UNIVERSITY OF BIRMINGHAM

Transition metal dichalcogenides: nanostructuring strategies and engineering for water electrolysis

by

Daniel Escalera López

A thesis submitted to the University of Birmingham for the degree of DOCTOR OF PHILOSOPHY

Centre for Hydrogen and Fuel Cell Research
School of Chemical Engineering
University of Birmingham
January 2019

Abstract

Transition metal dichalcogenides (TMDs) are a family of ubiquitous and inexpensive inorganic layered materials, with an ever-growing set of physicochemical properties. Namely, the edge site confined hydrogen evolution reaction (HER) electrocatalysis found in pristine TMDs is of high interest to replace the scarce precious metals currently employed in proton exchange membrane electrolysers. The core of this thesis is devoted to the maximization of the electrocatalytic activity of TMDs, here being MoS_2 and WS_2, towards the HER in acidic electrolytes by use of physical and electrochemical techniques. Activation of the electrochemically inert sulfur edge sites in MoS_2 was undertaken by preparation of Ni-MoS_2 hybrid nanoclusters using a dual-target magnetron sputtering and gas condensation technique. The HER enhancement observed is limited by the sulfur-deficient inherent nature of the size-selected MoS_2 nanoclusters, which hampers their crystallinity and electrochemical stability, amended here by a post-sulfidation treatment consisting of sulfur evaporation and annealing. Edge site exposure is alternatively explored for crystalline TMD flakes by fabrication of nanopillar/nanocone array structures, investigating their morphology-dependent mass transport properties and chalcogen-dependent HER catalysis. Insight on the pH-dependent HER activity and stability of electrodeposited amorphous molybdenum sulfide is thoroughly investigated, proposing the moieties responsible for the observed HER catalysis. Lastly, the potential of tungsten sulfide decoration to mitigate iridium corrosion under acidic oxygen evolution reaction conditions is evaluated.

Acknowledgements

I would firstly like to extend my most sincere gratitude to my supervisors Dr. Neil V. Rees and Prof. Richard E. Palmer for providing me with the opportunity to carry out my PhD and having trust in my capabilities. I would also like to thank Dr. Andrey Kaplan for taking over Prof. Palmer after his departure, and his support in the last year of my thesis. This work would not have been possible without the support from the EPSRC.

From Prof. Palmer I very much appreciate his drive to push my scientific abilities and rigour to become a better researcher. From Dr. Rees I strongly admire his patience, insight and unconditional support regarding experimental and personal difficulties I encountered during my PhD, all of this with a great sense of humour and humanity. I believe that during our meetings we learned a bit more about each other, particularly my somehow strange professorial writing style and our off-topic wanderings into science and other assorted topics, which I very much enjoyed.

I would also like to extend my gratitude to my dear colleagues that have collaborated with me in this work as a joint project, Yubiao Niu and Dr. Sung Jin Park, along with my master students Ross Griffin, Zhiheng Lou and Adam Elmi. Much of their efforts and assistance greatly benefited the results presented here, and made me learn a great deal about professional collaborations and academic supervision.

My short placement in Copenhagen would not have become a reality without the eager and welcoming attitude of Dr. María Escudero Escribano, who always faced any obstacles we encountered to make it happen with optimism and a smile. I deeply thank all the members of Dr. Escribano's group for their great help and support, making my stay very enjoyable: Alejandro, Anders, Bethan, Jonathan, Kaspar, Kim and Nikolai. Among them, I feel

particularly indebted to Jonathan and Kim for their extensive knowledge and know-how, and their willingness to share it with me.

And this leads me to my colleagues from the Centre for Doctoral Training in Fuel Cells and their Fuels. During my 4 years in the group I have met individuals from multiple countries, backgrounds and beliefs, which I believe they have all contributed to open my mind to new ways of seeing life and the world in itself: a very big family away from home. Our explorations of Selly Oak and Harborne local amenities (a.k.a. Friyays) and multiple informal chats in the office, mostly dealing with how happy/miserable our PhD lives were, will be engraved in my memory. To name a few, Bernardo, Carolina, Kun, Miguel, Sathish and Sophie are great people which I am very pleased to have met and shared multiple discussions and meals with. In particular, Miguel, my compatriot, has been for me like an older brother, greatly helping me to settle down in the group and helping each other's projects with our respective (and sometimes limited!) knowledge. Obviously my cohort mates Aimee, Laura, Lois and James have been extremely helpful and understanding when my Spanish mannerisms and temper kicked in, enabling me to adapt to these international times we live in. I should not leave out Hal (the boxer) Robbs, very supportive when I first started my lab experiments, and the CDT football/social gang (Abby, Abu, Alan, Liam, Melissa, Naser, Oliver, Oujen, Pete, Sam) for the great times shared outside the office walls.

This work not only encapsulates a series of professional efforts to actively contribute to the scientific community, but also a set of personal experiences which have inevitably made an impact on me. A journey of self-discovery, in which I have encountered people like Alberto, Alessandra, Alex, Chema, Christina, Enda, Flavia, Friederike, Giulia, Hassan, Hugo, Iván, Leo, Luca (two of them!), Ozzy, Pilar, Mar, Marlise, Ramón, Roberto and Víctor, among many others. We have shared extraordinary times together, and I believe that our friendship will last despite of the increasing distance that sets us apart due to our careers. One of my greatest

hobbies here has been playing football, and the Mexican team and their members (Adolfo, Alejandro, Coral, Emanuel, Frida, Gio, Jorge, José, Ricky, Saúl, Sandy, to name a few) have made me forget about my daily life worries, very much appreciated in such long journey like a PhD.

And lastly, but not less important, I would like to thank my family and friends home. Being far away from home to pursue my goals, it means a lot to me all their encouragement and kind words in the good and the bad times. I cannot express with enough words my gratitude to my parents: their unconditional love, support and anchor during these years has deeply touched me.

My last words go to the reader. I hope that you find here some knowledge which can help you in your endeavours in the fascinating world of electrochemistry.

List of Publications

[1] **Daniel Escalera-López**, Yubiao Niu, Jinlong Yin, Kevin Cooke, Neil V. Rees and Richard E. Palmer. *"Enhancement of the Hydrogen Evolution Reaction from Ni-MoS_2 Hybrid Nanoclusters"*. ACS Catalysis 6 (2016) 6008-6017.

[2] **Daniel Escalera-López**, Yubiao Niu, Sung Jin Park, Mark Isaacs, Karen Wilson, Richard E. Palmer and Neil V. Rees. *"Hydrogen evolution enhancement of ultra-low loading, size-selected molybdenum sulfide nanoclusters by sulfur enrichment"*. Applied Catalysis B: Environmental 235 (2018) 84-91.

[3] **Daniel Escalera-López**, Ross Griffin, Mark Isaacs, Karen Wilson, Richard E. Palmer and Neil V. Rees. *"MoS_2 and WS_2 nanocone arrays: Impact of surface topography on the hydrogen evolution electroatalytic activity and mass transport"*. Applied Materials Today 11 (2018) 70-81.

[4] **Daniel Escalera-López**, Ross Griffin, Mark Isaacs, Karen Wilson, Richard E. Palmer and Neil V. Rees. *"Electrochemical sulfidation of WS_2 nanoarrays: Strong dependence of hydrogen evolution activity on transition metal sulfide surface composition"*. Electrochemistry Communications 81 (2017) 106-111.

[5] **Daniel Escalera-López**, Zhiheng Lou and Neil V. Rees. *"Benchmarking the activity, stability and inherent electrochemistry of amorphous molybdenum sulfide for hydrogen production"*. Advanced Energy Materials 1 (2019) 1802614.

The content included in experimental chapters 5 to 9 is based upon the aforementioned publications. Contributions from other authors in the results presented are duly stated in Chapter 4 (Materials, equipment and methods).

Table of Contents

1. Introduction 1

1.1 Background of the research 1

1.2 Hydrogen production methods 4

1.2.1 Electrolytic-based methods 4

1.2.1.1 Alkaline electrolysers (AEs) 7

1.2.1.2 Proton exchange membrane (PEM) electrolysers 8

1.2.1.3 Solid oxide electrolysers (SOEs) 9

1.2.2 Prospects of hydrogen production 11

References 13

2. Literature review 16

2.1 Beyond critical metals: inorganic two-dimensional layered materials 16

2.2 Layered transition metal dichalcogenides: structural aspects 18

2.3 Hydrogen evolution reaction (HER): fundamentals and origin of TMD activity 20

2.4 Transition metal dichalcogenides: strategies for maximized edge site exposure 24

2.4.1 TMD edge site exposure maximization: top-down methods 24

2.4.2 TMD edge site exposure maximization: bottom-up methods 33

2.5 Transition metal dichalcogenides: strategies for maximizing the inherent electroactivity of the active sites 40

2.6 Group VI Transition metal dichalcogenides: strategies for activation of basal plane sites 44

2.7 Transition metal dichalcogenides and the oxygen evolution reaction: activity and stabilization of Ir-based state-of-the-art catalysts 49

References 52

3. Theoretical background 80

3.1 Electrochemical characterization 80

3.1.1 Fundamentals of electrochemistry 80

3.1.2 Reference electrodes (REs) 83

3.1.3 Electrochemical equilibrium: Nernst equation and its implications in RE operation 84

3.1.4 Counter electrode 86

3.1.5 Working electrode 87

3.1.6 Electrode kinetics: Butler-Volmer and the Tafel approximation 88

3.2 Electrochemical measurements 90
3.2.1 Mass transport limitations 91
3.2.2 Potential sweep methods 93
3.2.3 Criteria for electrochemical reversibility, and numerical elucidation of k^0_{app} 95
3.2.4 Electrode morphology-dependent mass transport properties 97
3.2.5 Electrochemical impedance spectroscopy 100
3.3 Physical characterization 104
3.3.1 Raman spectroscopy 104
3.3.2 X-ray photoelectron spectroscopy 107
3.3.3 Electron microscopy imaging 109
3.3.3.1 Scanning electron microscopy 109
3.3.3.2 Scanning transmission electron microscopy 110
3.4 Cluster beam deposition 113
References 118

4. Materials, equipment and methods 122
4.1 Working electrode preparation and modification 122
4.1.1 Glassy carbon electrode preparation 122
4.1.2 Glassy carbon working electrode assembly 122
4.2 Transition metal dichalcogenide nanoarray fabrication 123
4.3 Molybdenum sulfide nanoclusters fabrication 125
4.3.1 Nickel-molybdenum disulfide hybrid nanoclusters: dual-target magnetron sputtering deposition 125
4.3.2 Size-selected, sulfur-enriched molybdenum sulfide nanoclusters: single target magnetron sputtering deposition 127
4.4 Preparation of amorphous molybdenum sulfide thin films 128
4.5 Preparation of tungsten sulfide-decorated iridium electrodes 129
4.6 Equipment for electrochemical characterization 130
4.7 Chemicals and procedures for electrochemical characterization 132
4.7.1 Magnetron-sputtered molybdenum sulfide nanoclusters 132
4.7.1.1 Chemicals 132
4.7.1.2 Electrochemical characterization: nickel-molybdenum disulphide hybrid nanoclusters 133

4.7.1.3 Electrochemical characterization: size-selected, sulfur-enriched molybdenum sulfide nanocluster 133
4.7.2 Transition metal dichalcogenide nanoarrays 135
4.7.2.1 Chemicals 135
4.7.2.2 Electrochemical characterization procedures 136
4.7.3 Amorphous electrodeposited molybdenum sulfide 137
4.7.3.1 Chemicals 137
4.7.3.2 Electrochemical characterization procedures 138
4.7.4 Tungsten sulfide-decorated iridium electrodes 139
4.7.4.1 Chemicals 139
4.7.4.2 Electrochemical characterization procedures 139
4.8 Physical characterization 140
4.8.1 X-ray photoelectron spectroscopy (XPS) 140
4.8.2 Raman spectroscopy 141
4.8.3 Field emission gun scanning electron microscopy (FEG-SEM) 142
4.8.4 Aberration-corrected high-angle annular dark-field scanning transition electron microscopy (HAADF-STEM) 142
References 143

5. Ni-MoS_2 hybrid nanoclusters 144
5.1 Introduction 145
5.2 Results and discussion 146
5.2.1 Physical characterization of Ni, MoS_2 and Ni-MoS_2 hybrid nanoclusters: HAADF-STEM imaging 146
5.2.2 Physical characterization of Ni, MoS_2 and Ni-MoS_2 hybrid nanoclusters: XPS 153
5.2.3 Electrocatalytic activity to the hydrogen evolution reaction: influence of Ni incorporation 157
5.2.4 Electrochemical features of MoS_2 and Ni-MoS_2 hybrid nanoclusters: anodic stripping voltammetry (ASV) 163
5.3 Conclusions 170
References 172

6. Size-selected, sulfur-enriched molybdenum sulfide nanoclusters 176
6.1 Introduction 177
6.2 Results and discussion 178
6.2.1 Physical characterization of size-selected $(MoS_x)_{1000}$ nanoclusters: HAADF-STEM imaging and XPS 178

6.2.2 Electrocatalytic activity to the hydrogen evolution reaction: influence of sulfur enrichment 182
6.2.3 Evaluation of figures of merit and catalyst benchmarking 187
6.3 Conclusions 192
References 193
7. Plasma-etched MoS_2 and WS_2 crystals: implications of nanocone array profile in the mass transport and hydrogen evolution properties **197**
7.1 Introduction 198
7.2 Results and discussion 199
7.2.1 Fabrication and characterization of nanopillar arrays 199
7.2.2 Electrocatalytic activity for the hydrogen evolution reaction (HER) 206
7.2.3 Electron transfer properties of plama-etched TMDs 218
7.2.4 Analysis of 5-momth atmospherically aged samples 222
7.3 Conclusions 227
References 229
8. Atmospherically aged WS_2 nanocone arrays: study of electrochemical incorporation of sulfur **233**
8.1 Introduction 234
8.2 Results and discussion 235
8.2.1 Electrochemical sulfidation bath on MoS_2: voltammetric study 235
8.2.2 Electrochemical and physical monitoring of electrocatalytic and surface properties of sulfidated WS_2 nanoarrays 237
8.3 Conclusions 246
References 247
9. pH-dependent activity, stability and inherent electrochemistry of amorphous molybdenum sulfide for the hydrogen evolution **248**
9.1 Introduction 249
9.2 Results and discussion 250
9.2.1 Electrochemical growth of amorphous molybdenum sulfide 250
9.2.2 Anodically electrodeposited molybdenum sulfide (AE-MoS_x) inherent electrochemical activity: HER pre-catalytic peaks 253
9.2.3 AE-MoS_x inherent electrochemical activity: HER kinetics 260

9.2.4 AE-MoS_x inherent electrochemical activity: electro-oxidation 263
9.2.5 AE-MoS_x inherent electrochemical activity: electrochemical conditioning 272
9.2.5.1 AE-MoS_x electrochemical conditioning by oxidative-reductive and reductive cycling: EC, Raman and XPS analysis 274
9.2.5.2 AE-MoS_x electrochemical conditioning by electro-oxidative cycling: EC, Raman and XPS analysis 282
9.2.6 AE-MoS_x activity after electrochemical conditioning: descriptors for enhanced HER electrocatalysis 286
9.2.7 AE-MoS_x long-term HER performance: stability and accelerated durability testing 292
9.3 Conclusions 301
References 303
10. WS_{3-x} electrochemically-decorated iridium electrodes towards highly stable oxygen evolution electrocatalysts in acid 307
10.1 Introduction 308
10.2 Results and discussion 309
10.2.1 Electrochemical deposition of amorphous tungsten sulfide on iridium 309
10.2.1.1 Inherent electrochemistry of Ir substrate and $[WS_4]^{2-}$ precursor 309
10.2.1.2 Electrodeposition strategy and physical characterization of WS_{3-x} decorated Ir electrodes 315
10.2.2 Electrochemical testing of WS_{3-x} decorated Ir electrodes: oxygen evolution reaction (OER) 323
10.2.2.1 Short-term OER testing 323
10.2.2.2 Long-term OER testing 332
10.3 Conclusions 338
References 340
11. Conclusions and Outlook 344
11.1 Summary 344
11.2 Outlook and future work 351
Appendix
A. Non-electrolytic hydrogen production methods I
A.1 Hydrocarbon-based methods I

A.2 Biologically-based methods III
A.3 Alternative methods V
B. Layered transition metal dichalcogenides: optoelectronic properties VI
B.1 Electronic aspects of layered TMDs VI
B.2 Optical properties of layered TMDs IX
B.3 Other interesting properties and applications of layered TMDs XIV
C. Hybrid Ni-MoS_2 nanocluster composition calculation XVIII
D. Alternative XPS spectra peak devonvolution for Ni-MoS_2 and Ni nanoclusters XIX
E. Hydrogen turnover frequency (TOF) elucidation XX
E.1 Nickel-molybdenum disulfide hybrid nanoclusters XX
E.2 Size-selected, sulfur-enriched molybdenum sulfide nanoclusters XXIII
F. Hydrogen evolution reaction experiments: compilation of results XXVII
F.1 Nickel-molybdenum disulfide hybrid nanoclusters XXVII
F.2 Size-selected, sulfur-enriched molybdenum sulfide nanoclusters XXVIII
G. Electrochemical impedance spectroscopy of size-selected, sulfur enriched molybdenum sulfide nanoclusters: fitting parameters XXIX
H. Literature compilation and comparison of HER performance: state-of-the-art pure MoS_2 and MoS_2-based (hybrid/supported) catalysts XXX
I. Transition metal dichalcogenide nanoarrays XXXV
I.1 Elucidation of mass transport mechanism: peak current vs. square root of scan rate and transient chronoamperometry experiments XXXV
I.2 Elucidation of roughness factor by electrochemical capacitance measurements after solvent-phase electrochemical sulfidation XXXVII
J. AE-MoSx Raman mode values: compilation before/after electrochemical conditioning XXXIX
K. Tungsten sulfide-decorated iridium electrodes XLIII
K.1 Elucidation of OER normalized metrics: mass and specific activity XLIII
K.1.1 Mass activity calculation XLIII
K.1.2 Specific activity calculation XLIV
References XLIX

List of Figures

Figure 1.1. a) Time evolution of the global average surface temperature in the 1850-2017 period. b) Local warming observed in the 2006-2015 decade versus the average temperature in the pre-industrial period (1850-1900). Reproduced from ref. [1]. 2

Figure 1.2. a) Global primary energy consumption share in the 1965-2017 period, based on energy source (in %): oil (green), coal (black), natural gas (red), hydroelectricity (blue), nuclear energy (yellow) and renewable energy (orange). b) UK electricity generation share for the second quarter of 2018, based on energy source. Refs. [4] and [8]. 3

Figure 1.3. Pathways in the integrated energy system based on hydrogen produced from water electrolysis. Reproduced from ref. [19]. 6

Figure 1.4. Schematic of the operation principle of a) alkaline electrolyser cells (AECs), b) proton-exchange membrane electrolyser cells (PEMECs) and c) solid oxide electrolyser cells (SOECs). Reproduced from ref. [19].....7

Figure 2.1. Library of 2D layered materials formed by two compounds represented in the periodic table. Colour labelling: transition metal borides (orange), chalcogenides (blue), halides (green) and oxides (red). Elements coloured vertically act as anions, whereas elements coloured horizontally act as cations in the reported materials. MgB_2 (labelled with an asterisk) presents non-van der Waals interlayer interactions. Adapted from ref. [17]. 17

Figure 2.2. Schematic of the trigonal prismatic and octahedral (180° rotated trigonal prismatic) symmetry of the a) H and b) T phases found in TMDs. c) Crystallographic unit cells of the 1T, 2H and 3R TMD polytypes, along with their stacking sequence. Adapted from refs. [51,52].....19

Figure 2.3. a) "Volcano plot", here being experimental j_0 (in logarithmic scale) versus DFT-calculated $\Delta G_H{}^*$, for MoS_2 and metal electrocatalysts. b) Atomic ball model of a truncated MoS_2 hexagonal platelet ($Mo_{27}S_{54}$; Mo: blue, S: yellow) exposing the $(10\bar{1}0)$ Mo-edge and the $(\bar{1}010)$ S-edge. c) Alternative "volcano plot", here being experimental j_0 (in logarithmic scale) versus measured work function changes after hydrogen adsorption through a metal-water layer. Reproduced from refs. [68,74,75]. 23

Figure 2.4. a) Left to right: Schematic of the layer-dependent through-plane TMD electron transfer, HER polarization curves as a function of MoS_2 layer number and j_0 value dependence with layer number. b) TEM images obtained during in situ lateral sliding of a MoS_2 monolayer using a W probed dc biased at +10 V. c) Left: Centrifugation rate-dependent liquid exfoliated MoS_2 nanosheets dispersed in DMF. Right: Maximum length (blue), average length (black) and width (red) MoS_2 nanosheet size as a function of the centrifugation rate. d) Left: Surfactant-stabilized dispersions of multiple liquid exfoliated layered

TMDs and h-BN. Right: MoS_2 exfoliation yield dependence on sonication power, initial concentration (C_I) and sonication time (t_{sonic}). e) Room temperature ionic liquid exfoliated WS_2 nanodots, I) TEM imaged after 10000 rpm sequential centrifugation. II) Centrifugation rate-dependent (500-10000 rpm) HER catalysis after redispersion in DMF. III) HER polarization curves of 10000 rpm centrifuged fresh (black), 1 month aged (red) and 1 month aged after acetone washing (blue) WS_2 nanodots. Reproduced from refs. [85,90,92,94,95]. 26

Figure 2.5. a) Optical images and size distribution (inset) of n-BuLi exfoliated TaS_2 nanosheets. b) Coloured high-resolution TEM images showing the coexistence of the 2H (red), 1T (blue) and distorted 1T' (green) MoS_2 polymorphs after partial 2H→1T conversion upon 72h n-BuLi intercalation and exfoliation. c) HER polarization curves of chemically-exfoliated 1T (red) and 2H (blue, after annealing) MoS_2 monolayer nanosheets. d) HER performance of different exfoliated TMDs for a given intercalating agent (BuLi): $MoSe_2$ (blue), WS_2 (red) and WSe_2 (green). e) Alkali cation-dependent HER performance for alkali metal naphtanelide-exfoliated WS_2 nanosheets. f) Left: Illustration of the electronic affinity of phenyl ring-based functional groups covalently bound to exfoliated MoS_2 nanosheets. Right: Corresponding HER polarization curves obtained for the covalently-functionalized MoS_2 nanosheets. Reproduced from refs. [112,117,120,128,130,140]..... 30

Figure 2.6. a) Left: Illustration of the electrochemically-assisted lithiation method to exfoliate monolayer TMDs. Right: TEM image of electrochemically-assisted lithium exfoliated MoS_2 monolayer. b) Illustration of the electrochemically-assisted TMD exfoliation via volume-expanding generation of O_2 and SO_2 in a two-electrode cell submerged in Na_2SO_4 electrolyte. Inset: TEM image of exfoliated MoS_2 nanosheet. c) Top: Illustration of the self-limiting electro-ablation mechanism, yielding monolayer TMDs by in-situ H_2O_2 generation. Bottom: Anodic voltammogram of MoS_2, and the corresponding electro-oxidation feature in 1 M LiCl, and voltage-dependent (1.1-1.4 V held for 60 s) electro-ablation of MoS_2 multilayers. d) Top: Multilayered MoS_2 etching rate as a function of N_2/SF_6 plasma etching time. Bottom: Optical microscopy images of a ca. 90-layered MoS_2 flake before and after plasma etching. Reproduced from refs. [143,144,146,148,155]. 32

Figure 2.7. a) Top: Atmospheric-pressure CVD deposition setup based upon gas-phase TMD condensation on a substrate (here a vertical purple sheet), Bottom: Schematic of the edge-oriented MoS_2 platelets growth and SEM cross-section morphology analysis. b) CVD-grown MoS_2 deposition pattern obtained as function of the spatial location-induced MoO_3 concentration gradient in sections 1-6, and their corresponding SEM micrographs showing MoS_2 nanoplatelets shape evolution. c) Top: Shape evolution of MoS_2 nanoplatelets dependent on local chalcogen-to-metal vapour ratios, ranging from triangular to highly dendritic via star/branched triangular morphologies. Bottom: Morphology-dependent HER performance, and linear correlation between MoS_2 dendrite edge density and j_0. d) Top: Schematic of the spin coating-based thermal decomposition synthesis of $W_xMo_{(1-x)}S_2$ on reduced graphene

oxide (rGO). Bottom: HER and electrochemical impedance spectroscopy (EIS) of $W_xMo_{(1-x)}S_2$/rGO (blue) versus their MoS_2 (black) and WS_2 (red) analogues. Reproduced from refs. [160,171,177,191]. . 36

Figure 2.8. a) Left: Illustration of the stepped edge MoS_2 vertically-aligned array nanostructure (top), and high-resolution TEM and FE-SEM images showing their stepped nature and edge termination (bottom), Right: HER polarization curves obtained for stepped edge (red) versus flat edge (blue) and commercial (yellow) MoS_2 nanostructures. b-g) Compilation of TMD morphologies obtained by wet chemical synthesis: defect-rich nanosheets, in-plane edge-rich nanosheets, nanoflowers, hollow porous nanotubes, marigold-like nanoflowers and rhombic dodecahedra. Reproduced from refs. [193–197]. 37

Figure 2.9. a) Chemical structure of the edge-mimicking $(NH_4)_2[Mo_2S_{12}]$ cluster. b) Loading-dependent HER performance of the $[Mo_2S_{12}]^{2-}$ cluster catalyst. c) Chemical structure of the $[Mo_3S_{13}]^{2-}$ cluster (top and lateral perspective). d) Hydrogen TOF dependence on the XPS amorphous electrodeposited MoS_x content on high binding energy S_2^{2-} bridging and S^{2-} apical contents. Inset: HAADF-STEM image showing $[Mo_3S_{13}]^{2-}$ cluster-based structure on electrodeposited MoS_x. e) In operando Raman spectra recorded on amorphous electrodeposited MoS_x before (green) and during (blue) HER operation, showing H-S vibration band. Reproduced from refs. [198,199,205,207,208] 39

Figure 2.10. a) Plot of $\Delta G_H{}^*$ as a function of the TM-S edge binding energy ΔG_S. b) Left: TEM image of the vertically-aligned TM-doped MoS_2 nanosheets (lateral TM concentration profile on inset), Right: HER polarization curves before (black) and after Fe (red), Co (blue), Ni (cyan) or Cu (magenta) doping. c) Top: HER and EIS performance before (black) and after (red) multiwall CNTs functionalization of MoS_2 nanosheets, Bottom: Schematic and TEM image of MoS_2-multiwall CNTs composite. d) "Volcano plot" of hydrogen TOF per Mo atom as a function of support-dependent $[Mo_3S_{13}]^{2-}$ clusters $\Delta G_H{}^*$. e) Left: SEM micrograph of MoS_2-modified 3D nanoporous gold, Right: MoS_2 layer-dependent HER electrocatalysis of modified nanoporous gold substrate. Reproduced from refs. [218,232–235]. 42

Figure 2.11. a) Left: Aberration-corrected TEM image of MoS_2 with S vacancies (ca. 12 %), Right: HER performance before (blue) and after (red) tensile strain application (ca. 1.35 %). b) Left: Scanning tunnelling microscopy image showing O-incorporated atoms at S vacancy sites (dark triangles) of $MoS_{2-x}O_x$ crystals, Right: HER performance before (blue) and after (red) O-incorporation. c) Left: HAADF-STEM image of single Pt atom-doped MoS_2 nanosheets, Right: HER polarization curves before (magenta) and after (red) Pt doping, and d) Bottom: High-resolution TEM imaging of B-doped $MoSe_2$ nanosheets along with their EDX mapping, Top: HER cathodic voltammograms recorded before (green) and after (yellow) B incorporation. Reproduced from refs. [290,298,311,314]. 48

Figure 2.12. a) Schematic compiling the Ir electrodissolution pathways under OER operation: green and red arrows correspond to the dominating dissolution routes taking place at low and high OER overpotentials, respectively. Blue arrows show Ir intermediates and their associated reactions, observed

irrespective of the OER operation overpotential. b) Left: OER polarization curves of plasma-synthesized $W_{1-x}Ir_xO_{3-\delta}$ thin films. Right: OER stability testing by j_{geom} hold at +10 mA cm^{-2}, Electrolyte: 1 M H_2SO_4. c) Pourbaix diagrams (Potential vs. pH) of molybdenum-sulfur-oxygen-hydrogen (left) and tungsten-sulfur-oxygen-hydrogen systems (right). Reproduced from refs. [7,342,348]. 51

Figure 3.1. Two-electrode setup for the $Fe(CN)_6^{3-}/Fe(CN)_6^{4-}$ redox couple, and breakdown of the contributions of the measured potential $\Delta\phi_{total}$. 83

Figure 3.2. Simplified schematic of a three-electrode electrochemical setup. The illustrated cell operation corresponds to that used under potential-controlled hydrogen evolution testing conditions ($I_{WE} < 0$) with a glassy carbon displayed here as a WE. 91

Figure 3.3. Absolute voltage-time profiles of a) linear sweep voltammetry and b) cyclic voltammetry. c) Representative cyclic voltammogram obtained in a 5 mM $K_3[Fe(CN)_6]$ aqueous solution in a 3 mm glassy carbon working electrode. Scan rate: 25 mV s^{-1}..... 94

Figure 3.4. Schematic representation of the "diffusion domain approximation" for a microelectrode array, using diffusionally independent squared unit cells. Adapted from [12] 99

Figure 3.5. Schematic representation of the 4 diffusional regime cases found for microelectrode arrays, adapted from [16]..... 100

Figure 3.6. a) Illustration of the working principle of impedance spectroscopy. Graphical representation of AC signal and Nyquist plot features for ideal circuit elements as b) resistor, c) capacitor and d) inductor. Nyquist plot in d) plotted as Z'' vs. Z' for ease of representation. 102

Figure 3.7. a) Equivalent elements in the Randles circuit and b) Representative Nyquist plot obtained for a model Randles circuit..... 103

Figure 3.8. a) Molecular vibrations and corresponding vibration modes for single-layered (1L), bi-layered (2L) and bulk MX_2 materials: modes labelled with R are Raman-active, whilst those labelled IR are infrared-active; b) Layer-dependent relative frequency shift of in-plane E^1_{2g} and out-of-plane A_{1g} MoS_2 Raman modes; c) Raman spectra of monolayer 1T'-MoS_2 (black), monolayer 2H-MoS_2 (red), and bulk 2H-MoS_2 (black). Reproduced from refs. [20,22,23]..... 106

Figure 3.9. a) Schematic of the photoelectric effect employed as a basis for XPS measurements; b) Diagram of a conventional XPS instrument. Reproduced/adapted from refs. [32,36]. 108

Figure 3.10. Signals emitted after the interaction between the specimen and the electron beam, and their interaction volume (penetration depth). Reproduced from [41]. 110

Figure 3.11. a) JEOL 2100F aberration-corrected STEM used at the NPRL, and schematic of its key components; b) Schematic of the STEM imaging modes based on the beam collection angle θ; c)

Schematic of the working principle of Energy-dispersive X-ray spectroscopy: two electron from the L and K shell are ionised by the electron beam, where the generated vacancies are filled by electrons from the M and K shells, emitting Lα and Kα x-rays, respectively. Reproduced from refs. [44–46]..... 113

Figure 3.12. a) Schematic of the magnetron sputtering chamber: 1) magnetron target, 2) liquid nitrogen jacket, 3) cluster aggregation and nucleation region and 4) adjustable cluster beam nozzle; b) Schematic of the lateral Time-of-Flight mass filter chamber: 1,2) adjustable entrance/exit aperture slits, 3) Faraday cup array; 4,5 and 6) entrance, field-free drift and exit pulse region. Schematics adapted from ref. [57]. 114

Figure 3.13. Detailed schematic of the working principle utilized in the lateral Time-of-Flight mass filter. Adapted from ref. [60]..... 116

Figure 4.1. Custom-built silicon wafer vertical positioner employed for NS monolayer deposition. ... 124

Figure 4.2. Schematic of the dual-target magnetron sputtering and gas condensation cluster beam system (top view). It consists of four sections: magnetron sputtering, ion optics, lateral time-of-flight mass filter and cluster deposition. For all experiments described the mass filter is only used for cluster size monitoring, not for deposition. The clusters are instead deposited directly onto substrates in the chamber shown at the top of the figure..... 126

Figure 4.3. Cluster beam source schematic. It comprises five sections: magnetron sputtering and cluster formation, ion optics, Time-of-Flight mass filter, cluster deposition and cluster post-treatment. 127

Figure 4.4. Top: Diagram of the simplified transmission line circuit model employed for EIS fitting. Bottom: 3D schematic of the EIS equivalent circuit overlapped at a cross-section of the acidic electrolyte-(MoS_x) nanocluster-glassy carbon system..... 135

Figure 5.1. Compilation of mass spectra obtained by the time-of-flight mass filter during nanocluster deposition. From the spectra, MoS_2, Ni (8W) and Ni-MoS_2 (3W) show peak masses of around 4.8 x 10^4 amu ($(MoS_2)_{300}$), 1.3 x 10^5 amu ($\sim Ni_{2200}$) and 1.6 x 10^5 amu $\{(MoS_2)_{1000}\}$, respectively. The mass spectra of Ni (4W) is also plotted to show the effect of the power applied to this target..... 147

Figure 5.2. STEM images and size distribution in diameter based on the nanocluster surface area obtained by individual nanocluster counting at a given STEM image. MoS_2, Ni-MoS_2, and Ni (8W) have a peak value of 2.6 nm, 5.0 nm, and 4.2 nm respectively. Insets of STEM images are the FFT patterns of the corresponding clusters. 149

Figure 5.3. a) STEM image of hybrid Ni-MoS_2 hybrid nanocluster and b) example HAADF intensity line profile corresponding to the yellow region in a). The line profile shows step changes in nanocluster height, where layer numbers (0.65 nm theoretical interspacing) are labelled as a guide. c) STEM image of a side-on (perpendicularly oriented) MoS_2 nanocluster showing a layered structure..... 150

Figure 5.4. STEM image a) containing large and small nanoclusters used for EDX measurement. b)EDX mapping shows the composition of Ni-MoS_2 nanoclusters; Mo, S, and Ni are shown in green, blue, and red respectively. Signal in cyan comes from the overlap of Mo and S signals. Mo, S, and Ni signals are also shown separately in pannels c, d and e; where the nanocluster positions are marked by the yellow shapes. 152

Figure 5.5. High-resolution XPS spectra of Mo 3*d* (left) and S 2*p* (right) for fresh (top) and 14 h air exposed (bottom) for a) $(MoS_2)_{300}$ nanoclusters and b) $(Ni\text{-}MoS_2)_{1000}$ nanoclusters. Labels: raw spectra (solid black), cumulative peak fit (solid red), Mo^{4+} $3d_{5/2}$ (solid green), Mo^{4+} $3d_{3/2}$ (dashed green), Mo^{6+} $3d_{5/2}$ (solid orange), Mo^{6+} $3d_{3/2}$ (dashed orange), S $2p_{3/2}$ (solid yellow) and S $2p_{1/2}$ (dashed yellow). 154

Figure 5.6. High-resolution XPS spectra of Ni 2*p* fresh (top) and 14 h air exposed (bottom) Ni nanoclusters. Labels: raw spectra (solid black), cumulative peak fit (solid red), Ni^0 $2p_{3/2}$ peak deconvolution (solid blue), Ni^{2+} (NiO) $2p_{3/2}$ peak deconvolution (solid green) and Ni^{2+} $[Ni(OH)_2]$ $2p_{3/2}$ peak deconvolution (solid orange). 155

Figure 5.7. High-resolution XPS spectra of Ni 2*p* for fresh (top, solid magenta) and 14 h air exposed (bottom, solid orange) $(Ni\text{-}MoS_2)_{1000}$ nanoclusters. Dashed vertical line indicates peak position of metallic Ni (theoretical value: 852.7±0.4 eV).[10] 157

Figure 5.8. Linear sweep voltammograms recorded at 5 mm diameter glassy carbon (dashed black) samples modified with a) fresh $(MoS_2)_{300}$ (solid red), b) fresh $(Ni\text{-}MoS_2)_{1000}$ (solid magenta), c) Ni_{2200} (solid blue), d) 14-h air exposed $(MoS_2)_{300}$ (solid green), and e) 14-h air exposed $(Ni\text{-}MoS_2)_{1000}$ (solid orange) nanoclusters in the 0 to -1.2 V range vs. RHE. Scan rate: 25 mV s^{-1}. 161

Figure 5.9. Tafel plots (η vs. $\log|j_{geom}|$) of the Ni-doped/undoped MoS_2 nanoclusters evaluated in figure 6. Scan rate: 25 mV s^{-1}. 162

Figure 5.10. Anodic stripping voltammograms of 14-h air exposed a) $(MoS_2)_{300}$ nanoclusters (solid green) and b) $(Ni\text{-}MoS_2)_{1000}$ hybrid nanoclusters (solid orange) deposited on a 5 mm glassy carbon stub in the 0.4 to 1 V range vs. RHE. Scan rate: 50 mV s^{-1} 164

Figure 5.11. Peak deconvolution of the anodic stripping voltammogram (ASV) first scan of 14-h air exposed $(Ni\text{-}MoS_2)_{1000}$ hybrid nanoclusters deposited on a 5 mm glassy carbon stub in the 0.4 to 0.8 V range vs. RHE. Raw ASV (●) is deconvoluted in peaks I (solid blue), II (solid magenta), III (solid orange) and IV (solid green). Cumulative peak fit labelled in solid red. 169

Figure 6.1. Low magnification STEM images of size-selected $(MoS_x)_{1000}$ nanoclusters a) as-deposited and b) after sulfur evaporation and annealing. High magnification images for c) as-deposited and d) sulfur-evaporated and annealed $(MoS_x)_{1000}$ nanoclusters shown to compare modifications in crystallinity (FFT patterns of corresponding clusters shown in inset). Size distribution of non-overlapped independent

nanocluster counting on e) as-deposited and f) sulfur-evaporated and annealed $(MoS_x)_{1000}$ nanoclusters included for ease of comparison. 179

Figure 6.2. High magnification STEM images of size-selected $(MoS_x)_{1000}$ nanoclusters after sulfur evaporation and annealing showing a) Moiré patterns due to layer misorientation and b) layered structure when depositing in a side-on arrangement. c,d) HAADF intensity profile analysis of a,b) showing the 3-4 layered structure and corresponding interlayer spacing. 180

Figure 6.3. High-resolution Mo 3*d* (top) and S 2*p* (bottom) XPS spectra of a) as-deposited $(MoS_x)_{1000}$ nanoclusters, b) sulfurised, non-annealed $(MoS_x)_{1000}$ nanoclusters and c) sulfurised, annealed $(MoS_x)_{1000}$ nanoclusters. Labels: raw spectra (black), cumulative peak fit (red), Mo^{4+} $3d_{5/2:3/2}$ (green), $Mo^aO_bS_c$ $3d_{5/2:3/2}$ (blue), Mo^{6+} $3d_{5/2:3/2}$ (orange), S $2p_{3/2:1/2}$ (S^{2-}, yellow) and S $2p_{3/2:1/2}$ (S_2^{2-}, magenta). The faint peak at ca. 160 eV in the S 2*p* spectra corresponds to a background subtraction artifact. 182

Figure 6.4. a,b) Linear sweep voltammograms recorded at 5 mm diameter mirror-polished glassy carbon samples (black) modified with as-deposited $(MoS_x)_{1000}$ nanoclusters (blue) and sulfurised, annealed $(MoS_x)_{1000}$ nanoclusters (gold) at surface coverages of 5% (a) and 20% (b). Red arrows denote overpotential shift due to sulfurisation at $|j_{half\ max}|$. Scan rate: 50 mV s^{-1}. 184

Figure 6.5. a) Tafel plots (η vs. $\log|j_{geom}|$) of the different $(MoS_x)_{1000}$ nanoclusters plotted in Figure 6.4. Scan rate: 50 mV s^{-1}. b) Electrochemical impedance spectroscopy Nyquist spectra of samples in Figure 6.4 recorded at $\eta^{\sim}$ 700 mV vs. RHE. Labels in c,d): mirror-polished glassy carbon (black), as-deposited $(MoS_x)_{1000}$ nanoclusters at 5% (red) and 20% (purple) coverage, and sulfurised and annealed $(MoS_x)_{1000}$ nanoclusters at 5% (green) and 20% (blue) coverage. Asymmetric plotting of EIS spectra done for ease of interpretation of results. 186

Figure 6.6. a) Linear sweep voltammograms recorded at 5 mm diameter mirror-polished glassy carbon samples modified with 20% projected surface coverage as-deposited $(MoS_x)_{1000}$ nanoclusters (black), $(Ni\text{-}MoS_2)_{1000}$ hybrid nanoclusters (green) and sulfurised, annealed $(MoS_x)_{1000}$ nanoclusters (red). Blue arrow denotes overpotential shift at $|j_{half\ max}|$. b) Linear sweep voltammograms recorded at 5 mm diameter mirror-polished glassy carbon samples modified with sulfurised, annealed $(MoS_x)_{1000}$ nanoclusters at different projected surface area coverages: 5% (black), 10% (red) and 20% (blue). Scan rate: 50 mV s^{-1}. 188

Figure 6.7. Evaluation of short-term stability of $(MoS_x)_{1000}$ nanoclusters by comparison of the first (light blue) and eleventh (gold, as in Fig. 6.4) linear sweep voltammograms recorded at 5 mm diameter mirror-polished glassy carbon samples modified with a) as-deposited and b) sulfurised, annealed $(MoS_x)_{1000}$ nanoclusters with 20% projected surface coverage. Red arrow denotes overpotential shift at $|j_{half\ max}|$. Scan rate: 50 mV s^{-1}. 190

Figure 7.1. FE-SEM micrographs of 200 nm polystyrene-latex NS deposition on a) MoS_2 and b) WS_2 crystals..... 199

Figure 7.2. FE-SEM micrographs of SF_6/C_4F_8 plasma-etched MoS_2 crystals for a) 15 ± 1 s (45° tilt angle), b) 32 ± 1 s (80° tilt angle), c) 45 ± 1 s (85° tilt angle) and d) 60 ± 1 s (45° tilt angle) and SF_6/C_4F_8 plasma-etched WS_2 crystals for e) 16 ± 1 s, f) 31 ± 1 s, g) 46 ± 1 s and h) 61 ± 1 s (all imaged at 45° tilt angle). Image distortion in e) and f) is attributed to SEM distortions: such areas are not considered during nanopattern characterization. 202

Figure 7.3. High-resolution XPS spectra of W 4*f* (left) and S 2*p* (right) regions for SF_6/C_4F_8 plasma-etched WS_2 crystals: as-received (first row), 16 ± 1 s (second row), 31 ± 1 s (*R*= 2, *Z*= 6.4, third row), 31 ± 1 s (*R*= 1.4, *Z*= 5.1, fourth row) and 61 ± 1 s (fifth row). Labels: W^{4+} $4f_{7/2:5/2}$ WS_2 2H phase (green), W^{4+} $4f_{7/2:5/2}$ WS_2 1T phase (magenta), W^{4+} $4f_{7/2:5/2}$ from WO_2 (light blue), W 5*p* (orange), S $2p_{3/2:1/2}$ from S^{2-}(yellow) and S 2*p* from SO_x^{y-} (dark blue)..... 205

Figure 7.4. Linear sweep voltammograms of SF_6/C_4F_8 plasma-etched a) MoS_2 and b) WS_2 crystals in the 0 to -1.2 V voltage range vs. RHE. Dashed line (orange) indicates $|j_{geom}|$= 0.05 mA cm^{-2} (see text). Voltage scan rate: 50 mV s^{-1}. 207

Figure 7.5. Comparison of HER performance of a) 15 ± 1 s, b) 30 ± 1 s and c) 60 ± 1 s SF_6/C_4F_8 plasma-etched MoS_2 (solid black) and WS_2 (solid red) crystals in the 0 to -1.2 V voltage range vs. RHE. Scan rate: 50 mV s^{-1}. 209

Figure 7.6. Geometric peak current density $|j_P|$ vs. square root of the scan rate $\nu_{scan}^{1/2}$ plots for HER experimental (black) and theoretical values predicted by the irreversible Randles-Ševčík equation (blue) for a) 15 ± 1 s, c) 32 ± 1 s and e) 38 ± 1 s plasma-etched MoS_2 crystals; HER experimental (red=E_P + 50 mV; green= E_P + 100 mV) and theoretical irreversible Randles-Ševčík Case 4 (black) log-log plots of transient dimensionless current densities j/A_{domain} vs. dimensionless time τ for b) 15 ± 1 s and d) 32 ± 1 s plasma-etched MoS_2 crystal. 210

Figure 7.7. Plasma-etched WS_2 crystals geometric peak current density j_P vs. square root of the scan rate $\nu_{scan}^{1/2}$ plots for HER experimental (black) and theoretical values predicted by the irreversible Randles-Ševčík equation (blue). Etching conditions: a) 16 ± 1 s, b) 31 ± 1 s (*R*= 2, *Z*= 6.4), c) 31 ± 1 s (*R*= 1.4, *Z*= 5.1) and d) 61 ± 1 s..... 213

Figure 7.8. a) 31 ± 1 s (*R*= 2, *Z*= 6.4), b) 16 ± 1 s and c) 31 ± 1 s (*R*= 1.4, *Z*= 5.1) plasma-etched WS_2 crystal HER experimental (red=E_P + 50 mV; green= E_P + 100 mV) and theoretical (black, irreversible Randles-Ševčík Case 4; red, irreversible Randles-Ševčík Case 1) log-log plots of transient dimensionless current densities j/A_{domain} vs. dimensionless time τ..... 215

Figure 7.9. Tafel plots (η vs. $\log|j_{geom}|$) of a) MoS_2 and b) WS_2 SF_6/C_4F_8 freshly plasma-etched crystals. Voltage scan rate: 50 mV s^{-1}. 218

Figure 7.10. a) Peak to peak separations of the ferro/ferricyanide redox probe for plasma-etched MoS_2 (blue) and WS_2 (red) samples at υ_{scan}= 100m Vs^{-1}, b) Heterogeneous electron transfer rate constants k_{app}^{O} calculation for plasma-etched MoS_2 (purple) and WS_2 (green) samples obtained from the ψ vs. $\left[\left(\frac{\pi zFD\upsilon_{scan}}{RT}\right)\right]^{-1/2}$ plot slope (Inset: zoom of 9b for a $k_{app}^{O} \times 10^{-5}$ cms^{-1} scale bar to highlight MoS_2 values), and c) Calculated k_{app}^{O} values obtained by the Klinger and Kochi method for υ_{scan}= 100 mV s^{-1}. 219

Figure 7.11. Calculated values of k_{app}^{O} for the $[Fe(CN)_6]^{4-}/[Fe(CN)_6]^{3-}$ redox probe of fresh plasma-etched a) MoS_2 and b) WS_2 crystals (ψ vs. $\left[\left(\frac{\pi zFD\upsilon_{scan}}{RT}\right)\right]^{-1/2}$ plot, υ_{scan}= 100 mV s^{-1}), vs. the experimental nanopillar height obtained from tilt-angle corrected SEM micrographs..... 220

Figure 7.12. a) Linear sweep voltammograms in the 0 to -1.2 V voltage range vs. RHE and b) Tafel plots (η vs. $\log|j_{geom}|$) for WS_2 atmospherically-aged SF_6/C_4F_8 plasma-etched crystals. Dashed line (orange) indicates $|j_{geom}|$ = 0.05 mA cm^{-2} (see text). Voltage scan rate: 50 mV s^{-1}. 223

Figure 7.13. Comparison of HER performance of a) 16 ± 1 s, b) 31 ± 1 s (R= 2, Z= 6.4), c) 31 ± 1 s (R= 1.4, Z= 5.1) and d) 61 ± 1 s SF_6/C_4F_8 plasma-etched fresh (solid black) and 5-month aged (solid red) WS_2 crystals in the 0 to -1.2 V voltage range vs. RHE in 2 mM $HClO_4$/0.1M $NaClO_4$. Voltage scan rate: 50 mV s^{-1}. 224

Figure 7.14. FE-SEM micrographs of a) 16 ± 1 s, b) 31 ± 1 s (R= 2, Z= 6.4), c) 31 ± 1 s (R= 1.4, Z= 5.1) and d) 61 ± 1 s SF_6/C_4F_8 plasma-etched WS_2 crystals after 5 month atmospherical ageing and electrochemical testing. Tilt angle: 45°..... 225

Figure 8.1. Representative I-E curve obtained from the solvent-phase sulfidation method in a plasma-etched WS_2 crystal. Electrolyte: 10 mM $Na_2S_2O_3$, 0.1 M Na_2SO_4 and 1 mM H_2SO_4. The electrochemical window was selected based on the optimized conditions stated in ref. [1]. Scan rate: 25 mV s^{-1}, scanning direction indicated by arrow..... 236

Figure 8.2. Left column: Linear sweep voltammograms in the 0 to -1.2V voltage range of a) 31±1 s (R= 2, Z=6.4) and b) 61±1 s atmospherically aged, sulfidation treated plasma-etched WS_2 samples over a three week ambient exposure period. Right column: Tafel plots (η vs. $\log|j_{geom}|$) of c) 31±1 s (R= 2, Z=6.4) and d) 61±1 s atmospherically aged, sulfidation treated plasma-etched WS_2 samples over a three week ambient exposure period. Labels: pre-sulfidated (black), post-sulfidated (red), 8-day atmosphere exposed (green), 15-day atmosphere exposed (blue) and 22-day atmosphere exposed (magenta). Scan rate: 25 mV s^{-1}. 238

Figure 8.3. Comparison of: a-b) roughness-factor corrected HER peak current densities at υ_{scan}= 25mV s^{-1}, c-d) WO_2 surface content (left axis) and S^{2-}:W^{4+} XPS atomic photoemission ratios (right axis), and e-f) k^{O}_{app} values for the $[Fe(CN)_6]^{4-}$/$[Fe(CN)_6]^{3-}$ redox probe, for atmospherically aged, sulfidation treated plasma-etched WS_2 samples 31±1 s (R=2, Z=6.4, left column) and 61±1 s (right column), after weekly electrochemical testing over a three-week ambient exposure period. 240

Figure 8.4. Stacked high-resolution XPS spectra of W 4*f* and S 2*p* for a-b) 31 ± 1 s (R= 2, Z= 6.4) and c-d) 61 ± 1 s atmospherically aged, sulfidation treated, plasma-etched WS_2 samples over a three-week ambient exposure period. e-f) Comparison of total S:W XPS atomic photoemission ratios. 242

Figure 8.5. FE-SEM micrographs of a,c) 31 ± 1 s (R= 2, Z= 6.4) and b,d) 61 ± 1 s SF_6/C_4F_8 plasma-etched WS_2 crystals atmospherically aged plasma-etched WS_2 samples before (first row) and after solution-phase sulfidation (second row). Tilt angle: 45°. 244

Figure 9.1. a) Representative voltammograms obtained during the electrochemical deposition of MoS_x onto 0.25 cm^2 Si/Ti/Au electrodes by continuous voltage cycling from +0.1 V to -1 V vs. Ag/AgCl in 2mM $(NH_4)_2[MoS_4]$, 0.1 M $NaClO_4$. b) Representative first (black) and 25th (magenta) voltammograms obtained by continuous cycling within the +0.1 V to -1 V vs. Ag/AgCl electrochemical window for Si/Ti/Au electrodes in 0.1 M $NaClO_4$ (dashed lines) and 2mM $(NH_4)_2[MoS_4]$, 0.1 M $NaClO_4$ (solid lines) electrolytes. Scan rate: 50 mV s^{-1}. 251

Figure 9.2. Plotting of the experimental thickness of a) anodically electrodeposited molybdenum sulfide (AE-MoS_x, E= +0.1 V vs. Ag/AgCl) and b) cathodically electrodeposited molybdenum sulfide (CE-MoS_x, E= -1 V vs. Ag/AgCl) thin films grown Si/Ti/Au electrodes by potentiostatic electrodeposition as a function of the total charge density $< \sigma_q >$ passed. Error bars account for no less than three independent thickness measurements by surface profilometry. Electrolyte: 2mM $(NH_4)_2[MoS_4]$, 0.1 M $NaClO_4$. 252

Figure 9.3. Schematic of the coordination polymer structure of AE-MoS_x based on the $[Mo_3S_{13}]^{2-}$ cluster unit. Sulfur ligand types labelled as follows: apical S^{2-} (S^{2-}_{apical}), blue; bridging S_2^{2-} ($S_2^{2-}_{bridging}$), black; terminal S_2^{2-} ($S_2^{2-}_{terminal}$), red; unsaturated S^{2-} (S^{2-}_{unsat}), green. S-deficient Mo-sites (AE-MoS_x structural defects, referred as $Mo^{5+}O_xS_y$) represented by Mo^{5+}=O groups. 253

Figure 9.4. a) Linear sweep voltammograms recorded for pristine AE-MoS_x films (100 nm thick, catalyst loading ≈1.7 × 10^{-7} mol Mo cm^{-2} assuming 100% faradaic efficiency) across the 0-10 pH range by use of different buffered electrolyte solutions. b) Plotting of peak potential of the observed pre-catalytic redox features as a function of the buffered electrolyte pH. Scan rate: 50 mV s^{-1}. 255

Figure 9.5. Cathodic linear sweep voltammograms recorded after continuous cycling from 0.15 to -0.425 V vs. SCE of pristine AE-MoS_x films in 0.5 M H_2SO_4. Inset: zoom of the LSVs at the HER pre-catalytic peak region. Scan rate: 50 mV s^{-1}. 256

Figure 9.6. Representative linear sweep voltammograms recorded for pristine AE-MoS_x films (deep red) and bare Si/Ti/Au electrodes (dark yellow) across the 0-10 pH range by use of different buffered electrolyte solutions. Scan rate: 50 mV s^{-1}..... 257

Figure 9.7. High-resolution a) Mo 3*d* and b) S 2*p* XPS spectra of pristine AE-MoS_x thin films. Labels: raw spectra (black), cumulative peak fit (red), Mo^{4+} $3d_{5/2:3/2}$ (green), $Mo^aO_bS_c$ $3d_{5/2:3/2}$ (blue), Mo^{6+} $3d_{5/2:3/2}$ (orange), S $2p_{3/2:1/2}$ (S^{2-}, yellow), S $2p_{3/2:1/2}$ (S_2^{2-}, magenta) and S $2p_{3/2:1/2}$ (SO_x^{y-}, light blue). 258

Figure 9.8. a) Tafel plots (η vs. $\log|j_{geom}|$) for Si/Ti/Au (yellow), pristine AE-MoS_x (red) and AE-MoS_x under 1500 rpm stirring (green) across the 0-10 pH range. b) *iR* and Nersnstian-corrected HER linear sweep voltammograms recorded for AE-MoS_x under 1500 rpm electrolyte stirring. Scan rate: 50 mV s^{-1}. 260

Figure 9.9. a) Anodic stripping voltammogram of freshly-deposited AE-MoS_x films recorded from 0 to 1.2 V vs. SCE in 0.5 M H_2SO_4, b) Plot of AE-MoS_x electro-oxidation peak potential versus buffered electrolyte pH showing a gradient of -27 mV dec^{-1}. Scan rate: 50 mV s^{-1}..... 264

Figure 9.10. Representative anodic stripping voltammograms recorded for pristine AE-MoS_x films (deep red) and bare Si/Ti/Au electrodes (dark yellow) across the 0-10 pH range by use of different buffered electrolyte solutions. Voltage range: 0 to 1.5 V vs. SCE. Scan rate: 50 mV s^{-1}. 265

Figure 9.11. Anodic stripping voltammograms recorded for pristine AE-MoS_x films (deep red) and bare Si/Ti/Au electrodes (dark yellow) betweem the 3-5 pH range. Voltage range: 0 to 1.5 V vs. SCE. Scan rate: 50 mV s^{-1}..... 266

Figure 9.12. Stacked Raman spectra (532 nm laser excitation, 100-800 cm^{-1} range, intensity-normalized) of pristine (black) and electro-oxidized AE-MoS_x thin films across the 0-10 pH range. Dashed vertical lines refer to characteristic AE-MoS_x vibration modes, whilst asterisk labelling (*) identifies Raman modes ascribed to underlying Si substrate. 268

Figure 9.13. Cyclic voltammogram recorded for pristine AE-MoS_x films from 0.7 V to -1.2 V vs. SCE in a phosphate buffered electrolyte (pH≈7). Scan rate: 50 mV s^{-1}..... 269

Figure 9.14. a) Compilation of reverse scans obtained for post-LSV AE-MoS_x films (from -1.2 V to 0.7 V vs. SCE) across the 0-10 pH range Scan rate: 50 mV s^{-1}. Peak potential dependence of post-LSV AE-MoS_x electro-oxidative features labelled as b) $E_{peak,I}$ (blue) and c) $E_{peak,II}$ (magenta) as a function of the buffered electrolyte pH. Overlapped linear fits and experimental E-pH slopes displayed for ease of comparison. 270

Figure 9.15. Representative voltammograms obtained for post-LSV AE-MoS_x films during the evaluation of the electrochemical conditioning treatments: a) electro-oxidative, b) reductive, c) oxidative-

reductive (anodic potential vertex past $E_{peak,II}$) and d) oxidative-reductive (anodic potential vertex past $E_{peak,I}$). Electrolyte: pH 7 phosphate buffer saline. Scan rate: 50 mV s^{-1}. 273

Figure 9.16. Representative voltammograms obtained for post-LSV AE-MoS_x films during the oxidative-reductive electrochemical conditioning treatments (anodic potential vertex past $E_{peak,II}$). Scan rate: 50 mV s^{-1}. 275

Figure 9.17. Representative voltammograms obtained for post-LSV AE-MoS_x films during the reductive electrochemical conditioning treatments (cathodic potential vertex past $E_{peak,1}$). Scan rate: 50 mV s^{-1}. 276

Figure 9.18. a) Compilation of the 50th cathodic scans recorded during the oxidative-reductive electrochemical conditioning on pristine AE-MoS_x films across the 0-10 pH range, b) Representative voltammograms obtained for AE-MoS_x films during oxidative-reductive electrochemical conditioning in a pH 6 buffered electrolyte, c) Peak potential dependence of post-LSV AE-MoS_x HER pre-catalytic features $E_{peak,III}$ (●, * in Fig. 9a) and $E_{peak,IV}$ (▲, # in Fig. 9a) as a function of the buffered electrolyte pH. Scan rate: 50 mV s^{-1}. 277

Figure 9.19. Stacked Raman spectra (532 nm laser excitation, 100-800 cm^{-1} range, intensity-normalized) of pristine (black), and AE-MoS_x thin films electrochemically conditioned by a) oxidative-reductive cycling and b) reductive cycling across the 0-10 pH range. Dashed vertical lines refer to characteristic AE-MoS_x vibration modes. 281

Figure 9.20. Stacked Raman spectra (532 nm laser excitation, 100-800 cm^{-1} range, intensity-normalized) of pristine (black), and AE-MoS_x thin films electrochemically conditioned by electro-oxidative cycling across the 0-10 pH range. Dashed vertical lines refer to characteristic AE-MoS_x vibration modes..... 284

Figure 9.21. Representative voltammograms obtained for AE-MoS_x films before (red) and after (green) undergoing reductive electrochemical conditioning at in a) pH 0 (0.5 M H_2SO_4), b) pH=3 (82/18 v/v mixture of 0.1 M citric acid/0.1 M sodium citrate), c) pH=6 (11.5/88.5 v/v mixture of 0.1 M citric acid/0.1 M sodium citrate) and d) pH=9 (14.4/85.6 v/v mixture of 0.1 M HCl /0.05 M sodium tetraborate). Scan rate: 50 mV s^{-1}. 287

Figure 9.22. Summary of $\eta_{HER}@\,|2.5\ mA\ cm^{-2}|$as a function several AE-MoS_x descriptors across the 0-10 pH range after electro-oxidative AE-MoS_x conditioning: a) "high binding energy" $S_2^{2-}{}_{bridging}/S^{2-}{}_{apical}$ content, b) Mo^{4+} content, c) S^{2-}/S_2^{2-} : Mo^{4+} ratio, and d) total S : Mo ratio. At. % units correspond to relative XPS percentages within the Mo 3*d* and S 2*p* deconvoluted components. 288

Figure 9.23. Summary of $\eta_{HER}@\,|2.5\ mA\ cm^{-2}|$as a function several AE-MoS_x descriptors across the 0-10 pH range after oxidative-reductive AE-MoS_x conditioning: a) "high binding energy" $S_2^{2-}{}_{bridging}/S^{2-}{}_{apical}$ content, b) Mo^{4+} content, c) S^{2-}/S_2^{2-} : Mo^{4+} ratio, and d) total S : Mo ratio. At. % units correspond to relative XPS percentages within the Mo 3*d* and S 2*p* deconvoluted components. 290

Figure 9.24. Summary of $\eta_{HER}@|2.5\ mA\ cm^{-2}|$ as a function several AE-MoS_x descriptors across the 0-10 pH range after reductive AE-MoS_x conditioning: a) "high binding energy" $S_2^{2-}{}_{bridging}/S^{2-}{}_{apical}$ content, b) Mo^{4+} content, c) S^{2-}/S_2^{2-} : Mo^{4+} ratio, and d) total S : Mo ratio. At. % units correspond to relative XPS percentages within the Mo 3*d* and S 2*p* deconvoluted components. 291

Figure 9.25. a) Representative chronopotentiograms recorded during AE-MoS_x HER stability measurements (12 h galvanostatic electrolysis at j_{geom}= -10 mA cm^{-2}), b) Averaged (±10 min) initial (green) and final (red) overpotentials to sustain j_{geom}= -10 mA cm^{-2} for 12 h, c) Initial (blue) and final (orange) HER $\eta_{HER}@|5\ mA\ cm^{-2}|$obtained during accelerated durability testing on AE-MoS_x (3000 CVs, 100 mV s^{-1}). Values with * indicate approximate overpotentials due to experimental currents not achieving -5 mA cm^{-2} at the evaluated voltage window. d) Summary of $\eta_{HER}@|5\ mA\ cm^{-2}|$as a function $Mo^{5+}O_xS_y$ relative XPS content across the 0-10 pH range after accelerated durability testing. 293

Figure 9.26. Representative voltammograms obtained for AE-MoS_x films during accelerated durability potentiodynamic testing (3000 CVs, 100 mV s^{-1}). 295

Figure 9.27. Stacked Raman spectra (532 nm laser excitation, 100-1200 cm^{-1} range, intensity-normalized) of pristine (black), and AE-MoS_x thin films after accelerated durability testing (3000 CVs, 100 mV s^{-1}) across the 0-10 pH range. Dashed vertical lines refer to characteristic AE-MoS_x vibration modes. Raman features marked with an asterisk originated from a cosmic ray. 297

Figure 9.28. Summary of $\eta_{HER}@|5\ mA\ cm^{-2}|$as a function several AE-MoS_x descriptors across the 0-10 pH range after accelerated durability testing on AE-MoS_x(3000 CVs, 100 mV s^{-1}): a) "high binding energy" $S_2^{2-}{}_{bridging}/S^{2-}{}_{apical}$ content, b) Mo^{4+} content, c) S^{2-}/S_2^{2-} : Mo^{4+} ratio, and d) total S : Mo ratio. At. % units correspond to relative XPS percentages within the Mo 3*d* and S 2*p* deconvoluted components. 298

Figure 10.1 Representative voltammograms obtained on 0.25 cm^2 Si/Cr/Ir electrodes by continuous voltage cycling from 0 V to +2.5 V vs. RHE in a) 10 mM $(NH_4)_2[WS_4]$, 0.1 M $NaClO_4$ and b) 0.1 M $NaClO_4$ electrolytes; c) is analogous to a) using a voltage cycling window from -0.4 to +2.1 V vs. RHE (starting potential: +0.4 V). Scan rate: 50 mV s^{-1}. 310

Figure 10.2. High-resolution XPS spectra of a) W 4*f*, b) S 2*p* and c) Ir 4*f*. Labels: W^{4+} $4f_{7/2:5/2}$ (green), S $2p_{3/2:1/2}$ (SO_x^{y-}, yellow), Ir^0 $4f_{7/2:5/2}$ (blue). 312

Figure 10.3. Representative a) first and b) 15th (dark yellow) voltammograms obtained by continuous cycling within the 0 V to +2.5 V vs. RHE electrochemical window for 0.25 cm^2 Si/Cr/Ir electrodes in 0.1 M $NaClO_4$ (black) and 10 mM $(NH_4)_2[WS_4]$, 0.1 M $NaClO_4$ (dark yellow) electrolytes. Insets: zoom of the first and 15th voltammograms in the +0.4 to +1.80 V vs. RHE window. Scan rate: 50 mV s^{-1}. 313

Figure 10.4. Representative voltammograms obtained on 0.25 cm^2 Si/Cr/Ir electrodes by continuous voltage cycling in a 10 mM $(NH_4)_2[WS_4]$, 0.1 M $NaClO_4$ aqueous electrolyte in the voltage windows a) 0 to +1.6 V and b) 0.4 to +2.2 V vs. RHE (starting potential: +0.4 V). Scan rate: 50 mV s^{-1}. 315

Figure 10.5. a) j_{geom} – t profile obtained during use of pulse reverse potential electrodeposition procedure (+1.8 V, 500 ms; -0.2 V, 1000 ms) and b) E – t profiles obtained during use of pulse reverse current electrodeposition procedure (1000 ms on/off pulses) with current magnitudes of ±500 µA (blue), ±700 µA (green) and ±900 µA (red) on 0.25 cm^2 Si/Cr/Ir electrodes. 317

Figure 10.6. FE-SEM micrographs of as-received Si/Cr/Ir electrodes at a) 10000x, b) 25000x, c) 50000x and d) 100000x magnification..... 319

Figure 10.7. FE-SEM micrographs of Si/Cr/Ir electrodes after undergoing ±500-900 µA (pulse duration: 1000 ms), pulse reverse current electrodeposition experiments for a) 10 mins, b) 5 mins, c) 2.5 mins and d) 1 min. Micrographs image magnification: 50000x. 320

Figure 10.8. FE-SEM micrographs of Si/Cr/Ir electrodes after undergoing ±500 and 900 µA pulse reverse current electrodeposition experiments for 10 mins using a) 1000 ms, b) 250 ms and c) 62.5 ms current pulses. Micrographs image magnification: 50000x. 321

Figure 10.9. FE-SEM micrographs of Si/Cr/Ir electrodes after undergoing ±500 µA, 1000 ms pulse reverse current electrodeposition experiments for a) 10 mins, b) 5 mins, c) 2.5 mins and d) 1 min. Micrographs image magnification: 10000x (left), 25000x (middle) and 50000x (right). 322

Figure 10.10. Chronopotentiograms recorded for Si/Cr/Ir electrodes before and after undergoing ±500-900 µA pulse reverse current electrodeposition experiments, to sustain j_{geom}= +10 mA cm^{-2} for 2 h. Labels (total electrodeposition time): 10 mins (red), 5 mins (green), 2.5 mins (blue) and 1 min (orange). 324

Figure 10.11. Cyclic voltammograms recorded at pristine (black) and WS_{3-x} decorated (±500 µA, 1000 ms, 5 mins; dark yellow) Si/Cr/Ir electrodes a) before (broken line) and after (solid line) undergoing short-duty OER stability experiments: j_{geom}= +10 mA cm^{-2} sustained for 2 h; b) first OER voltammograms recorded for pristine and WS_{3-x} decorated (±700 µA, 250 ms, 10 mins). Voltage window: +1.0 to +1.6 V vs. RHE. Electrolyte: 0.1 M $HClO_4$. Scan rate: 10 mV s^{-1}..... 327

Figure 10.12. High-resolution XPS spectra of a) W 4*f*, b) S 2*p* and c) Ir 4*f* for pristine (top) and WS_{3-x} decorated (±500 µA, 1000 ms, 5 mins; bottom) Ir samples. Labels: W^{6+} $4f_{7/2:5/2}$ (orange), S $2p_{3/2:1/2}$ (S^{2-}, yellow), S $2p_{3/2:1/2}$ (S_2^{2-}, magenta), S $2p_{3/2:1/2}$ (SO_x^{y-}, dark blue), Ir^0 $4f_{7/2:5/2}$ (blue), Ir^{4+} $4f_{7/2:5/2}$ (green) and Ir^{3+} $4f_{7/2:5/2}$ (orange)..... 328

Figure 10.13. Cyclic voltammograms recorded at pristine (black) and WS_{3-x} decorated (±500 µA, 1000 ms, 5 mins; dark yellow) Si/Cr/Ir electrodes a) before (broken line) and after (solid line) undergoing

long-term OER stability experiments: j_{geom}= +10 mA cm^{-2} sustained for 12 h. Voltage window: +1.0 to +1.6 V vs. RHE. Scan rate: 10 mV s^{-1}.; b) first OER voltammograms recorded for pristine and WS_{3-x} decorated (±700 µA, 250 ms, 10 mins. Electrolyte: 0.1 M $HClO_4$. 334

Figure 10.14. FE-SEM micrographs of Si/Cr/Ir electrodes before, after 2 h and after 12 h OER stability testing of a) as-received and WS_{3-x} decorated electrodes by b) ±500 µA, 1000 ms, 5 mins, c) ±700 µA, 1000 ms, 10 mins, and d) ±900 µA, 1000 ms, 10 mins reverse current pulses. Micrographs image magnification: 50000x..... 335

List of Tables

Table 1.1. Compilation of reported operating parameters of alkaline electrolysers, PEM electrolysers and solid oxide electrolysers. Data compiled from multiple sources and reproduced in refs. [21] and [18]. 5

Table 1.2. Operating parameters of commercially available alkaline and PEM electrolyzers. Data compiled from refs. [20], [29], [31], [32] and manufacturer's brochures [33-37]. 10

Table 1.3. Comparison of hydrogen production technologies based on feedstock, efficiency, capital cost and hydrogen cost. Data compiled from refs. [38], [39], [40] and [20]. 11

Table 2.1. Crystallographic parameters and thickness-dependent band gap values (measured at room temperature) for the most utilized TMDs. Compiled from refs. [28-41]. 18

Table 2.2. Tafel slope theoretical values as a function of the HER rate-determining step. Refs. [53,54]. 21

Table 2.3. Compilation of TMD basal plane activation strategies, along with the underlying activation mechanisms, based upon structural engineering. 47

Table 2.4. Compilation of TMD basal plane activation strategies, along with the underlying activation mechanism, based upon incorporation of foreign metal/chalcogenide centers. 48

Table 5.1. Composition analysis of six hybrid Ni-MoS_2 nanoclusters based on HAADF-STEM images.. 152

Table 7.1. Compilation of height (h_{nanoc}), diameter and interspacing of the nanopillars obtained after plasma etching of MoS_2 and WS_2 crystals as a function of the SF_6/C_4F_8 plasma etching time. Etching time inaccuracy is related to the one second high ICP power and flow rate "strike step" required for the formation of the SF_6/C_4F_8 plasma. 200

Table 7.2. Relative XPS photoemission percentages for as-received and C_4F_8/SF_6 plasma-etched WS_2 crystals. 203

Table 7.3. Definition of dimensionless parameters used for transient chronoamperometry experiments. 211

Table 7.4. Compilation of heterogeneous electron transfer constants (k^o_{app}) for plasma-etched MoS2 and WS2 crystals. 221

Table 7.5. Compilation of height, diameter and interspacing of the nanopillars obtained after plasma etching and 5-month atmosphere exposure of WS_2 crystals as a function of the SF_6/C_4F_8 plasma etching time..... 226

Table 8.1. Compilation of HER onset potentials ($\eta_|$ at $|j| = 0.05\ mA\ cm^{-2}$) for 31±1 s (R= 2, Z= 6.4) and 61±1 s atmospherically aged, sulfidation treated, plasma-etched WS_2 samples after weekly electrochemical testing over a three week ambient period. 241

Table 8.2. Compilation of heterogeneous electron transfer constants (k^o_{app}) for atmospherically aged, sulfidation treated, plasma-etched WS_2 samples over a three week environment exposure period after elucidating the peak-to-peak separation of the $[Fe(CN)_6]^{4-}/[Fe(CN)_6]^{3-}$ redox probe..... 243

Table 8.3. Compilation of relative percentages of WS_2 polymorphs (metallic 1T and semiconducting 2H) obtained from XPS spectra for 31 ± 1 s (R= 2, Z= 6.4) and 61 ± 1 s atmospherically aged, sulfidation treated, plasma-etched WS_2 samples after weekly electrochemical testing over a three week ambient exposure period..... 243

Table 9.1. Compilation of the 50th cathodic relative peak current intensities for $E_{peak,III}$ $\left(\frac{I_{peak,III}}{I_{peak,III}+I_{peak,IV}}\right)$ and $E_{peak,IV}$ $\left(\frac{I_{peak,IV}}{I_{peak,III}+I_{peak,IV}}\right)$ as well as the ex-situ XPS relative ratio of the "low binding energy" ($S_2^{2-}{}_{terminal}/S^{2-}{}_{unsat}$) and "high binding energy" ($S_2^{2-}{}_{bridging}/S^{2-}{}_{apical}$) S $2p_{3/2:1/2}$ components obtained after oxidative-reductive electrochemical conditioning on pristine AE-MoS_x films across the 0-10 pH range. 279

Table 9.2. Relative XPS photoemission percentages of deconvoluted Mo 3d and S 2p components of AE-MoS_x thin films: pristine (a.r.) and after undergoing reductive conditioning across the 0-10 pH range. 280

Table 9.3. Relative XPS photoemission percentages of deconvoluted Mo 3d and S 2p components of AE-MoS_x thin films: pristine (a.r.) and after undergoing electro-oxidative conditioning across the 0-10 pH range. 283

Table 10.1. Compilation of the short-duty oxygen evolution activity of WS_{3-x} decorated Ir electrodes after use of ±500-900 µA pulse reverse current electrodeposition. E_{OER,t_0}, E_{OER,t_f} and ΔE_{OER} correspond to the averaged (± 10 s) initial, final and variation, respectively, of the OER overpotentials recorded to sustain j_{geom}= +10 mA cm^{-2} for 2 h. OER activity metrics (j_{geom}, mass activity, specific activity) are reported, for each sample, before (first row) and after (second row) short-duty OER stability measurements. 325

Table 10.2. Compilation of the roughness factor (R_f) values (obtained after integration of the hydrogen desorption region, 0.06 V to ca. 0.45 V vs RHE), their relative increase, and Tafel slope values for

pristine and WS_{3-x} decorated Ir electrodes before/after OER activity measurements, and after 2 h OER stability measurements. 326

Table 10.3. Compilation of the long-term oxygen evolution activity of WS_{3-x} decorated Ir electrodes after use of ±500-900 µA pulse reverse current electrodeposition at variable pulse timescales and total experiment durations. E_{OER,t_0}, E_{OER,t_f} and ΔE_{OER} correspond to the averaged (± 100 s) initial, final and variation, respectively, of the OER overpotentials recorded to sustain j_{geom}= +10 mA cm^{-2} for 12 h. OER activity metrics (j_{geom}, mass activity, specific activity) are reported, for each sample, before (first row) and after (second row) OER stability measurements. 336

Table 10.4. Compilation of the roughness factor (R_f) values (obtained after integration of the hydrogen desorption region, 0.06 V to ca. 0.45 V vs RHE), their relative increase, and Tafel slope values for pristine and WS_{3-x} decorated Ir electrodes before/after OER activity measurements, and after 12 h OER stability measurements. Values labelled with an asterisk (*) indicate that hydrogen desorption integration is affected by ohmic drop, unable to be fully corrected by post-experiment *iR* compensation. 337

Table 11.1. Compilation of TMD nanostructuring strategies undertaken in this thesis (Chapters 5 to 8), highlighting key findings, benefits and limitations versus the state-of-the-art. 349

Table 11.2. Compilation of TMD nanostructuring strategies undertaken in this thesis (Chapters 9 and 10), highlighting key findings, benefits and limitations versus the state-of-the-art. 350

List of Abbreviations

2D two-dimensional

AC/DC Alternating/Direct Current

AE(C) Alkaline Electrolyser (Cell)

AE-MoS_x Anodically Electrodeposited Molybdenum Sulfide

Anth Anthracenide

ASV Anodic Stripping Voltammetry

α Charge transfer coefficient

BSE Backscattered electrons

CE Counter Electrode

CE-MoS_x Cathodically Electrodeposited Molybdenum Sulfide

CNT Carbon Nanotube

CPE Constant Phase Element

CV Cyclic Voltammetry

CVD Chemical Vapour Deposition

D Diffusion coefficient

DFT Density Functional Theory

DMF N,N-dimethylformamide

δ Diffusion layer thickness

ΔE_{OER} Variation in the Oxygen Evolution Reaction overpotential

ΔE_P Peak-to-peak potential separation

$\Delta G_H{}^*$ Hydrogen Adsorption Free Energy Change

ECSA Electrochemical Active Surface Area

EDX Energy-Dispersive X-ray Spectroscopy

EIS Electrochemical Impedance Spectroscopy

EQCM Electrochemical Quartz Crystal Microbalance

FEG-SEM Field Emission Gun Scanning Electron Microscopy

FFT Fast Fourier Transform

FWHM Full Width at Half Maximum

GC Glassy Carbon

HAADF-STEM High-angle Annular Dark-Field Scanning Transmission Electron Microscopy

h-BN hexagonal Boron Nitride

HCP Hexagonal Close-Packed

HER Hydrogen Evolution Reaction

HET Heterogeneous Electron Transfer

H_{upd} Hydrogen underpotential deposition

$\eta_{half\ max}$ Peak half maximum overpotential

η_{onset} Onset overpotential

IA^+ Intercalated Alkali Cation

ICP Inductively Coupled Plasma

I_{WE}/E_{WE} Electrical current/potential at the working electrode

j_0 Exchange Current Density

j_{geom} Geometric current density

$j_{half\ max}$ Peak half maximum current density

j_P Peak current density

k^0_{app} Standard/apparent heterogenous electron transfer rate constant

LSV Linear Sweep Voltammetry

NP Nanoparticle

NPRL Nanoscale Physics Research Laboratory

NS Nanosphere

OCP Open Circuit Potential

OER Oxygen Evolution Reaction

PBS Phosphate Buffer Saline

PCET Proton-Coupled Electron Transfer

PE Pulsed Electrodeposition

PEME(C) Proton Exchange Membrane Electrolyser (Cell)

PGM Platinum Group Metal

PV Photovoltaics

PVD Physical Vapour Deposition

ψ Dimensionless kinetic parameter

R Radial coordinate

R_{ct} Charge Transfer Resistance

RE Reference Electrode

R_f Roughness factor

RF Radio Frequency

rGO reduced Graphene Oxide

RHE Reference Hydrogen Electrode

RTIL Room Temperature Ionic Liquid

SCE Saturated Calomel Electrode

SE Secondary electrons

SEM Scanning Electron Microscopy

SFC/ICP-MS Scanning Flow Cell/Inductively Coupled Plasma Mass Spectrometry

SHE Standard Hydrogen Electrode

SOE(C) Solid Oxide Electrolyser (Cell)

$\langle \sigma_q \rangle$ Integrated/Electrodeposition charge density

t-BuLi t-Butyl Lithium

TEM Transmission Electron Microscopy

TM Transition Metal

TMD Transition Metal Dichalcogenide

TOF Turnover Frequency

τ Dimensionless time

UHV Ultra-high Vacuum

vdW van der Waals

WE Working Electrode

XPS X-ray Photoelectron Spectroscopy

YSZ Yttria Stabilized Zirconia

z Stoichiometric number of electrons transferred in the electrochemical reaction

Z Normal coordinate

Z' Real component of electrochemical impedance

Z'' Imaginary component of electrochemical impedance

Chapter 1

Introduction

1.1 Background of the research

The impact of the industrial revolution in global warming is an undeniable and pressing concern. A very recent report from the Intergovernmental Panel on Climate Change has confirmed a 1±0.2 °C increase in the global average temperature in 2017 compared to pre-industrial levels (see Figure 1.1a),[1] with warming higher than the average (almost double) in specific regions and climate seasons (see Figure 1.1b).[1] In a business-as-usual scenario of anthropogenic emissions, this report suggests that 1.5 and 2 °C temperature increases will be achieved by 2040 and ca. 2070, respectively. Above 1.5 °C increase, experts anticipate disappearance of coral reefs, extinction of local species, sea level rise, aggravated climate events (heatwaves, heavy precipitation) and higher risks of water and food scarcity, amongst other effects.[2] Some can be mitigated if drastic action is taken to stabilize up to 1.5 °C the global temperature increase, commitment stated in the 2015 UN Paris agreement.[3]

However, the 2.2% and 1.6% growth of global primary energy consumption (for contribution by energy source, see Figure 1.2a) and carbon emissions in 2017,[4] respectively, present a contrasting reality. Oil, the highest relative contributor of primary energy consumption (ca. 34.2%), is being effectively depleted (98186 thousands of barrels/day consumed vs. 92649 produced), and its proven reserves would only last 50 more years at the present production rate. Interestingly, economic growth of emerging economies is mostly driven by use of carbon-intensive energy sources. For Brazil, China, India and Russia, coal, natural gas and oil account

for 62.9%, 86.4%, 91.9% and 87.4% of the primary energy consumption, respectively.[4] Consequently, a prompt transition towards a decarbonized and sustainable energy system is needed to sustain the everlasting increase of energy demand (projected to be a 16% by 2050)[5] whilst minimizing its impact on Earth's ecosystem.[6,7]

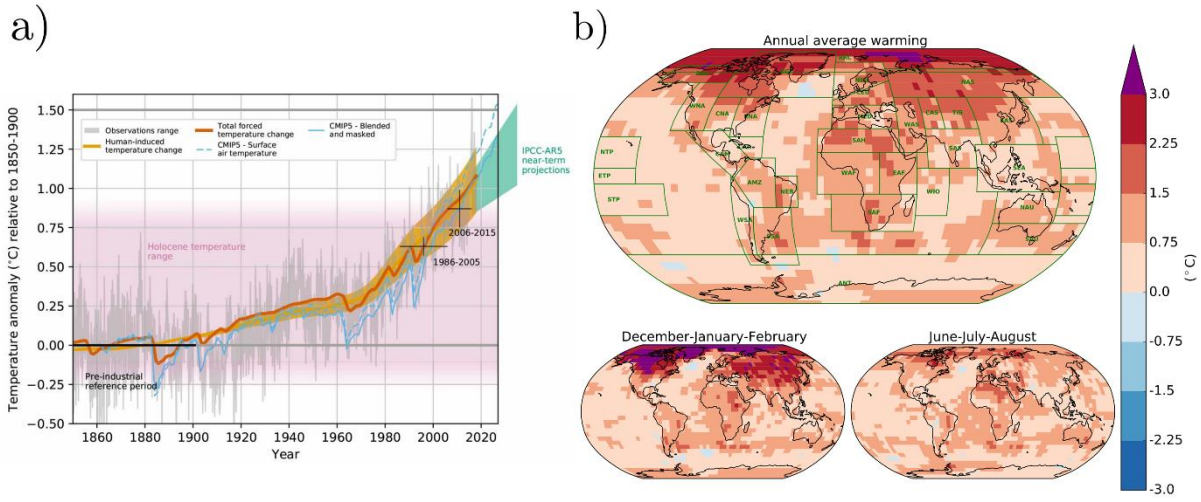

Figure 1.1. a) Time evolution of the global average surface temperature in the 1850-2017 period. b) Local warming observed in the 2006-2015 decade versus the average temperature in the pre-industrial period (1850-1900). Reproduced from ref. [1].

Green renewable energies such as hydrothermal, geothermal, wind or solar photovoltaics (PV) are one the keyplayers in this transition: these represent a 3.6% in the 2017 total energy consumption.[4] In the UK, despite being a net electricity importer, a 31.7% of the generated electricity corresponds to renewable energies (Figure 1.2b), presenting an energy capacity of 42.2 GW.[8,9] In both global and UK scenarios, renewables' generation power capacity is on the rise: 17% and 10% only in 2017, respectively. Their increasing deployment is driven by decreasing manufacturing costs (since 2010, solar PV and wind dropped down 70% and 25%) and competitive auction commissioning policies.[10] Thus, penetration of renewables in the electricity grid is today a reality which could dominate the future energy system.

The inherently intermittent nature of some renewable energies, however, might prevent to cover unpredictable peak energy demands (scenario coined as "lulls and slews".[11] Among the solutions, storage of renewable energy by on-site production of an energy carrier such as hydrogen during periods of low demand of the energy grid is one of the most praised. The main advantages of hydrogen use are its high gravimetric energy density compared with currently employed fossil fuels (1 Kg of hydrogen presents more chemical energy stored than 2.5 Kg of gasoline)[12] and the generation of water as a byproduct of its combustion. These are extremely valuable in the transportation sector, as not only would minimize carbon emissions but also improve the energy security given the price volatility and geopolitical instability of crude oil.[13] A hydrogen-based energy system, coined as the hydrogen economy,[14] has been envisioned as one of the most sustainable solutions to obtain a carbon-free energy cycle.[15,16] This, however, heavily relies on the hydrogen production method.

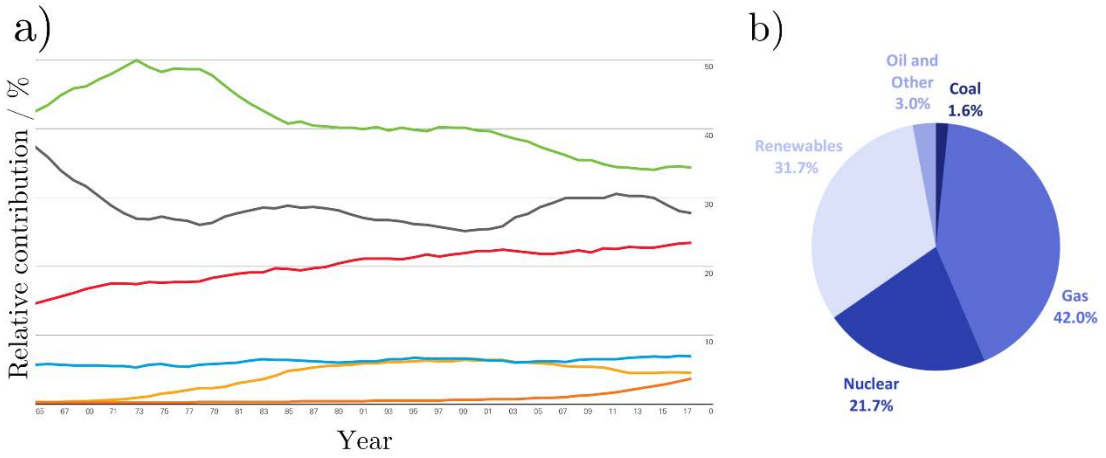

Figure 1.2. a) Global primary energy consumption share in the 1965-2017 period, based on energy source (in %): oil (green), coal (black), natural gas (red), hydroelectricity (blue), nuclear energy (yellow) and renewable energy (orange). b) UK electricity generation share for the second quarter of 2018, based on energy source. Refs. [4] and [8].

1.2 Hydrogen production methods

Hydrogen, although being the most abundant element in the universe, is mostly found on earth chemically bound to molecules (namely water and hydrocarbons) rather than in its molecular form. Different methods can be employed to generate hydrogen, with varying degrees of carbon footprint. We will herein outline those based on water electrolysis, but alternative hydrogen production methods are included in the appendix (section A) for completeness.

1.2.1 Electrolytic-based methods

Dating back to the pioneering experiments by van Troostwijk and Deiman in 1790,[17] water electrolysis consists on breaking water molecules into its elemental constituents, hydrogen and oxygen, by exerting an external voltage gradient between two immersed conducting electrodes. In the anode, oxygen evolution occurs, whilst hydrogen is produced at the cathode. The overall process is the following

$$H_2O \rightarrow H_2 + \frac{1}{2}O_2 \quad \Delta H = -288\, kJ\, mol^{-1} \quad (1.1)$$

Water electrolysis is plausible from multiple sources. Pure water, as it is weakly dissociated into protons and hydroxide ions (self-ionization constant $K_W = 1 \times 10^{-14}$ at 298 K), can undergo electrolysis, but its high resistivity (18.2 MΩ cm) requires the addition of water-soluble ions to minimize ohmnic losses. Wastewater, brine and seawater, although widely available, require demineralization and desalination treatments to prevent competing reactions (e.g. chlorine generation) to occur.[18]

In the ideal scenario of the hydrogen economy, surplus electricity obtained by renewable energies can be stored in molecular hydrogen by on-demand and on-site water electrolysis, yielding no carbon emissions. Hydrogen, generally stored at 100MPa or alternatively into metal hydrides,[19] can later be re-integrated into the electricity grid by its direct combustion or its

use in energy conversion technologies such as hydrogen fuel cells. Alternatively, hydrogen can also be employed to manufacture high-value chemicals such as ammonia (Haber-Bosch process) or hydrocarbons (Fischer-Tropsch process), and oxygen in relevant processes such as steel forging and sulphuric acid production, among many others.[20] This paradigm is shown in Figure 1.3.[21]

Water electrolysis cells, known as electrolysers, can be classified by the operating temperature and nature of the electrolyte (Figure 1.4): low-temperature electrolysers (alkaline and proton exchange membrane) operate industrially in the 50-80°C range, whilst high-temperature electrolysers (solid oxide) in the 700-1000°C.[22] Table 1.1 presents an overview of these technologies, and table 1.2 the specifications of some commercially-available units.

Operating parameters	Alkaline Electrolysers	PEM Electrolysers	Solid Oxide Electrolysers
Temperature / °C	60-80	50-80	650-1000
Pressure / bar	< 30	< 200	< 25
Current density / A cm^{-2}	0.2-0.4	0.6-2.0	0.3-2.0
Cell voltage / V	1.8-2.4	1.8-2.2	0.7-1.5
Power density / W cm^{-2}	Up to 1.0	Up to 4.4	-
Voltage efficiency / $\%_{HHV}$	62-82	67-82	81-86
Hydrogen production rate / m^3 H_2 h^{-1}	< 760	< 40	< 40
Hydrogen purity / %	> 99.5	> 99.999	99.9
System energy consumption / kWh nr^3 H_2	4.5-6.6	4.2-6.6	2.5-3.5
Cold start-up time / min	15	< 20	> 60
System response,lifetime / h	s, 60000-90000	ms, 20000-60000	s, 10000-40000
Capital cost / € kW^{-1}	1000-1200	1860-2320	> 2000
Maturity of technology	Mature, commercial	Commercial	Demonstration

Table 1.1. Compilation of reported operating parameters of alkaline electrolysers, PEM electrolysers and solid oxide electrolysers. Data compiled from multiple sources and reproduced in refs. [23] and [18].

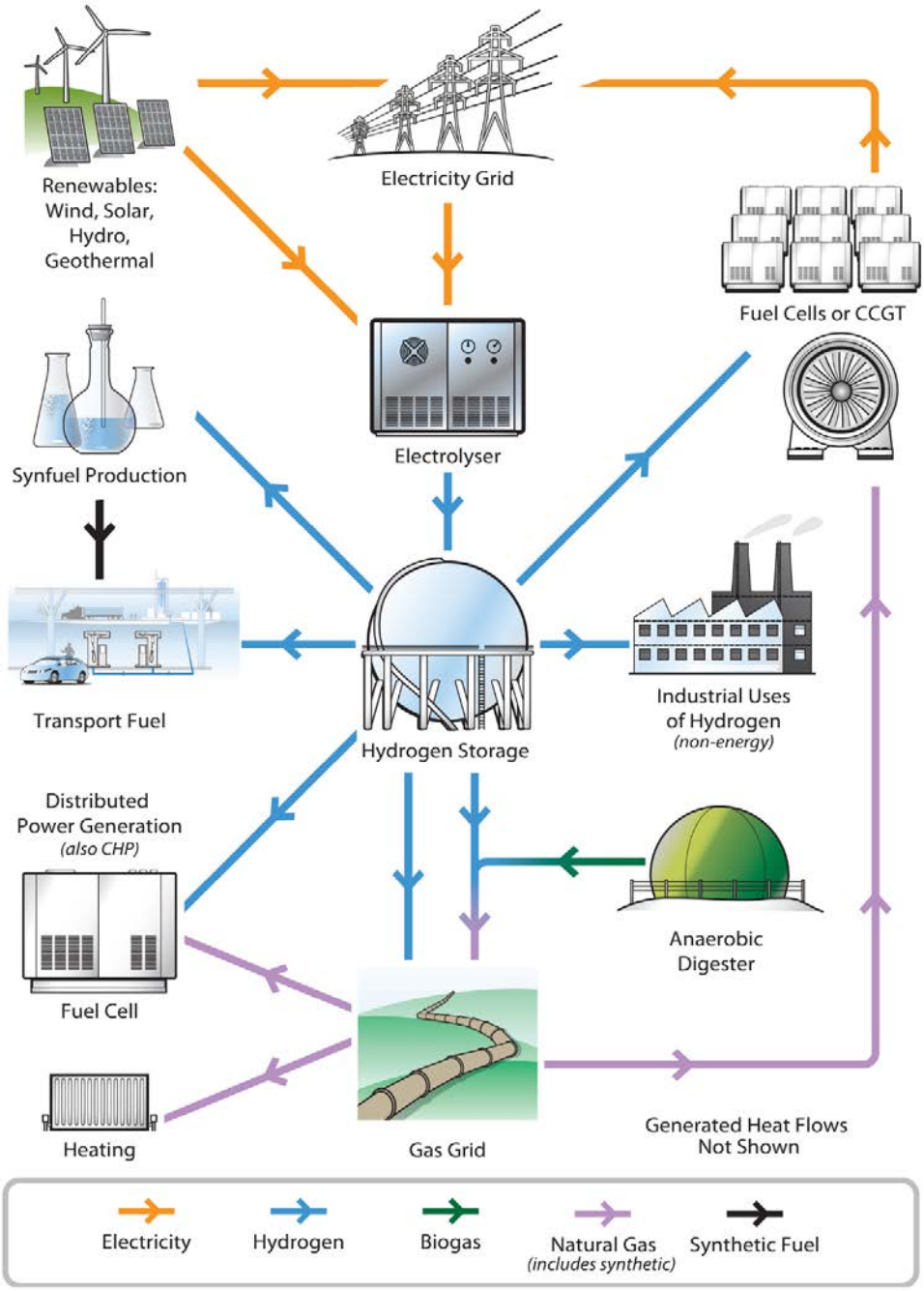

Figure 1.3. Pathways in the integrated energy system based on hydrogen produced from water electrolysis. Reproduced from ref. [21].

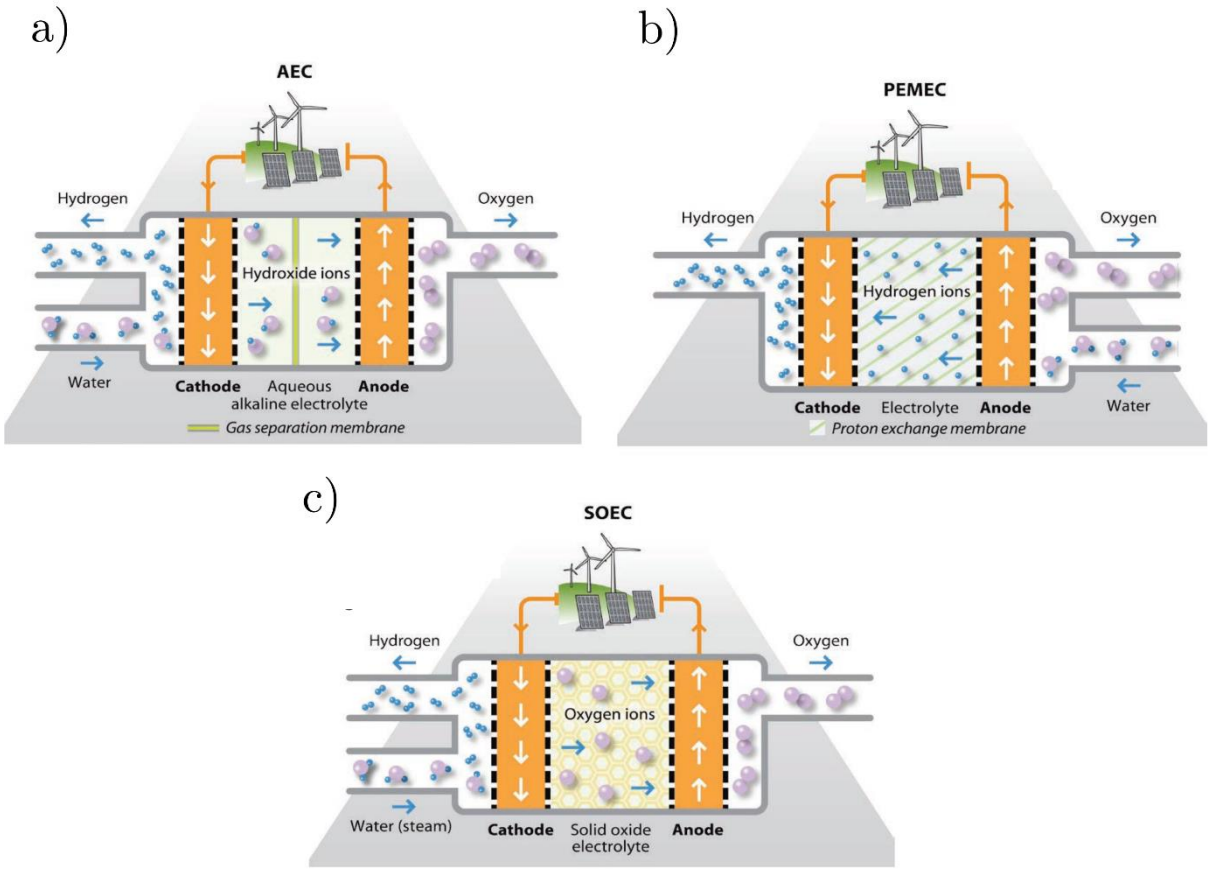

Figure 1.4. Schematic of the operation principle of a) alkaline electrolyser cells (AECs), b) proton-exchange membrane electrolyser cells (PEMECs) and c) solid oxide electrolyser cells (SOECs). Reproduced from ref. [21].

1.2.1.1 Alkaline electrolysers (AEs)

In alkaline electrolysers, an aqueous alkaline electrolyte normally composed of 25-30% KOH or NaOH is fed into the cathode where it is decomposed to hydrogen and OH^-. These anions then migrate through the electrolyte and a microporous separator (normally ceramic, with high chemical and thermal stability)[22] to reach the anode, where oxygen and water are generated. The half-cell reactions are the following

Cathode: $$2\,H_2O + 2\,e^- \rightarrow H_2 + 2\,OH^- \quad E^0_{SHE} = -0.828\,V \quad (1.2)$$

Anode: $$2\,OH^- \rightarrow \frac{1}{2}O_2 + H_2O + 2\,e^- \quad E^0_{SHE} = 0.401\,V \quad (1.3)$$

Hydrogen dissolved in the catholyte is recovered by dehumidification in a separate unit, and alkali electrolyte is replenished to compensate for leaking losses during recirculation.[24] In liquid alkaline electrolytes, carbonation and bubble formation during operation are major issues, as they irreversibly block and damage the electrodes increasing electron transfer resistance[22]: electrolyte concentrations up to 47% can be used to improve conductivity, but degradation of cell components is accelerated.[25]

Alkaline electrolysers are a consolidated technology since the 1920s, with low capital cost due to use of non-noble metal catalysts (e.g. Raney Ni) and robust stack designs.[26] Indeed, a 135MW electrolyser plant designed by Norsk Hydro operated from 1953 to 1991.[27] Lower current densities compared to PEM electrolysers are obtained, even when substituting the separator by a OH^- conducting membrane, and dynamic operation (desirable for coupling to intermittent renewable electricity) is discouraged due to worsened system efficiencies and hydrogen purities.[28]

1.2.1.2 Proton exchange membrane (PEM) electrolysers

PEM electrolysers are fed by water on the anode side, where oxygen and protons are generated. Contrasting with alkaline electrolysers, a solid polymer electrolyte formed by a perfluorinated sulfonic acid membrane (Nafion®) selectively conducts protons to the cathode, where hydrogen is produced. The half-cell reactions are the following

Cathode: $$2\,H^+ + 2\,e^- \rightarrow H_2 \qquad E^0_{SHE} = 0\,V \quad (1.4)$$

Anode: $$H_2O \rightarrow \frac{1}{2}O_2 + 2\,H^+ + 2\,e^- \quad E^0_{SHE} = 1.23\,V \quad (1.5)$$

The main advantage of PEM compared with alkaline electrolysers is the high purity of the hydrogen produced (99.999%) with no additional separation requirement. Other advantages are the higher operating currents and system efficiencies, and capability of operating under fluctuating power supply. However, shorter lifetimes, high purity water requirements to prevent

noble metal catalysts poisoning (e.g. Pt, Ir, Ru, Rh), and limited system scale-up due to higher operating pressures and complex design need to be addressed.[23]

1.2.1.3 Solid Oxide Electrolysers (SOEs)

Solid oxide electrolysers are conceptually solid oxide fuel cells operating in regenerative mode. The main advantage of SOEs with respect to AEs and PEMEs is that their high operating temperatures reduce the overpotential of the electrolytic reactions and, yielding higher electrical efficiencies (85-90%).[29,30] The overall mechanism resembles that of AEs: steam is fed onto the cathode (generally being nickel-yttria stabilized zirconia, Ni-YSZ), where hydrogen is evolved and the co-generated O^{2-} are conducted through a ceramic solid electrolyte (generally YSZ). When reaching the anode (made of a metal-doped lanthanum oxide, such as lanthanum strontium manganite), O^{2-} lose electrons to the external circuit to produce oxygen. Half-cell reactions are outlined below

Cathode: $$H_2O + 2\,e^- \rightarrow H_2 + O^{2-} \quad (1.6)$$

Anode: $$O^{2-} \rightarrow \frac{1}{2}O_2 + 2\,e^- \quad (1.7)$$

The main drawbacks of SOEs are the high operating temperatures needed which decrease the overall hydrogen production efficiency up to 60%,[24] the use of scarce materials, and cell assembly complexity (sealing, chrome migration). The former can be amended if a high-grade external heat is provided, such as waste heat from nuclear and coal-fired power plants, in which case efficiencies can go over 100%, but high-temperature renewable heat is scarce.[31] Stabilization of SOEs under thermal cycling and decrease in required operating temperatures are sought to enable their commercialization.[28,32]

Manufacturer	Type of electrolyser	Electrolyser power / kW	System energy consumption / kWh m^{-3} H_2	H_2 output pressure / bar
Avalence	Alkaline	2-25	56.4-60.5 kWh Kg^{-1}	≤ 690
AREVA H2Gen	PEM	1000	4.4	≤ 35
Acta Energy 200	PEM	1.06	5.3	≤ 30
Hydrog(e)nics HySTAT 60-10 (4 stacks)	Alkaline	300	5.0-5.4	10-27
Hydrog(e)nics HyLYZER 5000-30 (2 stacks)	PEM	5000	5.0-5.4	30
ITM Power HGas	PEM	100-100000	4.4	20-50
Proton OnSite	PEM	2200	5.3	30
Nel Hydrogen A-150-500	Alkaline	190-2135	3.8-4.4	1-200
Toshiba H_2One	PEM	Up to 5000	4.76	8
Siemens SILYZER 200	PEM	**1250**	**5.1**	≤ 35

Table 1.2. Operating parameters of commercially available alkaline and PEM electrolyzers. Data compiled from refs. [22], [31], [33], [34] and manufacturer's brochures [35–39].

1.2.2 Prospects of hydrogen production

The previous section have shown the multiple existing routes to produce hydrogen. A summary of the techno-economic status of several hydrogen production methods is shown in Table 1.3.

Hydrogen production method	Feedstock	Efficiency	Capital cost / M$	Hydrogen cost / $ Kg^{-1}
Steam reforming	Hydrocarbons	70-85	226.4 (with CCS)	2.27
			180.7 (without CCS)	2.08
ATR of methane with CCS	Hydrocarbons	60-75	183.8	1.48
Biomass gasification	Woody biomass	35-50	149.3	1.77
Biomass pyrolysis	Woody biomass	35.50	53.4	1.25
Direct bio-photolysis	Water + algae	0.5	50$ m^{-2}	2.13
Indirect bio-photolysis	Water + algae	0.5	135$ m^{-2}	1.42
Dark fermentation	Organic biomass	60-80	-	2.57
Photo-fermentation	Organic biomass	0.1	-	2.83
Nuclear/solar thermolysis	Water	45	39.6/16	2.17/7.98
Alkaline Electrolysers	Water + electricity	50-60	Table 1.2	3.68 (main grid)
				5.75 (renewables)
PEM Electrolysers	Water + electricity	55-70	Table 1.2	4.72 (main grid)
				8.74 (renewables)
Solid Oxide Electrolysers	Water + electricity + heat	**40-60**	**Table 1.2**	-

Table 1.3. Comparison of hydrogen production technologies based on feedstock, efficiency, capital cost and hydrogen cost. Data compiled from refs. [40], [41], [42] and [22].

Hydrocarbon-based methods present, to this date, the lowest hydrogen production costs, which supports their dominance over renewable-based methods. However, depletion of fossil fuels and the subsequent transition towards a carbon-free energy system will necessarily shift the production load towards methods based on renewable energies. In this regard, water electrolysis stands out as one of the most viable technologies given the high efficiencies and potential for scale-up. A recently reported expert elicitation study suggests that although alkaline

electrolysers will be the dominant electrolysis technology up to 2020, from 2030 onwards PEM electrolyzers will dominate the market. This is due to foreseen improvements in system efficiencies, lifetimes, scale-up and lower production costs in conjunction with the characteristic flexible power input operation.[23] One of the main drivers for PEM electrolysers capital cost reduction has been identified to be the minimization, if not replacement, of the platinum group metal (PGM) catalyst loading employed, which for PEM fuel cells stacks accounts for up to 49% of the high-volume manufacturing costs.[43] The next section will give an overview of catalysts for PEM electrolysers, with special focus on a family of earth-abundant, platinum-free materials known as transition metal dichalcogenides.

References

[1] K.Z. M. Allen, O. P. Dube, W. Solecki, F. Aragón–Durand, W. Cramer, S. Humphreys, M. Kainuma, J. Kala, N. Mahowald, Y. Mulugetta, R. Perez, M. Wairiu, Framing and Context, Glob. Warm. 1.5 °C - IPCC's Spec. Assess. Rep. (2018).

[2] Ove Hoegh-Guldberg, D. Jacob, M. Taylor, et al, Impacts of 1.5°C global warming on natural and human systems, Glob. Warm. 1.5 °C - IPCC's Spec. Assess. Rep. (2018).

[3] U.N. UN, Convention on Climate Change: Climate Agreement of Paris., (2015) 1–27. doi:10.1017/s0020782900004253.

[4] BP, BP Statistical Review of World Energy June 2018, Stat. Rev. World Energy. (2018) 1–56.

[5] Hydrogen Council, How hydrogen empowers the energy transition, (2017) 28. http://hydrogencouncil.com/wp-content/uploads/2017/11/Hydrogen-scaling-up-Hydrogen-Council.pdf.

[6] J. Markard, The next phase of the energy transition and its implications for research and policy, Nat. Energy. (2018) 1–6. doi:10.1038/s41560-018-0171-7.

[7] S. Chu, Y. Cui, N. Liu, The path towards sustainable energy, Nat. Mater. 16 (2016) 16–22. doi:10.1038/nmat4834.

[8] BEIS, Electricity Statistics 2018 Q2: Section 5 - Electricity, (2018) 0–8. https://assets.publishing.service.gov.uk/government/uploads/system/uploads/attachment_data/file/743579/Electricity.pdf.

[9] BEIS, Electricity Statistics 2018 Q2: Section 6 - Renewables, (2018) 0–9. https://assets.publishing.service.gov.uk/government/uploads/system/uploads/attachment_data/file/743591/Renewables.pdf.

[10] IEA, Market Report: Renewables 2018, (2018) 10. doi:10.1787/coal_mar-2017-en.

[11] D. MacKay, Sustainable Energy: Without the hot air, 1st ed, 2008. doi:10.1109/PES.2004.1373296.

[12] T. da Silva Veras, T.S. Mozer, D. da Costa Rubim Messeder dos Santos, A. da Silva César, Hydrogen: Trends, production and characterization of the main process worldwide, Int. J. Hydrogen Energy. 42 (2017) 2018–2033. doi:10.1016/j.ijhydene.2016.08.219.

[13] M. Ball, M. Weeda, The hydrogen economy - Vision or reality?, Int. J. Hydrogen Energy. 40 (2015) 7903–7919. doi:10.1016/j.ijhydene.2015.04.032.

[14] J. O'M. Bockris, The Hydrogen Economy, in: Environ. Chem., Springer, Boston, MA, 1977: pp. 549–582. doi:https://doi.org/10.1007/978-1-4615-6921-3_17.

[15] E. Cetinkaya, I. Dincer, G.F. Naterer, Life cycle assessment of various hydrogen production methods, Int. J. Hydrogen Energy. 37 (2012) 2071–2080. doi:10.1016/j.ijhydene.2011.10.064.

[16] J. Dufour, D.P. Serrano, J.L. Gálvez, J. Moreno, C. García, Life cycle assessment of processes for hydrogen production. Environmental feasibility and reduction of greenhouse gases emissions, Int. J. Hydrogen Energy. 34 (2009) 1370–1376. doi:10.1016/j.ijhydene.2008.11.053.

[17] A.P. van Troostwijk, J.R. Deiman, Sur une manière de décomposer l'eau en air inflammable & en air vital, Obs. Phys. 35 (1789) 369–378.

[18] I. Dincer, C. Acar, Review and evaluation of hydrogen production methods for better sustainability, Int. J. Hydrogen Energy. 40 (2014) 11094–11111. doi:10.1016/j.ijhydene.2014.12.035.

[19] V. Molkov, J.B. Saffers, Hydrogen jet flames, Int. J. Hydrogen Energy. 38 (2013) 8141–8158. doi:10.1016/j.ijhydene.2012.08.106.

[20] A.M. Clark, The provision of oxygen for industrial processes, Chem. Eng. Sci. 3 (1954) 118–125. doi:10.1016/S0009-2509(54)80011-X.

[21] FuelCellToday, Water Electrolysis & Renewable Energy Systems, 2013. http://www.fuelcelltoday.com/media/1871508/water_electrolysis___renewable_energy_systems.pdf.

[22] M. Bodner, A. Hofer, V. Hacker, H2 generation from alkaline electrolyzer, Wiley Interdiscip. Rev. Energy Environ. 4 (2015) 365–381. doi:10.1002/wene.150.

[23] O. Schmidt, A. Gambhir, I. Staffell, A. Hawkes, J. Nelson, S. Few, Future cost and performance of water electrolysis: An expert elicitation study, Int. J. Hydrogen Energy. 42 (2017) 30470–30492.

[24] J.D. Holladay, J. Hu, D.L. King, Y. Wang, An overview of hydrogen production technologies, Catal. Today. 139 (2009) 244–260. doi:10.1016/j.cattod.2008.08.039.

[25] M.N. Manage, D. Hodgson, N. Milligan, S.J.R. Simons, D.J.L. Brett, A techno-economic appraisal of hydrogen generation and the case for solid oxide electrolyser cells, Int. J. Hydrogen Energy. 36 (2011) 5782–5796. doi:10.1016/j.ijhydene.2011.01.075.

[26] K. Zeng, D. Zhang, Recent progress in alkaline water electrolysis for hydrogen production and applications, Prog. Energy Combust. Sci. 36 (2010) 307–326. doi:10.1016/j.pecs.2009.11.002.

[27] Nel Hydrogen, The world's most efficient and reliable electrolyser, 2016. http://nelhydrogen.com/assets/uploads/2017/01/Nel_Electrolyser_brochure.pdf.

[28] M. Lehner, R. Tichler, H. Steinmüller, M. Koppe, Power-to-Gas: Technology and Business Models, Springer International Publishing, 2014. doi:10.1007/978-3-319-03995-4.

[29] R. Hino, K. Haga, H. Aita, K. Sekita, 38. R&D on hydrogen production by high-temperature electrolysis of steam, Nucl. Eng. Des. 233 (2004) 363–375. doi:10.1016/j.nucengdes.2004.08.029.

[30] V. Utgikar, T. Thiesen, Life cycle assessment of high temperature electrolysis for hydrogen production via nuclear energy, Int. J. Hydrogen Energy. 31 (2006) 939–944. doi:10.1016/j.ijhydene.2005.07.001.

[31] S.P.S. Badwal, S. Giddey, C. Munnings, Emerging technologies, markets and commercialization of solid-electrolytic hydrogen production, Wiley Interdiscip. Rev. Energy Environ. 7 (2018) 1–19. doi:10.1002/wene.286.

[32] M.A. Laguna-Bercero, Recent advances in high temperature electrolysis using solid oxide fuel cells: A review, J. Power Sources. 203 (2012) 4–16. doi:10.1016/j.jpowsour.2011.12.019.

[33] NREL, Technology Brief: Analysis of Current-Day Commercial Electrolyzers, 2004. https://www.nrel.gov/docs/fy04osti/36705.pdf.

[34] Toshiba, Toshiba starts H2One independent energy supply, Fuel Cells Bull. 2015 (2015) 1. doi:10.1016/S1464-2859(15)30067-5.

[35] Acta S.p.A., Electrolysör Datenblatt EL250-500-1000, (n.d.). http://www.actaspa.com/.

[36] Proton On-Site, High Capacity Hydrogen Systems M Series PEM Electrolysers, (n.d.) 1–4. http://www.protononsite.com/sites/default/files/2016-10/pd-0600-0114_rev_a.pdf.

[37] AREVA, PEM Electrolysers, 2006. http://www.arevah2gen.com/wp-content/uploads/2017/02/AREVA_H2GEN_FICHE_PRODUIT_FRANCE_HD.pdf.

[38] Hydrogenics, HyPM Fuel Cell Power Modules, 2011. https://www.h2fc-fair.com/hm10/images/pdf/hydrogenics02.pdf.

[39] Siemens, Silyzer 300, n.d. https://www.siemens.com/content/dam/webassetpool/mam/tag-siemens-com/smdb/corporate-core/sustainable_energy/hydrogensolutions/broschüren/ct-ree-18-047-db-silyzer-300-db-de-en-rz.pdf.

[40] P. Nikolaidis, A. Poullikkas, A comparative overview of hydrogen production processes, Renew. Sustain. Energy Rev. 67 (2017) 597–611. doi:10.1016/j.rser.2016.09.044.

[41] A.M. Abdalla, S. Hossain, O.B. Nisfindy, A.T. Azad, M. Dawood, A.K. Azad, Hydrogen production, storage, transportation and key challenges with applications: A review, Energy Convers. Manag. 165 (2018) 602–627. doi:10.1016/j.enconman.2018.03.088.

[42] A. Bakenne, W. Nuttall, N. Kazantzis, Sankey-Diagram-based insights into the hydrogen economy of today, Int. J. Hydrogen Energy. 41 (2016) 7744–7753. doi:10.1016/j.ijhydene.2015.12.216.

[43] J. Spendelow, J. Marcinkoski, DOE Fuel Cell Technologies Office Record 14012: Fuel Cell System Cost - 2013, 2013.

Chapter 2

Literature review

This chapter will initially devote to provide a solid background on the origin and structural properties of two-dimensional transition metal dichalcogenides (TMDs) later presenting, to the best of our knowledge, the most representative research efforts based on their significance and their application in HER electrocatalysis.[1–9] In particular, the strategies explored to promote exposure of the HER-active edge sites, maximize the inherent electroactivity of the edge sites and activate the electrocatalytically inert basal planes.

2.1 Beyond critical metals: inorganic two-dimensional layered materials

The scientific community has dedicated intensive efforts to find alternative earth-abundant materials which can compete or even surpass the physicochemical properties of the well-established, yet increasingly scarce, PGMs. The first major breakthrough in this quest was made in 2004 by Novoselov and Geim with the experimental isolation of graphene by a mechanical exfoliation route.[10] Graphene consists of a two-dimensional (2D) atomically thin layer of sp^2 carbons in a honeycomb lattice arrangement, where each carbon atom is only bonded to three atoms.[11] This atomic arrangement in the single-layer domain confers graphene unprecedented properties compared with the sp^3 carbon counterparts: high electron mobility (at room temperature, 2.5×10^5 cm^2 V s^{-1}), high stability towards application of high-density electrical currents (10^6 times higher than copper) and stress/strain (Young modulus:

1TPa, intrinsic strength: 130 GPa), high specific surface areas (> 2600 m^2 g^{-1}), high transparency and full impermeability to gases, amongst others.[12,13] This striking anisotropy of graphene was exploited for multiple applications,[14] and paved the way to explore other inorganic layered materials. This was soon anticipated by Novoselov et al., employing the micromechanical cleavage technique, previously optimized for graphene production; to insulate single layers of "2D atomic crystals" of materials such as hexagonal boron nitride (h-BN), molybdenum disulfide (MoS_2) or niobium selenide.[15] Indeed, h-BN was quickly implemented as a high-quality graphene support for optoelectronic applications, as this stacked heterostructure induced a band gap in the initially semi-metallic (zero band gap) graphene.[16]

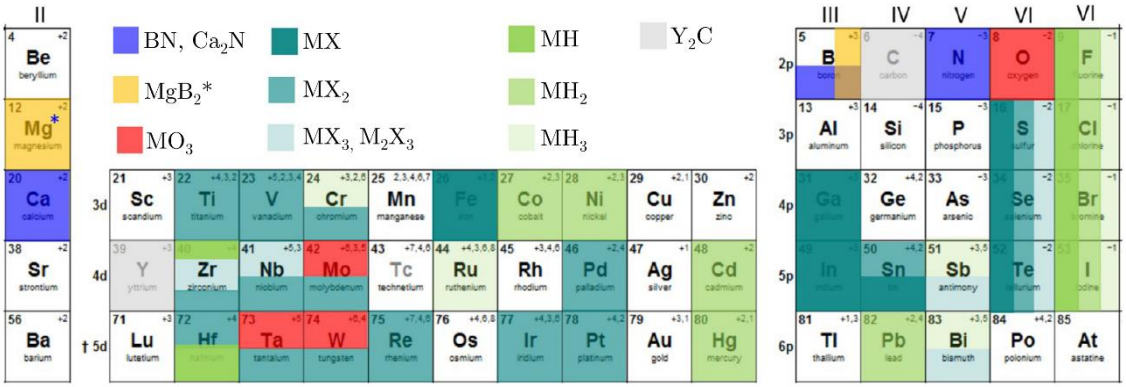

Figure 2.1. Library of 2D layered materials formed by two compounds represented in the periodic table. Colour labelling: transition metal borides (orange), chalcogenides (blue), halides (green) and oxides (red). Elements coloured vertically act as anions, whereas elements coloured horizontally act as cations in the reported materials. MgB_2 (labelled with an asterisk) presents non-van der Waals interlayer interactions. Adapted from ref. [17].

Recent reports account for more than 150 (and counting) 2D-layered materials which can be isolated to single layers (see Figure 2.1 for graphical representation).[18] Among these, the most renowned are the transition metal dichalcogenides (TMDs or MX_2, M= Mo, W, Ti, Zr, Hf, V, Nb, Ta, Re, Fe, Co, Ni, Zn; X= S, Se, Te),[19] MXenes (2D metal carbides, carbonitrides and

nitrides),[20,21] and most recently the monoelemental 2D semiconductors (Xenes: silicene, germanene, phosphorene, stanene, arsenene, antimonene).[22–27] Herein we will focus on the TMD 2D-layered family of materials.

2.2 Layered transition metal dichalcogenides: structural aspects

Transition metal dichalcogenide (MX_2) monolayers are constituted by transition metal cation centres (M) sandwiched between two hexagonally closed-packed layers of chalcogenide anions (X), forming an X-M-X atomic trilayer.[28] Analogous to graphite, intralayer bonds mostly present a covalent nature, whereas adjacent TMD layers are stacked by weak van der Waals (vdW) forces[29]: for MoS_2, interlayer forces are 100 times weaker than intralayer.[30] TMD monolayers are generally 6-8 Å thick (for MoS_2/$MoSe_2$/$MoTe_2$ ≈ 6.5/7.0/8.0 Å,[31–33] whilst for WS_2,WSe_2/WTe_2 ≈ 7/8 Å),[34–36] and the interlayer spacing, defined here as the distance between the atomic planes formed by M in two neighbouring layers, is of ≈6.5 Å. Crystallographic parameters for some relevant TMDs are compiled in Table 2.1.

2D TMD	Interlayer spacing / Å	M-X bond length / Å	Band gap / eV			
			Bulk	Trilayer	Bilayer	Monolayer
2H-MoS_2	6.15	2.42	1.23	1.46	1.59	1.89
2H-$MoSe_2$	6.47	2.49	1.09	1.34	1.46	1.57
2H-$MoTe_2$	7.28	2.72	0.93	1.02	1.05	1.08
2H-WS_2	6.16	2.40	1.35	1.53	1.73	1.98
2H-WSe_2	7.00	2.49	1.20	1.45	1.54	1.66
2H-WTe_2	7.02	2.71-2.82	Semimetal/metal (≈ 0.5)			

Table 2.1. Crystallographic parameters and thickness-dependent band gap values (measured at room temperature) for the most utilized TMDs. Compiled from refs. [37–50],

Layered TMDs present several polymorphs dependent on the metal coordination and interlayer stacking sequence: the most commonly reported are the 1T, 2H and 3R. In this nomenclature, the digit corresponds to the number of X-M-X layers involved in the stacking sequence along

the z axis (crystallographic unit cell), whereas the letter is related to the crystallographic symmetry. The 2H and 3R polytypes present a hexagonal trigonal prismatic (D_{3h} symmetry group, Figure 2.2a) and rhombohedral atomic arrangement (C^5_{3v} symmetry group, monolayers in trigonal prismatic phase), respectively, whilst the 1T polytype presents an octahedral structure (D_{3d} symmetry group), (Figure 2.2b).[7] The relative atomic arrangement of the X-M-X within a stacking sequence is expressed by three letters: capital letters correspond to the chalcogen, and lower-case letters to the metal. For a monolayered 1T-MX_2, the stacking sequence notation is AbC (no overlapping between X atom layers); for 2H-MX_2 this is now AbA BaB (X atoms overlap with M atoms of the neighbouring layer), and for 3H-MX_2 is AbA CaC BcB (see Figure 2.2c).

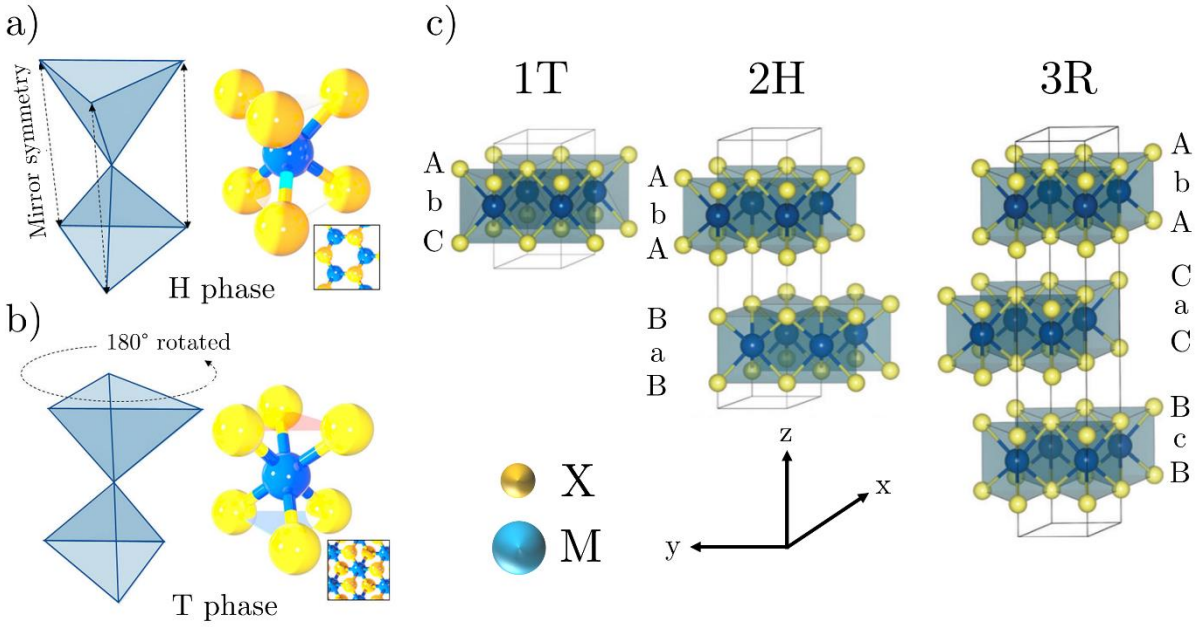

Figure 2.2. Schematic of the trigonal prismatic and octahedral (180° rotated trigonal prismatic) symmetry of the a) H and b) T phases found in TMDs. c) Crystallographic unit cells of the 1T, 2H and 3R TMD polytypes, along with their stacking sequence. Adapted from refs. [51,52].

TMDs from group IV (M= Ti, Zr, Hf) are mostly found in the 1T phase, whereas those from group VI (Mo, W) are generally present in nature in the 2H phase. This trend excludes WTe_2 (orthorhombic, T_d) and CrX_2 (metastable 1T phase). Surprisingly, TMDs from group V exhibit either a 1T phase (VX_2) or 2H phase (NbX_2, TaX_2).[51] For MoS_2, one of the most employed TMDs, both 2H and 3R are naturally occurring phases, 2H being the most abundant given its higher thermodynamic stability, and 1T is metastable. 3R- and 1T-MoS_2 phases can be converted to 2H- by use of heating treatments.[53,54]

The different symmetry and layer stacking arrangement induces contrasting electronic, optical and magnetic properties between TMD polymorphs, making them an extremely versatile family of layered materials. These, whilst not being the focus of this work, have been covered in the appendix for completeness (section B Appendix). We will now focus on the (electro)catalytic properties of TMDs, in particular those related to the electrochemically assisted hydrogen evolution reaction.

2.3 Hydrogen evolution reaction (HER): fundamentals and origin of TMD activity

The hydrogen evolution reaction (HER) is a multi-step, inner sphere electrochemical reaction which occurs at the cathode of (photo)electrochemical water splitting devices. It comprises the reduction of protons (in acidic media) or water (in alkaline media) to molecular hydrogen. The most widely accepted reaction mechanisms in acid and alkaline solutions are outlined below[55]:

1) Volmer reaction (electrochemical adsorption of monoatomic hydrogen)

$$H_3O^+ (aq.) + e^- + * \rightleftharpoons H^* + H_2O (l)$$ (Acidic media, 2.1a)

$$H_2O (l) + e^- + * \rightleftharpoons H^* + OH^-$$ (Alkaline media, 2.1b)

followed by either 2) or 3)

2) Heyrovský reaction (electrochemical hydrogen desorption)

$$H^* + H_3O^+ (aq.) + e^- + * \rightleftharpoons H_2 + H_2O (l) + * \quad \text{(Acidic media, 2.2a)}$$

$$H^* + H_2O (l) + e^- + * \rightleftharpoons H_2 + OH^- + * \quad \text{(Alkaline media, 2.2b)}$$

3) Tafel reaction (chemical hydrogen desorption, recombination)

$$H^* + H^* \rightleftharpoons H_2 + 2^* \quad \text{(Acidic and alkaline media, 2.3)}$$

Where $*$ and H^* designate an available active site and a chemisorbed hydrogen atom on an active site, respectively.

The pathways under which HER takes place are highly dependent on the (electro)chemical and electronic properties of the electrode material.[56] It is well established by theoretical microkinetic modelling[57] and experimental measurements, however,[58] that Tafel slopes (b) are intimately related to the HER rate-determining step (for theoretical values, see Table 2.2). Thus, experimental elucidation of b by gradient analysis of the η vs. $\log j_{geom}$ graphical representation (i.e. geometric current densities j_{geom} recorded at the kinetically-controlled HER overpotentials η) enables to allocate a characteristic HER mechanism to an electrocatalyst. Caution must be taken in Tafel slope analysis, as experimental values are affected by mass transport/uncompensated resistance limitations,[59] monoatomic hydrogen coverages,[57] catalyst surface structure and electrode preparation method.[2]

Rate-determining step		
Volmer reaction	Heyrovský reaction	Tafel reaction
$b = -\frac{2.303RT}{\alpha F} \approx 120\ mV\ dec^{-1}$	$b = -\frac{2.303RT}{(1+\alpha)F} \approx 40\ mV\ dec^{-1}$	$b = -\frac{2.303RT}{2F} \approx 30\ mV\ dec^{-1}$

Table 2.2. Tafel slope theoretical values as a function of the HER rate-determining step. Refs. [60,61].

Among the multiple HER descriptors historically evaluated,[62] the hydrogen adsorption free energy change ($\Delta G_H{}^*$), informing of the bond strength between the electrocatalyst surface and monoatomic hydrogen (M-H), was originally proposed by Parsons[63] and Gerischer,[64] and thoroughly investigated by Trasatti[65] to correlate the physicochemical properties of the known HER-active metals with their HER exchange current densities (j_0, obtained at the intercept of the Tafel plot), an experimental descriptor of the reaction rate in equilibrium. Based upon Sabatier's principle,[66] if hydrogen binding energy is very weak, then reaction 1) (hydrogen adsorption) should limit the overall process. On the other hand, if hydrogen binding energy is very strong, 2) or 3) (hydrogen desorption-recombination) will control the reaction rate.

According to this, the optimal HER catalyst should have a zero $\Delta G_H{}^*$ (thermo-neutral condition) so that hydrogen binding energy is neither too weak to facilitate proton-electron transfer processes nor too strong to guarantee a facile M-H bond breaking for the release of molecular hydrogen. Graphical plotting of experimental j_0 HER values versus Density Functional Theory (DFT) calculated $\Delta G_H{}^*$ for various metal surfaces yields the so-called "volcano plot" curve (see Figure 2.3a). The good correlation observed for HER activity trends not only enables the benchmarking of existing electrocatalysts,[67] but also serves as a predictive tool for the discovery of novel HER electrocatalysts, [68–72].

It should be noted, however, that the $\Delta G_H{}^*$-based volcano plot presents some limitations regarding unambiguous explanation of the HER reaction rates.[73] An alternative "volcano

plot" was reported, using experimentally measured modifications in the work function upon hydrogen electroadsorption through a water layer instead of $\Delta G_H{}^*$, with improved scaling relations (Figure 2.3c).[74]

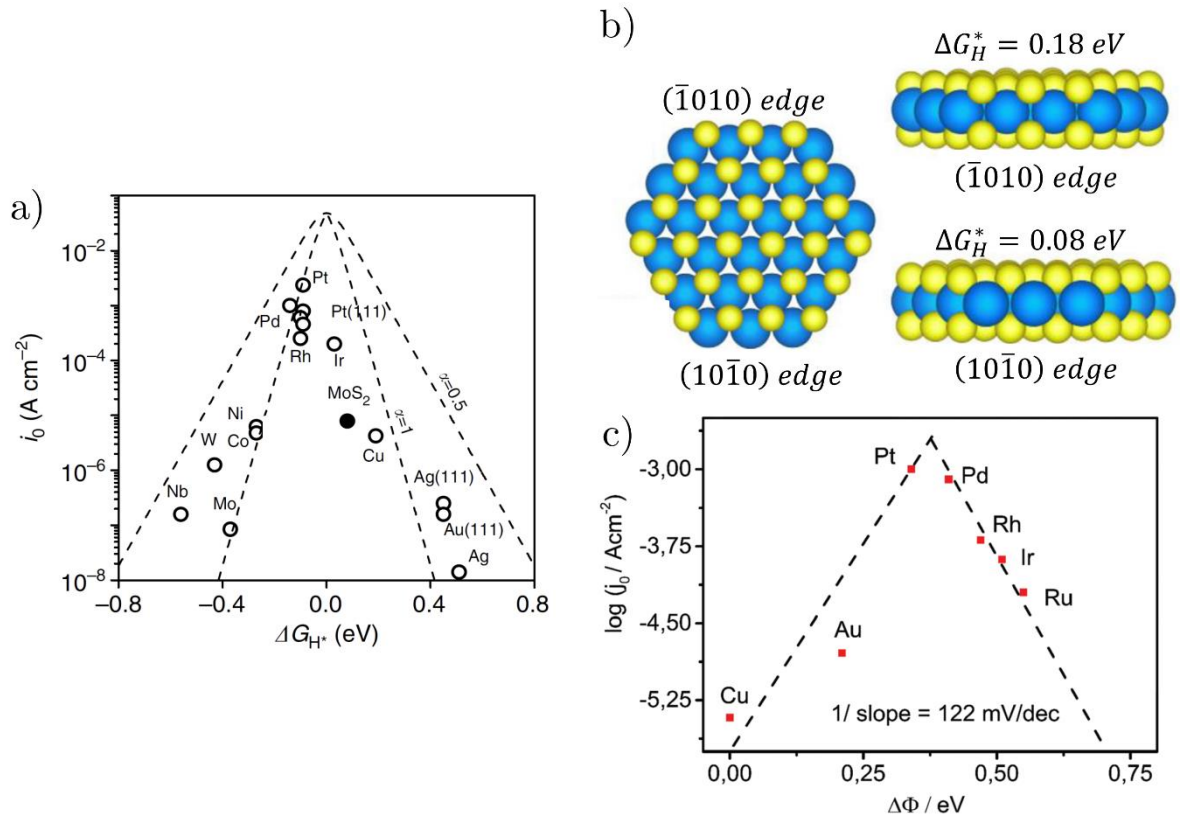

Figure 2.3. a) "Volcano plot", here being experimental j_0 (in logarithmic scale) versus DFT-calculated $\Delta G_H{}^*$, for MoS_2 and metal electrocatalysts. b) Atomic ball model of a truncated MoS_2 hexagonal platelet ($Mo_{27}S_{54}$; Mo: blue, S: yellow) exposing the $(10\bar{1}0)$ Mo-edge and the $(\bar{1}010)$ S-edge. c) Alternative "volcano plot", here being experimental j_0 (in logarithmic scale) versus measured work function changes after hydrogen adsorption through a metal-water layer. Reproduced from refs. [68,74,75].

Indeed, the use of TMDs as earth-abundant electrocatalysts for the HER was discovered by pioneering DFT calculations that evidenced an almost thermo-neutral $\Delta G_H{}^*$ value at the MoS_2 edges (Figure 2.3b) .[76] It was proposed that the HER would preferentially occur at the $(10\bar{1}0)$ Mo-edge, as its calculated $\Delta G_H{}^*$ value (0.08 eV) is closer to zero than that found at the

$(\bar{1}010)$ S-edge (0.18 eV).[77] Later experimental studies on truncated triangular MoS_2 nanoplatelets deposited on Au (111) in ultra-high vacuum (UHV) confirmed a linear correlation between the sulfided Mo-edge length predominantly present and the experimental HER j_0 values.[78] As alterations of the MoS_2 nanoplatelets dimensions yielded higher edge-to-basal plane ratios retaining the edge structure, this provided experimental proof that the Mo-edge is the HER active site, whilst the thermodynamically stable, defect-free (0001) 2H-phase basal plane[79] is catalytically inactive.[80,81] Unfortunately, the preferential exposure of the TMD edge sites for HER electrocatalysis is thermodynamically unfavourable, as the edge surface energy of MoS_2 is two orders of magnitude higher than that of the basal plane surface.[82,83]

2.4 Transition metal dichalcogenides: strategies for maximized edge site exposure

2.4.1 TMD edge site exposure maximization: top-down methods

As described in Section 2.2, naturally occurring 2D TMDs are encountered as layered stacks bound by weak vdW forces. The stacking arrangement, crystalline phase and number of layers yielded substantially modified physicochemical properties, also including their catalytic behaviour. The most important one is the conductivity anisotropy: TMD interlayer conductivities were found to be 2200 lower than along the X-M-X plane.[84] For chemical vapour deposited MoS_2 HER electrocatalysis, this resulted in worsened performances by a factor of ca. 4.47 after the deposition of each additional monolayer (Figure 2.4a).[85] Therefore, top-down methods to exfoliate layered 2D TMDs into few-to-single layered flakes would greatly benefit from improved electrical properties but also higher volumetric edge site exposure, as HER turnover frequency values (TOF) are inversely proportional to the number of layers[86] and the mean TMD nanosheet dimensions.[87]

Conceptually speaking, the most simple methods to achieve this are micro/nanomechanical cleavage, based upon the Scotch tape peeling method[15] and the use of a piezoelectrically micro-positioned ultra-sharp tungsten tip under high-resolution (TEM) imaging, respectively. Clean, highly-controlled production of few-to-monolayer TMDs with lateral dimensions up to ≈500 µm are achieved,[88,89] selectively yielding monolayers when applying a tip voltage bias (Figure 2.4b).[90]

A less technically challenging strategy to produce few-to-single layer TMDs is liquid phase exfoliation. Proposed by Coleman and co-workers, this consists on the shear-driven dispersion of bulk TMD single crystals in a solvent by use of a sonicating probe or a mechanical mixer, followed by size separation under sequential centrifugation and collection of supernatants. Initially surveyed using ca. 30 solvents of different polarities, these yielded air-insensitive and almost defect-free suspensions of several TMDs and h-BN.[91] Later investigations maximized the TMD concentration in solvent (ca. 40 mg ml^{-1} in MoS_2), with TMD nanoflake dimensions inversely proportional to the centrifugation rate employed (Figure 2.4c)[92] and experimentally proved by optical extinction spectroscopy.[93] Exfoliation yields, improved for a given centrifugation rate by higher TMD initial concentrations, higher sonication power and longer sonication times (Figure 2.4d),[94] are heavily affected by the solvent employed.

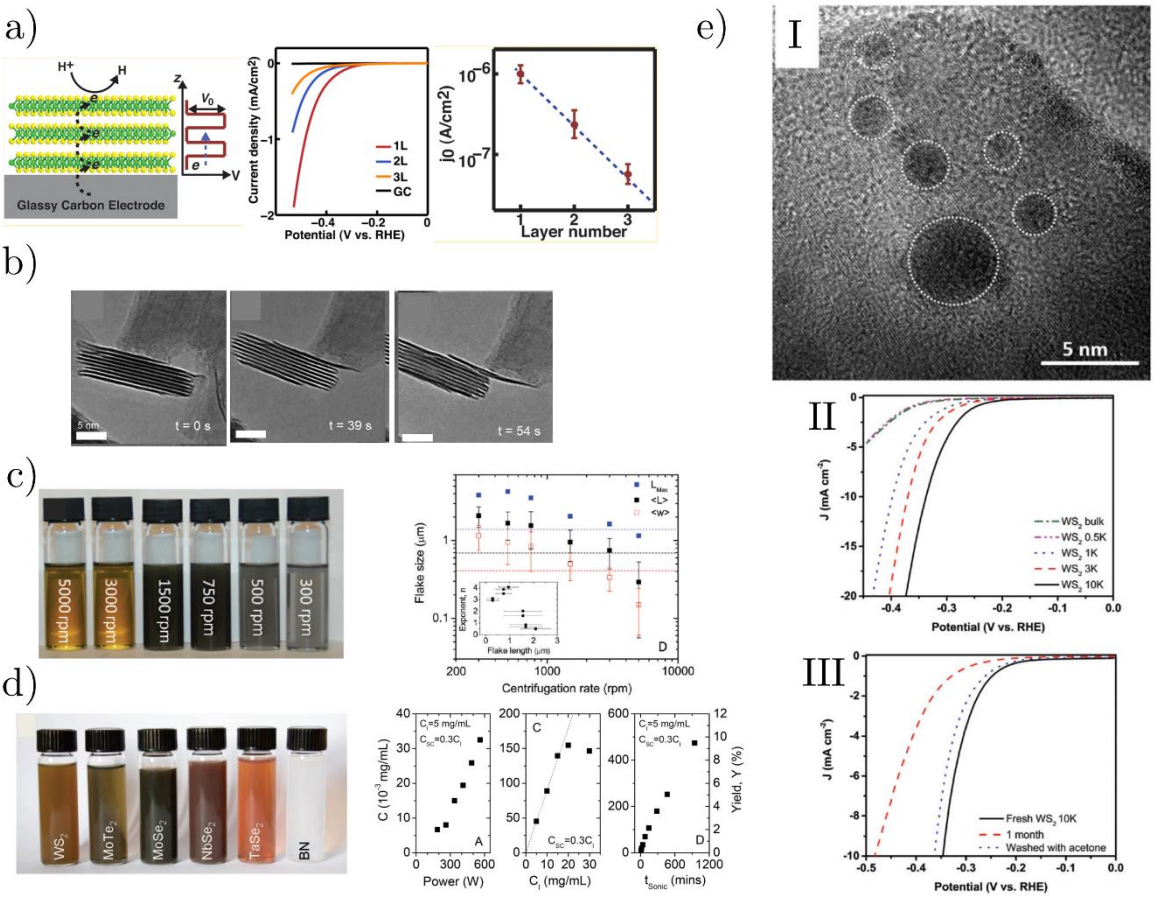

Figure 2.4. a) Left to right: Schematic of the layer-dependent through-plane TMD electron transfer, HER polarization curves as a function of MoS_2 layer number and j_0 value dependence with layer number. b) TEM images obtained during in situ lateral sliding of a MoS_2 monolayer using a W probed dc biased at +10 V. c) Left: Centrifugation rate-dependent liquid exfoliated MoS_2 nanosheets dispersed in DMF. Right: Maximum length (blue), average length (black) and width (red) MoS_2 nanosheet size as a function of the centrifugation rate. d) Left: Surfactant-stabilized dispersions of multiple liquid exfoliated layered TMDs and h-BN. Right: MoS_2 exfoliation yield dependence on sonication power, initial concentration (C_I) and sonication time (t_{sonic}). e) Room temperature ionic liquid exfoliated WS_2 nanodots, I) TEM imaged after 10000 rpm sequential centrifugation. II) Centrifugation rate-dependent (500-10000 rpm) HER catalysis after redispersion in DMF. III) HER polarization curves of 10000 rpm centrifuged fresh (black), 1 month aged (red) and 1 month aged after acetone washing (blue) WS_2 nanodots. Reproduced from refs. [85,90,92,94,95].

TMDs obtained by gradient centrifugation,[96] i.e. size resolution by mass-dependent sedimentation, were employed in numerous HER electrocatalysis studies.[97–99] Recent studies on the effect of sonication time and dispersing solvent in HER catalysis were evaluated: sonication times which yielded smaller WS_2 NP size distributions presented enhanced performances,[100] whilst choice of solvent negatively shifted η at -10 mA cm^{-2} by 150 mV (-0.57 V in acetonitrile vs. -0.72 V in methanol) ascribed to solvent-dependent dispersion and adsorption effects.[101] In case of DMF, ageing of WS_2 nanosheet dispersions tend to restack, trapping DMF adsorbates and residues at the interlayers which overall hamper through-plane electron transfer (Figure 2.4e).[95] Detrimental performances (250 mV negatively shifted η) were also found for ionic surfactant-modified exfoliated MoS_2 nanosheets due to surfactant-induced active sites blocking.[102] Alternatively, monolayers obtained from partially-amorphous MoS_2 presented improved hydrogen production compared with fully-crystalline counterparts.[103] Thus, experimental parameters responsible for improved exfoliation yields and selective control of size distributions are pending challenges in liquid exfoliation,[104,105] as these result in dramatic modifications in HER catalysis.

Few-to-single layer TMDs can also be chemically produced by intercalation of electron-donating guest species such as alkali metals, Lewis bases and organolithium compounds into the TMD interlayer gaps[48,106]: negatively charged electron acceptors cannot be intercalated due to electrostatic repulsion with the chalcogen layers.[107] Alkaline and organolithium intercalation of TMDs, dating back to the 1970's,[108,109] is based upon the violent exothermic reaction between the intercalated alkali cations (IA^+) after water/moisture exposure to produce volume-expanding alkali hydroxides and hydrogen, (see reaction 2.4) obtaining negatively-charged single layers[110] which can be collected by (induced) precipitation as interlayer-expanded restacked MX_2.[111]

$$IA_xMX_2 + x\,H_2O \rightarrow MX_2\,(nanosheets) + x/2\,H_2 + x\,IAOH \quad (2.4)$$

Intercalating agent-induced TMD interlayer expansion is generally promoted by ultrasonication, but recent investigations on group IV-VI TMDs have shown that manual shaking under controlled lithiating conditions enable to obtain large-sized monolayers (e.g. > 100 μm for TaS_2, Figure 2.5a).[112] Alkali-assisted Mo/WX_2 interlayer expansion is also accompanied by a partial phase transition from the semiconducting 2H polytype to the hydrophilic 1T metallic polytype (Figure 2.5b),[54,113,114] retained after restacking,[115] and reported to be 10^7 times more conductive.[116] For MoS_2, complete transformation of the 2H basal planes to the distorted 1T' phase can be achieved by extended Li intercalation times,[117] where Li^+ occupies the interlayer S-S tetrahedron sites.[118]

1T-MoS_2 and 1T-WS_2 monolayers obtained by Li intercalation presented excellent HER performances with respect to the 2H polytypes: 187 mV overpotential at 10 mA cm^{-2} with b= 43 mV dec^{-1} (Figure 2.5c),[119,120] and ca. 200 mV overpotential at 10 mA cm^{-2} with b= 55 mV dec^{-1},[121] respectively, related to the high density of active sites and lower charge transfer resistance (R_{ct}). Another study, employing a liquid-ammonia-assisted-lithiation method,[122] reported the preparation of mesoporous (holey) 1T- and 2H-MoS_2 monolayers, in which synergistic HER improvements were found between 1T phase and sulfur vacancies presence.[123] Exfoliated TMDs were alternatively produced by a KOH,[124] NH_3 [125] and superacid-assisted methods.[126]

The degree and type of intercalating agents has undisputed implications in HER electrocatalysis, extensively investigated by Pumera and co-workers. Initial investigations focused in MoS_2 by use of different Li intercalation compounds: methyl, n- and t-butyl lithium (t-BuLi). It was observed that t-BuLi intercalation produced smaller TMD nanosheet lateral sizes and layer numbers (1-8), which resulted in lower overpotentials (160 mV vs. 280 mV in bulk) and Tafel slopes (94 vs. 151 mV dec^{-1}).[127] Posterior investigations with other TMDs (MX_2, M= Mo, W; X= S, Se) using t-BuLi as an intercalant initially correlated improved HER

catalysis with higher exfoliation yields (Figure 2.5d),[128] later proven to be controlled by higher 1T phase contents arising from a more efficient 2H→1T conversion.[129] The influence of the intercalating alkali cation was also evaluated, observing again a good correlation between higher 1T phase contents and HER performances (best performers: Li^+ for MoS_2, Na^+ for WS_2) with larger hydrated interlayer interspacings and 1T phase stabilization upon cation-assisted proton intercalation (Figure 2.5e).[130]

Stabilization of the chemically-exfoliated TMD dispersions, critical for their long-term application, has been reported by covalent functionalization with organoiodides,[131] Bronsted acids,[132] ammonia,[133,134] thiol-terminated ligands,[135,136] diazonium salts,[137] and polymeric interspacers,[138] among others. The general origin of the increased stability is either the functionalization of the edge sites or partial relaxation of the metastable 1T phase to the 2H phase, achieving full conversion by thermal annealing.[139] Covalent functionalization with phenyl ring-based molecules containing electron-donating or withdrawing groups enabled to stabilize the HER-active 1T-MoS_2 phase, modulating its electrochemistry (Figure 2.5f): electron-donating groups facilitated electron-transfer kinetics (high TMD nanosheet conductance), and prevented the thermally-driven conversion to the 2H phase, which overall resulted in improved long-term HER stability.[140]

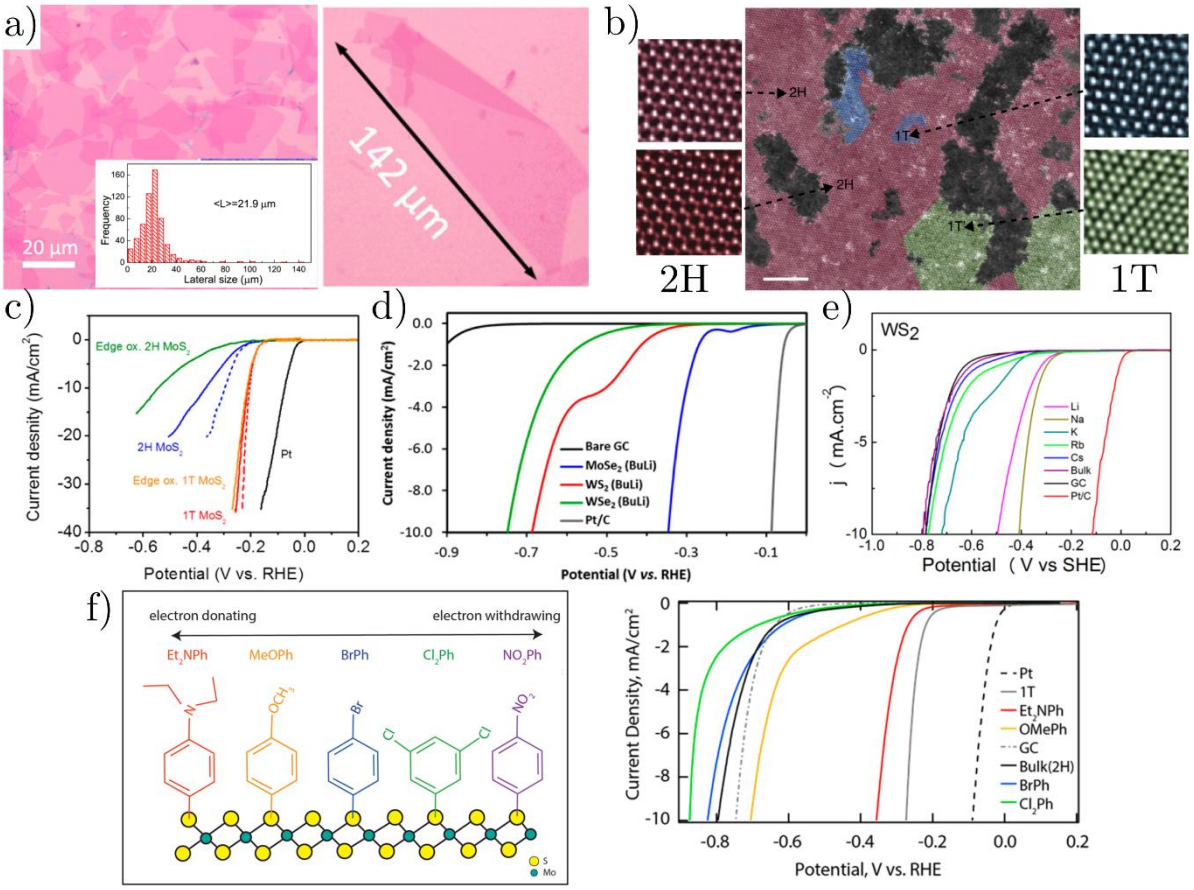

Figure 2.5. a) Optical images and size distribution (inset) of n-BuLi exfoliated TaS_2 nanosheets. b) Coloured high-resolution TEM images showing the coexistence of the 2H (red), 1T (blue) and distorted 1T' (green) MoS_2 polymorphs after partial 2H→1T conversion upon 72h n-BuLi intercalation and exfoliation. c) HER polarization curves of chemically-exfoliated 1T (red) and 2H (blue, after annealing) MoS_2 monolayer nanosheets. d) HER performance of different exfoliated TMDs for a given intercalating agent (BuLi): $MoSe_2$ (blue), WS_2 (red) and WSe_2 (green). e) Alkali cation-dependent HER performance for alkali metal naphtanelide-exfoliated WS_2 nanosheets. f) Left: Illustration of the electronic affinity of phenyl ring-based functional groups covalently bound to exfoliated MoS_2 nanosheets. Right: Corresponding HER polarization curves obtained for the covalently-functionalized MoS_2 nanosheets. Reproduced from refs. [112,117,120,128,130,140].

TMD exfoliation can also be induced by electrochemical methods, previously employed for graphene production,[141,142] such as electrochemically-assisted room temperature lithiation (Figure 2.6a),[143] and two-electrode anodization in aqueous (Figure 2.6b) or RTIL electrolytes.[144,145] The underlying mechanisms are based on the intercalation of in-situ generated Li^+, or the volume-expanding O_2 production from oxygen/hydroxyl radicals (as well as anions) within the electrolyte after applying a negative or positive bias on a TMD electrode, respectively. High-quality MoS_2 monolayers with a 92% yield, as well as lateral sizes within 5-50 µm were obtained. A particular case of TMD electrochemical exfoliation was found when MS_2 and MSe_2 (M = Mo, W) were selectively anodized to monolayers using TiN working electrodes in 1M LiCl electrolyte.[146,147] This, referred as self-limiting electro-ablation, was suggested to occur due to strong TMD-TiN interactions that limit the hydrogen peroxide TMD electro-oxidation up to the monolayer level (Figure 2.6c).[148]

Other alternative top-down TMD nanostructuring strategies have been explored, relying on physical methods. In brief, laser ablation was employed to successfully produce highly-crystalline 2 nm MoS_2 quantum dots,[149] whilst steam etching yields defective basal planes.[150] Alternatively, plasma etching successfully depletes TMD material by either exposing HER-active sulfur-vacancies with inert gases (Ar or H_2 plasma),[151,152] partially incorporating oxygen moieties at the TMD outermost surface (O_2 plasma),[153,154] or full layer-by-layer etching of the TMDs by formation of volatile MF_x compounds (N_2/SF_6 plasma, see Figure 2.6d).[155] Further insights on their HER activities will be given in Section 2.6.

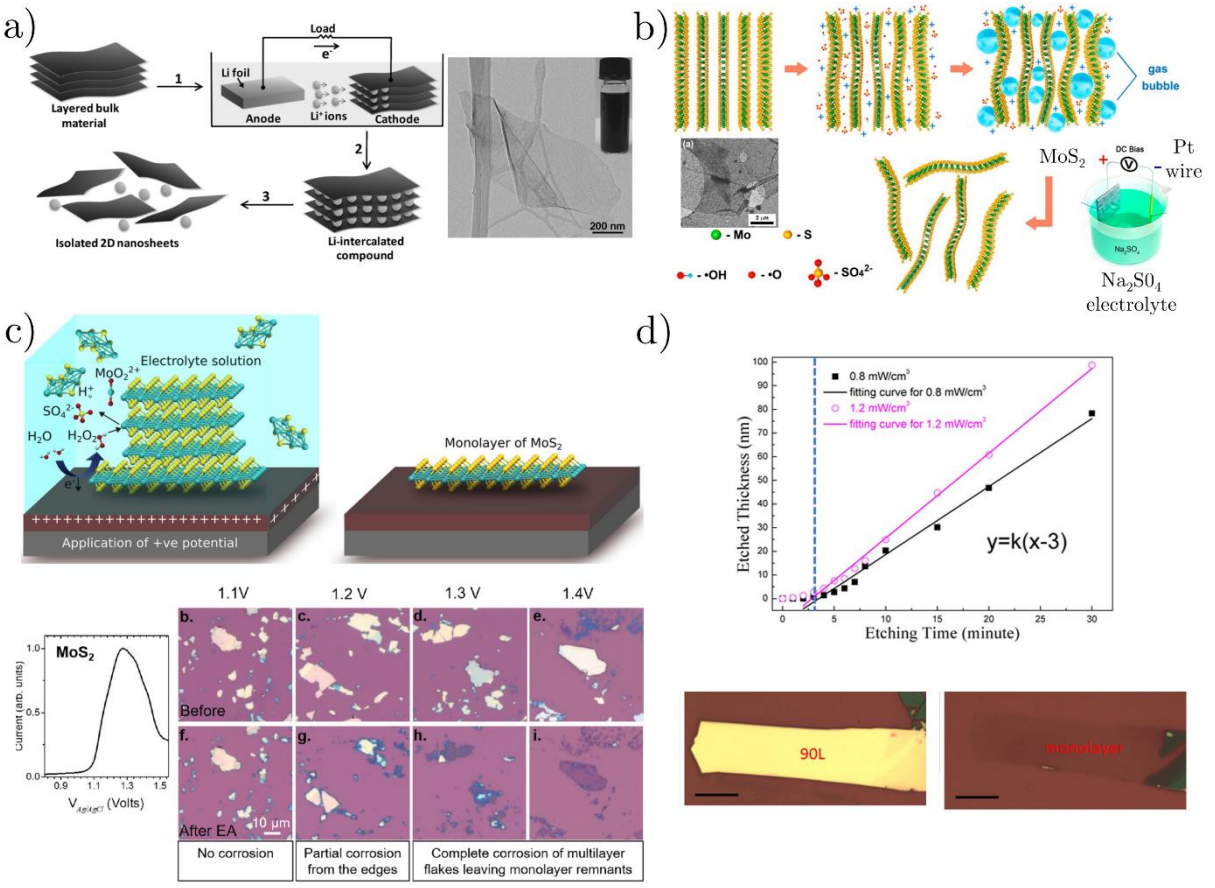

Figure 2.6. a) Left: Illustration of the electrochemically-assisted lithiation method to exfoliate monolayer TMDs. Right: TEM image of electrochemically-assisted lithium exfoliated MoS_2 monolayer. b) Illustration of the electrochemically-assisted TMD exfoliation via volume-expanding generation of O_2 and SO_2 in a two-electrode cell submerged in Na_2SO_4 electrolyte. Inset: TEM image of exfoliated MoS_2 nanosheet. c) Top: Illustration of the self-limiting electro-ablation mechanism, yielding monolayer TMDs by in-situ H_2O_2 generation. Bottom: Anodic voltammogram of MoS_2, and the corresponding electro-oxidation feature in 1 M LiCl, and voltage-dependent (1.1-1.4 V held for 60 s) electro-ablation of MoS_2 multilayers. d) Top: Multilayered MoS_2 etching rate as a function of N_2/SF_6 plasma etching time. Bottom: Optical microscopy images of a ca. 90-layered MoS_2 flake before and after plasma etching. Reproduced from refs. [143,144,146,148,155].

2.4.2 TMD edge site exposure maximization: bottom-up methods

It is clear from Section 2.4.1 that exposure of the metastable 1T phase edge sites in the most employed TMDs (MoS_2 and WS_2), is key to obtain HER electrocatalysis. As top-down methods rely on the inherent phase of the starting TMDs, bottom-up TMD preparation methods provide a nanoengineering approach to selectively produce HER active phases with a suitable morphology for catalysis. Indeed, 1T-MoS_2 obtained by hydrothermal synthesis outperformed its analogue obtained by lithium intercalation for the HER.[156] Three main bottom-up methods have been reported in the literature: chemical/physical vapour deposition (CVD/PVD), thermal decomposition and wet-chemical synthesis.

CVD of TMDs is generally undertaken by either I) gas-phase reaction and condensation of vaporized transition metal and chalcogenide solid precursors under inert conditions, or II) temperature-induced chalcogenide incorporation of pre-formed metal nanoplatelets or nanofilms (normally produced by PVD) by use of a chalcogen carrier gas under reducing or inert atmosphere (H_2X/H_2 or H_2X/Ar), generating nanoplatelet or nanofilm structures. An excellent example of CVD-nanoengineered TMDs are the vertically aligned, edge-terminated MoS_2 and $MoSe_2$ films reported by Kong et al. The 1T edge sites are optimally exposed towards the electrolyte with a continuous electron-conducting path which circumvents the high through-plane resistivity of horizontally-aligned TMDs,[157] which significantly improved after Li electrochemical intercalation post-treatment (widened interlayer spacing, 2H→1T phase conversion)[158] or deposition in curved/rough surfaces (higher surface areas).[159]

Similar benefits have been obtained in other edge-oriented TMD nanofilms (Figure 2.7a).[160–162] Large-scale, high-quality TMD monolayers have been obtained by CVD,[31,36,85,163–166] with templates assisting the formation highly-ordered mesoporous nanostructures[167] or layer-controlled nanoparticles.[86] In all cases, deposition parameters deeply affect catalytically-relevant parameters such as morphology, composition[168] and crystallinity.[169] For example,

increasing operating temperatures,[170] larger relative distances between chalcogen precursor and metal surface (Figure 2.7b),[171] and lower H_2S:H_2 ratios[172] promoted morphology shifts from triangular to round-shaped in MoS_2 nanoplatelets. An Evans-Polanyi based site-dependent deposition barrier model enabled to construct a theoretical "kinetic phase diagram" dependent on MoO_3 and S partial pressures, were quantitative correlations with experimental morphologies were achieved and applicable to other CVD-grown TMDs.[173]

Diffusion-limited twin defect derived crystal growth, unaccounted in this model and modified by chalcogen-to-metal vapour ratios,[174] is responsible for the formation of fractal-like dendritic MoS_2 structures (Figure 2.7c).[175] These present high edge-to-basal plane ratios beneficial for HER catalysis,[176] yielding j_0 as high as 32 µA cm^{-2}, ca. 40 times higher the triangular counterpart and among the best for unmodified monolayer MoS_2.[177] Alternatively, use of mixed chalcogenide powders/stream gas enabled to obtain ternary ($MoS_{2(1-x)}Se_{2x}$, $WS_{2(1-x)}Se_{2x}$)[178,179] and quaternary alloys ($Mo_xW_{(1-x)}S_{2y}Se_{2(1-y)}$)[180] with tuneable optoelectronic and HER activities. Highly-crystalline, thickness-controlled wafer-scale TMD nanosheet films were obtained by atomic layer deposition,[181] molecular beam epitaxy[182] or PVD methods such as pulsed layer deposition,[183] with high purities but scarce HER application due to their cost-intensive nature.[184,185]

PVD methods comprise the sublimation of TMD targets or powders by a plasma (magnetron sputtering, see section 3.4) or a heat source (thermal evaporation), with a subsequent condensation onto a substrate in UHV or inert gas atmosphere, and mainly reported for group VI TMDs.[186] For magnetron sputtered MX_2, there is a preferential evaporation of X, yielding sub-stoichiometric nanoclusters[187] or films[188,189] with amorphous structure, whilst morphology and stoichiometries for thermal-evaporated TMDs are similarly controlled as in CVD (operating temperatures, condensation length, carrier gas flux/composition).

Thermal decomposition is based upon the thermolysis of a MX_2 precursor powder or aqueous solution in presence/absence of H_2. The HER performances obtained with this method are noteworthy: a freezed-dried, thermally decomposed MoS_2 aerogel presented extremely high surface areas (≈ 700 m^2 g^{-1}) and HER performances (100 mA cm^{-2} at 260 mV),[190] whereas a $W_xMo_{(1-x)}S_2$-rGO composite an extraordinary low overpotential (96 mV at 10 mA cm^{-2}) and Tafel slope (38.7 mV dec^{-1}) (Figure 2.7d).[191] A recent temperature-dependent crystallinity study showed that maximized HER performances were obtained for 300°C annealed films, where a trade-off between intrinsic activities (higher TOF) and active edge site density (crystallinity degree) was found.[192]

Lastly, wet-chemical synthesis methods are aqueous (hydrothermal) or organic (solvothermal) solvent-based methods by reaction of appropriate TMD chemical precursors under high-pressure conditions (achieved in autoclaves) or inert atmospheres (colloidal synthesis) with high potential to scale-up. These yield edge- and defect-rich nanostructures with tuneable morphologies, which for group VI TMDs contain the metallic 1T phase responsible for HER catalysis (see Figures 2.8a-g). In general, longer reaction times and higher temperatures in wet-chemical synthesis methods yield improved crystallinities and higher stacking degrees. Wet-chemical synthesis methods were also implemented to produce composites with highly-conducting supports or transition metals, covered in the next sections.

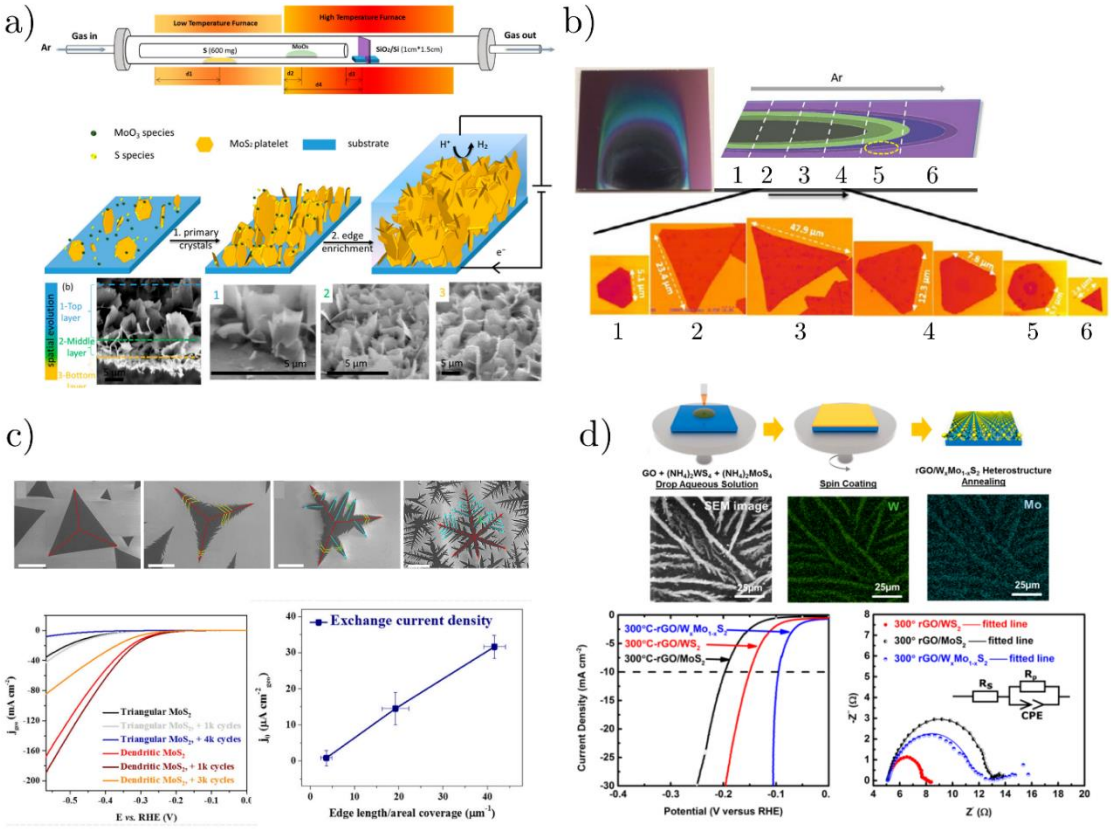

Figure 2.7. a) Top: Atmospheric-pressure CVD deposition setup based upon gas-phase TMD condensation on a substrate (here a vertical purple sheet), Bottom: Schematic of the edge-oriented MoS_2 platelets growth and SEM cross-section morphology analysis. b) CVD-grown MoS_2 deposition pattern obtained as function of the spatial location-induced MoO_3 concentration gradient in sections 1-6, and their corresponding SEM micrographs showing MoS_2 nanoplatelets shape evolution. c) Top: Shape evolution of MoS_2 nanoplatelets dependent on local chalcogen-to-metal vapour ratios, ranging from triangular to highly dendritic via star/branched triangular morphologies. Bottom: Morphology-dependent HER performance, and linear correlation between MoS_2 dendrite edge density and j_0. d) Top: Schematic of the spin coating-based thermal decomposition synthesis of $W_xMo_{(1-x)}S_2$ on reduced graphene oxide (rGO). Bottom: HER and electrochemical impedance spectroscopy (EIS) of $W_xMo_{(1-x)}S_2$/rGO (blue) versus their MoS_2 (black) and WS_2 (red) analogues. Reproduced from refs. [160,171,177,191].

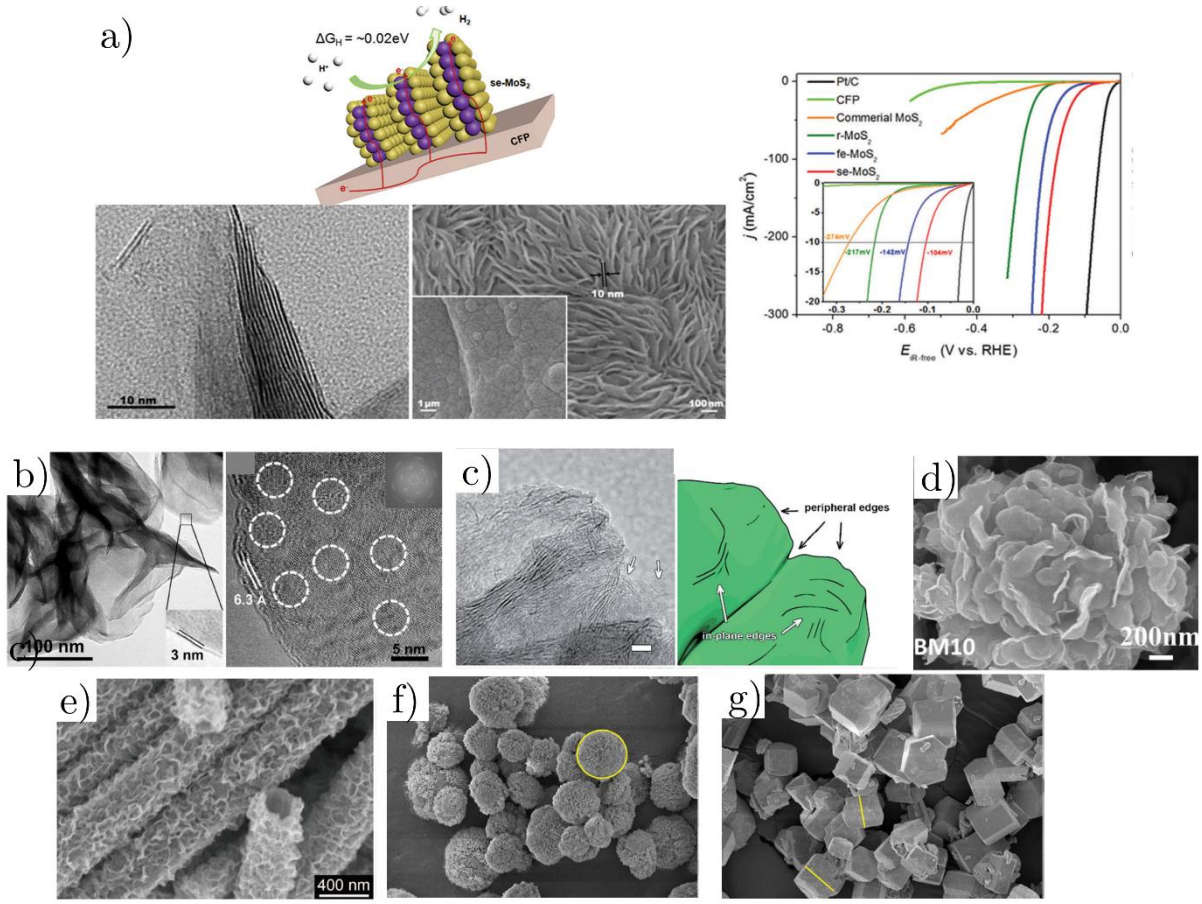

Figure 2.8. a) Left: Illustration of the stepped edge MoS_2 vertically-aligned array nanostructure (top), and high-resolution TEM and FE-SEM images showing their stepped nature and edge termination (bottom), Right: HER polarization curves obtained for stepped edge (red) versus flat edge (blue) and commercial (yellow) MoS_2 nanostructures. b-g) Compilation of TMD morphologies obtained by wet chemical synthesis: defect-rich nanosheets, in-plane edge-rich nanosheets, nanoflowers, hollow porous nanotubes, marigold-like nanoflowers and rhombic dodecahedra. Reproduced from refs. [193–197].

On a separate note, molecular catalysts with edge-mimicking structures are an alternative strategy to maximize group VI TMD activities, as the under-coordinated motifs obtained are intrinsically free of basal planes. The pioneering work by Karunadasa et al., who proposed the Mo-edge analogue $[(PY_5Me_2)MoS_2]^{2+}$, was followed by the synthesis of $[Mo_2S_{12}]^{2-}$ (Figure 2.9a-b)[198] and $[Mo_3S_{13}]^{2-}$ clusters (Figure 2.9c)[199] with improved TOF values per Mo unit (ca. 3 s^{-1} at η=200 mV). Amorphous MS_3 thin films prepared by wet-chemical synthesis[200,201] or electrodeposition from $[MS_4]^{2-}$ aqueous solutions,[202–204] the latter constituted by $[Mo_3S_{13}]^{2-}$ polymeric domains in MoS_3,[205] also presented improved HER performances. The preliminarily ascribed role of terminal S_2^{2-} ligands as the HER active sites in acid[169,206] or under-coordinated Mo atoms[205] was later related to higher S_2^{2-} bridging and S^{2-} apical contents (Figure 2.9d)[198,207] and finally to the S_2^{2-} bridging bond cleaving induced by proton electroadsorption by in operando Raman experiments (Figure 2.9e),[208] which results in S loss and an irreversible structural conversion from MoS_3 to MoS_{2+x} responsible for electrocatalysis.[209,210]

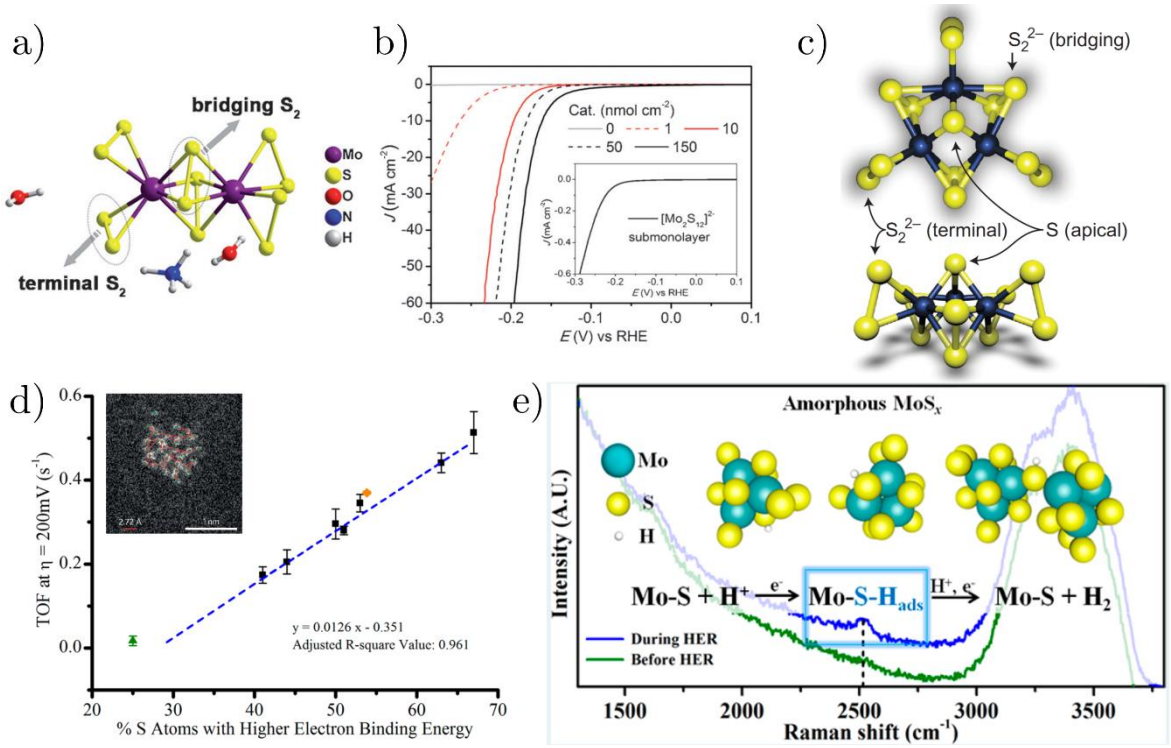

Figure 2.9. a) Chemical structure of the edge-mimicking $(NH_4)_2[Mo_2S_{12}]$ cluster. b) Loading-dependent HER performance of the $[Mo_2S_{12}]^{2-}$ cluster catalyst. c) Chemical structure of the $[Mo_3S_{13}]^{2-}$ cluster (top and lateral perspective). d) Hydrogen TOF dependence on the XPS amorphous electrodeposited MoS_x content on high binding energy S_2^{2-} bridging and S^{2-} apical contents. Inset: HAADF-STEM image showing $[Mo_3S_{13}]^{2-}$ cluster-based structure on electrodeposited MoS_x. e) In operando Raman spectra recorded on amorphous electrodeposited MoS_x before (green) and during (blue) HER operation, showing H-S vibration band. Reproduced from refs. [198,199,205,207,208]

2.5 Transition metal dichalcogenides: strategies for maximizing the inherent electroactivity of the active sites

The activity of TMD active sites towards the HER can be maximized if $\Delta G_H{}^*$ values are optimized to reach the ideal thermo-neutral value and the electron-transfer between the active sites and the conducting electrode is accelerated.

Group V TMDs (namely VS_2, TaS_2 and NbS_2), known to be inherently metallic, present close-to-zero $\Delta G_H{}^*$ values in the basal planes based on DFT calculations (-0.14, 0.17 and 0.01 eV for VS_2, NbS_2 and TaS_2, respectively)[211] which makes them highly active to the HER, as their activity is not limited to the edge sites: η=50-65 mV at 10 mA cm^{-2} with 10-55 µg cm^{-2} loadings (NbS_2 and TaS_2),[212,213] and η = 58 mV at 10 mA cm^{-2} with b = 34 mV dec^{-1} (VS_2),[214] which for TaS_2 can be further maximized using the 3R polytype due to improved hydrogen electroadsorption,[215] mimicking results obtained for MoS_2/WS_2.[216] These outstanding performances cannot be matched by pristine group VI TMDs (MoX_2, WX_2), where the 2H semiconducting basal planes are inactive.

DFT calculations showed that MoS_2 and WSe_2 should preferentially catalyse the HER in the Mo-edge and Se-edge, respectively,[76,217] whilst for WS_2 and $MoSe_2$ both edge sites should be indistinctively active.[77,217] Sub-stoichiometric transition metal (TM) doping was found to decrease $\Delta G_H{}^*$ in the MoS_2/WS_2 S-edge sites to quasi thermo-neutral values: 0.10 and 0.07 eV, respectively when using Co.[77] Posterior DFT calculations inversely correlated $\Delta G_H{}^*$ with ΔG_S, a thermodynamic descriptor related to the TM-S binding energy: a weakening in the doping metal-S bond strengthens the H-S bond at the S-edge, lowering $\Delta G_H{}^*$ close to thermo-neutral values for dopants such as group VII (Mn, Re) and group VIII-X (Fe, Co, Ni, Pt, Rh, etc) TMs (Figure 2.10a).[218] This $\Delta G_H{}^*$ comparable to the undoped MoS_2 Mo-edge not only activates them to the HER[77] but also results, for PVD nanoclusters, in a morphology

modification from triangular to hexagonal due to the thermodynamic stabilization of the S-edge.[219] Non-selective edge doping is obtained by co-electrochemical deposition using $[MoS_4]^{2-}$ and Fe/Co/Ni[220] or Pt[221] precursors in an aqueous solution, yielding up to 7-fold improved j_{geom} and Pt-comparable activities for $Pt_{0.1}MoS_{2.5}$, respectively.

Other strategies for non-selective TM doping reported for HER enhancement are the preparation of TMD/TM core-shells;[222] TMD-TM sub-stoichiometric composites prepared by wet chemical synthesis;[223] TM interlayer intercalation (Co, Ni, Pd, Pt)[224–226] or doping to stabilize the HER-active 1T polytype (Nb, Re, Ta or V)[53,227]; and electrochemically-induced Ag,[228] Ni,[229] Pt [230] or Pd[231] decoration of TMD nanosheets. Selective edge doping was achieved in edge-terminated, vertically-aligned MoS_2 nanosheets where the 2-fold (Cu) and ca. 3-fold (Fe,Co,Ni) j_0 enhancement was directly correlated to the S-edge sites activation (Figure 2.10b).[232]

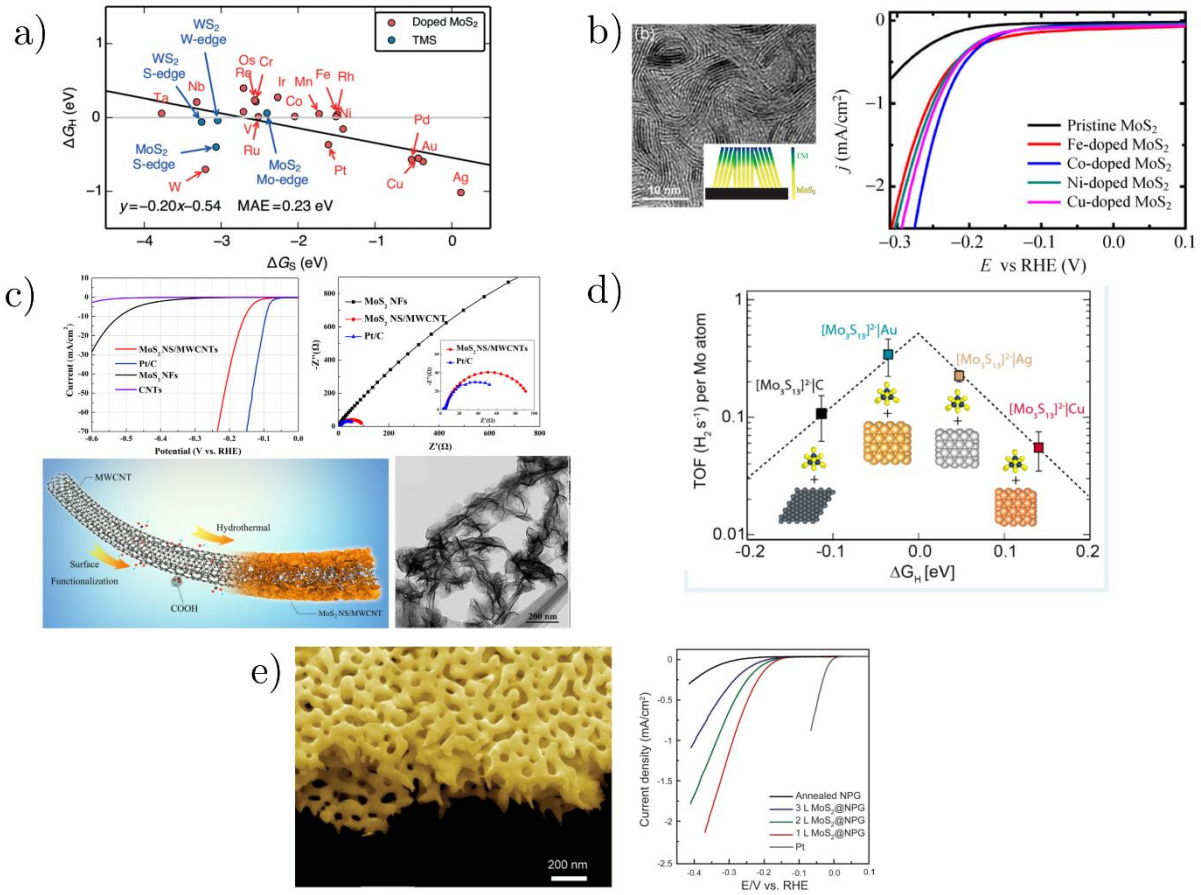

Figure 2.10. a) Plot of $\Delta G_H{}^*$ as a function of the TM-S edge binding energy ΔG_S. b) Left: TEM image of the vertically-aligned TM-doped MoS_2 nanosheets (lateral TM concentration profile on inset), Right: HER polarization curves before (black) and after Fe (red), Co (blue), Ni (cyan) or Cu (magenta) doping. c) Top: HER and EIS performance before (black) and after (red) multiwall CNTs functionalization of MoS_2 nanosheets, Bottom: Schematic and TEM image of MoS_2-multiwall CNTs composite. d) "Volcano plot" of hydrogen TOF per Mo atom as a function of support-dependent $[Mo_3S_{13}]^{2-}$ clusters $\Delta G_H{}^*$. e) Left: SEM micrograph of MoS_2-modified 3D nanoporous gold, Right: MoS_2 layer-dependent HER electrocatalysis of modified nanoporous gold substrate. Reproduced from refs. [218,232–235].

Alternatively, non-metallic anion doping was also employed for improving HER activities. Chalcogenide anions such as Se, more metallic than S, improved MoS_2 electron transfer rates,[236] whereas MoS_2 p-type doping with N via N_2 plasma[237] or wet chemical synthesis (metal precursor and thiourea)[238] decreased $\Delta G_H{}^*$ on the S-edge from -0.778 to 0.06 eV,[239] activating their HER activity alongside with improved conductivities.[240,241] Molybdenum phosphosulfides ($MoS_{2(1-x)}P_x$), prepared by post-sulfidation of MoP,[242] electrochemical deposition from $[MoS_4]^{2-}$ and sodium hypophosphite[243] or thermal annealing[244,245] also presented equivalent benefits for HER catalysis, notably higher stabilities. In some cases, however, TM doping (Nb, Ta) or metallic impurities have been found detrimental for HER catalysis.[246,247]

TMD anchoring with highly-conducting materials aimed to accelerate the charge transfer kinetics between the TMD active sites and the electrode, one of the limiting factors of layered materials, by providing an interconnected network.[248,249] HER enhancements after conductive composite fabrication generally manifested as significantly reduced R_{ct} and Tafel slope values (close to 40 mV dec^{-1} as found in the Volmer- Heyrovský mechanism).

Carbon-based supports, given their inexpensive nature and allotropy, were extensively employed: graphdiyne,[250] rGO,[60,251] (N-doped) carbon nanotubes (CNTs) (Figure 2.10c),[252] (N-doped) carbon nanofiber paper/cloth/foam,[158,193] carbon black[253] and carbonized wood microchannels,[254] among others.

Catalyst-support interactions, if strong, can also result in almost thermo-neutral $\Delta G_H{}^*$ values: NbS_2-Hf/$ZrSe_2$ and TaS_2-$HfSe_2$ heterostructures,[255] as well as Mo-edges on MoS_2-Au[256] presented the most favourable $\Delta G_H{}^*$ according to DFT calculations, the latter experimentally corroborated by improved HER performances by 3-fold increase in TOF vs. a glassy carbon support (Figure 2.10d).[234] Nanoporous Au-supported TMDs were fabricated accordingly,[162,257] where an additional strain-induced local 2H→1T MoS_2 phase transitions

synergistically maximized the HER performances (Figure 2.10e).[258] Other TMD conducting supports reported are black phosphorous,[259] h-BN,[260] CN,[261,262] MoO_2,[263] Si,[264], Ti_3C_2, [265] and TiO_2.[266]

Surprisingly, electrochemically-induced proton[267] and alkali cations[268] intercalation also decreased the charge transfer resistance and $\Delta G_H{}^*$ to more thermo-neutral values, without modifications of the TMD polytype or interlayer spacing.

2.6 Group VI Transition metal dichalcogenides: strategies for activation of basal plane sites

Activation of the electrocatalytically-inert group VI TMD basal planes to the HER has devoted significant attention in recent years. This was initially achieved by triggering the 2H→1T polytype conversion after chemical intercalation (see section 2.4.1), tensile/compressive strain,[222,235,269–272] or chemical vapour exposure,[273] which also modulated their optoelectronic[274,275] and magnetic properties[276–278] (see section B Appendix). The most relevant basal plane activation strategies, involving structural engineering and incorporation of foreign metal/chalcogenide centers, are compiled in Tables 2.3 and 2.4.

Basal plane activation method	Activation mechanism	Experimental strategy employed	References
Tensile strain	Energy downshift of the unoccupied TMD defect levels, facilitated proton reduction [279]	Synthesis of nanostructures with intrinsically distorted structure (e.g. nanospheres, crumpled/concave-distorted nanosheets, amorphous MoS_x on Au nanopillars)	[280–282]
Lattice defects	S vacancy and edge sites exposure	Multiple synthetic routes	[123,194,283–287]
S vacancy generation	Under-coordinated M sites reach $\Delta G_H^* = 0$ under optimal strain The relatively low S vacancy formation energy (2.12 eV)[288] is significantly decreased when forming a vacancy row.[289]	Exposure to inert plasma source (Ar, H_2)	[151,152,290–292]
		Cation exchange resin	[293,294]
		Electrochemical conditioning: cathodic potentials (-1 V vs. RHE, Figure 2.11a), 0 to 2.2 V vs. RHE voltage cycling.	[295,296]

Table 2.3. Compilation of TMD basal plane activation strategies, along with the underlying activation mechanisms, based upon structural engineering.

Basal plane activation method	Activation mechanism	Experimental strategy employed	References
Oxygen incorporation ($MoS_{2-x}O_x$ solid solution)	Local n-doping. increased electron affinity at the basal plane, reduced ΔG_H^*, assistance in S vacancy formation (Figure 2.11b)	Spontaneous replacement of X atoms on the basal planes under long-term ambient exposure (1 year)	[287,297–299]
Single-atom metal doping (substitution at metal site)	Vicinal chalcogenide atoms ΔG_H^* reduction to thermo-neutral values [272]: 0.1, -0.02 and ca. 0 eV for Ni, Pd and Pt, respectively	Dopants: Co, Cr, Er, Mn, Ni, Nb, Pd, Pt, (Figure 2.11c), Re and V.	Co,[300,301] Cr,[302] Er,[303] Mn,[240,304] Ni,[305–307] Nb,[308] Pd,[226,309,310] Pt,[311] Re[312] and V.[302]
Single-atom chalcogenide substitution	• B: basal plane active site (Figure 2.11d) • P: substantial decrease in the nearest-neighbour chalcogen ΔG_H^* • N/P: induced compressive strain to narrow the electronic band gap and improve intralayer charge transfer rates.[239,244] • F, N co-doping: sygnergistic activation of N as the basal plane active site (ΔG_H^* ca. -0.145 eV).[313]	Multiple synthetic routes	B,[314] F,[313] N,[267,286,288] and P. [244,316]

Table 2.4. Compilation of TMD basal plane activation strategies, along with the underlying activation mechanism, based upon incorporation of foreign metal/chalcogenide centers.

Basal plane-activated TMDs present remarkable HER peformances. Intralayer oxygen-incorporated $MoS_{2-x}O_x$ solid solution presents a 3-fold j_{geom} increase at η=200 mV, similarly to that obtained for oxygen-incorporated 1T-WS_2: a 2-fold increase in j_0 versus the undoped counterpart suggests improved conductivities to be the doping effect.[317] For Pd single-atom doping of MoS_2, a close-to-Pt performance was achieved: 40 mV onset potential, b= 41 mV dec^{-1} and j_0= 426.58 µA cm^{-2}.[309] As for the chalcogenide substitutional dopants, P-MoS_2, N,Mn-MoS_2 and B-$MoSe_2$ presented HER electrocatalysis comparable to those of group V TMDs: 43, 66, and 84 mV η at -10 mA cm^{-2}; and b= 34, 50 and 39 mV dec^{-1}, respectively.[240,314,316]

Briefly, Janus TMDs (i.e. sandwiched X-M-Y structures, X/Y being different chalcogenides) have been theoretically[318,319] and later experimentally demonstrated to present HER-active basal planes,[320] with activities to be exploited in future investigations.

The underlying activation mechanisms are, yet, still a matter of debate. As an example, the HER enhancements obtained from cathodic preconditioning activation, related to S vacancy generation in MS_2 TMDs, are in stark contrast with previously reported electrochemical activation treatments by Chia et al., where the enhancements were ascribed to stabilized 1T phases[321] and a higher availability of Mo-edge sites.[322] Analogously, unambiguous understanding of the nature of any mixed n- and p-type doping, such as N/F co-doping, is concealed as n- and p-type dopants should in theory present opposing doping effects on TMDs. Basal plane activation in TMDs is, consequently, a promising research field but efforts need to be made in deeper understanding of the activation mechanisms to fully harness their potential.

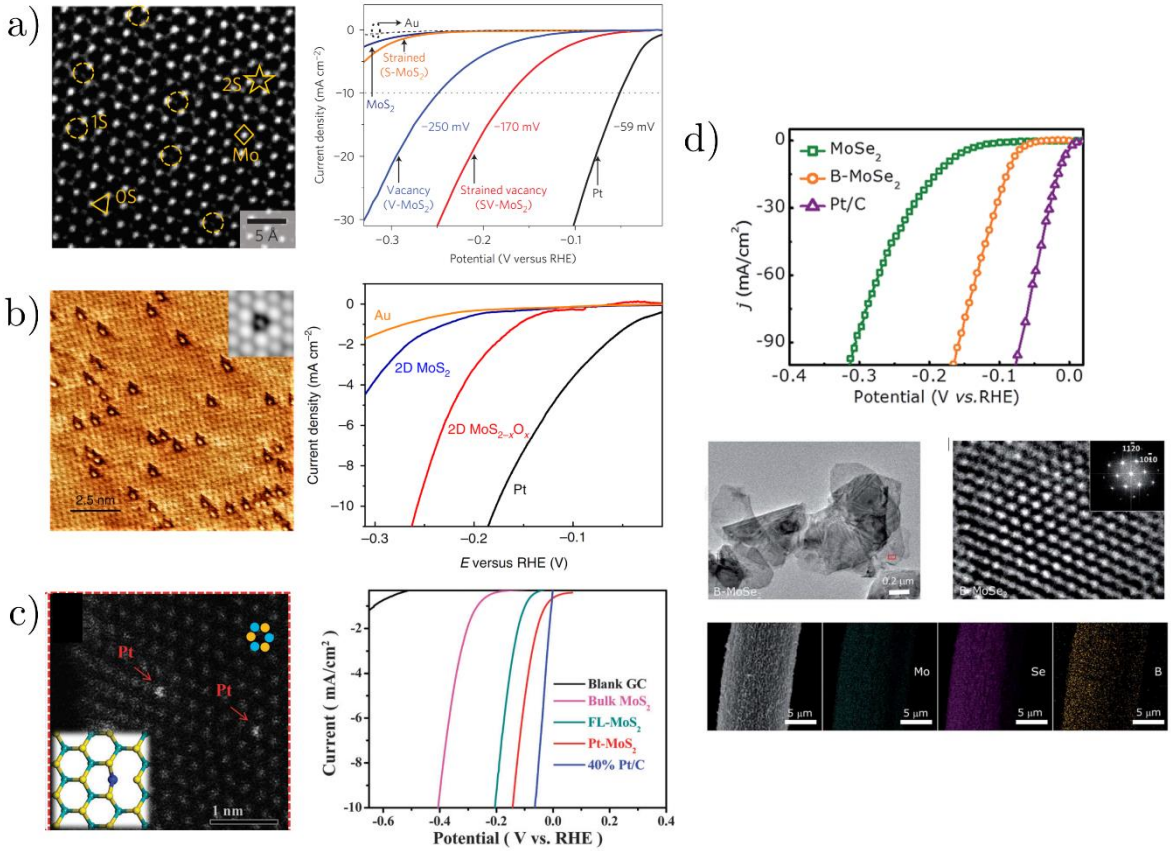

Figure 2.11. a) Left: Aberration-corrected TEM image of MoS_2 with S vacancies (ca. 12 %), Right: HER performance before (blue) and after (red) tensile strain application (ca. 1.35 %). b) Left: Scanning tunnelling microscopy image showing O-incorporated atoms at S vacancy sites (dark triangles) of $MoS_{2-x}O_x$ crystals, Right: HER performance before (blue) and after (red) O-incorporation. c) Left: HAADF-STEM image of single Pt atom-doped MoS_2 nanosheets, Right: HER polarization curves before (magenta) and after (red) Pt doping, and d) Bottom: High-resolution TEM imaging of B-doped $MoSe_2$ nanosheets along with their EDX mapping, Top: HER cathodic voltammograms recorded before (green) and after (yellow) B incorporation. Reproduced from refs. [290,298,311,314].

2.7 Transition metal dichalcogenides and the oxygen evolution reaction: activity and stabilization of Ir-based state-of-the-art catalysts

Replacement of PGM catalysts has driven research regarding the activity of TMDs towards oxygen evolution reaction (OER) electrocatalysis. In alkaline environments, materials such as MoS_2,[323] $CoSe_2$,[324] Ni_3Te_2,[325] $Ni_xFe_{1-x}S_2$,[326] Ni_3S_2 on Ni foam,[327] $Co_{1-x}V_xSP$[328] or CoX_2/NiX_2 (X = S, Se, Te)[329] were employed, among many others, with excellent activities and stabilities. Although still under debate, general consensus in the literature suggests that observed activities are a result of in situ partial/total TMD electro-oxidation under OER conditions to generate a porous metal (oxy)hydroxide layer responsible for the OER with high surface areas and active site exposures.[330] However, the majority of these (oxy)hydroxides are unstable in acid, preventing their implementation in PEM electrolyser technologies.

In such harsh acidic electrolytes, RuO_x and IrO_x are the state-of-the-art OER monoelemental materials,[331] as Pt (the HER and ORR metal champion) undergoes PtO_x formation which passivates its activity.[332] The benefits of acidic PEM electrolyser operation (see Chapter 1) are limited by the dissolution rates of RuO_x/IrO_x catalysts. Whilst OER activities present the trend Ru > Ir ≈ RuO_2> IrO_2, their dissolution rates increase as IrO_2 « RuO_2 < Ir « Ru.[333] Indeed, highly-active materials normally present an OER mechanism where lattice oxygen from surface metal oxides generated during OER operation (Ru, Ir)[334,335] or inherently present in the catalyst structure (perovskites)[336] assist in oxygen production: this is known as lattice oxygen evolution reaction, which aggravates their electrodissolution due to internal restructuring,[337] and is thermodynamically favourable.[338] For Ru, dissolution is ascribed to the OER-triggered formation of the volatile RuO_4 compound,[335] which can be stabilized by use of an overlayer of IrO_x,[339] thermal oxidation treatment[340] or mixed metal alloys/oxides.[73,341] In the case of Ir, the electrodissolution has been proven to be

overpotential-dependent (Figure 2.12a): high overpotentials favour the dissolution via IrO_3 oxidation to IrO_4^{-2}, whilst low overpotentials the formation of $Ir^{5+}O_2OH$ and ultimately the metastable $HIrO_2$ species to leach as Ir^{3+}.[342] Improved Ir stabilities were obtained for core-shell structures,[343] Ir-Ni mixed oxide thin films[344] or nanowires,[345] and Ir alloys such as $Ir_{0.7}Sn_{0.3}O_{2-x}$,[346] $IrO_x/SrIrO_3$,[347] or more recently $W_{1-x}Ir_xO_{3-\delta}$ (Figure 2.12b),[348] and composites such as IrO_2/MoO_3.[349] These contain the earth-abundant MoO_3 and WO_3, the resulting electro-oxidation products of group VI TMDs in acid (see Pourbaix diagrams in Figure 2.12c),[7,350,351] WO_3 being corrosion-resistant under both anodic and cathodic potentials[352] with robust OER photoelectrocatalytic activity[353] synergistically maximized when incorporating Ir.[354,355] To date, the exact stabilization mechanism of Ir-modified surfaces is still unknown, but use of earth-abundant oxides such as WO_3 as passivating agents towards improved Ir stabilities is of particular interest.

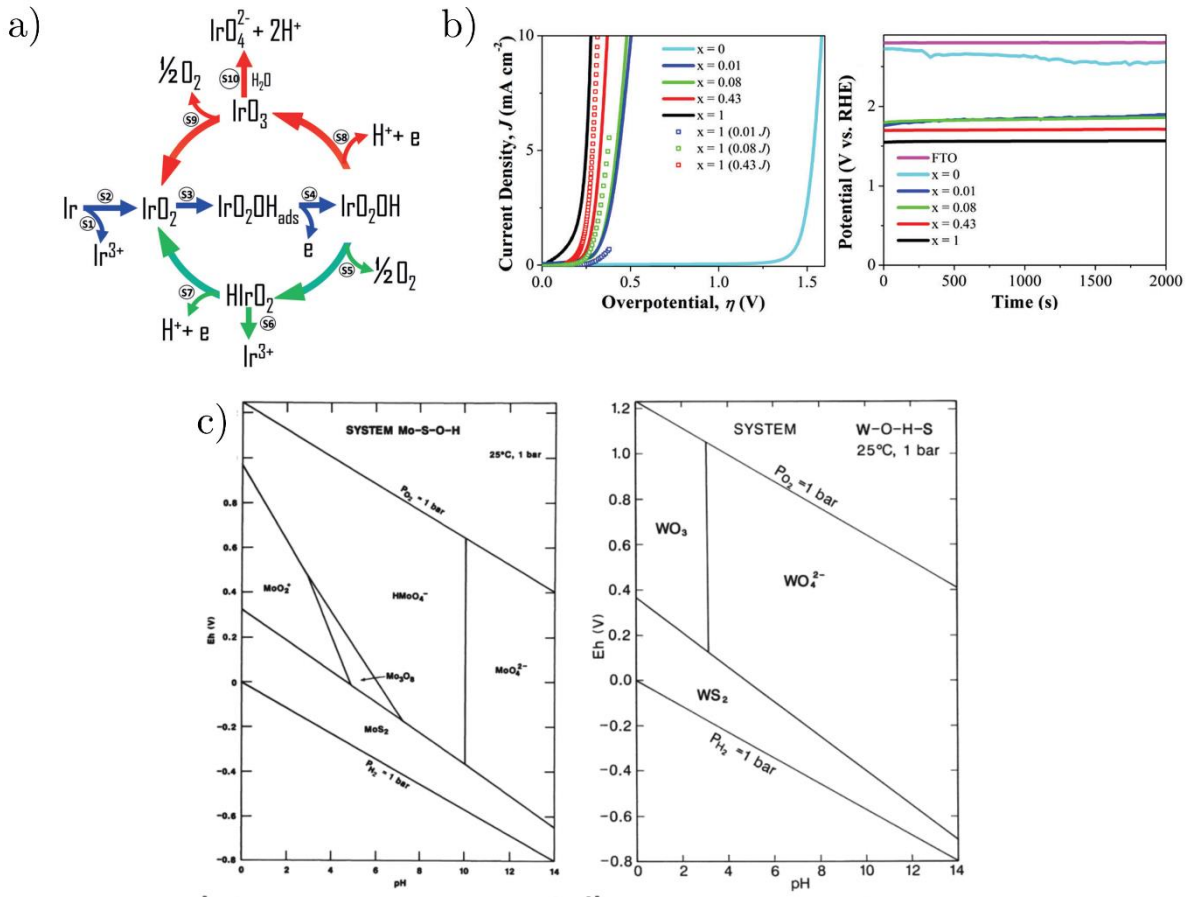

Figure 2.12. a) Schematic compiling the Ir electrodissolution pathways under OER operation: green and red arrows correspond to the dominating dissolution routes taking place at low and high OER overpotentials, respectively. Blue arrows show Ir intermediates and their associated reactions, observed irrespective of the OER operation overpotential. b) Left: OER polarization curves of plasma-synthesized $W_{1-x}Ir_xO_{3-\delta}$ thin films. Right: OER stability testing by j_{geom} hold at +10 mA cm^{-2}, Electrolyte: 1 M H_2SO_4. c) Pourbaix diagrams (Potential vs. pH) of molybdenum-sulfur-oxygen-hydrogen (left) and tungsten-sulfur-oxygen-hydrogen systems (right). Reproduced from refs. [7,342,348].

References

[1] M. Samadi, N. Sarikhani, M. Zirak, H. Zhang, H.L. Zhang, A.Z. Moshfegh, Group 6 transition metal dichalcogenide nanomaterials: Synthesis, applications and future perspectives, Nanoscale Horizons. 3 (2018) 90–204. doi:10.1039/c7nh00137a.

[2] J.D. Benck, T.R. Hellstern, J. Kibsgaard, P. Chakthranont, T.F. Jaramillo, Catalyzing the Hydrogen Evolution Reaction (HER) with Molybdenum Sulfide Nanomaterials, ACS Catal. 4 (2014) 3957–3971. http://pubs.acs.org/doi/abs/10.1021/cs500923c (accessed December 15, 2015).

[3] Y. Dou, L. Zhang, X. Xu, Z. Sun, T. Liao, S.X. Dou, Atomically thin non-layered nanomaterials for energy storage and conversion, Chem. Soc. Rev. 46 (2017) 7338–7373. doi:10.1039/c7cs00418d.

[4] H. Wang, H. Yuan, S. Sae Hong, Y. Li, Y. Cui, Physical and chemical tuning of two-dimensional transition metal dichalcogenides, Chem. Soc. Rev. 44 (2015) 2664–2680. doi:10.1039/c4cs00287c.

[5] D. Voiry, A. Mohite, M. Chhowalla, Phase engineering of transition metal dichalcogenides, Chem. Soc. Rev. 44 (2015) 2702–2712. doi:10.1039/c5cs00151j.

[6] D. Voiry, J. Yang, M. Chhowalla, Recent Strategies for Improving the Catalytic Activity of 2D TMD Nanosheets Toward the Hydrogen Evolution Reaction, Adv. Mater. (2016) 6197–6206. doi:10.1002/adma.201505597.

[7] X. Chia, A.Y.S. Eng, A. Ambrosi, S.M. Tan, M. Pumera, Electrochemistry of Nanostructured Layered Transition-Metal Dichalcogenides, Chem. Rev. 115 (2015) 11941–11966. doi:10.1021/acs.chemrev.5b00287.

[8] H. Wang, L. Gao, Recent developments in electrochemical hydrogen evolution reaction, Curr. Opin. Electrochem. 7 (2018) 7–14. doi:10.1016/j.coelec.2017.10.010.

[9] Y. Xue, Q. Zhang, W. Wang, H. Cao, Q. Yang, L. Fu, Opening Two-Dimensional Materials for Energy Conversion and Storage: A Concept, Adv. Energy Mater. 7 (2017) 1–23. doi:10.1002/aenm.201602684.

[10] K.S. Novoselov, A.K. Geim, S. V. Morozov, D. Jiang, Y. Zhang, S. V. Dubonos, I. V. Grigorieva, A. A. Firsov, Electric Field Effect in Atomically Thin Carbon Films, Nature. 306 (2004) 666–668. doi:10.1126/science.1102896.

[11] P. Miró, M. Audiffred, T. Heine, An atlas of two-dimensional materials, Chem. Soc. Rev. 43 (2014) 6537–6554. doi:10.1039/c4cs00102h.

[12] K.S. Novoselov, V.I. Fal'Ko, L. Colombo, P.R. Gellert, M.G. Schwab, K. Kim, A roadmap for graphene, Nature. 490 (2012) 192–200. doi:10.1038/nature11458.

[13] H.K. Chae, D.Y. Siberio-Pérez, J. Kim, Y. Go, M. Eddaoudi, A.J. Matzger, M. O'Keeffe, Omar M. Yaghi, A route to high surface area, porosity and inclusion of large molecules in crystals, Nature. 427 (2004) 523–527. doi:10.1038/nature02294.1.

[14] L.A. Ponomarenko, A.K. Geim, A.A. Zhukov, R. Jalil, S. V. Morozov, K.S. Novoselov,

I. V. Grigorieva, E.H. Hill, V. V. Cheianov, V.I. Fal'Ko, K. Watanabe, T. Taniguchi, R. V. Gorbachev, Tunable metalinsulator transition in double-layer graphene heterostructures, Nat. Phys. 7 (2011) 958–961. doi:10.1038/NPHYS2114.

[15] K.S. Novoselov, D. Jiang, F. Schedin, T.J. Booth, V. V Khotkevich, S. V Morozov, A.K. Geim, Two-dimensional atomic crystals, Proc. Natl. Acad. Sci. U. S. A. 102 (2005) 10451–10453. doi:10.1073/pnas.0502848102.

[16] C.R. Dean, A.F. Young, I. Meric, C. Lee, L. Wang, S. Sorgenfrei, K. Watanabe, T. Taniguchi, P. Kim, K.L. Shepard, J. Hone, Boron nitride substrates for high-quality graphene electronics, Nat. Nanotechnol. 5 (2010) 722–726. doi:10.1038/nnano.2010.172.

[17] D.L. Duong, S.J. Yun, Y.H. Lee, Van der Waals Layered Materials: Opportunities and Challenges, ACS Nano. 11 (2017) 11803–11830. doi:10.1021/acsnano.7b07436.

[18] W. Choi, N. Choudhary, G.H. Han, J. Park, D. Akinwande, Y.H. Lee, Recent development of two-dimensional transition metal dichalcogenides and their applications, Mater. Today. 20 (2017) 1–15. doi:10.1016/j.mattod.2016.10.002.

[19] S.Z. Butler, S.M. Hollen, L. Cao, Y. Cui, J.A. Gupta, H.R. Gutiérrez, T.F. Heinz, S.S. Hong, J. Huang, A.F. Ismach, E. Johnston-Halperin, M. Kuno, V. V. Plashnitsa, R.D. Robinson, R.S. Ruoff, S. Salahuddin, J. Shan, L. Shi, M.G. Spencer, M. Terrones, W. Windl, J.E. Goldberger, Progress, challenges, and opportunities in two-dimensional materials beyond graphene, ACS Nano. 7 (2013) 2898–2926. doi:10.1021/nn400280c.

[20] H. Tang, Q. Hu, M. Zheng, Y. Chi, X. Qin, H. Pang, Q. Xu, MXene–2D layered electrode materials for energy storage, Prog. Nat. Sci. Mater. Int. 28 (2018) 133–147. doi:10.1016/j.pnsc.2018.03.003.

[21] B. Anasori, M.R. Lukatskaya, Y. Gogotsi, 2D metal carbides and nitrides (MXenes) for energy storage, Nat. Rev. Mater. 2 (2017) 16098. doi:10.1038/natrevmats.2016.98.

[22] S. Balendhran, S. Walia, H. Nili, S. Sriram, M. Bhaskaran, Elemental analogues of graphene: Silicene, germanene, stanene, and phosphorene, Small. 11 (2015) 640–652. doi:10.1002/smll.201402041.

[23] J. Zhao, H. Liu, Z. Yu, R. Quhe, S. Zhou, Y. Wang, C.C. Liu, H. Zhong, N. Han, J. Lu, Y. Yao, K. Wu, Rise of silicene: A competitive 2D material, Prog. Mater. Sci. 83 (2016) 24–151. doi:10.1016/j.pmatsci.2016.04.001.

[24] A. Khandelwal, K. Mani, M.H. Karigerasi, I. Lahiri, Phosphorene – The two-dimensional black phosphorous: Properties, synthesis and applications, Mater. Sci. Eng. B Solid-State Mater. Adv. Technol. 221 (2017) 17–34. doi:10.1016/j.mseb.2017.03.011.

[25] A.H. Woomer, T.W. Farnsworth, J. Hu, R.A. Wells, C.L. Donley, S.C. Warren, Phosphorene: Synthesis, Scale-Up, and Quantitative Optical Spectroscopy, ACS Nano. 9 (2015) 8869–8884. doi:10.1021/acsnano.5b02599.

[26] S. Zhang, Z. Yan, Y. Li, Z. Chen, H. Zeng, Atomically thin arsenene and antimonene: Semimetal-semiconductor and indirect-direct band-gap transitions, Angew. Chemie - Int. Ed. 54 (2015) 3112–3115. doi:10.1002/anie.201411246.

[27] F.F. Zhu, W.J. Chen, Y. Xu, C.L. Gao, D.D. Guan, C.H. Liu, D. Qian, S.C. Zhang, J.F. Jia, Epitaxial growth of two-dimensional stanene, Nat. Mater. 14 (2015) 1020–1025. doi:10.1038/nmat4384.

[28] X. Sun, Z. Wang, Z. Li, Y.Q. Fu, Origin of Structural Transformation in Mono-and Bi-Layered Molybdenum Disulfide, Sci. Rep. 6 (2016) 2–10. doi:10.1038/srep26666.

[29] D.M. Andoshe, J.-M. Jeon, S.Y. Kim, H.W. Jang, Two-dimensional transition metal dichalcogenide nanomaterials for solar water splitting, Electron. Mater. Lett. 11 (2015) 323–335. doi:10.1007/s13391-015-4402-9.

[30] J.L. Verble, T.J. Wietling, P.R. Reed, Rigid-layer lattice vibrations and van der waals bonding in hexagonal MoS2, Solid State Commun. 11 (1972) 941–944. doi:10.1016/0038-1098(72)90294-3.

[31] A. Tarasov, P.M. Campbell, M.-Y. Tsai, Z.R. Hesabi, J. Feirer, S. Graham, W.J. Ready, E.M. Vogel, Highly Uniform Trilayer Molybdenum Disulfide for Wafer-Scale Device Fabrication, Adv. Funct. Mater. 24 (2014) 6389–6400. doi:10.1002/adfm.201401389.

[32] Y.H. Chang, W. Zhang, Y. Zhu, Y. Han, J. Pu, J.K. Chang, W.T. Hsu, J.K. Huang, C.L. Hsu, M.H. Chiu, T. Takenobu, H. Li, C.I. Wu, W.H. Chang, A.T.S. Wee, L.J. Li, Monolayer MoSe2grown by chemical vapor deposition for fast photodetection, ACS Nano. 8 (2014) 8582–8590. doi:10.1021/nn503287m.

[33] C.H. Naylor, W.M. Parkin, J. Ping, Z. Gao, Y.R. Zhou, Y. Kim, F. Streller, R.W. Carpick, A.M. Rappe, M. Drndić, J.M. Kikkawa, A.T.C. Johnson, Monolayer single-crystal 1T′-MoTe2grown by chemical vapor deposition exhibits weak antilocalization effect, Nano Lett. 16 (2016) 4297–4304. doi:10.1021/acs.nanolett.6b01342.

[34] N. Peimyoo, W. Yang, J. Shang, X. Shen, Y. Wang, T. Yu, Chemically Driven Tunable Light Emission of Charged and Neutral Excitons in Monolayer WS2, ACS Nano. 8 (2014) 11320–11329.

[35] H. Fang, S. Chuang, T.C. Chang, K. Takei, T. Takahashi, A. Javey, High-performance single layered WSe2p-FETs with chemically doped contacts, Nano Lett. 12 (2012) 3788–3792. doi:10.1021/nl301702r.

[36] J. Zhou, F. Liu, J. Lin, X. Huang, J. Xia, B. Zhang, Q. Zeng, H. Wang, C. Zhu, L. Niu, X. Wang, W. Fu, P. Yu, T.R. Chang, C.H. Hsu, D. Wu, H.T. Jeng, Y. Huang, H. Lin, Z. Shen, C. Yang, L. Lu, K. Suenaga, W. Zhou, S.T. Pantelides, G. Liu, Z. Liu, Large-Area and High-Quality 2D Transition Metal Telluride, Adv. Mater. 29 (2017). doi:10.1002/adma.201603471.

[37] K.F. Mak, C. Lee, J. Hone, J. Shan, T.F. Heinz, Atomically thin MoS2: A new direct-gap semiconductor, Phys. Rev. Lett. 105 (2010) 2–5. doi:10.1103/PhysRevLett.105.136805.

[38] P. Tonndorf, R. Schmidt, P. Bottger, X. Zhang, J. Borner, A. Liebig, M. Albrecht, C. Kloc, O. Gordan, D.R.T. Zahn, S.M. de Vasconcellos, Rudolf Bratschitsch, Photoluminescence emission and Raman response of monolayer MoS2, MoSe2, and WSe2, Opt. Express. 21 (2013) 4908–4916. doi:10.1201/9781315113722.

[39] O. Knop, R.D. MacDonald, Chalkogenides of the Transition Elements. III. Molybdenum Ditelluride, Can. J. Chem. 39 (1961) 897–904.

[40] J. Augustin, V. Eyert, T. Boker, W. Frentrup, H. Dwelk, C. Janowitz, R. Manzke, Electronic band structure of the layered compound Td-WTe2, Phys. Rev. B. 62 (2000) 10812–10823. doi:10.1038/s41467-017-00745-8.

[41] W.G. Dawson, D.W. Bullett, Electronic structure and crystallography of MoTe2and

WTe2, J. Phys. C Solid State Phys. 20 (1987) 6159–6174. doi:10.1088/0022-3719/20/36/017.

[42] B. E. Brown, The crystal structures of NbT2 and TaTe2, Acta Crystallogr. 20 (1966) 264–267. doi:10.1107/S0365110X66000501.

[43] W. Zhao, Z. Ghorannevis, L. Chu, M. Toh, C. Kloc, P.H. Tan, G. Eda, Evolution of electronic structure in atomically thin sheets of ws2and wse2, ACS Nano. 7 (2013) 791–797. doi:10.1021/nn305275h.

[44] K.K. Kam, B.A. Parkinson, Detailed photocurrent spectroscopy of the semiconducting group VIB transition metal dichalcogenides, J. Phys. Chem. 86 (1982) 463–467. doi:10.1021/j100393a010.

[45] C. Ruppert, O.B. Aslan, T.F. Heinz, Optical properties and band gap of single- and few-layer MoTe2 crystals, Nano Lett. 14 (2014) 6231–6236. doi:10.1021/nl502557g.

[46] P.B. James, M.T. Lavik, The crystal structure of MoSe2, Acta Crystallogr. 16 (1963) 1183–1183.

[47] W.J. Schutte, J.L. De Boer, F. Jellinek, Crystal structures of tungsten disulfide and diselenide, J. Solid State Chem. 70 (1987) 207–209. doi:10.1016/0022-4596(87)90057-0.

[48] K.D. Rasamani, F. Alimohammadi, Y. Sun, Interlayer-expanded MoS2, Mater. Today. 20 (2017) 83–91. doi:10.1016/j.mattod.2016.10.004.

[49] J.W. Seo, Y.W. Jun, S.W. Park, H. Nah, T. Moon, B. Park, J.G. Kim, Y.J. Kim, J. Cheon, Two-dimensional nanosheet crystals, Angew. Chemie - Int. Ed. 46 (2007) 8828–8831. doi:10.1002/anie.200703175.

[50] L.F. Mattheiss, Band structures of transition-metal-dichalcogenide layer compounds, Phys. Rev. B. 8 (1973) 3719–3740. doi:10.1103/PhysRevB.8.3719.

[51] G.H. Han, D.L. Duong, D.H. Keum, S.J. Yun, Y.H. Lee, Van der Waals Metallic Transition Metal Dichalcogenides, Chem. Rev. 118 (2018) 6297–6336. doi:10.1021/acs.chemrev.7b00618.

[52] A. Kuc, T. Heine, The electronic structure calculations of two-dimensional transition-metal dichalcogenides in the presence of external electric and magnetic fields, Chem. Soc. Rev. 44 (2015) 2603–2614. doi:10.1039/c4cs00276h.

[53] A.N. Enyashin, L. Yadgarov, L. Houben, I. Popov, M. Weidenbach, R. Tenne, M. Bar-Sadan, G. Seifert, New Route for Stabilization of 1T-WS2 and MoS2 Phases, J. Phys. Chem. C. 115 (2011) 24586–24591. doi:Doi 10.1021/Jp2076325.

[54] F. Wypych, R. Schöllhorn, 1T-MoS2, a new metallic modification of molybdenum disulfide, J. Chem. Soc. Chem. Commun. (1992) 1386–1388. doi:10.1039/c39920001386.

[55] W. Schmickler, E. Santos, Interfacial Electrochemistry, 2nd ed., Springer-Verlag Berlin Heidelberg, 2010.

[56] Y. Zheng, Y. Jiao, M. Jaroniec, S.Z. Qiao, Advancing the electrochemistry of the hydrogen-evolution reaction through combining experiment and theory., Angew. Chemie (International Ed.). 54 (2015) 52–65. doi:10.1002/anie.201407031.

[57] T. Shinagawa, A.T. Garcia-Esparza, K. Takanabe, Insight on Tafel slopes from a microkinetic analysis of aqueous electrocatalysis for energy conversion., Sci. Rep. 5

(2015) 13801. doi:10.1038/srep13801.

[58] B.E. Conway, B. V Tilak, Interfacial processes involving electrocatalytic evolution and oxidation of H2 , and the role of chemisorbed H, Electrochim. Acta. 47 (2002) 3571–3594.

[59] J. Zheng, Y. Yan, B. Xu, Correcting the Hydrogen Diffusion Limitation in Rotating Disk Electrode Measurements of Hydrogen Evolution Reaction Kinetics, J. Electrochem. Soc. 162 (2015) F1470–F1481. doi:10.1149/2.0501514jes.

[60] Y. Li, H. Wang, L. Xie, Y. Liang, MoS2 nanoparticles grown on graphene: an advanced catalyst for the hydrogen evolution reaction, J. Am. Chem. Soc. 133 (2011) 7296–7299. http://pubs.acs.org/doi/abs/10.1021/ja201269b (accessed December 15, 2015).

[61] S. Fletcher, Tafel slopes from first principles, J. Solid State Electrochem. 13 (2009) 537–549. doi:10.1007/s10008-008-0670-8.

[62] O.A. Petrii, G.A. Tsirlina, Electrocatalytic activity prediction for hydrogen electrode reaction: intuition, art, science, Electrochim. Acta. 39 (1994) 1739–1747. doi:10.1016/0013-4686(94)85159-X.

[63] R. Parsons, The rate of electrolytic hydrogen evolution and the heat of adsorption of hydrogen, Trans. Faraday Soc. 54 (1958) 1053–1063. doi:10.1007/s13398-014-0173-7.2.

[64] H. Gerischer, Mechanismus der Elektrolytischen Wasserstoffabscheidung und Adsorptionsenergie von Atomarem Wasserstoff, Bull. Des Sociétés Chim. Belges. 67 (1958) 506–527.

[65] Sergio Trasatti, Work Function, Electronegativity, and Electrochemical Behaviour of Metals. III. Electrolytic Hydrogen Evolution in Acid Solutions, J. Electroanal. Chem. Interfacial Electrochem. 39 (1972) 163–184. doi:10.1016/S0306-9877(98)90212-2.

[66] P. Sabatier, Encyclopédie de Science Chimique Appiquée: La Catalyse en Chimie Organique, Librairie Polytechnique, 1913.

[67] J.K. Nørskov, T. Bligaard, a. Logadottir, J.R. Kitchin, J.G. Chen, S. Pandelov, U. Stimming, Trends in the Exchange Current for Hydrogen Evolution, J. Electrochem. Soc. 152 (2005) J23. doi:10.1149/1.1856988.

[68] Y. Zheng, Y. Jiao, Y. Zhu, L.H. Li, Y. Han, Y. Chen, A. Du, M. Jaroniec, S.Z. Qiao, Hydrogen evolution by a metal-free electrocatalyst, Nat. Commun. 5 (2014) 1–8. doi:10.1038/ncomms4783.

[69] J. Kibsgaard, C. Tsai, K. Chan, J.D. Benck, J.K. Nørskov, F. Abild-Pedersen, T.F. Jaramillo, Designing an improved transition metal phosphide catalyst for hydrogen evolution using experimental and theoretical trends, Energy Environ. Sci. 8 (2015) 3022–3029. doi:10.1039/c5ee02179k.

[70] H. Duan, D. Li, Y. Tang, Y. He, S. Ji, R. Wang, H. Lv, P.P. Lopes, A.P. Paulikas, H. Li, S.X. Mao, C. Wang, N.M. Markovic, J. Li, V.R. Stamenkovic, Y. Li, High-Performance Rh2P Electrocatalyst for Efficient Water Splitting, J. Am. Chem. Soc. 139 (2017) 5494–5502. doi:10.1021/jacs.7b01376.

[71] Z.W. Seh, K.D. Fredrickson, B. Anasori, J. Kibsgaard, A.L. Strickler, M.R. Lukatskaya, Y. Gogotsi, T.F. Jaramillo, A. Vojvodic, Two-Dimensional Molybdenum Carbide (MXene) as an Efficient Electrocatalyst for Hydrogen Evolution, ACS Energy Lett. 1

(2016) 589–594. doi:10.1021/acsenergylett.6b00247.

[72] Y. Ito, T. Ohto, D. Hojo, M. Wakisaka, Y. Nagata, L. Chen, K. Hu, M. Izumi, J.I. Fujita, T. Adschiri, Cooperation between holey graphene and NiMo alloy for hydrogen evolution in an acidic electrolyte, ACS Catal. 8 (2018) 3579–3586. doi:10.1021/acscatal.7b04091.

[73] N. Danilovic, R. Subbaraman, D. Strmcnik, V.R. Stamenkovic, N.M. Markovic, Electrocatalysis of the HER in acid and alkaline media, J. Serbian Chem. Soc. 78 (2013) 2007–2015. doi:10.2298/JSC131118136D.

[74] A.R. Zeradjanin, A. Vimalanandan, G. Polymeros, A.A. Topalov, K.J.J. Mayrhofer, M. Rohwerder, Balanced work function as a driver for facile hydrogen evolution reaction - Comprehension and experimental assessment of interfacial catalytic descriptor, Phys. Chem. Chem. Phys. 19 (2017) 17019–17027. doi:10.1039/c7cp03081a.

[75] A. Gupta, T.B. Rawal, C.J. Neal, S. Das, T.S. Rahman, S. Seal, Molybdenum disulfide for ultra-low detection of free radicals: Electrochemical response and molecular modeling, 2D Mater. 4 (2017). doi:10.1088/2053-1583/aa636b.

[76] B. Hinnemann, P. Moses, J. Bonde, K.P. Jørgensen, J.H. Nielsen, S. Horch, I. Chorkendorff, J.K. Nørskov, Biomimetic hydrogen evolution: MoS2 nanoparticles as catalyst for hydrogen evolution, J. Am. Chem. Soc. 127 (2005) 5308–5309. http://pubs.acs.org/doi/abs/10.1021/ja0504690.

[77] J. Bonde, P.G. Moses, T.F. Jaramillo, J. Norskov, I. Chorkendorff, Hydrogen evolution on nano-particulate transition metal sulfides, Faraday Discuss. 140 (2008) 219–231. doi:10.1039/b814058h.

[78] T.F. Jaramillo, K.P. Jørgensen, J. Bonde, J.H. Nielsen, S. Horch, I. Chorkendorff, Identification of Active Edge Sites for Electrochemical H 2 Evolution from MoS2 Nanocatalysts, Science (80-.). 317 (2007) 100–103.

[79] S. Helveg, J. Lauritsen, E. Laegsgaard, I. Stensgaard, J. Norskov, B. Clausen, H. Topsoe, F. Besenbacher, Atomic-scale structure of single-layer MoS2 nanoclusters, Phys. Rev. Lett. 84 (2000) 951–4. doi:10.1103/PhysRevLett.84.951.

[80] P. Raybaud, J. Hafner, G. Kresse, S. Kasztelan, H. Toulhoat, Ab Initio Study of the H2–H2S/MoS2 Gas–Solid Interface: The Nature of the Catalytically Active Sites, J. Catal. 189 (2000) 129–146. doi:10.1006/jcat.1999.2698.

[81] H. Tributsch, J.C. Bennett, Electrochemistry and Photochemistry of MoS2 Layer Crystals. I, J. Electroanal. Chem. 81 (1977) 97–111.

[82] K. Weiss, J.M. Phillips, Calculated specific surface energy of molybdenite (<math display="inline"> <mrow> <msub> <mrow> <mi mathvariant="normal">MoS</mi> </mrow> <mrow> <mn>2</mn> </mrow> </msub> </mrow> </math>), Phys. Rev. B. 14 (1976) 5392–5395. doi:10.1103/PhysRevB.14.5392.

[83] J.A. Spirko, M.L. Neiman, A.M. Oelker, K. Klier, Electronic structure and reactivity of defect MoS2: I. Relative stabilities of clusters and edges, and electronic surface states, Surf. Sci. 542 (2003) 192–204. doi:10.1016/S0039-6028(03)00957-9.

[84] S.R.G. Thakurta, Electrical Properties of Molybdenite, Indian J. Phys. 43 (1969) 169–172.

[85] Y. Yu, S.Y. Huang, Y. Li, S.N. Steinmann, W. Yang, L. Cao, Layer-dependent electrocatalysis of MoS2 for hydrogen evolution, Nano Lett. 14 (2014) 553–558. doi:10.1021/nl403620g.

[86] B. Seo, G.Y. Jung, Y.J. Sa, H.Y. Jeong, J.Y. Cheon, J.H. Lee, H.Y. Kim, J.C. Kim, H.S. Shin, S.K. Kwak, S.H. Joo, Monolayer-precision synthesis of molybdenum sulfide nanoparticles and their nanoscale size effects in the hydrogen evolution reaction, ACS Nano. 9 (2015) 3728–3739. doi:10.1021/acsnano.5b00786.

[87] Z. Gholamvand, D. McAteer, A. Harvey, C. Backes, J.N. Coleman, Electrochemical Applications of Two-Dimensional Nanosheets: The Effect of Nanosheet Length and Thickness, Chem. Mater. 28 (2016) 2641–2651. doi:10.1021/acs.chemmater.6b00009.

[88] S.B. Desai, S.R. Madhvapathy, M. Amani, D. Kiriya, M. Hettick, M. Tosun, Y. Zhou, M. Dubey, J.W. Ager, D. Chrzan, A. Javey, Gold-Mediated Exfoliation of Ultralarge Optoelectronically-Perfect Monolayers, Adv. Mater. 28 (2016) 4053–4058. doi:10.1002/adma.201506171.

[89] D.M. Tang, D.G. Kvashnin, S. Najmaei, Y. Bando, K. Kimoto, P. Koskinen, P.M. Ajayan, B.I. Yakobson, P.B. Sorokin, J. Lou, D. Golberg, Nanomechanical cleavage of molybdenum disulphide atomic layers, Nat. Commun. 5 (2014) 1–8. doi:10.1038/ncomms4631.

[90] J.P. Oviedo, S. Kc, N. Lu, J. Wang, K. Cho, R.M. Wallace, M.J. Kim, In Situ TEM Characterization of Shear-Stress-Induced Interlayer Sliding in the Cross Section View of Molybdenum Disul fi de, (2014).

[91] J.N. Coleman, M. Lotya, A. O'Neill, S.D. Bergin, P.J. King, U. Khan, K. Young, A. Gaucher, S. De, R.J. Smith, I. V. Shvets, S.K. Arora, G. Stanton, H.Y. Kim, K. Lee, G.T. Kim, G.S. Duesberg, T. Hallam, J.J. Boland, J.J. Wang, J.F. Donegan, J.C. Grunlan, G. Moriarty, A. Shmeliov, R.J. Nicholls, J.M. Perkins, E.M. Grieveson, K. Theuwissen, D.W. McComb, P.D. Nellist, V. Nicolosi, Two-dimensional nanosheets produced by liquid exfoliation of layered materials, Science (80-.). 331 (2011) 568–571. doi:10.1126/science.1194975.

[92] A. O'Neill, U. Khan, J.N. Coleman, Preparation of High Concentration Dispersions of Exfoliated MoS2 with Increased Flake Size, Chem. Mater. 24 (2012) 2414–2421. doi:10.1021/cm301515z.

[93] C. Backes, R.J. Smith, N. McEvoy, N.C. Berner, D. McCloskey, H.C. Nerl, A. O'Neill, P.J. King, T. Higgins, D. Hanlon, N. Scheuschner, J. Maultzsch, L. Houben, G.S. Duesberg, J.F. Donegan, V. Nicolosi, J.N. Coleman, Edge and confinement effects allow in situ measurement of size and thickness of liquid-exfoliated nanosheets, Nat. Commun. 5 (2014) 1–10. doi:10.1038/ncomms5576.

[94] R.J. Smith, P.J. King, M. Lotya, C. Wirtz, U. Khan, S. De, A. O'Neill, G.S. Duesberg, J.C. Grunlan, G. Moriarty, J. Chen, J. Wang, A.I. Minett, V. Nicolosi, J.N. Coleman, Large-scale exfoliation of inorganic layered compounds in aqueous surfactant solutions, Adv. Mater. 23 (2011) 3944–3948. doi:10.1002/adma.201102584.

[95] W. Liu, J. Benson, C. Dawson, A. Strudwick, A.P.A. Raju, Y. Han, M. Li, P. Papakonstantinou, The effects of exfoliation, organic solvents and anodic activation on the catalytic hydrogen evolution reaction of tungsten disulfide, Nanoscale. 9 (2017) 13515–13526. doi:10.1039/C7NR04790H.

[96] K.G. Zhou, M. Zhao, M.J. Chang, Q. Wang, X.Z. Wu, Y. Song, H.L. Zhang, Size-dependent nonlinear optical properties of atomically thin transition metal dichalcogenide nanosheets, Small. 11 (2015) 694–701. doi:10.1002/smll.201400541.

[97] T. Wang, L. Liu, Z. Zhu, P. Papakonstantinou, J. Hu, H. Liu, M. Li, Enhanced electrocatalytic activity for hydrogen evolution reaction from self-assembled monodispersed molybdenum sulfidenanoparticles on an Au electrode, Energy Environ. Sci. 6 (2013) 625–633. doi:10.1039/C2EE23513G.

[98] J. Benson, M. Li, S. Wang, P. Wang, P. Papakonstantinou, Electrocatalytic Hydrogen Evolution Reaction on Edges of a Few Layer Molybdenum Disulfide Nanodots., ACS Appl. Mater. Interfaces. 7 (2015) 14113–22. doi:10.1021/acsami.5b03399.

[99] T. Wang, D. Gao, J. Zhuo, Z. Zhu, P. Papakonstantinou, Y. Li, M. Li, Size-Dependent Enhancement of Electrocatalytic Oxygen-Reduction and Hydrogen-Evolution Performance of MoS2 Particles., Chem. - A Eur. J. 19 (2013) 11939–48. doi:10.1002/chem.201301406.

[100] S.X. Leong, C.C. Mayorga-Martinez, Z. Sofer, J. Luxa, S.M. Tan, M. Pumera, A study of the effect of sonication time on the catalytic performance of layered WS_2 from various sources, Phys. Chem. Chem. Phys. 19 (2017) 2768–2777. doi:10.1039/C6CP07385A.

[101] X.J. Chua, M. Pumera, The effect of varying solvents for MoS_2 treatment on its catalytic efficiencies for HER and ORR, Phys. Chem. Chem. Phys. 19 (2017) 6610–6619. doi:10.1039/C6CP08205J.

[102] G.B. De-Mello, L. Smith, S.J. Rowley-Neale, J. Gruber, S.J. Hutton, C.E. Banks, Surfactant-exfoliated 2D molybdenum disulphide (2D-MoS2): The role of surfactant upon the hydrogen evolution reaction, RSC Adv. 7 (2017) 36208–36213. doi:10.1039/c7ra05085b.

[103] X. Hai, W. Zhou, K. Chang, H. Pang, H. Liu, L. Shi, F. Ichihara, J. Ye, Engineering the crystallinity of MoS_2 monolayers for highly efficient solar hydrogen production, J. Mater. Chem. A. 5 (2017) 8591–8598. doi:10.1039/C7TA00953D.

[104] C. Backes, T.M. Higgins, A. Kelly, C. Boland, A. Harvey, D. Hanlon, J.N. Coleman, Guidelines for exfoliation, characterization and processing of layered materials produced by liquid exfoliation, Chem. Mater. 29 (2017) 243–255. doi:10.1021/acs.chemmater.6b03335.

[105] L. Niu, J.N. Coleman, H. Zhang, H. Shin, M. Chhowalla, Z. Zheng, Production of Two-Dimensional Nanomaterials via Liquid-Based Direct Exfoliation, Small. 12 (2016) 272–293. doi:10.1002/smll.201502207.

[106] E. Benavente, M.A.S. Ana, F. Mendizábal, G. González, Intercalation chemistry of molybdenum disulfide, Coord. Chem. Rev. 224 (2002) 87–109. doi:10.1016/j.advengsoft.2017.12.003.

[107] M.J. McKelvy, W.S. Glaunsinger, Molecular Intercalation Reactions in Lamellar Compounds, Annu. Rev. Phys. Chem. 41 (1990) 497–523.

[108] F.R. Gamble, J.H. Osiecki, M. Cais, R. Pisharody, F.J. Disalvo, T.H. Geballe, Intercalation Complexes of Lewis Bases and Layered Sulfides: A Large Class of New, New Ser. 174 (1971) 493–497. https://www.jstor.org/stable/pdf/1733537.pdf?refreqid=excelsior%3A5871bec215d49e18da1fe9f46a94dc35.

[109] M.B. Dines, Lithium intercalation via -Butyllithium of the layered transition metal dichalcogenides, Mater. Res. Bull. 10 (1975) 287–291. doi:10.1016/0025-5408(75)90115-4.

[110] P. Joensen, R.F. Frindt, S.R. Morrison, Single layer MoS2, Mater. Res. Bull. 21 (1986) 457–461. doi:10.1016/0025-5408(86)90011-5.

[111] J. Heising, M.G. Kanatzidis, Exfoliated and restacked MoS2 and WS2: Ionic or neutral species? Encapsulation and ordering of hard electropositive cations, J. Am. Chem. Soc. 121 (1999) 11720–11732. doi:10.1021/ja991644d.

[112] J. Peng, J. Wu, X. Li, Y. Zhou, Z. Yu, Y. Guo, J. Wu, Y. Lin, Z. Li, X. Wu, C. Wu, Y. Xie, Very Large-Sized Transition Metal Dichalcogenides Monolayers from Fast Exfoliation by Manual Shaking, J. Am. Chem. Soc. 139 (2017) 9019–9025. doi:10.1021/jacs.7b04332.

[113] M.A. Py, R.R. Haering, Structural destabilization induced by lithium intercalation in MoS2 and related compounds, Can. J. Phys. 61 (1983) 76–84.

[114] R. Bissessur, M.G. Kanatzidis, J.L. Schindler, C.R. Kannewurf, Encapsulation of polymers into MoS2and metal to insulator transition in metastable MoS2, J. Chem. Soc. Chem. Commun. (1993) 1582–1585. doi:10.1039/C39930001582.

[115] J. Heising, M.G. Kanatzidis, Structure of restacked MoS2 and WS2 elucidated by electron crystallography, J. Am. Chem. Soc. 121 (1999) 638–643. doi:10.1021/ja983043c.

[116] M. Acerce, D. Voiry, M. Chhowalla, Metallic 1T phase MoS2nanosheets as supercapacitor electrode materials, Nat. Nanotechnol. 10 (2015) 313–318. doi:10.1038/nnano.2015.40.

[117] S.S. Chou, N. Sai, P. Lu, E.N. Coker, S. Liu, K. Artyushkova, T.S. Luk, B. Kaehr, C.J. Brinker, Understanding catalysis in a multiphasic two-dimensional transition metal dichalcogenide, Nat. Commun. 6 (2015) 1–8. doi:10.1038/ncomms9311.

[118] L. Wang, Z. Xu, W. Wang, X. Bai, Atomic mechanism of dynamic electrochemical lithiation processes of MoS2 nanosheets, J. Am. Chem. Soc. 136 (2014) 6693–6697. doi:10.1021/ja501686w.

[119] M.A. Lukowski, A.S. Daniel, F. Meng, A. Forticaux, L. Li, S. Jin, Enhanced Hydrogen Evolution Catalysis from Enhanced Hydrogen Evolution Catalysis from Chemically Exfoliated Metallic MoS 2 Nanosheets, J. Am. Chem. Soc. 135 (2013) 10274. doi:10.1021/ja404523s.

[120] D. Voiry, M. Salehi, R. Silva, T. Fujita, M. Chen, Conducting MoS2 nanosheets as catalysts for hydrogen evolution reaction, Nano Lett. 13 (2013) 6222–6227. http://pubs.acs.org/doi/abs/10.1021/nl403661s.

[121] D. Voiry, H. Yamaguchi, J. Li, R. Silva, D.C.B. Alves, T. Fujita, M. Chen, T. Asefa, V.B. Shenoy, G. Eda, M. Chhowalla, Enhanced catalytic activity in strained chemically exfoliated WS_2 nanosheets for hydrogen evolution., Nat. Mater. 12 (2013) 850–5. doi:10.1038/nmat3700.

[122] Y. Yin, J. Han, X. Zhang, Y. Zhang, J. Zhou, D. Muir, R. Sutarto, Z. Zhang, S. Liu, B. Song, Facile synthesis of few-layer-thick carbon nitride nanosheets by liquid ammonia-assisted lithiation method and their photocatalytic redox properties, RSC Adv. 4 (2014) 32690–32697. doi:10.1039/c4ra06036a.

[123] Y. Yin, J. Han, Y. Zhang, X. Zhang, P. Xu, Q. Yuan, L. Samad, X. Wang, Y. Wang, Z. Zhang, P. Zhang, X. Cao, B. Song, S. Jin, Contributions of Phase, Sulfur Vacancies, and Edges to the Hydrogen Evolution Reaction Catalytic Activity of Porous Molybdenum Disulfide Nanosheets, J. Am. Chem. Soc. 138 (2016) 7965–7972. doi:10.1021/jacs.6b03714.

[124] Z. Cui, H. Chu, S. Gao, Y. Pei, J. Ji, Y. Ge, P. Dong, P.M. Ajayan, J. Shen, M. Ye, Large-scale controlled synthesis of porous two-dimensional nanosheets for the hydrogen evolution reaction through a chemical pathway, Nanoscale. 10 (2018) 6168–6176. doi:10.1039/c8nr01182f.

[125] Y. Xu, L. Wang, X. Liu, S. Zhang, C. Liu, D. Yan, Y. Zeng, Y. Pei, Y. Liu, S. Luo, Monolayer MoS2with S vacancies from interlayer spacing expanded counterparts for highly efficient electrochemical hydrogen production, J. Mater. Chem. A. 4 (2016) 16524–16530. doi:10.1039/c6ta06534a.

[126] G. Pagona, C. Bittencourt, R. Arenal, N. Tagmatarchis, Exfoliated semiconducting pure 2H-MoS2 and 2H-WS2 assisted by chlorosulfonic acid, Chem. Commun. 51 (2015) 12950–12953. doi:10.1039/c5cc04689k.

[127] A. Ambrosi, Z. Sofer, M. Pumera, Lithium intercalation compound dramatically influences the electrochemical properties of exfoliated MoS2., Small. 11 (2015) 605–12. doi:10.1002/smll.201400401.

[128] A.Y.S. Eng, A. Ambrosi, Z. Sofer, P. Simek, M. Pumera, Electrochemistry of Transition Metal Dichalcogenides : Strong Dependence on the Metal-to-Chalcogen Composition and Exfoliation Method, ACS Nano. 8 (2014) 12185–12198.

[129] A. Ambrosi, Z. Sofer, M. Pumera, 2H → 1T phase transition and hydrogen evolution activity of MoS2, MoSe2, WS2 and WSe2 strongly depends on the MX2 composition., Chem. Commun. 51 (2015) 8450–3. doi:10.1039/c5cc00803d.

[130] J. Luxa, P. Vosecký, V. Mazánek, D. Sedmidubský, M. Pumera, Z. Sofer, Cation-Controlled Electrocatalytical Activity of Transition-Metal Disulfides, ACS Catal. 8 (2018) 2774–2781. doi:10.1021/acscatal.7b04233.

[131] D. Voiry, A. Goswami, R. Kappera, C.D.C.C.E. Silva, D. Kaplan, T. Fujita, M. Chen, T. Asefa, M. Chhowalla, Covalent functionalization of monolayered transition metal dichalcogenides by phase engineering, Nat. Chem. 7 (2015) 45–49. doi:10.1038/nchem.2108.

[132] J.I. Paredes, J.M. Munuera, S. Villar-Rodil, L. Guardia, M. Ayán-Varela, A. Pagán, S.D. Aznar-Cervantes, J.L. Cenis, A. Martínez-Alonso, J.M.D. Tascón, Impact of Covalent Functionalization on the Aqueous Processability, Catalytic Activity, and Biocompatibility of Chemically Exfoliated MoS2Nanosheets, ACS Appl. Mater. Interfaces. 8 (2016) 27974–27986. doi:10.1021/acsami.6b08444.

[133] A. Anto Jeffery, C. Nethravathi, M. Rajamathi, Two-dimensional nanosheets and layered hybrids of MoS2 and WS2 through exfoliation of ammoniated MS2 (M = Mo,W), J. Phys. Chem. C. 118 (2014) 1386–1396. doi:10.1021/jp410918c.

[134] P.L. Cullen, K.M. Cox, M.K. Bin Subhan, L. Picco, O.D. Payton, D.J. Buckley, T.S. Miller, S.A. Hodge, N.T. Skipper, V. Tileli, C.A. Howard, Ionic solutions of two-dimensional materials, Nat. Chem. 9 (2017) 244–249. doi:10.1038/nchem.2650.

[135] S.S. Chou, M. De, J. Kim, S. Byun, C. Dykstra, J. Yu, J. Huang, V.P. Dravid, Ligand

conjugation of chemically exfoliated MoS2, J. Am. Chem. Soc. 135 (2013) 4584–4587. doi:10.1021/ja310929s.

[136] X. Chen, N.C. Berner, C. Backes, G.S. Duesberg, A.R. McDonald, Functionalization of Two-Dimensional MoS2: On the Reaction between MoS2 and Organic Thiols, Angew. Chemie - Int. Ed. 55 (2016) 5803–5808. doi:10.1002/anie.201510219.

[137] K.C. Knirsch, N.C. Berner, H.C. Nerl, C.S. Cucinotta, Z. Gholamvand, N. McEvoy, Z. Wang, I. Abramovic, P. Vecera, M. Halik, S. Sanvito, G.S. Duesberg, V. Nicolosi, F. Hauke, A. Hirsch, J.N. Coleman, C. Backes, Basal-Plane Functionalization of Chemically Exfoliated Molybdenum Disulfide by Diazonium Salts, ACS Nano. 9 (2015) 6018–6030. doi:10.1021/acsnano.5b00965.

[138] P. Joo, K. Jo, G. Ahn, D. Voiry, H. Jeong, S. Ryu, M. Chhowalla, B. Kim, Functional Polyelectrolyte Nanospaced MoS2 Multilayers for Enhanced Photoluminescence, Nano Lett. 14 (2014) 6456–6462. http://pubs.acs.org/doi/abs/10.1021/nl502883a (accessed April 21, 2015).

[139] G. Eda, H. Yamaguchi, D. Voiry, T. Fujita, M. Chen, M. Chhowalla, Photoluminescence from chemically exfoliated MoS 2, Nano Lett. 11 (2011) 5111–5116. doi:10.1021/nl201874w.

[140] E.E. Benson, H. Zhang, S.A. Schuman, S.U. Nanayakkara, N.D. Bronstein, S. Ferrere, J.L. Blackburn, E.M. Miller, Balancing the Hydrogen Evolution Reaction, Surface Energetics, and Stability of Metallic MoS2Nanosheets via Covalent Functionalization, J. Am. Chem. Soc. 140 (2018) 441–450. doi:10.1021/jacs.7b11242.

[141] K. Parvez, R. Li, S.R. Puniredd, Y. Hernandez, F. Hinkel, S. Wang, X. Feng, K. Müllen, Electrochemically exfoliated graphene as solution-processable, highly conductive electrodes for organic electronics, ACS Nano. 7 (2013) 3598–3606. doi:10.1021/nn400576v.

[142] K. Parvez, Z.S. Wu, R. Li, X. Liu, R. Graf, X. Feng, K. Müllen, Exfoliation of graphite into graphene in aqueous solutions of inorganic salts, J. Am. Chem. Soc. 136 (2014) 6083–6091. doi:10.1021/ja5017156.

[143] Z. Zeng, Z. Yin, X. Huang, H. Li, Q. He, G. Lu, F. Boey, H. Zhang, Single-layer semiconducting nanosheets: High-yield preparation and device fabrication, Angew. Chemie - Int. Ed. 50 (2011) 11093–11097. doi:10.1002/anie.201106004.

[144] N. Liu, P. Kim, J.H. Kim, J.H. Ye, S. Kim, C.J. Lee, Large-area atomically thin MoS2 nanosheets prepared using electrochemical exfoliation, ACS Nano. 8 (2014) 6902–6910. doi:10.1021/nn5016242.

[145] D. Gopalakrishnan, D. Damien, B. Li, H. Gullappalli, V.K. Pillai, P.M. Ajayan, M.M. Shaijumon, Electrochemical synthesis of luminescent MoS $_2$ quantum dots, Chem. Commun. 51 (2015) 6293–6296. doi:10.1039/C4CC09826A.

[146] S. Das, M.K. Bera, S. Tong, B. Narayanan, G. Kamath, A. Mane, A.P. Paulikas, M.R. Antonio, S.K.R.S. Sankaranarayanan, A.K. Roelofs, A Self-Limiting Electro-Ablation Technique for the Top-Down Synthesis of Large-Area Monolayer Flakes of 2D Materials, Sci. Rep. 6 (2016) 1–9. doi:10.1038/srep28195.

[147] Y.T. Huang, A. Dodda, D.S. Schulman, A. Sebastian, F. Zhang, D. Buzzell, M. Terrones, S.P. Feng, S. Das, Anomalous Corrosion of Bulk Transition Metal Diselenides Leading to Stable Monolayers, ACS Appl. Mater. Interfaces. 9 (2017) 39059–39068.

doi:10.1021/acsami.7b13107.

[148] D.S. Schulman, D. May-Rawding, F. Zhang, D. Buzzell, N. Alem, S. Das, Superior Electro-Oxidation and Corrosion Resistance of Monolayer Transition Metal Disulfides, ACS Appl. Mater. Interfaces. 10 (2018) 4285–4294. doi:10.1021/acsami.7b17660.

[149] G. Ou, P. Fan, X. Ke, Y. Xu, K. Huang, H. Wei, W. Yu, H. Zhang, Defective molybdenum sulfide quantum dots as highly active hydrogen evolution electrocatalysts, Nano Res. 11 (2018) 751–761. doi:10.1007/s12274-017-1684-2.

[150] Z. Wang, Q. Li, H. Xu, C. Dahl-Petersen, Q. Yang, D. Cheng, D. Cao, F. Besenbacher, J. V. Lauritsen, S. Helveg, M. Dong, Controllable etching of MoS2 basal planes for enhanced hydrogen evolution through the formation of active edge sites, Nano Energy. 49 (2018) 634–643. doi:10.1016/j.nanoen.2018.04.067.

[151] C.C. Cheng, A.Y. Lu, C.C. Tseng, X. Yang, M.N. Hedhili, M.C. Chen, K.H. Wei, L.J. Li, Activating basal-plane catalytic activity of two-dimensional MoS2 monolayer with remote hydrogen plasma, Nano Energy. 30 (2016) 846–852. doi:10.1016/j.nanoen.2016.09.010.

[152] Q. Ma, P.M. Odenthal, J. Mann, D. Le, C.S. Wang, Y. Zhu, T. Chen, D. Sun, K. Yamaguchi, T. Tran, M. Wurch, J.L. McKinley, J. Wyrick, K. Magnone, T.F. Heinz, T.S. Rahman, R. Kawakami, L. Bartels, Controlled argon beam-induced desulfurization of monolayer molybdenum disulfide, J. Phys. Condens. Matter. 25 (2013). doi:10.1088/0953-8984/25/25/252201.

[153] N. Choudhary, M.R. Islam, N. Kang, L. Tetard, Y. Jung, S.I. Khondaker, Two-dimensional lateral heterojunction through bandgap engineering of MoS2 via oxygen plasma, J. Phys. Condens. Matter. 28 (2016). doi:10.1088/0953-8984/28/36/364002.

[154] H. Zhu, X. Qin, L. Cheng, A. Azcatl, J. Kim, R.M. Wallace, Remote Plasma Oxidation and Atomic Layer Etching of MoS2, ACS Appl. Mater. Interfaces. 8 (2016) 19119–19126. doi:10.1021/acsami.6b04719.

[155] S. Xiao, P. Xiao, X. Zhang, D. Yan, X. Gu, F. Qin, Z. Ni, Z.J. Han, K.K. Ostrikov, Atomic-layer soft plasma etching of MoS 2, Sci. Rep. 6 (2016) 1–8. doi:10.1038/srep19945.

[156] C.K. Chua, A.H. Loo, M. Pumera, Top-Down and Bottom-Up Approaches in Engineering 1 T Phase Molybdenum Disulfide (MoS $_2$): Towards Highly Catalytically Active Materials, Chem. - A Eur. J. (2016) 1–7. doi:10.1002/chem.201602764.

[157] D. Kong, H. Wang, J. Cha, M. Pasta, K. Koski, Synthesis of MoS2 and MoSe2 films with vertically aligned layers, Nano Lett. 13 (2013) 1341–1347. http://pubs.acs.org/doi/abs/10.1021/nl400258t (accessed December 15, 2015).

[158] H. Wang, Z. Lu, D. Kong, J. Sun, T.M. Hymel, Y. Cui, Electrochemical Tuning of MoS2 Nanoparticles on Three-Dimensional Substrate for Efficient Hydrogen Evolution, ACS Nano. 8 (2014) 4940–4947.

[159] H. Wang, D. Kong, P. Johanes, J.J. Cha, G. Zheng, K. Yan, N. Liu, MoSe 2 and WSe 2 Nano fi lms with Vertically Aligned Molecular Layers on Curved and Rough Surfaces, Nano Lett. 13 (2013) 3426–3433. doi:10.1021/nl401944f.

[160] S. Li, S. Wang, M.M. Salamone, A.W. Robertson, S. Nayak, H. Kim, S.C.E. Tsang, M. Pasta, J.H. Warner, Edge-Enriched 2D MoS2Thin Films Grown by Chemical Vapor

Deposition for Enhanced Catalytic Performance, ACS Catal. 7 (2017) 877–886. doi:10.1021/acscatal.6b02663.

[161] Y. Yang, H. Fei, G. Ruan, C. Xiang, J.M. Tour, Edge-oriented MoS2 nanoporous films as flexible electrodes for hydrogen evolution reactions and supercapacitor devices, Adv. Mater. 26 (2014) 8163–8168. doi:10.1002/adma.201402847.

[162] Y. Huan, J. Shi, X. Zou, Y. Gong, Z. Zhang, M. Li, L. Zhao, R. Xu, S. Jiang, X. Zhou, M. Hong, C. Xie, H. Li, X. Lang, Q. Zhang, L. Gu, X. Yan, Y. Zhang, Vertical 1T-TaS2 Synthesis on Nanoporous Gold for High-Performance Electrocatalytic Applications, Adv. Mater. 30 (2018) 1–9. doi:10.1002/adma.201705916.

[163] Y.H. Lee, X.Q. Zhang, W. Zhang, M.T. Chang, C. Te Lin, K. Di Chang, Y.C. Yu, J.T.W. Wang, C.S. Chang, L.J. Li, T.W. Lin, Synthesis of large-area MoS 2 atomic layers with chemical vapor deposition, Adv. Mater. 24 (2012) 2320–2325. doi:10.1002/adma.201104798.

[164] Y. Gong, Z. Lin, G. Ye, G. Shi, S. Feng, Y. Lei, A.L. Elías, N. Perea-Lopez, R. Vajtai, H. Terrones, Z. Liu, M. Terrones, P.M. Ajayan, Tellurium-Assisted Low-Temperature Synthesis of MoS 2 and WS 2 Monolayers, ACS Nano. 9 (2015) 11658–11666. doi:10.1021/acsnano.5b05594.

[165] S.J. Yun, S.H. Chae, H. Kim, J.C. Park, J.H. Park, G.H. Han, J.S. Lee, S.M. Kim, H.M. Oh, J. Seok, M.S. Jeong, K.K. Kim, Y.H. Lee, Synthesis of centimeter-scale monolayer tungsten disulfide film on gold foils, ACS Nano. 9 (2015) 5510–5519. doi:10.1021/acsnano.5b01529.

[166] J.C. Park, S.J. Yun, H. Kim, J.H. Park, S.H. Chae, S.J. An, J.G. Kim, S.M. Kim, K.K. Kim, Y.H. Lee, Phase-Engineered Synthesis of Centimeter-Scale 1T′- and 2H-Molybdenum Ditelluride Thin Films, ACS Nano. 9 (2015) 6548–6554. doi:10.1021/acsnano.5b02511.

[167] Y. Shi, Y. Wan, R. Liu, B. Tu, D. Zhao, Synthesis of highly ordered mesoporous crystalline WS2 and MoS2 via a high-temperature reductive sulfuration route, J. Am. Chem. Soc. 129 (2007) 9522–9531. http://pubs.acs.org/doi/abs/10.1021/ja072910n (accessed December 15, 2015).

[168] I.S. Kim, V.K. Sangwan, D. Jariwala, J.D. Wood, S. Park, K.S. Chen, F. Shi, F. Ruiz-Zepeda, A. Ponce, M. Jose-Yacaman, V.P. Dravid, T.J. Marks, M.C. Hersam, L.J. Lauhon, Influence of stoichiometry on the optical and electrical properties of chemical vapor deposition derived MoS2, ACS Nano. 8 (2014) 10551–10558. doi:10.1021/nn503988x.

[169] Y. Li, Y. Yu, Y. Huang, R.A. Nielsen, W.A. Goddard, Y. Li, L. Cao, Engineering the Composition and Crystallinity of Molybdenum Sulfide for High-Performance Electrocatalytic Hydrogen Evolution, ACS Catal. 5 (2015) 448–455. doi:10.1021/cs501635v.

[170] S. Xie, M. Xu, T. Liang, G. Huang, S. Wang, G. Xue, N. Meng, Y. Xu, H. Chen, X. Ma, D. Yang, High-quality round-shaped monolayer MoS2 domain and its transformation, Nanoscale. (2015) 219–225. doi:10.1039/C5NR05701A.

[171] S. Wang, Y. Rong, Y. Fan, M. Pacios, H. Bhaskaran, K. He, J.H. Warner, Shape evolution of monolayer MoS2crystals grown by chemical vapor deposition, Chem. Mater. 26 (2014) 6371–6379. doi:10.1021/cm5025662.

[172] J.V. Lauritsen, M.V. Bollinger, E. Lægsgaard, K.W. Jacobsen, J.K. Nørskov, B.S. Clausen, H. Topsøe, F. Besenbacher, Atomic-scale insight into structure and morphology changes of MoS2 nanoclusters in hydrotreating catalysts, J. Catal. 221 (2004) 510–522. doi:10.1016/j.jcat.2003.09.015.

[173] A. Govind Rajan, J.H. Warner, D. Blankschtein, M.S. Strano, Generalized Mechanistic Model for the Chemical Vapor Deposition of 2D Transition Metal Dichalcogenide Monolayers, ACS Nano. 10 (2016) 4330–4344. doi:10.1021/acsnano.5b07916.

[174] J. Ma, X. Li, L. Gan, S. Zhang, Y. Cao, Z. Nie, X. Wang, D. Ma, L. He, J. Nie, C. Xiong, R. Dou, Controlling the dendritic structure and the photo-electrocatalytic properties of highly crystalline MoS2on sapphire substrate, 2D Mater. 5 (2018). doi:10.1088/2053-1583/aacc90.

[175] J. Wang, X. Cai, R. Shi, Z. Wu, W. Wang, G. Long, Y. Tang, N. Cai, W. Ouyang, P. Geng, B.N. Chandrashekar, A. Amini, N. Wang, C. Cheng, Twin Defect Derived Growth of Atomically Thin MoS2 Dendrites, ACS Nano. 12 (2018) 635–643. doi:10.1021/acsnano.7b07693.

[176] Y. Zhang, Q. Ji, G.F. Han, J. Ju, J. Shi, D. Ma, J. Sun, Y. Zhang, M. Li, X.Y. Lang, Y. Zhang, Z. Liu, Dendritic, transferable, strictly monolayer MoS2flakes synthesized on SrTiO3single crystals for efficient electrocatalytic applications, ACS Nano. 8 (2014) 8617–8624. doi:10.1021/nn503412w.

[177] W. Xu, S. Li, S. Zhou, J.K. Lee, S. Wang, S.G. Sarwat, X. Wang, H. Bhaskaran, M. Pasta, J.H. Warner, Large Dendritic Monolayer MoS2Grown by Atmospheric Pressure Chemical Vapor Deposition for Electrocatalysis, ACS Appl. Mater. Interfaces. 10 (2018) 4630–4639. doi:10.1021/acsami.7b14861.

[178] H. Li, X. Duan, X. Wu, X. Zhuang, H. Zhou, Q. Zhang, X. Zhu, W. Hu, P. Ren, P. Guo, L. Ma, X. Fan, X. Wang, J. Xu, A. Pan, X. Duan, Growth of alloy MoS2xSe2(1-x)nanosheets with fully tunable chemical compositions and optical properties, J. Am. Chem. Soc. 136 (2014) 3756–3759. doi:10.1021/ja500069b.

[179] F. Wang, J. Li, F. Wang, T.A. Shifa, Z. Cheng, Z. Wang, K. Xu, X. Zhan, Q. Wang, Y. Huang, C. Jiang, J. He, Enhanced Electrochemical H $_2$ Evolution by Few-Layered Metallic WS $_{2(1-x)}$ Se $_{2x}$ Nanoribbons, Adv. Funct. Mater. 25 (2015) 6077–6083. doi:10.1002/adfm.201502680.

[180] S. Susarla, A. Kutana, J.A. Hachtel, V. Kochat, A. Apte, R. Vajtai, J.C. Idrobo, B.I. Yakobson, C.S. Tiwary, P.M. Ajayan, Quaternary 2D Transition Metal Dichalcogenides (TMDs) with Tunable Bandgap, Adv. Mater. 29 (2017) 1–8. doi:10.1002/adma.201702457.

[181] J.G. Song, J. Park, W. Lee, T. Choi, H. Jung, C.W. Lee, S.H. Hwang, J.M. Myoung, J.H. Jung, S.H. Kim, C. Lansalot-Matras, H. Kim, Layer-controlled, wafer-scale, and conformal synthesis of tungsten disulfide nanosheets using atomic layer deposition, ACS Nano. 7 (2013) 11333–11340. doi:10.1021/nn405194e.

[182] R. Yue, A.T. Barton, H. Zhu, A. Azcatl, L.F. Pena, J. Wang, X. Peng, N. Lu, L. Cheng, R. Addou, S. Mcdonnell, L. Colombo, J.W.P. Hsu, J. Kim, M.J. Kim, R.M. Wallace, C.L. Hinkle, HfSe 2 Thin Films : 2D Transition Metal Dichalcogenides Grown by Molecular Beam Epitaxy, ACS Nano. 9 (2015) 474–480. doi:10.1021/nn5056496.

[183] M.I. Serna, S.H. Yoo, S. Moreno, Y. Xi, J.P. Oviedo, H. Choi, H.N. Alshareef, M.J. Kim,

M. Minary-Jolandan, M.A. Quevedo-Lopez, Large-Area Deposition of MoS2by Pulsed Laser Deposition with in Situ Thickness Control, ACS Nano. 10 (2016) 6054–6061. doi:10.1021/acsnano.6b01636.

[184] C. MacIsaac, J.R. Schneider, R.G. Closser, T.R. Hellstern, D.S. Bergsman, J. Park, Y. Liu, R. Sinclair, S.F. Bent, Atomic and Molecular Layer Deposition of Hybrid Mo–Thiolate Thin Films with Enhanced Catalytic Activity, Adv. Funct. Mater. 28 (2018) 1–10. doi:10.1002/adfm.201800852.

[185] D.H. Kwon, Z. Jin, S. Shin, W.-S. Lee, Y.-S. Min, A comprehensive study on atomic layer deposition of molybdenum sulfide for electrochemical hydrogen evolution, Nanoscale. 8 (2016) 7180–7188. doi:10.1039/C5NR09065B.

[186] J.R. Brent, N. Savjani, P. O'Brien, Synthetic approaches to two-dimensional transition metal dichalcogenide nanosheets, Prog. Mater. Sci. 89 (2017) 411–478. doi:10.1016/j.pmatsci.2017.06.002.

[187] M.J. Cuddy, K.P. Arkill, Z.W. Wang, H.-P. Komsa, A. V Krasheninnikov, R.E. Palmer, Fabrication and atomic structure of size-selected, layered MoS2 clusters for catalysis., Nanoscale. 6 (2014) 12463–12469. doi:10.1039/c4nr04317k.

[188] M.A. Baker, R. Gilmore, C. Lenardi, W. Gissler, XPS investigation of preferential sputtering of S from MoS2 and determination of MoSx stoichiometry from Mo and S peak positions, Appl. Surf. Sci. 150 (1999) 255–262. doi:10.1016/S0169-4332(99)00253-6.

[189] M. Regula, C. Ballif, J.H. Moser, F. Lévy, Structural, chemical, and electrical characterisation of reactively sputtered WSxthin films, Thin Solid Films. 280 (1996) 67–75. doi:10.1016/0040-6090(95)08206-9.

[190] M.A. Worsley, S.J. Shin, M.D. Merrill, J. Lenhardt, A.J. Nelson, L.Y. Woo, A.E. Gash, T.F. Baumann, C.A. Orme, Ultralow density, monolithic WS<inf>2</inf>, MoS<inf>2</inf>, and MoS<inf>2</inf>/graphene aerogels, ACS Nano. 9 (2015) 4698–4705. doi:10.1021/acsnano.5b00087.

[191] Y. Lei, S. Pakhira, K. Fujisawa, X. Wang, O.O. Iyiola, N. Perea López, A. Laura Elías, L. Pulickal Rajukumar, C. Zhou, B. Kabius, N. Alem, M. Endo, R. Lv, J.L. Mendoza-Cortes, M. Terrones, Low-temperature Synthesis of Heterostructures of Transition Metal Dichalcogenide Alloys (WxMo1-xS2) and Graphene with Superior Catalytic Performance for Hydrogen Evolution, ACS Nano. 11 (2017) 5103–5112. doi:10.1021/acsnano.7b02060.

[192] Y.-H. Choi, J. Cho, A.M. Lunsford, M. Al-Hashimi, L. Fang, S. Banerjee, Mapping the electrocatalytic activity of MoS 2 across its amorphous to crystalline transition, J. Mater. Chem. A. 5 (2017) 5129–5141. doi:10.1039/C6TA10316B.

[193] J. Hu, B. Huang, C. Zhang, Z. Wang, Y. An, D. Zhou, H. Lin, M.K.H. Leung, S. Yang, Engineering stepped edge surface structures of MoS2 sheet stacks to accelerate the hydrogen evolution reaction, Energy Environ. Sci. 10 (2017) 593–603. doi:10.1039/C6EE03629E.

[194] J. Xie, H. Zhang, S. Li, R. Wang, X. Sun, M. Zhou, J. Zhou, X.W.D. Lou, Y. Xie, Defect-rich MoS2 ultrathin nanosheets with additional active edge sites for enhanced electrocatalytic hydrogen evolution., Adv. Mater. 25 (2013) 5807–13. doi:10.1002/adma.201302685.

[195] H. Huang, L. Chen, C. Liu, X. Liu, S. Fang, W. Liu, Y. Liu, Hierarchically

Nanostructured MoS2 with Rich In-plane Edges as a High-performance Electrocatalyst for Hydrogen Evolution Reaction, J. Mater. Chem. A. 4 (2016) 14577–14585. doi:10.1039/C6TA06174E.

[196] J.M. Wu, Y.G. Sun, W.E. Chang, J.T. Lee, Piezoelectricity induced water splitting and formation of hydroxyl radical from active edge sites of MoS2nanoflowers, Nano Energy. 46 (2018) 372–382. doi:10.1016/j.nanoen.2018.02.010.

[197] P. Karfa, R. Madhuri, P.K. Sharma, A. Tiwari, Designing of transition metal dichalcogenides based different shaped trifunctional electrocatalyst through "adjourn-reaction" scheme, Nano Energy. 33 (2017) 98–109. doi:10.1016/j.nanoen.2017.01.012.

[198] Z. Huang, W. Luo, L. Ma, M. Yu, X. Ren, M. He, S. Polen, K. Click, B. Garrett, J. Lu, K. Amine, C. Hadad, W. Chen, A. Asthagiri, Y. Wu, Dimeric [Mo2S12]2- Cluster: A Molecular Analogue of MoS2 Edges for Superior Hydrogen-Evolution Electrocatalysis, Angew. Chemie - Int. Ed. 54 (2015) 15181–15185. doi:10.1002/anie.201507529.

[199] J. Kibsgaard, T.F. Jaramillo, F. Besenbacher, Building an appropriate active-site motif into a hydrogen-evolution catalyst with thiomolybdate [Mo3S13]2— clusters, Nat. Chem. 6 (2014) 248–253. doi:10.1038/nchem.1853.

[200] J.D. Benck, Z. Chen, L.Y. Kuritzky, A.J. Forman, T.F. Jaramillo, Amorphous Molybdenum Sul fi de Catalysts for Electrochemical Hydrogen Production: Insights into the Origin of their Catalytic Activity, ACS Catal. 2 (2012) 1916–1923.

[201] Q.T. Nguyen, P.D. Nguyen, D. Nguyen, Q.D. Truong, T.T. Kim Chi, T.T.D. Ung, I. Honma, N.Q. Liem, P.D. Tran, Novel Amorphous Molybdenum Selenide as an Efficient Catalyst for Hydrogen Evolution Reaction, ACS Appl. Mater. Interfaces. 10 (2018) 8659–8665. doi:10.1021/acsami.7b18675.

[202] D. Merki, S. Fierro, H. Vrubel, X. Hu, Amorphous molybdenum sulfide films as catalysts for electrochemical hydrogen production in water, Chem. Sci. 2 (2011) 1262–1267. doi:10.1039/C1SC00117E.

[203] S.M. Tan, M. Pumera, Bottom-up Electrosynthesis of Highly Active Tungsten Sulfide (WS3-x) Films for Hydrogen Evolution, ACS Appl. Mater. Interfaces. 8 (2016) 3948–3957. doi:10.1021/acsami.5b11109.

[204] S.M. Tan, M. Pumera, Composition-Graded MoWSxHybrids with Tailored Catalytic Activity by Bipolar Electrochemistry, ACS Appl. Mater. Interfaces. 9 (2017) 41955–41964. doi:10.1021/acsami.7b09435.

[205] P.D. Tran, T. V. Tran, M. Orio, S. Torelli, Q.D. Truong, K. Nayuki, Y. Sasaki, S.Y. Chiam, R. Yi, I. Honma, J. Barber, V. Artero, Coordination polymer structure and revisited hydrogen evolution catalytic mechanism for amorphous molybdenum sulfide, Nat. Mater. 15 (2016) 640–646. doi:10.1038/nmat4588.

[206] B. Lassalle-Kaiser, D. Merki, H. Vrubel, S. Gul, V.K. Yachandra, X. Hu, J. Yano, Evidence from in situ X-ray absorption spectroscopy for the involvement of terminal disulfide in the reduction of protons by an amorphous molybdenum sulfide electrocatalyst, J. Am. Chem. Soc. 137 (2015) 314–321. doi:10.1021/ja510328m.

[207] L.R.L. Ting, Y. Deng, L. Ma, Y.J. Zhang, A.A. Peterson, B.S. Yeo, Catalytic Activities of Sulfur Atoms in Amorphous Molybdenum Sulfide for the Electrochemical Hydrogen Evolution Reaction, ACS Catal. 6 (2016) 861–867. doi:10.1021/acscatal.5b02369.

[208] Y. Deng, L.R.L. Ting, P.H.L. Neo, Y.-J. Zhang, A.A. Peterson, B.S. Yeo, Operando Raman Spectroscopy of Amorphous Molybdenum Sulfide (MoSx) during the Electrochemical Hydrogen Evolution Reaction: Identification of Sulfur Atoms as Catalytically Active Sites for H + Reduction, ACS Catal. (2016) 7790–7798. doi:10.1021/acscatal.6b01848.

[209] H.G.S. Casalongue, J.D. Benck, C. Tsai, R.K.B. Karlsson, S. Kaya, M.L. Ng, L.G.M. Pettersson, F. Abild-Pedersen, J.K. Nørskov, H. Ogasawara, T.F. Jaramillo, A. Nilsson, Operando Characterization of an Amorphous Molybdenum Sulfide Nanoparticle Catalyst during the Hydrogen Evolution Reaction, J. Phys. Chem. C. 118 (2014) 29252–29259. doi:10.1021/jp505394e.

[210] H. Vrubel, X. Hu, Growth and activation of an amorphous molybdenum sulfide hydrogen evolving catalyst, ACS Catal. 3 (2013) 2002–2011. doi:10.1021/cs400441u.

[211] H. Pan, Metal dichalcogenides monolayers: Novel catalysts for electrochemical hydrogen production, Sci. Rep. 4 (2014) 1–6. doi:10.1038/srep05348.

[212] Y. Liu, J. Wu, K.P. Hackenberg, J. Zhang, Y.M. Wang, Y. Yang, K. Keyshar, J. Gu, T. Ogitsu, R. Vajtai, J. Lou, P.M. Ajayan, B.C. Wood, B.I. Yakobson, Self-optimizing, highly surface-active layered metal dichalcogenide catalysts for hydrogen evolution, Nat. Energy. 6 (2017) 17127. doi:10.1038/nenergy.2017.127.

[213] J. Shi, X. Wang, S. Zhang, L. Xiao, Y. Huan, Y. Gong, Z. Zhang, Y. Li, X. Zhou, M. Hong, Q. Fang, Q. Zhang, X. Liu, L. Gu, Z. Liu, Y. Zhang, Two-dimensional metallic tantalum disulfide as a hydrogen evolution catalyst, Nat. Commun. 8 (2017) 958. doi:10.1038/s41467-017-01089-z.

[214] Y. Qu, M. Shao, Y. Shao, M. Yang, J. Xu, C.T. Kwok, X. Shi, Z. Lu, H. Pan, Ultra-high electrocatalytic activity of VS2 nanoflowers for efficient hydrogen evolution reaction, J. Mater. Chem. A. 5 (2017) 15080–15086. doi:10.1039/c7ta03172f.

[215] Y. Feng, S. Gong, E. Du, X. Chen, R. Qi, K. Yu, Z. Zhu, 3R TaS2Surpasses the Corresponding 1T and 2H Phases for the Hydrogen Evolution Reaction, J. Phys. Chem. C. 122 (2018) 2382–2390. doi:10.1021/acs.jpcc.7b10833.

[216] R.J. Toh, Z. Sofer, J. Luxa, D. Sedmidubský, M. Pumera, 3R phase of MoS $_2$ and WS $_2$ outperforms the corresponding 2H phase for hydrogen evolution, Chem. Commun. 53 (2017) 3054–3057. doi:10.1039/C6CC09952A.

[217] C. Tsai, K. Chan, F. Abild-Pedersen, J.K. Nørskov, Active edge sites in MoSe2 and WSe2 catalysts for the hydrogen evolution reaction: a density functional study., Phys. Chem. Chem. Phys. 16 (2014) 13156–64. doi:10.1039/c4cp01237b.

[218] C. Tsai, K. Chan, J.K. Nørskov, F. Abild-Pedersen, Rational design of MoS 2 catalysts: tuning the structure and activity via transition metal doping, Catal. Sci. Technol. 5 (2015) 246–253. doi:10.1039/C4CY01162G.

[219] J. Lauritsen, J. Kibsgaard, G. Olesen, P. Moses, B. Hinnemann, S. Helveg, J. Norskov, B. Clausen, H. Topsoe, E. Lagsgaard, Location and coordination of promoter atoms in Co- and Ni-promoted MoS2-based hydrotreating catalysts, J. Catal. 249 (2007) 220–233. doi:10.1016/j.jcat.2007.04.013.

[220] D. Merki, H. Vrubel, L. Rovelli, S. Fierro, X. Hu, Fe, Co, and Ni ions promote the catalytic activity of amorphous molybdenum sulfide films for hydrogen evolution, Chem. Sci. 3 (2012) 2515. doi:10.1039/c2sc20539d.

[221] X. Chia, N.A.A. Sutrisnoh, M. Pumera, Tunable Pt–MoS $_x$ Hybrid Catalysts for Hydrogen Evolution, ACS Appl. Mater. Interfaces. 10 (2018) 8702–8711. doi:10.1021/acsami.7b19346.

[222] H. Zhu, G. Gao, M. Du, J. Zhou, K. Wang, W. Wu, X. Chen, Y. Li, P. Ma, W. Dong, F. Duan, M. Chen, G. Wu, J. Wu, H. Yang, S. Guo, Atomic-Scale Core/Shell Structure Engineering Induces Precise Tensile Strain to Boost Hydrogen Evolution Catalysis, Adv. Mater. 30 (2018) 1–9. doi:10.1002/adma.201707301.

[223] L. Yu, B.Y. Xia, X. Wang, X.W. Lou, General Formation of M-MoS3 (M = Co, Ni) Hollow Structures with Enhanced Electrocatalytic Activity for Hydrogen Evolution, Adv. Mater. 28 (2016) 92–97. doi:10.1002/adma.201504024.

[224] N.H. Attanayake, A.C. Thenuwara, A. Patra, Y. V. Aulin, T.M. Tran, H. Chakraborty, E. Borguet, M.L. Klein, J.P. Perdew, D.R. Strongin, Effect of Intercalated Metals on the Electrocatalytic Activity of 1T-MoS 2 for the Hydrogen Evolution Reaction, ACS Energy Lett. (2018) 7–13. doi:10.1021/acsenergylett.7b00865.

[225] Z. Chen, K. Leng, X. Zhao, S. Malkhandi, W. Tang, B. Tian, L. Dong, L. Zheng, M. Lin, B.S. Yeo, K.P. Loh, Interface confined hydrogen evolution reaction in zero valent metal nanoparticles-intercalated molybdenum disulfide, Nat. Commun. 8 (2017) 1–9. doi:10.1038/ncomms14548.

[226] D. Wang, X. Wang, Y. Lu, C. Song, J. Pan, C. Li, M. Sui, W. Zhao, F. Huang, Atom-scale dispersed palladium in a conductive Pd0.1TaS2 lattice with a unique electronic structure for efficient hydrogen evolution, J. Mater. Chem. A. 5 (2017) 22618–22624. doi:10.1039/C7TA06447K.

[227] X. Chia, N.A.A. Sutrisnoh, Z. Sofer, J. Luxa, M. Pumera, Morphological Effects and Stabilization of the Metallic 1T Phase in Layered V-, Nb-, and Ta-Doped WSe2for Electrocatalysis, Chem. - A Eur. J. 24 (2018) 3199–3208. doi:10.1002/chem.201704158.

[228] I. Roger, M.D. Symes, Silver leakage from Ag/AgCl reference electrodes as a potential cause of interference in the electrocatalytic hydrogen evolution reaction, ACS Appl. Mater. Interfaces. 9 (2017) 472–478. doi:10.1021/acsami.6b13438.

[229] Y. Li, L. Wang, A. Song, M. Xia, Z. Li, G. Shao, The study on the active origin of electrocatalytic water splitting using Ni-MoS2as example, Electrochim. Acta. 268 (2018) 268–275. doi:10.1016/j.electacta.2018.02.084.

[230] D. Hou, W. Zhou, X. Liu, K. Zhou, J. Xie, G. Li, S. Chen, Pt nanoparticles/MoS2 nanosheets/carbon fibers as efficient catalyst for the hydrogen evolution reaction, Electrochim. Acta. 166 (2015) 26–31. doi:10.1016/j.electacta.2015.03.067.

[231] X. Liu, S. Gao, P. Yang, B. Wang, J.Z. Ou, Z. Liu, Y. Wang, Synergetic coupling of Pd nanoparticles and amorphous MoSxtoward highly efficient electrocatalytic hydrogen evolution reactions, Appl. Mater. Today. 13 (2018) 158–165. doi:10.1016/j.apmt.2018.09.001.

[232] H. Wang, C. Tsai, D. Kong, K. Chan, F. Abild-Pedersen, J.K. Nørskov, Y. Cui, Transition-metal doped edge sites in vertically aligned MoS2 catalysts for enhanced hydrogen evolution, Nano Res. 8 (2015) 566–575. doi:10.1007/s12274-014-0677-7.

[233] J. Cao, J. Zhou, Y. Zhang, X. Liu, A Clean and Facile Synthesis Strategy of MoS2 Nanosheets Grown on Multi-Wall CNTs for Enhanced Hydrogen Evolution Reaction Performance, Sci. Rep. 7 (2017) 1–8. doi:10.1038/s41598-017-09047-x.

[234] T.R. Hellstern, J. Kibsgaard, C. Tsai, D.W. Palm, L.A. King, F. Abild-Pedersen, T.F. Jaramillo, Investigating Catalyst–Support Interactions To Improve the Hydrogen Evolution Reaction Activity of Thiomolybdate [Mo3S13]2– Nanoclusters, ACS Catal. (2017) 7126–7130. doi:10.1021/acscatal.7b02133.

[235] Y. Tan, P. Liu, L. Chen, W. Cong, Y. Ito, J. Han, X. Guo, Z. Tang, T. Fujita, A. Hirata, M.W. Chen, Monolayer MoS 2 films supported by 3D nanoporous metals for high-effi ciency electrocatalytic hydrogen production, Adv. Mater. 26 (2014) 8023–8028. doi:10.1002/adma.201403808.

[236] X. Ren, Q. Ma, H. Fan, L. Pang, Y. Zhang, Y. Yao, X. Ren, S. (Frank) Liu, A Se-doped MoS 2 nanosheet for improved hydrogen evolution reaction, Chem. Commun. 51 (2015) 15997–16000. doi:10.1039/C5CC06847A.

[237] A. Azcatl, X. Qin, A. Prakash, C. Zhang, L. Cheng, Q. Wang, N. Lu, M.J. Kim, J. Kim, K. Cho, R. Addou, C.L. Hinkle, J. Appenzeller, R.M. Wallace, Covalent Nitrogen Doping and Compressive Strain in MoS2by Remote N2Plasma Exposure, Nano Lett. 16 (2016) 5437–5443. doi:10.1021/acs.nanolett.6b01853.

[238] S. Qin, W. Lei, D. Liu, Y. Chen, In-situ and tunable nitrogen-doping of MoS2 nanosheets., Sci. Rep. 4 (2014) 7582. doi:10.1038/srep07582.

[239] W. Xiao, P. Liu, J. Zhang, W. Song, Y.P. Feng, D. Gao, J. Ding, Dual-Functional N Dopants in Edges and Basal Plane of MoS2Nanosheets Toward Efficient and Durable Hydrogen Evolution, Adv. Energy Mater. 7 (2017). doi:10.1002/aenm.201602086.

[240] T. Sun, J. Wang, X. Chi, Y. Lin, Z. Chen, X. Ling, C. Qiu, Y. Xu, L. Song, W. Chen, C. Su, Engineering the Electronic Structure of MoS2Nanorods by N and Mn Dopants for Ultra-Efficient Hydrogen Production, ACS Catal. 8 (2018) 7585–7592. doi:10.1021/acscatal.8b00783.

[241] R. Li, L. Yang, T. Xiong, Y. Wu, L. Cao, D. Yuan, W. Zhou, Nitrogen doped MoS2nanosheets synthesized via a low-temperature process as electrocatalysts with enhanced activity for hydrogen evolution reaction, J. Power Sources. 356 (2017) 133–139. doi:10.1016/j.jpowsour.2017.04.060.

[242] J. Kibsgaard, T.F. Jaramillo, Molybdenum phosphosulfide: an active, acid-stable, earth-abundant catalyst for the hydrogen evolution reaction., Angew. Chemie (International Ed.). 53 (2014) 14433–7. doi:10.1002/anie.201408222.

[243] U.K. Sultana, A.P. O'Mullane, Electrochemical Formation of Amorphous Molybdenum Phosphosulfide for Enabling the Hydrogen Evolution Reaction in Alkaline and Acidic Media, ACS Appl. Energy Mater. 1 (2018) 2849–2858. doi:10.1021/acsaem.8b00489.

[244] R. Ye, P. Del Angel-Vicente, Y. Liu, M.J. Arellano-Jimenez, Z. Peng, T. Wang, Y. Li, B.I. Yakobson, S.H. Wei, M.J. Yacaman, J.M. Tour, High-Performance Hydrogen Evolution from MoS2(1-x)PxSolid Solution, Adv. Mater. 28 (2016) 1427–1432. doi:10.1002/adma.201504866.

[245] L. Bian, W. Gao, J. Sun, M. Han, F. Li, Z. Gao, L. Shu, N. Han, Z.X. Yang, A. Song, Y. Qu, J.C. Ho, Phosphorus-Doped MoS2Nanosheets Supported on Carbon Cloths as Efficient Hydrogen-Generation Electrocatalysts, ChemCatChem. 10 (2018) 1571–1577. doi:10.1002/cctc.201701680.

[246] X.J. Chua, J. Luxa, A.Y.S. Eng, S.M. Tan, Z. Sofer, M. Pumera, Negative Electrocatalytic Effects of p-Doping Niobium and Tantalum on MoS 2 and WS 2 for the

Hydrogen Evolution Reaction and Oxygen Reduction Reaction, ACS Catal. (2016) 5724–5734. doi:10.1021/acscatal.6b01593.

[247] R.J. Toh, Z. Sofer, J. Luxa, M. Pumera, Ultrapure Molybdenum Disulfide Shows Enhanced Catalysis for Hydrogen Evolution over Impurities-Doped Counterpart, ChemCatChem. 9 (2017) 1168–1171. doi:10.1002/cctc.201601561.

[248] Y. Ouyang, Q. Li, L. Shi, C. Ling, J. Wang, Molybdenum sulfide clusters immobilized on defective graphene: A stable catalyst for the hydrogen evolution reaction, J. Mater. Chem. A. 6 (2018) 2289–2294. doi:10.1039/c7ta09828f.

[249] Y. Zhou, J.L. Silva, J.M. Woods, J. V. Pondick, Q. Feng, Z. Liang, W. Liu, L. Lin, B. Deng, B. Brena, F. Xia, H. Peng, Z. Liu, H. Wang, C.M. Araujo, J.J. Cha, Revealing the Contribution of Individual Factors to Hydrogen Evolution Reaction Catalytic Activity, Adv. Mater. 30 (2018) 1–9. doi:10.1002/adma.201706076.

[250] H. Yu, Y. Xue, L. Hui, C. Zhang, Y. Li, Z. Zuo, Y. Zhao, Z. Li, Y. Li, Efficient Hydrogen Production on a 3D Flexible Heterojunction Material, Adv. Mater. 30 (2018) 1–7. doi:10.1002/adma.201707082.

[251] L. Liao, J. Zhu, X. Bian, L. Zhu, M.D. Scanlon, H.H. Girault, B. Liu, MoS 2 Formed on Mesoporous Graphene as a Highly Active Catalyst for Hydrogen Evolution, Adv. Funct. Mater. 23 (2013) 5326–5333. doi:10.1002/adfm.201300318.

[252] D. McAteer, Z. Gholamvand, N. McEvoy, A. Harvey, E. O'Malley, G.S. Duesberg, J.N. Coleman, Thickness Dependence and Percolation Scaling of Hydrogen Production Rate in MoS 2 Nanosheet and Nanosheet–Carbon Nanotube Composite Catalytic Electrodes, ACS Nano. 10 (2016) 672–683. doi:10.1021/acsnano.5b05907.

[253] P. Cao, J. Peng, J. Li, M. Zhai, Highly conductive carbon black supported amorphous molybdenum disulfide for efficient hydrogen evolution reaction, J. Power Sources. 347 (2017) 210–219. doi:10.1016/j.jpowsour.2017.02.056.

[254] L. Yang, A. Mukhopadhyay, Y. Jiao, J. Hamel, M. Benamara, Y. Xing, H. Zhu, Aligned and Stable Metallic MoS2 on Plasma-treated Mass Transfer Channels for Hydrogen Evolution Reaction, J. Mater. Chem. A. 5 (2017) 25359–25367. doi:10.1039/C7TA08400E.

[255] S.H. Noh, J. Hwang, J. Kang, M.H. Seo, D. Choi, B. Han, Tuning the catalytic activity of heterogeneous two-dimensional transition metal dichalcogenides for hydrogen evolution, J. Mater. Chem. A. 6 (2018) 20005–20014. doi:10.1039/c8ta07141a.

[256] C. Tsai, F. Abild-Pedersen, J.K. Nørskov, Tuning the MoS 2 Edge-Site Activity for Hydrogen Evolution via Support Interactions, Nano Lett. 14 (2014) 1381–1387.

[257] F. Scaglione, Y. Xue, F. Celegato, P. Rizzi, L. Battezzati, Amorphous molybdenum sulphide @ nanoporous gold as catalyst for hydrogen evolution reaction in acidic environment, J. Mater. Sci. 53 (2018) 12388–12398. doi:10.1007/s10853-018-2490-2.

[258] Y. Tan, P. Liu, L. Chen, W. Cong, Y. Ito, J. Han, X. Guo, Z. Tang, T. Fujita, A. Hirata, M.W. Chen, Monolayer MoS2 films supported by 3D nanoporous metals for high-efficiency electrocatalytic hydrogen production., Adv. Mater. 26 (2014) 8023–8. doi:10.1002/adma.201403808.

[259] R. He, J. Hua, A. Zhang, C. Wang, J. Peng, W. Chen, J. Zeng, Molybdenum Disulfide-Black Phosphorus Hybrid Nanosheets as a Superior Catalyst for Electrochemical

Hydrogen Evolution, Nano Lett. 17 (2017) 4311–4316. doi:10.1021/acs.nanolett.7b01334.

[260] S. Wang, X. Wang, J.H. Warner, W.E.T. Al, All Chemical Vapor Deposition Growth of MoS2:h-BN Vertical van der Waals Heterostructures, ACS Nano. 9 (2015) 5246–5254. doi:10.1021/acsnano.5b00655.

[261] X. Qian, J. Ding, J. Zhang, Y. Zhang, Y. Wang, E. Kan, X. Wang, J. Zhu, Ultrathin molybdenum disulfide/carbon nitride nanosheets with abundant active sites for enhanced hydrogen evolution, Nanoscale. 10 (2018) 1766–1773. doi:10.1039/c7nr07213a.

[262] Y. Hou, A.B. Laursen, J. Zhang, G. Zhang, Y. Zhu, X. Wang, S. Dahl, I. Chorkendorff, Layered nanojunctions for hydrogen-evolution catalysis, Angew. Chemie - Int. Ed. 52 (2013) 3621–3625. doi:10.1002/anie.201210294.

[263] R.D. Nikam, A.Y. Lu, P.A. Sonawane, U.R. Kumar, K. Yadav, L.J. Li, Y.T. Chen, Three-Dimensional Heterostructures of MoS2 Nanosheets on Conducting MoO2 as an Efficient Electrocatalyst to Enhance Hydrogen Evolution Reaction, ACS Appl. Mater. Interfaces. 7 (2015) 23328–23335. doi:10.1021/acsami.5b07960.

[264] X.-Q. Bao, D.Y. Petrovykh, P. Alpuim, D.G. Stroppa, N. Guldris, H. Fonseca, M. Costa, J. Gaspar, C. Jin, L. Liu, Amorphous oxygen-rich molybdenum oxysulfide Decorated p-type silicon microwire Arrays for efficient photoelectrochemical water reduction, Nano Energy. 16 (2015) 130–142. doi:10.1016/j.nanoen.2015.06.014.

[265] N.H. Attanayake, S.C. Abeyweera, A.C. Thenuwara, B. Anasori, Y. Gogotsi, Y. Sun, D.R. Strongin, Vertically aligned MoS2 on Ti3C2 (MXene) as an improved HER catalyst, J. Mater. Chem. A. 6 (2018) 16882–16889. doi:10.1039/c8ta05033c.

[266] S. Ng, M. Krbal, R. Zazpe, J. Prikryl, J. Charvot, F. Dvořák, L. Strizik, S. Slang, H. Sopha, Y. Kosto, V. Matolin, F.K. Yam, F. Bures, J.M. Macak, MoSexOy-Coated 1D TiO2Nanotube Layers: Efficient Interface for Light-Driven Applications, Adv. Mater. Interfaces. 5 (2018) 1–8. doi:10.1002/admi.201701146.

[267] G. Li, D. Zhang, Y. Yu, S. Huang, W. Yang, L. Cao, Activating MoS2 for pH-Universal Hydrogen Evolution Catalysis, J. Am. Chem. Soc. 139 (2017) 16194–16200. doi:10.1021/jacs.7b07450.

[268] D.A. Henckel, O.M. Lenz, K.M. Krishnan, B.M. Cossairt, Improved HER Catalysis through Facile, Aqueous Electrochemical Activation of Nanoscale WSe2, Nano Lett. 18 (2018) 2329–2335. doi:10.1021/acs.nanolett.7b05213.

[269] D. Voiry, H. Yamaguchi, J. Li, R. Silva, D.C.B. Alves, T. Fujita, M. Chen, T. Asefa, V.B. Shenoy, G. Eda, M. Chhowalla, Enhanced catalytic activity in strained chemically exfoliated WS2 nanosheets for hydrogen evolution., Nat. Mater. 12 (2013) 850–855. doi:10.1038/nmat3700.

[270] A. Apte, V. Kochat, P. Rajak, A. Krishnamoorthy, P. Manimunda, J.A. Hachtel, J.C. Idrobo, S.A. Syed Amanulla, P. Vashishta, A. Nakano, R.K. Kalia, C.S. Tiwary, P.M. Ajayan, Structural Phase Transformation in Strained Monolayer MoWSe $_2$ Alloy, ACS Nano. (2018) acsnano.8b00248. doi:10.1021/acsnano.8b00248.

[271] L. Oakes, R. Carter, T. Hanken, A.P. Cohn, K. Share, B. Schmidt, C.L. Pint, Interface strain in vertically stacked two-dimensional heterostructured carbon-MoS2 nanosheets controls electrochemical reactivity, Nat. Commun. 7 (2016) 7. doi:10.1038/ncomms11796.

[272] G. Gao, Q. Sun, A. Du, Activating catalytic inert basal plane of molybdenum disulfide to optimize hydrogen evolution activity via defect doping and strain engineering, J. Phys. Chem. C. 120 (2016) 16761–16766. doi:10.1021/acs.jpcc.6b04692.

[273] A.L. Friedman, A.T. Hanbicki, F.K. Perkins, G.G. Jernigan, J.C. Culbertson, P.M. Campbell, Evidence for Chemical Vapor Induced 2H to 1T Phase Transition in MoX2(X = Se, S) Transition Metal Dichalcogenide Films, Sci. Rep. 7 (2017) 1–9. doi:10.1038/s41598-017-04224-4.

[274] B. Akdim, R. Pachter, S. Mou, Theoretical analysis of the combined effects of sulfur vacancies and analyte adsorption on the electronic properties of single-layer MoS $_2$, Nanotechnology. 27 (2016) 185701. doi:10.1088/0957-4484/27/18/185701.

[275] J.-W. Wei, Z.-W. Ma, H. Zeng, Z.-Y. Wang, Q. Wei, P. Peng, Electronic and optical properties of vacancy-doped WS2 monolayers Electronic and optical properties of vacancy-doped WS 2 monolayers, Cit. AIP Adv. 2 (2012). doi:10.1063/1.4768261doi.org/10.1063/1.4768261.

[276] L. Cai, J. He, Q. Liu, T. Yao, L. Chen, W. Yan, F. Hu, Y. Jiang, Y. Zhao, T. Hu, Z. Sun, S. Wei, Vacancy-induced ferromagnetism of MoS2 nanosheets, J. Am. Chem. Soc. 137 (2015) 2622–2627. doi:10.1021/ja5120908.

[277] Y. Ma, Y. Dai, M. Guo, C. Niu, J. Lu, B. Huang, Electronic and magnetic properties of perfect, vacancy-doped, and nonmetal adsorbed MoSe2, MoTe2 and WS2 monolayers, Phys. Chem. Chem. Phys. 13 (2011) 15546–15553. doi:10.1039/c1cp21159e.

[278] H. Zheng, B. Yang, D. Wang, R. Han, X. Du, Y. Yan, Tuning magnetism of monolayer MoS2 by doping vacancy and applying strain, Appl. Phys. Lett. 104 (2014) 4–9. doi:10.1063/1.4870532.

[279] K.Y. Kim, J. Lee, S. Kang, Y.W. Son, H.W. Jang, Y. Kang, S. Han, Role of Hyper-Reduced States in Hydrogen Evolution Reaction at Sulfur Vacancy in MoS2, ACS Catal. 8 (2018) 4508–4515. doi:10.1021/acscatal.8b00883.

[280] Y.-C. Chen, A.-Y. Lu, P. Lu, X. Yang, C.-M. Jiang, M. Mariano, B. Kaehr, O. Lin, A. Taylor, I.D. Sharp, L.-J. Li, S.S. Chou, V. Tung, Structurally Deformed MoS 2 for Electrochemically Stable, Thermally Resistant, and Highly Efficient Hydrogen Evolution Reaction, Adv. Mater. 29 (2017) 1703863. doi:10.1002/adma.201703863.

[281] H. Li, M. Du, M.J. Mleczko, A.L. Koh, Y. Nishi, E. Pop, A.J. Bard, X. Zheng, Kinetic Study of Hydrogen Evolution Reaction over Strained MoS2 with Sulfur Vacancies Using Scanning Electrochemical Microscopy, J. Am. Chem. Soc. 138 (2016) 5123–5129. doi:10.1021/jacs.6b01377.

[282] Y. Kim, D.H.K. Jackson, D. Lee, M. Choi, T.W. Kim, S.Y. Jeong, H.J. Chae, H.W. Kim, N. Park, H. Chang, T.F. Kuech, H.J. Kim, In Situ Electrochemical Activation of Atomic Layer Deposition Coated MoS2 Basal Planes for Efficient Hydrogen Evolution Reaction, Adv. Funct. Mater. 27 (2017) 1–10. doi:10.1002/adfm.201701825.

[283] J.H. Han, H.K. Kim, B. Baek, J. Han, H.S. Ahn, M.H. Baik, J. Cheon, Activation of the Basal Plane in Two Dimensional Transition Metal Chalcogenide Nanostructures, J. Am. Chem. Soc. 140 (2018) 13663–13671. doi:10.1021/jacs.8b05477.

[284] Y. Bao, M. Yang, S.J.R. Tan, Y.P. Liu, H. Xu, W. Liu, C.T. Nai, Y.P. Feng, J. Lu, K.P. Loh, Substoichiometric Molybdenum Sulfide Phases with Catalytically Active Basal Planes, J. Am. Chem. Soc. 138 (2016) 14121–14128. doi:10.1021/jacs.6b09042.

[285] M.A.R. Anjum, H.Y. Jeong, M.H. Lee, H.S. Shin, J.S. Lee, Efficient Hydrogen Evolution Reaction Catalysis in Alkaline Media by All-in-One MoS $_2$ with Multifunctional Active Sites, Adv. Mater. 1707105 (2018) 1707105. doi:10.1002/adma.201707105.

[286] Y. Li, K. Yin, L. Wang, X. Lu, Y. Zhang, Y. Liu, D. Yan, Y. Song, S. Luo, Engineering MoS 2 nanomesh with holes and lattice defects for highly active hydrogen evolution reaction, Appl. Catal. B Environ. (2018). doi:10.1016/j.apcatb.2018.05.080.

[287] G. Ye, Y. Gong, J. Lin, B. Li, Y. He, S.T. Pantelides, W. Zhou, R. Vajtai, P.M. Ajayan, Defects Engineered Monolayer MoS $_2$ for Improved Hydrogen Evolution Reaction, Nano Lett. 16 (2016) 1097–1103. doi:10.1021/acs.nanolett.5b04331.

[288] J. Hong, Z. Hu, M. Probert, K. Li, D. Lv, X. Yang, L. Gu, N. Mao, Q. Feng, L. Xie, J. Zhang, D. Wu, Z. Zhang, C. Jin, W. Ji, X. Zhang, J. Yuan, Z. Zhang, Exploring atomic defects in molybdenum disulphide monolayers, Nat. Commun. 6 (2015) 1–8. doi:10.1038/ncomms7293.

[289] D. Le, T.B. Rawal, T.S. Rahman, Single-layer MoS2 with sulfur vacancies: Structure and catalytic application, J. Phys. Chem. C. 118 (2014) 5346–5351. doi:10.1021/jp411256g.

[290] H. Li, C. Tsai, A.L. Koh, L. Cai, A.W. Contryman, A.H. Fragapane, J. Zhao, H.S. Han, H.C. Manoharan, F. Abild-Pedersen, J.K. Nørskov, X. Zheng, Activating and optimizing MoS2 basal planes for hydrogen evolution through the formation of strained sulphur vacancies., Nat. Mater. 15 (2015) 48–53. doi:10.1038/nmat4465.

[291] A.Y. Lu, X. Yang, C.C. Tseng, S. Min, S.H. Lin, C.L. Hsu, H. Li, H. Idriss, J.L. Kuo, K.W. Huang, L.J. Li, High-Sulfur-Vacancy Amorphous Molybdenum Sulfide as a High Current Electrocatalyst in Hydrogen Evolution, Small. 12 (2016) 5530–5537. doi:10.1002/smll.201602107.

[292] H.-P. Komsa, J. Kotakoski, S. Kurasch, O. Lehtinen, U. Kaiser, A. V. Krasheninnikov, Two-Dimensional Transition Metal Dichalcogenides under Electron Irradiation: Defect Production and Doping, Phys. Rev. Lett. 109 (2012) 035503. doi:10.1103/PhysRevLett.109.035503.

[293] L. Lin, N. Miao, Y. Wen, S. Zhang, P. Ghosez, Z. Sun, D.A. Allwood, Sulfur-Depleted Monolayered Molybdenum Disulfide Nanocrystals for Superelectrochemical Hydrogen Evolution Reaction, ACS Nano. 10 (2016) 8929–8937. doi:10.1021/acsnano.6b04904.

[294] L. Lin, N. Miao, J. Huang, S. Zhang, Y. Zhu, D.D. Horsell, P. Ghosez, Z. Sun, D.A. Allwood, A photocatalyst of sulphur depleted monolayered molybdenum sulfide nanocrystals for dye degradation and hydrogen evolution reaction, Nano Energy. 38 (2017) 544–552. doi:10.1016/j.nanoen.2017.06.008.

[295] C. Tsai, H. Li, S. Park, J. Park, H.S. Han, J.K. Nørskov, X. Zheng, F. Abild-Pedersen, Electrochemical generation of sulfur vacancies in the basal plane of MoS2 for hydrogen evolution, Nat. Commun. 8 (2017) 15113. doi:10.1038/ncomms15113.

[296] X. Gan, H. Zhao, T.W. Lo, K.H.W. Ho, L.Y.S. Lee, D. Lei, K.-Y. Wong, 2H/1T Phase Transition of Multilayer MoS2 by Electrochemical Incorporation of S vacancies, ACS Appl. Energy Mater. 1 (2018) 4754–4765. doi:10.1021/acsaem.8b00875.

[297] J. Gao, B. Li, J. Tan, P. Chow, T.M. Lu, N. Koratkar, Aging of Transition Metal Dichalcogenide Monolayers, ACS Nano. 10 (2016) 2628–2635. doi:10.1021/acsnano.5b07677.

[298] J. Pető, T. Ollár, P. Vancsó, Z.I. Popov, G.Z. Magda, G. Dobrik, C. Hwang, P.B. Sorokin, L. Tapasztó, Spontaneous doping of the basal plane of MoS2 single layers through oxygen substitution under ambient conditions, Nat. Chem. (2018). doi:10.1038/s41557-018-0136-2.

[299] W. Shi, Z. Wang, Effect of oxygen doping on the hydrogen evolution reaction in MoS2monolayer, J. Taiwan Inst. Chem. Eng. 82 (2018) 163–168. doi:10.1016/j.jtice.2017.11.015.

[300] X. Hai, W. Zhou, S. Wang, H. Pang, K. Chang, F. Ichihara, J. Ye, Rational design of freestanding MoS2monolayers for hydrogen evolution reaction, Nano Energy. 39 (2017) 409–417. doi:10.1016/j.nanoen.2017.07.021.

[301] G. Liu, A.W. Robertson, M.M.J. Li, W.C.H. Kuo, M.T. Darby, M.H. Muhieddine, Y.C. Lin, K. Suenaga, M. Stamatakis, J.H. Warner, S.C.E. Tsang, MoS2 monolayer catalyst doped with isolated Co atoms for the hydrodeoxygenation reaction, Nat. Chem. 9 (2017) 810–816. doi:10.1038/NCHEM.2740.

[302] A.W. Robertson, Y.C. Lin, S. Wang, H. Sawada, C.S. Allen, Q. Chen, S. Lee, G. Do Lee, J. Lee, S. Han, E. Yoon, A.I. Kirkland, H. Kim, K. Suenaga, J.H. Warner, Atomic Structure and Spectroscopy of Single Metal (Cr, V) Substitutional Dopants in Monolayer MoS2, ACS Nano. 10 (2016) 10227–10236. doi:10.1021/acsnano.6b05674.

[303] G. Bai, S. Yuan, Y. Zhao, Z. Yang, S.Y. Choi, Y. Chai, S.F. Yu, S.P. Lau, J. Hao, 2D Layered Materials of Rare-Earth Er-Doped MoS2 with NIR-to-NIR Down- and Up-Conversion Photoluminescence, Adv. Mater. (2016) 7472–7477. doi:10.1002/adma.201601833.

[304] K. Zhang, S. Feng, J. Wang, A. Azcatl, N. Lu, R. Addou, N. Wang, C. Zhou, J. Lerach, V. Bojan, M.J. Kim, L.Q. Chen, R.M. Wallace, M. Terrones, J. Zhu, J.A. Robinson, Manganese Doping of Monolayer MoS2: The Substrate Is Critical, Nano Lett. 15 (2015) 6586–6591. doi:10.1021/acs.nanolett.5b02315.

[305] T.H.M. Lau, X. Lu, J. Kulhavý, S. Wu, L. Lu, T.-S. Wu, R. Kato, J.S. Foord, Y.-L. Soo, K. Suenaga, S.C.E. Tsang, Transition metal atom doping of the basal plane of MoS<inf>2</inf>monolayer nanosheets for electrochemical hydrogen evolution, Chem. Sci. 9 (2018) 4769–4776. doi:10.1039/c8sc01114a.

[306] Q. Wang, Z.L. Zhao, S. Dong, D. He, M.J. Lawrence, S. Han, C. Cai, S. Xiang, P. Rodriguez, B. Xiang, Z. Wang, Y. Liang, M. Gu, Design of active nickel single-atom decorated MoS2as a pH-universal catalyst for hydrogen evolution reaction, Nano Energy. 53 (2018) 458–467. doi:10.1016/j.nanoen.2018.09.003.

[307] H. Zhang, L. Yu, T. Chen, W. Zhou, X.W. (David) Lou, Surface Modulation of Hierarchical MoS2 Nanosheets by Ni Single Atoms for Enhanced Electrocatalytic Hydrogen Evolution, Adv. Funct. Mater. 1807086 (2018) 1–8. doi:10.1002/adfm.201807086.

[308] S. Sasaki, Y. Kobayashi, Z. Liu, K. Suenaga, Y. Maniwa, Y. Miyauchi, Y. Miyata, Growth and optical properties of Nb-doped WS2 monolayers, Appl. Phys. Express. 9 (2016) 071201. doi:10.7567/APEX.9.071201.

[309] K. Qi, S. Yu, Q. Wang, W. Zhang, J. Fan, W.T. Zheng, X. Cui, Decoration of the inert basal plane of defect-rich MoS $_2$ with Pd atoms for achieving Pt-similar HER activity, J. Mater. Chem. A. 4 (2016) 4025–4031. doi:10.1039/C5TA10337A.

[310] Z. Luo, Y. Ouyang, H. Zhang, M. Xiao, J. Ge, Z. Jiang, J. Wang, D. Tang, X. Cao, C. Liu, W. Xing, Chemically activating MoS2via spontaneous atomic palladium interfacial doping towards efficient hydrogen evolution, Nat. Commun. 9 (2018) 1–8. doi:10.1038/s41467-018-04501-4.

[311] J. Deng, H. Li, J. Xiao, Y. Tu, D. Deng, H. Yang, H. Tian, J. Li, P. Ren, X. Bao, Triggering the electrocatalytic hydrogen evolution activity of the inert two-dimensional MoS 2 surface via single-atom metal doping, Energy Environ. Sci. 8 (2015) 1594–1601. doi:10.1039/C5EE00751H.

[312] S.Z. Yang, Y. Gong, P. Manchanda, Y.Y. Zhang, G. Ye, S. Chen, L. Song, S.T. Pantelides, P.M. Ajayan, M.F. Chisholm, W. Zhou, Rhenium-Doped and Stabilized MoS2 Atomic Layers with Basal-Plane Catalytic Activity, Adv. Mater. 1803477 (2018) 1–7. doi:10.1002/adma.201803477.

[313] Y. Wang, S. Liu, X. Hao, J. Zhou, D. Song, D. Wang, L. Hou, F. Gao, Fluorine- and Nitrogen-Codoped MoS2with a Catalytically Active Basal Plane, ACS Appl. Mater. Interfaces. 9 (2017) 27715–27719. doi:10.1021/acsami.7b06795.

[314] D. Gao, B. Xia, C. Zhu, Y. Du, P. Xi, D. Xue, J. Ding, J. Wang, Activation of the MoSe2basal plane and Se-edge by B doping for enhanced hydrogen evolution, J. Mater. Chem. A. 6 (2018) 510–515. doi:10.1039/c7ta09982g.

[315] P. Zhang, B. Xu, G. Chen, C. Gao, M. Gao, Large-scale synthesis of nitrogen doped MoS2quantum dots for efficient hydrogen evolution reaction, Electrochim. Acta. 270 (2018) 256–263. doi:10.1016/j.electacta.2018.03.097.

[316] P. Liu, J. Zhu, J. Zhang, P. Xi, K. Tao, D. Gao, D. Xue, P Dopants Triggered New Basal Plane Active Sites and Enlarged Interlayer Spacing in MoS $_2$ Nanosheets toward Electrocatalytic Hydrogen Evolution, ACS Energy Lett. 2 (2017) 745–752. doi:10.1021/acsenergylett.7b00111.

[317] P. V Sarma, C.S. Tiwary, S. Radhakrishnan, P.M. Ajayan, M.M. Shaijumon, Oxygen incorporated WS2 Nanoclusters with Superior Electrocatalytic Properties for Hydrogen Evolution Reaction, Nanoscale. (2018) 9516–9524. doi:10.1039/C8NR00253C.

[318] D. Er, H. Ye, N.C. Frey, H. Kumar, J. Lou, V.B. Shenoy, Prediction of Enhanced Catalytic Activity for Hydrogen Evolution Reaction in Janus Transition Metal Dichalcogenides, Nano Lett. 18 (2018) 3943–3949. doi:10.1021/acs.nanolett.8b01335.

[319] W. Chen, X. Hou, X. Shi, H. Pan, Two-Dimensional Janus Transition Metal Oxides and Chalcogenides: Multifunctional Properties for Photocatalysts, Electronics, and Energy Conversion, ACS Appl. Mater. Interfaces. 10 (2018) 35289–35295. doi:10.1021/acsami.8b13248.

[320] J. Zhang, S. Jia, I. Kholmanov, L. Dong, D. Er, W. Chen, H. Guo, Z. Jin, V.B. Shenoy, L. Shi, J. Lou, Janus Monolayer Transition-Metal Dichalcogenides, ACS Nano. 11 (2017) 8192–8198. doi:10.1021/acsnano.7b03186.

[321] X. Chia, A. Ambrosi, D. Sedmidubský, Z. Sofer, M. Pumera, Precise tuning of the charge transfer kinetics and catalytic properties of MoS2 materials via electrochemical methods, Chemistry. 20 (2014) 17426–17432. doi:10.1002/chem.201404832.

[322] X. Chia, A. Ambrosi, Z. Sofer, J. Luxa, M. Pumera, Catalytic and Charge Transfer Properties of Transition Metal Dichalcogenides Arising from Electrochemical Pretreatment, ACS Nano. 9 (2015) 5164–5179.

[323] B. Mohanty, M. Ghorbani-Asl, S. Kretschmer, A. Ghosh, P. Guha, S. Panda, B. Jena, A. V. Krasheninnikov, B.K. Jena, MoS 2 Quantum Dots as an Efficient Catalyst Material for Oxygen Evolution Reaction, ACS Catal. (2018) acscatal.7b03180. doi:10.1021/acscatal.7b03180.

[324] Y. Liu, H. Cheng, M. Lyu, S. Fan, Q. Liu, W. Zhang, Y. Zhi, C. Wang, C. Xiao, S. Wei, B. Ye, Y. Xie, Low overpotential in vacancy-rich ultrathin CoSe2 nanosheets for water oxidation, J. Am. Chem. Soc. 136 (2014) 15670–15675. doi:10.1021/ja5085157.

[325] U. De Silva, J. Masud, N. Zhang, Y. Hong, W.P.R. Liyanage, M. Asle Zaeem, M. Nath, Nickel telluride as a bifunctional electrocatalyst for efficient water splitting in alkaline medium, J. Mater. Chem. A. 6 (2018) 7608–7622. doi:10.1039/c8ta01760c.

[326] T. Wang, G. Nam, Y. Jin, X. Wang, P. Ren, M.G. Kim, J. Liang, X. Wen, H. Jang, J. Han, Y. Huang, Q. Li, J. Cho, NiFe (Oxy) Hydroxides Derived from NiFe Disulfides as an Efficient Oxygen Evolution Catalyst for Rechargeable Zn–Air Batteries: The Effect of Surface S Residues, Adv. Mater. 30 (2018) 1–9. doi:10.1002/adma.201800757.

[327] J. Zhang, Y. Li, T. Zhu, Y. Wang, J. Cui, J. Wu, H. Xu, X. Shu, Y. Qin, H. Zheng, P.M. Ajayan, Y. Zhang, Y. Wu, 3D Coral-Like Ni3S2on Ni Foam as a Bifunctional Electrocatalyst for Overall Water Splitting, ACS Appl. Mater. Interfaces. 10 (2018) 31330–31339. doi:10.1021/acsami.8b09361.

[328] N.Q. Tran, V.Q. Bui, H.M. Le, Y. Kawazoe, H. Lee, Anion–Cation Double Substitution in Transition Metal Dichalcogenide to Accelerate Water Dissociation Kinetic for Electrocatalysis, Adv. Energy Mater. 8 (2018) 1–10. doi:10.1002/aenm.201702139.

[329] W. Chen, Y. Liu, Y. Li, J. Sun, Y. Qiu, C. Liu, G. Zhou, Y. Cui, In Situ Electrochemically Derived Nanoporous Oxides from Transition Metal Dichalcogenides for Active Oxygen Evolution Catalysts, Nano Lett. 16 (2016) 7588–7596. doi:10.1021/acs.nanolett.6b03458.

[330] B.R. Wygant, K. Kawashima, C.B. Mullins, Catalyst or Precatalyst? The Effect of Oxidation on Transition Metal Carbide, Pnictide, and Chalcogenide Oxygen Evolution Catalysts, ACS Energy Lett. (2018) 2956–2966. doi:10.1021/acsenergylett.8b01774.

[331] C.C.L. McCrory, S. Jung, J.C. Peters, T.F. Jaramillo, Benchmarking heterogeneous electrocatalysts for the oxygen evolution reaction., J. Am. Chem. Soc. 135 (2013) 16977–16987. doi:10.1021/ja407115p.

[332] Z.W. She, J. Kibsgaard, C.F. Dickens, I. Chorkendorff, J.K. Nørskov, T.F. Jaramillo, Combining theory and experiment in electrocatalysis: Insights into materials design, Science (80-.). 355 (2017). doi:10.1126/science.aad4998.

[333] S. Cherevko, S. Geiger, O. Kasian, N. Kulyk, J.-P. Grote, A. Savan, B.R. Shrestha, S. Merzlikin, B. Breitbach, A. Ludwig, K.J.J. Mayrhofer, Oxygen and hydrogen evolution reactions on Ru, RuO2, Ir, and IrO2 thin film electrodes in acidic and alkaline electrolytes: A comparative study on activity and stability, Catal. Today. 262 (2016) 170–180. doi:10.1016/j.cattod.2015.08.014.

[334] S. Fierro, T. Nagel, H. Baltruschat, C. Comninellis, Investigation of the oxygen evolution reaction on Ti/IrO2 electrodes using isotope labelling and on-line mass spectrometry, Electrochem. Commun. 9 (2007) 1969–1974. doi:10.1016/j.elecom.2007.05.008.

[335] M. Wohlfahrt-Mehrens, J. Heitbaum, Oxygen evolution on Ru and RuO2electrodes studied using isotope labelling and on-line mass spectrometry, J. Electroanal. Chem. 237

(1987) 251–260. doi:10.1016/0022-0728(87)85237-3.

[336] A. Grimaud, O. Diaz-Morales, B. Han, W.T. Hong, Y.L. Lee, L. Giordano, K.A. Stoerzinger, M.T.M. Koper, Y. Shao-Horn, Activating lattice oxygen redox reactions in metal oxides to catalyse oxygen evolution, Nat. Chem. 9 (2017) 457–465. doi:10.1038/nchem.2695.

[337] S. Cherevko, A.R. Zeradjanin, A.A. Topalov, N. Kulyk, I. Katsounaros, K.J.J. Mayrhofer, Dissolution of noble metals during oxygen evolution in acidic media, ChemCatChem. 6 (2014) 2219–2223. doi:10.1002/cctc.201402194.

[338] T. Binninger, R. Mohamed, K. Waltar, E. Fabbri, P. Levecque, R. Kötz, T.J. Schmidt, Thermodynamic explanation of the universal correlation between oxygen evolution activity and corrosion of oxide catalysts, Sci. Rep. 5 (2015) 1–7. doi:10.1038/srep12167.

[339] M. Escudero-Escribano, A.F. Pedersen, E.A. Paoli, R. Frydendal, D. Friebel, P. Malacrida, J. Rossmeisl, I.E.L. Stephens, I. Chorkendorff, Importance of Surface IrO x in Stabilizing RuO 2 for Oxygen Evolution, J. Phys. Chem. B. 122 (2018) 947–955. doi:10.1021/acs.jpcb.7b07047.

[340] E.A. Paoli, F. Masini, R. Frydendal, D. Deiana, C. Schlaup, M. Malizia, T.W. Hansen, S. Horch, I.E.L. Stephens, I. Chorkendorff, Oxygen evolution on well-characterized mass-selected Ru and RuO2 nanoparticles, Chem. Sci. 6 (2015) 190–196. doi:10.1039/C4SC02685C.

[341] C. Spöri, J.T.H. Kwan, A. Bonakdarpour, D.P. Wilkinson, P. Strasser, The Stability Challenges of Oxygen Evolving Catalysts: Towards a Common Fundamental Understanding and Mitigation of Catalyst Degradation, Angew. Chemie - Int. Ed. 56 (2017) 5994–6021. doi:10.1002/anie.201608601.

[342] O. Kasian, J.P. Grote, S. Geiger, S. Cherevko, K.J.J. Mayrhofer, The Common Intermediates of Oxygen Evolution and Dissolution Reactions during Water Electrolysis on Iridium, Angew. Chemie - Int. Ed. 57 (2018) 2488–2491. doi:10.1002/anie.201709652.

[343] Y.T. Kim, P.P. Lopes, S.A. Park, A.Y. Lee, J. Lim, H. Lee, S. Back, Y. Jung, N. Danilovic, V. Stamenkovic, J. Erlebacher, J. Snyder, N.M. Markovic, Balancing activity, stability and conductivity of nanoporous core-shell iridium/iridium oxide oxygen evolution catalysts, Nat. Commun. 8 (2017) 1–8. doi:10.1038/s41467-017-01734-7.

[344] T. Reier, Z. Pawolek, S. Cherevko, M. Bruns, T. Jones, D. Teschner, S. Selve, A. Bergmann, H.N. Nong, R. Schlögl, K.J.J. Mayrhofer, P. Strasser, Molecular insight in structure and activity of highly efficient, low-Ir Ir-Ni oxide catalysts for electrochemical water splitting (OER), J. Am. Chem. Soc. 137 (2015) 13031–13040. doi:10.1021/jacs.5b07788.

[345] S.M. Alia, S. Shulda, C. Ngo, S. Pylypenko, B.S. Pivovar, Iridium-Based Nanowires as Highly Active, Oxygen Evolution Reaction Electrocatalysts, ACS Catal. 8 (2018) 2111–2120. doi:10.1021/acscatal.7b03787.

[346] O. Kasian, S. Geiger, M. Schalenbach, A.M. Mingers, A. Savan, A. Ludwig, S. Cherevko, K.J.J. Mayrhofer, Using Instability of a Non-stoichiometric Mixed Oxide Oxygen Evolution Catalyst As a Tool to Improve Its Electrocatalytic Performance, Electrocatalysis. 9 (2018) 139–145. doi:10.1007/s12678-017-0394-6.

[347] L.C. Seitz, C.F. Dickens, K. Nishio, Y. Hikita, J. Montoya, A. Doyle, C. Kirk, A. Vojvodic, H.Y. Hwang, J.K. Norskov, T.F. Jaramillo, A highly active and stable

IrOx/SrIrO3 catalyst for the oxygen evolution reaction, Science (80-.). 353 (2016) 1011–1014.

[348] S. Kumari, B.P. Ajayi, B. Kumar, J.B. Jasinski, M.K. Sunkara, J.M. Spurgeon, A low-noble-metal W $_{1-x}$ Ir $_{x}$ O $_{3-\delta}$ water oxidation electrocatalyst for acidic media via rapid plasma synthesis, Energy Environ. Sci. 10 (2017) 2432–2440. doi:10.1039/C7EE02626A.

[349] M. Tariq, W.Q. Zaman, W. Sun, Z. Zhou, Y. Wu, L.M. Cao, J. Yang, Unraveling the Beneficial Electrochemistry of IrO2/MoO3Hybrid as a Highly Stable and Efficient Oxygen Evolution Reaction Catalyst, ACS Sustain. Chem. Eng. 6 (2018) 4854–4862. doi:10.1021/acssuschemeng.7b04266.

[350] W.A. Badawy, F.M. Al-Kharafi, Corrosion and passivation behaviors of molybdenum in aqueous solutions of different pH, Electrochim. Acta. 44 (1998) 693–702. doi:10.1016/S0013-4686(98)00180-7.

[351] M. Zafir Mohamad Nasir, Z. Sofer, M. Pumera, Effect of Electrolyte pH on the Inherent Electrochemistry of Layered Transition-Metal Dichalcogenides (MoS 2 , MoSe 2 , WS 2 , WSe 2), ChemElectroChem. 2 (2015) 1713–1718. doi:10.1002/celc.201500259.

[352] A.K. Nayak, M. Verma, Y. Sohn, P.A. Deshpande, D. Pradhan, Highly active tungsten oxide nanoplate electrocatalysts for the hydrogen evolution reaction in acidic and near neutral electrolytes, ACS Omega. 2 (2017) 7039–7047. doi:10.1021/acsomega.7b01151.

[353] S.S. Thind, K. Rozic, F. Amano, A. Chen, Fabrication and photoelectrochemical study of WO3-based bifunctional electrodes for environmental applications, Appl. Catal. B Environ. 176–177 (2015) 464–471. doi:10.1016/j.apcatb.2015.04.033.

[354] H. Tong, Y. Jiang, Q. Zhang, J. Li, W. Jiang, D. Zhang, N. Li, L. Xia, Enhanced Interfacial Charge Transfer on a Tungsten Trioxide Photoanode with Immobilized Molecular Iridium Catalyst, ChemSusChem. 10 (2017) 3268–3275. doi:10.1002/cssc.201700721.

[355] J.M. Spurgeon, J.M. Velazquez, M.T. McDowell, Improving O2 production of WO3 photoanodes with IrO2 in acidic aqueous electrolyte, Phys. Chem. Chem. Phys. 16 (2014) 3623. doi:10.1039/c3cp55527e.

Chapter 3

Theoretical background

3.1 Electrochemical characterization

The theoretical concepts outlined in this section have been adapted from multiple reference textbooks in electrochemistry.[1–6]

3.1.1 Fundamentals of electrochemistry

Electrochemistry is a scientific discipline concerning the study of electron transfer across an interface. Depending on the interface studied, we can classify the electrochemical processes as homogeneous (electron transfer occurs at the same phase, e.g liquid-liquid) or heterogeneous (electron transfer occurs at the interface of two different phases, e.g solid-liquid, solid-gas).

The majority of the practical applications of electrochemistry are based upon the use of heterogeneous interfaces: these are either two ionic conductors (as found, for example, in solid-state batteries) or an ionic conductor and an electron conductor. From now on we will focus on the latter scenario, specifically in the heterogeneous interface formed by a solid electron conductor (electrode) and a liquid ionic conductor (electrolyte).

The reactions studied in electrochemistry, analogously to any other chemical reaction, satisfy an equilibrium. For the classical example of inserting an inert metallic wire (e.g. platinum

electrode) into an aqueous electrolyte solution containing the anions $Fe(CN)_6^{3-}$ and $Fe(CN)_6^{4-}$ (a redox couple), this can be expressed as:

$$Fe(CN)_6^{3-}(aq.) + e^- \rightleftharpoons Fe(CN)_6^{4-}(aq.) \quad (3.1)$$

Depending upon the relative $Fe(CN)_6^{3-}/Fe(CN)_6^{4-}$ concentrations, the reaction will balance so that the rate under which $Fe(CN)_6^{4-}$ donates electrons to the metallic electrode is equal to that of electrons being transferred from the metallic electrode to $Fe(CN)_6^{3-}$. As the nature of these reactions involves the transfer of charged particles from/to a surface, this results a net electrical charge separation. Such charge separation consequently yields a difference in electrical potential between the metal surface ϕ_m and the solution ϕ_s at the electrode-electrolyte interface, $\Delta\phi_{m/s}$:

$$\Delta\phi_{m/s} = \phi_m - \phi_s \quad (3.2)$$

This absolute equilibrium potential, although presenting a precise finite value, cannot be measured experimentally unless an additional electrode is immersed in the solution to obtain a closed conducting electrical circuit. This results in a two-electrode electrochemical cell, the simplest experimental setup in electrochemistry.

Let us consider the individual contributions to the electrochemical cell potential. After the incorporation of a second electrode connected to an equipment capable of measuring a potential gradient (volt meter), we have generated two additional interfaces:

$$\Delta\phi_{total} = \Delta\phi_{m/s} + \Delta\phi_{s/m'} + \Delta\phi_{m'/m} \quad (3.3)$$

where $\Delta\phi_{s/m'}$ is the electrical potential gradient at the second electrode/electrolyte interface, and $\Delta\phi_{m'/m}$ the metal-metal contact potential difference.

By applying a marginal alteration to the electrochemical cell potential, unless $\Delta\phi_{s/m'}$ and $\Delta\phi_{m'/m}$ are negligible, $\Delta\phi_{m/s}$ can't be elucidated. It is satisfied that $\Delta\phi_{m'/m} \approx 0$ when m and m' are made of the same material (the electrochemical potential of the electron in both m an

m' is equivalent $\mu_e^m = \mu_e^{m\prime}$). Thus, an experimental value of $\Delta\phi_{m/s}$ can be obtained if $\Delta\phi_{s/m\prime}$ is known. However, metallic electrodes are polarizable surfaces, where any electrochemical potential will result in an equivalent modification in $\Delta\phi_{s/m\prime}$. This is clearly inadequate for electrochemical experimentation, as $\Delta\phi_{total}$ cannot be directly related to $\Delta\phi_{m/s}$.

Conversely, ideally non-polarizable electrodes, where the charge transfer across their interface is infinitely fast, present no modification in their electrical potential. Hence, irrespective of the electrical current passed then, their potential is fixed so that $\Delta\phi_{s/m\prime} = constant$

These electrodes are commonly known as reference electrodes (REs), because they provide a reference from which to report the electrical potential of any electrode at the other side of the electrochemical cell (half-cell). Although ideally non-polarizable electrodes do not formally exist, several electrochemical systems satisfy the non-polarizability conditions at reasonable current ranges. If a RE is used instead of m', Eq. 3.3 can then be rearranged as

$$\Delta\phi_{total} = \Delta\phi_{m/s} + \Delta\phi_{s/RE} + \Delta\phi_{RE/m} = \Delta\phi_{m/s} - \phi_m + (\Delta\phi_{s/RE} + \phi_{RE}) \quad (3.4)$$

As $\Delta\phi_{s/RE} + \phi_{RE} = constant$ in reference electrodes,

$$\Delta\phi_{total} = \Delta\phi_{m/s} - \phi_m + constant \quad (3.5)$$

Consequently, the experimentally measured potential does not correspond to the absolute value of $\Delta\phi_{m/s}$ as previously anticipated, so any $\Delta\phi_{total}$ measurements using a RE are restricted to changes in $\Delta\phi_{m/s} - \phi_m$. A schematic of the two-electrode setup using a RE is shown in figure 3.1.

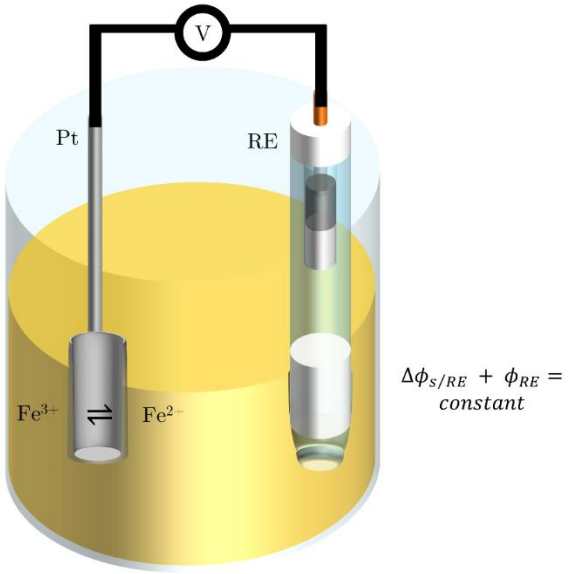

Figure 3.1. Two-electrode setup for the $Fe(CN)_6^{3-}/Fe(CN)_6^{4-}$ redox couple, and breakdown of the contributions of the measured potential $\Delta\phi_{total}$.

3.1.2 Reference electrodes (REs)

The RE historically employed is the so-called normal hydrogen electrode or standard hydrogen electrode (SHE). Its potential is defined by convention to be zero at all temperatures, based on the following reaction:

$$H_2\ (a = 1), Pt \mid H^+(a = 1, aq.);\ \ 2H^+(aq.) + 2e^- \rightleftharpoons H_2(g);\ E^0_{H^+/H_2} = 0\ V \quad (3.6)$$

SHE is experimentally fabricated by immersing a platinized platinum electrode into an acidic solution of unit activity (generally 1.18M HCl) and applying a 1 atm positive flow of hydrogen gas over the electrode surface. The safety concerns and technical difficulties of using a continuous hydrogen flow motivated the replacement of the SHE in daily electrochemical experimentation for alternative systems. Those employed in this thesis are the saturated silver/silver chloride (Ag/AgCl sat.) and the saturated calomel electrode (SCE). Both systems present well-defined potentials versus the SHE.

For Ag/AgCl sat.:

$$Ag|AgCl|Cl^{-}(a=1,sat);\ AgCl(s)+e^{-} \rightleftharpoons Ag\ (s)+\ Cl^{-}(aq.)\ ;\ E^{0}_{Ag/AgCl} vs.SHE = +0.197\ V \quad (3.7)$$

For the SCE:

$$Hg\ (l)|Hg_2Cl_2|Cl^{-}(a=1,sat);\ Hg_2Cl_2(s)+2e^{-} \rightleftharpoons 2\ Hg\ (l)+2\ Cl^{-}(aq.)\ ;\ E^{0}_{SCE} vs.SHE = +0.242\ V \quad (3.8)$$

Among the properties which REs need to satisfy to qualify as quasi-ideally non-polarizable interfaces, they must fulfil the following:

- High exchange current density values (i.e. fast electrode kinetics) to present high sensitivity to voltage perturbations at the electrode of interest (working electrode, WE)
- Contain oxidized and reduced forms of a specific element in high concentration to prevent drift from electrochemical equilibrium (i.e. changes in electrode potential)
- Present redox couples with solids and ideal liquids to present activities close to 1 to behave close to ideal conditions

3.1.3 Electrochemical equilibrium: Nernst equation and its implications in RE operation

As mentioned in section 3.1.1, electrochemical equilibrium is formally a specific case of a chemical equilibrium. For a generic chemical reaction of i number or reactants R which yield j products P, with stoichiometric coefficients ν_i and ν_j

$$\sum_i \nu_i R_i \ \rightarrow \sum_i \nu_j P_j \quad (3.9)$$

The Gibbs free energy of reaction $\Delta_r G$ under non-equilibrium conditions is defined as follows

$$\Delta_r G \ = \Delta_r G^0 + RT \ln Q_r = \Delta_r G^0 - RT \ln \frac{\prod_j \left(a_{P_j}^{\nu_j}\right)}{\prod_i \left(a_{R_i}^{\nu_i}\right)} \quad (3.10)$$

where $\Delta_r G^0$ is the standard Gibbs free energy change R the ideal gas constant (8.3145 J K^{-1} mol^{-1}), T the temperature (in degrees Kelvin), and $a_{P_j}^{v_j}$, $a_{R_i}^{v_i}$ the activities of products and reactants under non-equilibrium conditions.

In electrochemical systems, equation 3.11 establishes the relationship between $\Delta_r G$ and the cell electrical potential under operation E (i.e. electromotive force, emf), which in electrochemical systems under equilibrium conditions yields the standard cell potential E^0

$$\Delta_r G = -zFE \quad (3.11); \qquad \Delta_r G^0 = -zFE^0 \quad (3.12)$$

where z is the stoichiometric number of electrons transferred in the electrochemical reaction and F the Faraday constant (96485 C mol^{-1}). It can be concluded that electrochemical cells with positive emf values are thermodynamically favourable (spontaneous, generation of electrical current), whereas negative emf values require and external driving force to be triggered (i.e. external power supply)

By combination of eqs. 3.10 to 3.12 we obtain the following expression, known as the Nernst equation, which under electrochemical equilibrium (flow of minimal net electrical current) enables to obtain the equilibrium constant K_{eq}

$$E = E^0 - \frac{RT}{zF} \ln \frac{\Pi_j \left(a_{P_j}^{v_j}\right)}{\Pi_i \left(a_{R_i}^{v_i}\right)}; \qquad in\ equilibrium: E_{eq} = E^0 - \frac{RT}{zF} \ln K_{eq} \quad (3.13)$$

E is a dynamic value dependent on the electrochemical reaction rate (depletion of electroactive reactants), whilst E_{eq} is a stable value, commonly known as the open circuit potential (OCP) of the electrochemical cell.

We can now use this expression to analyse the properties of the electrochemical processes involved in REs

An expansion of the Nernst equation for the SHE yields the following

$$E = E^0_{SHE} - \frac{RT}{F}\ln\left\{\frac{P^{1/2}_{H_2}}{a_{H^+}}\right\} \quad (3.14)$$

As the hydrogen partial pressure in SHE $P^{1/2}_{H_2}$ is 1, a further conversion of natural logarithm to decimal leads to

$$E_{RHE} = E^0_{SHE} - \frac{2.303RT}{F} log\left\{\frac{1}{a_{H^+}}\right\} \quad (3.15)$$

which at 298 K and knowing the definition of $pH = log\left\{\frac{1}{a_{H^+}}\right\}$

$$E_{RHE} = E^0_{SHE} - 0.059pH \quad (3.16)$$

Consequently, the reference hydrogen electrode (RHE potential is pH-dependent: a 59 mV negative shift in E_{RHE} is found per pH unit increase. Alternatively, the Nernst equation of the redox processes for both Ag/AgCl sat. and SCE, yields

$$E_{Ag/AgCl\ or\ SCE} = E^0_{Ag/AgCl\ or\ SCE} - \frac{RT}{F}\ln\{a_{Cl^-}\} \quad (3.17)$$

which clearly shows the importance of using saturated chloride concentrations to mitigate any modification in a_{Cl^-} and the equilibrium potential. If high electrical currents are passed through any of the REs, however, the electrochemically-driven depletion/ formation H^+ or Cl^- will irreversibly modify the RE experimental potentials. Then, an additional electrode is needed to mitigate this drift: the counter electrode or auxiliary electrode.

3.1.4 Counter electrode

The incorporation of a counter electrode (CE) to the previously described two-electrode cell yields the classical three-electrode electrochemical cell setup. The CE not only ensures that a marginal current is passed through the RE to minimize its voltage drift, but also closes the electrical circuit by adopting the voltage necessary to pass the opposite electrical current to that exerted at the working electrode.

Consequently, the materials used as CEs should be either electrochemically inert to the system evaluated at the working electrode or stable at the operating electrochemical window. Else, after long-term operation, oxidised/reduced forms of the CE obtained by electrolysis can migrate within the electrolyte and ultimately interfere with the electrochemistry at the working electrode.

The CE materials should also present and excellent electrical conductivity and high surface area, so that the electrode kinetics at the working electrode are not limited by the electrochemical reaction occurring at the CE. For metals, a mesh morphology is desirable.

In this thesis we have employed both platinum mesh and glassy carbon counter electrode materials. For long-term experiments, following up recent reports which demonstrated significant Pt dissolution, redeposition and doping at non-PGM WEs under HER operating conditions,[7,8] the Pt mesh is encapsulated in a fritted glassware. Alternatively, glassy carbon is used owing to its electrochemical inertness despite of the smaller surface area and electrical conductivity.

3.1.5 Working electrode

The working electrode (WE) is the electrode which either serves as a support for the reaction of interest to occur, or triggers the redox process by being the electrocatalytic material. In the first scenario, a WE must be electrochemically inert to the electrochemical reaction, and present a wide electrochemical stability window to prevent additional current contributions during electrochemical experimentation. In the present thesis, we have selected glassy carbon and gold as working electrodes, both being inert to the hydrogen evolution reaction, which is catalysed by nanostructured molybdenum sulfide materials. In the second case, iridium and its modification with tungsten sulfide nuclei are the surface of interest purposefully chosen to catalyse the oxygen evolution reaction.

In all cases, the WEs allow to gather insights on crucial aspects of electrochemical reactions such as the electrode kinetics and mass transport phenomena.

3.1.6 Electrode kinetics: Butler-Volmer and the Tafel approximation

The reaction rates of electrochemical processes, as introduced in Section 3.1.3, are dependent on the external potential applied. Assuming that the electron transfer kinetics is the rate-limiting step of the electrochemical reaction, a macroscopic model can describe the overall electrode kinetics and its potential dependence. If we express the electrochemical reaction as

$$O(aq.) + e^-(m) \underset{k_{ox}}{\overset{k_{red}}{\rightleftharpoons}} R(aq.) \quad (3.18)$$

where k_{red} and k_{ox} are the heterogeneous electrochemical reaction rate constants of the reductive (forward) and oxidative (backward) electron transfer reactions. Analogously to chemical reactions, the overall reaction rate v, and consequently the net current I, is the difference between the oxidative (v_{ox}) and reductive (v_{red}) processes for a given electrode area A

$$v = \frac{I}{FA} = \frac{I_{ox} - I_{red}}{FA} = v_{ox} - v_{red} = k_{ox}[R]_0 - k_{red}[O]_0 \quad (3.19)$$

where $[R]_0$ and $[O]_0$ are the initial bulk concentrations of reductive and oxidative species, v_{ox} and v_{red} the oxidative and reductive reaction rates, with their corresponding oxidative and reductive currents I_{ox} and I_{red}

Transition state theory can then be implemented onto the deduction to elucidate the terms involved in the electrochemical reaction rate constants. For a given reaction, the reactant must overcome an energy barrier with an activation free energy $\Delta G_r^{\ddagger}$, which satisfies the following Arrhenius-type expressions

$$k_{ox} = A_f \exp\left(\frac{-\Delta G_{ox}^{\ddagger}}{RT}\right) \quad (3.20); \; k_{red} = A_f \exp\left(\frac{-\Delta G_{red}^{\ddagger}}{RT}\right) \quad (3.21)$$

A_f being a pre-exponential factor accounting for the collision frequency of electroactive species with the surface of the electrode.

The activation free energies of the oxidative ($\Delta G_{ox}^{\ddagger}$) and reductive ($\Delta G_{red}^{\ddagger}$) electrochemical processes are necessarily correlated with the interfacial electrode overpotential η (i.e. the electrochemical driving force), defined here as the difference between the applied potential E and the formal potential E_f^0, yielding

$$k_{ox} = k_{app}^0 \, exp\left(\frac{(1-\alpha)zF\eta}{RT}\right) \text{ (3.22)}; \;\; k_{red} = k_{app}^0 \, exp\left(\frac{-\alpha zF\eta}{RT}\right) \text{ (3.23)}$$

where the charge transfer coefficient α $(0 < \alpha < 1)$ informs of the relative geometric and electronic resemblance of the transition state compared with the initial and final electrochemical products. α values close to 0 indicate a transition state similar to the reactants, whilst α values close to one inform of a transition state similar to the products. Unless specific knowledge of the electrochemical reaction is known, α is assumed to be 0.5 (i.e. the transition state lies halfway the reaction coordinate). k_{app}^0 is the standard (or apparent) rate constant, which informs of the electrochemical reaction lability: high values of k_{app}^0 involve reactions which reach equilibrium in short timescales, and vice versa

Expressions 3.22 and 3.23 can be incorporated in the definition of the overall reaction rate,

$$I = FA_{geom}k_{app}^0 \left\{[R]_0 exp\left(\frac{(1-\alpha)zF\eta}{RT}\right) - [O]_0 \, exp\left(\frac{-\alpha zF\eta}{RT}\right)\right\} \text{ (3.24)}$$

which, normalized by the electrode area A_{geom} and with further rearrangements give the Butler-Volmer equation

$$j = j_0 \left\{exp\left(\frac{(1-\alpha)zF\eta}{RT}\right) - exp\left(\frac{-\alpha zF\eta}{RT}\right)\right\} \text{ (3.25)}$$

The Butler-Volmer equation can be further simplified for limiting scenarios. When applying large oxidative or reductive overpotentials, as $exp(-x) \longrightarrow 0$, the reductive or oxidative

component of the equation, respectively, can be regarded as negligible. The resulting expressions are known as the anodic and cathodic Tafel equations

Anodic Tafel:

$$log\, j = log\, j_0 + \frac{(1-\alpha)zF}{2.303RT}\eta \quad (3.26)$$

Cathodic Tafel:

$$log\, j = log\, j_0 - \frac{\alpha zF}{2.303RT}\eta \quad (3.27)$$

Thus, representation of $log\, j$ vs. η enables to elucidate the exchange current density j_0 (exponential of the intercept value) and a slope intimately correlated with α known as the Tafel slope. Further insights on the significance of both j_0 and Tafel slope were given in Section 2.3.

3.2 Electrochemical measurements

The standard three-electrode electrochemical cell setup enables electrochemical testing of the reaction of interest at the working electrode (see Figure 3.2). A potentiostat/galvanostat, an electronic-based instrument, is used in electrochemical experimentation to control the voltage (potentiostat) or current (galvanostat) established between the WE and the CE, whilst keeping a feedback loop of marginal current flow between the WE and RE so that the WE acts as a reference point in the course of electrochemical experimentation. A pre-determined voltage/current program is fed to the potentiostat/galvanostat by means of a PC-controlled software, chosen according to the information to be extracted from the electrochemical system: kinetic or mass-transport related.

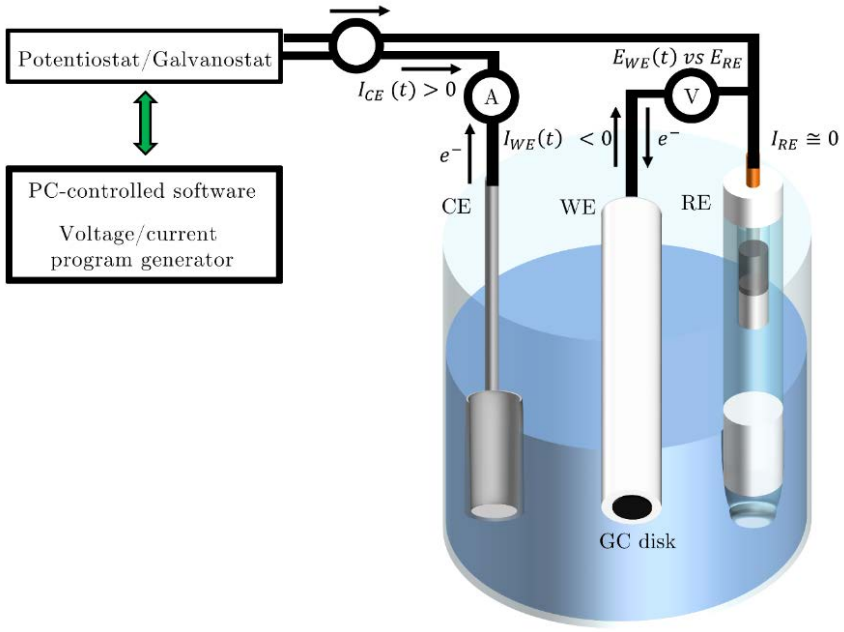

Figure 3.2. Simplified schematic of a three-electrode electrochemical setup. The illustrated cell operation corresponds to that used under potential-controlled hydrogen evolution testing conditions ($I_{WE} < 0$) with a glassy carbon displayed here as a WE.

3.2.1 Mass transport limitations

In previous sections we had assumed that the electrochemical processes studied were limited by the electron transfer kinetics. However, the rate under which electroactive species reach the electrode-electrolyte interface affects the overall electrochemical reaction. Three main transport processes can contribute: diffusion, migration and convection.

The contribution of migration and convection, which involve mass transport of the electroactive species by electrostatic and density gradients, respectively, can be mitigated. Addition of an excess, approximately 2 orders of magnitude higher concentration, of inert electrolyte (supporting electrolyte) results in all electrostatic ion transport being allocated to these spectator species, leaving the electroactive species unaffected by migration effects and sustaining the electroneutrality at the interface.

Natural convective effects can be mitigated in quiescent conditions by using a thermostatted cell (water jacket) to minimize temperature gradients, but experiments beyond the 20 s timescale might present additional convective contributions due to stray vibrations. Experiments under forced convection, such as those performed in a rotating disk electrode, present well-defined hydrodynamic profiles which allow to accurately predict the convective contribution to the electrochemical currents.

Hence, diffusion effects arising from concentration gradients from the bulk electrolyte to the electrode-electrolyte interface are the major contributors to the overall electrochemical current profiles shown in figure 3.3c.

Linear diffusion, as found in planar electrodes, and its time-dependence are described by Fick's 1st and 2nd law:

$$J = -D\frac{\partial C}{\partial x} \quad (3.28)$$

$$\frac{\partial C}{\partial t} = D\frac{\partial^2 C}{\partial x^2} \quad (3.29)$$

where J is the flux of species per unit of area and time, $\frac{\partial C}{\partial x}$ the concentration gradient along a direction x, D the diffusion coefficient of the species, and $\frac{\partial C}{\partial t}$ the time-dependent concentration.

For the semi-infinite planar diffusion scenario, where the electrolyte away from the electrode-electrolyte interface is regarded as unperturbed, the electrical current response with time upon an applied potential step from absent to diffusion-controlled currents is described by the Cottrell equation

$$|I_{Cottrell}| = \frac{zFAD_{ox/red}^{1/2}C_{ox/red,bulk}}{\pi^{1/2}t^{1/2}} \quad (3.30)$$

where $C_{ox/red,bulk}$ is the concentration of the electroactive species in bulk

The time-dependent current response of non-planar electrodes, where the linear diffusion regime is not applicable, will be covered in Section 3.2.4.

3.2.2 Potential sweep methods

The most commonly voltage programmes used in electrochemical experimentation are potential sweep methods, in particular linear sweep voltammetry (LSV) and cyclic voltammetry (CV).

LSV and CV involve a linear variation of the cell voltage (i.e. voltage ramp) with time, referred as scan rate, which aims to investigate variations in the WE electrical current as a function of the applied voltage. For LSV, the potential-time profile is linear (Figure 3.3a), whilst for CV if both initial and final potentials are identical it presents a symmetrical triangular profile (Figure 3.3b). A representative cyclic voltammogram of a solution containing $Fe(CN)_6^{3-}$ and $Fe(CN)_6^{4-}$ in quiescent conditions is shown in figure 3.3c. The voltammetric shape, for a given scan direction, presents three distinctive regions. The first region (labelled as I in Figure 3.3c) presents an almost negligible current as the η is similar to E_f^0: the driving force is not sufficiently high to drive any faradaic redox process. The second region (II in Figure 3.3c) presents an exponential shape as described by the Butler-Volmer equation: $|\eta| \geq E_f^0$, and consequently the electrochemical reaction rate $k_{ox/red}$ increases as η reach higher absolute values. Finally, the third region (III in Figure 3.3c) presents a maximum current followed by a decay, yielding a wave profile: $|\eta| \gg E_f^0$, and the electrochemical reaction rate is so high that the mass transport of the electroactive species limits the redox process. This wave profile is known as the diffusion decay peak profile, and has important implications in CV interpretation.

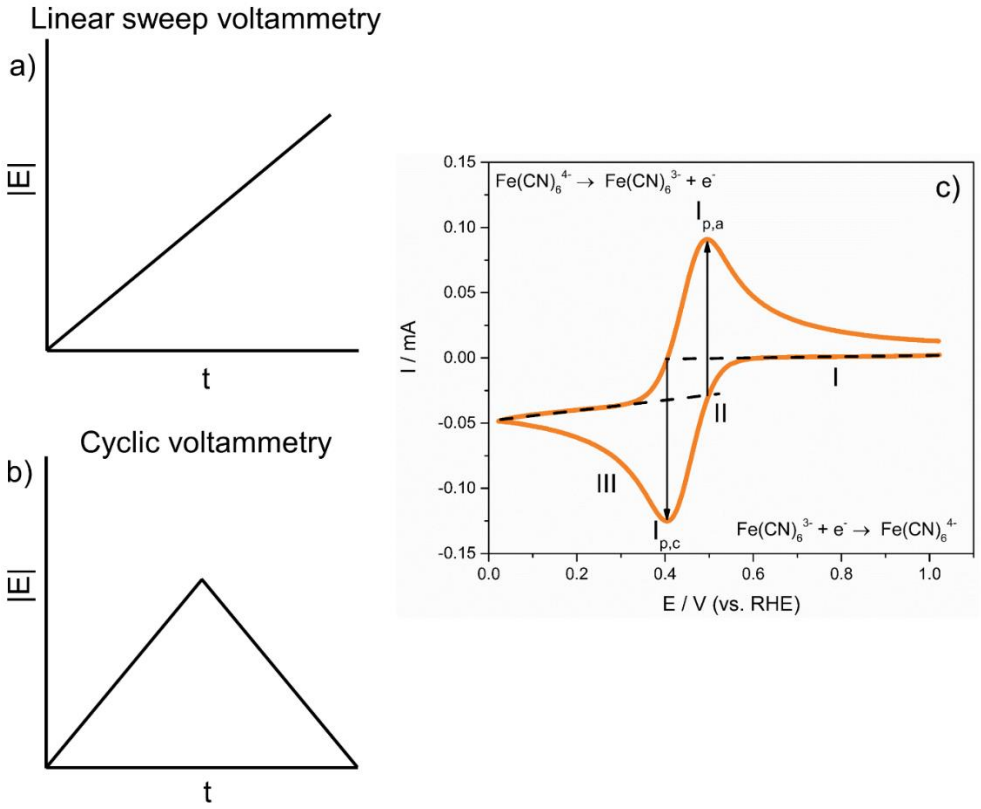

Figure 3.3. Absolute voltage-time profiles of a) linear sweep voltammetry and b) cyclic voltammetry. c) Representative cyclic voltammogram obtained in a 5 mM $K_3[Fe(CN)_6]$ aqueous solution in a 3 mm glassy carbon working electrode. Scan rate: 25 mV s^{-1}

Indeed, a relationship between the voltage scan rate v_{scan} and the peak current intensity of a redox process I_p is found for highly reversible and totally irreversible redox systems in semi-infinite linear diffusion conditions, known as the Randles-Ševčík equation

$$\text{Highly reversible: } |I_P| = 2.69 \times 10^5 \, z^{3/2} \, A_{geom} \, C_{ox/red,bulk} D_{ox/red}^{1/2} \, v_{scan}^{1/2} \quad (3.31)$$

$$\text{Totally irreversible: } |I_P| = 2.99 \times 10^5 \, \alpha^{1/2} \, A_{geom} \, C_{ox/red,bulk} D_{ox/red}^{1/2} \, v_{scan}^{1/2} \quad (3.32)$$

The Randles-Ševčík equation is essential as it enables the elucidation of electrochemically-relevant parameters such as diffusion coefficients and geometric electrode areas.

3.2.3 Criteria for electrochemical reversibility, and numerical elucidation of k^0_{app}

In the previous section, the concept of electrochemical reversibility and irreversibility in redox couples was introduced. Qualitatively, fully reversible electrochemical reactions are those that present fast enough electrode kinetics (large k^0_{app} values) so that the redox product of the forward scan is fully oxidized/reduced by reversing the scan direction. Conversely, fully irreversible electrochemical reactions are those where the reverse scan shows no redox process: once the oxidation/reduction has occurred, it cannot be reversed. These present small k^0_{app} values.

The degree of electrochemical reversibility can be evaluated by several criteria, adding to that of the Randles-Ševčík equation, as follows:

For fully reversible reactions:

- The peak-to-peak separation ΔE_P between the anodic $E_{P,a}$ and the cathodic peak $E_{P,c}$ is constant and independent on the scan rate (Tomeš criterion): $\Delta E_P = 59/z\ mV$
- The peak anodic $I_{P,a}$ to cathodic $I_{P,c}$ current ratio equals 1

For irreversible reactions:

- ΔE_P between the anodic $E_{P,a}$ and the cathodic peak $E_{P,c}$ (if reverse peak is present) dependent on the scan rate: $\Delta E_P > 120/z\ mV$
- $E_{P,c}$ (assuming a one-electron, cathodic reaction) displaces negatively by $30/\propto mV$ per tenfold increase in v_{scan}

However, most real electrochemical systems lie in the quasi-reversible scenario.

In our present research, insights on the electron transfer properties of TMDs are essential to correlate electrocatalytic enhancements of the HER with faster charge transfer kinetics, and

elucidating the heterogeneous electron transfer rate constant k_{app}^{0} of a quasi-reversible redox mediator such as $[Fe(CN)_6]^{4-}/[Fe(CN)_6]^{3-}$ provides an adequate metric.

For quasi-reversible systems, Nicholson and Shain elucidated a method to calculate k_{app}^{0} values by correlating the scan rate with a dimensionless kinetic parameter ψ using the expression

$$\psi = k_{app}^{O}\left(\frac{D_o}{D_R}\right)^{\alpha/2}\left[\left(\frac{\pi z F D_o v_{scan}}{RT}\right)\right]^{-1/2} \quad (3.33)$$

where D_{ox} and D_{red} are the diffusion coefficient for the oxidized and reduced species.[9]

A dataset was constructed which correlated ψ as a function of ΔE_P in the $61 \leq \Delta E_P \leq 212\ mV$ range upon varying v_{scan}. In practice, experimental ΔE_P values are compared to the ψ vs ΔE_P dataset to interpolate ψ and finally obtain k_{app}^{O} from the aforementioned equation.

Lavagnini et al. recently reported an empirical equation which provided a continuous ψ vs ΔE_P function in the $\Delta E_P\ 60 - 210\ mV$ range[10]

$$\psi = \frac{(-0.6288 + 0.0021\ z\Delta E_P)}{(1 - 0.017\ z\Delta E_P)} \quad (3.34)$$

Investigations by Klinger and Kochi proposed an alternative expression for electrochemically irreversible systems ($\psi < 0.1$ and $\Delta E_P > 210\ mV$)[11] derived from Nicholson and Shain's initial equation, providing a direct k_{app}^{O} elucidation from ΔE_P at a given scan rate:

$$k_{app}^{O} = 2.18\left(\frac{\alpha z F D v_{scan}}{RT}\right)^{1/2} exp\left[-\left(\frac{\alpha^2 F}{RT}\right) n\Delta E_P\right] \quad (3.35)$$

where ΔE_P is given in V.

A rearrangement of this expression in combination with Nicholson and Shain equation provides a graphical method to obtain k_{app}^{O} by plotting ψ vs. $\left[\left(\frac{\pi z F D v_{scan}}{RT}\right)\right]^{-1/2}$ for any range of scan rates utilized[10]

$$\psi = 2.18\left(\frac{\alpha}{\pi}\right)^{1/2} exp\left[-\left(\frac{\alpha^2 F}{RT}\right) z\Delta E_P\right] \quad (3.36)$$

$$\psi = k_{app}^{O}\left[\left(\frac{\pi zFDv_{scan}}{RT}\right)\right]^{-1/2} \quad (3.37)$$

3.2.4 Electrode morphology-dependent mass transport properties

Contrary to planar macroscopic electrodes, electrodes with a micrometric size (microelectrodes) and three-dimensional geometry present diffusion profiles that can no longer be described by one spatial coordinate. For microelectrodes, such as disk microelectrodes, mass transport towards the radius has a significant contribution, since the relative edge dimensions are comparable to those of the electrode cross-section and are no longer negligible: the smaller the radius, the higher the contribution. Fick's second law now needs to be expressed by cylindrical coordinates r and z_{coord}, referring to the radial coordinate and perpendicular coordinate from the disk centre.

$$\frac{\partial C}{\partial t} = D\left[\frac{\partial^2 C}{\partial r^2} + \frac{1}{r}\frac{\partial C}{\partial r} + \frac{\partial^2 C}{\partial {z_{coord}}^2}\right] \quad (3.38)$$

At very short timescales ($<$ 60 µs), microelectrodes behave similarly to planar electrodes in the potential step experiments: their response is equal to that predicted by the Cottrell equation (3.30).

However, at longer timescales ($>$ 60 ms) the radial diffusion contribution dominates the microelectrode response, yielding a steady-state diffusion (current) dependent on the microelectrode radius r_{el},

$$I = 4zF\, C_{ox/red,bulk} D_{ox/red} r_{el} \quad (3.39)$$

Microelectrodes reach this radial (convergent) diffusion regime at fast timescales, which is beneficial in the study of fast redox processes. In addition, the small dimensions of microelectrodes also minimize the contribution of non-faradaic processes (capacitance, ohmic drop) which also enable higher electrochemical signal-to-noise ratios.

The benefits of microelectrodes can be further exploited if these are fabricated as well-defined arrays. However, the mass transport response of microelectrode arrays will be dependent on the microelectrode dimensions and interspacings, as well as the timescales of the electrochemical experiments. This complex scenario was simplified by Compton el al. using the "diffusion domain approximation".[12–14]

Briefly, a regular array of microelectrodes with centre-to-centre spacing d is subdivided into N hexagonal ($A_{hex} = \frac{\sqrt{3}}{2}d^2$) or square unit cells ($A_{sqr} = d^2$), where N is the number of electrodes in the array. These unit cells are converted into circular (for microdisk arrays) or cylindrical (for micropillar arrays) diffusion domains with an equivalent area to that of A_{hex} or A_{sqr} and radius r_{domain}, leading to diffusion domain areas $A_{domain} = \pi r_{domain}^2$. These domains are considered diffusionally independent and equivalent, which implies a zero net flux across the walls of the domains (Figure 3.4). Consequently, this approximation simplifies a challenging three-dimensional problem to a two-dimensional one due to the cylindrical symmetry of the domains, obtaining the total microelectrode array current by multiplying the computationally-calculated current of one microelectrode by N.

Several experimental behaviours can be observed for microelectrode arrays. These are dependent on the experiment timescale (voltage scan rate) and the relative dimensions of the microelectrodes and their diffusion layer thickness δ. The latter corresponds to the region of the electrode-electrolyte interface affected by the electrochemical process, with concentrations of redox species that differ from the bulk. Although it does not present a defined thickness, δ is normally estimated as $\delta \approx \sqrt{\pi D t}$: it is clear that δ is intimately related to the voltage scan rate, as it is a time-dependent property. Based on these considerations, four microelectrode array cases can be identified (Figure 3.5).

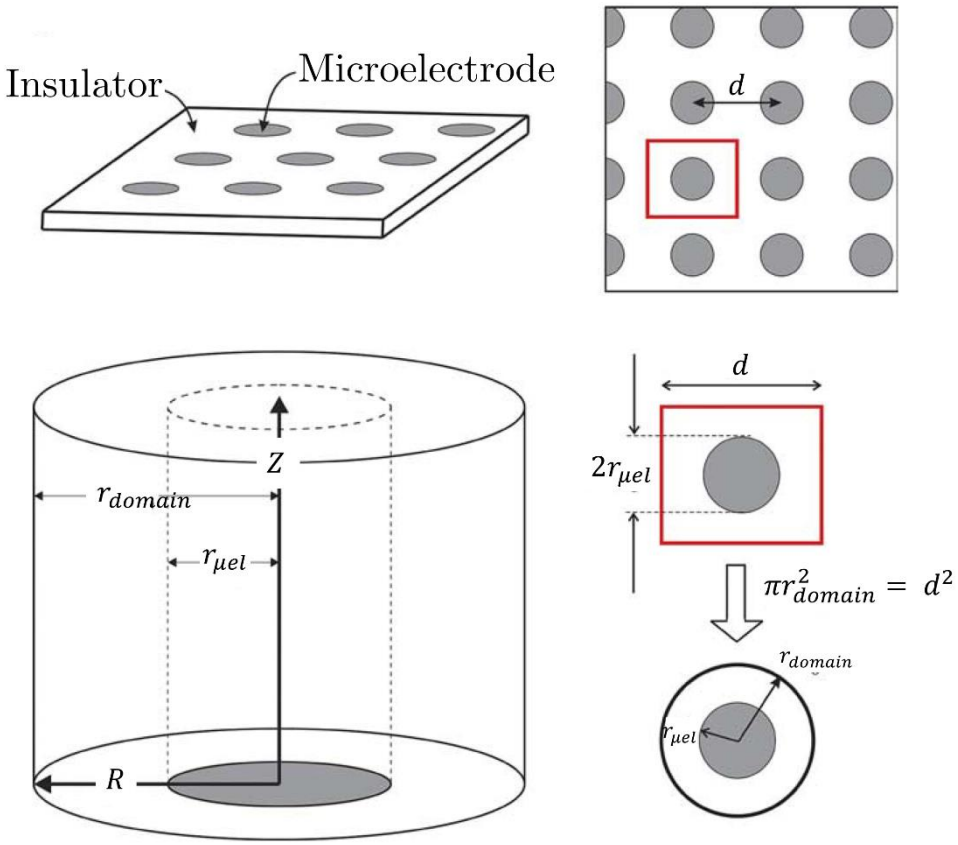

Figure 3.4. Schematic representation of the "diffusion domain approximation" for a microelectrode array, using diffusionally independent squared unit cells. Adapted from [12].

Case 1 is observed when thickness δ is smaller than the microelectrode size and interspacing, resulting in each microelectrode in the array having independent and individual planar diffusion layers. This is only observed at very short timescales (very fast scan rates). For case 2, the diffusion layer thickness δ is larger than the microelectrode dimensions but smaller than their interspacing, leading to a convergent diffusion profile per each microelectrode. In case 3 the initially independent radial diffusion layers formed by each microelectrode start to overlap as the diffusion layer thickness is larger than the microelectrode interspacing, observing a mixed mass transport behaviour. Cases 2 and 3 are observed at fast-to-moderate timescales/scan rates. Finally, case 4 corresponds to timescales under which the diffusion layer thickness δ is larger than both the size and interspacing of the microelectrodes, resulting in a complete overlap

of the microelectrode diffusion layers towards a semi-infinite planar diffusion regime, characteristic of macroelectrodes.

The diffusion domain approximation, however, is not valid when the number of electrodes in the perimeter of the array is not negligible compared to the total number. This was referred as Case 5, where a nanoelectrode array which should have presented a macroelectrode behaviour (case 4) presented a steady state response (case 2).[15]

The latter scenario will be of significance in the analysis of the mass transport response of the TMD nanopillar arrays fabricated in this thesis.

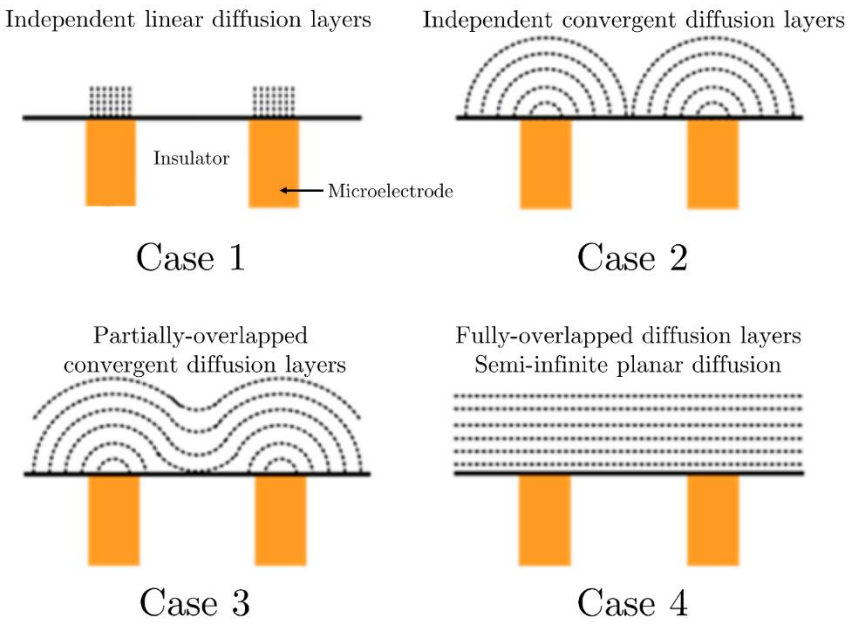

Figure 3.5. Schematic representation of the 4 diffusional regime cases found for microelectrode arrays, adapted from [16].

3.2.5 Electrochemical impedance spectroscopy

Electrochemical impedance spectroscopy (EIS) is a non-invasive technique that enables frequency-dependent information of an electrochemical system to be obtained. It consists of the application of a frequency perturbation of small amplitude to a preset direct current (DC)

potential input E_t, known as the across function, and evaluate modifications in the alternating current (AC) output I_t, known as the through function, before and after passing through the electrochemical system of interest (Figure 3.6a). The electrochemical system presents time (and consequently frequency) dependent phenomena, which can be represented as a set of elements in an electrical circuit. Thus, EIS can provide information relevant to the magnitude and kinetics of each physical phenomena involved in the electrochemical cell.

The value of the total impedance Z_{EIS} is defined as the ratio between the across function E_t and the through function I_t following the expression

$$Z_{EIS} = \frac{E_t}{I_t} = \frac{E_0 \sin(\omega t)}{I_0 \sin(\omega t + \varphi)} \quad (3.40)$$

where E_0 and I_0 are the voltage and current amplitude, ω the angular frequency (i.e. $2\pi f$, f being the frequency in Hz) of the sinusoidal wave, and φ the phase angle.

For ease of interpretation, and by use of complex exponentials (with the imaginary unit $j = \sqrt{-1}$), the total impedance Z_{EIS} with phase angle θ can be separated into two terms: one with the sole contribution of magnitude (Z', real), and another related to the phase angle (Z'', imaginary).

$$Z_{EIS} = |Z_{EIS}|\, exp(j\theta) = |Z_{EIS}|\, cos(x) + |Z|\, j\, sin(x) = Z' + Z'' \quad (3.41)$$

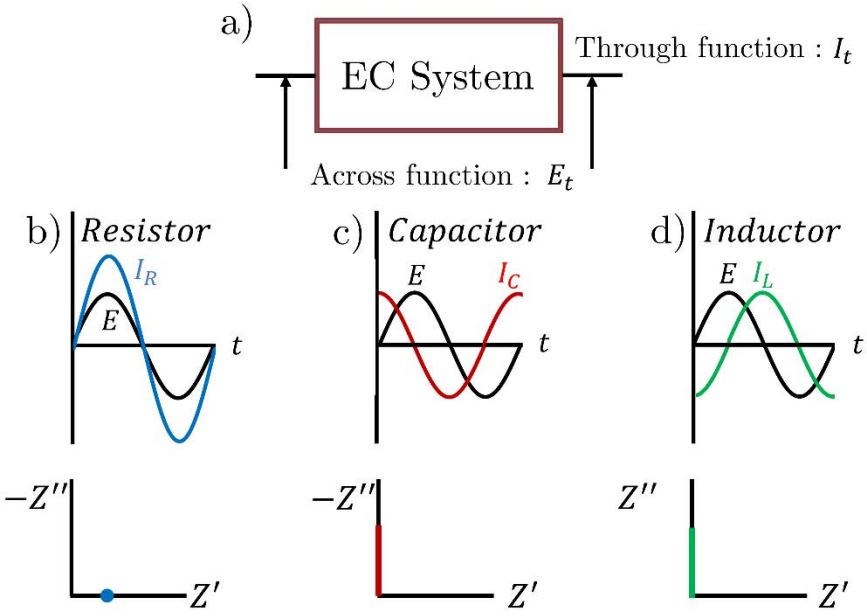

Figure 3.6. a) Illustration of the working principle of impedance spectroscopy. Graphical representation of AC signal and Nyquist plot features for ideal circuit elements as b) resistor, c) capacitor and d) inductor. Nyquist plot in d) plotted as Z'' vs. Z' for ease of representation.

Graphical representation of $-Z''$ vs. Z', known as the Nyquist plot, allows direct elucidation of the resistive components and capacitive/inductive components by mathematical treatment.

The impedance of a resistor Z_R, a capacitor Z_C, and an inductor Z_L present the following frequency-dependent responses

$$Z_R = R;\ Z_C = -\frac{j}{\omega C};\ Z_L = j\omega L \quad (3.42)$$

where R, C and L are the values of resistance, capacitance and inductance, respectively.

Thus, if the electrochemical system behaves as a pure resistor, the amplitude of the output signal is modified whereas the phase angle is unaffected: this would be a single point in the Nyquist real axis (Figure 3.6b). However, if it presented a behaviour of elements such as a capacitor (Figure 3.6c) or an inductor (Figure 3.6d), the phase angle would be negatively or

positively shifted, respectively, whilst the output signal amplitude would be unaffected: these would appear as a straight line in the Nyquist plot.

However, electrochemical systems cannot normally be represented by one circuit element alone, as several physical phenomena co-exist. Thus, a set of circuit elements is needed, either in series or in parallel, to construct an equivalent circuit which correlates with the physical phenomena.

The most employed and simple one is the so-called Randles circuit (see Figure 3.7). The R_{sol} element accounts prominently for the electrolyte resistance, as well as of the resistance of the cabling components along the electrochemical circuit. The non-faradaic charge-discharge of the electrical double layer is accounted by the capacitor C_{dl} (or constant phase element, CPE, if the capacitor is non-ideal), and the faradaic-driven charge transfer and mass transport resistances by the pure resistor R_{ct} and the Warburg element Z_w elements parallel to C_{dl}. However, other electrochemical processes such as multi-step electron transfer or adsorption processes, demand more complex equivalent circuits to provide full physical meaning.

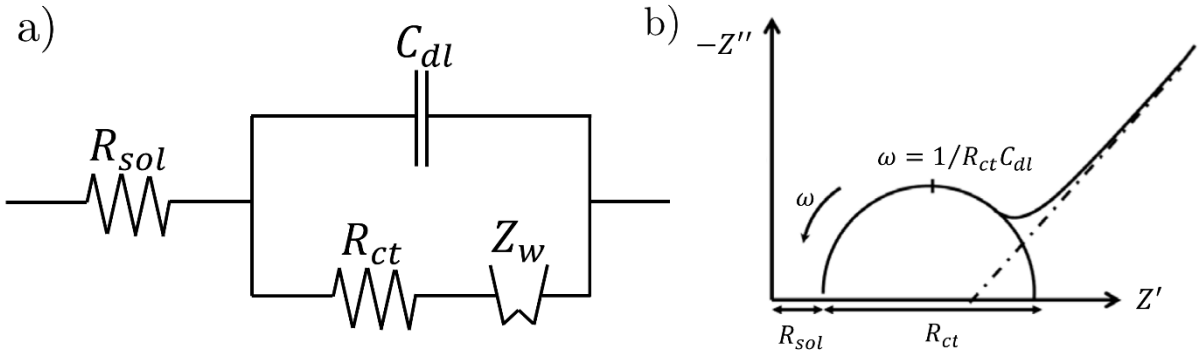

Figure 3.7. a) Equivalent elements in the Randles circuit and b) Representative Nyquist plot obtained for a model Randles circuit.

In the research presented here, EIS is mostly employed in our electrochemical analysis to apply the ohmic compensation correction ($-IR_{sol}, R_{sol}$ obtained at the high-frequency Z' intercept) and evaluate the electron transfer properties of TMDs by observing modifications in R_{ct} values.

3.3 Physical characterization

3.3.1 Raman spectroscopy

Raman spectroscopy is based on the inelastic scattering of an incident collimated light beam upon interaction with a surface, leading wavenumber modifications of the scattered light higher than 1 cm^{-1}. It is a non-destructive technique that can successfully characterize gas, liquid and solid phases and, unlike techniques such as X-ray diffraction or electron microscopies, samples in the µg weight range.

First experimental evidence of this non-coherent light scattering was demonstrated by C.V. Raman and K.R. Ramanathan in 1928, by use of a focused sunlight beam into several types of liquids and placing two complementary light filters between the incident and scattering light paths.[17] Modern Raman spectrometers collect the scattered light from a sample upon irradiation with a laser of specific wavelength. The interaction of the incident photons with the sample of interest can either lead to a negative (Stokes) or a positive (anti-Stokes) shift in the frequency of the scattered photons: this indicates that the scattered photons present a lower or a higher energy, respectively, than the incident photons. Stokes and anti-Stokes scattering lines are symmetrical, with frequencies independent on the incident light beam frequency.[18] A Raman spectrometer separates the scattered light beam by means of a holographic grating, which is later directed towards a CCD array detector that gives an intensity read-out of each wavelength detected: plotting of the relative scattered light intensities versus the wavenumber shift of the incident laser provides the Raman spectrum.[19]

In molecules or solids, the inelastic interaction of the incident beam arises from the excitation of specific vibration modes (e.g. translations, rotations or (a)symmetrical bond stretchings) or lattice vibrations, respectively, the latter modelled as quantized quasi-particles known as

phonons. The total number of active vibration/phonon modes (to infrared or Raman scattering) are obtained by applying symmetry operations on the given molecule or crystal unit cell. By doing so, a point group symmetry is identified, with a corresponding set of irreducible representations: in essence, the simplest mathematical form to express the symmetry changes caused by the excitation of a specific vibration mode[20] The expression which describes the induced electrical dipole moment P_k of a vibration/phonon mode k with respect to the normal vibration coordinate Q_k when an incident light beam E_{beam} of electric field amplitude $E_{0,beam}$, frequency ν_{beam}, and phase angle φ_k interacts with the sample follows

$$P_k = \alpha_k * E_{beam} = \alpha_0 * E_{0,beam}\cos(\nu_{beam}t) + P_{k0}\cos[(\nu_0 - \nu_k)t + \varphi_k] + P_{k0}\cos[(\nu_0 + \nu_k)t + \varphi_k]$$

$$\text{where } P_{k0} = \frac{1}{2}Q_{k0}\alpha_k^{'} * E_{0,beam} \quad (3.43)$$

The first term of the expression corresponds to Rayleigh scattering, whereas the second and third correspond to Stokes and anti-Stokes scattering (Raman active). It can clearly be seen that the latter are only present when $\alpha_k' = {\partial\alpha_{ij}}/{\partial Q_k} \neq 0$. This is known as the Raman scattering selection rule: vibration/phonon modes are only active to Raman if the molecular polarizability α, that is the relative charge distribution distortion of the molecule/solid at a given external electric field, is modified between the ground and excited state. [21]

Raman spectroscopy has proven to be a powerful technique to characterize layered two-dimensional materials such as graphene. In the case of layered TMDs, the fact that bulk MX_2 presents a D_{6h} point group symmetry, whereas in few-layered (even) 2N-MX_2 is D_{3d} and (odd) 2N+1-MX_2 is D_{3h} due to a reduction in symmetry clearly indicates that relevant information can be extracted by its use. A compilation of the vibration modes found in MX_2 materials can be found in Figure 3.8a.

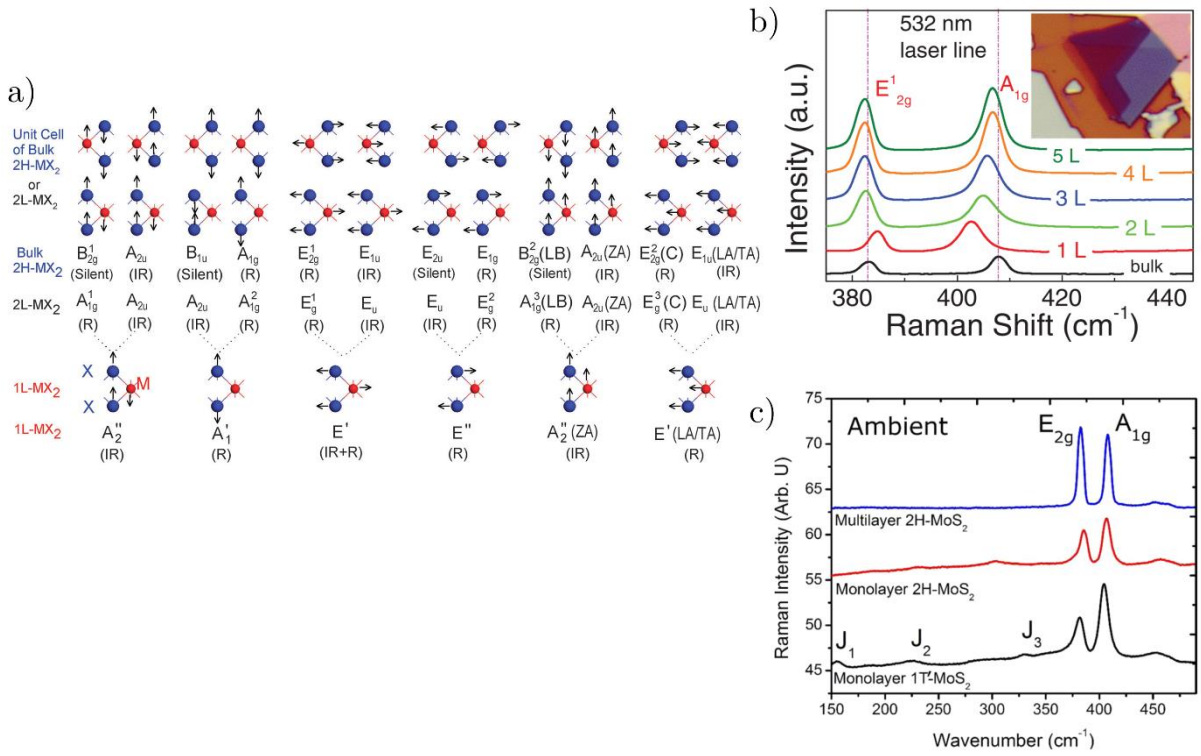

Figure 3.8. a) Molecular vibrations and corresponding vibration modes for single-layered (1L), bi-layered (2L) and bulk MX_2 materials: modes labelled with R are Raman-active, whilst those labelled IR are infrared-active; b) Layer-dependent relative frequency shift of in-plane E^1_{2g} and out-of-plane A_{1g} MoS_2 Raman modes; c) Raman spectra of monolayer 1T'-MoS_2 (black), monolayer 2H-MoS_2 (red), and bulk 2H-MoS_2 (black). Reproduced from refs. [20,22,23].

The most relevant morphological properties of TMDs obtained by Raman spectroscopy are the following:

- Number of TMD layers present (Figure 3.8b): a layer-dependent variation on the relative frequency of the in-plane E^1_{2g} and out-of-plane A_{1g} MoS_2 Raman modes was found up to 4 layers, compared to bulk MoS_2.[24] With increasing layer number, E^1_{2g} is red-shifted (lower frequency) whereas A_{1g} is blue-shifted (higher frequency). The relative frequency shift $\Delta\nu$ was found independent on the laser employed.[22] The

number of layers, in the case of MoS_2, can be obtained by $\Delta\nu(A_{1g} - E^1_{2g}) = 25.8 - 8.4/N$, N being the number of layers.

- Identification of TMD polymorphs: 1T (tetragonal, point group D_{3d}), 2H and 3R (hexagonal and rhombohedral, respectively, point group D_{3h}) polytypes of TMDs, as they present different symmetries they will consequently present different Raman modes. For 1T-MoS_2, three additional bands (at 153, 226, 330 cm^{-1} known as J1, J2 and J3 respectively) were observed[23] compared to 2H-MoS_2 (Figure 3.8c). Similar bands have been found in other TMDs. [25,26]
- Identification of sulfur ligands: molecular-type TMD materials such as the cluster-based $[Mo_3S_{13}]^{2-}$ present sulfur atoms with different chemical functionality, distinguishable in the Raman spectrum.[27,28]
- Laser-induced phase transitions: amorphous MoS_2 and 2H-$MoTe_2$ were demonstrated to undergo a transition to crystalline and 1T-$MoTe_2$ after laser irradiation, respectively.[25,29] This was due to thermal and Te vacancy generation effects, presenting clear Raman signatures.

3.3.2 X-ray photoelectron spectroscopy

X-ray photoelectron spectroscopy (XPS), also known as ESCA (electron spectroscopy for chemical analysis), is a surface characterization technique developed by Kai Siegbahn and co-workers at Uppsala University in the late 1950's.[30,31] XPS yields near-surface information regarding the elemental composition, chemical and electronic environment (i.e. oxidation state), and semi-quantitative elemental concentrations. Its working principle is based upon the photoelectric effect discovered by Albert Einstein in 1905 (see Figure 3.9a).[32] An incident monochromatic X-ray radiation of energy $h\nu$ interacts with the core-level electrons of the

surface atoms contained within the sample, ejected as photoelectrons with discrete kinetic energy E_k. The photoelectron binding energy BE is calculated as

$$BE = h\nu - E_k - E_\Phi \quad (3.44)$$

where E_Φ is the work function of the instrument (minimum energy required to eject an electron from the instrument), and BE is independent on the instrument.

A given element will present quantized photoelectron binding energies related to every core atomic orbital, detected in the XPS spectrum as a set of "fingerprint" peaks dependent on $h\nu$ (see Figure 3.9b). Although the probing depth of X-rays is in the order of µm, the ejected photoelectron escape depth ($E_k \sim 0 - 1480\ eV$) is of not more than 10 nm: photoelectrons at higher depths lose kinetic energy as they displace within the solid and are finally re-absorbed.[33] This explains the high surface specificity of XPS, as only the information on the outermost 10 nm region of the probed material is detected. Indeed, with the exception of H and He, XPS elemental sensitivity is as low as 0.5 atomic %.[34] This is particularly suited for disciplines as electrochemistry, where the electroactivity is limited to the interface.[35]

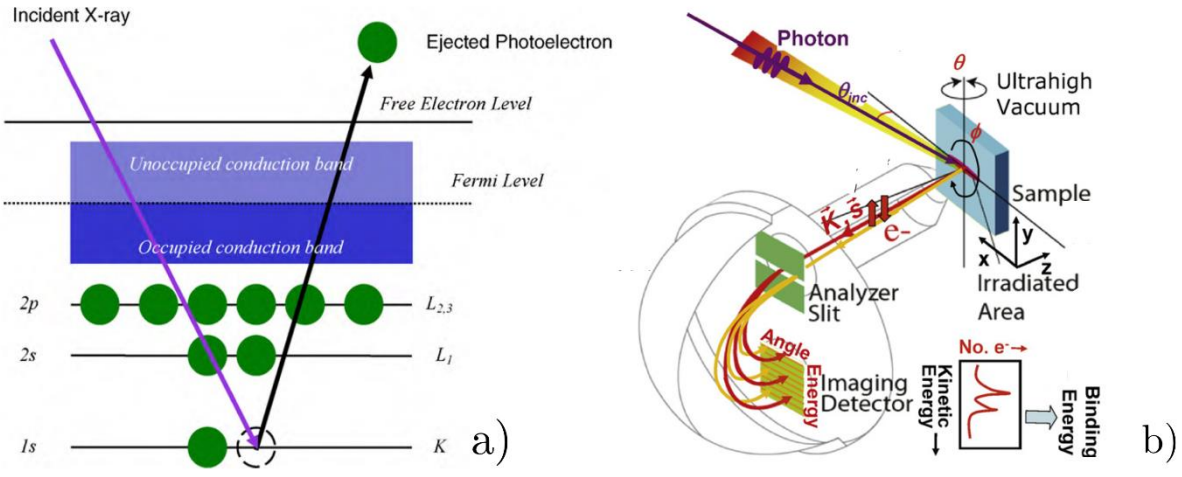

Figure 3.9. a) Schematic of the photoelectric effect employed as a basis for XPS measurements; b) Diagram of a conventional XPS instrument. Reproduced/adapted from refs. [32,36].

The elucidation of characteristic chemical environment, and consequently oxidation state, of each element detected in XPS arises from modifications of core-level electron binding energies with the atom effective charge: positively charged atoms will require higher energies to eject electrons compared with those negatively charged.[37] Thus, positive BE shifts indicate higher elemental oxidation states and vice versa.

In this research, XPS spectra of TMDs are acquired to evaluate oxidation state changes upon nanostructuring and electrochemical testing, as well as the chalcogen-to-metal ratios and degree of transition metal doping. In analogy to Raman spectroscopy, XPS spectra are distinctive for different TMD polymorphs: for MoS_2, the Mo $3d_{5/2;3/2}$ spin-orbit doublet is found to be downshifted ca. 1eV in the metallic 1T phase compared to the semiconducting 2H phase.[38]

3.3.3 Electron microscopy imaging

3.3.3.1 Scanning electron microscopy

Scanning electron microscopy (SEM) is a high vacuum surface characterisation technique that rasters a high-energy focused electron beam, accelerated by an applied voltage (≈1 to 30 kV) which interacts with a (generally) conductive specimen. The electron-sample interaction results in the emission of both photon and electron signals, containing information of the sample relative to its topography and composition (see Figure 3.10). The most relevant ones for surface imaging are those obtained by detection of backscattered (BSE) and secondary (SE) electrons. BSE are high-angle elastically-deflected electrons from the incident electron beam by atom nuclei in the specimen. The ratio between the BSEs and the incident electron beam is dependent on the atomic number Z_{atom}: higher Z_{atom} values (heavier elements) deflect more BSEs than lower Z_{atom} values.[39] Detection and analysis of BSEs provides, consequently, information regarding the sample composition: this is known as phase or Z_{atom} contrast.

Secondary electrons are low-energy electrons (< 50 eV) ejected from the specimen by the inelastically-scattered primary electron beam. As the mean free path of SEs is very small (1 to 10 nm),[40] their ejection (and subsequent detection) is surface topography-dependent: rougher or higher points in the specimen will eject more SEs compared to flat or low specimen areas. Thus, images obtained by detection and analysis of SEs provide surface topography contrast.

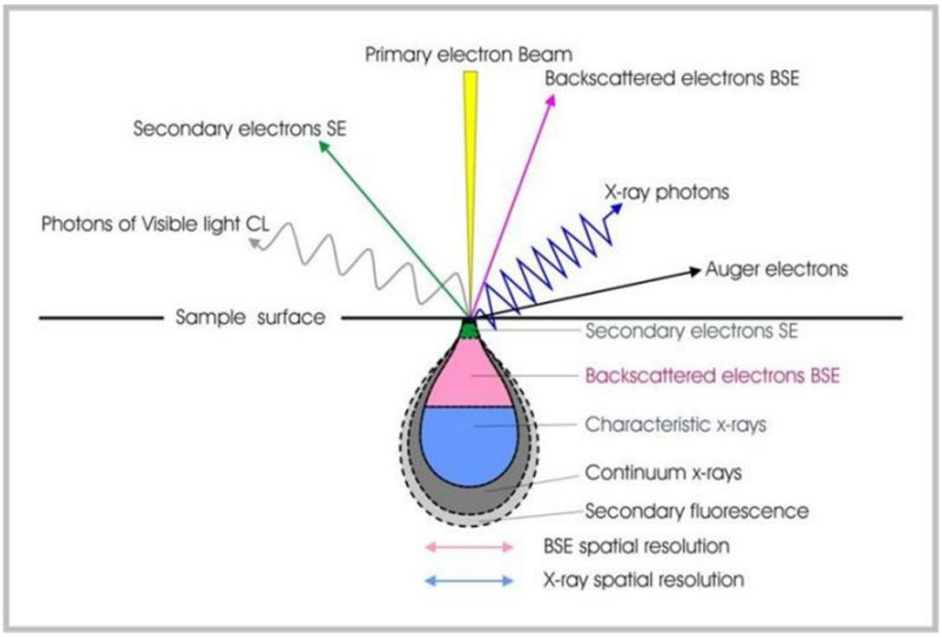

Figure 3.10. Signals emitted after the interaction between the specimen and the electron beam, and their interaction volume (penetration depth). Reproduced from [41].

In our present research, SEM imaging by SEs is employed to investigate the aspect-ratio of the plasma-etched TMD nanopillar arrays, the degree of decoration of tungsten sulfide nuclei on iridium substrates, as well as the impact of electrochemical testing in the surface roughness and morphology of the working electrodes.

3.3.3.2 Scanning transmission electron microscopy

Scanning transmission electron microscopy (STEM) is a high-resolution imaging technique based on the use of a very focused, high-energy electron beam probe to scan a thin specimen area. Signals obtained from the transmitted beam are collected point-by-point (as in SEM) to

form an image. STEM presents several advantages compared with conventional Transmission Electron Microscopy (TEM).

Firstly, the resulting image is not magnified by post-specimen lenses. Thus, as STEM is not affected by the aberration of these lenses, its theoretical resolution should be related to the wavelength of the incident electrons: for 200keV accelerating voltage, as used in NPRL's JEOL 2100 STEM (see Figure 3.11a), this should correspond to 2.51 pm. However, aberrations arising from the electron-probe formation limit STEM resolution: these are either spherical or chromatic. Spherical aberration occurs due to imperfections in the magnetic field exerted by the condensor lenses which yields a higher refraction angle for lens off-axis than near-axis electrons, whilst chromatic aberration arises from the energy dispersion (non-monochromatic nature, ≈ 0.3-1 eV) of the electron beam. Both lead to a dispersion of the beam at the focal point, which can be mitigated: the STEM employed in this work is spherical aberration-corrected (Cs), which provides a final spatial resolution of less than 0.1 nm (≈ 0.8 Å). Thus, aberration corrected(AC)-STEM enables atomic resolution imaging.

Secondly, STEM allows simultaneous collection of multiple signals depending on the relative deflection angle of the transmitted electron beam after interacting with the specimen nuclei and electron cloud (see Figure 3.11b): bright field (directly transmitted electron beam, collection angle θ ≈ 1-5 mrad), annular dark field (elastically scattered electron beam, θ ≈ 15-50 mrad) and high-angle annular dark field (HAADF, highly scattered electron beam, θ > 50 mrad).[42] In particular, HAADF-STEM imaging is also known as Z-contrast imaging as HAADF intensity, based on Rutherford scattering, is proportional to Z^n ($n<2$), n being a value experimentally obtained for each STEM instrument after calibration. Thus, HAADF-STEM images are atomically-resolved, with intensities related to Z. In nanocluster imaging, the linear dependence of HAADF intensity and cluster size[43] enables to elucidate, for single element clusters, three-dimensional profiles (i.e. cluster atomic structure).

Finally, chemical information can be gained from STEM by detection and mapping of the Energy-Dispersive X-rays (EDX). These are a result of the inelastic interaction between the focused electron beam and inner-shell electrons of atoms contained at the specimen: electron beam-induced ejection of an inner-shell electron is followed by an outer-shell, higher energy electron filling the generated vacancy (see Figure 3.11c). By doing so, the atom de-excites by releasing an X-ray photon, with an energy equivalent to the energy difference between the two electron states. Analogously to XPS, the element-dependent and quantized nature of the EDX enables elemental composition analysis, which in STEM is highly spatially-resolved. However, EDX-STEM presents a poor EDX energy (elemental) resolution due to the detector: in the case of the Bruker XFlash 4030 detector coupled to the STEM at NPRL, this is of 133 eV at Mn Kα.

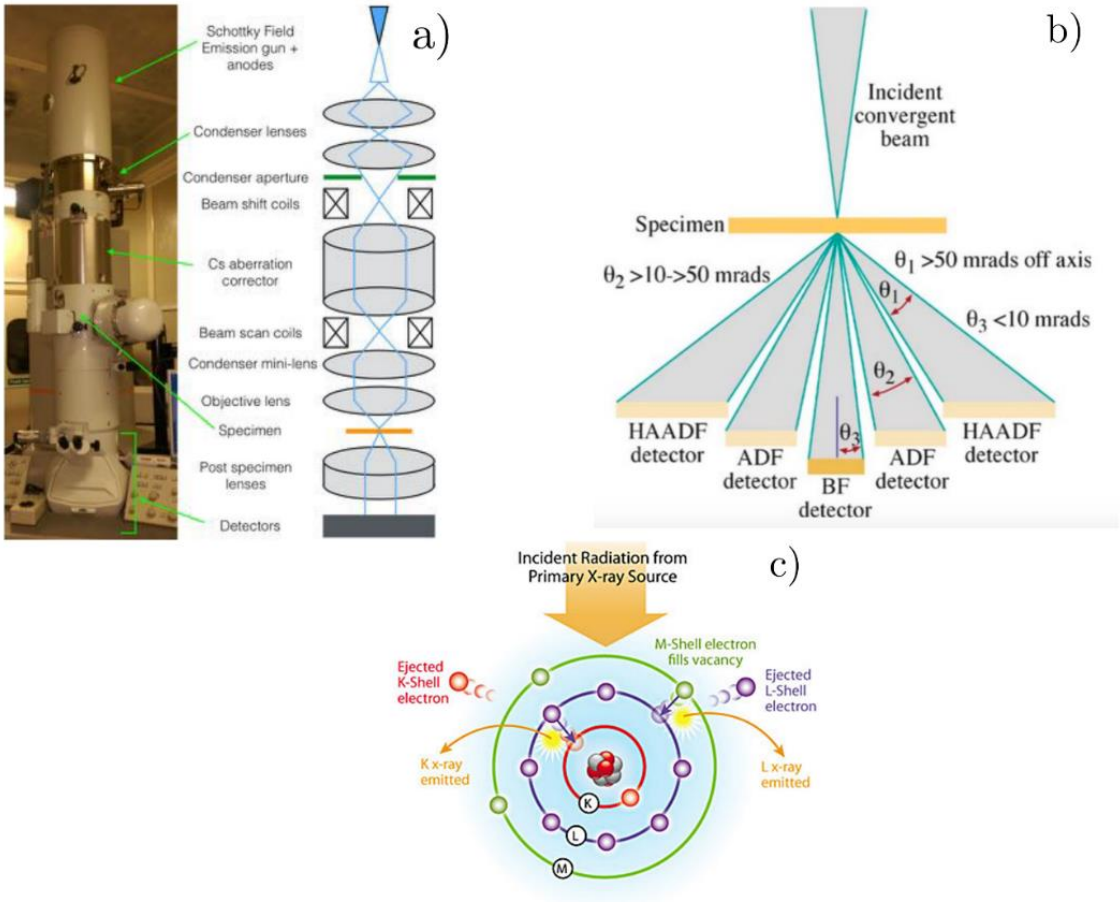

Figure 3.11. a) JEOL 2100F aberration-corrected STEM used at the NPRL, and schematic of its key components; b) Schematic of the STEM imaging modes based on the beam collection angle θ; c) Schematic of the working principle of Energy-dispersive X-ray spectroscopy: two electron from the L and K shell are ionised by the electron beam, where the generated vacancies are filled by electrons from the M and K shells, emitting Lα and Kα x-rays, respectively. Reproduced from refs. [44–46].

3.4 Cluster beam deposition

Physical production of nanoclusters has been carried out by techniques such as ball milling,[47,48] supersonic expansion nozzles and laser ablation.[49] However, nanocluster generation by magnetron sputtering and gas condensation cluster sources, used in the present work, is preferable as the size distributions and materials used to form the nanoclusters are less

restricted than in the aforementioned.[50] Clusters of Pt, Au, Ag, Pd, Pt-Ti and MoS_2, among others, have been fabricated with this technique at the NPRL.[43,51–56]

Its basic operation principle is the acceleration and collision of an inert gas plasma beam (in this case Ar^+), generated by a high DC or RF power, to a target of the material of interest mounted on a magnetron gun under ultra-high vacuum conditions (base pressure no more than 10^{-7} mbar). This occurs at the magnetron sputtering chamber (for schematic, see Figure 3.12a). Metallic targets are negatively biased to electrostatically attract Ar^+ plasma formed by DC, whereas periodical modifications in RF promote Ar^+ attraction and repulsion to non-conducting targets. The generated cloud of vaporised atoms is condensed by injection of cooled helium (He) gas to the sputtering chamber, where clusters aggregate via "three body collisions": two atoms of the sputtered material and a molecule of He. Although cooled He reduces the kinetic energy of the small atom aggregates, supplementary cooling by liquid nitrogen is needed to promote the condensation of larger clusters.

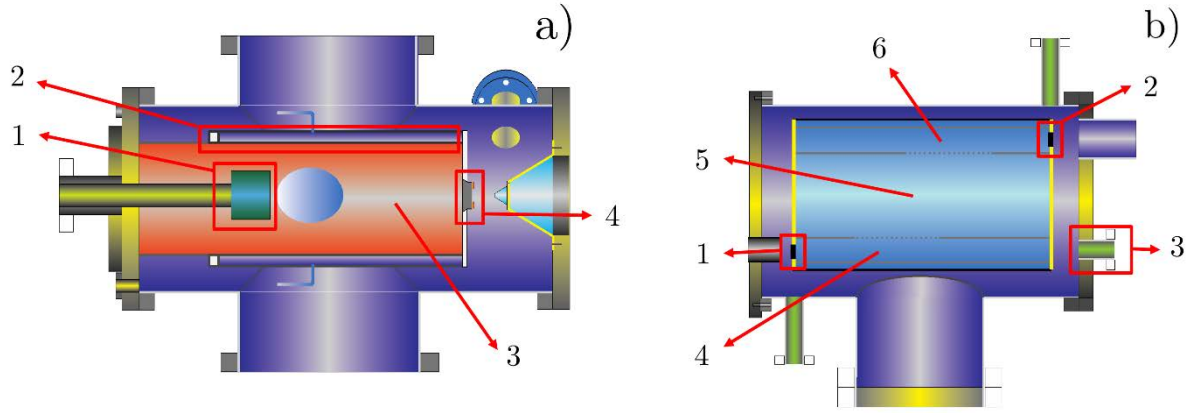

Figure 3.12. a) Schematic of the magnetron sputtering chamber: 1) magnetron target, 2) liquid nitrogen jacket, 3) cluster aggregation and nucleation region and 4) adjustable cluster beam nozzle; b) Schematic of the lateral Time-of-Flight mass filter chamber: 1,2) adjustable entrance/exit aperture slits, 3) Faraday cup array; 4,5 and 6) entrance, field-free drift and exit pulse region. Schematics adapted from ref. [57].

Cluster size distribution can be easily modified by altering the inlet pressures of Ar and He, and magnetron gun power. For higher Ar pressures, higher Ar^+ plasma flows are obtained, leading to higher sputtering rates and larger clusters. Same occurs with magneton power: higher powers result in a higher electric field gradient, which leads to higher higher Ar^+ plasma collision rates. Higher He pressures, on the other hand, yield smaller clusters with a narrower size distributions at a given sputtering rate.[58] This is explained by the higher He collision rates, which hinder the addition of atoms to the condensed atom aggregates. As ≈30% of the generated clusters are ionised by the Ar^+ plasma,[59] those positively-charged are collimated by an array of optical electrostatic lenses at the second vacuum chamber (ion optics).

The cluster beam then goes to the NPRL proprietary lateral Time-of-Flight (ToF) mass filter (schematic in Figure 3.12b, detailed illustration of the operating principle in Figure 3.13). The cluster mass selection is obtained by applying two opposing electrostatic pulses to the collimated, positively-charged horizontal cluster beam. The first perpendicular pulse, applied by a bottom plate parallel to the beam axis, generates a vertical deflection and acceleration of the clusters. The vertical trajectory of the clusters is dependent of their mass, which leads to a parallel spreading of cluster beams in the vertical axis: as all clusters experience the same electrostatic pulse, smaller clusters travel vertically more than the larger clusters. Next, a second perpendicular pulse, applied by a top plate parallel to the beam axis, cancels out the vertical motion of the beam of a given cluster size, which then exits the mass filter by an aperture towards the deposition chamber. Specific cluster masses can be selected by modifying the frequency and timescale of the electrostatic pulses.

The ToF mass filter resolution R is given by

$$R = \frac{M}{\Delta M} = \frac{x_{vert}}{\sqrt{\Delta x_{in} + \Delta x_{out}}} \quad (3.45)$$

where M and ΔM are the cluster mass and the cluster mass range exiting the mass filter, x_{vert} is the total vertical displacement of the selected cluster mass, and Δx_{in} and Δx_{out} the

dimensions of the entrance and exit apertures. In our present work, $R \approx$ 20-25. As an example, if we selected a cluster mass of 100 atoms, for $R \approx$ 20 we would obtain a size distribution of 100±2.5 atoms.

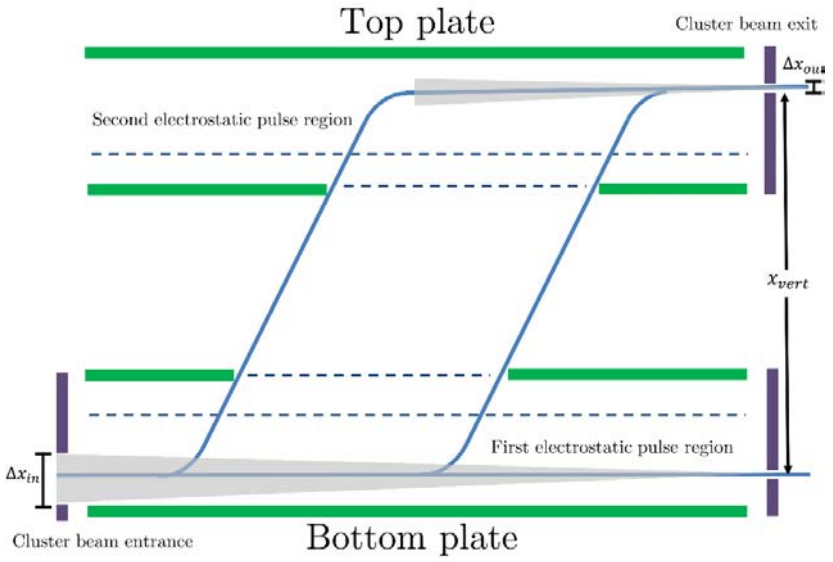

Figure 3.13. Detailed schematic of the working principle utilized in the lateral Time-of-Flight mass filter. Adapted from ref. [60].

Finally, the size-selected cluster beam is collimated at the deposition chamber, where it impacts the substrates acting as nanocluster supports, where mask holders confine the deposition area. To control the physical attachment degree (impact landing energy) of the nanoclusters to the support substrate, a positive voltage bias is applied to the substrate, ranging from 0 to 1500 V (0-1.5eV). Higher voltage biases lead to harder cluster pinning, whilst lower biases lead to soft landing.

In the present work we will be employing magnetron sputtering and gas condensation as the technique to deposit molecular materials such size-selected MoS_2 nanoclusters (for cluster source schematic, see Figure 4.3 Materials and methods section). In addition to this, formation of hybrid Ni-MoS_2 will also be explored: for such purpose, a modified cluster source simultaneously operating with dual targets (Ni and MoS_2) is employed (for dual-target cluster

source schematic, see Figure 4.2 Materials and methods section). Substrates employed are TEM grids, to evaluate cluster size distribution, morphology and elemental composition; and glassy carbon substrates to perform electrochemical experiments.

References

[1] A.C. Fisher, Electrode Dynamics, 1st ed., Oxford University Press, Oxford, 1996.

[2] C.M.A. Brett, A.M.O. Brett, Electroanalysis, 1st ed., Oxford University Press, Oxford, 1998.

[3] R.G. Compton, C.E. Banks, Understanding Voltammetry, 1st ed., World Scientific Publishing Co. Pte. Ltd., London, 2007.

[4] R.G. Compton, G.H.W. Sanders, Electrode Potentials, 1st ed., Oxford University Press, Oxford, 1996.

[5] C. Lefrou, P. Fabry, J.-C. Poignet, Electrochemistry: The Basics, With Examples, 1st ed., Springer Berlin Heidelberg, Grenoble, 2012.

[6] A.J. Bard, L.R. Faulkner, Electrochemical Methods: Fundamentals and Applications, 2nd ed., John Wiley and Sons Ltd., New York, 2001. doi:10.1016/B978-0-12-381373-2.00056-9.

[7] J.G. Chen, C.W. Jones, S. Linic, V.R. Stamenkovic, Best Practices in Pursuit of Topics in Heterogeneous Electrocatalysis, ACS Catal. 7 (2017) 6392–6393. doi:10.1021/acscatal.7b02839.

[8] R. Chen, C. Yang, W. Cai, H.-Y. Wang, J. Miao, L. Zhang, S. Chen, B. Liu, Use of Platinum as the Counter Electrode to Study the Activity of Nonprecious Metal Catalysts for the Hydrogen Evolution Reaction, ACS Energy Lett. 2 (2017) 1070–1075. doi:10.1021/acsenergylett.7b00219.

[9] R.S. Nicholson, Theory and Application of Cyclic Voltammetry for Measurement of Electrode Reaction Kinetics, Anal. Chem. 37 (1965) 1351–1355. doi:10.1021/ac60230a016.

[10] I. Lavagnini, R. Antiochia, F. Magno, An extended method for the practical evaluation of the standard rate constant from cyclic voltammetric data, Electroanalysis. 16 (2004) 505–506. doi:10.1002/elan.200302851.

[11] R.J. Klinger, J.K. Kochi, Electron-Transfer Kinetics from Cyclic Voltammetry. Quantitative Description of Electrochemical Reversibility, J. Phys. Chem. 85 (1981) 1731–1741. doi:10.1021/j150612a028.

[12] T.J. Davies, R.G. Compton, The cyclic and linear sweep voltammetry of regular and random arrays of microdisc electrodes: Theory, J. Electroanal. Chem. 585 (2005) 63–82. doi:10.1016/j.jelechem.2005.07.022.

[13] E.J.F. Dickinson, I. Streeter, R.G. Compton, Chronoamperometry and cyclic voltammetry at conical electrodes, microelectrodes, and electrode arrays: Theory, J. Phys. Chem. B. 112 (2008) 4059–4066. doi:10.1021/jp711936y.

[14] M.C. Henstridge, R.G. Compton, Mass Transport to micro- and nanoelectrodes and their arrays: A review, Chem. Rec. 12 (2012) 63–71. doi:10.1002/tcr.201100032.

[15] N. Godino, X. Borrise, F.X. Muñoz, F.J. Del Campo, R.G. Compton, Mass transport to nanoelectrode arrays and limitations of the diffusion domain approach: theory and experiment, J. Phys. Chem. C. 113 (2009) 11119–11125. doi:10.1021/jp9031354.

[16] A.S. Peinetti, R.S. Gilardoni, M. Mizrahi, F.G. Requejo, G.A. González, F. Battaglini, Numerical Simulation of the Diffusion Processes in Nanoelectrode Arrays Using an Axial Neighbor Symmetry Approximation, Anal. Chem. 88 (2016) 5752–5759. doi:10.1021/acs.analchem.6b00039.

[17] C. V. Raman, K. S. Krishnan, A New Type of Secondary Radiation, Nature. 121 (1928) 501–502. doi:10.1038/121501c0.

[18] S.-L. Zhang, Raman Spectroscopy and its Application in Nanostructures, John Wiley and Sons Ltd., Chichester, 2012.

[19] R.S. Das, Y.K. Agrawal, Raman spectroscopy: Recent advancements, techniques and applications, Vib. Spectrosc. 57 (2011) 163–176. doi:10.1016/j.vibspec.2011.08.003.

[20] X. Zhang, X.F. Qiao, W. Shi, J. Bin Wu, D.S. Jiang, P.H. Tan, Phonon and Raman scattering of two-dimensional transition metal dichalcogenides from monolayer, multilayer to bulk material, Chem. Soc. Rev. 44 (2015) 2757–2785. doi:10.1039/c4cs00282b.

[21] G. Gouadec, P. Colomban, Raman Spectroscopy of nanomaterials: How spectra relate to disorder, particle size and mechanical properties, Prog. Cryst. Growth Charact. Mater. 53 (2007) 1–56. doi:10.1016/j.pcrysgrow.2007.01.001.

[22] H. Li, Q. Zhang, C.C.R. Yap, B.K. Tay, T.H.T. Edwin, A. Olivier, D. Baillargeat, From bulk to monolayer MoS 2: Evolution of Raman scattering, Adv. Funct. Mater. 22 (2012) 1385–1390. doi:10.1002/adfm.201102111.

[23] A.P. Nayak, T. Pandey, D. Voiry, J. Liu, S.T. Moran, A. Sharma, C. Tan, C.H. Chen, L.J. Li, M. Chhowalla, J.F. Lin, A.K. Singh, D. Akinwande, Pressure-dependent optical and vibrational properties of monolayer molybdenum disulfide, Nano Lett. 15 (2015) 346–353. doi:10.1021/nl5036397.

[24] C. Lee, H. Yan, L. Brus, T. Heinz, J. Hone, S. Ryu, Anomalous lattice vibrations of single-and few-layer MoS2, ACS Nano. 4 (2010) 2695–700. doi:10.1021/nn1003937.

[25] S. Cho, S. Kim, J.H. Kim, J. Zhao, J. Seok, D.H. Keum, J. Baik, D. Choe, K.J. Chang, K. Suenaga, S.W. Kim, Y.H. Lee, H. Yang, Phase patterning for ohmic homojunction contact in MoTe2, Science (80-.). 349 (2015) 625–628.

[26] A.L. Friedman, A.T. Hanbicki, F.K. Perkins, G.G. Jernigan, J.C. Culbertson, P.M. Campbell, Evidence for Chemical Vapor Induced 2H to 1T Phase Transition in MoX2(X = Se, S) Transition Metal Dichalcogenide Films, Sci. Rep. 7 (2017) 1–9. doi:10.1038/s41598-017-04224-4.

[27] J. Kibsgaard, T.F. Jaramillo, F. Besenbacher, Building an appropriate active-site motif into a hydrogen-evolution catalyst with thiomolybdate [Mo3S13]2− clusters, Nat. Chem. 6 (2014) 248–253. doi:10.1038/nchem.1853.

[28] V.P. Fedin, B.A. Kolesov, Y. V. Mironov, V.Y. Fedorov, Synthesis and vibrational (IR and Raman) spectroscopic study of triangular thio-complexes [Mo3S13]2-containing92Mo,100Mo and34S isotopes, Polyhedron. 8 (1989) 2419–2423. doi:10.1016/S0277-5387(89)80005-1.

[29] D.N. Nguyen, L.N. Nguyen, P.D. Nguyen, T.V. Thu, A.D. Nguyen, P.D. Tran, Crystallization of Amorphous Molybdenum Sulfide Induced by Electron or Laser Beam and Its Effect on H2-Evolving Activities, J. Phys. Chem. C. 120 (2016) 28789–28794. doi:10.1021/acs.jpcc.6b08817.

[30] E. Sokolowski, C. Nording, K. Siegbahn, Magnetic Analysis of X-ray Produced Photo and Auger Electrons, Ark. För Fys. 12 (1957) 301.

[31] S. Hagström, C. Nordling, K. Siegbahn, Electron Spectroscopic Determination of the Chemical Valence State, Zeitschrift Für Phys. 178 (1964) 439–444. http://dx.doi.org/10.1007/BF01379473.

[32] C.J. Corcoran, H. Tavassol, M.A. Rigsby, P.S. Bagus, A. Wieckowski, Application of XPS to study electrocatalysts for fuel cells, J. Power Sources. 195 (2010) 7856–7879. doi:10.1016/j.jpowsour.2010.06.018.

[33] Paul van der Heide, X-ray Photoelectron Spectroscopy: An Introduction to Principles and Practices, 1st ed., John Wiley and Sons Ltd., 2011. doi:10.1002/9781118162897.

[34] S. Gross, L. Armelao, XPS as a powerful tool to investigate the surface properties of simple and mixed metal oxides; X-Ray Photoelectron Spectroscopy, in: J.M. .Wagner (Ed.), X-Ray

Photoelectron Spectrosc., Nova Science Publishers, 2010: pp. 126–185.

[35] K. Artyushkova, A. Serov, H. Doan, N. Danilovic, C.B. Capuano, T. Sakamoto, H. Kishi, S. Yamaguchi, S. Mukerjee, P. Atanassov, Application of X-ray photoelectron spectroscopy to studies of electrodes in fuel cells and electrolyzers, J. Electron Spectros. Relat. Phenomena. (2017). doi:10.1016/j.elspec.2017.12.006.

[36] C.S. Fadley, X-ray photoelectron spectroscopy: Progress and perspectives, J. Electron Spectros. Relat. Phenomena. 178–179 (2010) 2–32. doi:10.1016/j.elspec.2010.01.006.

[37] J.M. Hollander, W.L. Jolly, X-Ray Photoelectron Spectroscopy, Acc. Chem. Res. 3 (1970) 193–200.

[38] A. Ambrosi, Z. Sofer, M. Pumera, 2H → 1T phase transition and hydrogen evolution activity of MoS2, MoSe2, WS2 and WSe2 strongly depends on the MX2 composition., Chem. Commun. 51 (2015) 8450–3. doi:10.1039/c5cc00803d.

[39] L. Reimer, Scanning Electron Microscopy: Physics of Image Formation and Microanalysis, 2nd ed., Springer, Berlin, 1998.

[40] Andrew Zangwill, Physics at Surfaces, Cambridge University Press, 1988. doi:10.1017/CBO9780511622564.

[41] U. of Glasgow, Scanning Electron Microscopy, (n.d.). https://www.gla.ac.uk/schools/ges/researchandimpact/researchfacilities/isaac/services/scanningelectronmicroscopy/ (accessed October 13, 2018).

[42] R.J. Keyse, A.J. Garratt-Reed, P.J. Goodhew, G.W. Lorimer, Introduction to Scanning Transmission Electron Microscopy, 1st ed., BIOS Scientific Publishers, Oxford, 1998.

[43] Z.Y. Li, N.P. Young, M. Di Vece, S. Palomba, R.E. Palmer, a L. Bleloch, B.C. Curley, R.L. Johnston, J. Jiang, J. Yuan, Three-dimensional atomic-scale structure of size-selected gold nanoclusters., Nature. 451 (2008) 46–8. doi:10.1038/nature06470.

[44] Dawn Michelle Foster, Production and characterisation by scanning transmission electron microscopy of size-selected noble metal nanoclusters, University of Birmingham, 2017.

[45] D.B. Williams, C.B. Carter, Transmission Electron Microscopy: A Textbook for Materials Science, Springer Science & Business Media, 2009.

[46] Energy-dispersive X-ray spectroscopy, (n.d.). http://en.stonkcash.com/energy-dispersive-x-ray-spectrometry/ (accessed October 13, 2018).

[47] Y. Wang, Y. Li, C. Rong, J.P. Liu, Sm-Co hard magnetic nanoparticles prepared by surfactant-assisted ball milling, Nanotechnology. 18 (2007). doi:10.1088/0957-4484/18/46/465701.

[48] V. M. Chakka, B. Altuncevahir, Z.Q. Jin, Y. Li, J.P. Liu, Magnetic nanoparticles produced by surfactant-assisted ball milling, J. Appl. Phys. 99 (2006) 08E912. doi:10.1063/1.2170593.

[49] Walt A. de Heer, The physics of simple metal clusters: experimental aspects and simple models, Rev. Mod. Phys. 65 (1993) 611–676.

[50] S. Vajda, M.G. White, Catalysis Applications of Size-Selected Cluster Deposition, ACS Catal. 5 (2015) 7152–7176. doi:10.1021/acscatal.5b01816.

[51] K.-J. Hu, S.R. Plant, P.R. Ellis, C.M. Brown, P.T. Bishop, R.E. Palmer, The effects of 1-pentyne hydrogenation on the atomic structures of size-selected Au N and Pd N (N = 923 and 2057) nanoclusters, Phys. Chem. Chem. Phys. 16 (2014) 26631–26637. doi:10.1039/C4CP02686A.

[52] Z.W. Wang, R.E. Palmer, Intensity calibration and atomic imaging of size-selected Au and Pd clusters in aberration-corrected HAADF-STEM, J. Phys. Conf. Ser. 371 (2012) 012010. doi:10.1088/1742-6596/371/1/012010.

[53] M.J. Cuddy, K.P. Arkill, Z.W. Wang, H.-P. Komsa, A. V Krasheninnikov, R.E. Palmer, Fabrication and atomic structure of size-selected, layered MoS2 clusters for catalysis., Nanoscale. 6 (2014) 12463–12469. doi:10.1039/c4nr04317k.

[54] C.E. Blackmore, N. V Rees, R.E. Palmer, Modular construction of size-selected multiple-core Pt-TiO2 nanoclusters for electro-catalysis., Phys. Chem. Chem. Phys. (2015). doi:10.1039/c5cp00285k.

[55] S.J. Carroll, S. Pratontep, M. Streun, R.E. Palmer, Pinning of size-selected Ag clusters on graphite surfaces, J. Chem. Phys. 113 (2000) 7723–7727. doi:10.1063/1.1322657.

[56] S. Gibilisco, M. Di Vece, S. Palomba, G. Faraci, R.E. Palmer, Pinning of size-selected Pd nanoclusters on graphite, J. Chem. Phys. 125 (2006) 8–11. doi:10.1063/1.2337288.

[57] D. Escalera-López, Y. Niu, S.J. Park, M. Isaacs, K. Wilson, R.E. Palmer, N. V. Rees, Hydrogen evolution enhancement of ultra-low loading, size-selected molybdenum sulfide nanoclusters by sulfur enrichment, Appl. Catal. B Environ. 235 (2018) 84–91. doi:10.1016/j.apcatb.2018.04.068.

[58] C.E. Blackmore, Experimental and Theoretical Studies of the Atomic Structure of Platinum-based Nanoclusters, University of Birmingham, 2016.

[59] S. Pratontep, S.J. Carroll, C. Xirouchaki, M. Streun, R.E. Palmer, Size-selected cluster beam source based on radio frequency magnetron plasma sputtering and gas condensation, Rev. Sci. Instrum. 76 (2005) 045103. doi:10.1063/1.1869332.

[60] B. von Issendorff, R.E. Palmer, A new high transmission infinite range mass selector for cluster and nanoparticle beams, Rev. Sci. Instrum. 70 (1999) 4497. doi:10.1063/1.1150102.

Chapter 4

Materials, equipment and methods

4.1 Working electrode preparation and modification

4.1.1 Glassy carbon electrode preparation

Glassy carbon (GC) samples were fabricated from 5 and 7 mm diameter type 2 rods (Alfa Aesar, UK, 50 mm length). GC rods were cut into stubs of approximately 5 mm thickness with the aid of a diamond saw, under water flow to remove stray carbon particles and mitigate saw overheating under operation. GC stubs employed for direct electrochemical characterization were sequentially polished with 45, 30, 15, 9 and 3 µm MetaDi Supreme polycrystalline diamond suspensions on TriDent polishing pads (Buehler), followed by polishing with 1, 0.3 and 0.05 µm MicroPolish alumina slurry suspensions on MicroCloth polishing pads (Buehler). GC samples were mounted on a Buehler Vector LC 250 single force rotating sample holder (Spring load pressure: 15 N, Rotation speed: 60 rpm) by use of in-house manufactured polypropylene sample holder adaptors (38 mm diameter, 20 mm height, 3 mm sample holder thickness) coupled to a Buehler Metaserv 250 polisher under 250 rpm rotation speed. GC stubs were polished until a mirror-like finish was achieved.

4.1.2 Glassy carbon working electrode assembly

TMD nanoarray modified GC stubs electrical conductivity was improved by applying a colloidal silver ink (SPI Supplies, USA) at the TMD/GC edge junctions with a hypodermic needle under an optical microscope. For both TMD nanoarray and Ni-MoS_2 nanoclusters

experiments, the GC-modified stubs were electrically connected with silver ink to a 50 x 2 mm brass rod embedded in a 40 x 10 mm Teflon rod (Direct Plastics Ltd, United Kingdom). To prevent potential interference of silver and the GC lateral perimeter in the electrochemical experimentation, epoxy resin (Araldite) was applied to insulate the non-modified GC regions and ensure that only the TMD nanoarray crystal and nanocluster-modified cross section was exposed. For the remaining experiments (TMD nanoarray electrochemical sufidation monitoring and sulfur-enriched MoS_x nanoclusters), GC stubs were connected to a rotating disk capable OrigaTrod setup with a 7 mm diameter OrigaTip sample holder (OrigaLys ElectroChem SAS, France), or to a E4 series AFMSRCE modulated speed rotator coupled with a AFE3M shaft and an E4TQ ChangeDisk RDE tip (Pine Research Instrumentation Ltd., USA), respectively. No rotation was applied during electrochemical experimentation.

4.2 Transition metal dichalcogenide nanoarray fabrication

The TMD nanoarray fabrication has been adapted from a method developed within the Nanoscale Physics Research Laboratory (NPRL), and performed by MSc student Ross Griffin. MoS_2 (20x10 mm, SPI Supplies USA) and WS_2 (defect-free, 99.9995% purity, 2D Semiconductors USA) crystals were cut into rectangles of approximately 1.5 x 5 mm using a pristine scalpel blade and then attached to GC type 2 stubs (2mm thickness, 5-7mm diameter, Alfa Aesar, UK) with conductive carbon tape. TMD samples were mechanically cleaved under an optical microscope by insertion and lifting of a scalpel into the edges of the TMD samples to remove several TMD layers and obtain a flat surface for modification.

20 µL of a 1:1 (vol. ratio) mixture of a 216 ± 4 nm diameter polystyrene-latex nanosphere (NS) suspension (3000 Series Nanosphere, 1 wt. % in water, Thermo Scientific, UK) with absolute ethanol were transferred to a silicon wafer to form, by self-assembly, a NS monolayer with hexagonal close-packed (HCP) structure. All silicon wafers were cleaned first by piranha solution (H_2SO_4 96% vol. /H_2O_2 30% vol. 3:1) and later by oxygen plasma (Technics Plasma

100-E, 100 W Induced Coupled Plasma, 60 s) to ensure a residue-free hydrophilic surface feasible for surface modification. Prior to use, the NS suspension was ultrasonicated to ensure isotropic NS distribution.

Nanospheres deposition onto the TMD-modified GC substrate was performed by attaching the NS-modified silicon wafer to a custom-built vertical positioner (Figure 4.1). The positioner was adjusted to immerse the wafer into a water-filled Petri dish (30 s) containing the TMD-modified GC stubs attached to the centre of the dish bottom, and the supernatant was extracted with a syringe to promote NS deposition onto the TMD surface by evaporation. Successful formation of a NS theoretical monolayer at the water-air interface was initially assessed by thin film light reflection interference under illumination with a tungsten lamp. SEM micrographs of the resulting samples were acquired to evaluate the coverage and compactness of the NS HCP arrangement (XL 30 SFEG, 5kV).

Figure 4.1. Custom-built silicon wafer vertical positioner employed for NS monolayer deposition

Etching of the NS-modified TMDs was performed in an Oxford Instruments Plasmalab NGP 80 Inductively Coupled Plasma (ICP)/ Radio Frequency (RF) etcher. Isotropic oxygen plasma etching for 40 s at 30 standard cubic centimetres per minute (sccm) O_2 flow rate and 100 W RF power was performed as an NS shrinking step. Next, exposure to an anisotropic plasma etching mixture of SF_6 (20 sccm) and C_4F_8 (30 sccm) performed under 200 W ICP and 20 W

RF power for variable times (15-60s) was carried out to obtain nanopillar arrays with variable aspect ratios. Both etching steps were performed under pressures of 15 mTorr and chiller temperatures of 20°C. SEM micrographs of the freshly etched and electrochemically tested samples were acquired to determine the aspect ratio (nanopillar height/base diameter) and interspacing (nanopillar base-to-base distance) of the individual nanostructures in the array (XL 30 SFEG and JEOL 7100F FEG-SEM, 5kV, tilt angles from 45° to 85°).

4.3 Molybdenum sulfide nanoclusters fabrication

4.3.1 Nickel-molybdenum disulfide hybrid nanoclusters: dual-target magnetron sputtering deposition

Ni, MoS_2 and hybrid Ni-MoS_2 nanoclusters were prepared using a custom-built cluster beam source at Teer Coatings Ltd (Worcestershire, UK) by PhD candidate Yubiao Niu. The system layout is shown in Figure 4.2.

Ni, MoS_2 and Ni-MoS_2 hybrid nanoclusters are generated within the first section of the source by sputtering with dual, independent magnetrons. During the preparation of pure Ni or MoS_2 clusters, only the magnetron sputtering source fitted with the respective target (Ni or MoS_2) was activated, leaving the other magnetron power supply switched off. For the deposition of Ni-MoS_2 hybrid clusters, the two magnetrons were operated simultaneously.

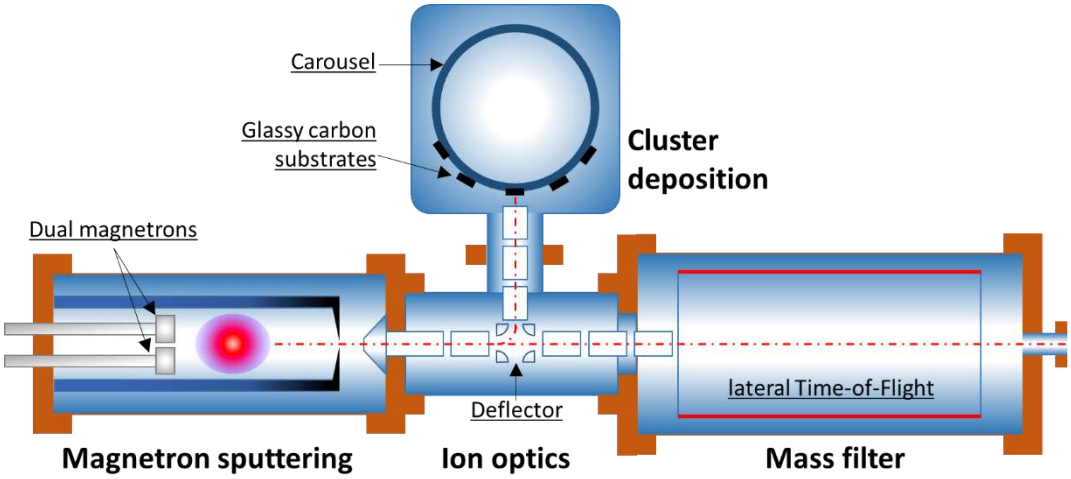

Figure 4.2. Schematic of the dual-target magnetron sputtering and gas condensation cluster beam system (top view). It consists of four sections: magnetron sputtering, ion optics, lateral time-of-flight mass filter and cluster deposition. For all experiments described the mass filter is only used for cluster size monitoring, not for deposition. The clusters are instead deposited directly onto substrates in the chamber shown at the top of the figure.

After leaving the magnetron sputtering chamber via a small nozzle (5 mm in diameter), positively charged clusters are accelerated and steered by the ion optical electrostatic lenses which surround the beam in the second vacuum chamber. Next, the ion beam is collimated and directed into the third vacuum chamber for mass selection. By using the lateral Time-of-Flight mass filter developed at the NPRL, (see Section 3.4) the mass distribution of clusters can be monitored in real time. When the desired cluster size distribution within the sampled ion beam is achieved, the high voltages applied to the deflector in the centre of the Ion Optics chamber are switched to deflection mode, so that the positively ionised fraction of the cluster beam is deflected horizontally towards the deposition chamber. Mirror-finished GC stubs (5 mm x 5 mm x 3 mm) are mounted on a carousel that can rotate as well as translate vertically. The rotation speed of the carousel and its vertical motion are carefully controlled to ensure an even cluster distribution on the substrates. Additionally, a high voltage bias is applied to the carousel in order to control the impact energy of the clusters landing on the GC stubs. During the

cluster deposition, a condensation length (i.e. the distance between sputtering target surface and the exit nozzle) of 24 cm was used and a pressure of approximately 0.23 mbar was maintained in the condensation chamber, with 70 standard cubic centimetres per minute (sccm) Ar flow and 10 sccm He flow. For all the samples, an average cluster spacing of 2.5 nm was targeted. According to this cluster spacing and the mass spectra, the mass loadings are 1.28 μg cm^{-2}, 3.45 μg cm^{-2}, and 4.25 μg cm^{-2} for Ni, MoS_2 and Ni-MoS_2 hybrid nanoclusters, respectively.

4.3.2 Size-selected, sulfur-enriched molybdenum sulfide nanoclusters: single target magnetron sputtering deposition

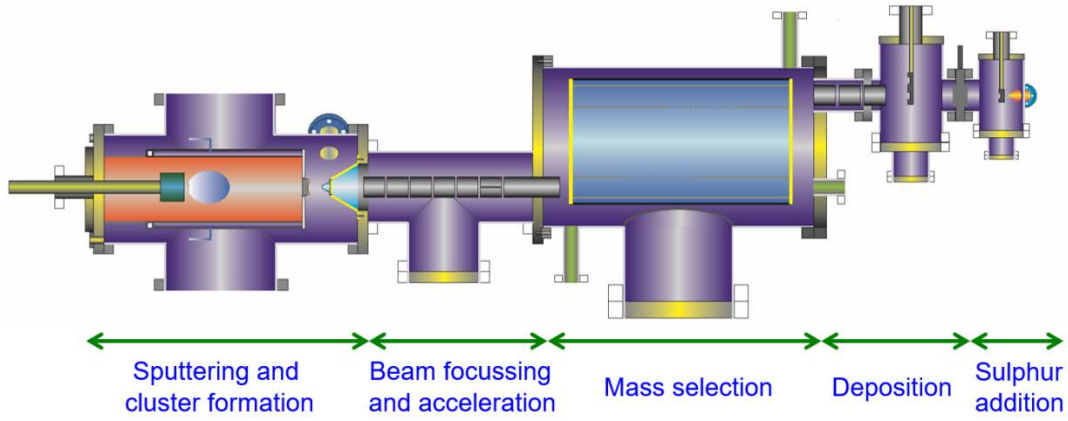

Figure 4.3. Cluster beam source schematic. It comprises five sections: magnetron sputtering and cluster formation, ion optics, Time-of-Flight mass filter, cluster deposition and cluster post-treatment.

Size-selected MoS_2 nanoclusters were produced using a DC (45 W) magnetron sputtering and gas condensation cluster beam source as shown in Figure 4.3, by PhD candidate Yubiao Niu and Dr. Sung Jin Park at the NPRL from a 2-inch sputtering MoS_2 target (PI-KEM, 99.9% purity). Ar and He flows to promote MoS_2 target sputtering and nanocluster aggregation were 180 sccm and 160 sccm, respectively. The positively charged clusters were accelerated with ion optical electrostatic lenses and then size-selected with a lateral time-of-flight mass filter (see

Section 3.4). A mass of 160000 amu, corresponding to 1000 MoS_2 units (designated as $(MoS_2)_{1000}$), was selected for depositing onto an amorphous carbon coated TEM grids (Agar Scientific, 200 Mesh Cu) and onto mirror-finished GC stubs (5 mm x 5 mm x 3 mm). The mass resolution of the mass filter is of approx. 20: for the as-deposited MoS_2, this yields a cluster deposition size distribution of 160000±8000 amu. The loading of the TEM grid samples was approx. 5% projected surface area coverage (i.e., approx. 5% of the surface covered by clusters), while the loadings of the GC samples were 5%, 10% and 20% projected surface area. The clusters were deposited onto amorphous carbon covered TEM grids and GC stubs with an impact energy of 1.0 eV and 1.5 eV per MoS_2 unit, respectively. Sulfur addition was conducted in a sulfur atmosphere created by evaporating sulfur using a home-built in-situ thermal evaporator (5 min). Annealing (7 min, 215 ± 5 °C) was performed with an electron beam bombardment heating stage. The temperature was monitored using a pyrometer (IMPAC Pyrometer, IPE 140).

4.4 Preparation of amorphous molybdenum sulfide thin films

Amorphous molybdenum sulfide (MoS_x) thin films were deposited onto Si/Ti (10 nm)/Au (100 nm) substrates by electrochemical deposition from a freshly-prepared, deaerated electrolyte solution containing 2mM $(NH_4)_2[MoS_4]$ (99.97% trace metal analysis, Sigma-Aldrich) and 0.1 M $NaClO_4$ (ACS ≥98%, Sigma-Aldrich). In this setup, a double-junction saturated Ag/AgCl reference electrode (Sigma-Aldrich) and a bright Pt mesh counter electrode (Alfa Aesar, U.K.) were employed. Analogously to HER experiments, the Pt counter electrode was encapsulated in a glass vial with a fritted junction to prevent Pt re-deposition onto the deposited MoS_x thin films. A deposition area on Si/Ti/Au chips (5 × 5 mm) was selectively exposed to the electrolyte by insulating the remaining working electrode surface with hydrophobic Teflon tape. Electrodeposition was carried out with neither rotation nor N_2 bubbling to prevent alterations

in the deposition rate from the effects of convection. Preliminary deposition rate studies were performed by depositing MoS_x thin films at various charge densities. Anodic electrodeposition (AE) was performed at a constant voltage of +0.1 V vs. Ag/AgCl, whilst cathodic electrodeposition (CE) was performed at -1 V vs. Ag/AgCl. MoS_x thin film thickness vs. charge density plots (Figure 9.2 Chapter 9) were obtained after three independent height profile measurements of each MoS_x-modified sample using a Dektak 3ST surface Profilometer (Veeco, USA). For inherent electrochemistry and HER experiments on AE-MoS_x, an approx. thickness of 100 nm (33.7 mC cm^{-2}) was employed in all samples, assuming a 100% Faradaic deposition efficiency.

4.5 Preparation of tungsten sulfide-decorated iridium electrodes

Tungsten sulfide (WS_x) nuclei were deposited onto Si (0.5 mm)/Si thermal oxidation layer (1 μm)/ Cr (10 nm)/Ir (100 nm) substrates by electrochemical deposition from a freshly-prepared, deaerated electrolyte solution containing 10mM $(NH_4)_2[WS_4]$ (99.9% trace metals basis, Sigma-Aldrich) and 0.1 M $NaClO_4$ (≥99.0% AnalaR Normapur, VWR Chemicals). In this setup, an in-house fabricated reversible hydrogen electrode (RHE) encapsulated in a fritted double junction (electrolyte: 0.1 M $NaClO_4$) and a 3 mm diameter GC counter electrode (Alfa Aesar, U.K.) were employed. A deposition area on Si/Cr/Ir chips (5 × 5 mm) was selectively exposed to the electrolyte by insulating the remaining working electrode surface with hydrophobic Teflon tape. Electrodeposition was carried out under quiescent conditions to prevent alterations in the deposition rate from the effects of forced convection. Preliminary WS_x deposition studies were performed by depositing thin films by continuous cyclic voltammetry experiments within the -0.4 V to +2.5 V vs. RHE voltage window. Galvanostatic pulsed electrodeposition was performed by symmetrically alternating the working electrode current intensity in the 500-900 μm current range. Several current pulse time durations (0.0625, 0.125, 0.25, 0.5 and 1s) and

total electrodeposition times (1, 2.5, 5 and 10 mins) were employed to evaluate modifications in WS_x nuclei size and coverages.

4.6 Equipment for electrochemical characterization

Electrochemical measurements at the University of Birmingham were carried out with a PC-controlled PGSTAT128N potentiostat/galvanostat using a Nova 2.1 software (Metrohm Autolab B.V, Netherlands) whilst those at the University of Copenhagen were recorded in an ECi-200 potentiostat/galvanostat using the software EC4U 4.1.90.1 (Nordic Electrochemistry ApS, Denmark). In both cases three-electrode thermostatted electrochemical cells were employed (water jacket, 23 ± 2° C). Oxygen-free conditions during electrochemical experimentation were achieved after purging the electrochemical cell with N_2 (99.998% purity, Oxygen-free grade, BOC Gases plc) or Ar (99.999% purity, ≤ 2 ppm oxygen, Alphagaz 1 Argon), and maintained by applying a positive atmosphere of the inert gas above the electrolyte surface. All electrochemical glassware was cleaned overnight by use of a dilute solution of $KMnO_4$ (ACS ≥ 99%, Sigma-Aldrich) in concentrated H_2SO_4 (> 95% analytical grade, Fisher Scientific) followed by thorough rinsing with ultrapure water (University of Birmingham), or by overnight soaking in an acidified saturated solution of $KMnO_4$ (≥ 99%, crystalline, extra pure, Merck) followed by rinsing in a 1 L aqueous solution containing H_2SO_4 (0.5mL, 95% technical grade, VWR Chemicals) and H_2O_2 (30 mL), and copious rinsing with ultrapure water (University of Copenhagen).

The reference electrodes used in this work are as follows: commercial SCE reference (RE-2BP, BAS Inc., Japan) for HER experiments at the University of Birmingham, commercial double junction saturated Ag/AgCl reference (Z113107-1EA, Sigma-Aldrich) for solvent-phase electrochemical sulfidation and molybdenum sulfide electrodeposition experiments, and in-house fabricated RHE for experiments at the University of Copenhagen. The latter is obtained

by flame sealing the narrow end of a previously snapped Pasteur pipette containing a protruding 1 mm Pt wire (Alfa Aesar), which is rinsed and filled up with the same electrolyte as used for electrochemical experiments (for this work either 0.1 M $NaClO_4$ or 0.1 M $HClO_4$). Next, the Pt-modified Pasteur is inserted onto a glass vessel (i.e. fritted double junction or Luggin capillary) filled with analogous electrolyte to prevent electrolyte cross-contamination and RHE voltage drift, and connected to a two-electrode electrochemical cell to undergo in-situ hydrogen production at the Pasteur reservoir by electrolysis (WE potential: -2 V, 5-10 mins) using a Pt wire counter electrode (CE).

Unless otherwise stated, all HER potentials reported for non-RHE electrodes are corrected versus the RHE using the Nernstian shift correction: $E_{RHE} = E_{0,ref} + 0.059pH$, where $E_{0,ref}$ is the standard electrode potential of the reference electrode versus the standard hydrogen electrode. Experimental deviations in the in-house RHE reference were accounted for by acquisition of 10 cyclic voltammograms from -0.25 V to 0.15 V (starting potential: 0.05 V) after 10 minutes purging with H_2 to reach solution saturation. Real RHE values were elucidated by averaging the experimental voltage values obtained at 0 A for the 10^{th} forward/backward scan.

The counter electrodes used in this work are a 52 mesh woven Pt gauze (0.1 mm wire diameter) connected to a 0.25 mm Pt wire (Alfa Aesar), or 3 mm glassy carbon rod. For experiments under which Pt contamination at the working electrode (WE) due to dissolution and re-deposition are foreseeable (i.e. long term HER and electrochemical deposition experiments), the Pt mesh was encapsulated in a glass tube with a fritted junction.

The WEs used are modified GC stubs (*vide supra*), Si (1 mm)/Si thermal oxidation layer (1 μm)/ Ti (10 nm)/Au (100 nm) and Si (0.5 mm)/Si thermal oxidation layer (1 μm)/ Cr (10 nm)/Ir (100 nm) wafers prepared by sputtering deposition and mechanical dicing (5 x 15 mm, IMB-CNM, Universitat Autònoma de Barcelona, Spain). Prior to use, Si/Ti/Au and Si/Cr/Ir

chips were ultrasonicated sequentially in acetone (3 times, 3 mins), isopropanol (2 mins) and finally rinsed in ultrapure water to eliminate the polymeric resin coated onto the substrates, used for preventing particle contamination from mechanical dicing and surface scratching during wafer transportation.

4.7. Chemicals and procedures for electrochemical characterization

4.7.1 Magnetron-sputtered molybdenum sulfide nanoclusters

4.7.1.1 Chemicals

A 2 mM $HClO_4$ (ACS ≥ 70%, Sigma-Aldrich), 0.1 M $NaClO_4$ (ACS ≥ 98%, Sigma-Aldrich) solution (pH 2.7) was used in all experiments, freshly prepared with ultrapure water (Millipore Mili-Q Direct 8, resistivity not less than 18.2 MΩ cm). This fully supported, non-coordinating anion-containing, low proton concentration electrolyte was chosen in contrast to the more commonly reported high proton concentration electrolytes in hydrogen evolution experiments (0.5 M H_2SO_4, pH ≈ 0.3; 0.1 M $HClO_4$, pH ≈ 1) as previous experiments on $(MoS_x)_y$ nanoclusters yielded more reproducible electrochemical results, enabling accurate elucidation of the HER reaction kinetic parameters. Acidic electrolytes with lack of a supporting electrolyte (in our case 0.1 M $NaClO_4$) are reported to distort any kinetic analysis due to migration effects of the electroactive species.[1]

4.7.1.2 Electrochemical characterization: nickel-molybdenum disulfide hybrid nanoclusters

The $(MoS_2)_{300}$, Ni_{2200} and $(Ni\text{-}MoS_2)_{1000}$ nanocluster-modified electrodes were preconditioned with 10 cycles between -0.045 and -1.645 V vs. SCE at a scan rate of 50 mVs^{-1}. Electrocatalytic measurements were made at a range of voltage scan rates from 2 to 1200 mVs^{-1}. This experimental procedure was applied to both freshly deposited and 14 h air-exposed samples.

Anodic stripping voltammetry experiments, consisting of 10 cycles in the 0 to 1.2 V voltage range vs. SCE, were performed in both on the 14 h air-exposed electrochemically tested MoS_2 and Ni-doped MoS_2 samples to estimate their turnover frequency (TOF) and elucidate their electrochemical features. All voltammograms were later plotted with respect to the reversible hydrogen electrode (RHE).

4.7.1.3 Electrochemical characterization: size-selected, sulfur-enriched molybdenum sulfide nanoclusters

Nanocluster-modified GC electrodes were preconditioned prior to HER experiments with 10 cycles from -0.045 to -1.645V (vs. SCE) at a voltage scan rate of 50 mVs^{-1} to obtain a stabilized performance. HER electrocatalysis measurements were then recorded at a range of voltage scan rates from 2 to 1200 mVs^{-1}, and electrochemical impedance spectroscopy measurements (EIS) were acquired in the -0.1 to -1.4 V vs. SCE with 100 mV steps, using a frequency range of 10^{-1} to 10^5 Hz (voltage amplitude = 10 mV) with the aid of the FRA32 Autolab module to apply the *iR* compensation correction on all HER voltammograms. All GC samples were immediately tested after nanocluster modification, being transported to the electrochemical cell in a N_2-saturated sealed container to avoid exposure to air.

The experimental EIS data was fitted employing the commercial software ZView (Scribner Associates Inc., USA). A linear transmission model commonly used for porous systems,[2,3] recently applied to describe EIS on amorphous MoS_x thin films,[4,5] was adapted for its use on our non-porous system as the conventional Randles circuit provided a poor fit of the experimental data. (Figure 4.4) The circuit comprises three main impedances representing the contributions of the electrolyte, MoS_x nanocluster catalysts, and catalyst-electrode interface. R_{sol} and CPE_{sol} are the elements which describe the electrolyte resistance and the charge-discharge of the electrical double layer, respectively. The electron transfer resistance and inherent MoS_x through-plane resistance are included in R_{ct}, whereas the faradaic capacitance behavior of the layered MoS_x nanocluster structure is accounted for by CPE_{ct}. Finally, the electron transfer resistance and capacitance at the MoS_x nanoclusters' bottommost layer-GC electrode contact interface are described by R_c and CPE_{ct}, respectively.

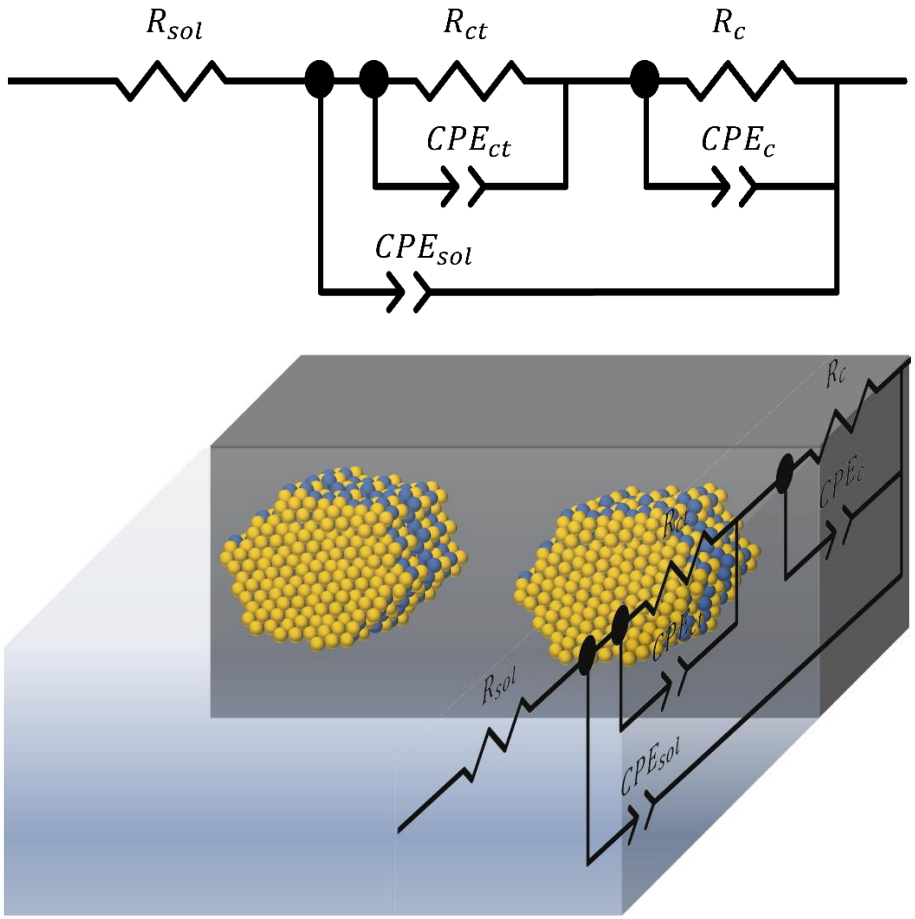

Figure 4.4. Top: Diagram of the simplified transmission line circuit model employed for EIS fitting. Bottom: 3D schematic of the EIS equivalent circuit overlapped at a cross-section of the acidic electrolyte-(MoS_x) nanocluster-glassy carbon system.

4.7.2 Transition metal dichalcogenide nanoarrays

4.7.2.1 Chemicals

All hydrogen evolution experiments were performed in a 2 mM $HClO_4$ (ACS ≥70%, Sigma-Aldrich), 0.1 M $NaClO_4$ (ACS ≥98%, Sigma-Aldrich) electrolyte. Heterogeneous electron transfer (HET) rates were investigated in 10 mM $K_4Fe(CN)_6/K_3Fe(CN)_6$ (BioUltra ≥99.5%,

Sigma-Aldrich) electrolyte supported by a pH 7.2 phosphate buffer (50 mM potassium phosphate monobasic/potassium phosphate dibasic trihydrate, ≥99%, Sigma-Aldrich). All electrolytes were freshly prepared with ultrapure water (resistivity not less than 18.2 MΩ·cm, Millipore Milli-Q Direct 8).

4.7.2.2 Electrochemical characterization procedures

The TMD electrodes were preconditioned for HER experiments with 10 cycles between -0.045 and -1.645 V versus SCE at a voltage scan rate of 50 mV s^{-1}, and tested at a range of voltage scan rates (2 - 1200 mV s^{-1}). Elucidation of heterogeneous electron transfer rate constants (k^{o}_{app}) was conducted by performing five cyclic voltammograms in the phosphate buffer-supported 10 mM $K_4Fe(CN)_6/K_3Fe(CN)_6$ electrolyte at scan rates ranging from 10 to 300 mV s^{-1}, correlating the peak to peak separation of the $K_4Fe(CN)_6/K_3Fe(CN)_6$ redox features with the dimensionless parameter ψ. This was performed using two methods reported in the literature: Nicholson and Shain,[6] and Klinger and Kochi[7] (see Section 3.2.3). A diffusion coefficient of 7.26×10^{-6} cm^2 s^{-1} for the $[Fe(CN)_6]^{3-/4-}$ redox pair was used in the calculation,[8] assuming a charge transfer coefficient (α) of 0.5. The least squares linear regression of the HER peak current density (j_P) vs. the square root of the scan rate ($v_{scan}^{1/2}$) was fitted with the Randles-Ševčík expression for irreversible redox processes[9] using $\alpha = 0.27$ (WS_2) and $\alpha = 0.3$ (MoS_2), both obtained after modelling the HER CVs obtained at 10, 50 and 100 mV s^{-1} scan rates with the DigiElch 7 software (Gamry Instruments Ltd., USA) according to a planar geometry.

During the solvent-phase electrochemical sulfidation studies, additional electrochemical capacitance (-0.2 to +0.2 V vs. RHE, voltage scan rates from 10-500 mV s^{-1}) and electrochemical impedance spectroscopy measurements (acquired from 0 to -1.645 V vs. SCE

,100 mV steps, frequency range: 10^{-1} to 10^{5} Hz, voltage amplitude = 10 mV) to account for roughness factor and *iR* compensation corrections during the three-week electrochemical and XPS testing period.

4.7.3 Amorphous electrodeposited molybdenum sulfide

4.7.3.1 Chemicals

Electrolytes employed for pH-controlled inherent electrochemistry and HER measurements were prepared as follows. For pH≈0, a 0.5 M H_2SO_4 (95% v/v, Fisher Scientific) acid solution was employed. pH 1-2 solutions were obtained by mixing aliquots of 0.2 M HCl (37% v/v ACS, Sigma-Aldrich) and 0.2 M KCl (anhydrous, ACS ≥ 99%, Sigma-Aldrich) electrolytes. pH 3-6 buffered electrolytes were obtained by mixing varying volumes of 0.1 M citric acid monohydrate (ACS ≥ 99%, Sigma-Aldrich) and 0.1 M sodium citrate dihydrate (≥ 99% FG, Sigma-Aldrich) solutions. The phosphate buffered saline (PBS) pH 7 electrolyte was prepared by mixing 6.15 mL of a 1 M potassium phosphate dibasic trihydrate (≥ 99%, for molecular biology, Sigma-Aldrich), and 3.85 mL of a 1 M potassium phosphate monobasic (≥ 99%, for cell culture, Sigma-Aldrich). Finally, pH 8-10 buffered electrolytes were prepared by mixing 0.05 M sodium tetraborate (anhydrous, BioUltra ≥ 99%, Sigma-Aldrich) with 0.1 M HCl (for pH 8-9) or 0.1 M NaOH (ACS ≥ 97%, pellets, Sigma-Aldrich) (for pH 10). All electrolytes were brought to volume in 100 mL volumetric flasks with ultrapure water (Millipore Mili-Q Direct 8, resistivity not less than 18.2 MΩ cm), testing their final pH using a 3-point calibrated Mettler-Toledo FiveEasy FE20 pH bench meter coupled to a Mettler-Toledo LE438 pH electrode (Greifensee, Switzerland).

4.7.3.2 Electrochemical characterization procedures

pH-dependent inherent electrochemical activity of as-prepared electrodeposited MoS_x thin films was evaluated by acquiring one cyclic voltammogram from 0.7 to -1.2 V vs. SCE. For MoS_x activation pre-treatment studies, a 50 cyclic voltammogram protocol was employed, where both anodic and cathodic limits were modified based on the inherent electrochemical features observed in the voltammogram of the as-prepared sample. Three main pretreatments were investigated: electro-oxidative (lower voltage selected close to OCP values, upper voltage selected past the electro-oxidation features), oxidative-reductive (lower voltage selected past the first cathodic pre-wave peak, upper voltage selected past the electro-oxidation features) and reductive (lower voltage selected past the first cathodic pre-wave peak, upper voltage selected close to OCP values). Linear sweep voltammograms ($E_{anodic} = E_{SCE} + E_{H^+/H_2} - 0.059pH$, to $E_{cathodic} = -1.2\,V - 0.059pH$) and electrochemical impedance spectroscopy measurements (voltage range: -0.1 to -1.4 V vs. SCE, 200 mV steps, frequency range: 10^{-1} to 10^5 Hz, voltage amplitude = 10 mV) were recorded before and after the activation pretreatment step to account for modifications in both HER activities and *iR* compensation corrections.

For long-term potentiodynamic durability testing, an initial linear sweep voltammogram was recorded from 0.7 to -1.2 V vs. SCE on as-prepared MoS_x thin films under 1500 rpm exerted by a magnetic stirring bar controlled by a stirring plate to establish the anodic and cathodic limits. The upper voltage limit was selected close to OCP values, whereas the cathodic limit was selected to achieve HER geometric current densities of -10 mA cm^{-2}. Under these conditions, 3000 cyclic voltammograms were recorded at 1500 rpm and positive N_2 pressure for all the electrolytes tested at a voltage scan rate of 100 mV s^{-1}. For stability measurements, a 12 hour chronopotentiometry experiment was set to monitor the overpotential required to

sustain a constant HER geometric current density of -10 mA cm^{-2}, with experimental conditions equivalent to those used for potentiodynamic experiments (1500 rpm, positive N_2 pressure).

All electrochemical experiments were repeated no less than three times to ensure reproducibility.

4.7.4 Tungsten sulfide-decorated iridium electrodes

4.7.4.1 Chemicals

All oxygen evolution experiments were performed in a 0.1 M $HClO_4$ electrolyte (70%, Suprapur®, Merck). All electrolytes were freshly prepared with ultrapure water (resistivity not less than 18.2 MΩ·cm, Millipore Milli-Q Direct 8).

4.7.4.2 Electrochemical characterization procedures

All Ir samples were preconditioned prior to oxygen evolution reaction (OER) electrochemical testing by recording 20 cyclic voltammograms from 0 to 0.7 V vs. RHE at a voltage scan rate of 50 mV s^{-1}. This electrochemical preconditioning was followed by the acquisition of 20 cyclic voltammograms from 0.025 to 0.55 V vs. RHE at a voltage scan rate of 50 mV s^{-1}. This aims to evaluate the electrochemical active surface area (ECSA) of the Ir electrodes, and is repeated before/after any OER testing measurement. ECSA is estimated for the 20^{th} cycle by integrating the hydrogen desorption region from 0.06 V to the potential where the hydrogen desorption concludes. Next, OER activity is evaluated by the acquisition of 10 cyclic voltammograms from 1 to 1.6 V vs. RHE at a voltage scan rate of 10 mV s^{-1}. After the corresponding repetition of the ECSA measurements, Ir electrodes OER stability is monitored by a short term (2 hours) or long term (12 hours) chronopotentiometry experiment set to monitor the overpotential

required to sustain a constant OER geometric current density of +10 mA cm^{-2}. For long term stability experiments, a 1000 rpm stirring rate was employed. After all OER stability measurements, ECSA and OER activity measurements (the latter only for 3 cycles) were recorded to evaluate modifications in the Ir electrodes surface and electrocatalysis. *iR* compensation corrections on all voltammograms were accounted for by software-assisted subtraction (EC4 View, version 1.2.68.1) of the high-frequency EIS component of the Nyquist plot (-Z''= 0).

4.8. Physical Characterization

4.8.1 X-ray photoelectron spectroscopy (XPS)

XPS measurements were performed with the following instruments: Kratos Axis HSi (Mg Kα, 1253.6 eV achromatic radiation) for Ni-MoS_2 and TMD nanoarray samples and Kratos Axis SUPRA for sulfur-enriched MoS_x nanoclusters (EBRI, Aston University, Dr. Mark Isaacs and Mr. James Hunns); Thermo Scientific K-Alpha system (NEXUS, Newcastle University); Kratos AXIS ULTRA (NMRC, University of Nottingham, Dr. Emily Smith) for amorphous electrodeposited MoS_x samples; and Thermo Scientific Theta Probe (DTU, Dr. Kim Degn Jensen) for WS_{3-x} decorated Ir samples. Unless otherwise stated, all XPS spectrometers used a microfocused monochromatic aluminium X-ray source (Al Kα, 1486.6 eV, 12 kV), a charge neutralizer filament to prevent surface charging, and working pressures below 5×10^{-9} mbar. Three independent and non-overlapping XPS analysis positions were acquired, using spot sizes of 100 μm (Kratos HSi), 30 μm^2 (Kratos SUPRA), 400 × 800 μm (Thermo Scientific) and 0.5 mm^2 (Kratos ULTRA) on each sample. For low resolution survey spectra, 160 eV (Kratos HSi and SUPRA))/150 eV (Thermo Scientific)/80 eV (Kratos ULTRA)/100 eV (Thermo Scientific DTU) pass energies and 0.4 eV (Thermo Scientific)/0.5 eV (Kratos)/1 eV (Thermo Scientific

DTU) step sizes were employed (dwell time: 10 ms), whereas for high-resolution spectra pass energies and step sizes of 20 eV (Kratos HSi and SUPRA)/40 eV (Thermo Scientific)/20 eV (Kratos)/100 eV (Thermo Scientific DTU) and 0.1 eV were selected (dwell time: 100 ms). All high-resolution spectra were energy-corrected to the adventitious C 1s peak set to 284.6 eV, and processed using the CASA XPS software (version 2.3.18PR1.0).

For high resolution spectra peak deconvolution, Shirley backgrounds were selected and Gaussian-Lorentzian (30) and Doniach-Šunjić modified Gaussian-Lorentzian lineshapes were employed for Mo *3d*/Ni *2p*/S *2p* and W *4f*/Ir *4f*, respectively. Mo *3d* spectra were fitted by applying a 3:2 area ratio constraint and 3.1 eV separation on the $3d_{5/2:3/2}$ spin-orbit doublets, whereas S 2p spectra were fitted by applying a 2:1 area ratio constraint and 1.2 eV separation on the $2p_{3/2:1/2}$ spin-orbit doublets.[10–12] W *4f* and Ir *4f* spectra were deconvoluted by applying a 2.17 eV and 3.0 eV $4f_{7/2:5/2}$ spin-orbit doublet separation, respectively, and a 4:3 area ratio constraint.[13]

4.8.2 Raman spectroscopy

Raman spectroscopy measurements were conducted on a Renishaw inVia Raman microscope (Renishaw, UK) using a 532 nm laser (65 mW power) and an interchangeable 50 cm^{-1} low pass filter (Renishaw, UK) previously calibrated by the 520 cm^{-1} peak found in a Si wafer standard. Low resolution survey spectra were recorded in the 100-2500 cm^{-1} and 100-1200 cm^{-1} wavelength ranges by three cumulative acquisitions of 10s. For high-resolution Raman spectra at the characteristic MoS_x vibrational frequencies (100-800 cm^{-1}), three cumulative acquisitions of 30 s were employed. In all cases, two non-overlapping regions were investigated per MoS_x thin film sample, using a 20x objective lens and 10% laser power. Higher magnification lenses at the selected laser power and exposure times lead to lased-induced amorphous MoS_x crystallization as reported by Nguyen et al.[14]

4.8.3 Field emission gun scanning electron microscopy (FEG-SEM)

FEG-SEM micrographs were acquired to determine the nanopillar height/base diameter (aspect ratio) and nanopillar base-to-base distance (interspacing) of the TMD nanoarrays, as well as the surface modification and roughening upon electrochemical sulfidation or degradation on TMD nanoarrays and WS_{3-x}-modified Ir electrodes, respectively. For TMD nanoarrays imaging, XL 30 SFEG (Phillips, the Netherlands) and JEOL 7100F FEG-SEM (JEOL Ltd., Japan) microscopes were utilized, in both cases using electron accelerating voltages of 5 kV and tilt angles from 45° to 85°. Micrographs were taken in conjunction with the technical staff, Dr. Nigel Neate and Mr. Martin Roe, at the NMRC (University of Nottingham). For WS_{3-x}-modified Ir electrodes imaging, a FEI Nova NanoSEM 600 microscope (Thermo Fisher Scientific, USA) was autonomously operated under electron accelerating voltages of 10 kV, spot sizes of 3.5 μm and beam currents of 0.16 mA at the Center for Electron Nanoscopy (DTU, Valby, Denmark).

4.8.4 Aberration-corrected high-angle annular dark-field scanning transmission electron microscopy (HAADF-STEM)

Amorphous carbon-coated TEM grids (Agar Scientific, 200 Cu mesh) coated with as-deposited, sulfur-enriched and Ni-incorporated (hybrid) MoS_x nanoclusters size distribution, morphology and crystallinity presented in this work was assessed by PhD candidate Yubiao Niu at the NPRL using a spherical aberration-corrected 200 kV JEOL 2100F STEM in the HAADF mode. Elemental composition of the aforementioned nanoclusters was evaluated by energy-dispersive X-ray spectroscopy (EDX).

References

[1] E.J.F. Dickinson, J.G. Limon-Petersen, N. V Rees, R.G. Compton, How Much Supporting Electrolyte Is Required to Make a Cyclic Voltammetry Experiment Quantitatively " Diffusional "? A Theoretical and Experimental Investigation, J. Phys. Chem. C. 113 (2009) 11157–11171.

[2] J. Bisquert, G. Garcia-Belmonte, F. Fabregat-Santiago, A. Compte, Anomalous transport effects in the impedance of porous film electrodes, Electrochem. Commun. 1 (1999) 429–435.

[3] J. Bisquert, G. Garcia-Belmonte, F. Fabregat-Santiago, N.S. Ferriols, P. Bogdanoff, E.C. Pereira, Doubling Exponent Models for the Analysis of Porous Film Electrodes by Impedance. Relaxation of TiO2 Nanoporous in Aqueous Solution, J. Phys. Chem. B. 104 (2000) 2287–2298. doi:10.1021/jp993148h.

[4] A.P. Murthy, J. Theerthagiri, J. Madhavan, K. Murugan, Highly active MoS2 /carbon electrocatalysts for the hydrogen evolution reaction – insight into the effect of the internal resistance and roughness factor on the Tafel slope, Phys. Chem. Chem. Phys. 19 (2017) 1988–1998. doi:10.1039/C6CP07416B.

[5] H. Vrubel, T. Moehl, M. Grätzel, X. Hu, Revealing and accelerating slow electron transport in amorphous molybdenum sulphide particles for hydrogen evolution reaction, Chem. Commun. 49 (2013) 8985. doi:10.1039/c3cc45416a.

[6] R.S. Nicholson, Theory and Application of Cyclic Voltammetry for Measurement of Electrode Reaction Kinetics, Anal. Chem. 37 (1965) 1351–1355. doi:10.1021/ac60230a016.

[7] R.J. Klinger, J.K. Kochi, Electron-Transfer Kinetics from Cyclic Voltammetry. Quantitative Description of Electrochemical Reversibility, J. Phys. Chem. 85 (1981) 1731–1741. doi:10.1021/j150612a028.

[8] S.J. Konopka, B. McDuffie, Diffusion coefficients of ferri- and ferrocyanide ions in aqueous media, using twin-electrode thin-layer electrochemistry, Anal. Chem. 42 (1970) 1741–1746. doi:10.1021/ac50160a042.

[9] A.J. Bard, L.R. Faulkner, Electrochemical Methods: Fundamentals and Applications, 2nd ed., John Wiley and Sons Ltd., New York, 2001. doi:10.1016/B978-0-12-381373-2.00056-9.

[10] H.W. Wang, P. Skeldon, G.E. Thompson, XPS studies of MoS2 formation from ammonium tetrathiomolybdate solutions, Surf. Coatings Technol. 91 (1997) 200–207. doi:10.1016/S0257-8972(96)03186-6.

[11] W. Grunert, A.Y. Stakheev, R. Feldhaus, K. Anders, E.S. Shpiro, K.M. Minachev, Analysis of Mo(3d) XPS Spectra of Supported Mo Catalysts: An Alternative Approach, J. Phys. Chem. 95 (1991) 1323–1328. doi:10.1021/j100156a054.

[12] G.C. Stevens, T. Edmonds, Electron spectroscopy for chemical analysis spectra of molybdenum sulfides, J. Catal. 37 (1975) 544–547. doi:10.1016/0021-9517(75)90190-6.

[13] V. Pfeifer, T.E. Jones, J.J. Velasco Vélez, C. Massué, R. Arrigo, D. Teschner, F. Girgsdies, M. Scherzer, M.T. Greiner, J. Allan, M. Hashagen, G. Weinberg, S. Piccinin, M. Hävecker, A. Knop-Gericke, R. Schlögl, The electronic structure of iridium and its oxides, Surf. Interface Anal. 48 (2016) 261–273. doi:10.1002/sia.5895.

[14] D.N. Nguyen, L.N. Nguyen, P.D. Nguyen, T.V. Thu, A.D. Nguyen, P.D. Tran, Crystallization of Amorphous Molybdenum Sulfide Induced by Electron or Laser Beam and Its Effect on H2-Evolving Activities, J. Phys. Chem. C. 120 (2016) 28789–28794. doi:10.1021/acs.jpcc.6b08817.

Chapter 5

Ni-MoS_2 hybrid nanoclusters

5.1 Introduction

As-prepared MoS_2 materials present several limitations in their hydrogen evolution reaction (HER) activity, most importantly the electroactive inertness of both basal planes and S-edge sites. Density functional theory (DFT) calculations predicted the activation of the latter by doping with transition metals (TMs) due to a decrease in the hydrogen adsorption free energy (ΔG_H) closer to thermo-neutral values, where the HER activity is optimal. For metals such as Fe, Co or Ni, experimental studies have observed a 3-fold HER enhancement as compared with the undoped MoS_2 counterparts.[1] However, reported TM-doping methodologies in the literature comprise multi-step, solvent-assisted procedures which are complex and in some cases prevent accurate nanoparticle size control.

This chapter devotes to the preparation of transition metal-doped molybdenum sulfide (MoS_2) nanoclusters. In particular, we evaluate the viability of using a one-step, solvent-free methodology by employing a dual-target, magnetron-sputtering and gas condensation deposition technique in collaboration with Teer Coatings Ltd. Physical and electrochemical experiments aim to evaluate the viability of the physical deposition strategy proposed, as well as the synergistic effect between the transition metal used as a dopant (in this work Ni) and the MoS_2 material in the electrochemical production of hydrogen in acidic media.

5.2 Results and discussion

5.2.1 Physical characterization of Ni, MoS_2 and Ni-MoS_2 hybrid nanoclusters: HAADF-STEM imaging

Pristine MoS_2 and Ni nanoclusters, along with Ni-MoS_2 hybrid nanoclusters were prepared with the custom-built dual-target magnetron sputtering and gas condensation cluster source at Teer Coatings Ltd. (for cluster source schematic and deposition parameters, see Section 4.3.1 Materials and methods).

The proprietary time-of-flight mass filter coupled to the cluster source enabled real-time monitoring of the mass of nanoclusters before their deposition onto the selected substrates (in this work mirror-finished glassy carbon electrodes). By modification of the sputtering power, nanoclusters of selected size distributions were deposited. Figure 5.1 shows the mass spectra obtained for the samples deposited to be employed in the HER measurements. During the preparation of pure MoS_2 samples, a sputtering power of 8W was applied to the MoS_2 target and a peak mass of 4.8 x 10^4 amu, equivalent to $(MoS_2)_{300}$, was found in the mass spectra (300 being the number of MoS_2 units contained in one MoS_2 nanocluster) . The pure Ni sample was prepared similarly, and a resulting Ni peak mass of 1.3 x 10^5 amu, equivalent to $\sim Ni_{2200}$, was found (2200 being the number of Ni atoms in one Ni nanocluster). When the sputtering power for the Ni target was changed from 4W to 8W, the peak mass shifted from 6 x 10^4 amu to 1.3 x 10^5 amu, and the peak beam current shifted from 11 pA to 90 pA. Thus, higher sputtering power on the Ni target generates more numerous, and larger, Ni nanoclusters. Consequently, a lower sputtering power of only 3W on the Ni target was used in the preparation of the hybrid Ni-MoS_2 nanoclusters in order to avoid an excess of Ni nanoclusters, while 8W of sputtering power was used on the MoS_2 target. The peak mass of the hybrid Ni-MoS_2 nanoclusters was located at 1.6 x 10^5 amu, equivalent to a mass of $(MoS_2)_{1000}$ (1000 equivalent MoS_2 units per

Ni-MoS_2 nanocluster) or Ni_{2712} (2712 equivalent Ni atoms per Ni-MoS_2 nanocluster). In the following sections of this chapter we will refer to the Ni, MoS_2 and hybrid Ni-MoS_2 nanoclusters as Ni_{2200}, $(MoS_2)_{300}$ and $(Ni\text{-}MoS_2)_{1000}$, respectively, for convenience.

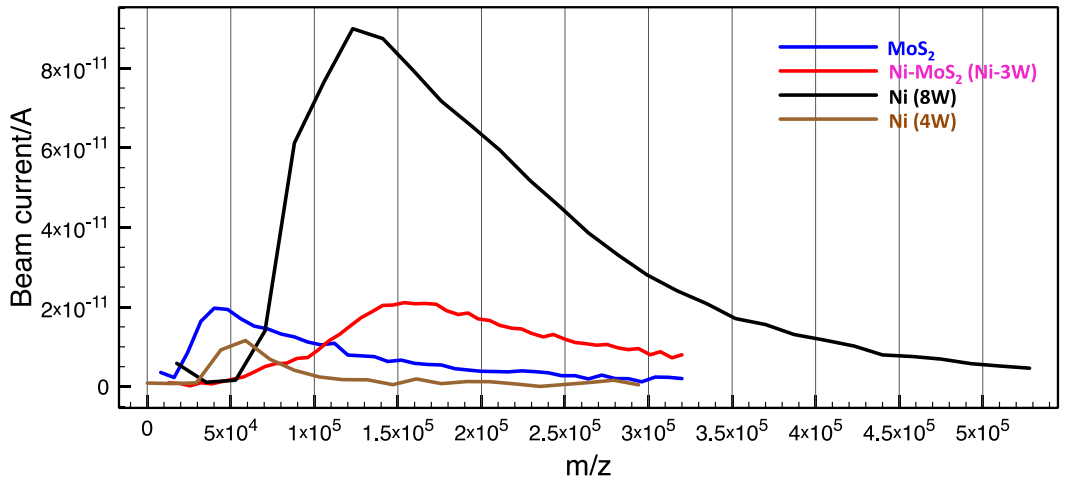

Figure 5.1. Compilation of mass spectra obtained by the time-of-flight mass filter during nanocluster deposition. From the spectra, MoS_2, Ni (8W) and Ni-MoS_2 (3W) show peak masses of around 4.8 x 10^4 amu ($(MoS_2)_{300}$), 1.3 x 10^5 amu (~Ni_{2200}) and 1.6 x 10^5 amu $\{(MoS_2)_{1000}\}$, respectively. The mass spectra of Ni (4W) is also plotted to show the effect of the power applied to this target.

The STEM images in Figure 5.2 show (top to bottom) the morphologies of MoS_2 nanoclusters, Ni-MoS_2 hybrid nanoclusters and Ni nanoclusters. An HAADF-STEM image is a Z_{atom}-contrast image, whereby the image intensity depends on the atomic number of elements,[2] and in practice the images are dominated by Mo atoms: its Z_{atom} is 1.63 and ca. 3 times higher than that of Ni and S, respectively. HAADF-STEM image intensities, at a given atomic column, were also shown to be proportional to the number of atoms contained in each column,[3,4] consequently providing thickness contrast: in our case the number of MoS_2 layers. The HAADF-STEM intensity line profile analysis across one MoS_2 nanocluster, shown in Figure 5.3, indicates an incomplete multi-layer structure equivalent to 3-4 layers based on the

theoretical interspacing for bulk MoS_2 (0.65 nm). This assumption, given that the amorphous nature of the MoS_2-based nanoclusters could yield non-stacked layers, is reasonable given the clear observation of layers on side-on deposited MoS_2 nanoclusters, with layer interspacings of 0.67 nm (Figure 5.3c). Thus, we can conclude that MoS2 nanoclusters present a layered stacking with amorphous structure within layers. Ni-MoS_2 nanoclusters present a broadly similar non-crystalline morphology to that of the pure MoS_2 nanoclusters, while Ni nanoclusters show a quite distinct crystalline structure. Fast Fourier Transform (FFT) analysis of STEM images in Figure 5.2 and 5.3 (STEM image intensity modulus as a function of the spatial frequency, providing information of the lattice fringe symmetry of a given material equivalent to that obtained by selected area electron diffraction) and comparison with the crystalline lattice parameters of MoS_2 polymorphs 1T and 2H show that no clear extended crystalline structure could be found on either MoS_2 or Ni-MoS_2 nanoclusters: their diffuse ring FFT pattern contrasts with that observed for Ni nanoclusters, which presents a well-defined set of diffraction spots. This implies that Ni is atomically added to the MoS_2 nanoclusters when the hybrid Ni-MoS_2 nanoclusters are formed, as aggregation of Ni islands onto MoS_2 nanoclusters would result in clear and localized crystalline regions onto an overall MoS_2 amorphous matrix matching those of pristine Ni. Insight on the local crystalline structure on both MoS_2 and hybrid Ni-MoS_2 nanoclusters could be evaluated by local FFT pattern analysis or alternative techniques such as STM or AFM, beyond the scope of this research due to their complexity. Based on the projected surface areas of tens of nanoclusters of each kind (i.e. the nanoclusters software-calculated, brightness contrast-based cross section at the TEM grid plane), the average diameter distributions are shown in Figure 5.2. The peak values in the distributions for MoS_2 nanoclusters, Ni-MoS_2 nanoclusters and Ni nanoclusters are 2.6 nm, 5.0 nm, and 4.2 nm respectively.

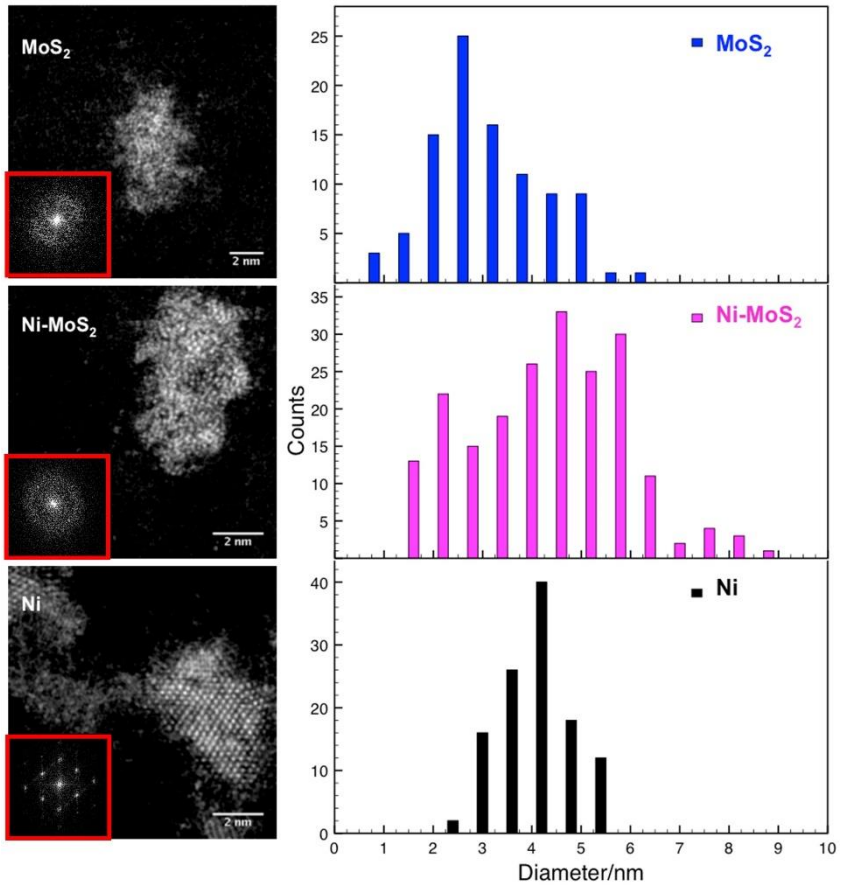

Figure 5.2. STEM images and size distribution in diameter based on the nanocluster surface area obtained by individual nanocluster counting at a given STEM image. MoS_2, Ni-MoS_2, and Ni (8W) have a peak value of 2.6 nm, 5.0 nm, and 4.2 nm respectively. Insets of STEM images are the FFT patterns of the corresponding clusters.

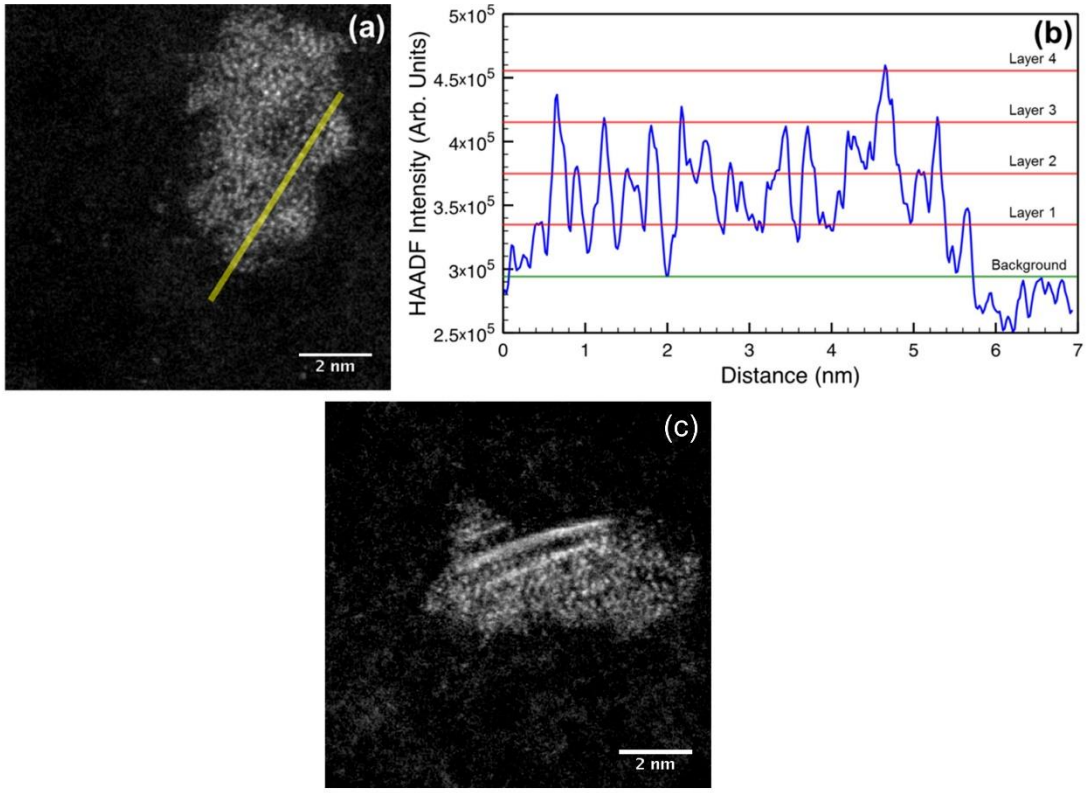

Figure 5.3. a) STEM image of hybrid Ni-MoS_2 hybrid nanocluster and b) example HAADF intensity line profile corresponding to the yellow region in a). The line profile shows step changes in nanocluster height, where layer numbers (0.65 nm theoretical interspacing) are labelled as a guide. c) STEM image of a side-on (perpendicularly oriented) MoS_2 nanocluster showing a layered structure.

In order to confirm the existence of Ni in the hybrid Ni-MoS_2 nanoclusters, EDX analysis was conducted, and the result is shown in Figure 5.4. Mo, S, and Ni signals are found in the same clusters, which indicate Ni-MoS_2 hybrid nanoclusters were made successfully. The characteristic energy difference between the Mo L-edge and S L-edge is only 14 eV, which is smaller than the energy resolution of the EDX instrument (133 eV). Other characteristic Mo X-ray emission lines which would enable independent detection of Mo and S, such as the $K_{\alpha 1}$ (17.48 keV), cannot be used as the EDX detector employed can only detect X-ray emissions in the 1keV-10 keV range. Consequently, Mo and S signals cannot be distinguished by EDX, and

the cyan dots in Figure 5.4b are due to the signal overlap of Mo and S. Ni signals are found both in MoS_2 areas and between them, which means Ni might locate on or between MoS_2 nanoclusters. Figures 5.4c to 5.4e display the individual elemental maps. Nanocluster shape mismatch between HAADF-STEM image shown in Figure 5.4a and Figures 5.4b to 5.4e is ascribed to STEM image drift during EDX measurement and related to a mechanical drift of the STEM piezoelectric stage. Compared with the large nanoclusters, the small nanocluster located at the bottom of each image is much less abundant in Ni, which is found primarily at MoS_2 edge sites and between nanoclusters. Besides the signals found in the nanoclusters (marked by the yellow shapes), signals can be found outside the nanoclusters; these signals may come from small clusters originating from the deposition process or electron beam sputtering of the deposited nanoclusters. Since Mo and S signals are overlapped with each other, the exact nanocluster compositions cannot be obtained from EDX analysis, which could be resolved by use of electron energy loss spectroscopy (EELS), but our STEM instrument does not present an EELS detector. To identify the composition of the hybrid Ni-MoS_2 nanoclusters, a method based on atom counting and STEM intensity measurement was employed (see section C Appendix). By this method, the compositions of six nanoclusters of varying size were calculated and are listed in Table 5.1.The outcome is that there is no fixed ratio of Ni atoms to MoS_2 units in the hybrid nanoclusters, but in general the proportion of Ni increases with nanocluster size, which agrees with the EDX results. This atom counting assumes that the dominant HAADF-STEM intensity is that of Mo across the MoS_2-based nanoclusters, which could be a source of error, but provides a reasonable estimation of the hybrid nanoclusters compositions.

Ni-MoS_2 cluster	Ratio of number of Ni atoms to number of MoS_2 units
$Ni_{22}(MoS_2)_{373}$	0.06
$Ni_{30}(MoS_2)_{378}$	0.08
$Ni_{720}(MoS_2)_{461}$	1.56
$Ni_{648}(MoS_2)_{844}$	0.77
$Ni_{1235}(MoS_2)_{1163}$	1.06
$Ni_{2181}(MoS_2)_{1458}$	1.5

Table 5.1. Composition analysis of six hybrid Ni-MoS_2 nanoclusters based on HAADF-STEM images.

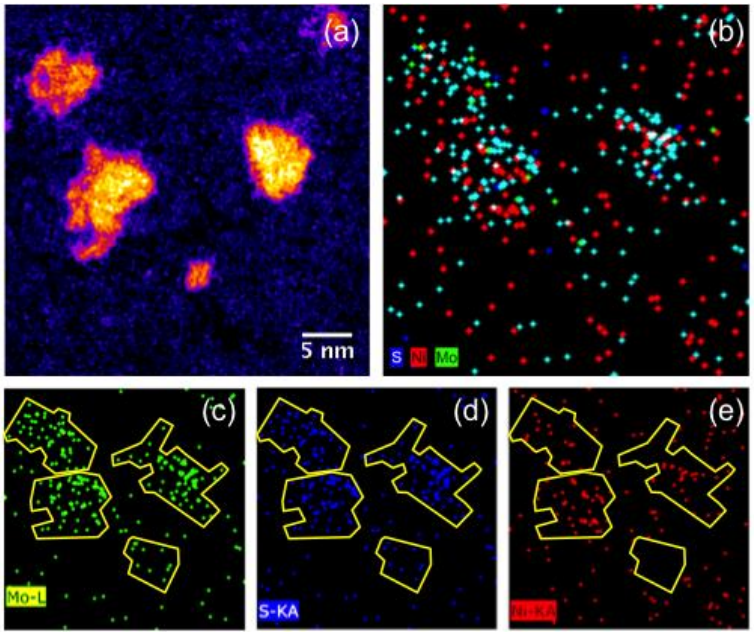

Figure 5.4. STEM image a) containing large and small nanoclusters used for EDX measurement. b) EDX mapping shows the composition of Ni-MoS_2 nanoclusters; Mo, S, and Ni are shown in green, blue, and red respectively. Signal in cyan comes from the overlap of Mo and S signals. Mo, S, and Ni signals are also shown separately in pannels c, d and e; where the nanocluster positions are marked by the yellow shapes.

5.2.2 Physical characterization of Ni, MoS_2 and Ni-MoS_2 hybrid nanoclusters: XPS

The chemical composition and oxidation state of the untested nanoclusters deposited on TEM grids analyzed by STEM imaging were further characterized by XPS. High-resolution spectra in the Mo 3*d* and S 2*p* region for fresh and 14 h air-exposed $(MoS_2)_{300}$ and $(Ni\text{-}MoS_2)_{1000}$ nanoclusters and are shown in Figure 5.5a and 5.5b. The fresh Mo 3*d* XPS spectrum can be deconvoluted into four components after the inclusion of the photoemission current characteristic of the carbon tape used to immobilize the TEM grids: one Mo $3d_{5/2}$ and Mo $3d_{3/2}$ spin-orbit doublet found at ~229.8 eV and ~232.9 eV with binding energies consistent with the binding energies found for the $(MoS_2)_{300}$ nanoclusters (Figure 5.5a) and characteristic of the Mo^{4+} oxidation state found in MoS_2 materials,[5] and an additional doublet at ~233.1 eV and ~236.2 eV related to the Mo^{6+} oxidation state found in MoO_3.[6] An upward shift of 0.2 eV and ~0.4 eV in the Mo^{4+} and Mo^{6+} components on $(Ni\text{-}MoS_2)_{1000}$ and $(MoS_2)_{300}$ nanoclusters, respectively, after air exposure as well as a photoemission intensity increase of the latter doublet indicate an oxidation state increase in both MoS_2 and Ni-MoS_2 nanoclusters. This is supported by analysis of the Mo^{4+}:Mo^{6+} XPS atomic photoemission percentages (at. %), which reveal a conversion of MoS_2 into MoO_3 from Ni-MoS_2 fresh samples (Mo^{4+}/Mo^{6+} 78.1/21.9 at. %) to air exposed (Mo^{4+}/Mo^{6+} 54.9/45.1 at. %). The fresh S 2*p* spectrum can be deconvoluted into two components at ~160.7 eV and ~161.9 eV corresponding to the spin-orbit S $2p_{3/2}$:$2p_{1/2}$ doublet characteristic of the S^{2-} oxidation state,[7] and observing that an additional broad signal at ~167 eV related to oxidized sulfur species such as sulfites or sulfates[8] is also found on $(MoS_2)_{300}$ nanoclusters (Figure 5.5a). Quantification of the Mo^{4+}:S^{2-} peak areas confirmed the S-deficient nature of $(MoS_2)_{300}$ nanoclusters (1:0.90±0.02), while $(Ni\text{-}MoS_2)_{1000}$ nanoclusters present a 1:1.8±0.1 ratio similar to the Mo:S ratio expected in MoS_2 (1:2). Such difference in

the oxidation behavior could be ascribed to the presence of surface Ni atoms prone to oxidation which would mitigate S^{2-} oxidation under ambient conditions. The lack of definition in the spin-orbit S $2p_{3/2}$:$2p_{1/2}$ doublet found here had been previously ascribed in amorphous MoS_3 materials to the presence of mixed S^{2-}/S_2^{2-} oxidation states,[9] but in our case it could be due either to the low photoemission counts due to low sample loading (~4 μg cm^{-2}) or to the inherent amorphous nature of the (Ni-)MoS_2 nanoclusters provided the S-deficiency of the samples. An alternative deconvolution of the high-resolution S $2p$ region including the possibility of mixed S^{2-}/S_2^{2-} oxidation states can be found in the appendix (Section D).

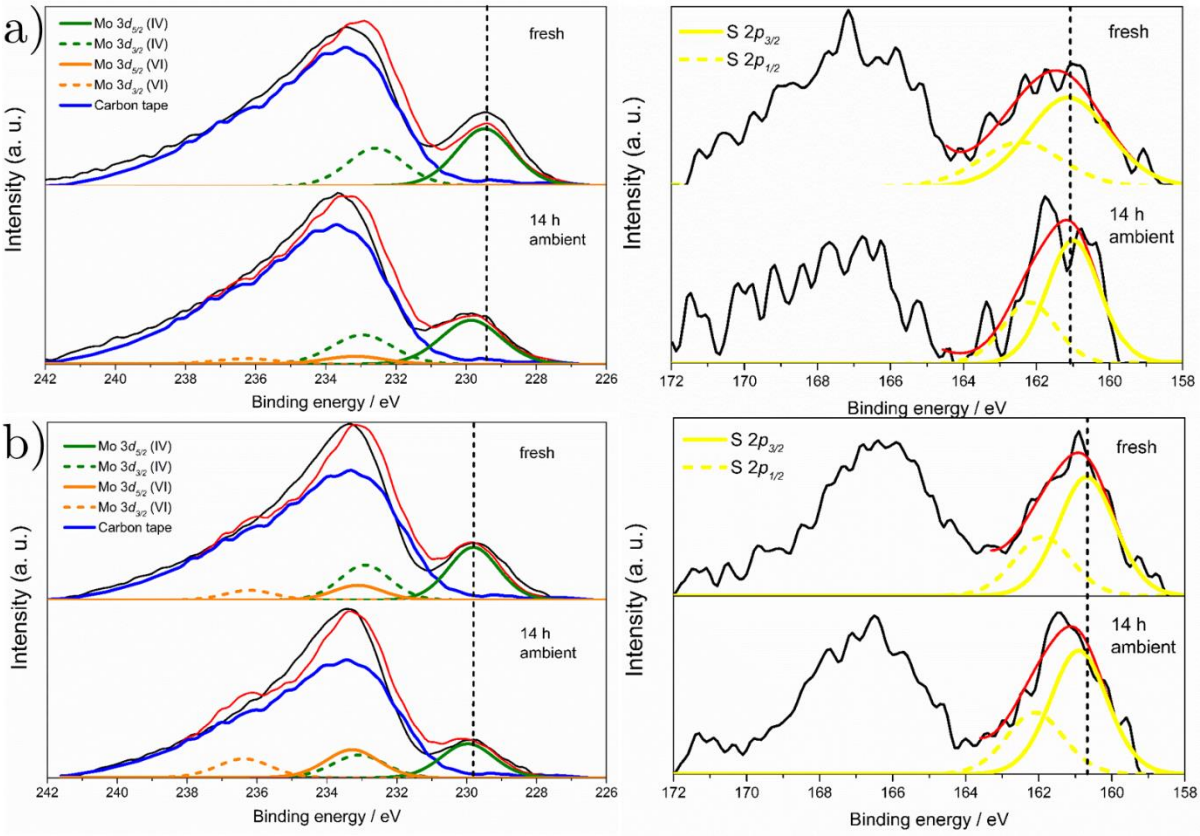

Figure 5.5. High-resolution XPS spectra of Mo $3d$ (left) and S $2p$ (right) for fresh (top) and 14 h air exposed (bottom) for a) $(MoS_2)_{300}$ nanoclusters and b) $(Ni\text{-}MoS_2)_{1000}$ nanoclusters. Labels: raw spectra (solid black), cumulative peak fit (solid red), Mo^{4+} $3d_{5/2}$ (solid green), Mo^{4+} $3d_{3/2}$ (dashed green), Mo^{6+} $3d_{5/2}$ (solid orange), Mo^{6+} $3d_{3/2}$ (dashed orange), S $2p_{3/2}$ (solid yellow) and S $2p_{1/2}$ (dashed yellow).

Analysis of the Ni 2*p* high-resolution spectra of both Ni and Ni-MoS_2 nanoclusters is paramount to evaluate the oxidation state of the Ni dopant atoms as well as to identify the presence of nickel species such as oxides and sulfides. Deconvolution of the Ni $2p_{3/2}$ component of the untested Ni nanoclusters (Figure 5.6, fitting parameters used from Biesinger et al.[10]) shows the predominance of oxidized species such as NiO and $Ni(OH)_2$, with Ni:NiO:$Ni(OH)_2$ relative composition percentages practically invariable after air exposure (12.4:36.2:51.4 fresh, 10.2:41.3:48.5 air exposed).

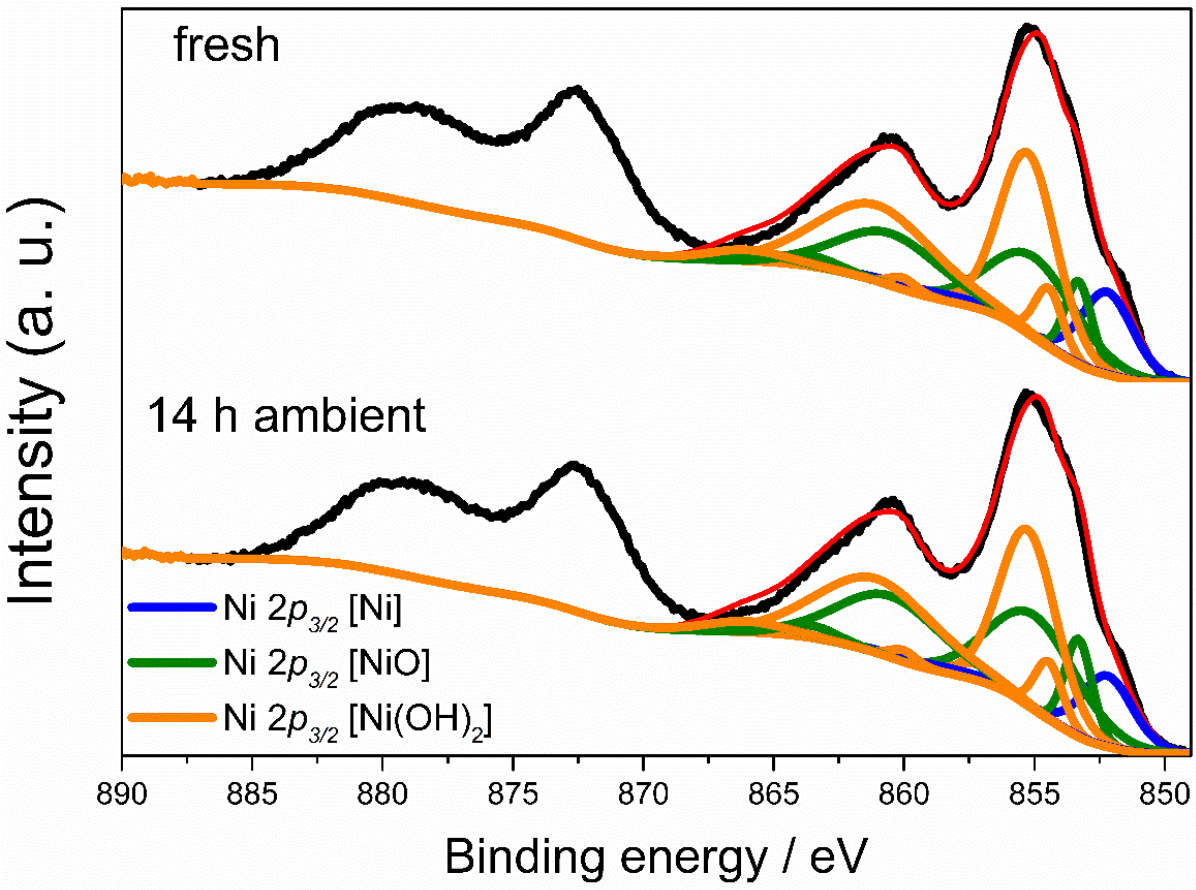

Figure 5.6. High-resolution XPS spectra of Ni 2*p* fresh (top) and 14 h air exposed (bottom) Ni nanoclusters. Labels: raw spectra (solid black), cumulative peak fit (solid red), Ni^0 $2p_{3/2}$ peak deconvolution (solid blue), Ni^{2+} (NiO) $2p_{3/2}$ peak deconvolution (solid green) and Ni^{2+} [$Ni(OH)_2$] $2p_{3/2}$ peak deconvolution (solid orange).

As for (Ni-MoS_2)$_{1000}$ nanoclusters (Figure 5.7), quantitative analysis of the Ni 2*p* region is not possible due to low signal-noise ratio ascribed to the low Ni content aimed during the hybrid nanocluster formation. The peak position of the Ni $2p_{3/2}$ component for the fresh (Ni-MoS_2)$_{1000}$ samples at ~852.8 eV and the lack of clearly defined satellite signals seem to suggest predominance of metallic Ni (theoretical value: 852.7±0.4 eV),[10] but air exposure leads to an upward shift of the Ni $2p_{3/2}$ component to ~854eV, similar to the 854.6 eV characteristic of the NiO principal XPS peak[11] as well as in increase in the Ni $2p_{3/2}$ and Ni $2p_{1/2}$ satellite intensities (~861 and ~872.5 eV, respectively) . This would indicate that under air exposure the doping Ni atoms spontaneously increase their oxidation state to Ni^{2+} as found in NiO species, agreeing with the behavior observed for bare Ni nanoclusters. Presence of a nickel sulfide phase cannot be discarded from XPS results as it is well reported that directly bonded S atoms leave the Ni $2p_{3/2}$ peak position unaltered,[12] and the S $2p_{3/2}$:$2p_{1/2}$ doublet overlap commonly reported in nickel sulfides[13] is also found in the bare (MoS_2)$_{300}$ nanoclusters. However, the upward shift of the Ni $2p_{3/2}$ component to binding energies similar to those of NiO species after air exposure makes the presence of a nickel sulfide phase unlikely. Thus, the Ni oxidation state conversion observed after 14 h air exposure will have significant repercussions in the electrocatalytic performance of the Ni-MoS_2 hybrid nanoclusters.

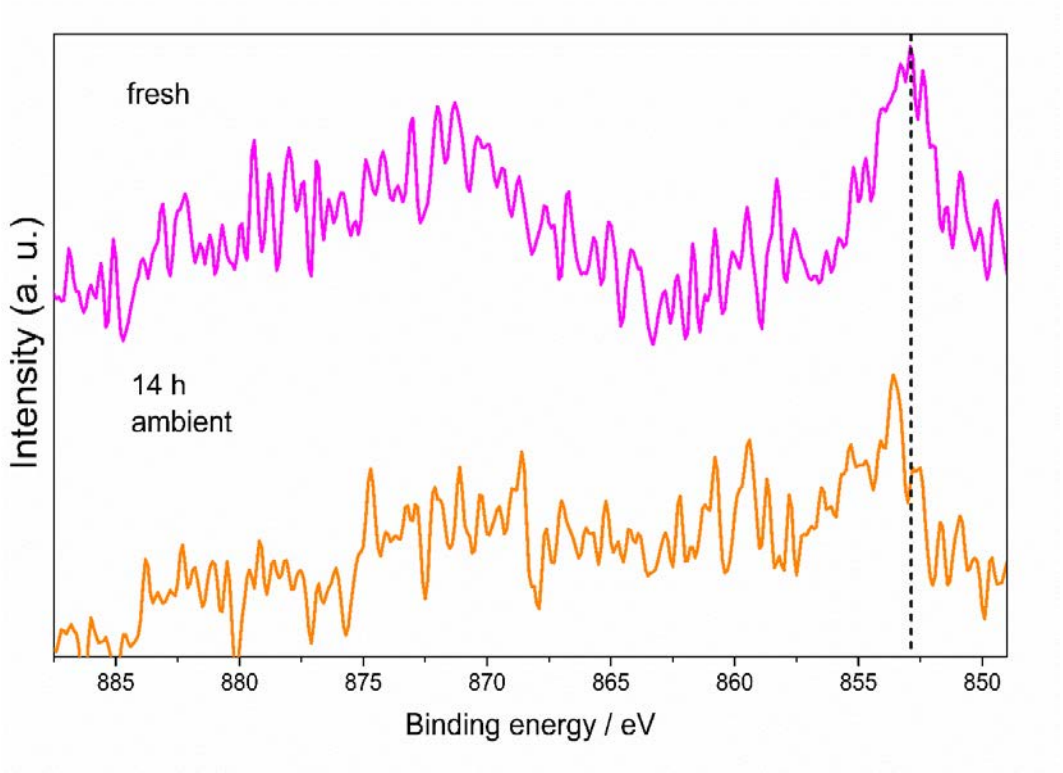

Figure 5.7. High-resolution XPS spectra of Ni 2*p* for fresh (top, solid magenta) and 14 h air exposed (bottom, solid orange) $(Ni\text{-}MoS_2)_{1000}$ nanoclusters. Dashed vertical line indicates peak position of metallic Ni (theoretical value: 852.7±0.4 eV).[10]

5.2.3 Electrocatalytic activity to the hydrogen evolution reaction: influence of Ni incorporation

Figure 5.8 shows the linear sweep voltammograms acquired in the 0 to -1.2 V range (normalized vs. RHE) at a scan rate of 25mV s^{-1} in 2mM $HClO_4$/0.1M $NaClO_4$ aqueous electrolyte for all samples tested. A diffusion decay peak profile is observed in all samples due to the low proton concentration present in the electrolyte ($[H^+] \approx 2 \times 10^{-6}\ mol\ cm^{-3}$), purposefully chosen to perform a better elucidation of the samples' kinetic parameters and surface coverage.

Freshly prepared $(MoS_2)_{300}$ nanoclusters (Fig. 8a) exhibit an onset potential of ca. 650 mV, reaching a peak half maximum current density ($|j_{half\ max}|$) of 0.31 mA cm^{-2} at an overpotential (η) of ca. 770 mV. The experimental onset potential is approx. 400 mV higher than that of 2H-MoS_2 nanosheets reported in the literature (ca. 200 mV vs RHE):[14–16] this originates from the MoS_2 preparation methodology and hence the degree of sulfur enrichment.

The main factors that hinder HER activity in MoS_2 materials are their intrinsic conductivity, chalcogen-to-metal ratio, edge site abundance and catalyst loading. Previous investigations from our research group demonstrated that magnetron-sputtered MoS_2 size-selected nanoclusters presented a 2-layer thickness in the 150-500 unit range.[17] This issue has again been observed in this investigation, where $(MoS_2)_{300}$ nanoclusters exhibit an incomplete multilayered structure ranging from 1 to 4 layers (Figure 5.3). As through-plane electron mobility in MoS_2 is 2200 times slower than in-plane,[18] the absence of single-layered clusters hampers the electrocatalytic activity. XPS analysis performed in this study have revealed that both $(MoS_2)_{300}$ and $(Ni\text{-}MoS_2)_{1000}$ nanoclusters are S-deficient. A high correlation between chalcogen-to-metal ratio and HER activity has been extensively reported. Eng et al. observed a substantial increase in both HER overpotential and Tafel slope in chalcogen deficient TMDs,[19] that can be ascribed in the case of MoS_2 to a deficiency of active sites and the formation of oxide species MoO_2/MoO_3 at the S-deficient sites unstable to cathodic potentials in acidic media,[20] experimentally confirmed by XPS measurements reported here.

Sulfur-rich MoS_2 nanostructures with enhanced HER activities and stability in acidic environment have been prepared by use of gas phase[21] or liquid phase[22] methods. However, evidence has shown that the morphology of MoS_2 is modified by the exposure and composition of the sulfur gas phase[23,24] or liquid phase.[22] Additionally, this would increase the potential formation of the HER-active nickel sulfide. Thus, ex-situ sulfidation treatments were not performed to guarantee that the HER enhancement in the samples is unambiguously due to the Ni-doping of the edge sites. In addition to this, reports by Vrubel et al. and Rowley-Neil

et al. revealed that the HER activity of the molybdenum sulfide catalysts is correlated with the catalyst loading: higher molybdenum sulfide catalyst loading lead to enhanced HER performance.[25,26] Thus, the HER performance of our nanoclusters cannot be unambiguously judged by the current density values obtained at the same overpotentials as those reported by the literature. Assuming a cluster interspacing of 2.5 nm, the mass loadings for Ni_{2200}, $(MoS_2)_{300}$ and $(Ni\text{-}MoS_2)_{1000}$ are 1.28 μg cm^{-2}, 3.45 μg cm^{-2} and 4.25 μg cm^{-2}, respectively. These values are at least one order of magnitude smaller than those reported in more competitive MoS_2 materials,[21,27] supporting our claims that the low catalyst loadings lead to overpotentials higher than those reported in the literature.

Electrochemical testing of the $(MoS_2)_{300}$ nanoclusters after the aforementioned testing and exposure to air for 14 hours indicates an enhancement in their electrocatalytic performance to the HER, with a $|j_{half\ max}|$ of ca. 0.40 mA cm^{-2} at $\eta \approx 749$ mV. This is due to the dissolution of the $(MoS_2)_{300}$ nanoclusters outermost layers due to the conversion of MoS_2 to MoO_3, compound soluble in acidic conditions. Yu et al. observed that electrochemical cycling of bilayered MoS_2 nanoflakes assisted in the oxidation of Mo^{4+} to Mo^{6+} ascribed to air exposure, leading to the complete loss of the MoS_2 outermost layer after re-immersion in the acidic electrolyte used. The loss of such layer resulted in enhanced HER performance and Tafel slope, concluding that the loss of a full MoS_2 monolayer increases the HER activity by a factor of ~4.47.[28] As the $(MoS_2)_{300}$ nanoclusters have been shown to consist of an incomplete multilayered structure (1 to 4 MoS_2 layers thick), any loss of the outermost layers will consequently enhance the HER activity.

Analogous voltammograms were recorded for $(Ni\text{-}MoS_2)_{1000}$ hybrid nanoclusters (Figure 5.8b). It can be seen that $(Ni\text{-}MoS_2)_{1000}$ hybrid nanoclusters exhibit a significant improvement in the electrocatalytic activity with respect to the undoped counterparts: the onset potential is reduced by ca. 100 mV and the $|j_{half\ max}|$ (0.35 mA cm^{-2}) is reached at $\eta \approx 680$ mV (100 mV less than $(MoS_2)_{300}$ nanoclusters). To confirm that the HER enhancement is due to the effective

Ni-doping of the S-edge sites and not to the presence of HER-active Ni nanoclusters in the sample, the response of a GC sample modified with Ni nanoclusters (average atomic mass units= 2200, Figure 5.8c) was evaluated. Ni_{2200} nanoclusters exhibited an onset potential and $|j_{half\ max}|$ similar to $(MoS_2)_{300}$ nanoclusters (0.36 mA cm^{-2}, $\eta \approx 770$ mV) but with faster HER kinetics (as per Tafel analysis, *vide infra*). This is evidenced by the fact that Ni_{2200} nanoclusters achieve a peak current density ($|j_p|$) of 0.72 mA cm^{-2} at $\eta \approx 870$ mV whereas $(MoS_2)_{300}$ nanoclusters only a $|j_p|$ =0.63 mA cm^{-2} at $\eta \approx 905$ mV. Thus, we can satisfactorily conclude that the HER enhancement observed in $(Ni\text{-}MoS_2)_{1000}$ nanoclusters is due to the increase in active edge sites density upon Ni-doping of the initially inactive S-edge sites.

Combined analysis of exchange current density (j_0) and turnover frequency (TOF) values provides insight on the predicted HER enhancement by Ni-doping as well as an indication of the intrinsic activity per-site[29]. Freshly-prepared $(MoS_2)_{300}$ and $(Ni\text{-}MoS_2)_{1000}$ nanoclusters presented similar j_0 values ($\approx 8\times10^{-10}$ A cm^{-2}), but after the above electrochemical experiments and 14-h air exposure $(Ni\text{-}MoS_2)_{1000}$ hybrid nanoclusters (Figure 5.8e) showed an almost 3-fold increase with respect to their initial j_0 value (2.1×10^{-9} vs. 7.6×10^{-10}). This significant HER enhancement is in good agreement with previous reports that indicated a 3-fold increase in active sites but a worse per-site activity due to the overall less thermo-neutral ΔG_H values[1]. TOF values of the 14-h air exposed samples support these conclusions: $(Ni\text{-}MoS_2)_{1000}$ nanoclusters exhibit a lower TOF value (60.3 H_2 s^{-1}) than $(MoS_2)_{300}$ nanoclusters (67.1 H_2 s^{-1}) at equivalent overpotentials (calculation performed at $(MoS_2)_{300}$ overpotential at $|j_{half\ max}|$), indicating an inferior per-site activity of the doped MoS_2 nanoclusters despite the increase in the density of edge sites. If TOF is calculated for $(Ni\text{-}MoS_2)_{1000}$ nanoclusters at their $|j_{half\ max}|$ overpotential, we obtain a value of 30.9 H_2 s^{-1}. All results are summarised in Table F.1 Section F Appendix.

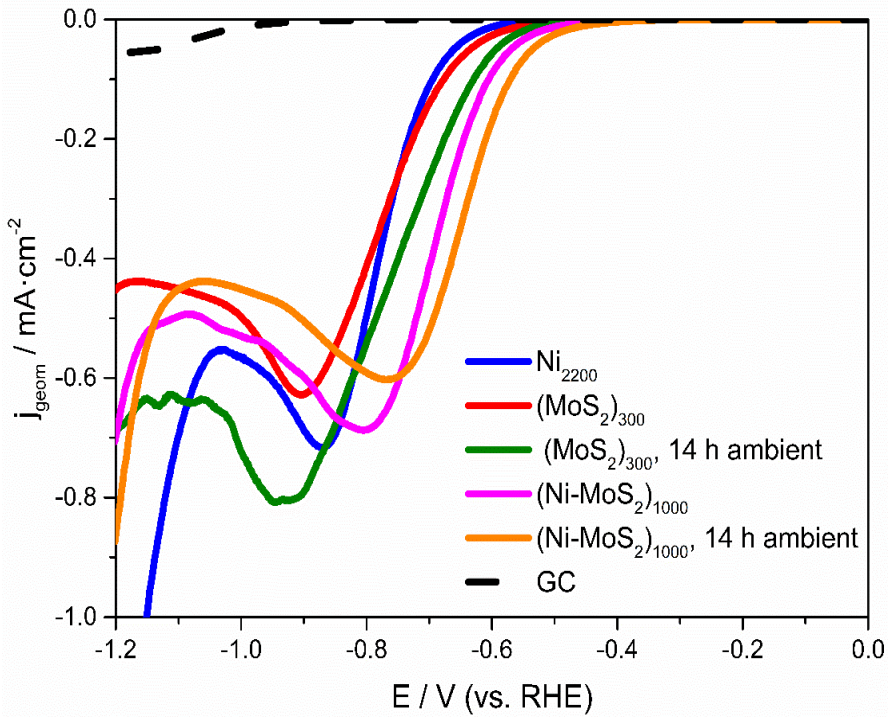

Figure 5.8. Linear sweep voltammograms recorded at 5 mm diameter glassy carbon (dashed black) samples modified with a) fresh $(MoS_2)_{300}$ (solid red), b) fresh $(Ni\text{-}MoS_2)_{1000}$ (solid magenta), c) Ni_{2200} (solid blue), d) 14-h air exposed $(MoS_2)_{300}$ (solid green), and e) 14-h air exposed $(Ni\text{-}MoS_2)_{1000}$ (solid orange) nanoclusters in the 0 to -1.2 V range vs. RHE. Scan rate: 25 mV s^{-1}.

Tafel slope analysis was then carried out to provide insight on the HER efficiency of the catalysts and on the HER reaction mechanism. Noble metals such as Pt follow the Volmer-Tafel mechanism, in which the rate determining step is the chemical hydrogen desorption from the catalyst surface, with Tafel slopes $b \approx 30$ mV dec^{-1}.[30] Tafel slope analysis of the 25mV s^{-1} cathodic scans (Figure 5.9) revealed that all the MoS_2 samples are in the 95-130 mV dec^{-1} range, $(MoS_2)_{300}$ exhibiting the lowest Tafel slope (94 mV dec^{-1}) after exposure to air for 14 hours. This compares to exfoliated MoS_2 layers reported to display Tafel slopes, $b \approx 120$ mV dec^{-1}, in agreement with the Volmer mechanism which dictates the monoatomic hydrogen

adsorption to be the limiting step.[31] Edge-rich nanosheets[32] and pure 1T-phase MoS_2[33] samples exhibited, respectively, $b \approx$ 55-60 mV dec^{-1} and b ≈ 40 mV dec^{-1}.

Electrodissolution of oxygen-rich HER inactive regions or electrochemical exfoliation of MoS_2 outermost layers, previously reported in the literature, might expose edge-abundant nanocluster regions with higher through-plane conductivity that could explain $(MoS_2)_{300}$ lower Tafel slope after air exposure.[28] Ni_{2200} samples present a Tafel slope of 106 mV dec^{-1}, similar to the $b \approx$ 120 mV dec^{-1} reported in the literature for electrodeposited Ni thin films.[34] When as-prepared Ni-doped/undoped MoS_2 nanoclusters are compared, Ni-doping does not decrease the Tafel slope value significantly, leaving the HER mechanism unchanged as reported previously.[1]

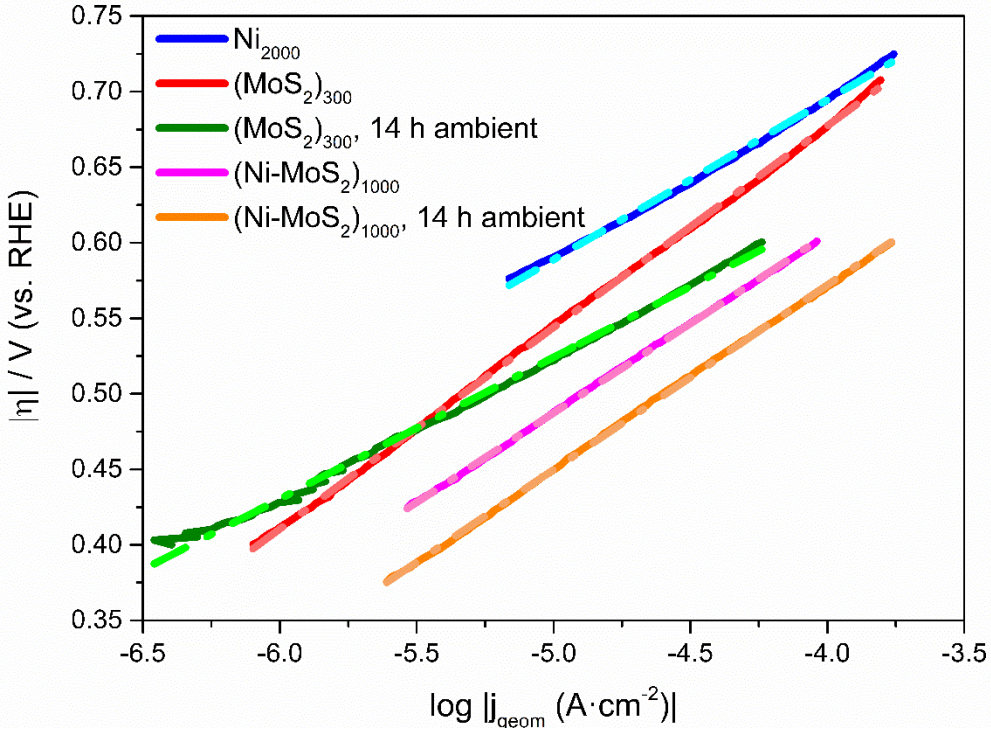

Figure 5.9. Tafel plots (η vs. $\log|j_{geom}|$) of the Ni-doped/undoped MoS_2 nanoclusters evaluated in figure 5.8. Scan rate: 25 mV s^{-1}.

The HER enhancement of $(Ni\text{-}MoS_2)_{1000}$ hybrid nanoclusters after 14 h air exposure is probably related to the Ni surface: reports suggest this could comprise a spontaneously formed

$NiO+Ni(OH)_2$ shell several atomic layers thick.[35] Oxygen present in the $NiO+Ni(OH)_2$ shell acts a proton-acceptor site, reported both theoretically and experimentally to catalyze HER.[36,37] The presence of NiO after 14 h air exposure of $(Ni\text{-}MoS_2)_{1000}$ hybrid nanoclusters has been confirmed by XPS measurements (see previous analysis), which is also expected to be found in the samples tested electrochemically. This effect would synergistically contribute to the HER enhancement already observed for 14 h air exposed $(MoS_2)_{300}$ related to dissolution of the MoS_2 outermost layers.

5.2.4 Electrochemical features of MoS_2 and Ni-MoS_2 hybrid nanoclusters: anodic stripping voltammetry (ASV)

ASV experiments were performed on the 14 h air-exposed samples to estimate numerically their TOF (for TOF calculation, see Section E.1 Appendix) and elucidate their electrochemical features. The choice of ASV for TOF estimation is based on the fundamentals of the technique and the nature of the nanoclusters. ASV, unlike other techniques reported in the literature for estimating TOF values (probe molecules adsorption, electrochemical capacitance measurement), allows to discriminate the contribution of the HER inactive basal sites and the HER active edge sites according to their electrochemical stability (anodic peak potential), avoiding active surface area overestimation that would lead to undervalued turnover frequencies. In addition to this, electrochemical features originated by the Ni atoms/clusters allocated in inactive sites can be effectively deconvoluted and withdrawn from the Ni-doped active sites response to enable a rigorous analysis. This analysis does not necessarily guarantee that all the sites electrochemically oxidised are available to the electrolyte due to geometric constraints, but it provides a reasonable estimation of the active sites present in the sample.

Figure 5.10a shows the anodic voltammograms obtained for $(MoS_2)_{300}$ nanocluster-modified GC electrode. The two oxidation peaks at ca. 0.72 V and 0.92 V vs. RHE these peaks correspond to the selective oxidation of the MoS_2 edge plane sites (Mo- edges) and basal plane sites respectively,[15] by the irreversible oxidation of Mo metal centres from oxidation state +4 to +6.[31] The metastable edge sites require lower overpotentials to drive their oxidation, whereas the thermodynamically favoured basal plane sites necessitate higher overpotentials for their electrochemical oxidation.[38]

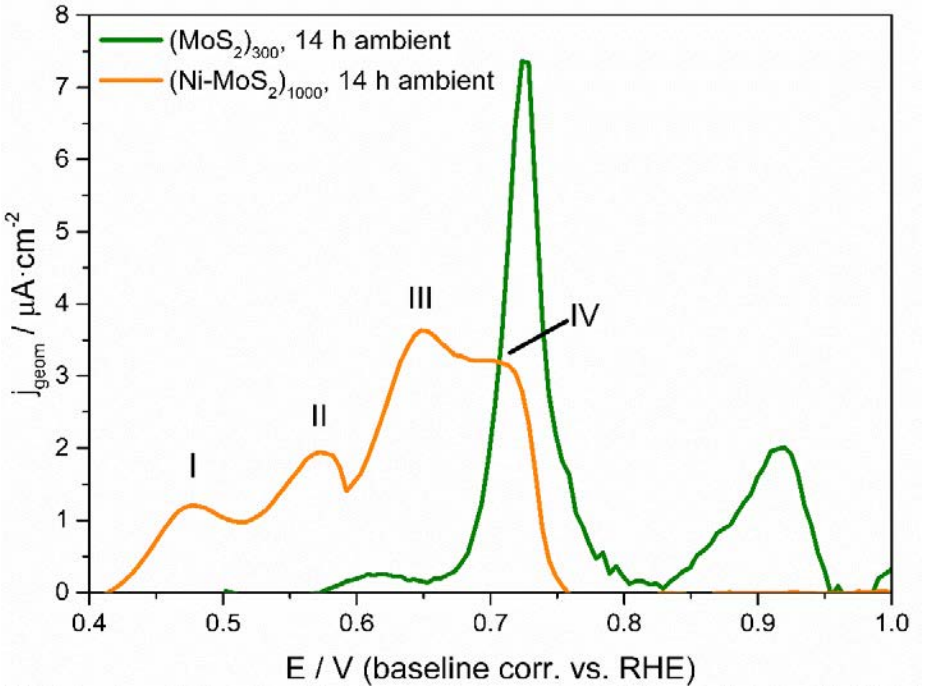

Figure 5.10. Anodic stripping voltammograms of 14-h air exposed a) $(MoS_2)_{300}$ nanoclusters (solid green) and b) $(Ni\text{-}MoS_2)_{1000}$ hybrid nanoclusters (solid orange) deposited on a 5 mm glassy carbon stub in the 0.4 to 1 V range vs. RHE. Scan rate: 50 mV s^{-1}.

Next, analogous experiments were conducted on the $(Ni\text{-}MoS_2)_{1000}$ hybrid nanoclusters-modified GC electrode, with the results given in Figure 5.10b. In contrast to the undoped MoS_2 nanoclusters, the ASV presents a broad signal in the 0.4 to 0.8 V region on the first anodic sweep, that is no longer present in further scans. Deconvolution of the voltammetric profile

reveals that the signal consists of four oxidation peaks at ca. 0.48 V (peak I), 0.57 V (peak II), 0.65 V (peak III) and 0.72 V (peak IV), respectively. The peak IV potential is in agreement to the oxidation of undoped edge plane sites experimentally observed in $(MoS_2)_{300}$ nanoclusters.

The absence of any other electrochemical features from bare MoS_2 implies that the remaining anodic peaks are necessarily related to oxidation processes at either bare Ni or Ni-doped MoS_2 sites. Thus, insight on the electro-oxidation reaction mechanism of bare Ni electrodes in acidic electrolyte is required to allocate the unidentified electro-oxidative features to a specific redox process.

The electrochemical features of Ni oxidation in acidic media have been reported to be dependent on the electrolyte, pH and experimental conditions (hydrodynamic parameters, voltage range, etc)[39–42]. The general electro-oxidation mechanism can be summarised as follows[42],

$$[Ni]_k + H_2O \rightleftharpoons [Ni]_k(H_2O)_{ad} \rightleftharpoons [Ni]_{k-1}Ni(OH)_{ad} + H^+_{aq} + 1e^- \quad (5.1)$$

$$[Ni]_{k-1}Ni(OH)_{ad} \rightleftharpoons [Ni]_{k-1}Ni(OH^+)_{ad} + 1e^- \quad (5.2)$$

$$[Ni]_{k-1}Ni(OH^+)_{ad} \rightleftharpoons [Ni]_{k-1} + NiOH^+_{aq} + H^+_{aq} \rightleftharpoons [Ni]_k + H_2O + Ni^{2+} \quad (5.3)$$

$$[Ni]_{k-1}Ni(OH^+)_{ad} + H_2O \rightarrow [Ni]_{k-1} + Ni(OH)_2 + H^+_{aq} \quad (5.4)$$

$$[Ni]_{k-1}[Ni(OH)_2] \rightleftharpoons [Ni]_k + 2OH^- + Ni^{2+} \quad (5.5)$$

$$[Ni]_{k-1}[Ni(OH)_2] \rightleftharpoons [Ni]_{k-1}[NiO] + H_2O \quad (5.6)$$

where the application of sufficiently positive potentials drives the two-electron Ni electro-oxidation in the presence of adsorbed water molecules. Formation of Ni(OH) and $Ni(OH^+)$ intermediates in redox reactions 5.1 and 5.2 is followed by either electrodissolution (reaction 5.3) or the formation and further chemical dissolution of a $Ni(OH)_2$ anodic layer (reactions 5.4, 5.5) by protons provided from the acidic media.

Voltammetric investigations in sulfuric acid (pH≤3) revealed two oxidation peaks at ca. 0.2 V and ca. 0.3-0.5 V vs. RHE, followed by a passivation current extending from 0.7 V vs. RHE upwards[43]. The first peak was reported to be the result of the competition between nickel electrodissolution and $Ni(OH)_2$ anodic layer formation, the former having the largest contribution, whereas the second peak was attributed to the $Ni(OH)_2$ layer growth depicted in 5.4[40,44]. The dissolution of this nickel hydroxide layer by 5.5 is interrupted by the reduction of $Ni(OH)_2$ phase water content at more positive potentials that yields a Ni_xO_y-based passive film (5.6).

In light of these reports, we ascribe peak I to the formation of the $Ni(OH)_2$ anodic layer originated from Ni nanoclusters/atoms not located at MoS_2 active edge sites (i.e. in MoS_2 basal planes or in direct contact with the GC electrode). Coverage of the basal plane sites by Ni atoms/aggregates is suspected to mask the inherent electrochemical activity of the MoS_2 basal planes, of which their electro-oxidative activity is absent in the $(Ni\text{-}MoS_2)_{1000}$ ASV. Further analysis of the integrated charge density $\langle\sigma_q\rangle$ of the ASV peaks supports this claim, as the $\langle\sigma_q\rangle$ value for peak I observed in the $(Ni\text{-}MoS_2)_{1000}$ hybrid nanoclusters ASV (approx. 9.7 μC cm^{-2}) is almost equivalent to that observed for the $(MoS_2)_{300}$ nanoclusters basal plane ASV ($\langle\sigma_q\rangle$ approx. 14.4 μC cm^{-2}), indicating an almost entire coverage of the MoS_2 basal plane sites by Ni.

Ni doping, according to recent DFT calculations of ΔG_H values in MoS_2 nanoclusters[1] and experimental reports, could effectively dope both the already-active Mo-edge sites and the initially inactive S-edge sites.[45,46] This results in two active sites per two MoS_2 units at the S-edge and one active site per two MoS_2 units at the Mo-edge with a theoretical Mo-edge:S-edge abundance ratio of 1:2. Activation of the thermodynamically favoured basal planes would have significant implications in the enhancement of the electrocatalytic activity of TMDs, as

all their surface would be active to the HER. Recent reports have successfully achieved the activation of the basal planes by incorporation of platinum in the in-plane structure[47] or the formation of strained sulfur vacancies in 2H-MoS_2.[48] However, the possibility of Ni doping of the basal planes, although briefly mentioned by Wang et al. as one of the main challenges in transition metal doping,[1] was not considered in this study as no theoretical or experimental reports provide evidence of MoS_2 basal planes activation after incorporation of Ni above the basal planes surface.

Assuming a correlation between the Mo-edge:S-edge natural abundance and electro-oxidative activity ratios we should expect, if the Ni-doped sites have distinctive electro-oxidative features with respect to pristine active sites, that unidentified peaks II and III satisfy a 1:2 anodic peak ratio. Peak deconvolution of the anodic stripping voltammogram, upon application of a 1:2 peak II:peak III area ratio constraint, provides a satisfactory fit with $R^2 \approx 0.990$ (Figure 5.11). We therefore conclude that peaks II and III correspond to the electro-oxidation of doped Mo-edge and S-edge sites, respectively. To the best of our knowledge, this is the first time that site-dependent electrochemical features have been observed on TM-doped MoS_2 materials.
The large difference in the undoped edge plane sites peak intensity between the $(MoS_2)_{300}$ and the $(Ni\text{-}MoS_2)_{1000}$ hybrid nanoclusters can be understood by analysis of the integrated charge density of the electro-oxidative peaks found in the ASV. We would expect that, due to the fact that Ni doping does not occur selectively on the edge sites, some Mo-edge sites remain undoped. As a consequence, the sum of the ASV response of the Ni doped and Ni undoped Mo-edge sites in $(Ni\text{-}MoS_2)_{1000}$ nanoclusters should be (assuming equivalent catalyst loading and surface coverage) equivalent to the ASV response of the undoped Mo-edge sites present in $(MoS_2)_{300}$ nanoclusters.

The integrated charge density of the ASV peak at 0.72 V vs. RHE observed in $(MoS_2)_{300}$ ascribed to the Mo-edge sites ($\langle \sigma_q \rangle$ approx. 32.7 μC cm^{-2}) is approximately equivalent to the

sum of the integrated charge densities of the ASV peaks II and IV in $(Ni\text{-}MoS_2)_{1000}$ nanoclusters, ascribed to the Ni-doped and Ni-undoped Mo-edge sites respectively (Ni-doped Mo-edge sites peak II: $\langle\sigma_q\rangle$ approx. 13.4 μC cm^{-2}, undoped Mo-edge sites peak IV: $\langle\sigma_q\rangle$ approx. 14.3 μC cm^{-2}, total charge density originated by Mo-edge sites: $\langle\sigma_q\rangle$ approx. 27.7 μC cm^{-2}). Differences observed are correlated with variations in the nanoclusters loading as well as peak integration.

Peak III in $(Ni\text{-}MoS_2)_{1000}$ nanoclusters, ascribed in this manuscript as the electro-oxidative feature of the Ni-doped S-edge sites, was initially electrocatalytically inert and thus contributed to the ASV basal plane peak acquired for the $(MoS_2)_{300}$ nanoclusters.

The possibility of one of the peaks being due to the oxidation of a nickel sulfide species formed by interaction of Ni and MoS_2 nanoclusters can be easily discarded by the peak positions: this process occurs at potentials ca. -0.05 V, out of our electrochemical window.[49]

This peak identification also provides some insight on the thermodynamic stability of Ni-doped Mo-edge and S-edge sites. Analogous to non-doped MoS_2 nanoclusters, the lower oxidation potential of peak II with respect to peak III would imply that the Ni-doped Mo-edge sites are more thermodynamically unstable than the Ni-doped S-edge sites. Kibsgaard et al. observed that M (M= Fe, Co, Ni, Cu) doped-MoS_2 nanoparticles prepared by physical vapour deposition exhibited, in terms of $(\bar{1}010)$ S-edge and $(10\bar{1}0)$ Mo-edge relative free energies, stabilized S-edge sites in MoS_2 with respect to Mo-edge sites, in agreement with the peak position order experimentally observed in the ASV.[50]

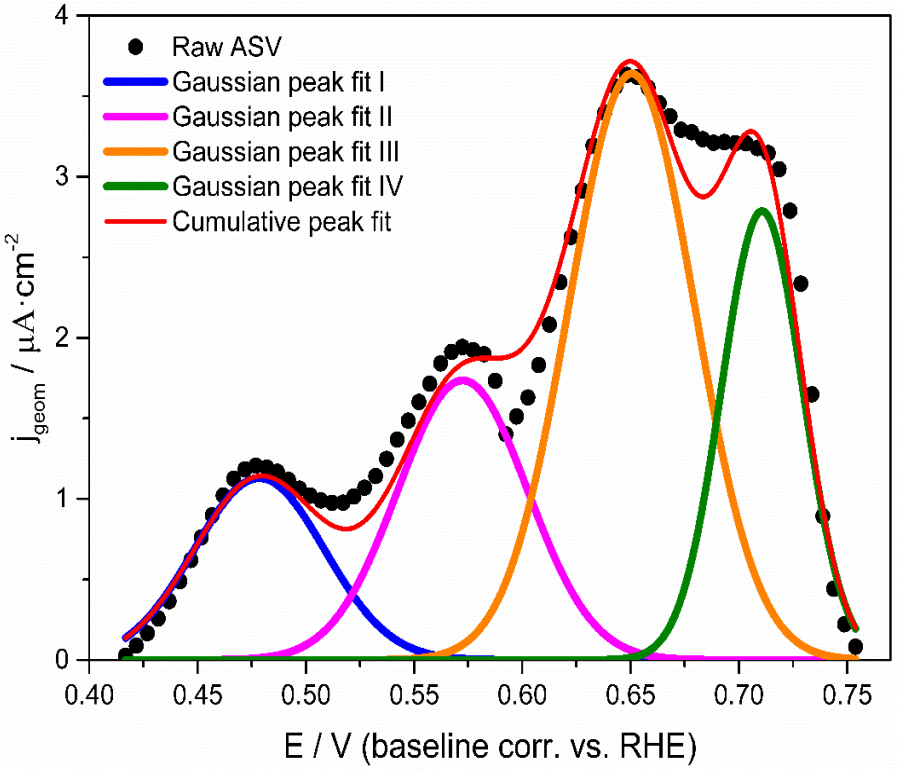

Figure 5.11. Peak deconvolution of the anodic stripping voltammogram (ASV) first scan of 14-h air exposed $(Ni\text{-}MoS_2)_{1000}$ hybrid nanoclusters deposited on a 5 mm glassy carbon stub in the 0.4 to 0.8 V range vs. RHE. Raw ASV (•) is deconvoluted in peaks I (solid blue), II (solid magenta), III (solid orange) and IV (solid green). Cumulative peak fit labelled in solid red.

As a final remark, we can now extract conclusions on the nature of the Ni incorporation onto MoS_2 nanoclusters. The magnetron sputtering technique employed here implicitly results in Ni non-selectively added onto the MoS_2 nanoclusters: this justifies the lack of a specific Ni to MoS_2 ratio within the Ni-MoS_2 nanoclusters across the size distributions obtained. Selective edge site decoration would imply a chemical interaction between Ni and the Mo (Mo-edge) or S (S-edge) sites, whereas Ni addition solely by physical interaction would yield distinguishable Ni and MoS_2 phases with no synergistic HER enhancement. In our case we believe we have a contribution of both, as the synergistic HER enhancement is still accompanied by the identification of the pristine Ni electrochemistry.

5.3 Conclusions

In this chapter we have evaluated a new methodology to obtain transition metal-doped MoS_2 nanoclusters. Indeed, the dual target magnetron sputtering and gas condensation deposition technique proposed allowed the successful deposition of Ni-MoS_2 hybrid nanoclusters in one step, obtaining a unimodal size distribution with an average cluster size of 1000 equivalent MoS_2 sub-units. Elemental mapping of the nanoclusters by EDX on the HAADF-STEM images demonstrated that the nanoclusters obtained by simultaneous sputtering of Ni and MoS_2 independent targets are a hybrid of both materials rather than their segregated components, with a Ni-MoS_2 ratio dependent on the nanocluster sizes due to the non-selective Ni incorporation onto MoS_2.

The activity of Ni-MoS_2 hybrid nanoclusters is on par with previous reports of electrocatalytic enhancement to HER after Ni doping: a significant shift in the onset potential (approx. 100 mV) followed by an almost 3-fold increase in exchange current densities as well as a practically unvaried Tafel slope ($\approx$ 120 mV dec^{-1}). This activity is only achieved when nanoclusters are exposed to atmospheric environment, suggesting that only when Ni dopant atoms/aggregates oxidise the Ni-doped edge sites become fully HER active, this supported by XPS measurements.

Anodic stripping voltammetry experiments revealed that HER active undoped and doped edge sites are electrochemically distinguishable according to their thermodynamic stability, following the order Ni-doped Mo-edge$<$ Ni-doped S-edge$<$ pristine Mo-edge. The successful electrochemical identification of S-edge doping and its subsequent correlation with the HER enhancement confirm the capability of dual target magnetron sputtering and gas condensation deposition technique for the preparation of TM-doped TMDs. Furthermore, anodic stripping voltammetry is identified as a powerful technique for probing TM-doped TMDs to tailor doping

parameters such as the degree of doping and the identification of the doped sites. The aforementioned results suggest that the origin of the Ni interaction with MoS_2 presents both chemical (dopant) and physical characteristics (unambiguous elucidation still pending), conforming to the non-selective doping nature of dual target magnetron sputtering.

References

[1] H. Wang, C. Tsai, D. Kong, K. Chan, F. Abild-Pedersen, J.K. Nørskov, Y. Cui, Transition-metal doped edge sites in vertically aligned MoS2 catalysts for enhanced hydrogen evolution, Nano Res. 8 (2015) 566–575. doi:10.1007/s12274-014-0677-7.

[2] Z.W. Wang, Z.Y. Li, S.J. Park, A. Abdela, D. Tang, R.E. Palmer, Quantitative Z-contrast imaging in the scanning transmission electron microscope with size-selected clusters, Phys. Rev. B - Condens. Matter Mater. Phys. 84 (2011) 2–4. doi:10.1103/PhysRevB.84.073408.

[3] Z.Y. Li, N.P. Young, M. Di Vece, S. Palomba, R.E. Palmer, a L. Bleloch, B.C. Curley, R.L. Johnston, J. Jiang, J. Yuan, Three-dimensional atomic-scale structure of size-selected gold nanoclusters., Nature. 451 (2008) 46–8. doi:10.1038/nature06470.

[4] D.S. He, Z.Y. Li, J. Yuan, Kinematic HAADF-STEM image simulation of small nanoparticles, Micron. 74 (2015) 47–53. doi:10.1016/j.micron.2015.04.005.

[5] N.M.D. Brown, N. Cui, A. Mckinley, An XPS study of the surface modification of natural MoS 2 following treatment in an RF-oxygen plasma, Appl. Surf. Sci. 134 (1998) 11–21.

[6] W. Grunert, A.Y. Stakheev, R. Feldhaus, K. Anders, E.S. Shpiro, K.M. Minachev, Analysis of Mo(3d) XPS Spectra of Supported Mo Catalysts: An Alternative Approach, J. Phys. Chem. 95 (1991) 1323–1328. doi:10.1021/j100156a054.

[7] M.A. Baker, R. Gilmore, C. Lenardi, W. Gissler, XPS investigation of preferential sputtering of S from MoS2 and determination of MoSx stoichiometry from Mo and S peak positions, Appl. Surf. Sci. 150 (1999) 255–262. doi:10.1016/S0169-4332(99)00253-6.

[8] D. Escalera-López, E. Gómez, E. Vallés, Electrochemical growth of CoNi and Pt – CoNi soft magnetic composites on an alkanethiol monolayer-modified ITO substrate, Phys. Chem. Chem. Phys. 17 (2015) 16575–16586. doi:10.1039/C5CP02291F.

[9] J.D. Benck, Z. Chen, L.Y. Kuritzky, A.J. Forman, T.F. Jaramillo, Amorphous Molybdenum Sul fi de Catalysts for Electrochemical Hydrogen Production: Insights into the Origin of their Catalytic Activity, ACS Catal. 2 (2012) 1916–1923.

[10] M.C. Biesinger, B.P. Payne, L.W.M. Lau, A. Gerson, R.S.C. Smart, X-ray photoelectron spectroscopic chemical state Quantification of mixed nickel metal, oxide and hydroxide systems, Surf. Interface Anal. 41 (2009) 324–332. doi:10.1002/sia.3026.

[11] A.P. Grosvenor, M.C. Biesinger, R.S.C. Smart, N.S. McIntyre, New interpretations of XPS spectra of nickel metal and oxides, Surf. Sci. 600 (2006) 1771–1779. doi:10.1016/j.susc.2006.01.041.

[12] N. Jiang, Q. Tang, M. Sheng, B. You, D. Jiang, Y. Sun, Nickel sulfides for electrocatalytic hydrogen evolution under alkaline conditions: a case study of crystalline NiS, NiS2, and Ni3S2 nanoparticles, Catal. Sci. Technol. 6 (2015) 1077–1084. doi:10.1039/C5CY01111F.

[13] N. Jiang, L. Bogoev, M. Popova, S. Gul, J. Yano, Y. Sun, Electrodeposited nickel-sulfide films as competent hydrogen evolution catalysts in neutral water, J. Mater. Chem. A. 2 (2014) 19407–19414. doi:10.1039/C4TA04339A.

[14] T.F. Jaramillo, K.P. Jørgensen, J. Bonde, J.H. Nielsen, S. Horch, I. Chorkendorff, Identification of active edge sites for electrochemical H2 evolution from MoS2 nanocatalysts., Science. 317 (2007) 100–102. doi:10.1126/science.1141483.

[15] J. Bonde, P.G. Moses, T.F. Jaramillo, J. Norskov, I. Chorkendorff, Hydrogen evolution on nano-particulate transition metal sulfides, Faraday Discuss. 140 (2008) 219–231. doi:10.1039/b814058h.

[16] M.A. Lukowski, A.S. Daniel, F. Meng, A. Forticaux, L. Li, S. Jin, Enhanced Hydrogen Evolution Catalysis from Chemically Exfoliated Metallic MoS 2 Nanosheets, J. Am. Chem. Soc. 135 (2013) 1–4.

[17] M.J. Cuddy, K.P. Arkill, Z.W. Wang, H.-P. Komsa, A. V Krasheninnikov, R.E. Palmer, Fabrication and atomic structure of size-selected, layered MoS2 clusters for catalysis., Nanoscale. 6 (2014) 12463–12469. doi:10.1039/c4nr04317k.

[18] S.R.G. Thakurta, Electrical Properties of Molybdenite, Indian J. Phys. 43 (1969) 169–172.

[19] A.Y.S. Eng, A. Ambrosi, Z. Sofer, P. Simek, M. Pumera, Electrochemistry of Transition Metal Dichalcogenides : Strong Dependence on the Metal-to-Chalcogen Composition and Exfoliation Method, ACS Nano. 8 (2014) 12185–12198.

[20] Z. Chen, D. Cummins, B.N. Reinecke, E. Clark, M.K. Sunkara, T.F. Jaramillo, Core-shell MoO 3-MoS 2 Nanowires for Hydrogen Evolution : A Functional Design for Electrocatalytic Materials, Nano Lett. 11 (2011) 4168–4175.

[21] J. Kibsgaard, Z. Chen, B.N. Reinecke, T.F. Jaramillo, Engineering the surface structure of MoS2 to preferentially expose active edge sites for electrocatalysis., Nat. Mater. 11 (2012) 963–969. doi:10.1038/nmat3439.

[22] H.A. Burch, M. Isaacs, K. Wilson, R.E. Palmer, N.V. Rees, Electrocatalytic regeneration of atmospherically aged MoS 2 nanostructures via solution-phase sulfidation, RSC Adv. 6 (2016) 26689–26695. doi:10.1039/C6RA03326A.

[23] S. Xie, M. Xu, T. Liang, G. Huang, S. Wang, G. Xue, N. Meng, Y. Xu, H. Chen, X. Ma, D. Yang, High-quality round-shaped monolayer MoS2 domain and its transformation, Nanoscale. (2015) 219–225. doi:10.1039/C5NR05701A.

[24] J.V. Lauritsen, M.V. Bollinger, E. Lægsgaard, K.W. Jacobsen, J.K. Nørskov, B.S. Clausen, H. Topsøe, F. Besenbacher, Atomic-scale insight into structure and morphology changes of MoS2 nanoclusters in hydrotreating catalysts, J. Catal. 221 (2004) 510–522. doi:10.1016/j.jcat.2003.09.015.

[25] H. Vrubel, X. Hu, Growth and activation of an amorphous molybdenum sulfide hydrogen evolving catalyst, ACS Catal. 3 (2013) 2002–2011. doi:10.1021/cs400441u.

[26] S.J. Rowley-Neale, D.A.C. Brownson, G.C. Smith, D.A.G. Sawtell, P.J. Kelly, C.E. Banks, 2D nanosheet molybdenum disulphide (MoS2) modified electrodes explored towards the hydrogen evolution reaction, Nanoscale. 7 (2015) 18152–18168. doi:10.1039/C5NR05164A.

[27] M.-R. Gao, J.-X. Liang, Y.-R. Zheng, Y.-F. Xu, J. Jiang, Q. Gao, J. Li, S.-H. Yu, An efficient molybdenum disulfide/cobalt diselenide hybrid catalyst for electrochemical hydrogen generation., Nat. Commun. 6 (2015) 5982. doi:10.1038/ncomms6982.

[28] Y. Yu, S.Y. Huang, Y. Li, S.N. Steinmann, W. Yang, L. Cao, Layer-dependent electrocatalysis of MoS2 for hydrogen evolution, Nano Lett. 14 (2014) 553–558. doi:10.1021/nl403620g.

[29] J.D. Benck, T.R. Hellstern, J. Kibsgaard, P. Chakthranont, T.F. Jaramillo, Catalyzing the Hydrogen Evolution Reaction (HER) with Molybdenum Sulfide Nanomaterials, ACS Catal. 4 (2014) 3957–3971. http://pubs.acs.org/doi/abs/10.1021/cs500923c (accessed December 15, 2015).

[30] B.E. Conway, B. V Tilak, Interfacial processes involving electrocatalytic evolution and oxidation of H2 , and the role of chemisorbed H, Electrochim. Acta. 47 (2002) 3571–3594.

[31] X. Chia, A. Ambrosi, Z. Sofer, J. Luxa, M. Pumera, Catalytic and Charge Transfer Properties

of Transition Metal Dichalcogenides Arising from Electrochemical Pretreatment, ACS Nano. 9 (2015) 5164–5179.

[32] M.-R. Gao, M.K.Y. Chan, Y. Sun, Edge-terminated molybdenum disulfide with a 9.4-Å interlayer spacing for electrochemical hydrogen production., Nat. Commun. 6 (2015) 7493. doi:10.1038/ncomms8493.

[33] D. Voiry, M. Salehi, R. Silva, T. Fujita, M. Chen, Conducting MoS2 nanosheets as catalysts for hydrogen evolution reaction, Nano Lett. 13 (2013) 6222–6227. http://pubs.acs.org/doi/abs/10.1021/nl403661s.

[34] E. Navarro-Flores, Z. Chong, S. Omanovic, Characterization of Ni, NiMo, NiW and NiFe electroactive coatings as electrocatalysts for hydrogen evolution in an acidic medium, J. Mol. Catal. A Chem. 226 (2005) 179–197. doi:10.1016/j.molcata.2004.10.029.

[35] S.L. Medway, C. a. Lucas, a. Kowal, R.J. Nichols, D. Johnson, In situ studies of the oxidation of nickel electrodes in alkaline solution, J. Electroanal. Chem. 587 (2006) 172–181. doi:10.1016/j.jelechem.2005.11.013.

[36] R. Subbaraman, D. Tripkovic, D. Strmcnik, K.-C. Chang, M. Uchimura, A.P. Paulikas, V. Stamenkovic, N.M. Markovic, Enhancing Hydrogen Evolution Activity in Water Splitting by Tailoring Li + -Ni(OH) 2 -Pt Interfaces, Science (80-.). 334 (2011) 1256–1260.

[37] P.A. Thiel, The Interaction of Water with Solid Surfaces: Fundamental Aspects, Surf. Sci. Rep. 7 (1990) 211–385.

[38] W. Kautek, H. Gerischer, Anisotropic Photocorrosion of n-Type MoS2, MoSe2 and WSe Single Crystal Surfaces: the Role of Cleavage Steps, Line and Screw Dislocations, Surf. Sci. 119 (1982) 46–60.

[39] R.C. V Piatti, J.J. Podesta, The Electrochemical Kinetic Behaviour of Nickel in Acid Aqueous Solutions Containing Chloride and Perchlorate Ions, Electrochim. Acta. 14 (1969) 541–560.

[40] M.R. Barbosa, S.G. Real, J.R. Vilche, A.J. Arvia, Comparative Potentiodynamic Study of Nickel in Still and Stirred Acid-Potassium Sulfate Solutions in the 0.4-5.7 pH Range, J. Electrochem. Soc. 135 (1988) 1077–1085. http://onlinelibrary.wiley.com/doi/10.1002/cbdv.200490137/abstract (accessed December 15, 2015).

[41] S.G. Real, M.R. Barbosa, A.J. Arvia, Influence of Chloride Concentration on the Active Dissolution and Passivation of Nickel Electrodes in Acid Sulfate Solutions, J. Electrochem. Soc. 137 (1990) 1696–1702.

[42] M.R. Barbosa, J.A. Bastos, J.J. García-Jareño, F. Vicente, Chloride role in the surface of nickel electrode, Electrochim. Acta. 44 (1998) 957–965.

[43] C.F. Zinola, A.M. Castro Luna, The Inhibition of Ni Corrosion in H2SO4 Solutions Containing Simple Non-saturated Substances, Corros. Sci. 37 (1995) 1919–1929.

[44] S.G. Real, J.R. Vilche, A.J. Arvia, The Characteristics of the Potentiodynamic Potential/Current Profiles Obtained with the Ni/0.5N H2SO4 Interface. A Contribution to the Mechanism of the Electrode Process, Corros. Sci. 20 (1980) 563–586.

[45] J. Lauritsen, J. Kibsgaard, G. Olesen, P. Moses, B. Hinnemann, S. Helveg, J. Norskov, B. Clausen, H. Topsoe, E. Lagsgaard, Location and coordination of promoter atoms in Co- and Ni-promoted MoS2-based hydrotreating catalysts, J. Catal. 249 (2007) 220–233. doi:10.1016/j.jcat.2007.04.013.

[46] H. Schweiger, P. Raybaud, H. Toulhoat, Promoter Sensitive Shapes of Co(Ni)MoS Nanocatalysts in Sulfo-Reductive Conditions, J. Catal. 212 (2002) 33–38. doi:10.1006/jcat.2002.3737.

[47] J. Deng, H. Li, J. Xiao, Y. Tu, D. Deng, H. Yang, H. Tian, J. Li, P. Ren, X. Bao, Triggering the

electrocatalytic hydrogen evolution activity of the inert two-dimensional MoS 2 surface via single-atom metal doping, Energy Environ. Sci. 8 (2015) 1594–1601. doi:10.1039/C5EE00751H.

[48] H. Li, C. Tsai, A.L. Koh, L. Cai, A.W. Contryman, A.H. Fragapane, J. Zhao, H.S. Han, H.C. Manoharan, F. Abild-Pedersen, J.K. Nørskov, X. Zheng, Activating and optimizing MoS2 basal planes for hydrogen evolution through the formation of strained sulphur vacancies., Nat. Mater. 15 (2015) 48–53. doi:10.1038/nmat4465.

[49] D. Giovanelli, N.S. Lawrence, S.J. Wilkins, L. Jiang, T.G.J. Jones, R.G. Compton, Anodic stripping voltammetry of sulphide at a nickel film: towards the development of a reagentless sensor., Talanta. 61 (2003) 211–20. doi:10.1016/S0039-9140(03)00269-8.

[50] J. Kibsgaard, A. Tuxen, K.G. Knudsen, M. Brorson, H. Topsøe, E. Lægsgaard, J. V. Lauritsen, F. Besenbacher, Comparative atomic-scale analysis of promotional effects by late 3d-transition metals in MoS2 hydrotreating catalysts, J. Catal. 272 (2010) 195–203. doi:10.1016/j.jcat.2010.03.018.

Chapter 6

Size-selected, sulfur-enriched molybdenum sulfide nanoclusters

6.1 Introduction

In the previous chapter the hydrogen evolution enhancement of Ni-MoS_2 hybrid nanoclusters was demonstrated by activating the initially HER-inert S-edge sites present in the MoS_2 nanoclusters. However, all magnetron-sputtered MoS_2 clusters were found to be S-deficient: in contact with atmospheric conditions, this results in the formation of molybdenum oxides which electrodissolve in acidic electrolytes. This ultimately hampers the MoS_2 nanocluster stability, key for their potential implementation in PEM electrolyser technologies. Although previous works in the literature have maximized the chalcogen-to-metal ratio by post-synthesis treatments (e.g. H_2S flow under elevated temperatures in quart tube furnace), these are not applicable to size-selected magnetron-sputtered deposited nanoclusters as their size distribution control would be irreversibly altered.

This chapter focuses on the incorporation of sulfur into S-deficient, size-selected molybdenum sulfide (MoS_x) nanoclusters obtained by magnetron sputtering, by use of a sulfur evaporation and annealing treatment under ultra-high vacuum conditions. Influence of the sulfur treatment and its implications in the MoS_x nanoclusters morphology and HER activity is monitored by physical and electrochemical techniques. A correlation between sulfide contents and degree of crystallinity with the observed HER electrocatalysis is discussed.

6.2 Results and discussion

6.2.1 Physical characterization of size-selected $(MoS_x)_{1000}$ nanoclusters: HAADF-STEM imaging and XPS

Figure 6.1 shows the aberration-corrected HAADF-STEM images of $(MoS_x)_{1000}$ nanoclusters obtained from the single target magnetron sputtering and gas condensation cluster source after time-of-flight mass selection (selected mass at cluster source, 160000 amu, equivalent to 1000 MoS_2 units per cluster) at 5% projected surface area coverage after deposition on amorphous carbon covered TEM grids. Figure 6.1a and 6.1b are acquired at low magnification before and after sulfur evaporation and annealing, respectively. It can be seen in both cases that nanoclusters diffused and aggregated after deposition onto the amorphous carbon TEM grid substrates: this effect will be disregarded for size distribution evaluation, as it would conceal the effect of sulfur evaporation and annealing in MoS_x size distributions.

The as-deposited MoS_x clusters are rather irregular with poorly ordered structures, and a peak diameter of 5.5 nm is given based on the projected surface area from our previous study where size distributions of more than 150 non-overlapped nanoclusters were evaluated (Figure 6.1e).[1] The size distributions of 3.8 and 7.8 nm correspond to fragmented $(MoS_x)_{1000}$ and clusters with a doubled mass, i.e. $(MoS_x)_{2000}$. The STEM image of as-deposited MoS_x cluster at a higher magnification (Figure 6.1c), together with its FFT pattern (inset), show the amorphous feature of the cluster and confirm the absence of extended crystalline order. The clusters have an uneven layered structure revealed by the HAADF intensity line profile, which agrees with previous first-principle simulation studies[2] and our previous observations for magnetron-sputtered MoS_2 nanoclusters.[3] Compared with the as-deposited clusters, the sulfurised clusters become larger with a mean diameter of 6.0 nm (see Figure 6.1f for size

distribution). This is due to the morphological reconstruction of MoS_x clusters with the added sulfur.

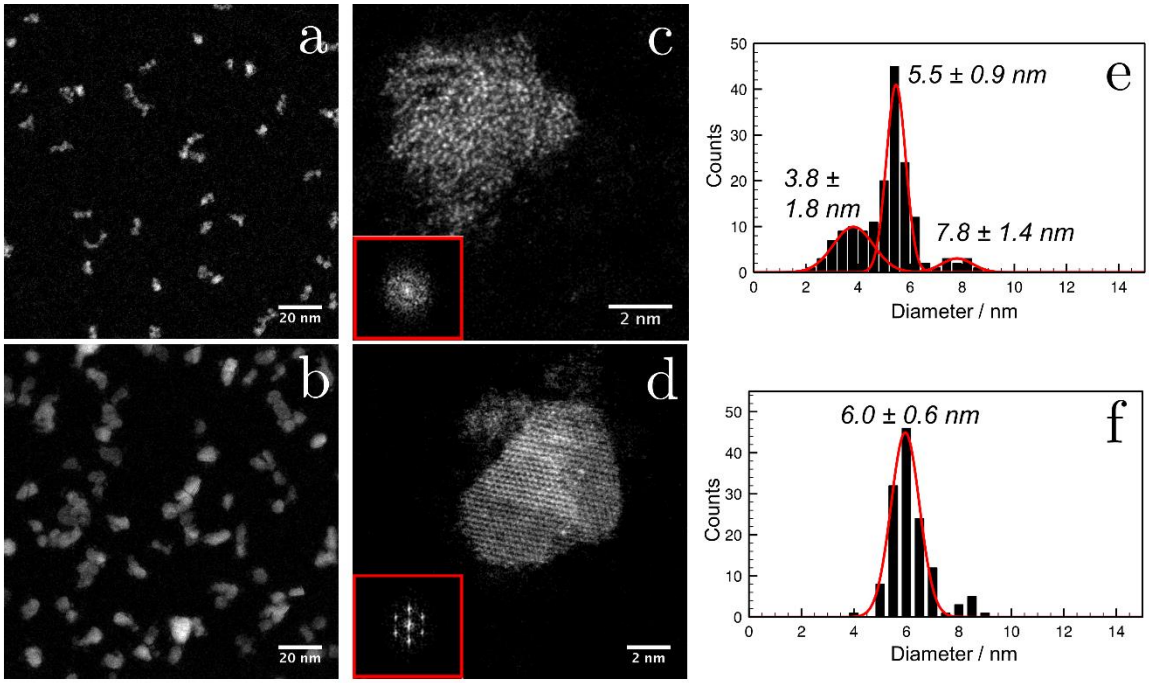

Figure 6.1. Low magnification STEM images of size-selected $(MoS_x)_{1000}$ nanoclusters a) as-deposited and b) after sulfur evaporation and annealing. High magnification images for c) as-deposited and d) sulfur-evaporated and annealed $(MoS_x)_{1000}$ nanoclusters shown to compare modifications in crystallinity (FFT patterns of corresponding clusters shown in inset). Size distribution of non-overlapped independent nanocluster counting on e) as-deposited and f) sulfur-evaporated and annealed $(MoS_x)_{1000}$ nanoclusters included for ease of comparison.

In contrast to the as-deposited clusters, the sulfurised clusters shown in Figure 6.1b and 6.1d present rather crystalline structures, which can also be confirmed by their FFT patterns (inset). The sulfurised clusters retain the layered structure of 3 to 4 layers-thick (Figures 6.2a and 6.2c), with layer-to-layer interspacings of 0.642 nm found on side-on nanoclusters (Figures 6.2 b and 6.2d), indicating that the sulfur treatment does not alter the nanoclusters layer arrangement. The Moiré pattern shown in Figure 6.2a indicates a misorientation between layers, which can be commonly found in the sulfurised clusters with 3 or more layers.[4] Given

that sulfur is long known to sublime at temperatures well below 100 °C,[5,6] we can conclude that the crystalline structures come from the chemical bond between the added sulfur and the clusters, and that the structural modification into crystalline clusters mainly takes place within the 2D layers.

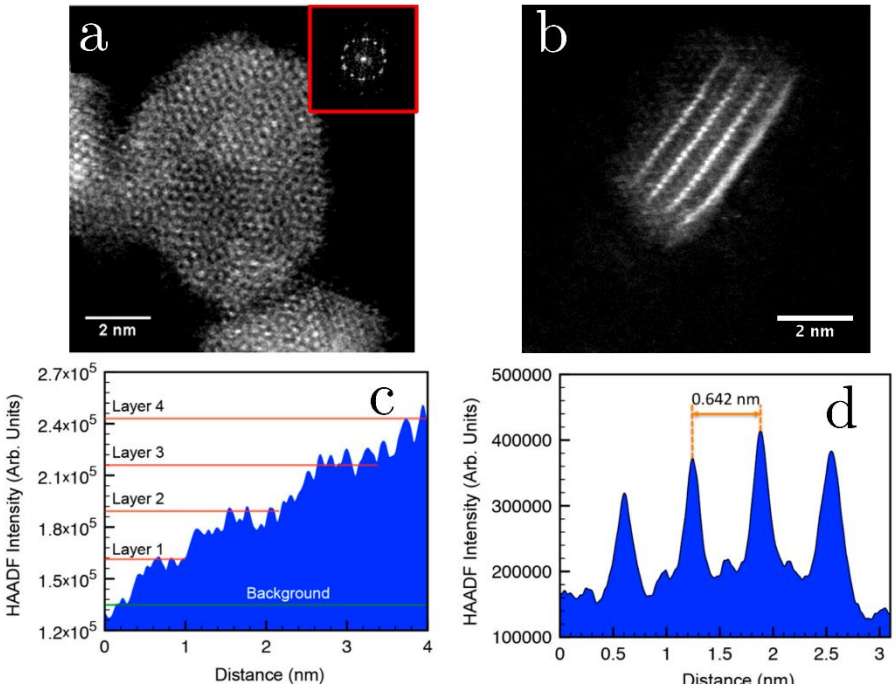

Figure 6.2. High magnification STEM images of size-selected $(MoS_x)_{1000}$ nanoclusters after sulfur evaporation and annealing showing a) Moiré patterns due to layer misorientation and b) layered structure when depositing in a side-on arrangement. c,d) HAADF intensity profile analysis of a,b) showing the 3-4 layered structure and corresponding interlayer spacing.

XPS measurements were acquired from molybdenum sulfide clusters deposited onto amorphous carbon TEM grids to investigate the degree of sulfur incorporation and potential modifications in the oxidation state of the clusters. The high-resolution Mo 3*d* and S 2*p* spectra of the as-deposited molybdenum sulfide nanoclusters reveal a complex surface composition (see Figure 6.3a). The Mo spectra (Figure 6.3, top row) could not be solely deconvoluted into the Mo^{4+} $3d_{5/2:3/2}$ spin-orbit doublet characteristic of MoS_2 materials (binding energies of ~229.8

and ~232.9 eV, respectively). Two additional doublets were needed, ascribed to $Mo^{a}O_{b}S_{c}$ (~231.5 and ~234.6 eV, where the superscript ^{a} represents the Mo oxidation state whereas the subscripts $_{b}$ and $_{c}$ the stoichiometry of O and S in the specific oxysulfide) and Mo^{6+} (~233.1 and ~236.2 eV) oxidation states reported in molybdenum compounds such as molybdenum oxysulfides[7] and MoO_3.[8] Analysis of the Mo^{4+}: $Mo^{a}O_{b}S_{c}$: Mo^{6+} relative percentages (at. %) from the XPS photoemission intensities yields a relative ratio of 53.8:25.2:21.0 at. %, corroborating the significant proportion of oxidized molybdenum species at the nanoclusters. The S spectra (Figure 6.3, bottom row) were deconvoluted using two $2p_{3/2:1/2}$ spin-orbit doublets related to the S^{2-} (~161.3 and ~162.5 eV) and S_2^{2-} (~162.6 and ~163.8 eV) oxidation states consistently reported for amorphous MoS_x thin films and nanoparticles,[9,10] yielding a S^{2-}/ S_2^{2-} relative ratio of 20:80. The broad S signal centered at ca. 170 eV is ascribed to oxidized sulfur species such as sulfites or sulfates (referred here as SO_x^{y-} for ease of convenience).[11] The XPS intensity ratio between the S-containing Mo species (Mo^{4+}/$Mo^{a}O_{b}S_{c}$) and the S^{2-}/ S_2^{2-} species yields a close-to-stoichiometric but still S-deficient ratio (1:1.9±0.1), similar to that found in our previous investigations.[3,12]

Likewise, high-resolution XPS spectra on the sulfur-evaporated and annealed $(MoS_x)_{1000}$ nanoclusters (Figure 6.3c) reveal an almost total conversion of oxidized Mo species to Mo^{4+} (Mo^{4+}: $Mo^{a}O_{b}S_{c}$: Mo^{6+} at. % ratio of 88.9:8.0:3.1), as well as an effective S-enrichment, obtaining a Mo^{4+}/$Mo^{a}O_{b}S_{c}$: S^{2-}/ S_2^{2-} ratio of 1: 4.9±0.1. As for the S^{2-}/ S_2^{2-} XPS intensity ratio, this is now 75:25. Further analysis of the sulfurised but non-annealed $(MoS_x)_{1000}$ nanoclusters sample (Fig. 6.3b) reveals that S incorporation onto the nanoclusters occurs at this stage to a certain extent (Mo^{4+}/$Mo^{a}O_{b}S_{c}$: S^{2-}/ S_2^{2-} ratio of 1: 3.3±0.1), but it leads neither to an effective depletion of oxygen-containing Mo species (Mo^{4+}: $Mo^{a}O_{b}S_{c}$: Mo^{6+} at. % ratio of 62.2:21.4:16.4), nor to full crystallization of the nanocluster structures.[1] Hence, it is concluded that the best methodology to produce S-enriched MoS_x nanoclusters with enhanced crystalline order is by the adoption of sequential sulfur evaporation and thermal annealing.

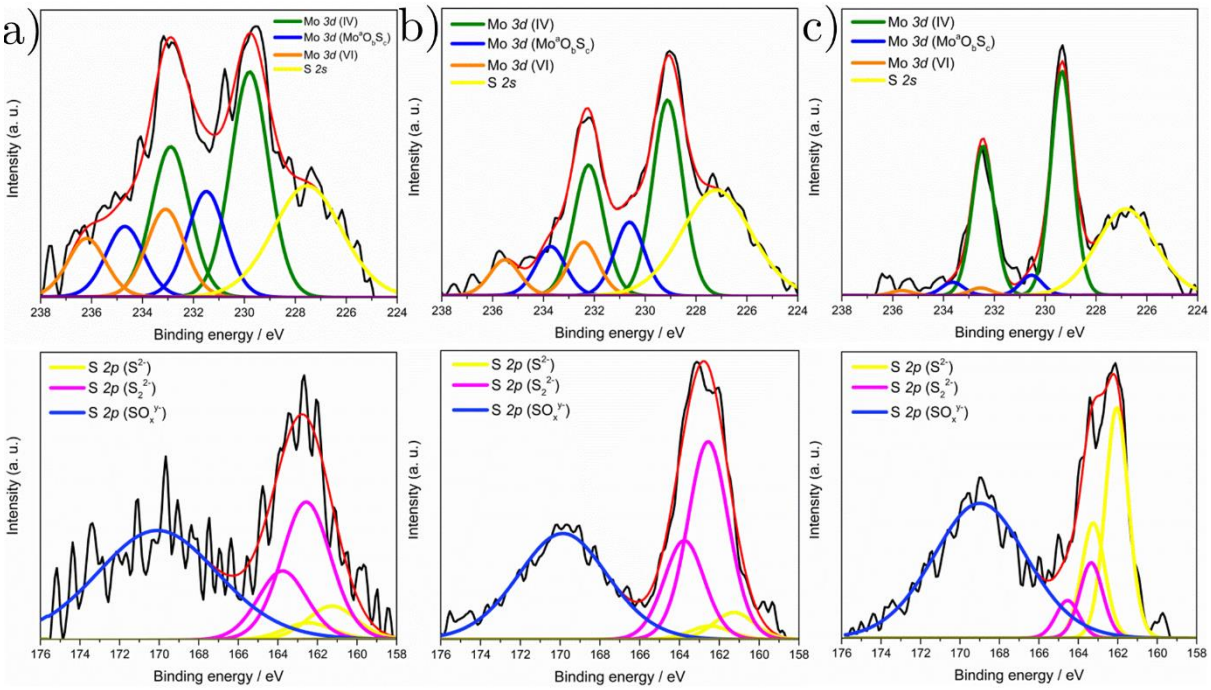

Figure 6.3. High-resolution Mo 3*d* (top) and S 2*p* (bottom) XPS spectra of a) as-deposited $(MoS_x)_{1000}$ nanoclusters, b) sulfurised, non-annealed $(MoS_x)_{1000}$ nanoclusters and c) sulfurised, annealed $(MoS_x)_{1000}$ nanoclusters. Labels: raw spectra (black), cumulative peak fit (red), Mo^{4+} $3d_{5/2:3/2}$ (green), $Mo^aO_bS_c$ $3d_{5/2:3/2}$ (blue), Mo^{6+} $3d_{5/2:3/2}$ (orange), S $2p_{3/2:1/2}$ (S^{2-}, yellow) and S $2p_{3/2:1/2}$ (S_2^{2-}, magenta). The faint peak at ca. 160 eV in the S 2*p* spectra corresponds to a background subtraction artifact.

6.2.2 Electrocatalytic activity to the hydrogen evolution reaction: influence of sulfur enrichment

The hydrogen evolution activity of the as-prepared and sulfur-enriched $(MoS_x)_{1000}$ nanoclusters was evaluated in a 3-electrode electrochemical setup, by recording linear sweep voltammograms between 0 to -1.2 V (scan rate= 50 mV s^{-1}) in a 2mM $HClO_4$/0.1 M $NaClO_4$ aqueous electrolyte (normalized vs. RHE and iR compensated, for further details, see 4.7.1.3

Materials and methods). The low proton concentration in the electrolyte used ($[H^+] \approx 2 \times 10^{-6}$ mol cm^{-3}, pH≈ 2.7) is responsible for the diffusion decay peak profile in Figures. 6.4a and 6.4b, analogous to that found with the Ni-MoS_2 magnetron-sputtered nanoclusters reported in the previous chapter.[12,13] The as-prepared samples present onset potentials, η_{onset} for current densities of $|j|=0.05$ mA cm^{-2}, of ca. 690 mV, which are ~60 mV positively shifted compared to the recorded η_{onset} for bare glassy carbon. This confirms that even at ultra-low loadings MoS_2 effectively catalyzes the HER. The peak half-maximum overpotentials ($\eta_{half\ max}$) and current densities ($|j_{half\ max}|$) metrics used in the previous chapter to describe the HER catalysis of our magnetron-sputtered nanoclusters[12] are found to be ca. 810 mV and 0.31 mA cm^{-2}, respectively (see Table E.2 Section E.2 Appendix).

These are in good agreement with the results obtained for $(MoS_{0.9})_{300}$ nanoclusters, which presented a higher cluster loading (ca. 3.5 μg cm^{-2}) but equivalent surface coverage given the smaller cluster sizes (~20%).[12] Interestingly, such ultra-low loadings of size-selected MoS_x nanoclusters used in the present work (5% coverage: ~84 ng cm^{-2}, 10% coverage: ~168 ng cm^{-2}, 20% coverage: ~335 ng cm^{-2}) already present HER activities comparable to those of $(MoS_{0.9})_{300}$ nanoclusters with loadings higher by 1 order of magnitude. Despite both smaller dimensions (~2.6 nm) and higher loadings, the S-deficient Mo:S ratio and cluster overlapping upon random surface landing can then explain the $(MoS_{0.9})_{300}$ nanoclusters' reported performance. After sulfur incorporation, all $(MoS_x)_{1000}$ nanoclusters exhibit remarkable improvements in their HER performance. A consistent 200 mV shift in the HER $\eta_{half\ max}$ was found independently of the sample loading (see Figures 6.4a-b).

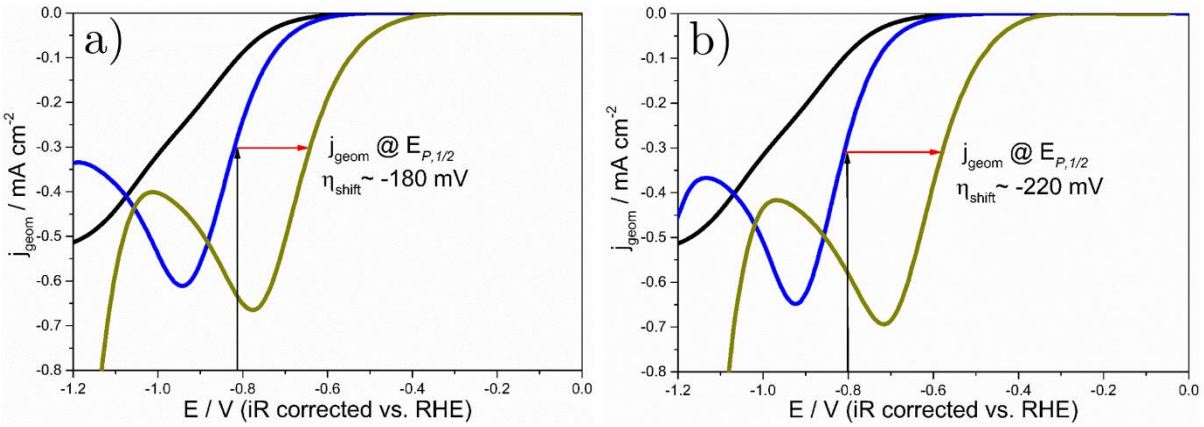

Figure 6.4. a,b) Linear sweep voltammograms recorded at 5 mm diameter mirror-polished glassy carbon samples (black) modified with as-deposited $(MoS_x)_{1000}$ nanoclusters (blue) and sulfurised, annealed $(MoS_x)_{1000}$ nanoclusters (gold) at surface coverages of 5% (a) and 20% (b). Red arrows denote overpotential shift due to sulfurisation at $|j_{half\ max}|$. Scan rate: 50 mV s^{-1}

To gather further insight about the HER kinetics and electron transfer properties, Tafel slope analysis and electrochemical impedance spectroscopy (EIS) experiments were carried out before and after sulfur enrichment of $(MoS_x)_{1000}$ nanoclusters. Tafel plots of the cathodic linear sweep voltammograms (η vs. $\log|j_{geom}|$, Figure 6.5a) show Tafel slopes in the 143-154 mV dec^{-1} range for all $(MoS_x)_{1000}$ nanocluster samples irrespective of both loading and sulfur modification, similar values to the one found for bare GC (≈154 mV dec $^{-1}$). This indicates that the sulfurisation treatment does not modify the mechanism under which the HER operates: for slopes close to b≈ 120 mV dec^{-1} this is the Volmer mechanism, its rate-limiting step being the electroadsorption of monoatomic hydrogen.[14] Previous reports on amorphous MoS_x catalysts have reported Tafel slopes of b≈40 mV dec $^{-1}$ (Volmer-Heyrovský rate-limiting step), significantly lower than the ones obtained for the as-deposited amorphous $(MoS_x)_{1000}$ nanoclusters.

Two main factors are responsible for this: the electrolyte pH and the inherent morphology or the clusters. Recent investigations by Dubouis et al. on electrodeposited, amorphous MoS_x materials have shown that the HER mechanism (and consequently the Tafel slope) is pH-dependent[15]: for pH≤1, the hydronium cation electroreduction governs the proton reduction with pH-independent Tafel slopes of b≈40 mV dec $^{-1}$; at higher pH values the lower proton concentration leads to mass transport limitations which ultimately result in the proton electroadsorption (i.e. Volmer rate-limiting HER step, b≈120 mV dec $^{-1}$) dominating the HER. Alternatively, the 40 mV dec^{-1} Tafel slopes reported on amorphous MoS_x are well known to arise from the $[Mo_3S_{13}]^{2-}$ cluster-based structure and the different sulfur moieties entailed.[16,17] The pH≥1 used for our electrolyte along with the trigonal prismatic coordination as found in 2H-MoS_2 for our size-selected MoS_x nanoclusters[3] support the ca. 143-154 mV dec^{-1} Tafel slopes obtained.

Electrochemical impedance spectroscopy (EIS) Nyquist plots were fitted with a simplified equivalent circuit model based on the recently-used linear transmission model[18,19] for amorphous/porous MoS_x structures (see Section 4.7.1.3 Materials and methods for further details).[20,21] Unlike the Randles circuit conventionally used to physically describe the HER on TMD materials, this circuit not only accounts for the charge transfer resistance (R_{ct}), but also for the contact resistance between the nanoclusters and the glassy carbon electrode interface (R_c). Such information is of physical relevance given the layer-dependent HER catalysis of TMDs and their inherently high through-plane resistance.[22–26] At -1.1 V vs. SCE (~ -0.7 V vs. RHE), a significant decrease in all EIS resistance components was found after the combined treatment of sulfur evaporation plus annealing on the $(MoS_x)_{1000}$ nanoclusters (Figure 6.5b, Table G.1 Section G Appendix): R_{ct} (~1240 vs. ~1180 Ω, 5% coverage; ~6060 vs. ~840 Ω, 20% coverage), and R_c (~4640 vs. ~3250 Ω, 5% coverage; ~12420 vs. ~6820 Ω, 20% coverage). We postulate the extended crystalline order of the sulfur-enriched nanocluster

structure to be the governing factor. The asymmetric nature of the EIS regarding the magnitude of the real and the imaginary axis components can be justified by the multifaceted nature of the nanoclusters: different crystalline orientations present different electron transfer properties, yielding an overlap of different total impedance contributions, accounted for in the linear transmission model employed.

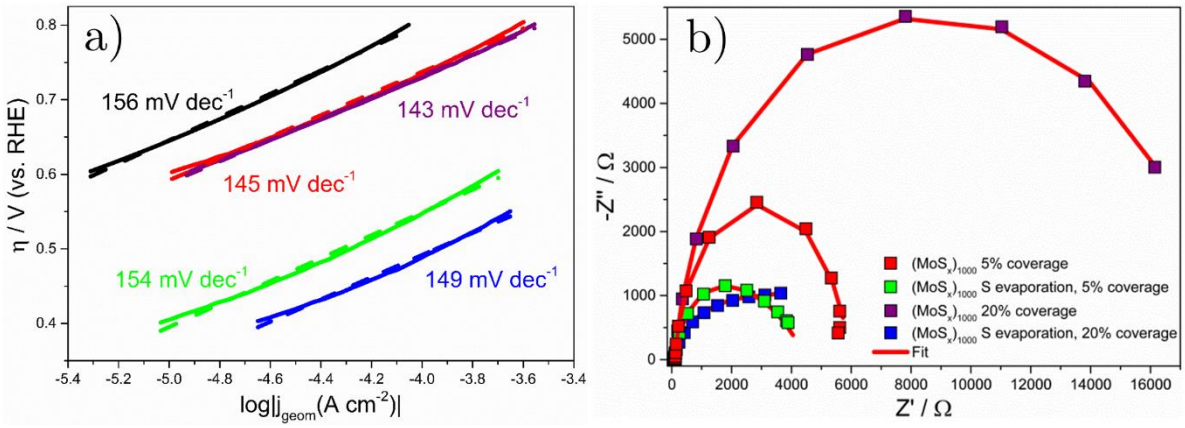

Figure 6.5. a) Tafel plots (η vs. $\log|j_{geom}|$) of the different $(MoS_x)_{1000}$ nanoclusters plotted in Figure 6.4. Scan rate: 50 mV s^{-1}. b) Electrochemical impedance spectroscopy Nyquist spectra of samples in Figure 6.4 recorded at η~ 700 mV vs. RHE. Labels in c,d): mirror-polished glassy carbon (black), as-deposited $(MoS_x)_{1000}$ nanoclusters at 5% (red) and 20% (purple) coverage, and sulfurised and annealed $(MoS_x)_{1000}$ nanoclusters at 5% (green) and 20% (blue) coverage. Asymmetric plotting of EIS spectra done for ease of interpretation of results.

This can be supported by both the FFT analysis of the nanoclusters imaged by HAADF-STEM and the high-resolution S 2*p* XPS results. The former shows, after sulfur incorporation, that the $(MoS_x)_{1000}$ nanocluster FFT pattern changes from a diffuse ring characteristic of highly amorphous materials to a well-defined set of diffraction spots ranging from single sets ascribed to aligned MoS_2 layers along the (100) plane (intralayer spacing: 0.25 nm) to dual sets related to misoriented stacking layer arrangements.[1] The high-resolution S 2*p* XPS data monitoring the S^{2-}/ S_2^{2-} intensity ratio, which serves as a descriptor of the degree of MoS_x crystallinity,

reveals an increased S^{2-} relative content after the sulfur evaporation treatment: 75:25 vs. the 20:80 found in pristine nanoclusters. Thus, the sulfur evaporation and annealing not only incorporates sulfur into the nanocluster structures but also converts the characteristic amorphous MoS_x/MoS_3 S_2^{2-} moieties[10,27–29] to S^{2-} as found in crystalline MoS_2.[30] From these findings we can conclude that the sulfur evaporation and subsequent annealing of $(MoS_x)_{1000}$ nanoclusters results in an overall improvement in their charge transfer properties. A previous report on polymorphic MoS_2 (a system which resembles the non-crystalline nature of our as-deposited nanoclusters) revealed that electron hopping only occurs between metallic 1T domains bounded by semiconducting 2H regions, and therefore is limited .[31]

On a separate note, it is also noteworthy to explore which are the potential HER active sites in our MoS_x nanoclusters. For amorphous MoS_x, terminal S_2^{2-},[32] bridging S_2^{2-}[33] or unsaturated Mo^{IV} centers (i.e. S vacancies)[34] have been proposed as moieties responsible for hydrogen evolution, reaching no unambiguous consensus to date. For the as-prepared $(MoS_x)_{1000}$ nanoclusters, the presence of terminal/ bridging S_2^{2-} as found in our S 2*p* XPS spectra seems to indicate they might participate in the HER along with the well-established TMD unsaturated S^{2-} active sites.[35,36] In the case of our S-enriched $(MoS_x)_{1000}$ nanoclusters, the almost total conversion of the partially-oxidized $Mo^aO_bS_c$ and S_2^{2-} species to Mo^{4+} and S^{2-} as found in crystalline MoS_2 and subsequent HER enhancement lead us to believe that the main HER actives are the unsaturated S^{2-} moieties.

6.2.3 Evaluation of figures of merit and catalyst benchmarking

Further catalyst benchmarking by turnover frequency (TOF) and exchange current density (j_0) analysis also demonstrates the HER enhancement observed. For 5% surface coverage, as-deposited $(MoS_x)_{1000}$ nanoclusters present TOF ≈ 3.0 H_2 s^{-1} and $j_0 \approx 8.8 \times 10^{-10}$ A cm^{-2} at $\eta_{half\ max}$= 825 mV, whereas for an equivalent $\eta_{half\ max}$ the sulfur-modified $(MoSx)_{1000}$ nanoclusters

sample exhibits TOF ≈ 6.1 H_2 s^{-1} and $j_0 \approx 2.8 \times 10^{-8}$ A cm^{-2}. At 20% surface coverage, similar enhancements can be found (TOF ≈ 1.4 vs. 0.8 H_2 s^{-1} at $\eta_{half\ max}$= 814 mV; $j_0 \approx 5.2 \times 10^{-8}$ vs. 7.9×10^{-10} A cm^{-2}). The two-fold increase in TOF and more than 30-fold increase in j_0 indicates improved per-site activities and active site densities: positive shifts in onset potential values under given HER kinetics (i.e. same Tafel slope values) have been related to higher densities of active sites.[37] This, along with the onset potential shift, significantly surpasses the HER enhancement (ca. 70 mV at $|j_{half\ max}|$, see Figure 6.6a), found after S-edge site doping with Ni in $(Ni\text{-}MoS_2)_{1000}$ nanoclusters (3-fold increase in j_0 but lower TOF after doping),[12] indicating that the synergistic effect of sulfur enrichment and improved crystallinity prevails over a S-edge activation strategy on as-deposited MoS_x nanoclusters.

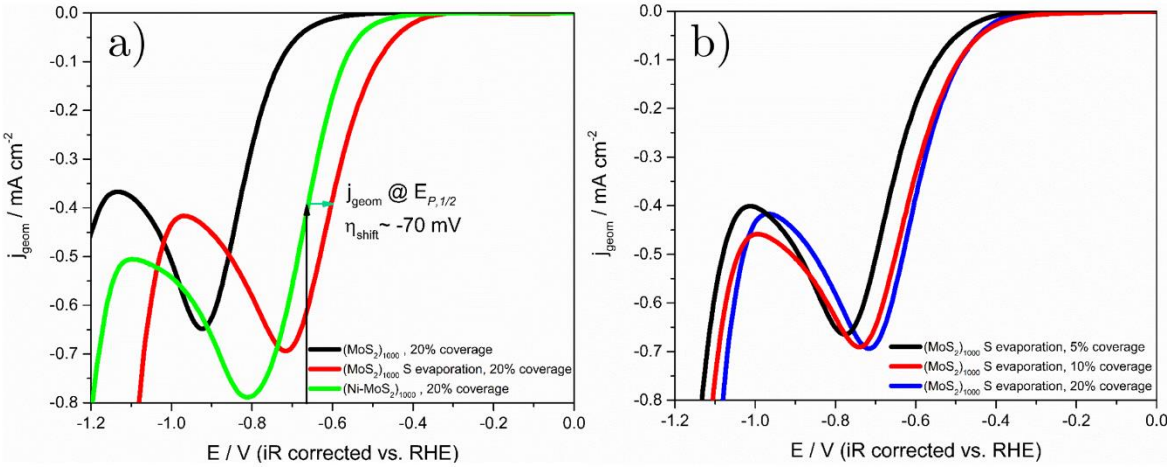

Figure 6.6. a) Linear sweep voltammograms recorded at 5 mm diameter mirror-polished glassy carbon samples modified with 20% projected surface coverage as-deposited $(MoS_x)_{1000}$ nanoclusters (black), $(Ni\text{-}MoS_2)_{1000}$ hybrid nanoclusters (green) and sulfurised, annealed $(MoS_x)_{1000}$ nanoclusters (red). Blue arrow denotes overpotential shift at $|j_{half\ max}|$. b) Linear sweep voltammograms recorded at 5 mm diameter mirror-polished glassy carbon samples modified with sulfurised, annealed $(MoS_x)_{1000}$ nanoclusters at different projected surface area coverages: 5% (black), 10% (red) and 20% (blue). Scan rate: 50 mV s^{-1}.

We finally proceeded to benchmark the performance of our $(MoS_x)_{1000}$ nanoclusters with recently-reported MoS_2-based catalysts from the literature. However, the ultra-low loadings utilized in this report preclude quantitative comparisons based on the HER metrics commonly cited (η at -10 mA cm^{-2} and $|j_{geom}|$ at 200 mV). It is well known that these metrics are heavily affected by the catalyst loading (for loading-dependent HER see Figure 6.6b),[9,38–41] catalyst layer thickness[22,42,43] and TMD morphologies.[29,44,45] Instead, we normalized all previous $|j_{geom}|$ reported values by mass activity (mA mg^{-1}), a metric widely accepted in the noble metal electrocatalysis community (see Table H.1 Appendix).[46,47] The mass activities found for $(MoS_x)_{1000}$ nanoclusters at η values as low as 400 mV (close to the HER onset) are, after sulfur evaporation and annealing, comparable with the best reported MoS_2 catalysts at 200 mV tested using a high proton concentration electrolyte. The values obtained are ca. 110 mA mg^{-1} at 5% coverage and ca. 70 mA mg^{-1} at 20% coverage (see Table F.2 Section F.2 Appendix). For $\eta_{half\ max}$, mass activities are in the 1000 mA mg^{-1} range: for 5% coverage, ca. 3620 mA mg^{-1} (pristine) and ca. 4010 mA mg^{-1} (sulfurised); for 20% coverage, ca. 980 mA mg^{-1} (pristine) and ca. 1040 mA mg^{-1} (sulfurised). This highlights the remarkable activities of the sulfurised $(MoS_x)_{1000}$ nanoclusters obtained at very low loadings.

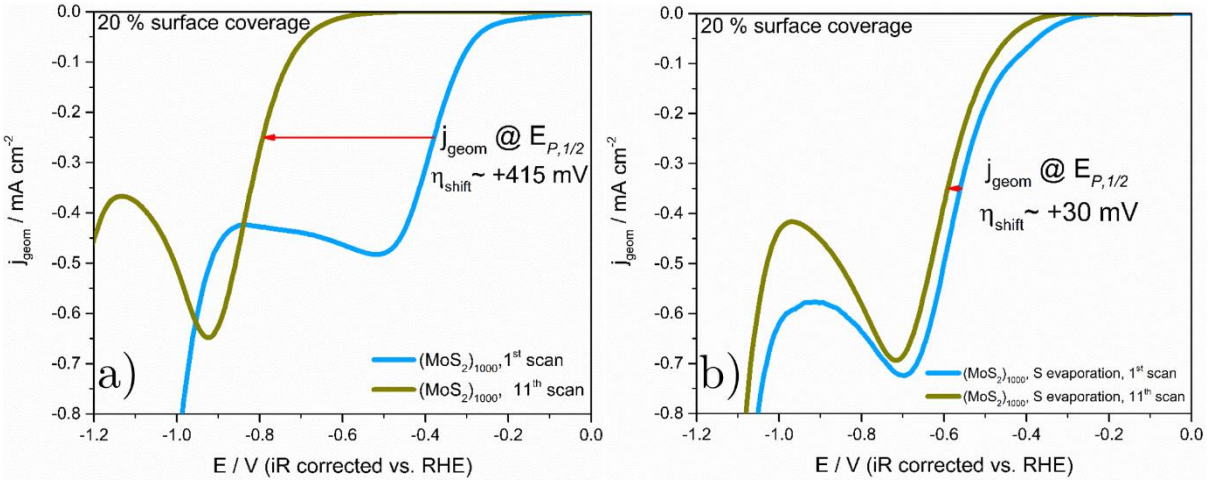

Figure 6.7. Evaluation of short-term stability of $(MoS_x)_{1000}$ nanoclusters by comparison of the first (light blue) and eleventh (gold, as in Fig. 6.4) linear sweep voltammograms recorded at 5 mm diameter mirror-polished glassy carbon samples modified with a) as-deposited and b) sulfurised, annealed $(MoS_x)_{1000}$ nanoclusters with 20% projected surface coverage. Red arrow denotes overpotential shift at $|j_{half\ max}|$. Scan rate: 50 mV s^{-1}.

The electrochemical stability of MoS_x electrocatalyts is also an important feature for evaluating prospective long-term HER performance. A preliminary comparison of the very first cathodic HER cycle recorded during our preconditioning step with the final pseudo-stationary LSV reported (11^{th} real HER cycle, as shown in Figures 6.4a and 6.4b) reveals clear differences in stability before and after sulfur evaporation and enrichment (Figure 6.7). For 20% surface coverage, as-deposited and S-defficient $(MoS_x)_{1000}$ nanoclusters present an extraordinarily high activity on their first cathodic polarization scan ($\eta_{half\ max} \approx$ 380 mV) which dramatically decays shown by a 415 mV overpotential shift at the 11^{th} scan (Figure 6.7a). This indicates that, despite of their high activity, the edge/defect-abundant nature of amorphous MoS_x nanoclusters also confers them a high electrochemical instability. Remarkably, the S-enriched crystalline $(MoS_x)_{1000}$ nanoclusters present a dramatically enhanced stability (Figure 6.7b): although their initial activity is not as high as the amorphous nanocluster counterparts, $\eta_{half\ max}$ is modified

less than 30 mV. We believe that the improved crystallinity and subsequent minor presence of dissolution-prone undercoordinated Mo sites after S-enrichment mitigates electrochemically-induced MoS_x leaching yielding higher stabilities.

6.3 Conclusions

In this chapter, the initially sulfur-deficient $(MoS_{1.9})_{1000}$ size-selected nanoclusters obtained by magnetron sputtering and gas condensation have been successfully sulfur-enriched under vacuum, by sequential use of sulfur evaporation and annealing treatments after their immediate deposition.

This treatment has been shown to induce extended crystalline order, compared with the initially amorphous nanocluster morphology, plus the incorporation of S^{2-} moieties at the $(MoS_x)_{1000}$ nanocluster surface to yield $Mo^{4+}/Mo^aO_bS_c$: S^{2-}/ S_2^{2-} ratios of 1: 4.9±0.1 instead of 1:1.9±0.1. The annealing step is found key to reducing fully the oxygen-containing Mo species to Mo^{4+} and maximizing sulfur incorporation at the nanoclusters surface. A consistent 200 mV positive shift in the HER onset overpotential was found irrespective of sample loading of S-enrichened $(MoS_x)_{1000}$ nanoclusters, whilst the Tafel slope remained unaffected by the sulfur treatment (ca. 145mV dec^{-1}). The 2-fold and more than 30-fold increases in TOF and j_0 values, respectively, surpass the HER enhancements previously reported after S-edge site activation by Ni in $(Ni\text{-}MoS_2)_{1000}$ hybrid nanoclusters from our previous chapter.

The results illuminate the critical role played by S-enrichment and crystallinity in MoS_x nanocluster hydrogen electrocatalysis: creating higher densities of proton-acceptor S sites and lower charge transfer resistances, as well as conferring higher electrochemical stabilities. Nanocluster benchmarking by mass activity emphasizes the remarkable performance of S-rich $(MoS_x)_{1000}$ size-selected nanoclusters at the ultra-low loading level (83.78 ng cm^{-2}, 5% surface coverage): 110.5 mA mg^{-1} at 400 mV overpotential, and 4010.5 mA mg^{-1} at $\eta_{\text{half max}}$= 652 mV.

These results are comparable to the state-of-the-art MoS_2-based catalysts, reflecting the significant activities of size-selected MoS_x nanoclusters obtained at ultra-low loadings, resembling previous enhancements reported for noble metals[48–50].

References

[1] Y. Niu, S. Park, R. Palmer, Modification of Deposited, Size-Selected MoS2 Nanoclusters by Sulphur Addition: An Aberration-Corrected STEM Study, Inorganics. 5 (2016) 1. doi:10.3390/inorganics5010001.

[2] Z. Wu, Y. Wang, Y. Ye, J. Feng, M. Zhang, Y. Luo, L. He, W. Cao, First-principles study of monolayer MoS2 with deficient and excessive Mon and Sn (n = -3 --> 3) clusters on 5 X 5 supercells, Comput. Mater. Sci. 121 (2016) 124–130. doi:10.1016/j.commatsci.2016.04.036.

[3] M.J. Cuddy, K.P. Arkill, Z.W. Wang, H.-P. Komsa, A. V Krasheninnikov, R.E. Palmer, Fabrication and atomic structure of size-selected, layered MoS2 clusters for catalysis., Nanoscale. 6 (2014) 12463–12469. doi:10.1039/c4nr04317k.

[4] M.J. Cuddy, Size-selected molybdenum disulfide clusters for hydrogen evolution, Nanoscale Physics Research Laboratory, School of Physics and Astronomy, University of Birmingham, 2013.

[5] R.P. Tucker, Notes on the Sublimation of Sulfur between 25° and 50° C, Ind. Eng. Chem. 21 (1929) 44–47. doi:10.1021/ie50229a014.

[6] R.N. Grugel, H. Toutanji, Sulfur "concrete" for lunar applications - Sublimation concerns, Adv. Sp. Res. 41 (2008) 103–112. doi:10.1016/j.asr.2007.08.018.

[7] E. Schmidt, C. Sourisseau, G. Meunier, A. Levasseur, Amorphous molybdenum oxysulfide thin films and their physical characterization, Thin Solid Films. 260 (1995) 21–25. doi:10.1016/0040-6090(94)06463-6.

[8] W. Grunert, A.Y. Stakheev, R. Feldhaus, K. Anders, E.S. Shpiro, K.M. Minachev, Analysis of Mo(3d) XPS Spectra of Supported Mo Catalysts: An Alternative Approach, J. Phys. Chem. 95 (1991) 1323–1328. doi:10.1021/j100156a054.

[9] H. Vrubel, X. Hu, Growth and activation of an amorphous molybdenum sulfide hydrogen evolving catalyst, ACS Catal. 3 (2013) 2002–2011. doi:10.1021/cs400441u.

[10] T. Weber, J.C. Muijsers, J.W. Niemantsverdriet, Structure of Amorphous MoS3, J. Phys. Chem. 99 (1995) 9194–9200.

[11] S.R. Kelemen, G.N. George, M.L. Gorbaty, Direct determination and quantification of sulphur forms in heavy petroleum and coals 1. The X-ray photoelectron spectroscopy (XPS) approach, Fuel. 69 (1990) 939–944.

[12] D. Escalera-López, Y. Niu, J. Yin, K. Cooke, N. V. Rees, R.E. Palmer, Enhancement of the Hydrogen Evolution Reaction from Ni-MoS $_2$ Hybrid Nanoclusters, ACS Catal. (2016) 6008–6017. doi:10.1021/acscatal.6b01274.

[13] C.E. Blackmore, N. V Rees, R.E. Palmer, Modular construction of size-selected multiple-core Pt-TiO2 nanoclusters for electro-catalysis., Phys. Chem. Chem. Phys. (2015). doi:10.1039/c5cp00285k.

[14] Y. Zheng, Y. Jiao, M. Jaroniec, S.Z. Qiao, Advancing the electrochemistry of the hydrogen-evolution reaction through combining experiment and theory., Angew. Chemie (International Ed.). 54 (2015) 52–65. doi:10.1002/anie.201407031.

[15] N. Dubouis, C. Yang, R. Beer, L. Ries, D. Voiry, A. Grimaud, Interfacial Interactions as an Electrochemical Tool To Understand Mo-Based Catalysts for the Hydrogen Evolution Reaction, ACS Catal. 8 (2017) 828–836. doi:10.1021/acscatal.7b03684.

[16] T.R. Hellstern, J. Kibsgaard, C. Tsai, D.W. Palm, L.A. King, F. Abild-Pedersen, T.F. Jaramillo, Investigating Catalyst–Support Interactions To Improve the Hydrogen Evolution Reaction Activity of Thiomolybdate [Mo3S13]2– Nanoclusters, ACS Catal. (2017) 7126–7130. doi:10.1021/acscatal.7b02133.

[17] J. Kibsgaard, T.F. Jaramillo, F. Besenbacher, Building an appropriate active-site motif into a hydrogen-evolution catalyst with thiomolybdate [Mo3S13]2– clusters, Nat. Chem. 6 (2014) 248–253. doi:10.1038/nchem.1853.

[18] J. Bisquert, G. Garcia-Belmonte, F. Fabregat-Santiago, A. Compte, Anomalous transport effects in the impedance of porous film electrodes, Electrochem. Commun. 1 (1999) 429–435. doi:S1388-2481(99)00084-3.

[19] J. Bisquert, G. Garcia-Belmonte, F. Fabregat-Santiago, N.S. Ferriols, P. Bogdanoff, E.C. Pereira, Doubling Exponent Models for the Analysis of Porous Film Electrodes by Impedance. Relaxation of TiO2 Nanoporous in Aqueous Solution, J. Phys. Chem. B. 104 (2000) 2287–2298. doi:10.1021/jp993148h.

[20] A.P. Murthy, J. Theerthagiri, J. Madhavan, K. Murugan, Highly active MoS2 /carbon electrocatalysts for the hydrogen evolution reaction – insight into the effect of the internal resistance and roughness factor on the Tafel slope, Phys. Chem. Chem. Phys. 19 (2017) 1988–1998. doi:10.1039/C6CP07416B.

[21] H. Vrubel, T. Moehl, M. Grätzel, X. Hu, Revealing and accelerating slow electron transport in amorphous molybdenum sulphide particles for hydrogen evolution reaction, Chem. Commun. 49 (2013) 8985. doi:10.1039/c3cc45416a.

[22] Y. Yu, S.Y. Huang, Y. Li, S.N. Steinmann, W. Yang, L. Cao, Layer-dependent electrocatalysis of MoS2 for hydrogen evolution, Nano Lett. 14 (2014) 553–558. doi:10.1021/nl403620g.

[23] D. Fu, J. Zhou, S. Tongay, K. Liu, W. Fan, T.J. King Liu, J. Wu, Mechanically modulated tunneling resistance in monolayer MoS2, Appl. Phys. Lett. 103 (2013) 32–35. doi:10.1063/1.4827301.

[24] R.M. and S. a Salam, Electrical Properties of Molybdenite, Proc. Phys. Soc. Sect. B. 66 (1953) 377. doi:10.1088/0370-1301/66/5/305.

[25] S.R.G. Thakurta, Electrical Properties of Molybdenite, Indian J. Phys. 43 (1969) 169–172.

[26] H. Tributsch, J.C. Bennett, Electrochemistry and Photochemistry of MoS2 Layer Crystals. I, J. Electroanal. Chem. 81 (1977) 97–111.

[27] L.R.L. Ting, Y. Deng, L. Ma, Y.J. Zhang, A.A. Peterson, B.S. Yeo, Catalytic Activities of Sulfur Atoms in Amorphous Molybdenum Sulfide for the Electrochemical Hydrogen Evolution Reaction, ACS Catal. 6 (2016) 861–867. doi:10.1021/acscatal.5b02369.

[28] J.D. Benck, Z. Chen, L.Y. Kuritzky, A.J. Forman, T.F. Jaramillo, Amorphous Molybdenum Sul fi de Catalysts for Electrochemical Hydrogen Production: Insights into the Origin of their Catalytic Activity, ACS Catal. 2 (2012) 1916–1923.

[29] Y. Li, Y. Yu, Y. Huang, R.A. Nielsen, W.A. Goddard, Y. Li, L. Cao, Engineering the Composition and Crystallinity of Molybdenum Sulfide for High-Performance Electrocatalytic Hydrogen Evolution, ACS Catal. 5 (2015) 448–455. doi:10.1021/cs501635v.

[30] M.A. Baker, R. Gilmore, C. Lenardi, W. Gissler, XPS investigation of preferential sputtering of S from MoS2 and determination of MoSx stoichiometry from Mo and S peak positions, Appl. Surf. Sci. 150 (1999) 255–262. doi:10.1016/S0169-4332(99)00253-6.

[31] J.S. Kim, J. Kim, J. Zhao, S. Kim, J.H. Lee, Y. Jin, H. Choi, B.H. Moon, J.J. Bae, Y.H. Lee, S.C. Lim, Electrical Transport Properties of Polymorphic MoS2, ACS Nano. 10 (2016) 7500–7506. doi:10.1021/acsnano.6b02267.

[32] B. Lassalle-Kaiser, D. Merki, H. Vrubel, S. Gul, V.K. Yachandra, X. Hu, J. Yano, Evidence from in situ X-ray absorption spectroscopy for the involvement of terminal disulfide in the reduction of protons by an amorphous molybdenum sulfide electrocatalyst, J. Am. Chem. Soc. 137 (2015) 314–321. doi:10.1021/ja510328m.

[33] Y. Deng, L.R.L. Ting, P.H.L. Neo, Y.-J. Zhang, A.A. Peterson, B.S. Yeo, Operando Raman Spectroscopy of Amorphous Molybdenum Sulfide (MoSx) during the Electrochemical Hydrogen Evolution Reaction: Identification of Sulfur Atoms as Catalytically Active Sites for H + Reduction, ACS Catal. (2016) 7790–7798. doi:10.1021/acscatal.6b01848.

[34] P.D. Tran, T. V. Tran, M. Orio, S. Torelli, Q.D. Truong, K. Nayuki, Y. Sasaki, S.Y. Chiam, R. Yi, I. Honma, J. Barber, V. Artero, Coordination polymer structure and revisited hydrogen evolution catalytic mechanism for amorphous molybdenum sulfide, Nat. Mater. 15 (2016) 1–8. doi:10.1038/nmat4588.

[35] D. Escalera-López, R. Griffin, M. Isaacs, K. Wilson, R.E. Palmer, N. V. Rees, Electrochemical sulfidation of WS2 nanoarrays: Strong dependence of hydrogen evolution activity on transition metal sulfide surface composition, Electrochem. Commun. 81 (2017) 106–111. doi:10.1016/j.elecom.2017.06.016.

[36] B. Hinnemann, P. Moses, J. Bonde, K.P. Jørgensen, J.H. Nielsen, S. Horch, I. Chorkendorff, J.K. Nørskov, Biomimetic hydrogen evolution: MoS2 nanoparticles as catalyst for hydrogen evolution, J. Am. Chem. Soc. 127 (2005) 5308–5309. http://pubs.acs.org/doi/abs/10.1021/ja0504690.

[37] D. Voiry, M. Salehi, R. Silva, T. Fujita, M. Chen, Conducting MoS2 nanosheets as catalysts for hydrogen evolution reaction, Nano Lett. 13 (2013) 6222–6227. http://pubs.acs.org/doi/abs/10.1021/nl403661s.

[38] M.-R. Gao, M.K.Y. Chan, Y. Sun, Edge-terminated molybdenum disulfide with a 9.4-Å interlayer spacing for electrochemical hydrogen production., Nat. Commun. 6 (2015) 7493. doi:10.1038/ncomms8493.

[39] J. Kibsgaard, Z. Chen, B.N. Reinecke, T.F. Jaramillo, Engineering the surface structure of MoS2 to preferentially expose active edge sites for electrocatalysis., Nat. Mater. 11 (2012) 963–969. doi:10.1038/nmat3439.

[40] J. Kibsgaard, T.F. Jaramillo, Molybdenum phosphosulfide: an active, acid-stable, earth-abundant catalyst for the hydrogen evolution reaction., Angew. Chemie (International Ed.). 53 (2014) 14433–7. doi:10.1002/anie.201408222.

[41] Y. Zhang, L. Zuo, Y. Huang, L. Zhang, F. Lai, W. Fan, T. Liu, In-Situ Growth of Few-Layered MoS2 Nanosheets on Highly Porous Carbon Aerogel as Advanced Electrocatalysts for Hydrogen Evolution Reaction, ACS Sustain. Chem. Eng. 3 (2015) 3140–3148. doi:10.1021/acssuschemeng.5b00700.

[42] D. McAteer, Z. Gholamvand, N. McEvoy, A. Harvey, E. O'Malley, G.S. Duesberg, J.N. Coleman, Thickness Dependence and Percolation Scaling of Hydrogen Production Rate in MoS 2 Nanosheet and Nanosheet–Carbon Nanotube Composite Catalytic Electrodes, ACS Nano. 10 (2016) 672–683. doi:10.1021/acsnano.5b05907.

[43] B. Seo, G.Y. Jung, Y.J. Sa, H.Y. Jeong, J.Y. Cheon, J.H. Lee, H.Y. Kim, J.C. Kim, H.S. Shin, S.K. Kwak, S.H. Joo, Monolayer-precision synthesis of molybdenum sulfide nanoparticles and their nanoscale size effects in the hydrogen evolution reaction, ACS Nano. 9 (2015) 3728–3739. doi:10.1021/acsnano.5b00786.

[44] G. Li, D. Zhang, Q. Qiao, Y. Yu, D. Peterson, A. Zafar, R. Kumar, S. Curtarolo, F. Hunte, S. Shannon, Y. Zhu, W. Yang, L. Cao, All The Catalytic Active Sites of MoS2 for Hydrogen Evolution, J. Am. Chem. Soc. 138 (2016) 16632–16638. doi:10.1021/jacs.6b05940.

[45] J. Xie, J. Zhang, S. Li, F. Grote, X. Zhang, H. Zhang, R. Wang, Y. Lei, B. Pan, Y. Xie,

Controllable disorder engineering in oxygen-incorporated MoS2 ultrathin nanosheets for efficient hydrogen evolution, J. Am. Chem. Soc. 135 (2013) 17881–17888. doi:10.1021/ja408329q.

[46] Y. Garsany, J. Ge, J. St-Pierre, R. Rocheleau, K.E. Swider-Lyons, Analytical Procedure for Accurate Comparison of Rotating Disk Electrode Results for the Oxygen Reduction Activity of Pt/C, J. Electrochem. Soc. 161 (2014) F628–F640. doi:10.1149/2.036405jes.

[47] K.J.J. Mayrhofer, D. Strmcnik, B.B. Blizanac, V. Stamenkovic, M. Arenz, N.M. Markovic, Measurement of oxygen reduction activities via the rotating disc electrode method: From Pt model surfaces to carbon-supported high surface area catalysts, Electrochim. Acta. 53 (2008) 3181–3188. doi:10.1016/j.electacta.2007.11.057.

[48] E.A. Paoli, F. Masini, R. Frydendal, D. Deiana, C. Schlaup, M. Malizia, T.W. Hansen, S. Horch, I.E.L. Stephens, I. Chorkendorff, Oxygen evolution on well-characterized mass-selected Ru and RuO2 nanoparticles, Chem. Sci. 6 (2015) 190–196. doi:10.1039/C4SC02685C.

[49] E. Kemppainen, A. Bodin, B. Sebok, T. Pedersen, B. Seger, B. Mei, D. Bae, P.C.K. Vesborg, J. Halme, O. Hansen, P.D. Lund, I. Chorkendorff, Scalability and feasibility of photoelectrochemical H2 evolution: the ultimate limit of Pt nanoparticle as an HER catalyst, Energy Environ. Sci. 8 (2015) 2991–2999. doi:10.1039/C5EE02188J.

[50] P. Hernandez-Fernandez, F. Masini, D.N. McCarthy, C.E. Strebel, D. Friebel, D. Deiana, P. Malacrida, A. Nierhoff, A. Bodin, A.M. Wise, J.H. Nielsen, T.W. Hansen, A. Nilsson, I.E.L. Stephens, I. Chorkendorff, Mass-selected nanoparticles of PtxY as model catalysts for oxygen electroreduction, Nat. Chem. 6 (2014) 732–738. doi:10.1038/nchem.2001.

Chapter 7

Plasma-etched MoS_2 and WS_2 crystals: implications of nanocone array profile in the mass transport and hydrogen evolution properties

7.1 Introduction

Maximization of the edge exposure is paramount in transition metal dichalcogenides (TMDs) to obtain improved HER activities. Among the plethora of strategies employed, physical techniques such as plasma etching have provided successful results.[1–3] Previous investigations at the NPRL have optimized the formation of reproducible nanopillar arrays assisted by nanosphere lithography masking and plasma etching treatments,[4–6] this being used in MoS_2 crystals.[7] By comparison with edge-abundant planar TMDs, the preparation of 3D nanoarrays not only promotes the exposure of TMD edge sites by defect formation, but also confers these surfaces amplified mass transport properties arising from their nanometric profile.

In this chapter we evaluate the formation of nanoarray structures by nanosphere lithography and plasma etching on two different TMD crystal surfaces: MoS_2 and WS_2. The influence of plasma etching parameters in the resulting TMD surface nanopattern and the subsequent effect in the surface composition, mass transport and HER electrocatalysis are discussed. Additionally, the effect of electrochemical testing in the TMD nanostructures topography and HER activity is investigated.

7.2 Results and discussion

7.2.1 Fabrication and characterization of nanopillar arrays

SEM micrographs of MoS_2 (Figure 7.1a) and WS_2 (Figure 7.1b) nanosheets after 220 nm nanospheres (NSs) deposition show the formation of monolayers with a very high degree of coverage and compactness. The long-established protocol used for the preparation of hexagonally close-packed 220 nm NSs monolayers over substrates with different physicochemical properties such as gold[8] and silicon[9] explains the successful few-to-single monolayer formation on the TMD surfaces studied. Point defects are present on the NS layers, arising from TMD surface defects and their lack of atomic planarity, and estimation of the NS layer number is limited by the resolution of the FE-SEM microscope.

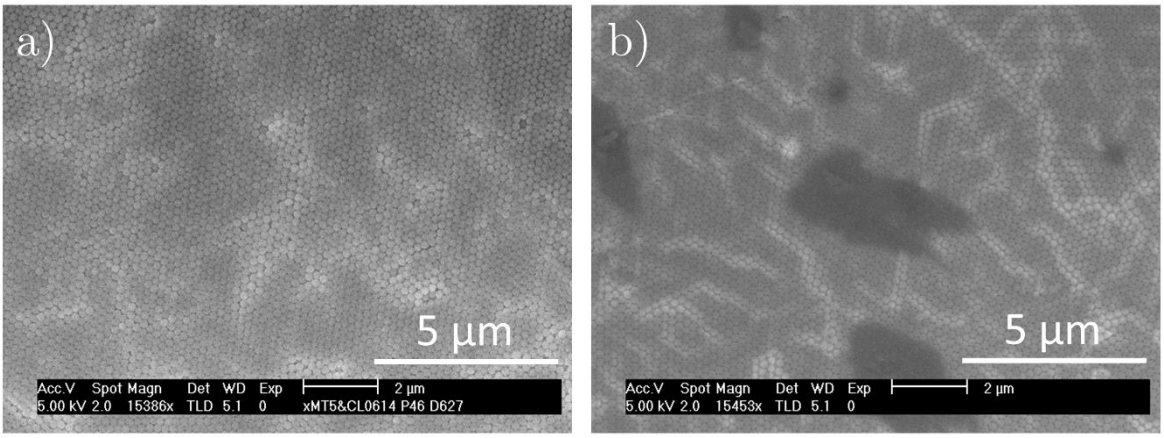

Figure 7.1. FE-SEM micrographs of 200 nm polystyrene-latex NS deposition on a) MoS_2 and b) WS_2 crystals

The effects of plasma etching parameters on the NS-modified TMD crystals were then investigated. The initial isotropic oxygen plasma etching step was equivalent for all samples (40 s, 100 W RF power), whilst the duration of the subsequent anisotropic SF_6/C_4F_8 plasma etching step was varied to explore the influence of the plasma exposure time on the final surface

nanopattern. Table 7.1 lists the etching parameters used and nanopillar dimensions obtained for MoS_2 and WS_2 crystals measured from SEM micrographs (representative SEM micrographs of the nanopillars are shown in Figure 7.2).

Material	SF_6/C_4F_8 plasma etching time / s	Angle-corrected nanopillar height/ nm	Nanopillar diameter / nm	Nanopillar interspacing / nm	Aspect ratio	Radial coordinate, R	Normal coordinate, Z	Figure
MoS_2	15 ± 1	270 ± 20	200 ± 30	23 ± 1	1.3 ± 0.3	1.3	2.7	7.2a
	32 ± 1	380 ± 40	200 ± 10	17 ± 5	1.9 ± 0.3	1.2	3.8	7.2b
	38 ± 1	360 ± 20	190 ± 10	42 ± 3	1.9 ± 0.2	1.4	3.8	-
	45 ± 1	250 ± 20	110 ± 10	23 ± 1	2.4 ± 0.2	1.4	4.5	7.2c
	60 ± 1	580 ± 20	230 ± 40	9 ± 1	2.5 ± 0.5	1.2	5.0	7.2d
WS_2	16 ± 1	300 ± 20	110 ± 10	110 ± 10	2.8 ± 0.3	2.3	5.5	7.2e
	31 ± 1	350 ± 30	110 ± 10	81 ± 4	3.1 ± 0.3	2	6.4	7.2f
	31 ± 1	380 ± 30	150 ± 20	34 ± 4	2.5 ± 0.3	1.4	5.1	-
	46 ± 1	180 ± 20	140 ± 20	57 ± 7	1.3 ± 0.3	1.6	2.6	7.2g
	61 ± 1	-	-	-	-			7.2h

Table 7.1. Compilation of height (h_{nanoc}), diameter and interspacing of the nanopillars obtained after plasma etching of MoS_2 and WS_2 crystals as a function of the SF_6/C_4F_8 plasma etching time. Etching time inaccuracy is related to the one second high ICP power and flow rate "strike step" required for the formation of the SF_6/C_4F_8 plasma.

Significant variations in morphology were found on varying the etching time. For MoS_2, short etching times (Figure 7.2a) created closely-spaced arrays of cylindrical pillars, whereas longer times resulted in arrays of cones with negligible interspacing. In addition, a nanopillar height maximum was achieved at approx. 30 s (Figure 7.2b), indicating that the SF_6/C_4F_8 etching could be subdivided into two regimes.

The first regime ($<$ 30 s etching time) involved both the MoS_2 etching as well as the etching of the remaining shrunken NSs monolayer. The transition from a nanocylinder array to a nanocone array, observed between 15 and 30 s etching, was driven by the survival of partially

etched NSs. In this regime, the slower NS erosion rate compared with MoS_2 appears to cause SF_6/C_4F_8 plasma etching of MoS_2 material to occur by a 'side-on' mechanism, leading to conical structures with increased aspect ratios; higher etching times lead to higher nanopillar heights.

The second regime (> 30 s etching time) occurs when the NSs have been fully etched away, leaving the conical array structures uncovered. This resulted in a preferential etching of the more reactive top section of the nanocones leading to a truncated nanocone array (see Figure 7.2c). As a consequence, in this regime higher etching times led to lower nanopillar heights with increased aspect ratios. Depletion of highly-reactive nanocone tips at very long etching times (Figure 7.2d) ultimately resulted in a top-down governed etching, obtaining very large nanopillars (>500 nm tall) with high aspect ratios.

For WS_2 crystals, all etching times led to nanocone array morphologies with a clear interspacing. Theoretical hardness values (based on Vickers' indentation method) would seem to indicate that bulk WS_2 is a harder material than bulk MoS_2 (HV_{max} values of 10391 and 9703 MPa respectively).[10] However, the shorter and further interspaced nanocones present in plasma-etched WS_2 compared to those found in MoS_2 at equivalent low etching times (Figures 7.2e and 7.2f), suggest a higher chemical reactivity (i.e. dissolution rate) of WS_2 to the SF_6/C_4F_8 plasma. This higher horizontal etching rate compared to MoS_2 then justifies the narrower nanocone diameters found at short etching times: 110 ± 10 nm (WS_2) vs. 200 ± 30 nm (MoS_2) for 15 ± 1 s SF_6/C_4F_8 plasma etching. An increase in etching time generated taller nanocones with shorter interspacings: this reflects a shift from a 'side-on' to a top-down etching profile. At long etching times (>45 s), the faster WS_2 etching rate results in the deformation of the array structure (Figure 7.2g) to form ultimately an amorphous structure (Figure 7.2h), preventing the formation of truncated nanocone array structures.

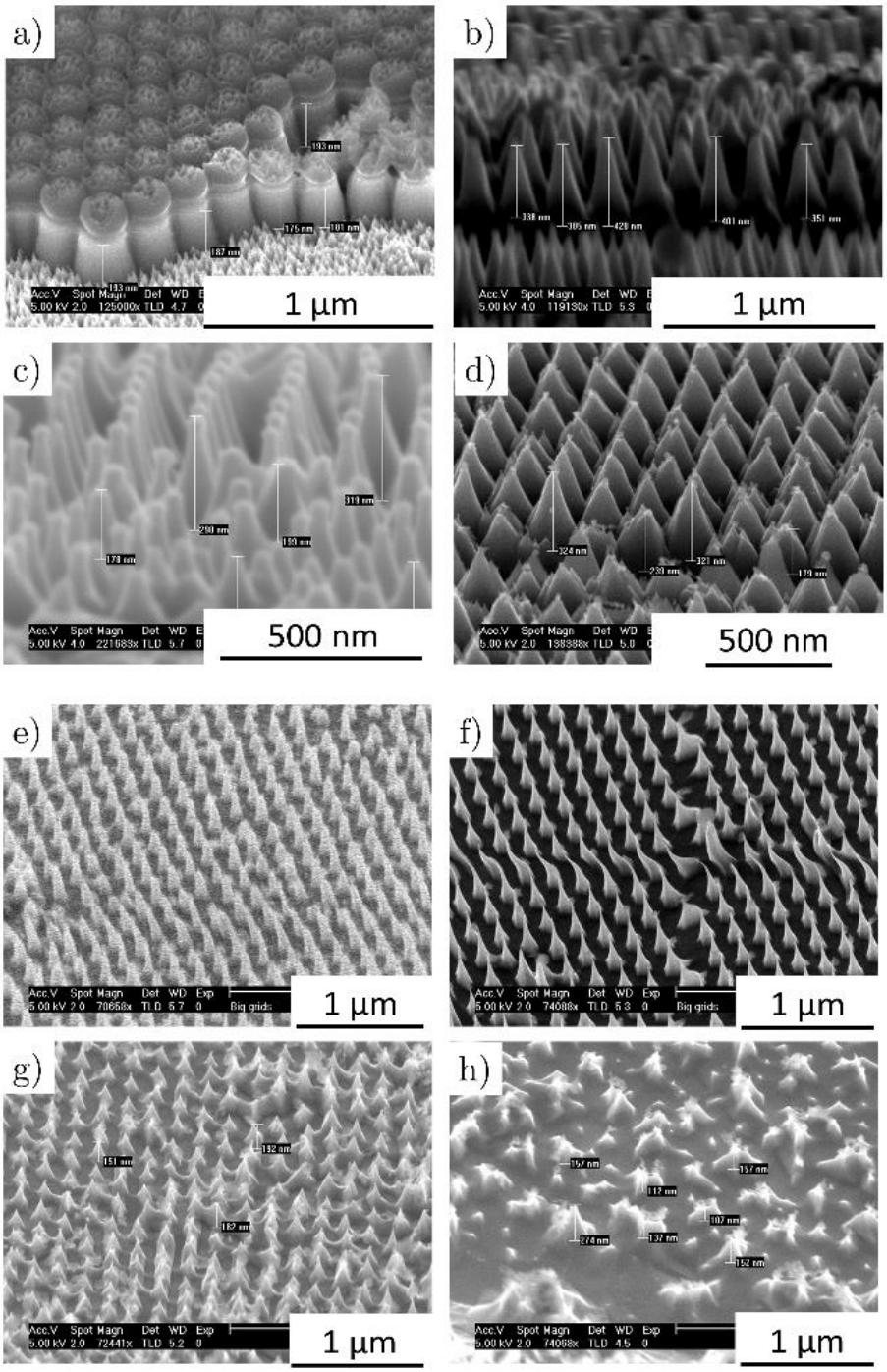

Figure 7.2. FE-SEM micrographs of SF_6/C_4F_8 plasma-etched MoS_2 crystals for a) 15 ± 1 s (45° tilt angle), b) 32 ± 1 s (80° tilt angle), c) 45 ± 1 s (85° tilt angle) and d) 60 ± 1 s (45° tilt angle) and SF_6/C_4F_8 plasma-etched WS_2 crystals for e) 16 ± 1 s, f) 31 ± 1 s, g) 46 ± 1 s and h) 61 ± 1 s (all imaged at 45° tilt angle). Image distortion in e) and f) is attributed to SEM distortions: such areas are not considered during nanopattern characterization.

XPS measurements were acquired to evaluate changes in the WS_2 samples' surface composition after plasma etching (Figure 7.3, see Table 7.2 for detailed analysis), in order to compare our previous results obtained on equivalent plasma-etched MoS_2.[7] The high-resolution W *4f* spectra of the as-received WS_2 crystal presents the characteristic W $4f_{7/2}$:$4f_{5/2}$ spin-orbit doublet of the semiconducting 2H phase (Figure 7.3a, binding energies of ~32.65 and ~34.8 eV, respectively),[11] with no observable contribution from any other WS_2 phases (1T) or W compounds (WO_x), whereas the S *2p* spectra exhibits the S $2p_{3/2}$:$2p_{1/2}$ spin orbit doublet (Figure 7.3b, 162.3 and 165.1 eV, respectively) from the S^{2-} oxidation state,[12] giving a W:S ratio of 1:2.0±0.1 expected for crystalline WS_2.[13]

	Relative XPS photoemission percentage / %				
Sample	WS_2 2H phase	WS_2 1T phase	WO_2	S^{2-}	SO_x^{y-}
As-received	100	0	0	100	0
16 ± 1 s	98.1	1.9	0	95.7	4.3
31 ± 1 s	97.0	0.9	2.1	89.2	10.8
(*R*= 2, *Z*= 6.4)					
31 ± 1 s	94.8	4.4	0.8	81.1	18.9
(*R*= 1.4, *Z*= 5.1)					
61 ± 1 s	98.3	1.7	0	80.1	19.9

Table 7.2. Relative XPS photoemission percentages for as-received and C_4F_8/SF_6 plasma-etched WS_2 crystals.

The XPS spectra for the freshly plasma-etched samples present, on the other hand, additional surface components. In the case of the W *4f* region (Figures 7.3c, 7.3e, 7.3g and 7.3i), spin-orbit doublets arising from the 1T phase (~31.65 and ~33.8 eV) and from WO_2 (~33.0 and ~35.2 eV)[14] can be detected. For the S *2p* region (Figures 7.3d, 7.3f, 7.3h and 7.3j), an additional broad signal centered at ~168 eV is found, related to S high oxidation states widely

ascribed to SO_x^{y-} species.[15,16] Thus, plasma-etching promotes the exposure of metallic 1T sites, presumably located at the nanopillars' surface, but also a conversion of a small fraction of WS_2 to WO_2. The latter is supported by an increase in the relative content of oxidized SO_x^{y-} species vs. S^{2-} species as the plasma-etching time increases (from 0% at t = 0 to 19.9% at t = 61 ± 1s, see Table 7.2). Compared to WS_2, however, previously reported freshly-fabricated plasma etched MoS_2 nanocone arrays present significantly higher MoO_x surface contents, with $MoS_2/MoO_2/MoO_3$ relative XPS molar percentages of 56.1/35.8/8.1.[7] This can be understood by the well-reported MoS_2 high reactivity with RF-oxygen [1] and ICP SF_6-based plasmas [2]: these treatments generate structural damage within the MoS_2 crystallite (e.g. broadening of the A_{1g} and $E^1{}_{2g}$ Raman vibration modes)[17] and formation of oxygen-containing MoO_xS_y species.[18] Such oxygen incorporation can be understood by the low energies required to form sulfur vacancies (2.12 eV)[19] which can be surpassed, for electrons generated by SF_6-based plasmas, with power densities as low as ~ 1.5mW cm^{-3} [2]. Thus, despite of exhibiting a slight broadening of the W $4f_{7/2}$:$4f_{5/2}$ FWHM values (~0.8 eV pristine vs. ~0.9 eV plasma-etched), WS_2 seems to present a minor structural damage and consequently a lower oxygen incorporation after plasma-etching.

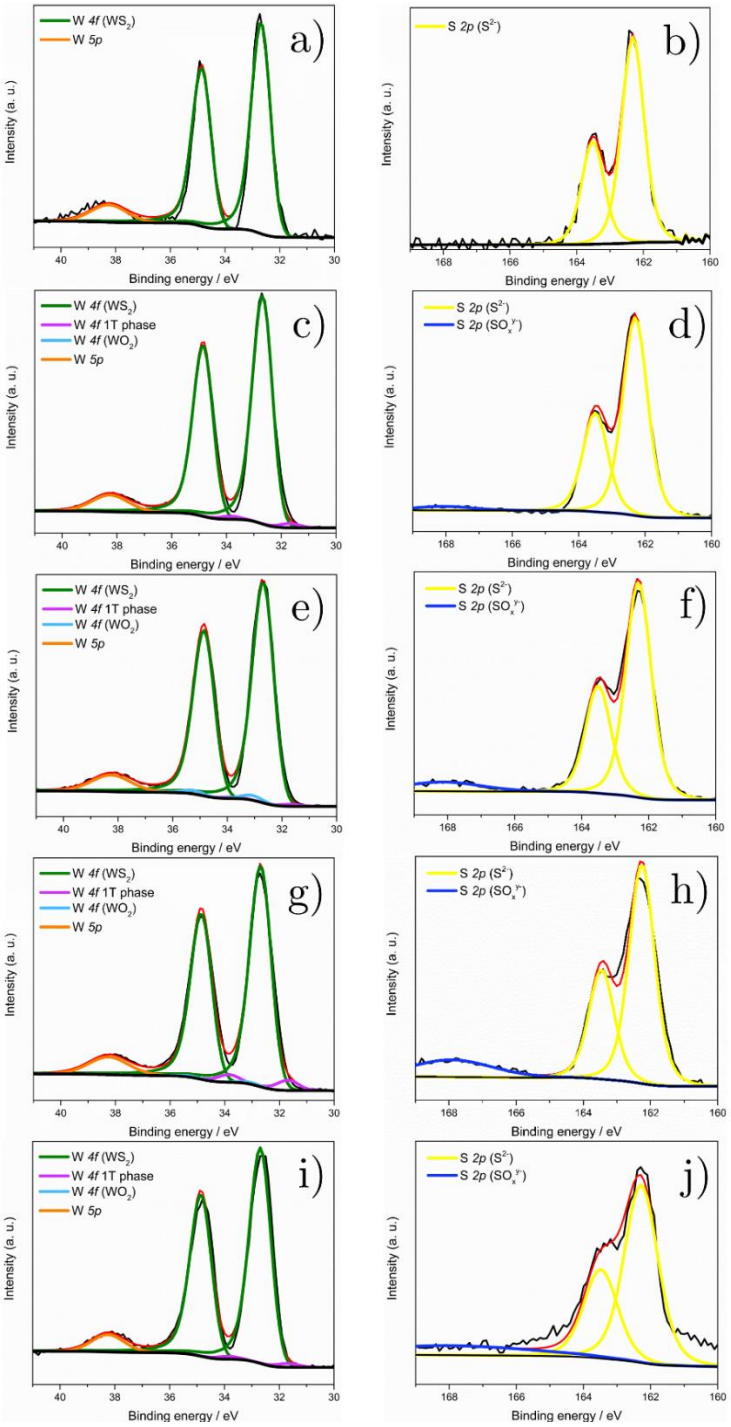

Figure 7.3. High-resolution XPS spectra of W 4f (left) and S 2p (right) regions for SF_6/C_4F_8 plasma-etched WS_2 crystals: as-received (first row), 16 ± 1 s (second row), 31 ± 1 s (R= 2, Z= 6.4, third row), 31 ± 1 s (R= 1.4, Z= 5.1, fourth row) and 61 ± 1 s (fifth row). Labels: W^{4+} $4f_{7/2:5/2}$ WS_2 2H phase (green), W^{4+} $4f_{7/2:5/2}$ WS_2 1T phase (magenta), W^{4+} $4f_{7/2:5/2}$ from WO_2 (light blue), W $5p$ (orange), S $2p_{3/2:1/2}$ from S^{2-}(yellow) and S 2p from SO_x^{y-} (dark blue).

The relatively low 1T phase contents for plasma-etched WS_2 samples (≤ 4%, Table 7.2) can be explained by the intrinsic surface-sensitive nature of XPS. As the average XPS maximum photoelectron space depth is of ca. 10 nm, XPS can only probe the outermost surface of the hundreds of nanometers-thick WS_2 nanocone arrays (i. e. the nanocone tip surface). Thus, XPS cannot quantify the 1T sites present at the nanocones' lower regions, which should be main contributors for both surface area and HER catalysis. Further evidence can be drawn from the actual 1T phase percentages obtained: highest 1T contents were found in the sample with lower aspect ratio (ca. 4.4% for 31 ± 1 s, aspect ratio=3.1 ± 0.3) and vice versa (ca. 0.9% for 31 ± 1 s, aspect ratio=2.5 ± 0.3), which contradicts the expected behavior of higher 1T site contents at higher aspect ratio structures. This can be understood by the wider nanocone tip surfaces found in structures with lower aspect ratios; these imply larger exposed areas at the sub-10 nm region than the sharp structures found in high aspect ratio nanocones, justifying the higher XPS 1T contents found in lower aspect ratio structures.

7.2.2 Electrocatalytic activity for the hydrogen evolution reaction (HER)

Plasma-etched MoS_2 and WS_2 crystals were electrochemically tested in a 2 mM $HClO_4$/ 0.1M $NaClO_4$ aqueous electrolyte to investigate the electrocatalytic enhancement of the hydrogen evolution reaction. Two main voltammetric features can be observed in the cathodic region with this electrolyte: a diffusional reduction wave at ca. -0.3 to -0.7 V (vs. RHE) due to the 2mM proton concentration followed by bulk solvent breakdown at ca. 300-400 mV higher overpotentials. Experiments reported in the literature generally utilize more concentrated electrolytes (0.1 M $HClO_4$ or 0.5 M H_2SO_4) to obtain current densities of -10 mA cm^{-2}_{geom}. This figure of merit represents the current density obtained from a 12.3% efficient solar to hydrogen

cost competitive energy conversion device.[20] The characteristic proton diffusion decay profile observed in this electrolyte, despite of not enabling to achieve the typical -10 mA cm^{-2} benchmarking current densities reported for TMDs, will enable to discern mass transport properties arising from the nanoarray geometries under study. These effects are vital in understanding the interplay between pure catalytic effects and mass transport, which would be masked at higher proton concentrations.

Figure 7.4 shows the linear sweep voltammograms (LSVs) obtained for as-received (unetched) as well as plasma-etched MoS_2 and WS_2 for different etching times at 50 mV s^{-1} scan rate. In both materials a shift in the HER onset potential is observed compared with the unetched samples, ≈ 200 mV for MoS_2 (-0.56 to -0.36 V) and ≈100 mV for WS_2 (-0.44 to -0.34 V), where the onset is measured at a HER current density of 0.05 mA cm^{-2} (see dashed line in Figure 7.4). The maximum HER shift is observed for the 15 s etched MoS_2 sample, ≈320 mV from -0.56 to -0.24 V. This indicates that the plasma etching treatment successfully exposes an increased number of active sites by generation of an edge-abundant nanopillar array, being more effective for MoS_2 than for WS_2.

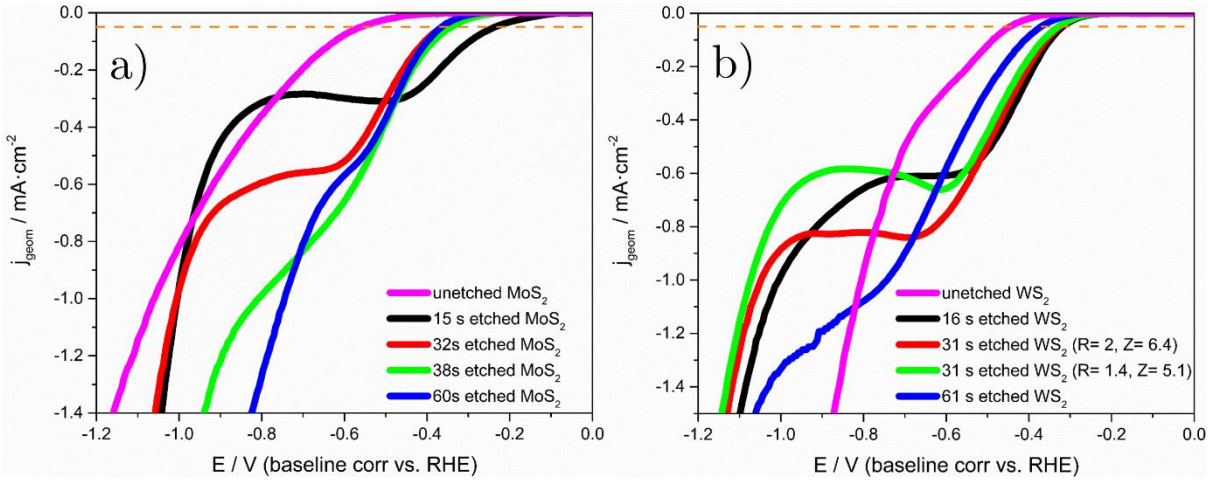

Figure 7.4. Linear sweep voltammograms of SF_6/C_4F_8 plasma-etched a) MoS_2 and b) WS_2 crystals in the 0 to -1.2 V voltage range vs. RHE. Dashed line (orange) indicates $|j_{geom}| = 0.05$ mA cm^{-2} (see text). Voltage scan rate: 50 mV s^{-1}.

For equivalent etching times, the WS_2 samples exhibit higher steady-state current density values than MoS_2 at a given scan rate (Figure 7.5). In order to discern if the origin of the enhanced HER currents in WS_2 samples is due to kinetic or mass transport effects derived from the high-aspect ratio nanoarrayed structures, we analysed the HER peak current variation with voltage scan rate (Randles-Ševčík equation) for the tested samples. Previous investigations on cylindrical micropillar[21,22] and microdisc[23,24] electrode arrays concluded that four different diffusional mass transport regimes could be distinguished, depending upon microelectrode height, radius and interelectrode distances.[24] All samples tested here, based on both nanopillar dimensions and experimental timescales, should satisfy case 4 where the diffusion layer thickness (δ) is larger than both the size and interspacing of the microelectrodes, resulting in a complete overlap of the microelectrode diffusion layers towards a semi-infinite planar diffusion regime, characteristic of macroelectrodes.

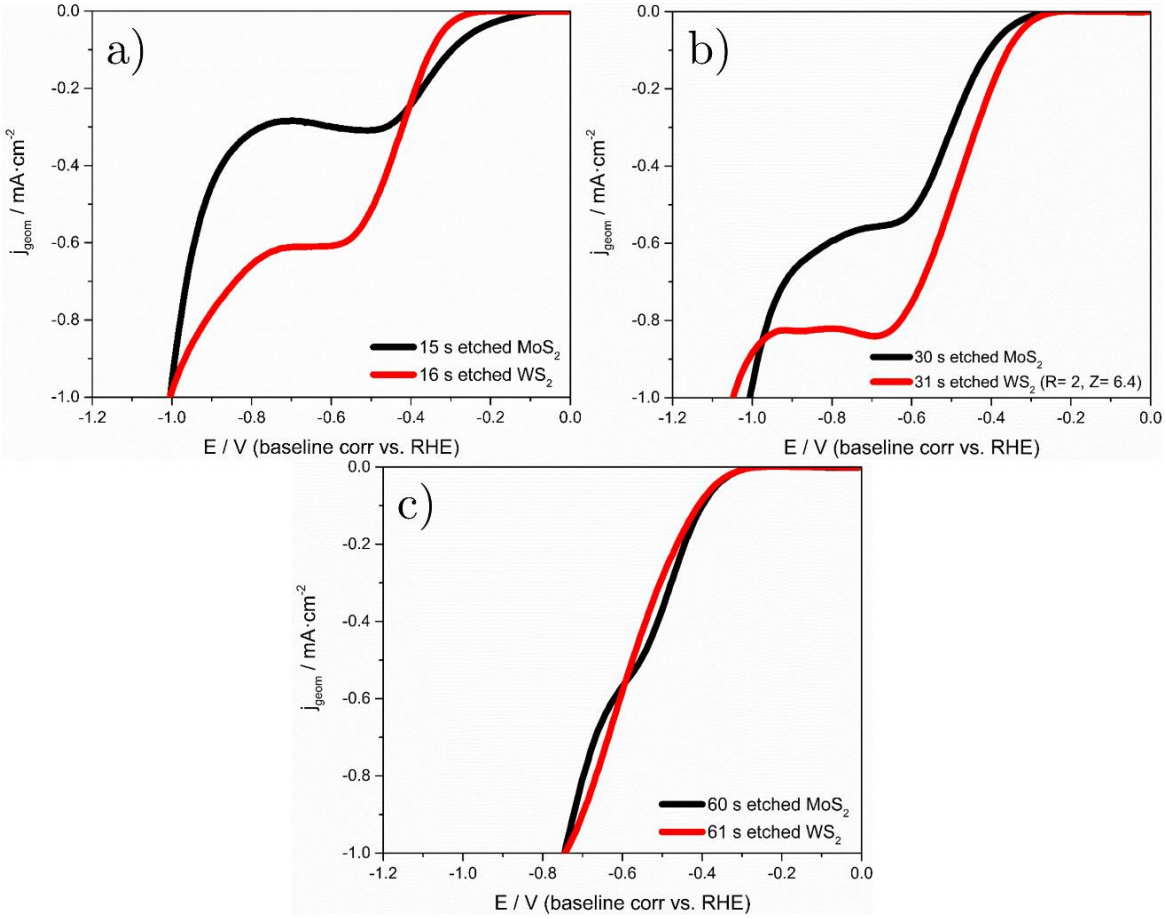

Figure 7.5. Comparison of HER performance of a) 15 ± 1 s, b) 30 ± 1 s and c) 60 ± 1 s SF_6/C_4F_8 plasma-etched MoS_2 (solid black) and WS_2 (solid red) crystals in the 0 to -1.2 V voltage range vs. RHE. Scan rate: 50 mV s^{-1}.

The experimental peak current (plotted here as geometric current densities $|j_P| = |I_P|/A_{geom}$ for normalization purposes) vs. square root of the scan rate ($\nu_{scan}^{1/2}$) plots of plasma-etched MoS_2 crystals (Figure 7.6) are in excellent agreement with those predicted by the irreversible Randles-Ševčík expression for a planar electrode of equivalent geometrical area, irrespective of the scan rate studied.

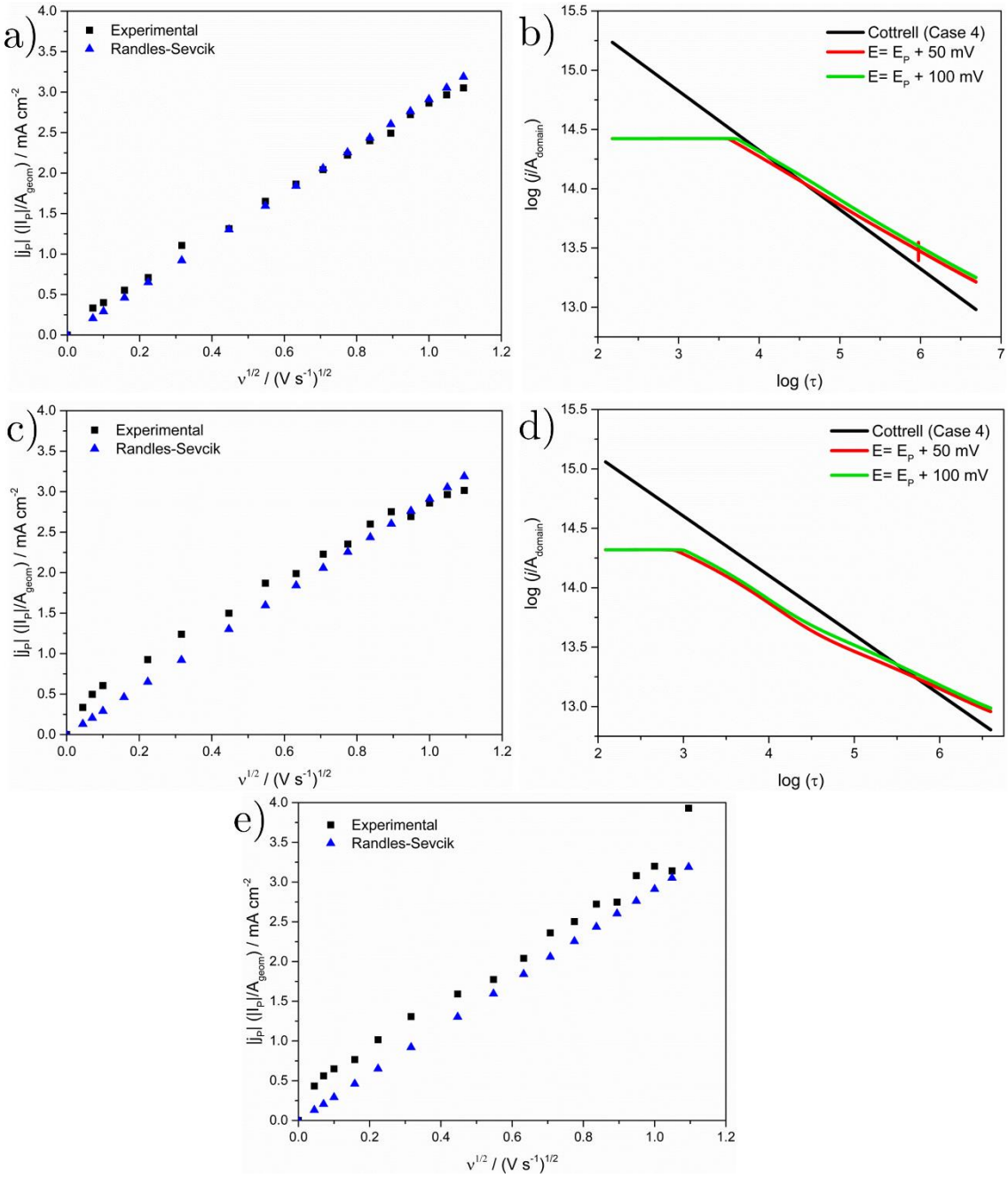

Figure 7.6. Geometric peak current density $|j_P|$ vs. square root of the scan rate $\nu_{scan}^{1/2}$ plots for HER experimental (black) and theoretical values predicted by the irreversible Randles-Ševčík equation (blue) for a) 15 ± 1 s, c) 32 ± 1 s and e) 38 ± 1 s plasma-etched MoS_2 crystals; HER experimental (red=E_P + 50 mV; green= E_P + 100 mV) and theoretical irreversible Randles-Ševčík Case 4 (black) log-log plots of transient dimensionless current densities j/A_{domain} vs. dimensionless time τ for b) 15 ± 1 s and d) 32 ± 1 s plasma-etched MoS_2 crystal.

This would indicate that neither the contribution of the nanopillars to the overall HER current with respect to the MoS_2 crystal geometrical area, nor possible pseudo-thin layer mass transport effects are significant. The radial diffusion profiles formed at individual nanocone overlap due to the narrow nanocone interspacing (≤ 40 nm), resulting in an overall semi-infinite planar diffusion regime (case 4 behaviour, see Section 3.2.4). Therefore, any HER enhancement observed for these samples is due to the exposure of active edge sites rather than to a mass transport enhancement.

The experimental $|j_P|$ vs. $v_{scan}^{1/2}$ plots for plasma-etched WS_2 crystals show increased current densities with respect to the theoretical irreversible Randles-Ševčík HER peak current densities of an equivalent planar electrode (Figure 7.7). These effects are more noticeable for samples with higher aspect ratios and at faster scan rates (v_{scan}> 50mV s^{-1}), in apparent contradiction of the expected case 4 behaviour deriving from the microelectrode array model.[25]

Parameter	Expression
Diffusion domain area, A_{domain}	d^2
Diffusion domain radius, r_{domain}	$\sqrt{d^2/\pi}$
Radial coordinate, R	r_{domain}/r_{nanoc}
Normal coordinate, Z	h_{nanoc}/r_{nanoc}
Dimensionless time, τ	$D_{H^+}t/r_{nanoc}^2$
Dimensionless current, j	$I/(2\pi F C_{H^+,bulk} D_{H^+} r_{nanoc})$

Table 7.3. Definition of dimensionless parameters used for transient chronoamperometry experiments.

In the downsizing from the microelectrode to the nanoelectrode scale, however, the equivalency and diffusional independence of each nanoelectrode in the array might no longer be satisfied. Investigations by Godino et al. on the concentration profiles of recessed nanoelectrode arrays with radius r= 50 nm and diameter d= 1000 nm at a scan rate v_{scan}= 1

V s^{-1} revealed that complete overlapping of the individual nanoelectrode diffusion layers led to a hemispherical diffusion layer characteristic of a microelectrode, contrary to the case 4 scenario predicted for an equivalent microelectrode array.[26] This indicated that, despite being diffusionally independent, the nanoelectrodes in the array are no longer equivalent, and that radial diffusion can be more important in nanoelectrode arrays than in microelectrode arrays.

A computational model accounting for the diffusional field overlapping of adjacent nanoelectrodes in an array was recently proposed, with improved prediction capability.[27] Further experimental investigations of scan rate, nanoelectrode interspacing and population effects confirmed the discrepancies with the microelectrode array behaviour. These are summarized as follows: i) slow scan rates ($\upsilon_{scan} <$ 1 V s^{-1}) enhanced the degree of nanoelectrode diffusion field overlap and inequality, favouring an overall microelectrode response, ii) larger interspacings promoted the diffusionally independent behaviour of each nanoelectrode in the array at a given scan rate, and iii) very densely populated arrays promoted, at slow scan rates, an unequal performance between nanoelectrodes in the inner positions and those in the nanoarray perimeter, where the inner nanoelectrodes resembled the behaviour predicted by the diffusion domain approximation.[26]

Accordingly, this indicates that the overall macroelectrode response obtained for the plasma-etched MoS_2 crystals is mainly due to the densely-packed nanopilllar array geometries obtained, irrespective of the etching time and aspect ratio. The highly overlapped diffusional layers generated by each nanopillar induced by the short interspacings (≤ 40 nm) along with the large dimensions of the MoS_2 crystal (i. e. high density of inner nanopillars) would counterbalance the radial diffusion contribution of the perimetric nanopillars in the overall HER current. Thus, it is hypothesized that only at very fast scan rates will the nanopillars exhibit diffusionally independent layers resembling the behaviour of cases 1 and 2 for microelectrode arrays.[26]

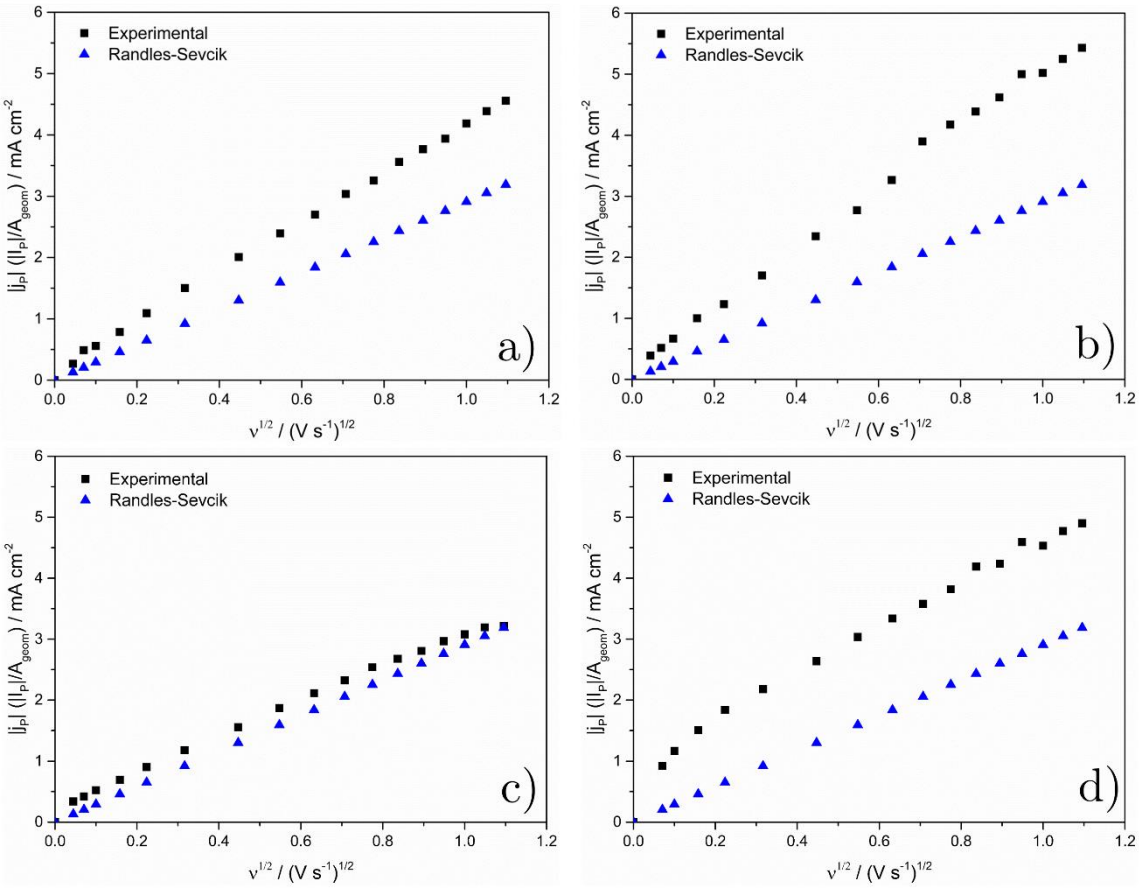

Figure 7.7. Plasma-etched WS_2 crystals geometric peak current density $|j_P|$ vs. square root of the scan rate $\nu_{scan}^{1/2}$ plots for HER experimental (black) and theoretical values predicted by the irreversible Randles-Ševčík equation (blue). Etching conditions: a) 16 ± 1 s, b) 31 ± 1 s (R= 2, Z= 6.4), c) 31 ± 1 s (R= 1.4, Z= 5.1) and d) 61 ± 1 s.

For the plasma-etched WS_2 samples, the clear correlation between increased HER peak current densities and higher aspect ratios at the investigated scan rates rules out an explanation solely based on the nanoarray population density. The WS_2 samples etched for 16s (R= 2.3, Z= 5.5) and 31s (R= 2.0, Z= 6.4) exhibit higher HER peak currents, the latter being the highest despite a smaller nanocone interspacing. This indicates that, apart from the smaller degree of overlap of the nanocone diffusion layers with respect to the MoS_2 samples, WS_2 nanocones with higher aspect ratios could present a larger contribution of radial diffusion as

well as a higher abundance of active edge sites, leading to higher HER currents. These findings would be consistent with effects i) and ii) mentioned previously, as well as with the smaller diffusional overlap predicted for higher aspect ratio nanocone arrays at a given scan rate.[28]

However, for the other 31s-etched WS_2 sample (R= 1.4, Z= 5.1), the densely packed nanocone arrays obtained (interspacing≈ 35 nm) lead to $|j_P|$ values similar to those predicted by the irreversible Randles-Ševčík expression, leading to an overall quasi-planar electrode performance similar to the MoS_2 etched samples. This suggests that the nanopillar interspacing is the governing factor for obtaining nanocone array diffusion regimes different from case 4, as the MoS_2 etched samples exhibit similar nanopillar heights but smaller aspect ratios than the plasma-etched WS_2 counterparts. The effect of the maximized radial diffusion flux to the nanocone apex for low α values (α ≤ 10°, where α is defined as the angle between the nanocone surface and its vertical axis) and its contribution to the overall HER current should be minimal compared with that of the nanocones' surface, as current is radius-dependent, and at the apex r≈0, supporting the key role of the nanocone interspacing in the overall diffusion regimes.[28]

Transient chronoamperometry experiments at potentials beyond that of the HER peak current (+50-100 mV) were performed to gain further insight on the mass transport regimes present at short timescales (t< 5 s). Dimensionless log-log plots of experimental current density vs. time are shown in Figures 7.6b, 7.6d and 7.8, along with the theoretical current plots for microelectrode arrays cases 1 and 4 (see Section I.1 Appendix): definitions of the dimensionless parameters used in the diffusion domain approximation are compiled in Table 7.3. The zero gradient regions observed at short timescales (t< 10 ms for MoS_2 and t< 300 ms for WS_2) are ascribed to non-Faradaic capacitive currents.[29]

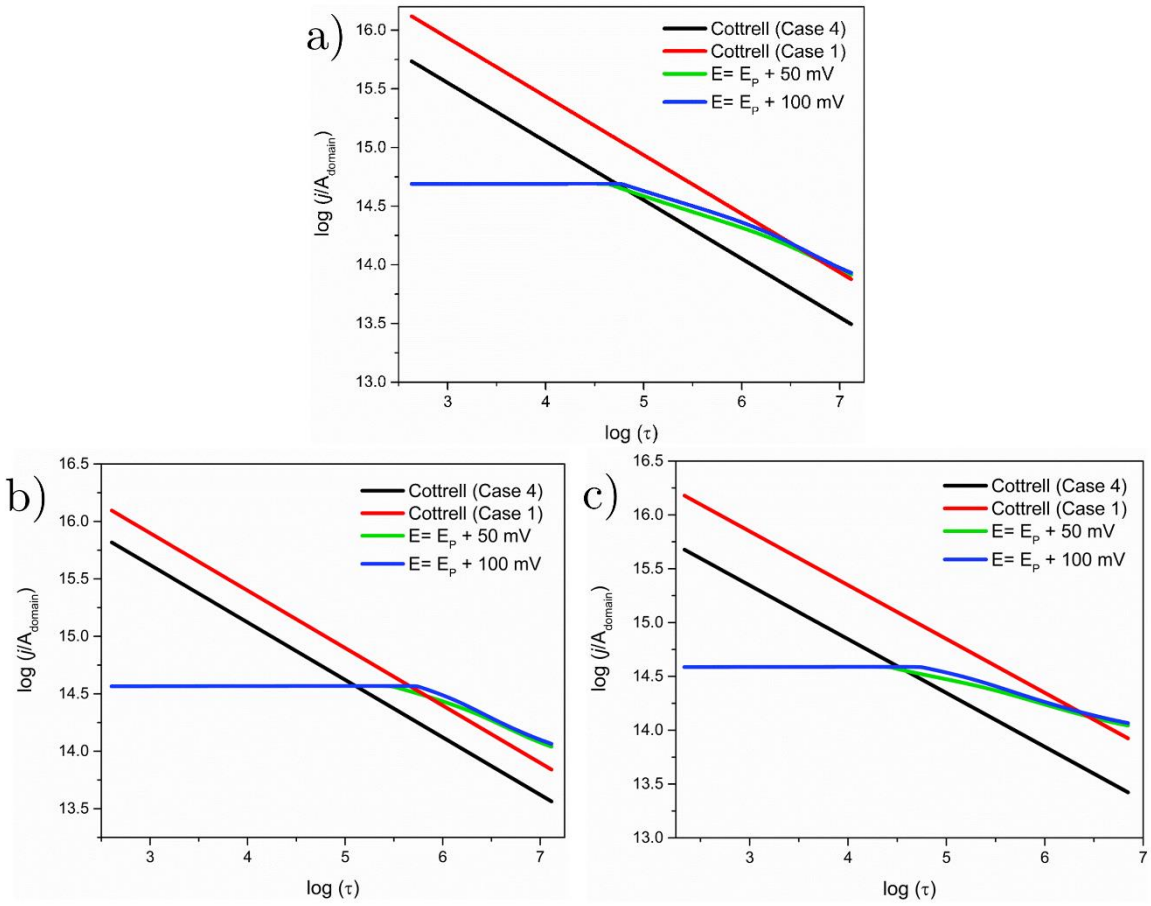

Figure 7.8. a) 31 ± 1 s (R= 2, Z= 6.4), b) 16 ± 1 s and c) 31 ± 1 s (R= 1.4, Z= 5.1) plasma-etched WS_2 crystal HER experimental (red=E_P + 50 mV; green= E_P + 100 mV) and theoretical (black, irreversible Randles-Ševčík Case 4; red, irreversible Randles-Ševčík Case 1) log-log plots of transient dimensionless current densities j/A_{domain} vs. dimensionless time τ.

The response of the MoS_2 etched samples (Figs. 7.6b and 7.6d) seems to converge with the currents predicted by case 4, departing from a Cottrellian regime (characterized by a log-log slope of -1/2) at short timescales through a transitional mass transport regime. The slope and extent of the transitional regime are reported to be intimately linked to nanopillar density and dimensions (radius and height), and thus are difficult to explain experimentally based on dimensionless parameters.[22] Experimental discrepancies with respect to case 4 could be

ascribed to the modification of the geometric area and nanocone geometry by electrochemically-induced restructuring under HER experiments.

Analogous experiments on the WS_2 samples revealed, beyond the capacitive charging current, an absence of Cottrellian behaviour at short timescales followed by a transitional mass transport regime as observed in the MoS_2 samples. For the 31s (R= 2.0, Z= 6.4) etched WS_2 sample (Figure 7.8a), the experimental current converges to the calculated current with a slope of ca. -1/2, indicating that macroscopically the sample behaves with an overall planar diffusion to the nanocones and intercone surfaces and therefore has an electroactive area equivalent to the real surface area.

The 16s (R= 2.3, Z= 5.5) sample (Figure 7.8b) exhibits experimental currents significantly higher than those predicted for planar diffusion, confirming the additional current contribution from radial diffusion. This suggests that the enhanced HER current of the 31s etched sample vs. the 16s etched sample is due to their nanocone larger aspect ratio which exposes more HER active sites rather than to a synergistic contribution from enhanced mass transport.

Finally, for the other 31s etched WS_2 sample (R= 1.4, Z= 5.1), the experimental current divergence from cases 1 and 4, having a log-log slope of approx. -1/4, which suggests a complex mass transport behaviour at short timescales (Figure 7.8c). We hypothesize that at longer timescales this would ultimately converge to a quasi-case 4 behaviour, based on the experimental irreversible Randles-Ševčík plots forced by the narrow nanocone interspacing.

Tafel slope analysis was performed to elucidate the HER efficiency of the catalysts and the HER reaction mechanism. Naturally occurring MoS_2 and WS_2 layers present Tafel slopes (b) of ≈ 120 mV dec^{-1}, characteristic of the Volmer mechanism in which the atomic hydrogen adsorption is the HER limiting step.[30] Pure 1T-phase MoS_2,[31] 1T-phase WS_2 and edge-rich nanosheet samples[32,33] were reported to exhibit slopes of ≈ 40 mV dec^{-1} , ≈ 55 mV dec^{-1} and ≈ 55-60 mV dec^{-1}, respectively .

By contrast, noble metals such as Pt display Tafel slopes of ≈ 30 mV dec^{-1}, following the Volmer-Tafel mechanism under which the desorption of molecular hydrogen is the reaction limiting step.[34] Tafel slope analysis (Figure 7.9) of the 50 mV s^{-1} LSVs reveal that SF_6/C_4F_8 plasma-etched WS_2 samples, with the exception of the 31 ± 1 s etched sample, show Tafel slope values lower than their MoS_2 counterparts. Thus, the HER mechanism and efficiency of the geometrically accessible active edge sites is closer to the best performing HER catalysts in WS_2 than in MoS_2.

For WS_2, values range between 80 and 125 mV dec^{-1}, indicating that the Volmer adsorption mechanism is the HER rate limiting step. Tafel plot values for MoS_2 are in some cases (unetched, 15 ± 1 s etched, 60 ± 1 s etched) higher than the b ≈ 120 mV dec^{-1} value expected, indicating a high TMD through-plane resistance that hinders electron transfer kinetics. The high Tafel slope for unetched MoS_2 (≈ 220 mV dec^{-1}) in comparison with unetched WS_2 (≈ 130 mV dec^{-1}) confirms that the significant HER shift obtained after plasma etching is due to the initially low MoS_2 activity.

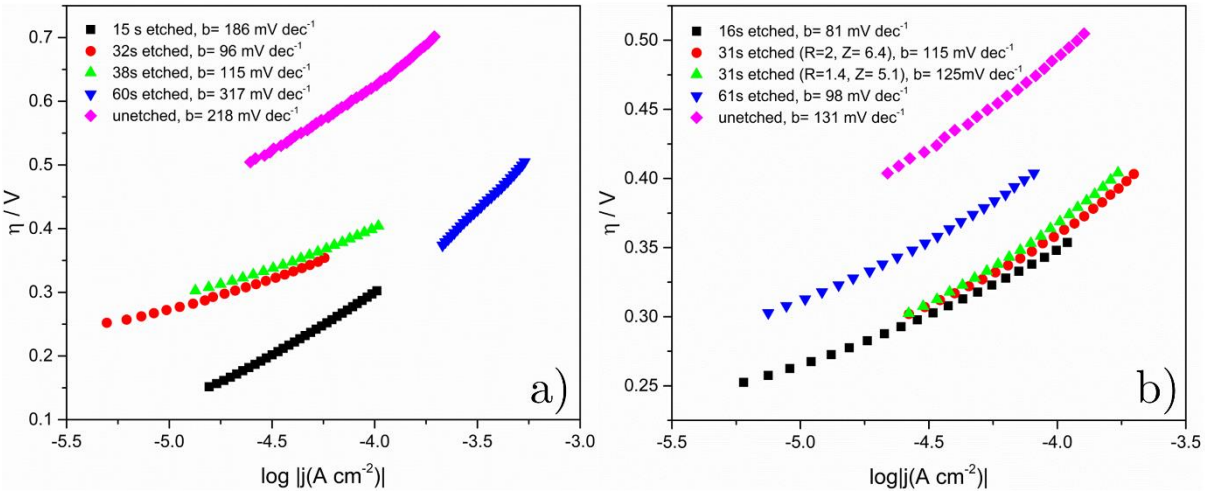

Figure 7.9. Tafel plots (η vs. $\log|j_{geom}|$) of a) MoS_2 and b) WS_2 SF_6/C_4F_8 freshly plasma-etched crystals. Voltage scan rate: 50 mV s^{-1}.

7.2.3 Electron transfer properties of plasma-etched TMDs

The experimental elucidation of electron transfer properties is essential to benchmark the inherent electrochemical properties of a material. Kinetic parameters have not been widely studied for TMDs[35–39] and are generally assessed by calculation of the (apparent) heterogeneous electron transfer (HET) constant k^o_{app} based on electrochemical experiments using redox mediators such as $Fe(CN)_6^{4-}/Fe(CN)_6^{3-}$.[40] Thus, the k^o_{app} calculation should enable the intrinsic electron transfer properties of SF_6/C_4F_8 plasma-etched TMDs to be correlated with their experimental HER performance. Calculation of k^o_{app} was carried out using the Nicholson and Shain method (for $\Delta E_P <$ 220 mV)[41] and the Klinger and Kochi analysis (for $\Delta E_P >$ 220 mV)[42]; for further details see section 3.2.3 Theoretical Background. Experimental ΔE_P values were obtained by performing cyclic voltammograms in an electrolyte containing the $Fe(CN)_6^{4-}/Fe(CN)_6^{3-}$ quasi-reversible redox mediator within scan rates of υ_{scan}=0.01-0.3 Vs^{-1}. This voltage window was selected to avoid overlapping with the inherent

electro-oxidative TMD features at E > +1.10 V vs SCE and the HER onset at E < -0.60 V vs SCE. Experimentally recorded ΔE_P values at υ_{scan}= 100mV s^{-1} and calculated k^o_{app} values obtained from the ψ vs. $\left[\left(\frac{\pi zFD\upsilon_{scan}}{RT}\right)\right]^{-1/2}$ plot are summarized in Figures 7.10a and 7.10b (see Table 7.4 for k^o_{app} values, and Figure 7.10c for Klinger and Kochi plot).

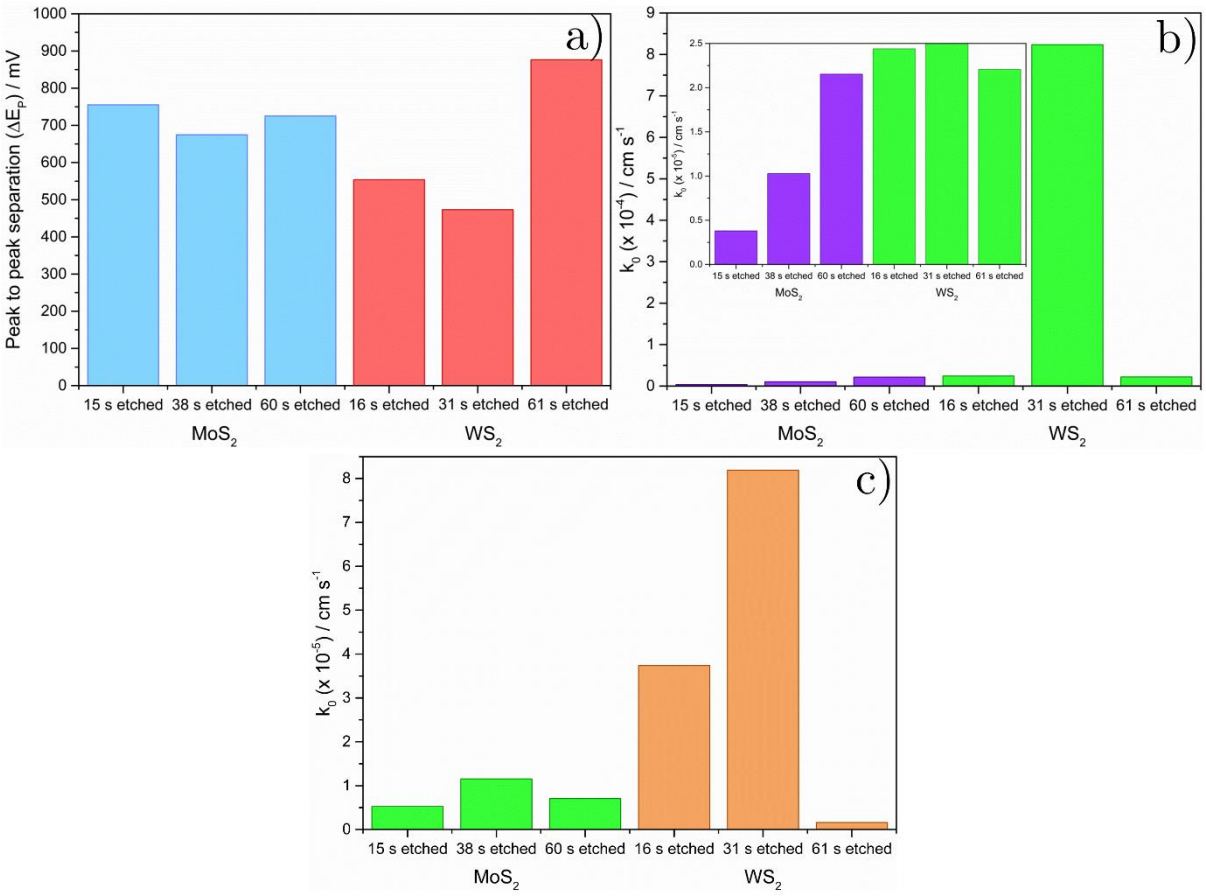

Figure 7.10. a) Peak to peak separations of the ferro/ferricyanide redox probe for plasma-etched MoS_2 (blue) and WS_2 (red) samples at υ_{scan}= 100 mVs^{-1}, b) Heterogeneous electron transfer rate constants k^o_{app} calculation for plasma-etched MoS_2 (purple) and WS_2 (green) samples obtained from the ψ vs. $\left[\left(\frac{\pi zFD\upsilon_{scan}}{RT}\right)\right]^{-1/2}$ plot slope (Inset: zoom of 9b for a k^o_{app} × 10^{-5} cms^{-1} scale bar to highlight MoS_2 values), and c) Calculated k^o_{app} values obtained by the Klinger and Kochi method for υ_{scan}= 100 mV s^{-1}.

Two conclusions can be extracted from the results. First, the plasma-etched WS_2 samples present faster electron transfer kinetics ($k^o_{app} > 2.2 \times 10^{-5}$ cm s^{-1}) than the MoS_2 samples, irrespective of nanopillar dimensions and etching conditions. This supports the HER experimental evidence which suggested that plasma-etched WS_2 is an inherently more electrochemically active material. Secondly, there is a positive correlation between k^o_{app} values and the nanopillar height (Figure 7.11). This seems to indicate that a higher abundance of active edge sites in taller nanopillars improves the electron transfer properties of TMDs (reported k^o_{app} values of bulk MoS_2 and WS_2 are, respectively, 2.1×10^{-5} cm s^{-1} and $<6.3 \times 10^{-6}$ cm s^{-1}),[35,37,43] consistent with previous findings in the literature which correlated a higher exposure of the metallic 1T phase edge sites with enhanced electrical conductivities.[12,31]

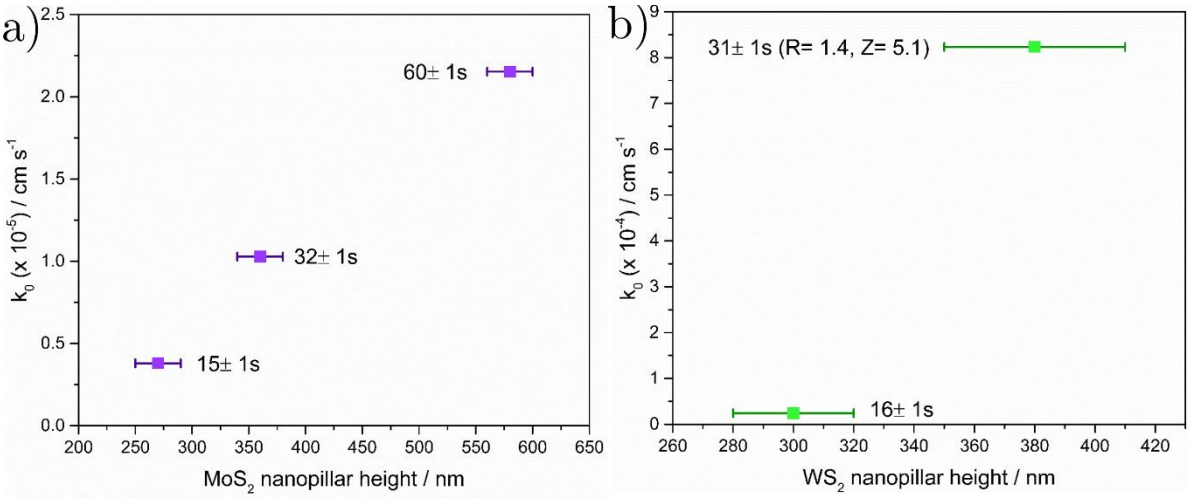

Figure 7.11. Calculated values of k^o_{app} for the $[Fe(CN)_6]^{4-}/[Fe(CN)_6]^{3-}$ redox probe of fresh plasma-etched a) MoS_2 and b) WS_2 crystals (ψ vs. $\left[\left(\frac{\pi zFDv_{scan}}{RT}\right)\right]^{-1/2}$ plot, v_{scan}= 100 mV s^{-1}), vs. the experimental nanopillar height obtained from tilt-angle corrected SEM micrographs.

The enhanced performance of plasma-etched WS_2 vs. MoS_2 crystals lies on their relative stability towards the oxygen plasma employed in the nanosphere shrinking process. Previous XPS studies confirmed the incorporation of oxygen into 2H-MoS_2 single crystals upon RF-oxygen plasma exposure, converting the S^{2-} and Mo^{4+} initial states to S^{6+}, Mo^{5+} and Mo^{6+}

characteristic of molybdenum sulfates ($Mo(SO_4)_2$), molybdenum oxysulfides (MoS_xO_y) and molybdenum oxides (Mo_xO_y), respectively.[18] Recent investigations in our group revealed that air exposed (>20 days) plasma-etched MoS_2 crystals presented an increased MoO_2 content to the detriment of MoS_2, achieving MoO_2/MoS_2 molar percentages of 51.97/45.52.[7] In the case of WS_2, XPS studies on the electrochemically tested, atmosphere-exposed samples revealed a very low WO_2 content (≤2 %),[44] confirming their higher stability against oxygen incorporation from the RF-oxygen plasma step.

Material	SF_6/C_4F_8 plasma etching time / s	R	Z	k^O_{app}, Klinger and Kochi (@ 100mV s^{-1}) / cm s^{-1}	k^O_{app}, ψ vs. $\left[\left(\frac{\pi zFDv_{scan}}{RT}\right)\right]^{-1/2}$ / cm s^{-1}
MoS_2	15 ± 1	1.3	2.7	5.27×10^{-6}	3.80×10^{-6}
	32 ± 1	1.2	3.8	-	-
	38 ± 1	1.4	3.8	1.15×10^{-5}	1.03×10^{-5}
	60 ± 1	1.2	5.0	7.07×10^{-6}	2.15×10^{-5}
WS_2	16 ± 1	2.3	5.5	3.74×10^{-5}	2.44×10^{-5}
	31 ± 1	2	6.4	-	-
	31 ± 1	1.4	5.1	8.19×10^{-5}	8.23×10^{-4}
	61 ± 1	-	-	1.63×10^{-6}	2.21×10^{-5}

Table 7.4. Compilation of heterogeneous electron transfer constants (k^O_{app}) for plasma-etched MoS2 and WS2 crystals.

With regards to the effect of oxygen incorporation on the HER activity of MoS_2, Latiff et al. reported that incremental MoO_2 contents in physical mixtures with bulk MoS_2 worsened the HER performance,[45] contrary to previous results obtained with oxygen-incorporated, few-layered MoS_2.[46] Thus, despite observing an HER enhancement after plasma-etching arising from a higher abundance of edge sites, MoS_2 nanopillar arrays present slower electron transfer properties due to their oxygen impurities compared with the plasma-etched WS_2 samples, following the same behaviour observed for bulk MoS_2.[45]

7.2.4 Analysis of 5-month atmospherically aged samples

An investigation of the influence of air exposure and electrochemically-induced restructuring on the electrocatalytic activity was carried out by testing the SF_6/C_4F_8 plasma-etched WS_2 crystals after 5 months' preservation in a desiccator (Figure 7.12a). WS_2 etched samples still present a shift in the HER onset potential compared with the unetched sample (≈ 60 mV, from -0.47 to -0.41 V), but lower than the one observed for the fresh samples (≈ 100 mV). This suggests a loss in the number of active edge sites due to electrochemical degradation, due for example to sample oxidation, as reported previously.[36,47] Comparison of LSVs obtained from fresh and aged etched WS_2 samples reveals a significant increase in current density values for samples subject to short etching times (Figure 7.13a and 7.13b), whereas samples etched for long times present a similar current density plateau but shifted to higher overpotentials (Figure 7.13c and 7.13d). Tafel plot analysis (Figure 7.12b) supports these results, as short etching time samples exhibit a lower Tafel slope after ageing (≈20 mV dec^{-1} lower for 31 ± 1 s (R= 2, Z= 6.4) etched sample), in contrast to the almost invariant Tafel slopes obtained for long etching time, aged samples (variations less than ≈5 mV dec^{-1}). The 16 ± 1 s etched WS_2 sample presents a higher current density plateau despite exhibiting a higher Tafel slope (100 mV dec^{-1} vs. 81 mV dec^{-1}).

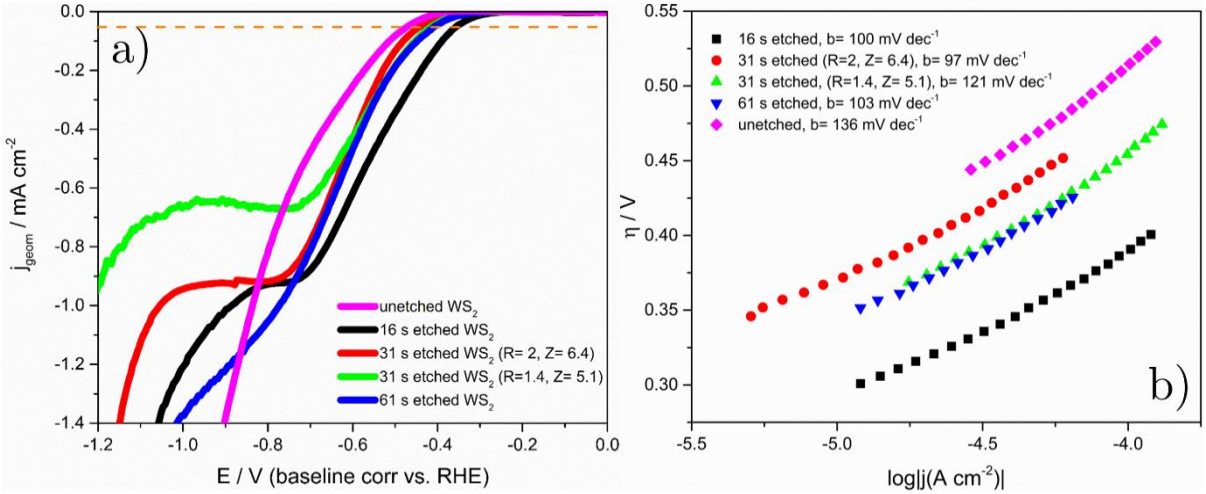

Figure 7.12. a) Linear sweep voltammograms in the 0 to -1.2 V voltage range vs. RHE and b) Tafel plots (η vs. $\log|j_{geom}|$) for WS_2 atmospherically-aged SF_6/C_4F_8 plasma-etched crystals. Dashed line (orange) indicates $|j_{geom}| = 0.05$ mA cm^{-2} (see text).Voltage scan rate: 50 mV s^{-1}.

We postulate that the electrochemical cycling cannot fully penetrate or restructure the tall, short interspaced nanocone arrays and amorphous morphologies obtained at long etching times but removes some active edge sites. This results in a minimal modification of morphology and active edge sites HER kinetics leading to a similar LSV profile shifted to higher overpotentials. On the other hand, both short and widely interspaced nanocone arrays are more prone to electrochemically-induced restructuring, leading to higher surface areas with lower active edge site densities.

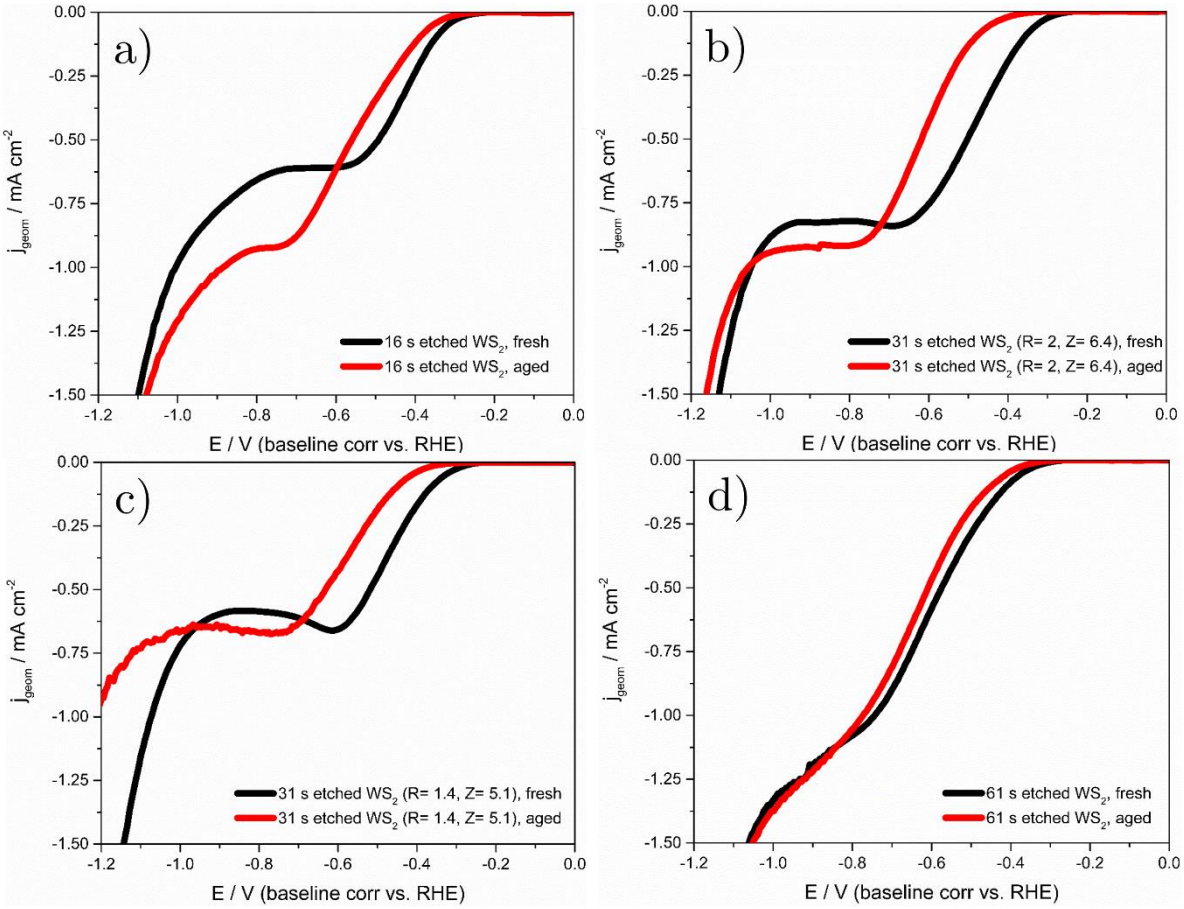

Figure 7.13. Comparison of HER performance of a) 16 ± 1 s, b) 31 ± 1 s (R= 2, Z= 6.4), c) 31 ± 1 s (R= 1.4, Z= 5.1) and d) 61 ± 1 s SF_6/C_4F_8 plasma-etched fresh (solid black) and 5-month aged (solid red) WS_2 crystals in the 0 to -1.2 V voltage range vs. RHE in 2 mM $HClO_4$/0.1M $NaClO_4$. Voltage scan rate: 50 mV s^{-1}.

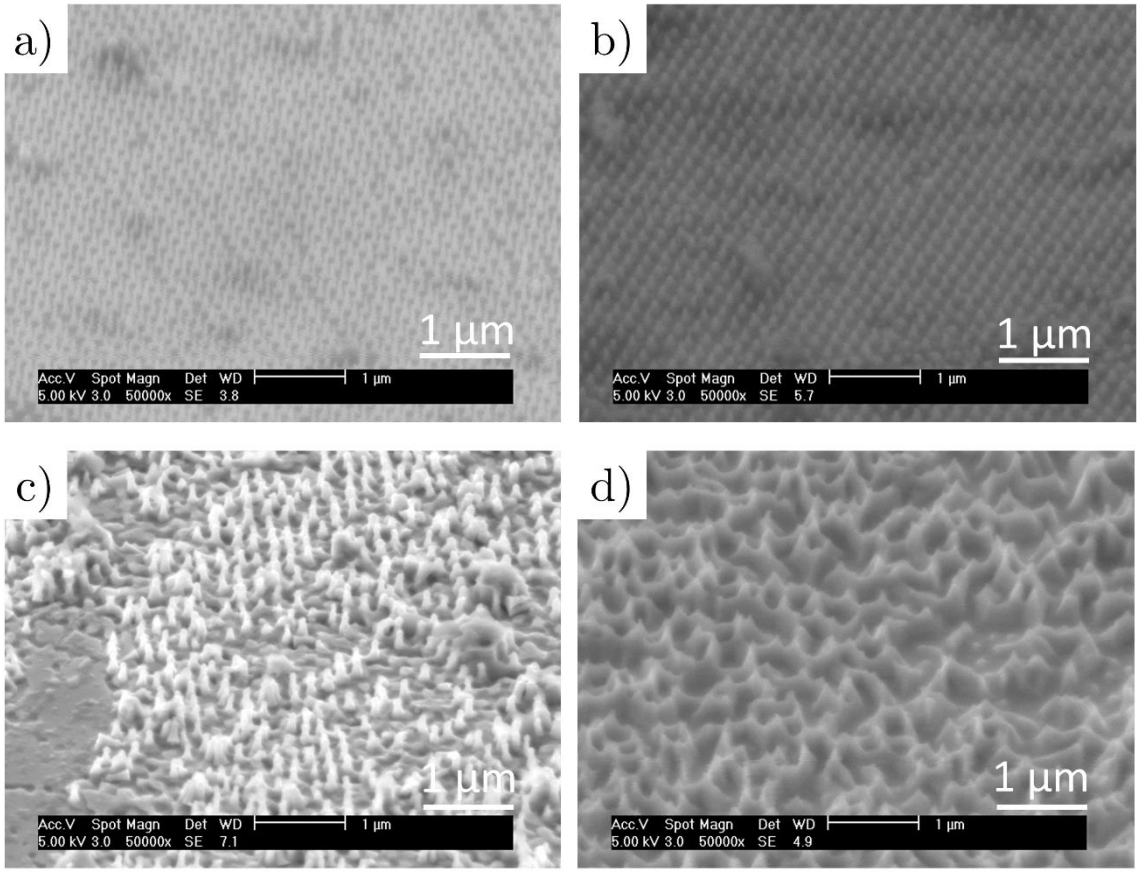

Figure 7.14. FE-SEM micrographs of a) 16 ± 1 s, b) 31 ± 1 s (R= 2, Z= 6.4), c) 31 ± 1 s (R= 1.4, Z= 5.1) and d) 61 ± 1 s SF_6/C_4F_8 plasma-etched WS_2 crystals after 5 month atmospherical ageing and electrochemical testing. Tilt angle: 45°.

SEM micrograph analysis (Figure 7.14) of the samples after electrochemical testing (Table 7.5) supports this: briefly etched samples exhibited significant modifications in the nanocone aspect ratio (for 16 ± 1 s, an increase from 2.8 ± 0.3 to 3.9 ± 0.4; for 31 ± 1 s with R= 2.0, Z= 6.4, a decrease from 3.1 ± 0.3 to 1.9 ± 0.2), while long-etched samples show almost invariant nanocone dimensions and morphologies. The evident modification in HER activity observed after short duty electrochemical tests suggests, then, that the plasma-etched TMD nanocone array nanostructures are indeed prone to surface modification under HER operating conditions due to electrochemical restructuring, this foreseeable to worsen at long operating times. Long term electrochemical testing of these samples are, consequently, out of the scope

of this chapter, as our focus is drawn to the nanocone array morphology role in the inherent mass transport and HER voltammetric profile, which is irreversibly altered if successive cycling experiments are performed.[44]

Material	SF_6/C_4F_8 plasma etching time / s	Angle-corrected nanopillar height/ nm	Nanopillar diameter / nm	Nanopillar interspacing / nm	Aspect ratio	R	Z
Aged WS_2	16 ± 1	420 ± 30	100 ± 10	75 ± 8	3.9 ± 0.4	2	8.4
	31 ± 1,	240 ± 30	125 ± 10	87 ± 9	1.9 ± 0.2	1.9	3.8
	31 ± 1	320 ± 20	120 ± 10	62 ± 8	2.7 ± 0.3	1.7	5.3
	61 ± 1	-	-	-	-	-	-

Table 7.5. Compilation of height, diameter and interspacing of the nanopillars obtained after plasma etching and 5-month atmosphere exposure of WS_2 crystals as a function of the SF_6/C_4F_8 plasma etching time.

7.3 Conclusions

In this chapter we have studied the fabrication of edge-abundant MoS_2 and WS_2 nanopillar arrays by nanosphere lithography and plasma etching treatments, and compared the resulting nanostructures and hydrogen evolution performances. Plasma-etching parameters are demonstrated to control the resulting nanopillar array morphologies. For MoS_2, these shifted from closely spaced nanocylinders to truncated nanocones, whereas for WS_2 a nanocone profile was always present. A maximum nanopillar height was achieved after complete depletion of the nanosphere masks (approx. 30 s SF_6/C_4F_8 etching): longer etching times led to truncated (MoS_2) or amorphous (WS_2) nanostructures. XPS measurements demonstrate that plasma-etching leads to the exposure of 1T metallic sites on WS_2, concurring with previous results obtained for MoS_2 [7].

Electrochemical experiments on freshly-etched samples showed a significant shift in the HER onset potential (≈200 mV for MoS_2 and ≈100 mV for WS_2). WS_2 enhanced HER activity with respect to MoS_2 at equivalent etching conditions was elucidated by Randles-Ševčík and transient chronoamperometry experiments: narrow interspaced nanopillar/truncated nanocone arrays obtained for MoS_2 (interspacing $\leq$ 40 nm) did not promote mass transport regimes different from microelectrode array Case 4 (i.e. planar macroelectrode). Thus, the HER enhancement observed solely stemmed from the higher exposure of active edge sites. However, the shorter but highly-interspaced WS_2 nanocone arrays presented in some cases significantly higher current densities than those expected for microelectrode array Case 4: here the diffusionally independent but inequivalent behaviour of individual naconones in a nanoelectrode array present a high contribution of hemispherical diffusion, neglected in the microelectrode array case. However, the correlation of enhanced HER and electron transfer properties with the aspect ratio of the MoS_2/WS_2 nanocone arrays suggests that the higher exposure of conductive 1T metallic edge sites dictates the HER performance.

Finally, morphology stability studies on electrochemically-tested, atmosphere exposed plasma-etched WS_2 crystals were performed. SEM imaging analysis indicates that surface restructuring upon electrochemical testing is only minimal on high aspect-ratio, closely-interspaced nanocone array structures obtained at long etching times. This translates onto HER experiments by the observation of equivalent LSV profiles shifted to higher overpotentials due to the loss of active WS_2 edge sites.

References

[1] S. Kim, M.S. Choi, D. Qu, C.H. Ra, X. Liu, M. Kim, Y.J. Song, W.J. Yoo, Effects of plasma treatment on surface properties of ultrathin layered MoS2, 2D Mater. 3 (2016) 035002. doi:10.1088/2053-1583/3/3/035002.

[2] S. Xiao, P. Xiao, X. Zhang, D. Yan, X. Gu, F. Qin, Z. Ni, Z.J. Han, K.K. Ostrikov, Atomic-layer soft plasma etching of MoS 2, Sci. Rep. 6 (2016) 1–8. doi:10.1038/srep19945.

[3] H. Zhu, X. Qin, L. Cheng, A. Azcatl, J. Kim, R.M. Wallace, Remote Plasma Oxidation and Atomic Layer Etching of MoS2, ACS Appl. Mater. Interfaces. 8 (2016) 19119–19126. doi:10.1021/acsami.6b04719.

[4] K. Seeger, R.E. Palmer, Fabrication of silicon cones and pillars using rough metal films as plasma etching masks, Appl. Phys. Lett. 74 (1999) 1627–1629. doi:10.1063/1.123638.

[5] K. Seeger, R.E. Palmer, Fabrication of ordered arrays of silicon nanopillars in silicon pillars, J. Phys. D. Appl. Phys. 32 (1999) L129–L132. doi:10.1088/0022-3727/32/24/102.

[6] A. Wellner, P.R. Preece, J.C. Fowler, R.E. Palmer, Fabrication of ordered arrays of silicon nanopillars in silicon-on-insulator wafers, Microelectron. Eng. 5758 (2001) 919–924. doi:10.1088/0022-3727/32/24/102.

[7] H.A. Burch, M. Isaacs, K. Wilson, R.E. Palmer, N.V. Rees, Electrocatalytic regeneration of atmospherically aged MoS 2 nanostructures via solution-phase sulfidation, RSC Adv. 6 (2016) 26689–26695. doi:10.1039/C6RA03326A.

[8] A. Frommhold, Nanotexturisation of Gold Surfaces and its Application to Neural Implants, Nanoscale Physics Research Laboratory, School of Physics and Astronomy, University of Birmingham, 2010.

[9] A. Frommhold, A.P.G. Robinson, E. Tarte, High aspect ratio silicon and polyimide nanopillars by combination of nanosphere lithography and intermediate mask pattern transfer, Microelectron. Eng. 99 (2012) 43–49. doi:10.1016/j.mee.2012.06.008.

[10] M.I. Petrescu, Theoretical hardness calculated from crystallo-chemical data for MoS 2 and WS2crystals and nanostructures, Acta Crystallogr. Sect. B Struct. Sci. 68 (2012) 501–510. doi:10.1107/S0108768112033149.

[11] A.P. Shpak, A.M. Korduban, L.M. Kulikov, T. V. Kryshchuk, N.B. Konig, V.O. Kandyba, XPS studies of the surface of nanocrystalline tungsten disulfide, J. Electron Spectros. Relat. Phenomena. 181 (2010) 234–238. doi:10.1016/j.elspec.2010.05.030.

[12] A. Ambrosi, Z. Sofer, M. Pumera, 2H → 1T phase transition and hydrogen evolution activity of MoS2, MoSe2, WS2 and WSe2 strongly depends on the MX2 composition., Chem. Commun. 51 (2015) 8450–3. doi:10.1039/c5cc00803d.

[13] K.M. McCreary, A.T. Hanbicki, G.G. Jernigan, J.C. Culbertson, B.T. Jonker, Synthesis of Large-Area WS2 monolayers with Exceptional Photoluminescence, Sci. Rep. 6 (2016) 19159. doi:10.1038/srep19159.

[14] A. Katrib, F. Hemming, P. Wehrer, L. Hilaire, G. Maire, The multi-surface structure and catalytic properties of partially reduced WO3, WO2 and WC + O2 or W + O2 as characterized by XPS, J. Electron Spectros. Relat. Phenomena. 76 (1995) 195–200. doi:10.1016/0368-2048(95)02451-4.

[15] A.A. Audi, P.M.A. Sherwood, X-ray photoelectron spectroscopic studies of sulfates and bisulfates interpreted by Xa and band structure calculations, Surf. Interface Anal. 29 (2000) 265–275. doi:10.1002/sia.1211.

[16] M.Y. Smirnov, A. V Kalinkin, A. V Pashis, A.M. Sorokin, A.S. Noskov, K.C. Kharas, V.I. Bukhtiyarov, Interaction of Al 2 O 3 and CeO 2 Surfaces with SO 2 and SO 2 + O 2 Studied by X-ray Photoelectron Spectroscopy, J. Phys. Chem. B. 109 (2005) 11712–11719. doi:10.1021/jp0508249.

[17] N. Choudhary, M.R. Islam, N. Kang, L. Tetard, Y. Jung, S.I. Khondaker, Two-dimensional lateral heterojunction through bandgap engineering of MoS2 via oxygen plasma, J. Phys. Condens. Matter. 28 (2016). doi:10.1088/0953-8984/28/36/364002.

[18] N.M.D. Brown, N. Cui, A. Mckinley, An XPS study of the surface modification of natural MoS 2 following treatment in an RF-oxygen plasma, Appl. Surf. Sci. 134 (1998) 11–21.

[19] J. Hong, Z. Hu, M. Probert, K. Li, D. Lv, X. Yang, L. Gu, N. Mao, Q. Feng, L. Xie, J. Zhang, D. Wu, Z. Zhang, C. Jin, W. Ji, X. Zhang, J. Yuan, Z. Zhang, Exploring atomic defects in molybdenum disulphide monolayers, Nat. Commun. 6 (2015) 1–8. doi:10.1038/ncomms7293.

[20] J.D. Benck, T.R. Hellstern, J. Kibsgaard, P. Chakthranont, T.F. Jaramillo, Catalyzing the Hydrogen Evolution Reaction (HER) with Molybdenum Sulfide Nanomaterials, ACS Catal. 4 (2014) 3957–3971. http://pubs.acs.org/doi/abs/10.1021/cs500923c (accessed December 15, 2015).

[21] R. Prehn, L. Abad, D. Sánchez-Molas, M. Duch, N. Sabaté, F.J. Del Campo, F.X. Muñoz, R.G. Compton, Microfabrication and characterization of cylinder micropillar array electrodes, J. Electroanal. Chem. 662 (2011) 361–370. doi:10.1016/j.jelechem.2011.09.002.

[22] D. Sánchez-Molas, J.P. Esquivel, N. Sabaté, F.X. Muñoz, F.J. del Campo, High Aspect-Ratio, Fully Conducting Gold Micropillar Array Electrodes: Silicon Micromachining and Electrochemical Characterization, J. Phys. Chem. C. 116 (2012) 18831–18846. doi:10.1021/jp305339k.

[23] D. Menshykau, X.-J. Huang, N. V Rees, F.J. del Campo, F.X. Muñoz, R.G. Compton, Investigating the concept of diffusional independence. Potential step transients at nano- and micro-electrode arrays: theory and experiment., Analyst. 134 (2009) 343–348. doi:10.1039/b816223a.

[24] T.J. Davies, R.G. Compton, The cyclic and linear sweep voltammetry of regular and random arrays of microdisc electrodes: Theory, J. Electroanal. Chem. 585 (2005) 63–82. doi:10.1016/j.jelechem.2005.07.022.

[25] C. Amatore, J.M. Savéant, D. Tessier, Charge Transfer at Partially Blocked Surfaces - A Model for the Case of Microscopic Active and Inactive Sites, J. Electroanal. Chem. 147 (1983) 39–51. doi:10.1016/S0022-0728(83)80055-2.

[26] N. Godino, X. Borrise, F.X. Muñoz, F.J. Del Campo, R.G. Compton, Mass transport to nanoelectrode arrays and limitations of the diffusion domain approach: theory and experiment, J. Phys. Chem. C. 113 (2009) 11119–11125. doi:10.1021/jp9031354.

[27] A.S. Peinetti, R.S. Gilardoni, M. Mizrahi, F.G. Requejo, G.A. González, F. Battaglini, Numerical Simulation of the Diffusion Processes in Nanoelectrode Arrays Using an Axial Neighbor Symmetry Approximation, Anal. Chem. 88 (2016) 5752–5759. doi:10.1021/acs.analchem.6b00039.

[28] E.J.F. Dickinson, I. Streeter, R.G. Compton, Chronoamperometry and cyclic voltammetry at conical electrodes, microelectrodes, and electrode arrays: Theory, J. Phys. Chem. B. 112 (2008) 4059–4066. doi:10.1021/jp711936y.

[29] A.J. Bard, L.R. Faulkner, Electrochemical Methods: Fundamentals and Applications, 2nd ed., John Wiley and Sons Ltd., New York, 2001. doi:10.1016/B978-0-12-381373-2.00056-9.

[30] T. Shinagawa, A.T. Garcia-Esparza, K. Takanabe, Insight on Tafel slopes from a microkinetic analysis of aqueous electrocatalysis for energy conversion., Sci. Rep. 5 (2015) 13801. doi:10.1038/srep13801.

[31] D. Voiry, M. Salehi, R. Silva, T. Fujita, M. Chen, Conducting MoS2 nanosheets as catalysts for hydrogen evolution reaction, Nano Lett. 13 (2013) 6222–6227. http://pubs.acs.org/doi/abs/10.1021/nl403661s.

[32] D. Voiry, H. Yamaguchi, J. Li, R. Silva, D.C.B. Alves, T. Fujita, M. Chen, T. Asefa, V.B. Shenoy, G. Eda, M. Chhowalla, Enhanced catalytic activity in strained chemically exfoliated WS_2 nanosheets for hydrogen evolution., Nat. Mater. 12 (2013) 850–5. doi:10.1038/nmat3700.

[33] M.-R. Gao, M.K.Y. Chan, Y. Sun, Edge-terminated molybdenum disulfide with a 9.4-Å interlayer spacing for electrochemical hydrogen production., Nat. Commun. 6 (2015) 7493. doi:10.1038/ncomms8493.

[34] B.E. Conway, B. V Tilak, Interfacial processes involving electrocatalytic evolution and oxidation of H2 , and the role of chemisorbed H, Electrochim. Acta. 47 (2002) 3571–3594.

[35] A.Y.S. Eng, A. Ambrosi, Z. Sofer, P. Simek, M. Pumera, Electrochemistry of Transition Metal Dichalcogenides : Strong Dependence on the Metal-to-Chalcogen Composition and Exfoliation Method, ACS Nano. 8 (2014) 12185–12198.

[36] X. Chia, A. Ambrosi, Z. Sofer, J. Luxa, M. Pumera, Catalytic and Charge Transfer Properties of Transition Metal Dichalcogenides Arising from Electrochemical Pretreatment, ACS Nano. 9 (2015) 5164–5179.

[37] M. Velický, M.A. Bissett, P.S. Toth, H. V. Patten, S.D. Worrall, A.N.J. Rodgers, E.W. Hill, I.A. Kinloch, K.S. Novoselov, T. Georgiou, L. Britnell, R.A.W. Dryfe, Electron transfer kinetics on natural crystals of MoS 2 and graphite, Phys. Chem. Chem. Phys. 17 (2015) 17844–17853. doi:10.1039/C5CP02490K.

[38] M. Velický, M.A. Bissett, C.R. Woods, P.S. Toth, T. Georgiou, I.A. Kinloch, K.S. Novoselov, R.A.W. Dryfe, Photoelectrochemistry of Pristine Mono- and Few-Layer MoS2, Nano Lett. 16 (2016) 2023–2032. doi:10.1021/acs.nanolett.5b05317.

[39] H. Li, M. Du, M.J. Mleczko, A.L. Koh, Y. Nishi, E. Pop, A.J. Bard, X. Zheng, Kinetic Study of Hydrogen Evolution Reaction over Strained MoS2 with Sulfur Vacancies Using Scanning Electrochemical Microscopy, J. Am. Chem. Soc. 138 (2016) 5123–5129. doi:10.1021/jacs.6b01377.

[40] S.J. Konopka, B. McDuffie, Diffusion coefficients of ferri- and ferrocyanide ions in aqueous media, using twin-electrode thin-layer electrochemistry, Anal. Chem. 42 (1970) 1741–1746. doi:10.1021/ac50160a042.

[41] R.S. Nicholson, Theory and Application of Cyclic Voltammetry for Measurement of Electrode Reaction Kinetics, Anal. Chem. 37 (1965) 1351–1355. doi:10.1021/ac60230a016.

[42] R.J. Klinger, J.K. Kochi, Electron-Transfer Kinetics from Cyclic Voltammetry. Quantitative Description of Electrochemical Reversibility, J. Phys. Chem. 85 (1981) 1731–1741. doi:10.1021/j150612a028.

[43] E. Parzinger, E. Mitterreiter, M. Stelzer, F. Kreupl, J.W. Ager, A.W. Holleitner, U. Wurstbauer, Hydrogen evolution activity of individual mono-, bi-, and few-layer MoS2towards photocatalysis, Appl. Mater. Today. 8 (2017) 132–140. doi:10.1016/j.apmt.2017.04.007.

[44] D. Escalera-López, R. Griffin, M. Isaacs, K. Wilson, R.E. Palmer, N. V. Rees, Electrochemical sulfidation of WS2 nanoarrays: Strong dependence of hydrogen evolution activity on transition metal sulfide surface composition, Electrochem. Commun. 81 (2017) 106–111. doi:10.1016/j.elecom.2017.06.016.

[45] N. Mohamad Latiff, L. Wang, C.C. Mayorga-Martinez, Z. Sofer, A.C. Fisher, M. Pumera, Valence

and oxide impurities in MoS2 and WS2 dramatically change their electrocatalytic activity towards proton reduction, Nanoscale. 8 (2016) 16752–16760. doi:10.1039/C6NR03086F.

[46] J. Xie, J. Zhang, S. Li, F. Grote, X. Zhang, H. Zhang, R. Wang, Y. Lei, B. Pan, Y. Xie, Controllable disorder engineering in oxygen-incorporated MoS2 ultrathin nanosheets for efficient hydrogen evolution, J. Am. Chem. Soc. 135 (2013) 17881–17888. doi:10.1021/ja408329q.

[47] L.R.L. Ting, Y. Deng, L. Ma, Y.J. Zhang, A.A. Peterson, B.S. Yeo, Catalytic Activities of Sulfur Atoms in Amorphous Molybdenum Sulfide for the Electrochemical Hydrogen Evolution Reaction, ACS Catal. 6 (2016) 861–867. doi:10.1021/acscatal.5b02369.

Chapter 8

Atmospherically aged WS_2 nanocone arrays: study of electrochemical incorporation of sulfur

8.1 Introduction

In the previous chapter we successfully prepared MoS_2 and WS_2 nanocone arrays, where the latter presented mass transport properties different from planar electrodes, arising from the wider nanocone interspacing. Electron microscopy imaging and electrochemical testing, however, showed the reconstruction of the TMD nanoarrayed structures and worsened HER performances, respectively, upon repeated use after environment exposure. Our research group successfully adapted an electrochemical sulfidation method to reinstate the HER activity of atmosphere-exposed, electrochemically tested MoS_2 nanoarrays.[1] However, its implementation onto other TMD surfaces was not investigated.

In this chapter we investigate the possibility of sulfur-enriching electrochemically-aged WS_2 nanoarrays with a room temperature solution-phase sulfidation method. Chalcogen-to-metal ratio, HER electrocatalysis and electron transfer modifications are assessed over a three-week period. The viability of the sulfide incorporation onto TMDs, as well as insights on the sulfidation mechanism in itself are discussed.

8.2 Results and discussion

8.2.1 Electrochemical sulfidation bath on WS_2: voltammetric study

In order to assess the viability of the electrochemical incorporation of sulfur onto the atmospherically aged and electrochemically restructured WS_2 nanoarray samples, we performed preliminary voltammetric studies on as-received WS_2 crystals.

The electrochemical sufidation bath, consisting of a solution containing 10 mM $Na_2S_2O_3$ and 0.1 M Na_2SO_4, is acidified in-situ with H_2SO_4 to achieve a pH 3, which drives the spontaneous decomposition of the $S_2O_3^{2-}$ anion to form colloidal sulfur (Eq. 8.1).[2]

$$S_2O_3^{2-}\,(aq) + H^+\,(aq) \rightleftharpoons S\,(s) + HSO_3^-\,(aq.) \quad (8.1)$$

The on-site generated colloidal sulfur can be further reduced to surface sulfide by applying a cathodic current (Eq. 8.2)

$$S\,(s) + 2e^- \rightleftharpoons +S^{2-}\,(aq) \quad (8.2)$$

Thus, the overall electrochemical incorporation of sulfide onto the selected working electrode surface proceeds by Eq. 8.3

$$S_2O_3^{2-}\,(aq) + H^+\,(aq) + 2e^- \rightleftharpoons S^{2-}\,(aq) + HSO_3^-\,(aq.) \quad (8.3)$$

A previous study from our group on electrochemically aged MoS_2 nanoarrays demonstrated that surface sulfide incorporation into the MoS_2 structure was maximized if the cathodic reduction of colloidal sulfur was preceded by an anodic sweep to fully oxidize the MoS_2 surface.[1] For MoS_2, electrochemically-induced surface oxidation (at E > +1 V vs Ag/AgCl) yields the acid-soluble MoO_4^{2-} species.[3] Consequently, the enhanced sulfur incorporation after surface oxidation suggests that the redeposition of MoO_4^{2-} species might assist in the overall sulfidation mechanism.

For WS_2, the cyclic voltammogram obtained during the solvent-phase sulfidation treatment, acquired in the voltage range from 1.25 V to -1.25 V vs Ag/AgCl (Figure 8.1), presents a redox profile analogous to that of MoS_2 [1]. The redox features observed are ascribed as follows. The anodic peak (I) at ca. 0.7 V vs Ag/AgCl corresponds to the conversion of W in WS_2 from 4+ to a 6+ oxidation state.[3] This proceeds by a complex electro-oxidative mechanism which generates WO_x moieties, mostly being the acid insoluble WO_3.[4] The first cathodic peak (II) at ca. 0.25 V vs Ag/AgCl, also found on the MoS_2 sulfidation process, can be related to the sulphur electroreduction,[1] whereas the second cathodic process (III) starting at ca. -0.5 V vs Ag/AgCl involves both the reduction of the tungsten oxide compounds WO_x formed in (I), expected to start at ca. -0.55V vs Ag/AgCl (Nernstian corrected to pH= 3)[4] and the bulk hydrogen evolution.

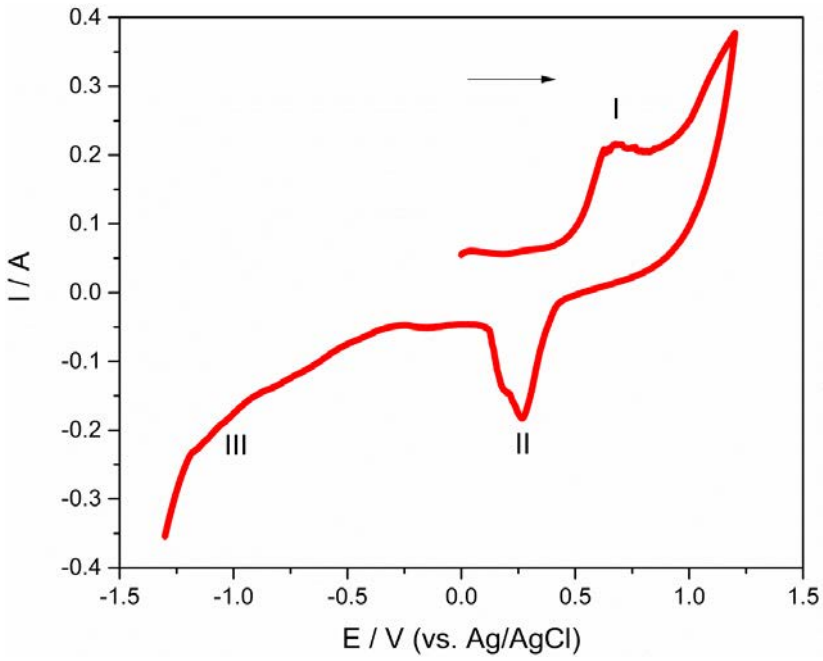

Figure 8.1. Representative I-E curve obtained from the solvent-phase sulfidation method in a plasma-etched WS_2 crystal. Electrolyte: 10 mM $Na_2S_2O_3$, 0.1 M Na_2SO_4 and 1 mM H_2SO_4. The electrochemical window was selected based on the optimized conditions stated in ref.[1]. Scan rate: 25 mV s^{-1}, scanning direction indicated by arrow.

Thus, we can preliminary conclude that the electrochemical sulfidation method previously employed on MoS_2 is susceptible to be used in WS_2.

8.2.2 Electrochemical and physical monitoring of electrocatalytic and surface properties of sulfidated WS_2 nanoarrays

The successful incorporation of sulfide moieties onto WS_2 by the solvent-phase sulfidation method was evaluated by monitoring the HER performance, oxidation state, and electron transfer properties over a one month period following the sulfidation treatment on atmospherically aged WS_2 samples previously tested in Chapter 7. Monitoring of the HER performance (Figures 8.2 and 8.3) provided the following observations. Firstly, freshly sulfidated samples did not necessarily present enhanced HER performances compared with pre-sulfidated samples. Secondly, the samples' HER peak current, after roughness factor correction to discard enhanced currents derived from surface area modifications (electrochemical capacitance measurements, see section I.2 Appendix), was inferior after a 3-week environmental exposure compared to the pre-sulfidated, atmospherically-exposed state (Figures 8.3a and 8.3b).

The cathodic feature appearing at E ca. -0.4 V vs RHE in the HER experiments (Figures 8.2a and 8.2b) is ascribed to the diffusion decay peak profile of proton reduction catalysed by the WS_2 active sites, characteristic of the fully-supported, low proton concentration electrolyte used (2 mM $HClO_4$, 0.1 M $NaClO_4$),[5] whilst the exponential cathodic current at higher overpotentials (onset at. ca. -0.7 V vs RHE) is ascribed to the water reduction reaction (i.e. solvent breakdown).[6] Indeed, the resolution of the diffusion decay proton reduction peak also seems correlated with the S^{2-}:W^{4+} ratio, and consequently to the active sites present.

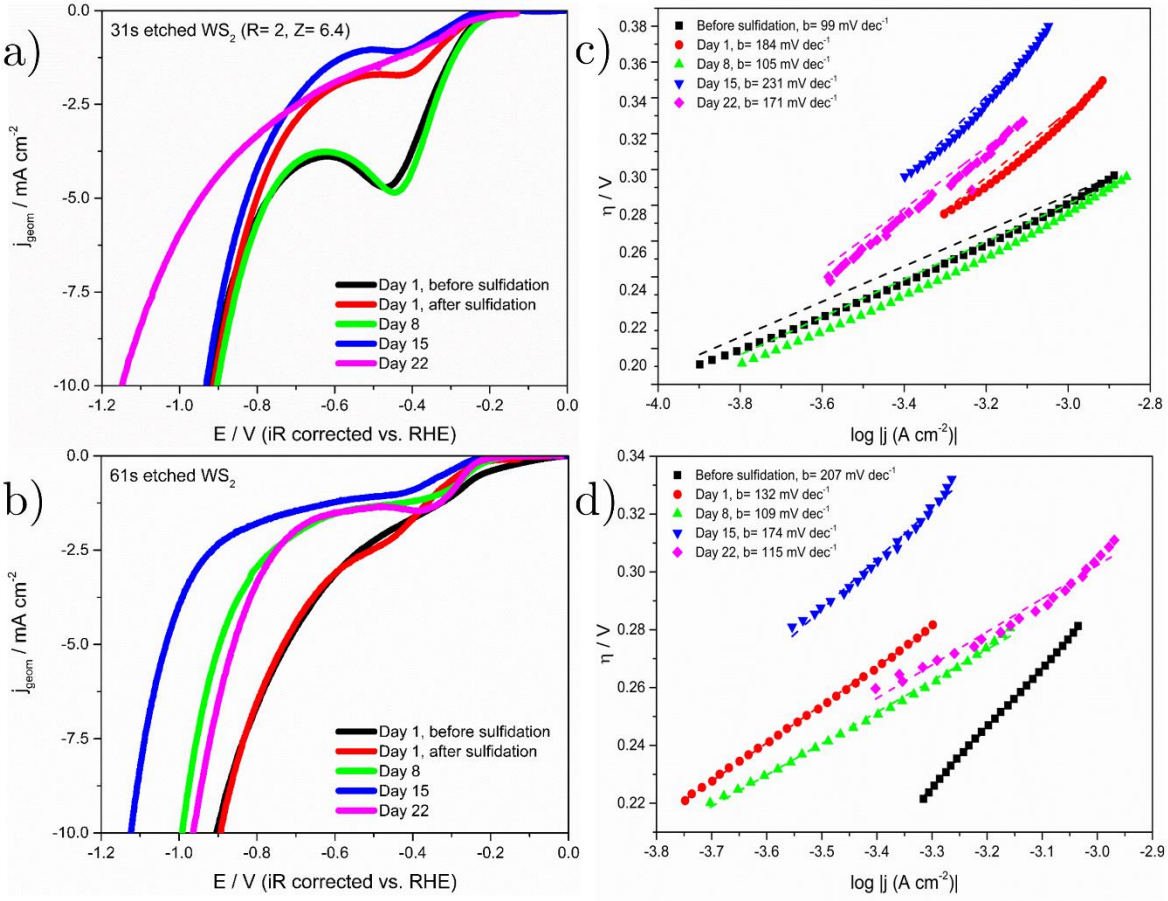

Figure 8.2. Left column: Linear sweep voltammograms in the 0 to -1.2V voltage range of a) 31±1 s (*R*= 2, Z=6.4) and b) 61±1 s atmospherically aged, sulfidation treated plasma-etched WS_2 samples over a three week ambient exposure period. Right column: Tafel plots (η vs. $\log|j_{geom}|$) of c) 31±1 s (*R*= 2, *Z*=6.4) and d) 61±1 s atmospherically aged, sulfidation treated plasma-etched WS_2 samples over a three week ambient exposure period. Labels: pre-sulfidated (black), post-sulfidated (red), 8-day atmosphere exposed (green), 15-day atmosphere exposed (blue) and 22-day atmosphere exposed (magenta). Scan rate: 25 mV s^{-1}.

Both phenomena can be understood by changes in the surface oxidation state revealed by XPS measurements. For the 31±1 s (*R*=2, *Z*=6.4) plasma-etched WS_2 sample, the peak current decays to half of its initial value following sulfidation (Figure 8.3a). This is correlated to a decrease in the total S:W ratio (1.5:1, see Figure 8.4e), and the appearance of WO_2 at the

crystal surface up to ca. 24% (W $4f_{7/2}$:$4f_{5/2}$ spin-orbit doublet at binding energies of ~33 and ~35.2 eV, respectively; Figures 8.3c and 8.4a).[7] This is in stark contrast with the high-resolution W 4*f* spectra of the pre-sulfidated plasma-etched WS_2 crystals, which present a stoichiometric total S:W ratio and can be deconvoluted by the semiconducting 2H phase W $4f_{7/2}$:$4f_{5/2}$ spin-orbit doublet (binding energies of ~32.65 and ~34.8 eV, respectively), with an additional contribution from the metallic 1T phase (W $4f_{7/2}$:$4f_{5/2}$ spin-orbit doublet binding energies: ~31.65 and ~33.8 eV). Previous reports on bulk and chemically-exfoliated WS_2 crystals suggest that incorporation of WO_2 is detrimental for the HER.[4,8] In the case of the 31±1 s sample, this is supported by the changed HER kinetics (Tafel slope increase from 100 to 185 mV dec^{-1}, Figure 8.2c) and higher onset potentials (η_{onset} from 173 to 207 mV, see Table 8.1).

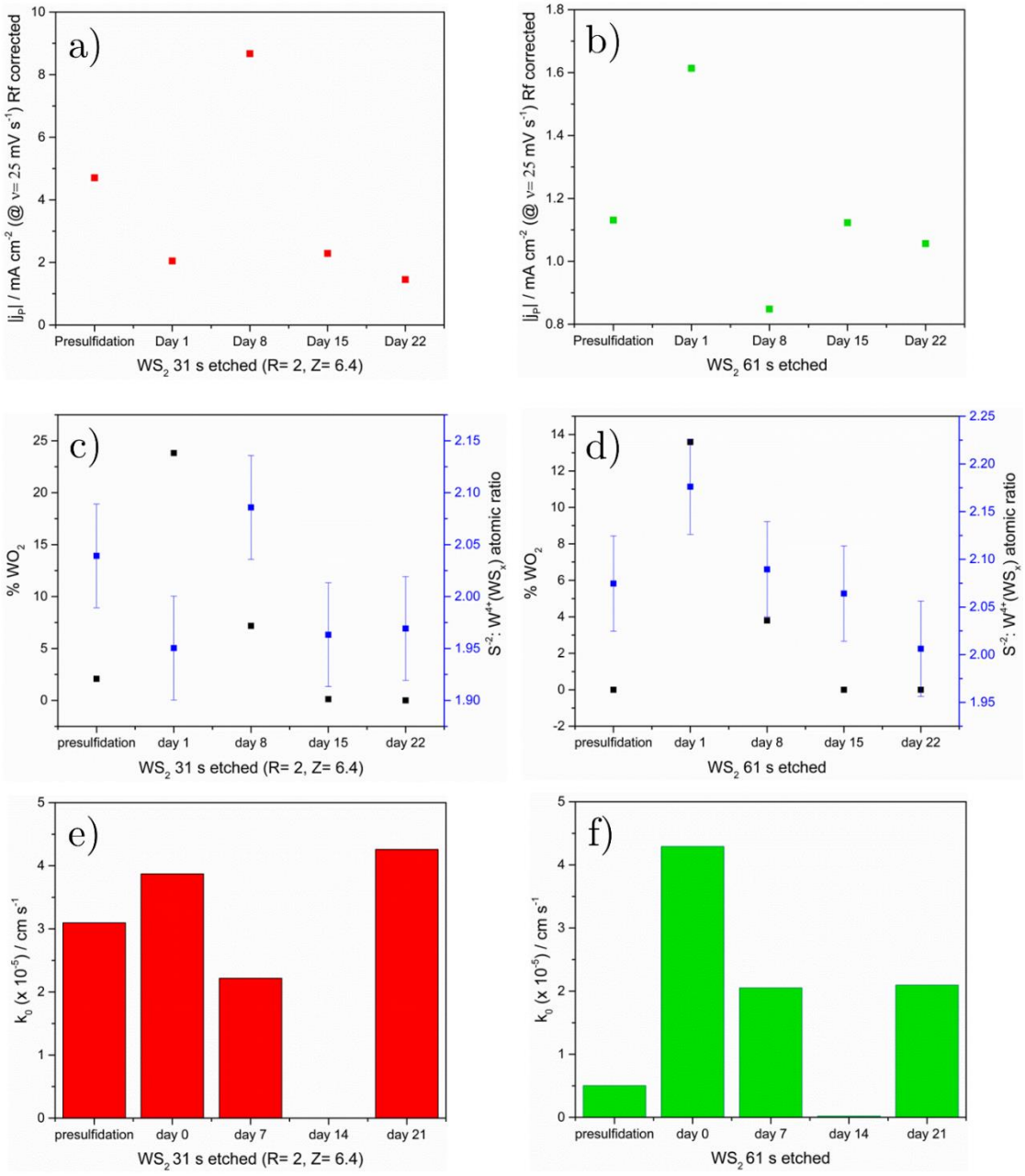

Figure 8.3. Comparison of: a-b) roughness-factor corrected HER peak current densities at υ_{scan}= 25mV s^{-1}, c-d) WO_2 surface content (left axis) and S^{2-}:W^{4+} XPS atomic photoemission ratios (right axis), and e-f) k^{O}_{app} values for the $[Fe(CN)_6]^{4-}/[Fe(CN)_6]^{3-}$ redox probe, for atmospherically aged, sulfidation treated plasma-etched WS_2 samples 31±1 s (R=2, Z=6.4, left column) and 61±1 s (right column), after weekly electrochemical testing over a three-week ambient exposure period.

		HER onset potential (η at $\|j\| = 0.05\ mA\ cm^{-2}$) / mV				
WS_2	SF_6/C_4F_8 plasma etching time / s	Pre-sulfidated	Day 1	Day 8	Day 15	Day 22
	31 ± 1	173	207	166	232	131
	61 ± 1	48	122	176	219	177

Table 8.1. Compilation of HER onset potentials (η at $|j| = 0.05\ mA\ cm^{-2}$) for 31±1 s (R= 2, Z= 6.4) and 61±1 s atmospherically aged, sulfidation treated, plasma-etched WS_2 samples after weekly electrochemical testing over a three week ambient period.

Conversely, the 61±1 s plasma-etched WS_2 sample presented higher peak currents (Figure 8.3b) and kinetics (Tafel slope 130 vs. initial 210 mV dec^{-1}, Figure 8.2d) following sulfidation, despite the decay in the total S:W ratio (from ca. 2:1 to 1.88:1, see Figure 8.4f) and the 14% increase in surface WO_2 content (Figures 8.3d and 8.4c).

This initially non-linear trend is found to be linked to the S:W ratio, if calculated solely using the W^{4+} XPS components characteristic of WS_2 (semiconducting 2H phase and metallic 1T phase). Sulfur-rich S:W ratios promote enhanced HER performance and vice versa, as it is widely agreed that sulfur is the proton-accepting site on the edge sites of crystalline TMDs. Maximum peak currents indeed coincide with the highest sulfur-to-metal ratios for both 31±1 s (S:W= 2.08:1, $j_p \approx$ 9 mA cm^{-2}, day 8) and 61±1 s samples (S:W= 2.18:1, $j \approx$ 1.6 mA cm^{-2}, freshly sulfidated). After these peak values, both post-sulfidated 31±1 s and 61±1 s etched samples exhibited an HER current decrease in subsequent electrochemical testing to values lower or comparable with the freshly sulfidated state, due to lower S:W ratios. This accords with previous investigations which correlated higher sulfur content in TMDs with improved hydrogen turnover frequencies,[9,10] and sulfur-depleted W-edge sites of electro-oxidized WS_2 with poor catalytic activity.[4] We hypothesize that the electrochemically-induced restructuring gradually depletes the WO_2 phase, initially exposing underlying WS_2 with high active site densities which are later reconstructed during atmospheric and experimental conditions to a more homogeneous nanostructure (Figure 8.5).

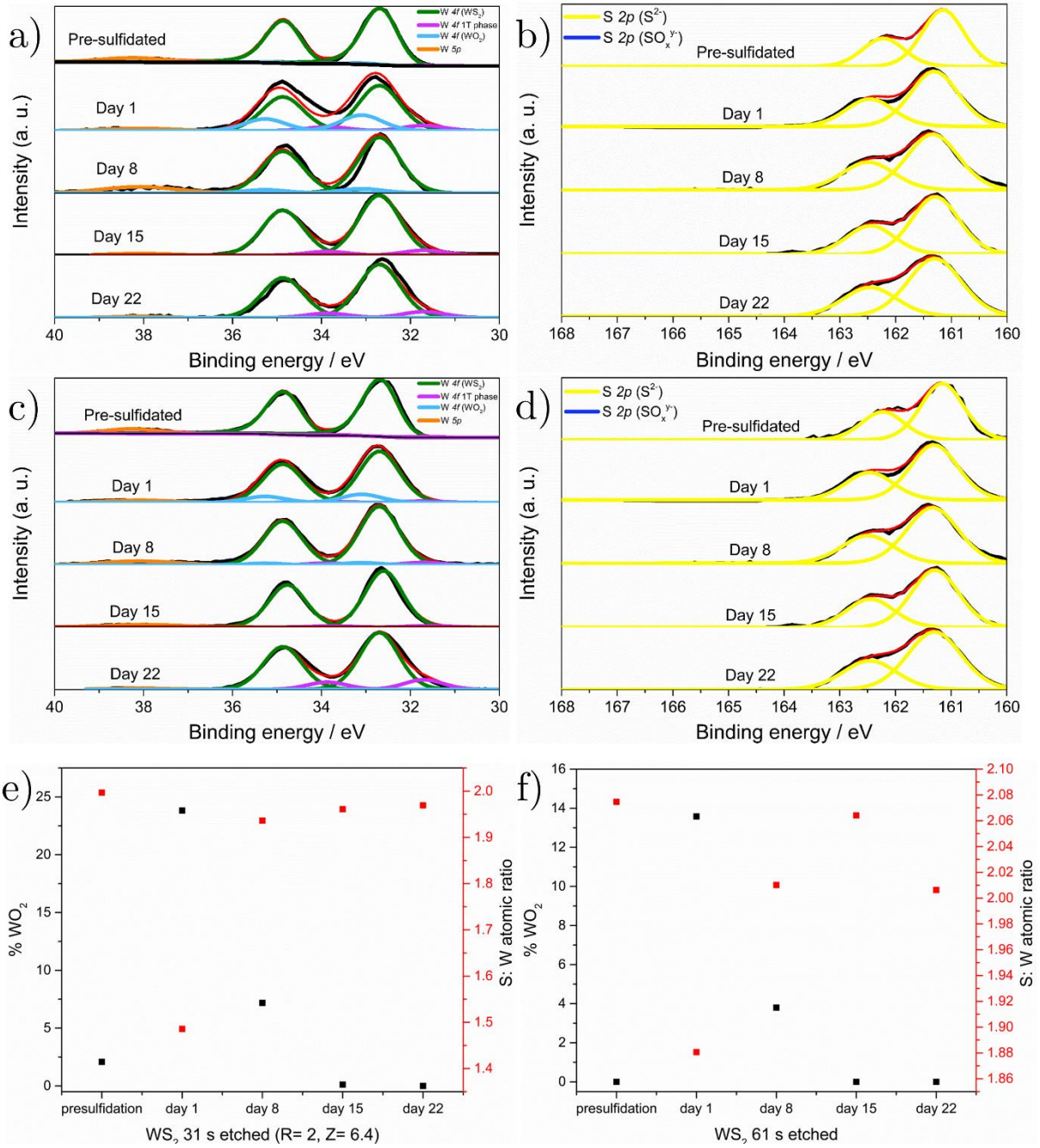

Figure 8.4. Stacked high-resolution XPS spectra of W 4*f* and S 2*p* for a-b) 31 ± 1 s (R= 2, Z= 6.4) and c-d) 61 ± 1 s atmospherically aged, sulfidation treated, plasma-etched WS_2 samples over a three-week ambient exposure period. e-f) Comparison of total S:W XPS atomic photoemission ratios.

With regard to the electron transfer kinetics, both samples exhibit higher k_{app}^{O} values (≈ 4×10^{-5} cms^{-1}) after undergoing the sulfidation treatment (Figures 8.3e and 8.3f, see Table 8.2 for values). This agrees with literature reports which found enhanced electrical conductivities of WO_x species vs. WS_2,[11] beneficial for mediating in the redox chemistry of surface sensitive species such as $Fe(CN)_6^{4-}/Fe(CN)_6^{3-}$. A gradual decrease in k_{app}^{O} values after two weeks of testing correlates with reduced WO_2 content at the crystal surface, whereas restored k_{app}^{O} values after three weeks can be attributed to the higher WS_2 metallic 1T polymorph contents (ca. 10-15%, see Table 8.3).

Sample	WS_2 31 ± 1 s (R = 2, Z = 6.4)		WS_2 61 ± 1 s	
	k_{app}^{O}, Klinger and Kochi (@ 100mV s^{-1}) / cm s^{-1}	k_{app}^{O}, ψ vs. $\left[\left(\frac{\pi zFDv_{scan}}{RT}\right)\right]^{-1/2}$ / cm s^{-1}	k_{app}^{O}, Klinger and Kochi (@ 100mV s^{-1}) / cm s^{-1}	k_{app}^{O}, ψ vs. $\left[\left(\frac{\pi zFDv_{scan}}{RT}\right)\right]^{-1/2}$ / cm s^{-1}
Pre-sulfidated	6.14×10^{-5}	3.10×10^{-5}	2.83×10^{-7}	5.04×10^{-6}
Day 1	1.06×10^{-5}	3.87×10^{-5}	3.41×10^{-5}	4.29×10^{-5}
Day 8	4.16×10^{-5}	2.22×10^{-5}	5.31×10^{-6}	2.05×10^{-5}
Day 15	4.17×10^{-9}	1.01×10^{-8}	8.73×10^{-8}	1.98×10^{-7}
Day 22	2.30×10^{-5}	4.26×10^{-5}	2.01×10^{-6}	2.10×10^{-5}

Table 8.2. Compilation of heterogeneous electron transfer constants (k_{app}^{O}) for atmospherically aged, sulfidation treated, plasma-etched WS_2 samples over a three week environment exposure period after elucidating the peak-to-peak separation of the $[Fe(CN)_6]^{4-}/[Fe(CN)_6]^{3-}$ redox probe.

			XPS photoemission percentage / %				
WS_2	SF_6/C_4F_8 plasma etching time / s	WS_2 polymorph	Pre-sulfidated	Day 1	Day 8	Day 15	Day 22
	31 ± 1	2H	97	73.4	89.3	92.2	89.9
		1T	0.9	2.8	3.5	7.7	10.1
	61 ± 1	2H	98.3	83.9	92	95.5	85.3
		1T	1.7	2.5	4.2	4.5	14.7

Table 8.3. Compilation of relative percentages of WS_2 polymorphs (metallic 1T and semiconducting 2H) obtained from XPS spectra for 31 ± 1 s (R= 2, Z= 6.4) and 61 ± 1 s atmospherically aged, sulfidation treated, plasma-etched WS_2 samples after weekly electrochemical testing over a three week ambient exposure period.

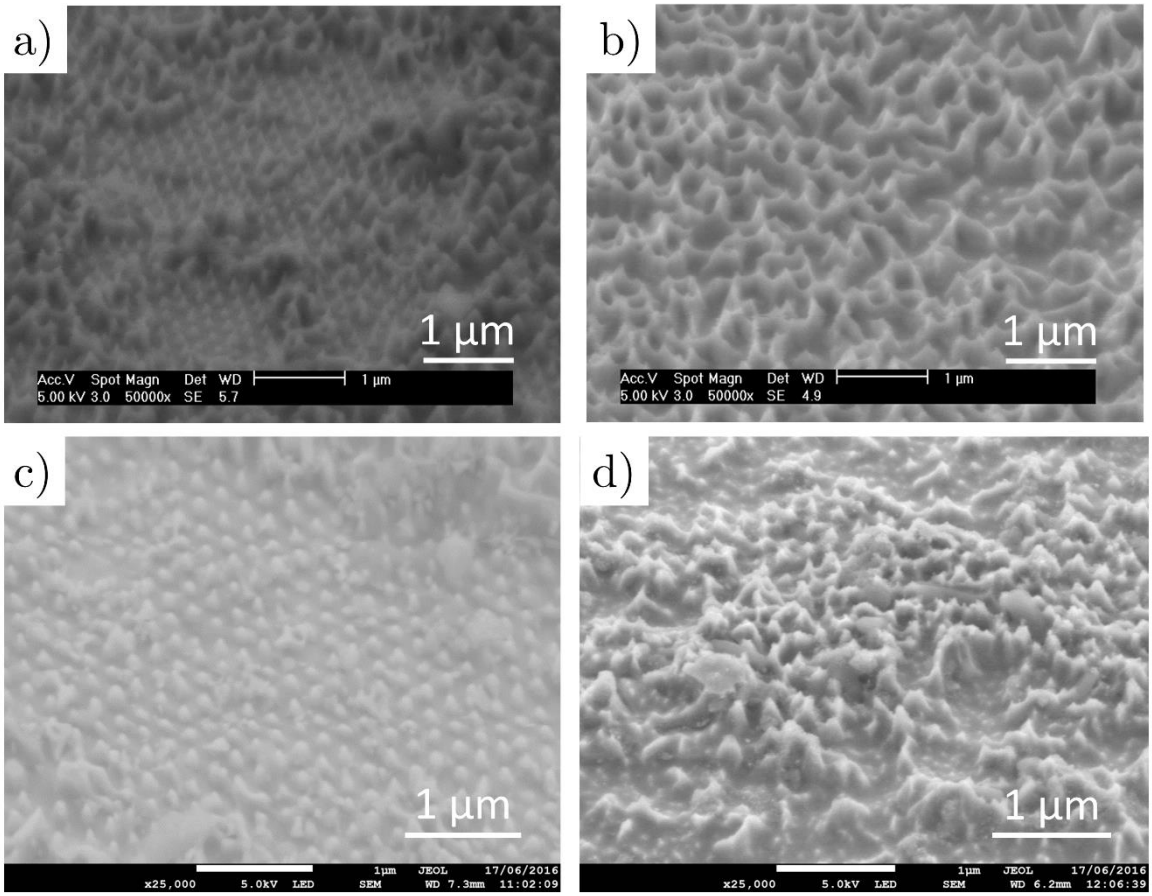

Figure 8.5. FE-SEM micrographs of a,c) 31 ± 1 s (R= 2, Z= 6.4) and b,d) 61 ± 1 s SF_6/C_4F_8 plasma-etched WS_2 crystals atmospherically aged plasma-etched WS_2 samples before (first row) and after solution-phase sulfidation (second row). Tilt angle: 45°.

These results suggest that this sulfidation method does not incorporate sulfur into the atmospherically aged WS_2 samples. Instead, it promotes the appearance of WO_x moieties at the WS_x surface which are reduced in the cathodic sweep. We hypothesize that in general, the sulfur incorporation is only effective when the electro-oxidative step of TMDs forms acid-soluble species, as sulfur incorporation into atmospherically-aged MoS_2 crystals was optimal when the cathodic voltage vertex surpassed the reduction potential of the TMD oxidised species (MoO_4^{2-}).[1] In the case of WS_2, the oxidised WO_x species generated during the electro-oxidative step are insoluble at pH≤3,[12] coinciding with the optimized pH value for the sulfidation electrolyte

(pH 3). Consequently, the electroreduced sulfur cannot be incorporated into the WO_x structure, and would dissolve under acidic conditions.[13] Hence, we predict that the electrochemical solvent-phase sulfidation method is only suited for MoX_2 (X = S, Se) rather than for WX_2 (X = S, Se).

8.3. Conclusions

In contrast to MoS_2, the application of the solution-phase, room-temperature electrochemical sulfidation method used in this chapter to obtain S-rich structures did not lead to S-rich WS_x but to S-deficient WS_x structures with high WO_2 surface content. The inferior HER performances but improved electron transfer properties are in agreement with the detrimental effect reported after WO_2 incorporation into WS_2 for the HER catalysis. The unsuccessful incorporation of electroreduced sulfide in the WS_x structure is suspected to arise from the nature of the sulfidation mechanism: redeposition of acid-soluble MoO_4^{2-} species for MoX_2 improves S^{2-} incorporation onto the surface, which is not possible in the case of WX_2 as the WO_x compounds formed are acid insoluble. This demonstrates the key role of the nature of the TMDs in the successful electrochemical incorporation of sulfur in their structure, and reveals that an electrochemistry-based sulfidation method universally applicable for any TMDs remains to be developed.

References

[1] H.A. Burch, M. Isaacs, K. Wilson, R.E. Palmer, N.V. Rees, Electrocatalytic regeneration of atmospherically aged MoS 2 nanostructures via solution-phase sulfidation, RSC Adv. 6 (2016) 26689–26695. doi:10.1039/C6RA03326A.

[2] T. Yukawa, K. Kuwabara, K. Koumoto, Electrodeposition of CuInS2 from aqueous solution (II) electrodeposition of CuInS2 film, Thin Solid Films. 286 (1996) 151–153. doi:10.1016/S0040-6090(96)08545-8.

[3] A.Y.S. Eng, A. Ambrosi, Z. Sofer, P. Simek, M. Pumera, Electrochemistry of Transition Metal Dichalcogenides: Strong Dependence on the Metal-to-Chalcogen Composition and Exfoliation Method, ACS Nano. 8 (2014) 12185–12198.

[4] X. Chia, A. Ambrosi, Z. Sofer, J. Luxa, M. Pumera, Catalytic and Charge Transfer Properties of Transition Metal Dichalcogenides Arising from Electrochemical Pretreatment, ACS Nano. 9 (2015) 5164–5179.

[5] E.J.F. Dickinson, J.G. Limon-Petersen, N. V Rees, R.G. Compton, How Much Supporting Electrolyte Is Required to Make a Cyclic Voltammetry Experiment Quantitatively " Diffusional "? A Theoretical and Experimental Investigation, J. Phys. Chem. C. 113 (2009) 11157–11171.

[6] N. Dubouis, C. Yang, R. Beer, L. Ries, D. Voiry, A. Grimaud, Interfacial Interactions as an Electrochemical Tool To Understand Mo-Based Catalysts for the Hydrogen Evolution Reaction, ACS Catal. 8 (2017) 828–836. doi:10.1021/acscatal.7b03684.

[7] A. Katrib, F. Hemming, P. Wehrer, L. Hilaire, G. Maire, The multi-surface structure and catalytic properties of partially reduced WO3, WO2 and WC + O2 or W + O2 as characterized by XPS, J. Electron Spectros. Relat. Phenomena. 76 (1995) 195–200. doi:10.1016/0368-2048(95)02451-4.

[8] N. Mohamad Latiff, L. Wang, C.C. Mayorga-Martinez, Z. Sofer, A.C. Fisher, M. Pumera, Valence and oxide impurities in MoS2 and WS2 dramatically change their electrocatalytic activity towards proton reduction, Nanoscale. 8 (2016) 16752–16760. doi:10.1039/C6NR03086F.

[9] L.R.L. Ting, Y. Deng, L. Ma, Y.J. Zhang, A.A. Peterson, B.S. Yeo, Catalytic Activities of Sulfur Atoms in Amorphous Molybdenum Sulfide for the Electrochemical Hydrogen Evolution Reaction, ACS Catal. 6 (2016) 861–867. doi:10.1021/acscatal.5b02369.

[10] H. Vrubel, X. Hu, Growth and activation of an amorphous molybdenum sulfide hydrogen evolving catalyst, ACS Catal. 3 (2013) 2002–2011. doi:10.1021/cs400441u.

[11] B. Seo, H.Y. Jeong, S.Y. Hong, A. Zak, S.H. Joo, Impact of a conductive oxide core in tungsten sulfide-based nanostructures on the hydrogen evolution reaction, Chem. Commun. 51 (2015) 8334–8337. doi:10.1039/C5CC02472B.

[12] M. Zafir Mohamad Nasir, Z. Sofer, M. Pumera, Effect of Electrolyte pH on the Inherent Electrochemistry of Layered Transition-Metal Dichalcogenides (MoS 2 , MoSe 2 , WS 2 , WSe 2), ChemElectroChem. 2 (2015) 1713–1718. doi:10.1002/celc.201500259.

[13] K. Osseo-Asare, Solution chemistry of tungsten leaching systems, Metall. Trans. B. 13 (1992) 555–564. doi:10.1007/BF02669168.

Chapter 9

pH-dependent activity, stability and inherent electrochemistry of amorphous molybdenum sulfide for the hydrogen evolution

9.1 Introduction

Aside from the most commonly studied 2H or 1T crystalline phases for MoS_2, $[Mo_3S_{13}]^{2-}$ cluster-based amorphous molybdenum sulfide polymorphs present intriguing properties for the HER. The high sulfur-to-molybdenum ratios with structures resembling the crystalline MoS_2 edges imply a high number of potential active sites, being reported as one of the best-performing HER molecular catalysts.[1] A one-step electrochemical deposition method yielded amorphous molybdenum sulfide (MoS_x) by anodic or cathodic decomposition of a $[MoS_4]^{2-}$ precursor,[2,3] presenting a $[Mo_3S_{13}]^{2-}$ polymeric-based structure. Despite of the promising HER activities reported, the intrinsic structural complexity of the electrodeposited MoS_x conceals the unambiguous role of the sulfur moieties in the HER activity across different electrolyte environments.

In this chapter we present a comprehensive study which aims to elucidate the electrochemical activity, stability and inherent electrochemistry of electrodeposited MoS_x thin films across the 0-10 pH range. Extensive use of electrochemical and ex-situ characterization techniques (Raman spectroscopy, XPS) is employed for such purpose. An initial study of the pH-dependent MoS_x inherent redox features followed by electrochemical conditioning strategies is evaluated to correlate specific modifications in surface morphologies and species with the resulting HER electrocatalysis. Finally, the knowledge gathered from these studies is incorporated in the understanding of the long-term HER performances and subsequent stabilities.

9.2 Results and discussion

9.2.1 Electrochemical growth of amorphous molybdenum sulfide

Preliminary electrochemical deposition studies were performed on Si/Ti/Au electrodes to evaluate the influence of experimental conditions (electrochemical setup, deposition parameters) in the amorphous molybdenum sulfide (MoS_x) thin film growth. Figure 9.1a shows a set of representative voltammograms obtained after continuous cycling from 0.1 V to -1 V vs. Ag/AgCl using an electrolytic bath containing 2mM $(NH_4)_2[MoS_4]$ as the MoS_x source,[2] and 0.1 M $NaClO_4$ as supporting electrolyte. In agreement with previous reports, the first scans exhibit small current density values lacking defined electrochemical features. However, subsequent scans show broad oxidation features in the reverse scan: one shoulder with peak at ca. -0.5 V and an oxidation feature between -0.2 and 0.1 V. A cathodic process is also observed between -0.2 and -1 V in the forward scan.

Analogous cycling in a 0.1 M $NaClO_4$ aqueous electrolyte shows negligible currents at the investigated voltage window (Figure 9.1b), confirming that the redox features found in the $(NH_4)_2[MoS_4]$ containing bath correspond to the electroactivity of the $[MoS_4]^{2-}$ anion.[3] The aforementioned first oxidation shoulder, more pronounced upon cycling, has been ascribed by EQCM measurements to non-faradaic capacitance currents of the increasingly thicker porous MoS_x deposited film.[4] Analogously, the remaining second oxidation and reduction features were ascribed to oxidative and reductive deposition mechanisms related to the $[MoS_4]^{2-}$ anion.

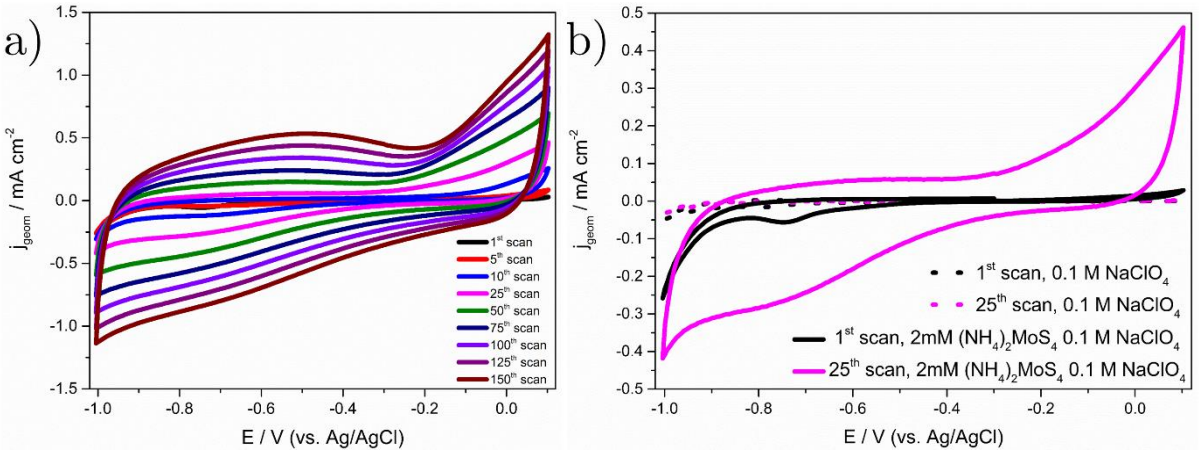

Figure 9.1. a) Representative voltammograms obtained during the electrochemical deposition of MoS_x onto 0.25 cm^2 Si/Ti/Au electrodes by continuous voltage cycling from +0.1 V to -1 V vs. Ag/AgCl in 2mM $(NH_4)_2[MoS_4]$, 0.1 M $NaClO_4$. b) Representative first (black) and 25th (magenta) voltammograms obtained by continuous cycling within the +0.1 V to -1 V vs. Ag/AgCl electrochemical window for Si/Ti/Au electrodes in 0.1 M $NaClO_4$ (dashed lines) and 2mM $(NH_4)_2[MoS_4]$, 0.1 M $NaClO_4$ (solid lines) electrolytes. Scan rate: 50 mV s^{-1}.

These electrochemical features described resemble those subsequently found in FTO,[5] glassy carbon[6] and Au[7] electrodes: this supports the previously suggested substrate-insensitive deposition mechanism of MoS_x, which was elucidated to operate by instantaneous nucleation and 3D-growth.[3] The suggested electrodeposition mechanisms are the following[4,5]:

$$[MoS_4]^{2-} \rightarrow MoS_3 + 1/8\,S_8 + 2e^- \,(anodic) \quad (9.1)$$

$$[MoS_4]^{2-} + 2H_2O + 2e^- \rightarrow MoS_2 + 2HS^- + 2OH^- \,(cathodic) \quad (9.2)$$

Further testing was performed to evaluate the deposition rate efficiency of both anodic electrodeposition (AE) and cathodic electrodeposition (CE) processes. This was done by preparing MoS_x thin films of different thicknesses (i. e. electrodeposition charge density $< \sigma_q >$) using potentiostatic deposition for varying durations enabled to investigate the deposition rate

efficiency. For AE-MoS_x the voltage was held at +0.1 V vs. Ag/AgCl, whereas for CE-MoS_x it was held at -1 V vs. Ag/AgCl. MoS_x thin film thickness vs. $< \sigma_q >$ plots of AE-MoS_x and CE-MoS_x (Figures 9.2a and 9.2b) clearly demonstrate the lower faradaic efficiency of the cathodic deposition mechanism: a 10-fold higher $< \sigma_q >$ is required on CE than AE to achieve 100 nm-thick MoS_x thin films (338.07 mC cm^{-2} vs. 33.70 mC cm^{-2}), in agreement with previous studies. For AE-MoS_x, assuming a faradaic efficiency of 100%, this corresponds to 1.7×10^{-7} mol Mo cm^{-2}. We conclude that AE-MoS_x is the preferred material due to its higher deposition efficiency and reportedly improved HER properties as compared to CE-MoS_x.[4]

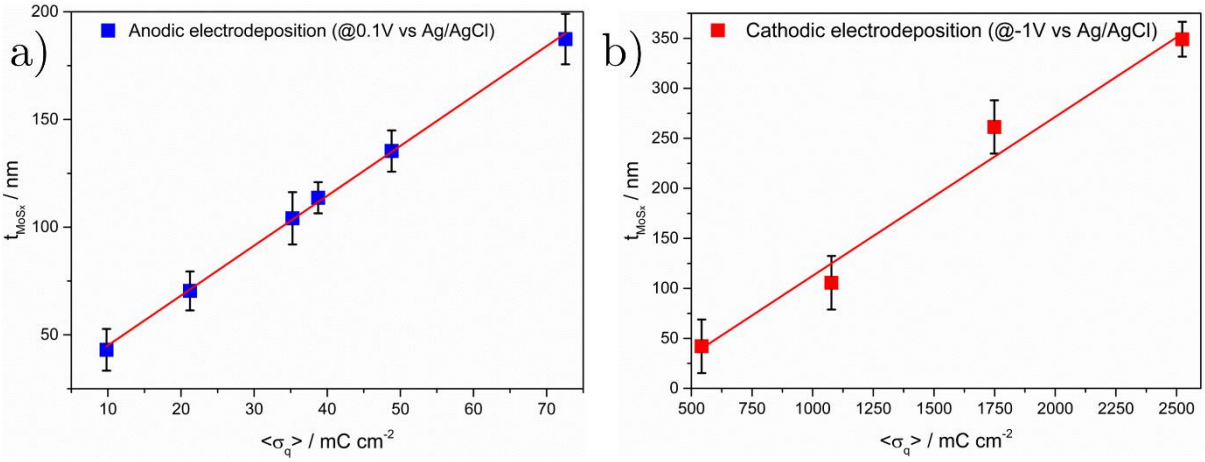

Figure 9.2. Plotting of the experimental thickness of a) anodically electrodeposited molybdenum sulfide (AE-MoS_x, E= +0.1 V vs. Ag/AgCl) and b) cathodically electrodeposited molybdenum sulfide (CE-MoS_x, E= -1 V vs. Ag/AgCl) thin films grown Si/Ti/Au electrodes by potentiostatic electrodeposition as a function of the total charge density $< \sigma_q >$ passed. Error bars account for no less than three independent thickness measurements by surface profilometry. Electrolyte: 2mM $(NH_4)_2[MoS_4]$, 0.1 M $NaClO_4$.

9.2.2 Anodically electrodeposited molybdenum sulfide (AE-MoS_x) inherent electrochemical activity: HER pre-catalytic peaks

The AE-MoS_x enhanced activity vs. CE-MoS_x has been systematically related to the higher content of proton-accepting S sites and the multiple S moieties found in the $[Mo_3S_{13}]^{2-}$ cluster-based polymeric structure of the electrodeposit (representative schematic in Figure 9.3).[8]

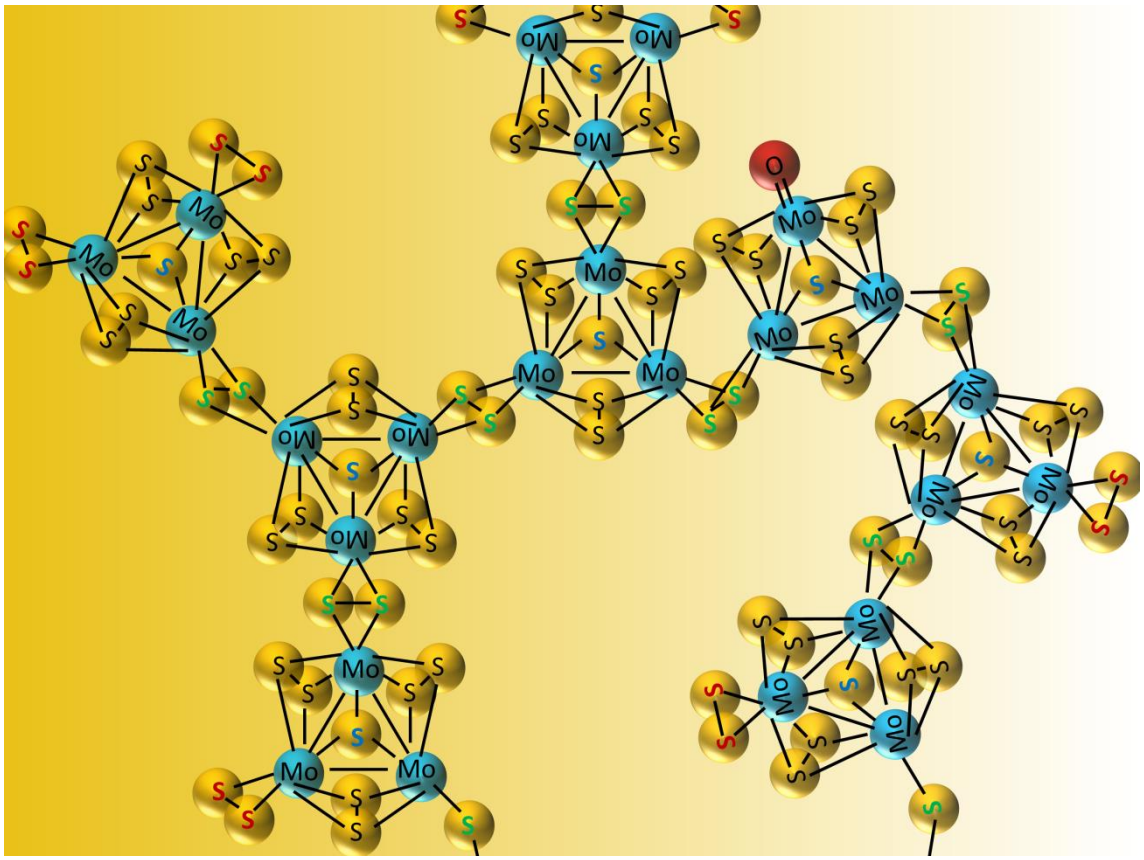

Figure 9.3. Schematic of the coordination polymer structure of AE-MoS_x based on the $[Mo_3S_{13}]^{2-}$ cluster unit. Sulfur ligand types labelled as follows: apical S^{2-} (S^{2-}_{apical}), blue; bridging S_2^{2-} ($S_2^{2-}_{bridging}$), black; terminal S_2^{2-} ($S_2^{2-}_{terminal}$), red; unsaturated S^{2-} (S^{2-}_{unsat}), green. S-deficient Mo-sites (AE-MoS_x structural defects, referred as $Mo^{5+}O_xS_y$) represented by Mo^{5+}=O groups.

In order to shed light on the electrochemical activity of AE-MoS_x comprehensive studies at different pHs were conducted by use of buffered electrolytes to minimise any local pH changes under HER operating conditions that may affect the AE-MoS_x inherent electrochemistry, morphology and/or surface species. Figure 9.4a shows a compilation of the hydrogen evolution linear sweep voltammograms (LSVs) recorded for 100 nm-thick AE-MoS_x films at a voltage scan rate of 50 mV s^{-1} using different buffered electrolytes in the 0-10 pH range after *iR* compensation.

In acidic media (pH < 5), one HER pre-wave peak can be observed, centred at $E_{peak,1}$ ≈ -0.37 V vs. SCE in 0.5 M H_2SO_4 (pH ≈ 0.3). From mildly acidic to alkaline conditions (5 ≤ pH ≤ 10), two more additional pre-catalytic events are identified at more cathodic potentials. For the pH 7 phosphate buffered electrolyte, their peaks are located at $E_{peak,2}$ ≈ -0.91 V and $E_{peak,3}$ ≈ -1.14 V vs. SCE, respectively. These peaks, as previously reported, only appear on the first HER cathodic scan, being absent in subsequent HER voltammograms (Figure 9.5 and Figure 9.15b).[8,9] This would initially indicate that, within the evaluated voltage window, the nature of the redox processes is irreversible. These are involved in the so-called irreversible "activation" step which converts the S-rich AE-MoS_3 to the HER-active MoS_{2+x} phase which presents a structure/stoichiometry closer to that of CE-MoS_x.[4,9]

To gather further understanding on the nature of the pre-catalytic reduction features, Figure 9.4b shows plots of their peak potential as a function of the pH. It is well known that pH-dependent gradients on the peak potential position can be related to the Nernst equation which describes proton-coupled electron transfer (PCET) mechanisms.[10–15] From it, information can be drawn on the number of protons and electrons involved in the electrochemically-triggered redox processes. For the first reduction process, $E_{peak,1}$ the slope gradient vs. the pH presents a -54 mV dec^{-1} dependence. This gradient is very close to the theoretical -59 mV dec^{-1} expected for redox processes involving an equivalent number of protons and electrons being

consumed. On the other hand, $E_{peak,2}$ and $E_{peak,3}$, found only in mildly acidic to alkaline pH conditions, present a ca. 0 mV dec^{-1} and +21 mV dec^{-1} dependence, respectively. Thus, $E_{peak,2}$ involves a reduction event in which no protons are involved, whereas $E_{peak,3}$ is related to a PCET mechanism involving a two-electron : one proton ratio.

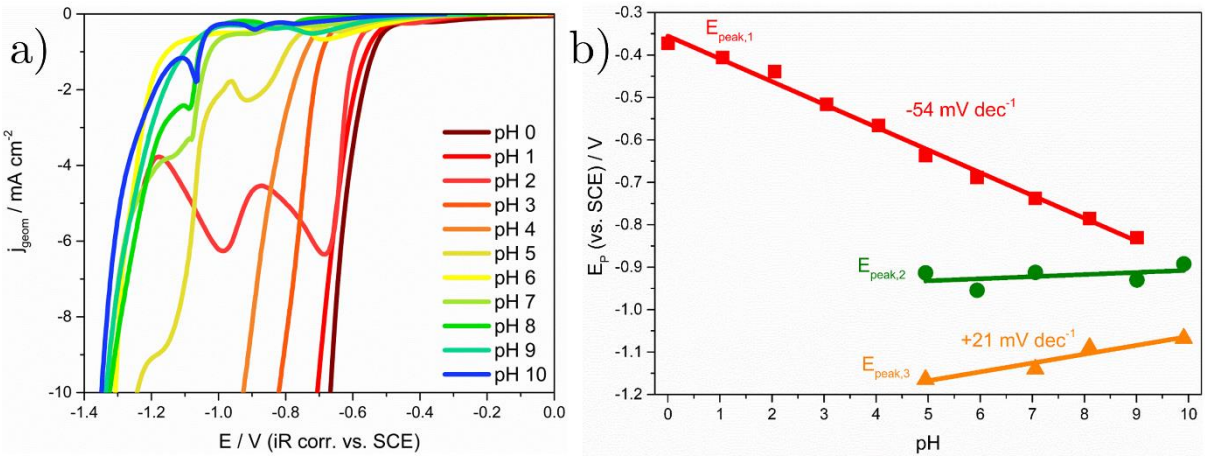

Figure 9.4. a) Linear sweep voltammograms recorded for pristine AE-MoS_x films (100 nm thick, catalyst loading ≈1.7 × 10^{-7} mol Mo cm^{-2} assuming 100% faradaic efficiency) across the 0-10 pH range by use of different buffered electrolyte solutions. b) Plotting of peak potential of the observed pre-catalytic redox features as a function of the buffered electrolyte pH. Scan rate: 50 mV s^{-1}.

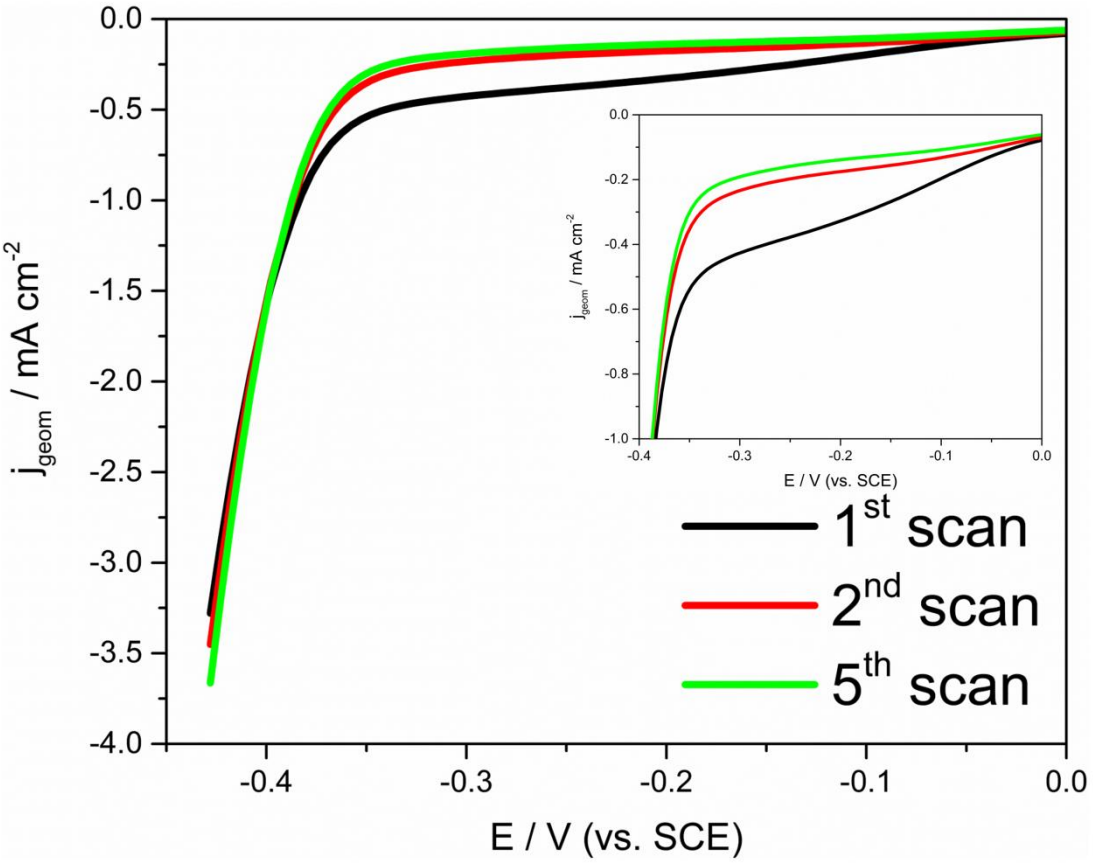

Figure 9.5. Cathodic linear sweep voltammograms recorded after continuous cycling from 0.15 to -0.425 V vs. SCE of pristine AE-MoS_x films in 0.5 M H_2SO_4. Inset: zoom of the LSVs at the HER pre-catalytic peak region. Scan rate: 50 mV s^{-1}.

Equivalent studies on unmodified Si/Ti/Au electrodes within the studied pH range confirm that the aforementioned peaks are not related to the inherent electrochemistry of the species present in the buffered electrolytes (Figure 9.6). In addition, the sharp nature of $E_{peak,3}$ would seem to indicate that the redox process involves a surface-bound species not influenced by diffusion of electroactive species: the release of protons proposed after pH gradient analysis would support the surface-confined nature of the process.

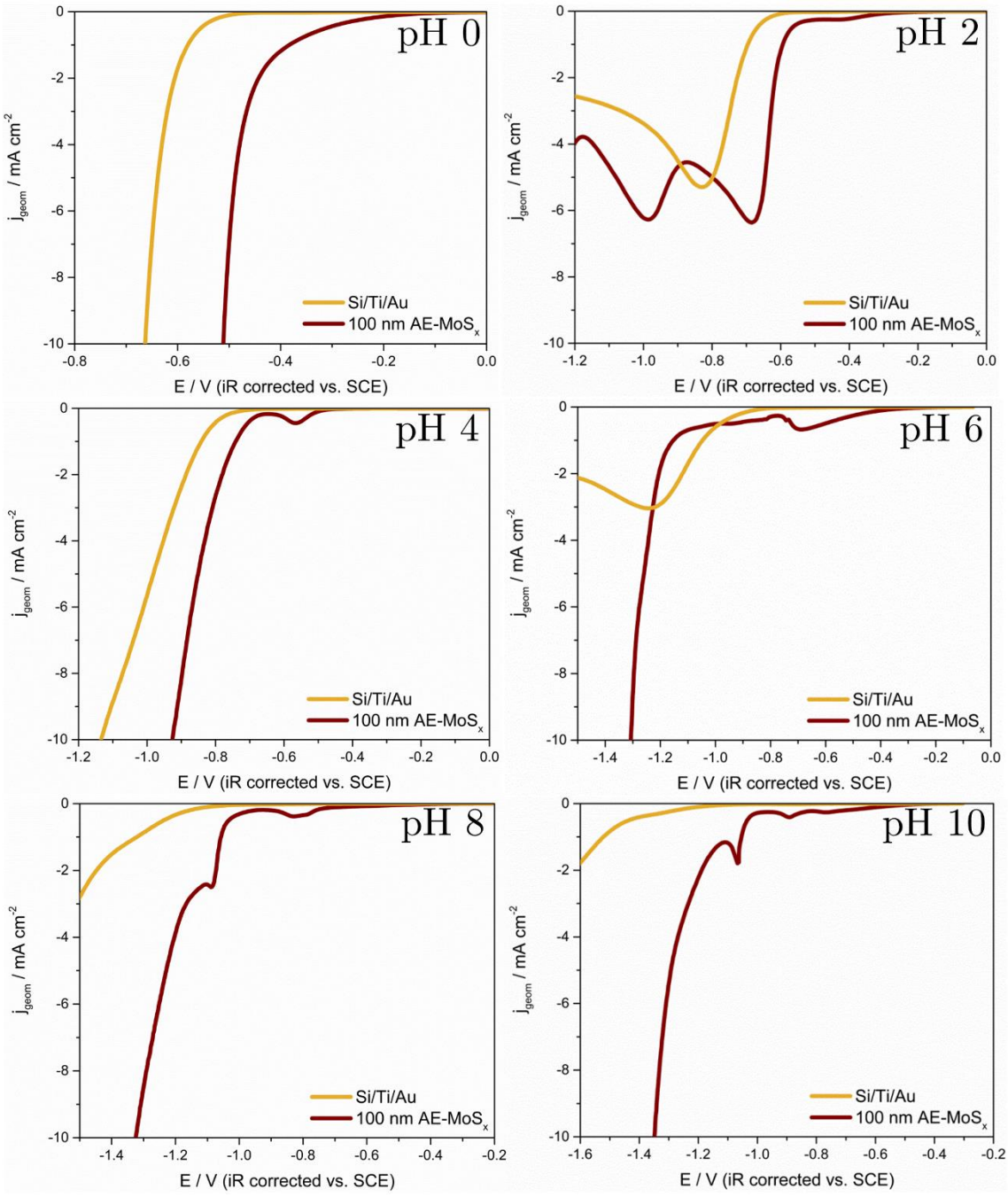

Figure 9.6. Representative linear sweep voltammograms recorded for pristine AE-MoS_x films (deep red) and bare Si/Ti/Au electrodes (dark yellow) across the 0-10 pH range by use of different buffered electrolyte solutions. Scan rate: 50 mV s^{-1}.

Having this in mind, we have proposed several potential candidates for the redox processes involved in each pre-catalytic feature. The in-situ proof of S-S bond cleaving from $S_2^{2-}{}_{bridging}$ and $S_2^{2-}{}_{terminal}$ at potentials equivalent to that of $E_{peak,1}$ leads us to ascribe the redox process

occurring at $E_{peak,1}$ to this process.[16] This involves a 2 H^+: 2e^- PCET reduction process (see reaction 9.3a), which would satisfy the approximate -59 mV dec^{-1} gradient experimentally observed.

$$Mo^{IV}(S-S)_{br/t}Mo^{IV} + 2\,H^+ + 2\,e^- \rightleftharpoons 2\,Mo^{IV} - SH \quad (9.3a)$$

However, the additional evidence of the removal of $S_2^{2-}{}_{terminal}$ ligands under HER operating conditions also suggests an alternative 2 H^+: 2e^- PCET reduction mechanism,[8] this time leading to formation of unsaturated Mo^{4+} centers (see reaction 9.3b)

$$Mo^{IV}[(S-S)_t]^{2-} + 2\,H^+ + 2\,e^- \rightarrow Mo^{IV} - \blacksquare + 2\,HS^- \quad (9.3b)$$

Whilst (9.3b) is an irreversible process, (9.3a) is an electrochemically reversible redox reaction. The degree of electrochemical reversibility/coexistence of these mechanisms and their implications in HER catalysis will be further investigated in sections 9.2.5 and 9.2.6 respectively.

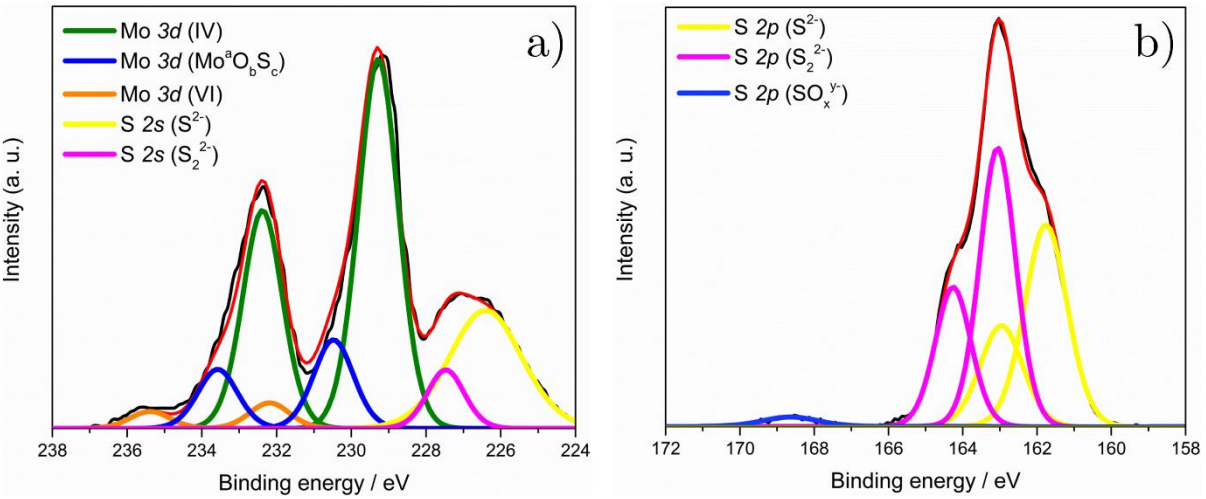

Figure 9.7. High-resolution a) Mo 3*d* and b) S 2*p* XPS spectra of pristine AE-MoS_x thin films. Labels: raw spectra (black), cumulative peak fit (red), Mo^{4+} $3d_{5/2:3/2}$ (green), $Mo^aO_bS_c$ $3d_{5/2:3/2}$ (blue), Mo^{6+} $3d_{5/2:3/2}$ (orange), S $2p_{3/2:1/2}$ (S^{2-}, yellow), S $2p_{3/2:1/2}$ (S_2^{2-}, magenta) and S $2p_{3/2:1/2}$ (SO_x^{y-}, light blue).

As for $E_{peak,2}$ and $E_{peak,3}$, their sole appearance at pH≥5 might indicate that either (i) the species responsible are only formed at these pH values after (9.3a, 9.3b) occur, or (ii) the species are unstable at pH≤5 and consequently not present at the AE-MoS_x surface until pH≥5 values are achieved. Surface composition analysis of pristine AE-MoS_x by XPS (Figure 9.7) suggests that the prepared films predominantly contain Mo^{4+} species, but Mo^{5+} oxysulfides and to a lesser extent MoO_3 are also present (Mo^{4+}: $Mo^{5+}O_xS_y$: Mo^{6+} XPS relative ratios 75.4: 18.6: 6.0, Figure 9.7a), giving Mo: S ratios of 1: 2.4±0.2. Previous evidence suggests that the AE-MoS_x undergoes a slow $Mo^{4+}\rightarrow Mo^{5+}\rightarrow Mo^{6+}$ transformation under atmospheric conditions[17] similar to that found in the $(NH_4)_2[MoS_4]$ precursor:[18] this could have partially occurred between MoS_x thin film preparation and XPS acquisition. The presence of $Mo^{5+}O_xS_y$ and MoO_3 at the outermost AE-MoS_x pristine surface is key as their stability is pH-dependent: MoO_3 is well known to be unstable in acidic media,[19] whereas $Mo^{5+}O_xS_y$ compounds are mostly soluble in acid unless structure-based properties confer enhanced stabilities.[20] Thus, the thermodynamically-favoured dissolution in acidic media eliminates their electrochemical contribution in electrolytes presenting pH $<$ 5,[21] leading us to hypothesis (ii). We propose, analogously to a previous report,[8] $E_{peak,2}$ to be due to the electrochemically-assisted reduction of $Mo^{5+}O_xS_y$ to Mo^{4+} species by reaction (9.4)

$$Mo^{V}O_bS_c + 1\,e^- \rightarrow Mo^{IV}O_bS_c \quad (9.4)$$

For $E_{peak,3}$, the proton-generating nature of the redox reaction involved limits the potential events occurring as Mo or S reduction events are normally proton-depleting. We herein tentatively propose that $Mo^{4+}O_xS_y$ could further reduce at more cathodic potentials to form MoO_2 (reaction 9.5)

$$Mo^{IV}OS + Mo^{IV}OS_2 + 2H_2O + 2\,e^- \rightarrow 2\,MoO_2 + 3\,HS^- + 1\,H^+ \quad (9.5)$$

9.2.3 AE-MoS_x inherent electrochemical activity: HER kinetics

It is also of particular relevance to monitor modifications in the HER kinetics as a function of the pH, as this might ultimately provide insights into the hydrogen evolution mechanism which ultimately dictates the electrocatalytic activity. Although previous reports describe almost unaltered Tafel slope values upon incremental MoS_2 loadings,[22] layer stacking,[19] and amorphous MoS_x S:Mo stoichiometry,[9,23] the influence of the electrolyte pH is rarely documented.

We investigated this by analysing the linear region of the η vs. $\log|j_{geom}|$ plot (i.e. Tafel plot, *b*) of *iR*-compensated LSVs acquired towards hydrogen evolving potentials, over a set of independent repeated measurements at the different buffered electrolytes studied. Figure 9.8a compiles the Tafel plots of bare Si/Ti/Au substrates and AE-MoS_x thin films, the latter under the presence and absence of 1500 rpm stirring, to identify potential contributions of both substrate and mass transport in the obtained values.

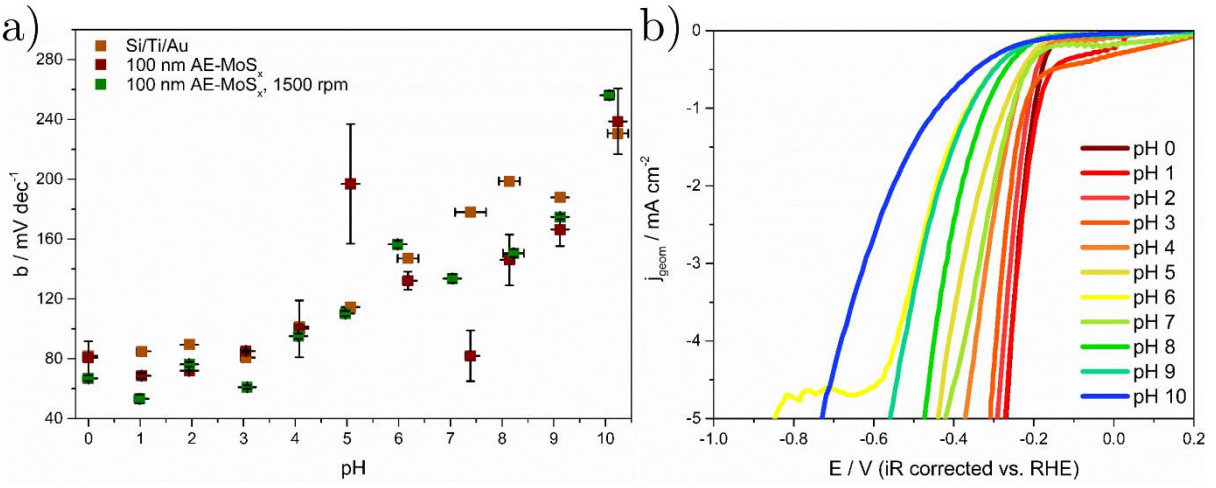

Figure 9.8. a) Tafel plots (η vs. $\log|j_{geom}|$) for Si/Ti/Au (yellow), pristine AE-MoS_x (red) and AE-MoS_x under 1500 rpm stirring (green) across the 0-10 pH range. b) *iR* and Nersnstian-corrected HER linear sweep voltammograms recorded for AE-MoS_x under 1500 rpm electrolyte stirring. Scan rate: 50 mV s^{-1}.

A plateau in the 0 ≤ pH ≤ 3 range, followed by an overall upward increase in the Tafel slope (*b)* values, was found when both Si/Ti/Au substrates and AE-MoS_x films were tested in more alkaline electrolytes. While *b* seems independent on the presence of AE-MoS_x up to pH 5, Si/Ti/Au substrates exhibit slightly higher values in neutral to alkaline environments. Although the exact HER pathway on bare Au is still under debate,[24] recent investigations in acidic electrolytes have found two characteristic Tafel slope values at low (b≈68 ± 5 mV dec^{-1}) and high current densities (b≈120 ± 2 mV dec^{-1}) due to hydrogen surface diffusion effects,[25,26] converging to a Tafel slope of b≈120 dec^{-1} in alkaline environments.[27] The averaged experimental b≈84 ± 4 mV dec^{-1} across the 0 ≤ pH ≤ 3 pH range, which ascends up to b≈230 ± 10 mV dec^{-1} at pH 10 deviate from the expected values.

Overall, AE-MoS_x films tested under stirring present Tafel slopes with lower dispersion and more reliable physical meaning compared to their quiescent counterparts (b≈65±10 mV dec^{-1} in the 0 ≤ pH ≤ 3 range closer to theoretical Volmer-Heyrovsky b≈40 mV dec^{-1} as reported for AE-MoS_x in acid).

We believe that the observed differences arise due to: (i) the irreversible transformation of AE-MoS_x to CE-MoS_x that occurs only after the first LSV scan (as plotted for the unstirred case) which modifies the intrinsic kinetics of the HER active sites, (ii) charge transfer differences across the working electrode material, (iii) mass transport effects due to measurements being recorded under quiescent conditions instead of under stirring and (iv) the nature of the working electrode. All of these, amongst others, have been suggested as potential sources of error to unambiguously compare Tafel slopes, specifically for ascribing them to reaction mechanisms.[28,29]

The Si/Ti/Au substrate, particularly in acidic conditions, indeed seems to govern the experimental Tafel slopes obtained after MoS_x modification across the 0-10 pH range. A similar conclusion was obtained in previous reports in acidic electrolytes upon use of supporting

working electrodes of different nature[30,31] and morphology.[32] Thus, the anomalous Tafel slopes found for the Si/Ti/Au with respect to Au might stem from the inherent morphology of the working electrode.

As for the Tafel slope trend with pH, it has been very recently studied on AE-MoS_x by Dubouis et al. by use of variable concentrations sulfuric acid in the $0 \leq pH \leq 4$ range.[33] It was suggested that whilst at very acidic pHs ($pH \leq 2$) the HER mechanism on AE-MoS_x operated by the electroreduction of the hydronium ion ($H_3O^+ + 1\,e^- \rightarrow 1/2\,H_2 + H_2O$), at $pH \geq 3$ the HER occurred via the water reduction/splitting mechanism ($H_2O + 1\,e^- \rightarrow 1/2\,H_2 + OH^-$). This implies that b should be pH-insensitive for $pH \leq 2$, whereas b should increase at $pH > 3$ due to increasingly lower proton concentrations yielding the proton electroadsorption rate-limiting step (i.e. Volmer step, $b \approx$ 120mV dec^{-1}) to govern the HER performance. This pH-dependent HER mechanism was previously reported for noble metal surfaces.[34–37] Despite of using electrolytes with different spectator species and ionic strengths, this trend is also found for our AE-MoS_x results under stirring: within the $0 \leq pH \leq 2$ range, Tafel slopes are almost constant $b \approx 65 \pm 10$ mV dec^{-1}, whilst at $pH > 2$ they increase approximately linearly yielding $b \approx 120$ mV dec^{-1} at pH 5.

For neutral to alkaline pHs, however, b exceeds 120mV dec^{-1}: as electron transfer coefficients in mildly acidic to alkaline conditions are reported to be almost pH independent,[38] mass transport limitations (i.e. proton concentration depletion at the electrode interface) and electrode surface species will necessarily play a role on the HER kinetics. Particularly, the low thermodynamic stability of AE-MoS_x and the presence of the previously unstable MoO_x and related species at the electrode surface will certainly modify both hydrogen active sites/coverages and charge transfer properties. Indeed, molybdenum oxides such as MoO_3 and MoO_2, stable in neutral to alkaline environments, exhibited Tafel slopes as high as $b \approx 160$ mV dec^{-1} and $b \approx 200$ mV dec^{-1}, respectively in 0.5 M H_2SO_4.[39] Thus, we believe that the presence

of Mo_xO_y surface species in neutral to alkaline environments with different HER active site kinetics, and the partial exposure of the underlying Au substrate due to AE-MoS_x instability, could explain the Tafel slopes observed.

This pH-dependence on the Tafel slope, HER mechanism, and surface species consequently supports the AE-MoS_x LSVs found under stirring after *iR* and Nernstian compensation (Figure 9.8b). As found by Dubouis et al., LSVs in the $0 \leq pH \leq 2$ range fully overlap due to invariable Tafel slope and HER kinetics, whereas for $pH \geq 3$ the HER mechanism and Tafel slope modification results in non-overlapping, negatively shifted LSVs towards higher pH values. Although the HER curves in neutral to alkaline should converge to the water reduction mechanism, the modification of the Mo species responsible for the HER and their coverage upon pH-dependent AE-MoS_x dissolution alter this trend.

9.2.4 AE-MoS_x inherent electrochemical activity: electro-oxidation

Next, we investigated the electro-oxidative processes of the 100 nm-thick AE-MoS_x films. For pristine AE-MoS_x, a LSV from ca. 0 V to 1.2 V vs. SCE reveals a broad anodic feature, in the 0.2 - 1.1 V voltage range, with its peak at ca. 0.7 V vs. SCE when tested in a 0.5 M H_2SO_4 electrolyte (Figure 9.9a). Plotting of the electro-oxidation band peak potential as a function of the pH gives an experimental gradient of -27 mV dec^{-1}, which closely matches the -29.5 mV dec^{-1} theoretical Nernstian slope characteristic of a 1 H^+: 2e^- PCET electro-oxidation mechanism (Figure 9.9b). Previous reports in the literature performed with crystalline MoS_2 materials under different pHs concur with our obtained results: a single broad electro-oxidative feature was reported, which satisfied a 1 H^+: 2e^- PCET ascribed to the oxidation of the Mo^{4+} moieties to Mo^{6+} by a complex redox mechanism.[40,41] To the best of our knowledge, our investigation is the first one to experimentally support the 1 H^+: 2e^- PCET electro-oxidation mechanism for pristine AE-MoS_x.

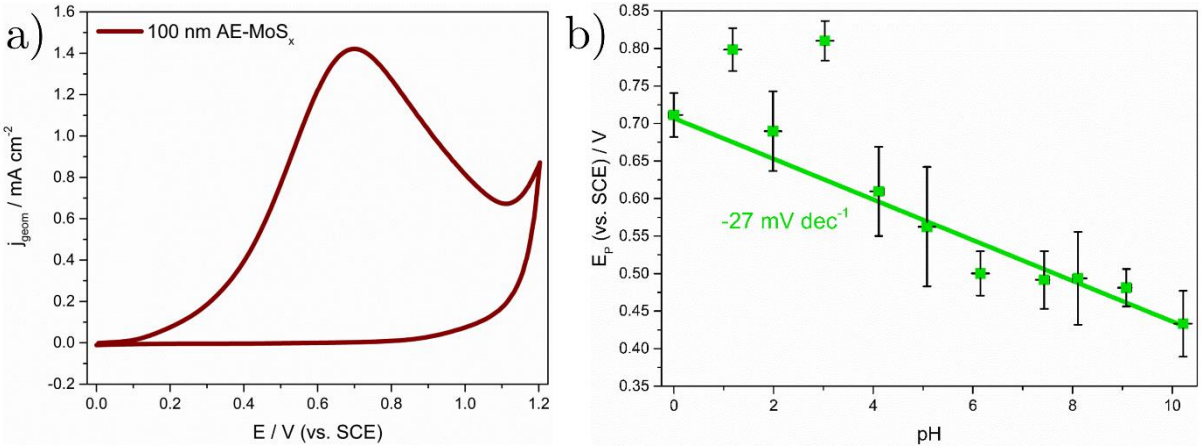

Figure 9.9. a) Anodic stripping voltammogram of freshly-deposited AE-MoS_x films recorded from 0 to 1.2 V vs. SCE in 0.5 M H_2SO_4, b) Plot of AE-MoS_x electro-oxidation peak potential versus buffered electrolyte pH showing a gradient of -27 mV dec^{-1}. Scan rate: 50 mV s^{-1}.

The oxidative shoulder found in the 1-1.2 V region is ascribed to the electro-oxidation of the underlying Au substrate: additional voltammograms recorded at higher anodic limits after their initial electro-oxidation (0 to 1.5 V vs. SCE, Figure 9.10) for both AE-MoS_x modified and pristine Si/Ti/Au electrodes corroborated its correspondence with the Au inherent electrochemical features.

Interestingly, AE-MoS_x samples that have been anodically stripped in the 3-6 pH range present an additional sharp electro-oxidative feature past the broad oxidation band peak maximum, best resolved at pH 4 and gradually faded at increased pH values (Figure 9.11). We hypothesize that the citric-citrate electrolyte used is responsible for this feature, by formation of a redox-active complex with the soluble Mo^{6+} species at the electrode-electrolyte interface. As the most abundant citric acid species at pH 4 corresponds to AH_2^- (monovalent anion), this is most likely to be the responsible Mo^{6+} complexing agent. Unambiguous identification of this feature along with that allocated to Au electro-oxidation are pending: control experiments on alternative substrates (e.g. glassy carbon) would prove their origin, this being beyond the scope of this thesis.

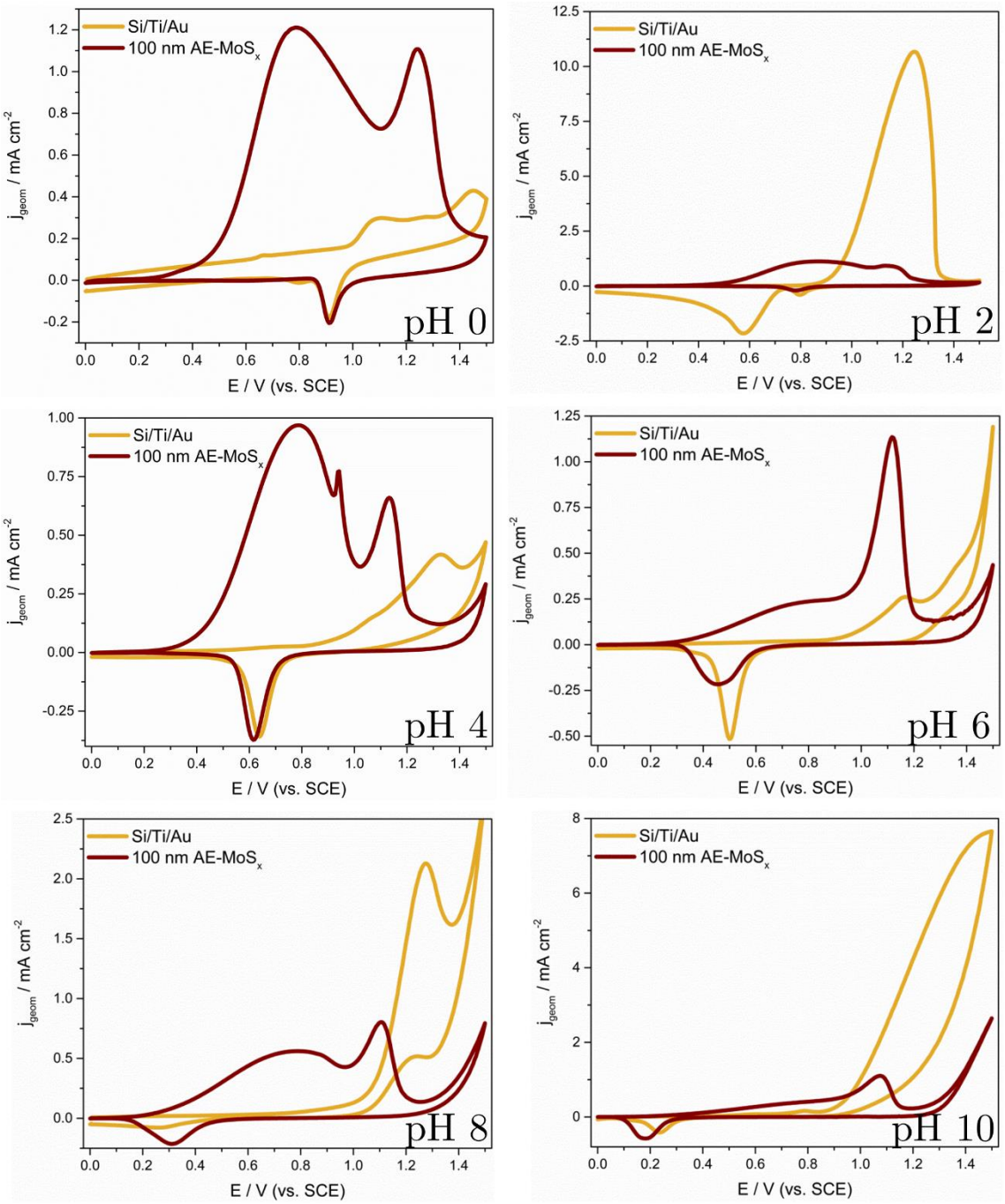

Figure 9.10. Representative anodic stripping voltammograms recorded for pristine AE-MoS_x films (deep red) and bare Si/Ti/Au electrodes (dark yellow) across the 0-10 pH range by use of different buffered electrolyte solutions. Voltage range: 0 to 1.5 V vs. SCE. Scan rate: 50 mV s^{-1}.

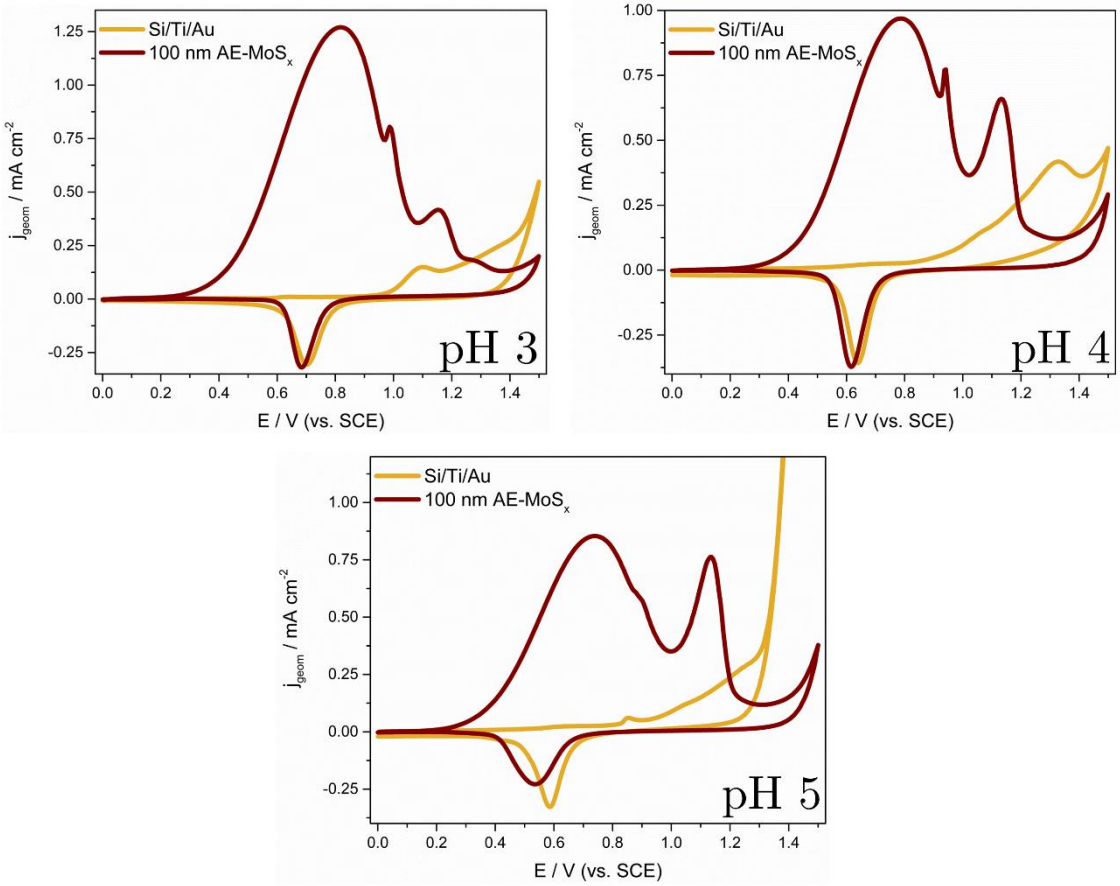

Figure 9.11. Anodic stripping voltammograms recorded for pristine AE-MoS_x films (deep red) and bare Si/Ti/Au electrodes (dark yellow) betweem the 3-5 pH range. Voltage range: 0 to 1.5 V vs. SCE. Scan rate: 50 mV s^{-1}.

To gain further insight on the implications of the complex electro-oxidation mechanism, ex-situ Raman spectra of the electro-oxidized AE-MoS_x films were recorded (Figure 9.12, see Section 4.8.2 for experimental details and Table J.1 Appendix for values), providing interesting results particularly for samples tested at pH ≥ 5. Under these conditions, several Raman vibration features arise and/or are severely altered: 1) the ν(Mo-Mo) band at ca. 201 cm^{-1} sharpens and increases its relative intensity, 2) the ν(Mo-S) band at ca. 358 cm^{-1} sharpens to the detriment of the remaining ν(Mo-S) bands, and undergoes a red-shift to ca. 354.8 cm^{-1}, 3) the out-of-plane A_{1g} mode appears at ca. 404 cm^{-1}, with relative intensities higher than those found for the in-plane E^2_{1g} mode at ca. 380 cm^{-1} and 4) additional Raman modes appear at ca.

341 (faint), 490 (strong) and 730 (strong) cm^{-1}, respectively. This unambiguously proves that electro-oxidation irreversibly changes the morphology of the cluster-based AE-MoS_x structure: the Raman signal intensity sharpening in features 1-3) inform that the resulting structure comprises morphologies with predominance of those vibration modes. As for 4), we believe that the weakening and disappearance of ν(Mo-S) and $\nu(S\text{-}S)_{terminal}$ vibration modes, respectively, are responsible for the 341 and 490 cm^{-1} bands. Additionally, the 730 cm^{-1} band should correspond to the partial oxidation of Mo^{4+} sites, as this vibration is not far away from the one expected for Mo=O (ca. 880 cm^{-1}). Thus, we can conclude that the 1 H^+: 2e^- PCET electro-oxidation mechanism for pristine AE-MoS_x primarily involves the disappearance of $S_2^{2-}{}_{terminal}$ and the formation of partially-oxidized molybdenum sites.

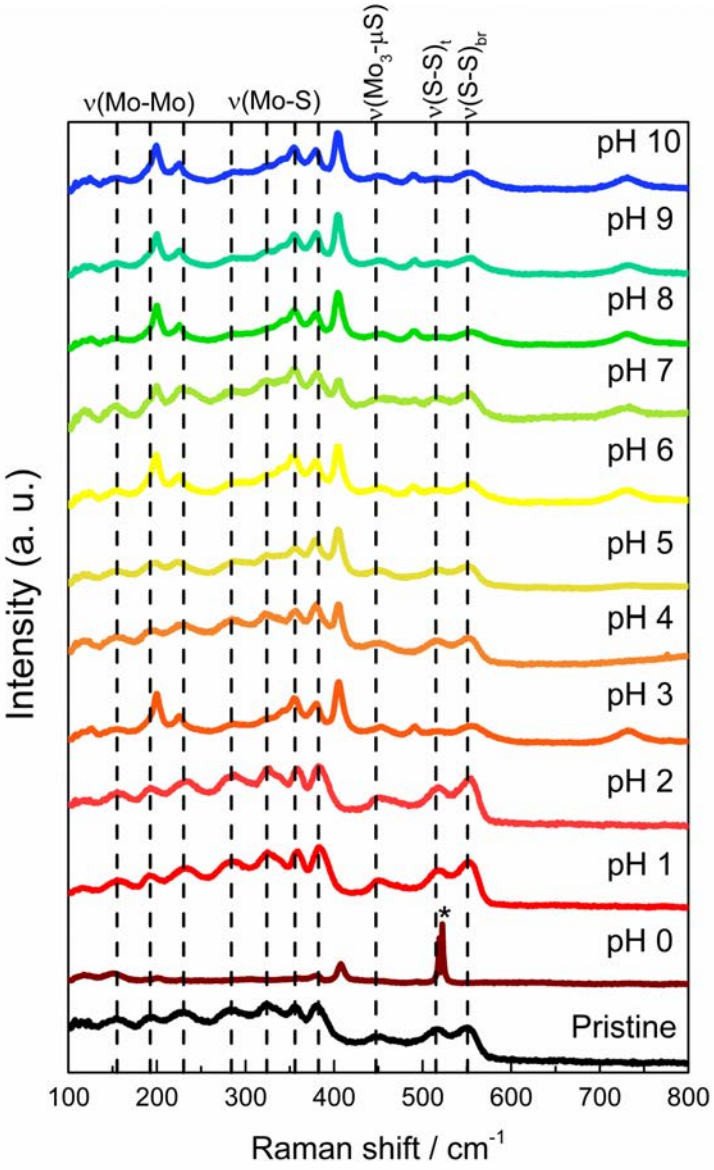

Figure 9.12. Stacked Raman spectra (532 nm laser excitation, 100-800 cm^{-1} range, intensity-normalized) of pristine (black) and electro-oxidized AE-MoS_x thin films across the 0-10 pH range. Dashed vertical lines refer to characteristic AE-MoS_x vibration modes, whilst asterisk labelling (*) identifies Raman modes ascribed to underlying Si substrate.

Alternatively, we investigated the electro-oxidative features after one LSV towards HER potentials (from 0.7 V to -1.2 V vs. SCE, scan rate 50 mV s^{-1}) by recording the reverse scan towards positive potentials (from -1.2 V to 0.7 V vs. SCE, scan rate 50 mV s^{-1}, referred in the discussion as post-LSV). Figure 9.13 shows a representative anodic voltammogram obtained in

a pH 7 phosphate buffered electrolyte: two well-resolved peaks can be identified, the first ($E_{peak,I}$) at ca. -0.16 V and the second ($E_{peak,II}$) at ca. 0.29 V. Surprisingly, $E_{peak,I}$ and $E_{peak,II}$ partially overlap for the remaining pH electrolytes investigated. These are equivalent to those previously found for AE-MoS_x being oxidatively stripped after applying a cathodic scan to HER potentials,[9,42] in stark contrast with the electro-oxidative behaviour found for pristine AE-MoS_x. This suggests that the AE-MoS_x electrochemical conditioning to hydrogen evolving potentials alters the electro-oxidation mechanism.

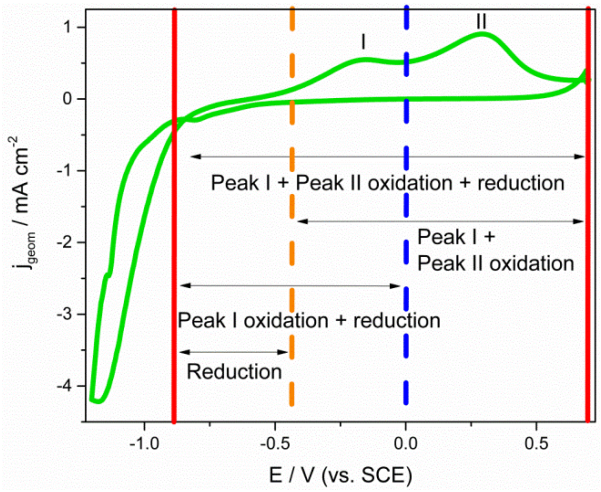

Figure 9.13. Cyclic voltammogram recorded for pristine AE-MoS_x films from 0.7 V to -1.2 V vs. SCE in a phosphate buffered electrolyte (pH≈7). Scan rate: 50 mV s^{-1}.

It was previously hypothesized that partial stripping to potentials past $E_{peak,I}$ selectively oxidized weakly Mo-bound low XPS binding energy unsaturated S^{2-} (S^{2-}_{unsat}) and $S_2^{2-}_{terminal}$ to MoO_x, whereas stripping past $E_{peak,II}$ lead to full conversion of AE-MoS_x to HER-inactive MoO_x.[9] A more recent study attributed these features to the irreversible oxidation of $S_2^{2-}_{terminal}$ and $S_2^{2-}_{bridging}$, respectively.[42] However, neither the pH-dependence of these reactions nor the electrochemical reversibility of reaction (9.3a) triggered by the initial LSV scan towards HER potentials were taken into consideration when proposing these reactions. To gather insight on these redox processes, we elucidated the pH-dependence of the post-LSV AE-MoS_x electro-oxidative features (Figure 9.14a) by plotting the electro-oxidation peak potentials versus the

electrolyte pH for both $E_{peak,I}$ (Figure 9.14b) and $E_{peak,II}$ (Figure 9.14c) after Gaussian peak deconvolution. For $E_{peak,I}$, a -56 ± 4 mV dec^{-1} dependence was observed between pH 2 and pH 8. This is in excellent agreement with a 1 H^+: 1e^- (or subsequent multiples) PCET electro-oxidation mechanism. However, this does not satisfy the widely established 1 H^+: 2e^- PCET mechanism under which the irreversible electro-oxidation of MoS_2 materials to Mo^{6+} is reported to proceed, as this would give a theoretical Nernstian slope of -29.5 mV dec^{-1}. [40,41,43]

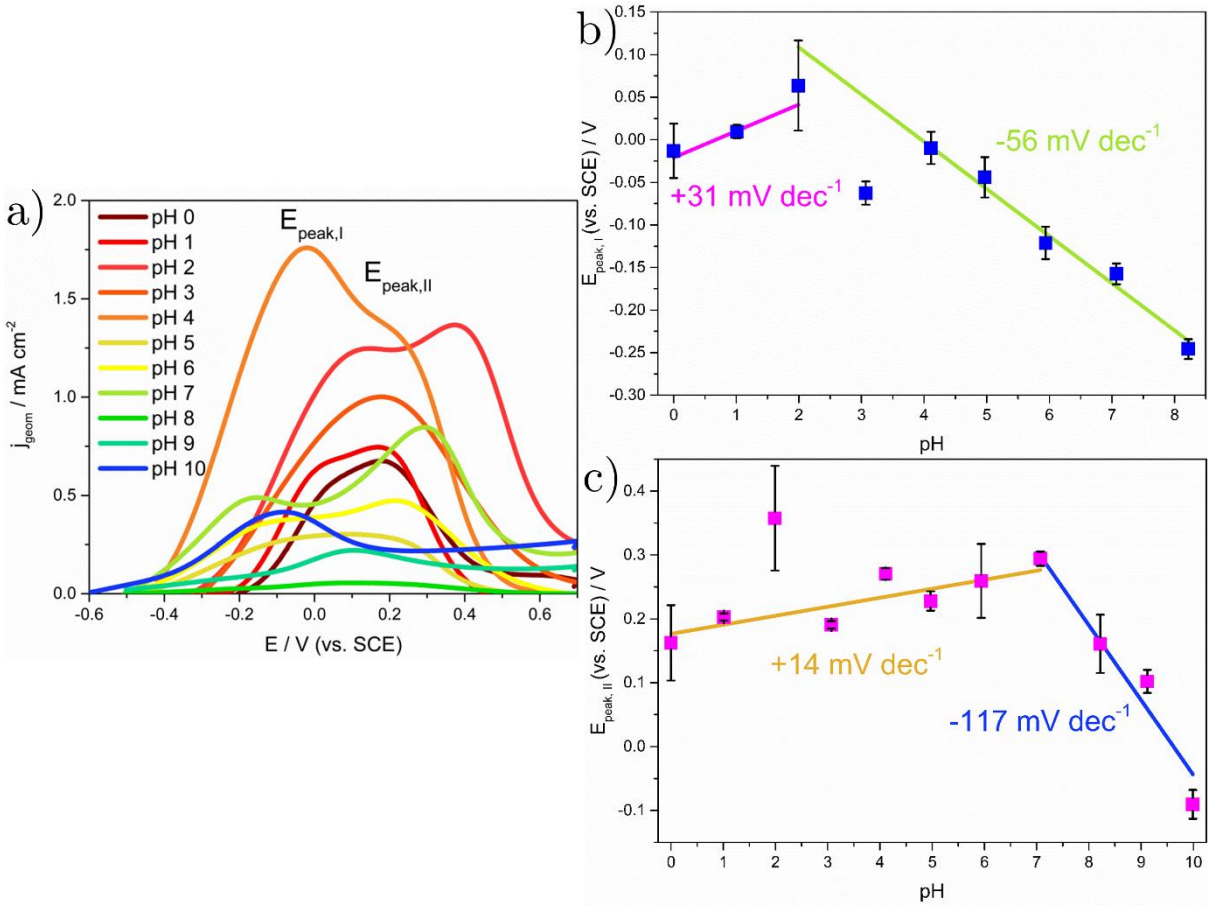

Figure 9.14. a) Compilation of reverse scans obtained for post-LSV AE-MoS_x films (from -1.2 V to 0.7 V vs. SCE) across the 0-10 pH range Scan rate: 50 mV s^{-1}. Peak potential dependence of post-LSV AE-MoS_x electro-oxidative features labelled as b) $E_{peak,I}$ (blue) and c) $E_{peak,II}$ (magenta) as a function of the buffered electrolyte pH. Overlapped linear fits and experimental E-pH slopes displayed for ease of comparison.

Thus, an alternative electro-oxidation event precedes the complete electrochemical oxidation of the AE-MoS_x thin film. Analysis of the voltammetric features found after cycling the post-LSV AE-MoS_x at variable voltage windows indicates that the electro-oxidation event responsible for $E_{peak,I}$ can only be found when AE-MoS_x has undergone cathodic cycling past the pre-catalytic peak $E_{peak,1}$ (Figure 9.15 section 9.2.5). Given the electrochemical reversibility of reaction (9.3a), we preliminarily suggest the electro-oxidation event $E_{peak,I}$ to be the reinstatement of the previously cleaved S-S bond in $S_2^{2-}{}_{bridging}$ and/or $S_2^{2-}{}_{terminal}$ (2 H^+: 2e^- PCET mechanism).

$$2\,Mo^{IV}-SH \rightleftharpoons Mo^{IV}(S-S)_{br/t}Mo^{IV} + 2\,H^+ + 2\,e^- \quad (9.6a)$$

However, the partial corrosion of the previously cleaved $S_2^{2-}{}_{bridging}$ and/or $S_2^{2-}{}_{terminal}$ sites giving MoO_2 also satisfies a close-to 1 H^+: 1e^- PCET electro-oxidation mechanism, and thus cannot be discarded.

$$Mo^{IV}-SH + 6\,H_2O \rightarrow MoO_2 + HSO_4^- + 12H^+ + 11e^- \quad (9.6b, \text{acidic pH})$$

$$Mo^{IV}-SH + 6\,H_2O \rightarrow MoO_2 + SO_4^{2-} + 13H^+ + 11e^- \quad (9.6b, \text{neutral pH})$$

As for $E_{peak,II}$, a clear -117±17 mV dec^{-1} gradient is found at neutral to alkaline pHs ($7 \leq pH \leq 10$). This satisfies a 2 H^+: 1e^- PCET mechanism: based on the thermodynamic instability seen for Mo species at positive potentials in alkaline environments,[21] we suggest the electro-oxidation of MoO_2 to the soluble MoO_4^{2-} anion to be the reaction taking place.

$$MoO_2 + 2\,H_2O \rightarrow \frac{1}{2}MoO_4^{2-} + 4\,H^+ + 2\,e^- \quad (9.7)$$

In acidic pH, $E_{peak,II}$ presents a slightly positive gradient of +14±5 mV dec^{-1}. This clearly deviates from the 1 H^+: 2e^- PCET mechanism generally ascribed to MoS_2 electrodissolution, and would theoretically imply a 1 proton-depleting, 3 electron-generating PCET mechanism. This informs of a complex electro-oxidation mechanism which cannot be unambiguously

described by one specific redox process. The most likely final electro-oxidation products are, according to thermodynamic stability, the acid-unstable MoO_3 ($pH \leq 1$) and the solution-soluble $HMoO_4^-$ ($1 \leq pH \leq 7$).[21,44]

9.2.5 AE-MoS_x inherent electrochemical activity: electrochemical conditioning

Having in mind the inherent electrochemical features found for AE-MoS_x, we proceeded to evaluate the impact of several voltammetric pre-treatments on pristine thin films. These not only intend to identify an optimal activation step to maximize the AE-MoS_x thin film HER activities, but also to corroborate the redox mechanisms proposed previously. For such purpose, a combined use of electrochemical techniques, ex-situ Raman and ex-situ X-ray photoelectron spectroscopies were employed to correlate positive/negative electrocatalytic effects with modifications in surface morphology and/or species. Multiple activation pre-treatments can be chosen by tuning the electrochemical parameters: in our study cyclic voltammetry is chosen over potentiostatic preconditioning procedures because of the need to monitor any electrochemical modifications of the redox features during preconditioning. Given the irreversible nature and close proximity to HER-evolving potentials of the events responsible for $E_{peak,2}$ and $E_{peak,3}$ (peaks absent after first cathodic scan), only voltammetric cycling within the voltage range comprising $E_{peak,1}$, $E_{peak,I}$ and $E_{peak,II}$ will be evaluated. For acidic/alkaline pHs, the overlap found for $E_{peak,I}$ and $E_{peak,II}$ implies that only three CV pretreatments can be evaluated: electro-oxidative, oxidative-reductive and reductive (for definitions, see experimental section). For pH 7, the absence of overlap between $E_{peak,I}$ and $E_{peak,II}$ will enable two different oxidative-reductive CV pre-treatments upon modification of the anodic potential vertex (past $E_{peak,I}$ or $E_{peak,II}$, respectively).

Figure 9.15 shows representative cyclic voltammograms obtained for the four electrochemical conditioning methods evaluated in a pH 7 phosphate buffered electrolyte (50 CVs at 50 mV s^{-1}), selected after identifying the voltage window of each redox feature by recording an initial voltammogram from 0.7 to -1.2 V (as depicted in Figure 9.13).

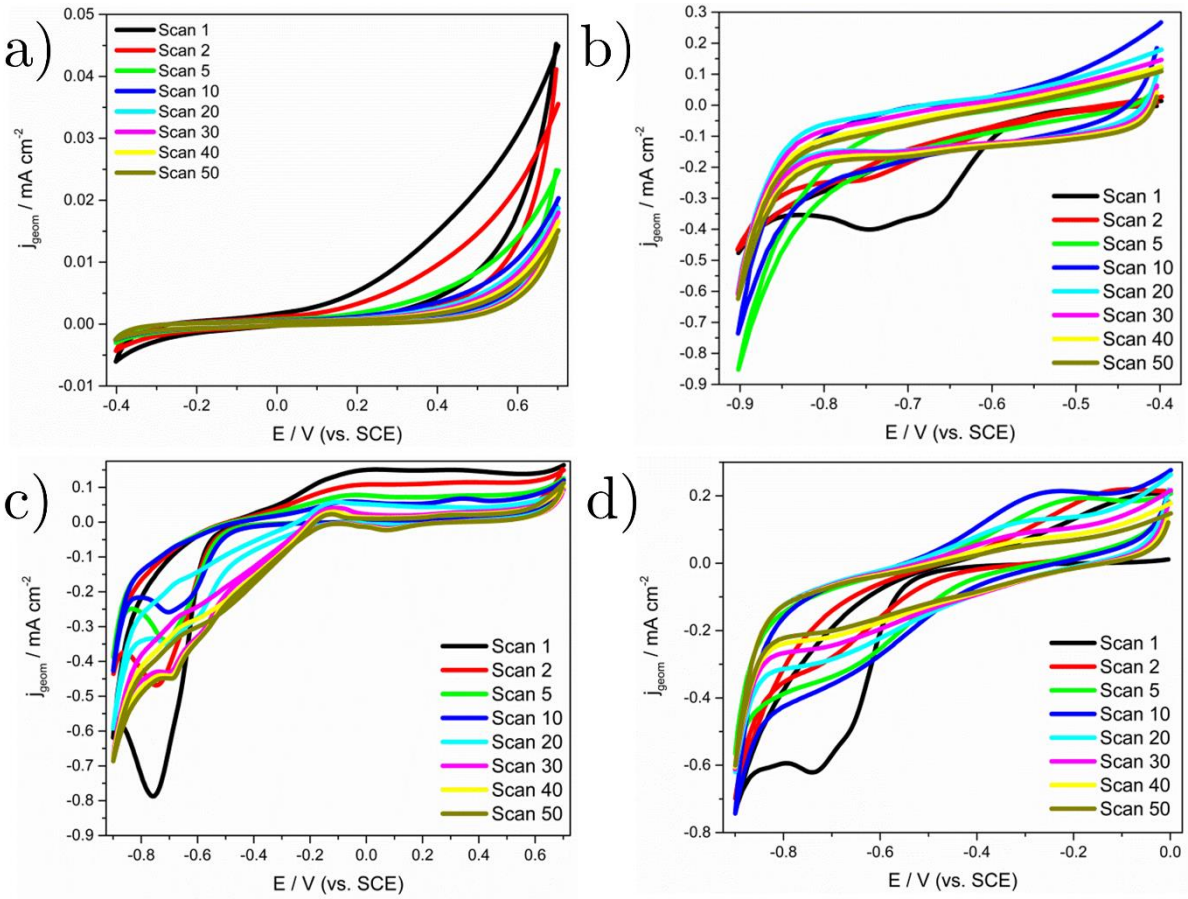

Figure 9.15. Representative voltammograms obtained for post-LSV AE-MoS_x films during the evaluation of the electrochemical conditioning treatments: a) electro-oxidative, b) reductive, c) oxidative-reductive (anodic potential vertex past $E_{peak,II}$) and d) oxidative-reductive (anodic potential vertex past $E_{peak,I}$). Electrolyte: pH 7 phosphate buffer saline. Scan rate: 50 mV s^{-1}.

For the electro-oxidation treatment (Figure 9.15a), it can be clearly seen that no electro-oxidative peaks can be found but an increasing anodic current instead. On the other hand,

these peaks can be found for both oxidative-reductive treatments (Figs. 9.15c and 9.15d). This suggests that the electro-oxidation features responsible for $E_{peak,I}$ and $E_{peak,II}$ only arise after the AE-MoS_x thin films have been previously cycled to cathodic potentials past the first pre-catalytic event $E_{peak,1}$ (Figure 9.15b), and/or that the voltage window under which the AE-MoS_x thin films are cycled alters their peak position. The oxidative-reductive cycling shown in Figure 9.15d clearly shows a co-dependence between the pre-catalytic event $E_{peak,1}$ and the electro-oxidative feature $E_{peak,I}$. Thus, we believe that $E_{peak,1}$ is indispensable for $E_{peak,I}$ to occur and vice-versa: this would initially support our claims that $E_{peak,1}$ corresponds to the electrochemically reversible S-S bond cleaving from $S_2^{2-}{}_{bridging}$ and $S_2^{2-}{}_{terminal}$ given by reactions (9.3a, 9.3b), and $E_{peak,I}$ to the reverse reaction (9.6a).

9.2.5.1 AE-MoS_x electrochemical conditioning by oxidative-reductive and reductive cycling: EC, Raman and XPS analysis

To further corroborate this, we analysed the voltammetric profiles of both oxidative-reductive (Figure 9.16) and reductive (Figure 9.17) cyclic pretreatments along with their respective XPS spectra.

For the oxidative-reductive voltammograms, it was observed that $E_{peak,1}$ split into two peaks after continuous cycling irrespective of the electrolyte pH (Figure 9.18a). For AE-MoS_x cycled in a pH 6 electrolyte (Figure 9.18b), the initially broad precatalytic peak found at $E_{peak,I} \approx$ -0.68 V for the first scan decomposed into $E_{peak,III} \approx$ -0.53 V and $E_{peak,IV} \approx$ -0.64 V. Peak III current density decreased, and peak position shifted positively upon cycling, whereas peak IV emerged as cycling progressed. Plotting of the pH-dependent $E_{peak,III}$ and $E_{peak,IV}$ position in the 0-10 pH range for the 50^{th} oxidative-reductive cathodic scan (Figure 9.18c) showed that both peaks presented a Nernstian gradient close to -59 mV dec^{-1} ($E_{peak,III} \approx$ -52±1 mV dec^{-1} , $E_{peak,IV} \approx$ -49±1 mV dec^{-1}), consequently leading to an almost constant peak separation. This satisfies

the 2 H^+: 2e^- PCET reduction mechanism under which the S-S bond cleaving/dissolution is suggested to occur.

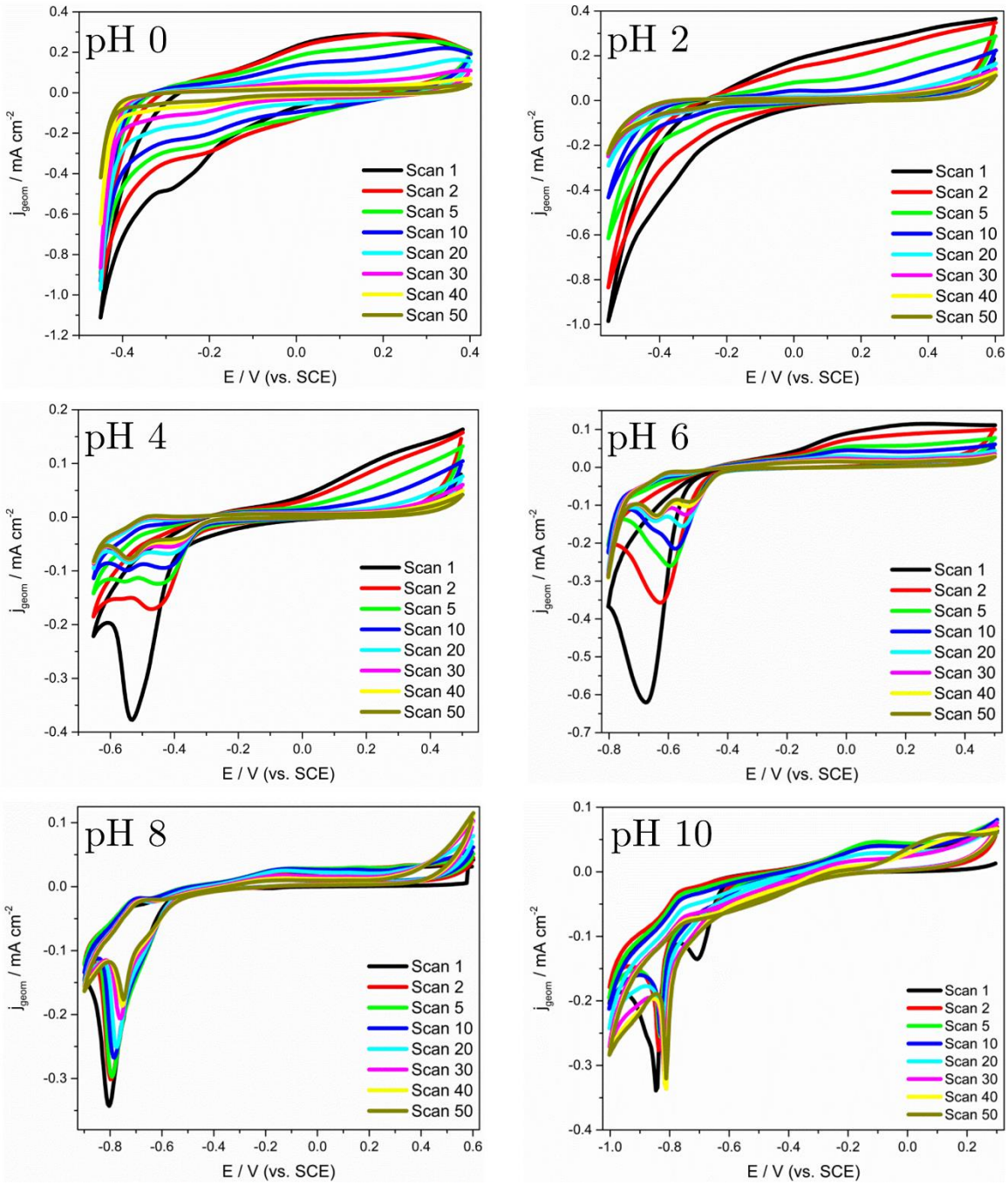

Figure 9.16. Representative voltammograms obtained for post-LSV AE-MoS_x films during the oxidative-reductive electrochemical conditioning treatments (anodic potential vertex past $E_{peak,II}$). Scan rate: 50 mV s^{-1}.

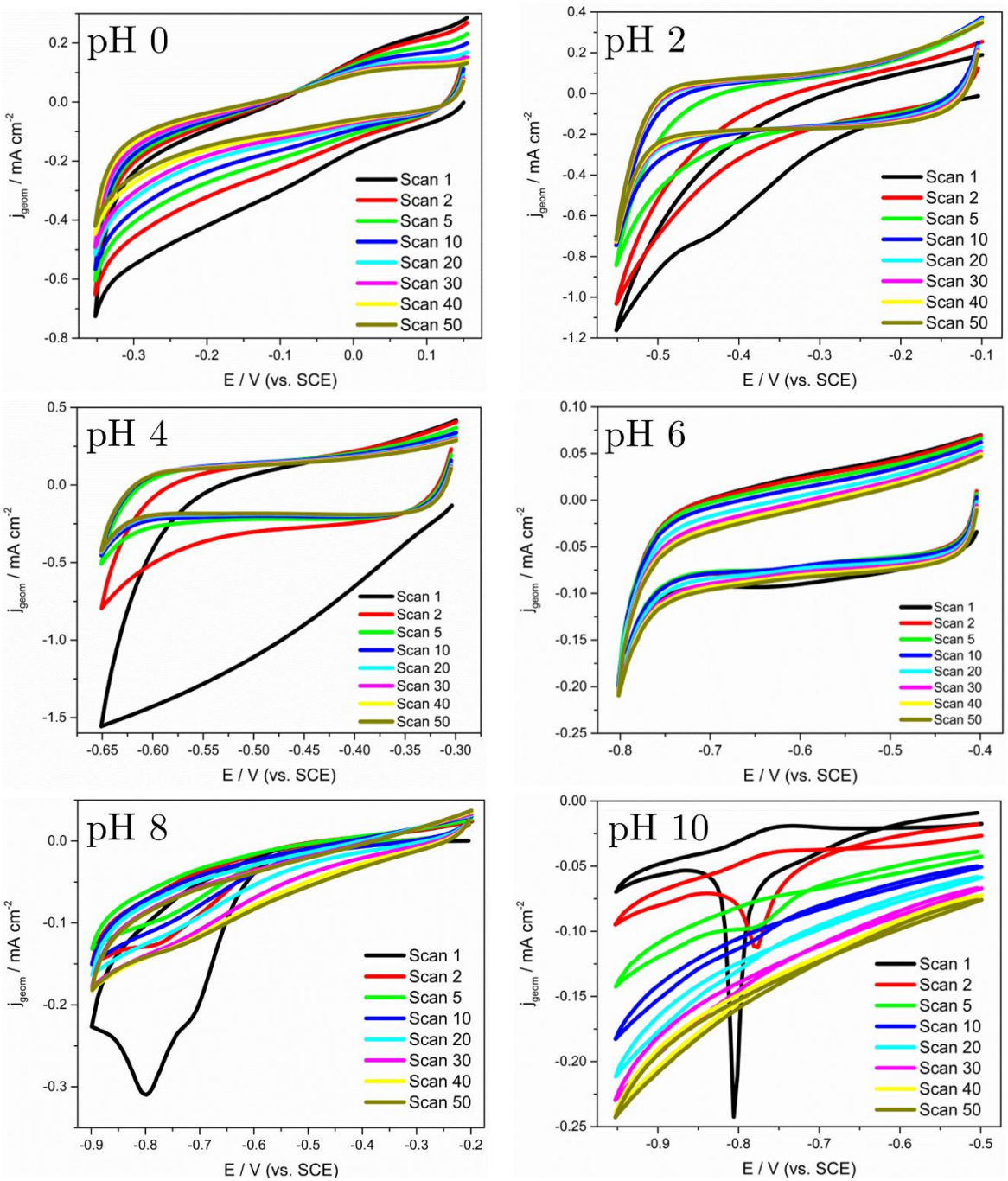

Figure 9.17. Representative voltammograms obtained for post-LSV AE-MoS_x films during the reductive electrochemical conditioning treatments (cathodic potential vertex past $E_{peak,1}$). Scan rate: 50 mV s^{-1}.

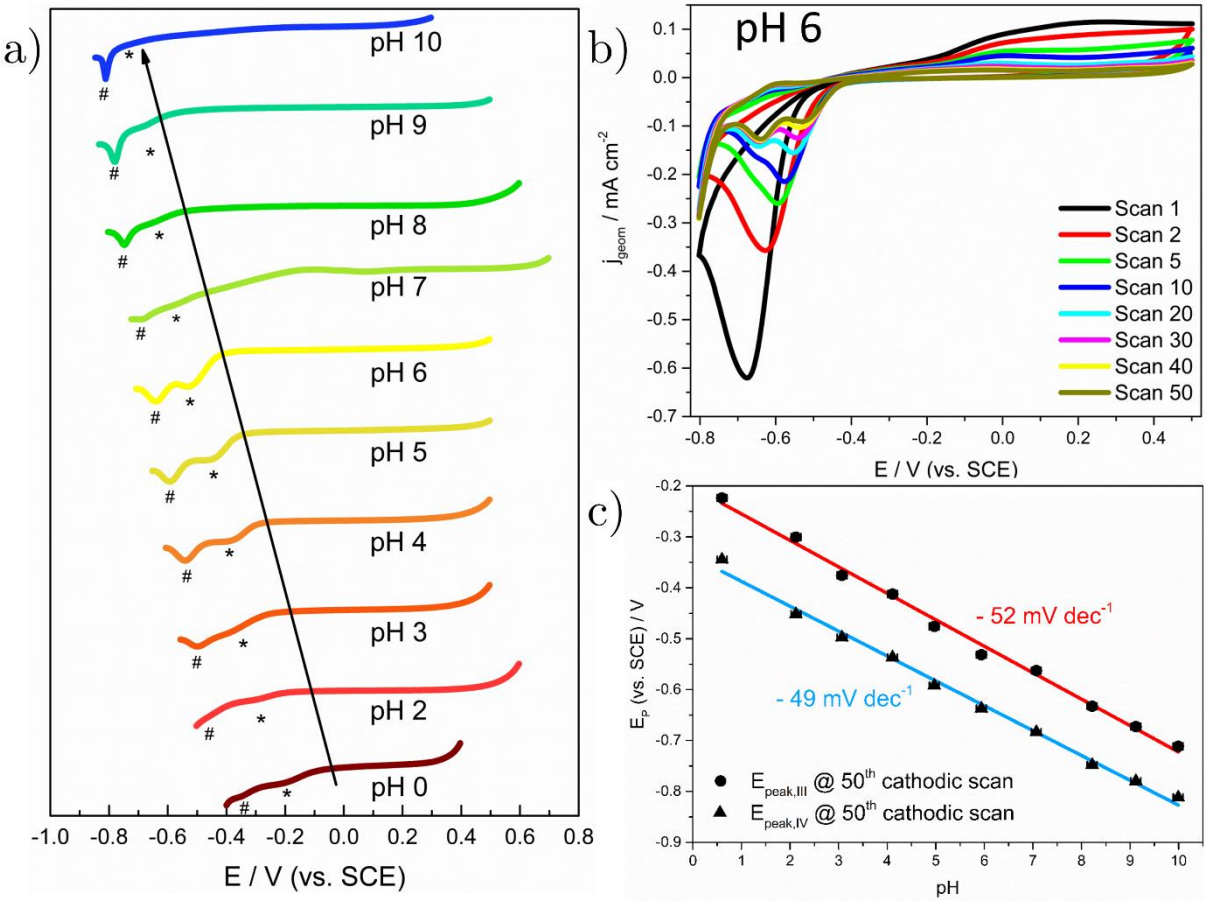

Figure 9.18. a) Compilation of the 50th cathodic scans recorded during the oxidative-reductive electrochemical conditioning on pristine AE-MoS_x films across the 0-10 pH range, b) Representative voltammograms obtained for AE-MoS_x films during oxidative-reductive electrochemical conditioning in a pH 6 buffered electrolyte, c) Peak potential dependence of post-LSV AE-MoS_x HER pre-catalytic features $E_{peak,III}$ (●, * in Fig. 9.18a) and $E_{peak,IV}$ (▲, # in Fig. 9.18a) as a function of the buffered electrolyte pH. Scan rate: 50 mV s^{-1}.

Finally, we compared the relative peak current intensities of $E_{peak,III}$ and $E_{peak,IV}$ to the relative abundance of the S_x^{y-} components found in XPS after electrochemical testing. Amorphous MoS_x materials are deconvoluted with two S $2p_{3/2:1/2}$ spin-orbit doublets (see Figure 9.7b): for pristine AE-MoS_x these correspond to a "low binding energy" doublet ascribed to both $S_2^{2-}{}_{terminal}$ and $S^{2-}{}_{unsat}$ with $2p_{3/2}$ and $2p_{1/2}$ binding energies of 161.7 ± 0.1 eV and 162.9 ± 0.1 eV, and a "high

binding energy" doublet ascribed to both $S_2^{2-}_{bridging}$ and apical S^{2-} (S^{2-}_{apical}) with $2p_{3/2}$ and $2p_{1/2}$ binding energies of 163.0 ± 0.1 eV and 164.2 ± 0.1 eV.[45,46] An excellent correlation between relative atomic abundance of the $S_2^{2-}_{terminal}/S^{2-}_{unsat}$ and $S_2^{2-}_{bridging}/S^{2-}_{apical}$ components after electrochemical conditioning and the relative $E_{peak,III}$ /$E_{peak,IV}$ current intensity at the 50th scan was found, respectively, in the 0-7 pH range (see Table 9.1). For alkaline pHs, the electrochemical oxidation of the MoS_x film by (9.6b) along with the thermodynamic instability of its reaction products driven by reaction (9.7) results in overall thin film dissolution and oxidation of S_x^{y-} components to SO_x^{y-} which prevents any quantitative XPS analysis. This led us to ascribe $E_{peak,III}$ and $E_{peak,IV}$ to the electrochemical cleaving of the S-S bond from $S_2^{2-}_{terminal}$ and $S_2^{2-}_{bridging}$, respectively. This is in good agreement with the inherent bonding strengths of $S_2^{2-}_{terminal}$ and $S_2^{2-}_{bridging}$: the Raman vibration of $S_2^{2-}_{terminal}$, $\nu(S\text{-}S)_{terminal} \approx 516$ cm^{-1}, appears at lower wavenumbers (i.e. softer binding energy) than that of $S_2^{2-}_{bridging}$, $\nu(S\text{-}S)_{bridging} \approx 555$ cm^{-1}, which indicates that $S_2^{2-}_{terminal}$ is more prone to undergo electrochemical cleaving at lower overpotentials than $S_2^{2-}_{bridging}$.

The higher content of the "high binding energy" $S_2^{2-}_{bridging}$/ S^{2-}_{apical} component vs. the "low binding energy" $S_2^{2-}_{terminal}/S^{2-}_{unsat}$ after oxidative-reductive cycling (averaged $S_2^{2-}_{terminal}/S^{2-}_{unsat}$:$S_2^{2-}_{bridging}$/ S^{2-}_{apical} ratio of 35:65 vs. 46:54 as found in pristine AE-MoS_x) along with the $E_{peak,III}$ current intensity decay upon continuous cycling suggests that S-S cleaving in $S_2^{2-}_{terminal}$ proceeds by the cathodic dissolution mechanism (9.3b) along with electro-oxidative dissolution (9.6b), the former favoured by successive cycling due to the increasingly more positive $E_{peak,III}$ position. For $E_{peak,IV}$, the conversion of $S_2^{2-}_{bridging}$ to S^{2-}_{unsat} appears to be partially reversible as in both oxidative-reductive and reductive cycling, the $E_{peak,IV}$ current intensity decreases steadily but the peak is still well resolved. In stark contrast, at the reductive cycling voltage region the HER pre-catalytic feature is almost irreversible: after the first scan, $E_{peak,1}$ current decreases substantially or is almost negligible (see Figures 9.15b and 9.17).

pH	$\left(\frac{I_{peak,III}}{I_{peak,III}+I_{peak,IV}}\right)$ / %	$\left(\frac{I_{peak,IV}}{I_{peak,III}+I_{peak,IV}}\right)$ / %	$S_2^{2-}_{terminal}/S^{2-}_{unsat}$ XPS / %	$S_2^{2-}_{bridging}/S^{2-}_{apical}$ XPS / %
0	39.7	60.3	39.4 ± 0.8	60.6 ± 0.8
1	n.a.	n.a.	59.1 ± 1.3	40.9 ± 1.3
2	27.6	72.4	39.3 ± 0.7	60.7 ± 0.7
3	36.6	63.4	35.2 ± 0.2	64.8 ± 0.2
4	35.0	65.0	34.2 ± 0.8	65.8 ± 0.8
5	37.0	63.0	37.2 ± 0.5	62.8 ± 0.5
6	40.7	59.3	38.7 ± 0.5	61.3 ± 0.5
7	40.7	59.3	47.8 ± 3.9	52.2 ± 3.9
8	27.0	73.0	40.5 ± 5.1	59.5 ± 5.1
9	24.6	75.4	43.4 ± 0.5	56.6 ± 0.5
10	23.6	76.4	33.0 ± 0.1	67.0 ± 0.1

Table 9.1. Compilation of the 50th cathodic relative peak current intensities for $E_{peak,III}$ $\left(\frac{I_{peak,III}}{I_{peak,III}+I_{peak,IV}}\right)$ and $E_{peak,IV}$ $\left(\frac{I_{peak,IV}}{I_{peak,III}+I_{peak,IV}}\right)$ as well as the ex-situ XPS relative ratio of the "low binding energy" ($S_2^{2-}_{terminal}/S^{2-}_{unsat}$) and "high binding energy" ($S_2^{2-}_{bridging}/S^{2-}_{apical}$) S $2p_{3/2:1/2}$ components obtained after oxidative-reductive electrochemical conditioning on pristine AE-MoS_x films across the 0-10 pH range.

Interestingly, the relative $S_2^{2-}_{terminal}/S^{2-}_{unsat}$: $S_2^{2-}_{bridging}/$ S^{2-}_{apical} XPS ratio is almost unchanged with respect to pristine AE-MoS_x after reductive cycling across the 0-10 pH range (averaged 49:51 over 0-10 pH results vs. initial 46:54, Table 9.2). This can be well understood if $S_2^{2-}_{bridging}$ and $S_2^{2-}_{terminal}$ cleaving selectively undergo mechanisms (9.3a) and (9.3b), respectively. The freshly formed S^{2-}_{unsat} moieties after $S_2^{2-}_{bridging}$ cleaving compensate the loss of $S_2^{2-}_{terminal}$ in the XPS S $2p_{3/2:1/2}$ components, keeping their relative ratio balanced.

Relative XPS photoemission percentage/ %					
pH	Mo^{4+}	$Mo^{5+}O_xS_y$	Mo^{6+}	$S_2^{2-}_{terminal}/S^{2-}_{unsat}$	$S_2^{2-}_{bridging}/S^{2-}_{apical}$
a.r.	75.4 ± 0.7	18.6 ± 0.2	6.0 ± 0.6	46.2 ± 0.7	53.8 ± 0.7
0	51.8 ± 0.9	4.9 ± 0.1	43.3 ± 0.8	46.4 ± 1.4	53.6 ± 1.4
1	38.4 ± 1.4	12.8 ± 0.7	48.8 ± 1.5	48.2 ± 0.6	51.8 ± 0.6
2	38.1 ± 2.3	8.1 ± 0.1	53.8 ± 2.2	65.4 ± 0.8	34.6 ± 0.8
3	44.9 ± 0.6	13.4 ± 1.5	46.7 ± 2.0	44.9 ± 0.2	55.1 ± 0.2
4	45.8 ± 0.5	12.2 ± 0.3	42.0 ± 0.8	55.5 ± 1.5	44.5 ± 1.5
5	36.3 ± 1.3	12.4 ± 0.6	51.3 ± 1.5	61.1 ± 1.2	38.9 ± 1.2
6	45.4 ± 3.7	9.6 ± 1.7	42.8 ± 2.1	53.1 ± 12	46.9 ± 12
7	14.7 ± 0.6	9.0 ± 1.0	76.3 ± 1.4	51.5 ± 3.3	48.5 ± 3.3
8	39.7 ± 3.8	6.4 ± 3.6	53.9 ± 0.2	43.9 ± 1.3	56.1 ± 1.3
9	55.8 ± 1.7	0	44.2 ± 1.7	45.8 ± 0.7	54.2 ± 0.7
10	36.7 ± 1.0	8.0 ± 0.4	55.3 ± 1.3	36.4 ± 6.1	63.6 ± 6.1

Table 9.2. Relative XPS photoemission percentages of deconvoluted Mo 3*d* and S 2*p* components of AE-MoS_x thin films: pristine (a.r.) and after undergoing reductive conditioning across the 0-10 pH range.

Investigation of the Raman spectra recorded for samples after having undergone oxidative-reductive (Figure 9.19a, Table J.2 Appendix) and reductive (Figure 9.19b, Table J.3 Appendix) electrochemical conditionings present multiple similarities. The gradual decrease towards higher pH values of both $\nu(S\text{-}S)_{terminal}$ and $\nu(S\text{-}S)_{bridging}$ Raman modes as compared to $\nu(S_{apical}\text{-}Mo)$, which ultimately disappear in neutral to alkaline pHs, corroborates the electrochemical cleaving of $S_2^{2-}_{terminal}$ and $S_2^{2-}_{bridging}$ moieties at hydrogen pre-catalytic potentials. It is also observed that both ν(Mo-Mo) and ν(Mo-S) vibration bands in the 150-225 cm^{-1} and 285-360 cm^{-1} wavenumber range, respectively, become increasingly unresolved towards higher pH values to ultimately become a broad band: this indicates the loss of the cluster-like structure as found in pristine AE-MoS_x. The lack of any ν(Mo-Mo) and ν(Mo-S) band sharpening, contrary to

that found for pristine films' electro-oxidation, suggests that morphological restructuring under these electrochemical conditioning protocols is less severe.

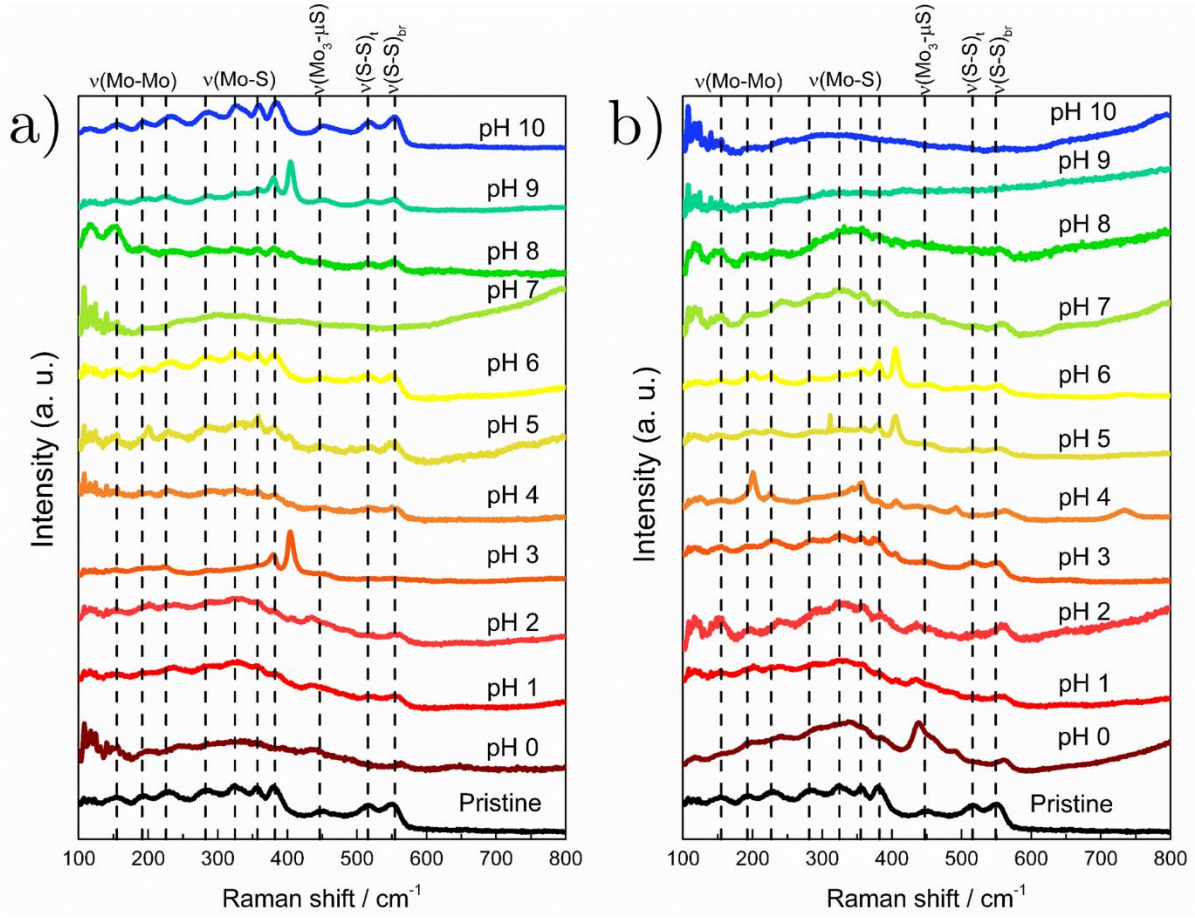

Figure 9.19. Stacked Raman spectra (532 nm laser excitation, 100-800 cm^{-1} range, intensity-normalized) of pristine (black), and AE-MoS_x thin films electrochemically conditioned by a) oxidative-reductive cycling and b) reductive cycling across the 0-10 pH range. Dashed vertical lines refer to characteristic AE-MoS_x vibration modes.

Interestingly, the $\nu(S_{apical}\text{-}Mo)$ vibrational band seems to split into two additional peaks: one red-shifted (ca. 437 cm^{-1}, sharp and intense) and another one blue-shifted (ca. 483 cm^{-1}), the latter poorly defined towards higher pHs. Tran and co-workers suggested that $S_2^{2-}{}_{terminal}$ dissolution under hydrogen evolving conditions modified the Mo_3 cluster geometry ultimately red-shifting the $\nu(S_{apical}\text{-}Mo)$ vibration.[8] Indeed, the fact that these bands selectively arise

upon reductive cycling within the pre-catalytic peak $E_{peak,1}$ voltage region informs us that this redox process is indeed directly responsible for the emerging Raman modes. The initial $\nu(S_{apical}$-Mo) vibration is greatly diminished, but still present at pH 0, which clearly indicates that the band at ca. 437 cm^{-1} is indeed a new Raman vibration arising from a weaker S_{apical}-Mo bond. Accordingly, we believe that the band at ca. 437 cm^{-1} corresponds to a Mo-S-Mo vibration arising after $S_2^{2-}{}_{bridging}/S^{2-}{}_{apical}$ cleavage, similar to the ν(Mo-S-Mo) stretching mode found for CE-MoS_x (ca. 425 cm^{-1}).[47] This would support previous reports which suggested a morphological conversion of AE-MoS_x to CE-MoS_x under HER potentials due to S loss and S-S bond cleavage. In the case of the band at ca. 483 cm^{-1}, as already discussed for the pristine electro-oxidation Raman scenario, it is hypothesized to be originated by partially-cleaved $S_2^{2-}{}_{terminal}$ moieties: ultimately this band disappears after full dissolution of $S_2^{2-}{}_{terminal}$ moieties.

As for the Mo^{4+}: $Mo^{5+}O_xS_y$: Mo^{6+} XPS relative photoemission ratios, no clear trend can be found neither for the oxidative-reductive nor for the reductive CV conditioning treatments as a function of the pH.

9.2.5.2 AE-MoS_x electrochemical conditioning by electro-oxidative cycling: EC, Raman and XPS analysis

As mentioned previously, the electro-oxidative voltammograms present no oxidation peaks but a rising anodic current. We believe, in this case, that the rising anodic current observed is in good agreement with the onset of the electro-oxidation broad band obtained for pristine AE-MoS_x. The absence of electro-oxidative features $E_{peak,I}$ and $E_{peak,II}$, after performing a preliminary CV from 0.7 to -1.2 V vs. SCE to establish the electro-oxidation cycling window, corroborate that these peaks only appear if immediately preceded by conditioning at HER potentials. Thus, electrochemical conditioning drastically modifies the electro-oxidation features of AE-MoS_x. However, this does not necessarily mean that the electro-oxidation events responsible for $E_{peak,I}$ and $E_{peak,II}$ do not occur.

Combined analysis of XPS and Raman measurements acquired after 50 CVs of electro-oxidative conditioning corroborate this. An increased XPS photoemission contribution from Mo^{6+} species along with a decay in the Mo^{4+} $3d_{5/2;3/2}$ spin-orbit doublet from pH 0 to pH 6 reveals and effective conversion of Mo^{4+} characteristic of $Mo^{IV}S_x$ to Mo^{6+} as found in molybdenum oxide compounds ($Mo_xO_y^{z-}$) (For compiled relative XPS percentages see Table 9.3).[48]

Relative XPS photoemission percentage/ %					
pH	Mo^{4+}	$Mo^{5+}O_xS_y$	Mo^{6+}	$S_2^{2-}{}_{terminal}/S^{2-}{}_{unsat}$	$S_2^{2-}{}_{bridging}/S^{2-}{}_{apical}$
a.r.	75.4 ± 0.7	18.6 ± 0.2	6.0 ± 0.6	46.2 ± 0.7	53.8 ± 0.7
0	38.1 ± 2.4	6.9 ± 1.3	55.0 ± 1.1	39.4 ± 0.8	60.6 ± 0.8
1	46.8 ± 1.1	15.4 ± 1.1	37.8 ± 2.2	50.4 ± 0.2	49.6 ± 0.2
2	35.7 ± 1.7	10.1 ± 0.7	54.2 ± 1.0	45 ± 0.7	55 ± 0.7
3	43.1 ± 2.7	10.4 ± 0.3	46.5 ± 2.6	36.3 ± 0.5	63.7 ± 0.5
4	32.1 ± 1.5	8.4 ± 0.9	59.5 ± 2.0	32.1 ± 1	67.9 ± 1
5	32.2 ± 1.4	9.8 ± 0.7	58.0 ± 2.1	41.9 ± 0.8	58.1 ± 0.8
6	18.9 ± 7.5	6.0 ± 1.0	77.6 ± 7.8	57.3 ± 5.3	42.7 ± 5.3
7	35.8 ± 3.7	11.3 ± 1.5	52.9 ± 5.3	40.4 ± 4.5	59.6 ± 4.5
8	41.2 ± 1.4	7.8 ± 0.1	51.0 ± 1.3	38.9 ± 0.7	61.1 ± 0.7
9	49.5 ± 2.5	11.6 ± 0.6	38.9 ± 4.2	40.7 ± 1	59.3 ± 1
10	31.6 ± 2.1	8.5 ± 0.8	60.0 ± 2.9	34.5 ± 1.5	65.5 ± 1.5

Table 9.3. Relative XPS photoemission percentages of deconvoluted Mo $3d$ and S $2p$ components of AE-MoS_x thin films: pristine (a.r.) and after undergoing electro-oxidative conditioning across the 0-10 pH range.

The steady increase of the Mo=O (ca. 800-850 cm^{-1}) and $Mo(=O)_2$ (ca. 900-950 cm^{-1}) Raman vibration modes characteristic of MoO_x species within the same pH range corroborates this Mo electro-oxidation. These are also accompanied by a significant intensity decrease of the ν(Mo-Mo) bands in the 150-225 cm^{-1} range along with the ν(Mo-S) vibration mode at 286 cm^{-1}, which further support structural modifications in the AE-MoS_x cluster-like structure induced by electro-oxidative cycling (see Figure 9.20).

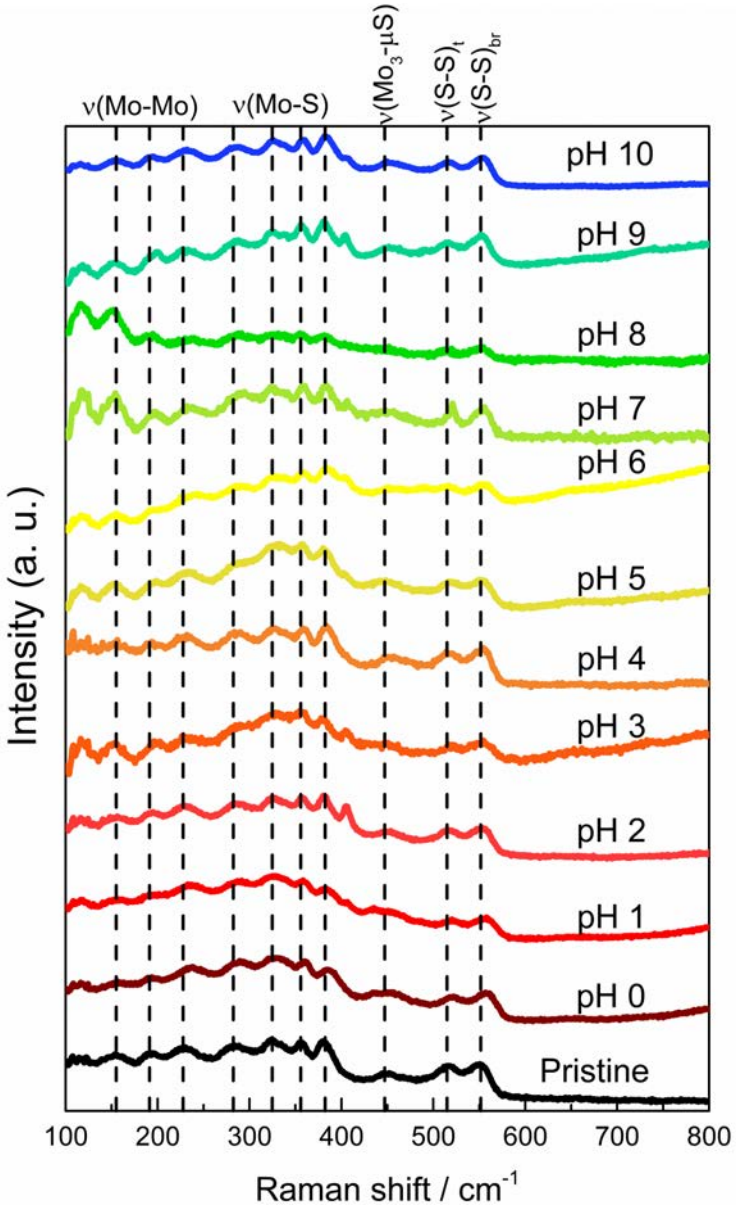

Figure 9.20. Stacked Raman spectra (532 nm laser excitation, 100-800 cm^{-1} range, intensity-normalized) of pristine (black), and AE-MoS_x thin films electrochemically conditioned by electro-oxidative cycling across the 0-10 pH range. Dashed vertical lines refer to characteristic AE-MoS_x vibration modes.

In the case of the S components, two electro-oxidation mechanisms seem to co-exist. In the acidic pH range (pH≤ 4), the electro-dissolution of the low binding energy $S_2^{2-}{}_{terminal}/S^{2-}{}_{unsat}$ S components as suggested in (9.6b) for $E_{peak,I}$ seems the overall S electro-oxidation: lower binding energy electrons are more readily removed than high binding electrons found in the S_2^{2-}

$_{bridging}/S^{2-}_{apical}$ XPS components. This conclusion is also qualitatively supported by the relative intensities of the $\nu(S_{apical}\text{-}Mo) \approx 447$ cm^{-1}, $\nu(S\text{-}S)_{terminal} \approx 516$ cm^{-1} and $\nu(S\text{-}S)_{bridging} \approx 555$ cm^{-1} vibrations: both $\nu(S\text{-}S)_{terminal}$ and $\nu(S\text{-}S)_{bridging}$ modes present relative intensities lower or equivalent to those initially obtained for the $\nu(S_{apical}\text{-}Mo)$ vibration. This would indicate that the $S_2^{2-}{}_{bridging}$/ $S_2^{2-}{}_{terminal}$ dissolution but minimal variation in $S^{2-}{}_{apical}$ content would lead to higher relative surface ratios of the "high binding energy" $S_2^{2-}{}_{bridging}/S^{2-}{}_{apical}$ S components.

However, in the mildly acidic pH range ($4 \leq pH \leq 6$) the increasingly higher $S_2^{2-}{}_{terminal}/S^{2-}{}_{unsat}$ S $2p_{3/2:1/2}$ relative XPS ratio to the detriment of the $S_2^{2-}{}_{bridging}/S^{2-}{}_{apical}$ component indicates that the unidentified complex electro-oxidation mechanism responsible for $E_{peak,II}$ governs the S component ratio, most likely by electro-dissolution of the more weakly bound $S^{2-}{}_{apical}$ moieties. The increasingly less-resolved $\nu(S_{apical}\text{-}Mo)$ Raman mode, particularly for pH 6, is in good agreement with these findings.

At pH $>$ 6, both Mo^{4+} and $S_2^{2-}{}_{bridging}/S^{2-}{}_{apical}$ XPS components again present higher relative percentages. These somewhat surprising results can be explained again by the thermodynamic instability of MoS_x in neutral to alkaline media. The favored electro-oxidation of MoO_2 to MoO_4^{2-} suggested in (9.7) towards more alkaline pH values implies that more Mo^{4+} is converted to the soluble MoO_4^{2-} which depletes from the electrodeposit surface and in turn does not contribute to neither XPS nor Raman spectra (Mo=O and $Mo(=O)_2$ vibration modes gradually fade towards alkaline pHs). The same occurs for the S components: towards alkaline environments the overall MoS_x electrodeposit dissolution again seems to promote the electro-oxidation of the lower binding energy (more readily oxidizable) $S_2^{2-}{}_{terminal}/S^{2-}{}_{unsat}$ components. The upward trend of the S^{2-}/S_2^{2-} : Mo^{4+} ratio towards alkaline pH values, yet the practically invariable total S:Mo ratio irrespective of pH suggests that both Mo and S electro-oxidize/dissolve at similar rates, but Mo moieties present at the outermost surface are primarily found at higher oxidation states as compared to S species in alkaline medium.

Thus, we conclude that in acidic pH values the overall MoS_x electro-oxidation is governed by the $S_2^{2-}{}_{terminal}/S^{2-}{}_{unsat}$ electro-dissolution (9.6b) accompanied by a steady Mo^{4+}/ Mo^{6+} conversion, whereas in mildly acidic to alkaline pHs the MoS_x electro-oxidation mostly proceeds by the prominent $Mo_xO_y^{z-}$ electro-dissolution.

9.2.6 AE-MoS_x activity after electrochemical conditioning: descriptors for enhanced HER electrocatalysis

After gathering understanding regarding the implications of the electrochemical cycling pre-treatments on the inherent morphology and oxidation state on AE-MoS_x samples, we proceeded to evaluate their impact on the HER electrocatalysis. Figure 9.21 shows representative LSVs (*iR* compensated) of AE-MoS_x samples before/after undergoing reductive electrochemically conditioned treatments at pH 0, 3, 6 and 9, respectively. It can be clearly concluded, by comparing the overpotentials required to achieve HER current densities of -2.5 mA cm^{-2} ($\eta_{HER}@\,|2.5\ mA\ cm^{-2}| = \eta_{initial} - \eta_{final}$), a figure of merit attainable at the HER overpotential window monitored for all pH values in this study, that the electrochemical conditioning treatments performed do have an effect on the HER electrocatalysis. Samples conditioned at very acidic pHs (pH 0) present the faintest modification in their performance; at mildly acidic conditions (pH 3) their overall effect is negative, whilst in quasi-neutral conditions (pH 6) there is a substantial enhancement in the HER electrocatalysis. Finally, for alkaline conditions (pH 9), the electrochemical conditionings studied are again detrimental for the HER electrocatalysis.

In an attempt to correlate any modification in HER electrocatalysis with physical properties of the AE-MoS_x samples, we plotted $\eta_{HER}@\,|2.5\ mA\ cm^{-2}|$ as a function of the most commonly used HER descriptors in the amorphous MoS_x literature across the studied pH range according to their XPS relative abundance: "high binding energy" $S_2^{2-}{}_{bridging}/S^{2-}{}_{apical}$, Mo^{4+}, S^{2-}/S_2^{2-} : Mo^{4+}

ratio (only including unoxidized Mo and S surface species), and total S : Mo ratio (accounting for oxidized Mo and S surface species).

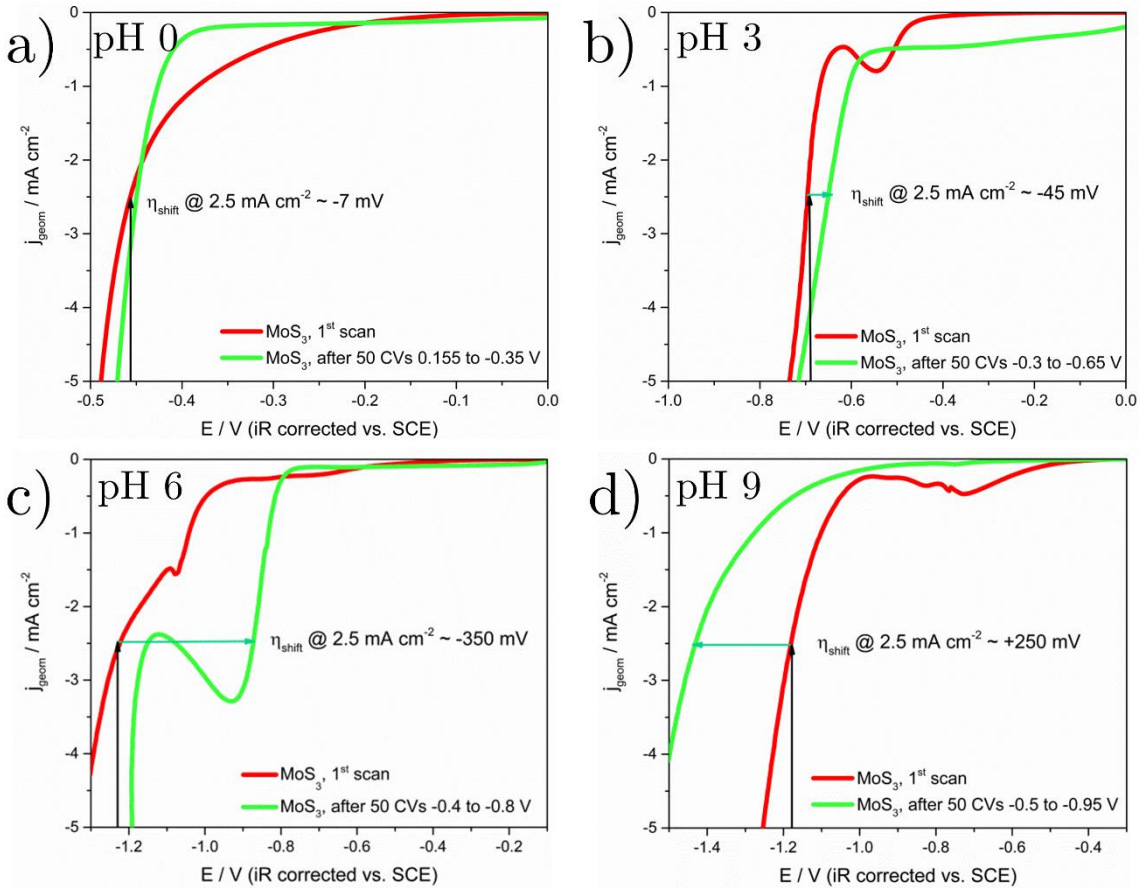

Figure 9.21. Representative voltammograms obtained for AE-MoS_x films before (red) and after (green) undergoing reductive electrochemical conditioning at in a) pH 0 (0.5 M H_2SO_4), b) pH=3 (82/18 v/v mixture of 0.1 M citric acid/0.1 M sodium citrate), c) pH=6 (11.5/88.5 v/v mixture of 0.1 M citric acid/0.1 M sodium citrate) and d) pH=9 (14.4/85.6 v/v mixture of 0.1 M HCl /0.05 M sodium tetraborate). Scan rate: 50 mV s^{-1}.

For samples undergoing the "electro-oxidation" cycling (Figure 9.22), there is a clear correlation between the HER electrocatalysis and the relative surface content of $S_2^{2-}{}_{bridging}/S^{2-}{}_{apical}$ and Mo^{4+} species. Surprisingly, the samples which presented enhanced HER electrocatalysis were the ones which presented lower Mo^{4+} and $S_2^{2-}{}_{bridging}/S^{2-}{}_{apical}$ species contents, and vice versa. This contradicts previous reports which correlated higher hydrogen turnover frequencies with

incremental $S_2^{2-}{}_{bridging}/S^{2-}{}_{apical}$ species and Mo^{4+} contents.[9] This leads us to believe that partially-oxidized, under-coordinated Mo moieties generated during electro-oxidation present promoted HER activities compared to the untreated AE-MoS_x cluster-like structure, somehow involving the generation of more active $S_2^{2-}{}_{terminal}/S^{2-}{}_{unsat}$ moieties.

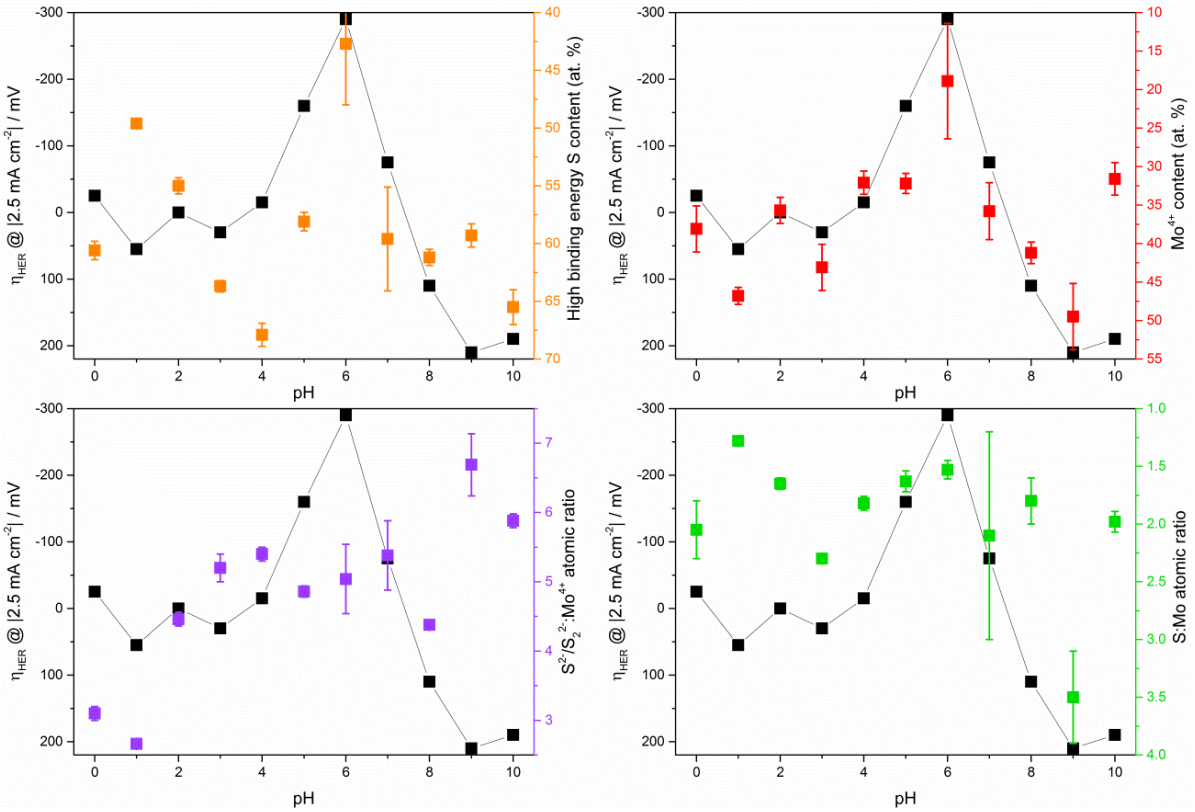

Figure 9.22. Summary of $\eta_{HER}@\,|2.5\,mA\,cm^{-2}|$as a function several AE-MoS_x descriptors across the 0-10 pH range after electro-oxidative AE-MoS_x conditioning: a) "high binding energy" $S_2^{2-}{}_{bridging}/S^{2-}{}_{apical}$ content, b) Mo^{4+} content, c) S^{2-}/S_2^{2-} : Mo^{4+} ratio, and d) total S : Mo ratio. At. % units correspond to relative XPS percentages within the Mo 3*d* and S 2*p* deconvoluted components.

For samples treated by the "oxidation-reduction" cycling (Figure 9.23), no clear trend can be found for the $S_2^{2-}{}_{bridging}/S^{2-}{}_{apical}$ and Mo^{4+} species relative surface content, but it seems to be present in the S^{2-}/S_2^{2-} : Mo^{4+} ratio instead: higher sulfide contents lead to improved HER

activity and viceversa. The well-established proton-accepting role of sulfur sites in MoS_2 electrocatalysis supports this experimental trend.[49,50] Finally, the AE-MoS_x samples electrochemically conditioned by "reductive" cycling (Figure 9.24) present HER electrocatalytic properties correlating with "high binding energy" $S_2^{2-}{}_{bridging}/S^{2-}{}_{apical}$ and S^{2-}/S_2^{2-} : Mo^{4+} ratio (the latter to a minor extent): higher sulfide contents and lower $S_2^{2-}{}_{bridging}/S^{2-}{}_{apical}$ promoted HER on AE-MoS_x. This trend is very valuable as it informs that not only sulfur is the main HER active site triggered under selective cathodic preconditioning, but also that the simultaneously electrochemically-induced $S_2^{2-}{}_{bridging}$ cleaving and $S_2^{2-}{}_{terminal}$ dissolution leads to unsaturated $S^{2-}{}_{unsat}$ moieties which are ultimately the proton-accepting sites.

It is also noteworthy to compare the maximum positive/negative electrocatalytic effects obtained as a function of the electrochemical preconditioning employed, giving an order as follows: reductive (from -350 mV to +250 mV) > electro-oxidative (from -290 mV to + 210 mV) > oxidative-reductive (from -220 mV to + 150 mV). Hence, selective electrochemical cycling within the pre-catalytic HER and electro-oxidative windows, trigger electrochemically-driven AE-MoS_x surface restructuring that govern the HER performance, namely $S_2^{2-}{}_{bridging}$ cleaving and $S_2^{2-}{}_{terminal}$ dissolution, and partially-oxidized under-coordinated Mo moieties generation, respectively. Analogous enhancements on crystalline MoS_2 were found upon reductive electrochemical treatments, initially allocated to lower chalcogen-to-metal ratios exposing more Mo-edge sites[43] and later ascribed to the basal plane activation by formation of S vacancies below -1V vs. RHE.[51] For oxidative-reductive conditioning, the partial electrochemical reversibility of the aforementioned phenomena limits their impact on the HER electrocatalysis, as their generation at anodic/cathodic regions will be inevitably followed by their partial depletion/reinstatement at the opposite voltage range.

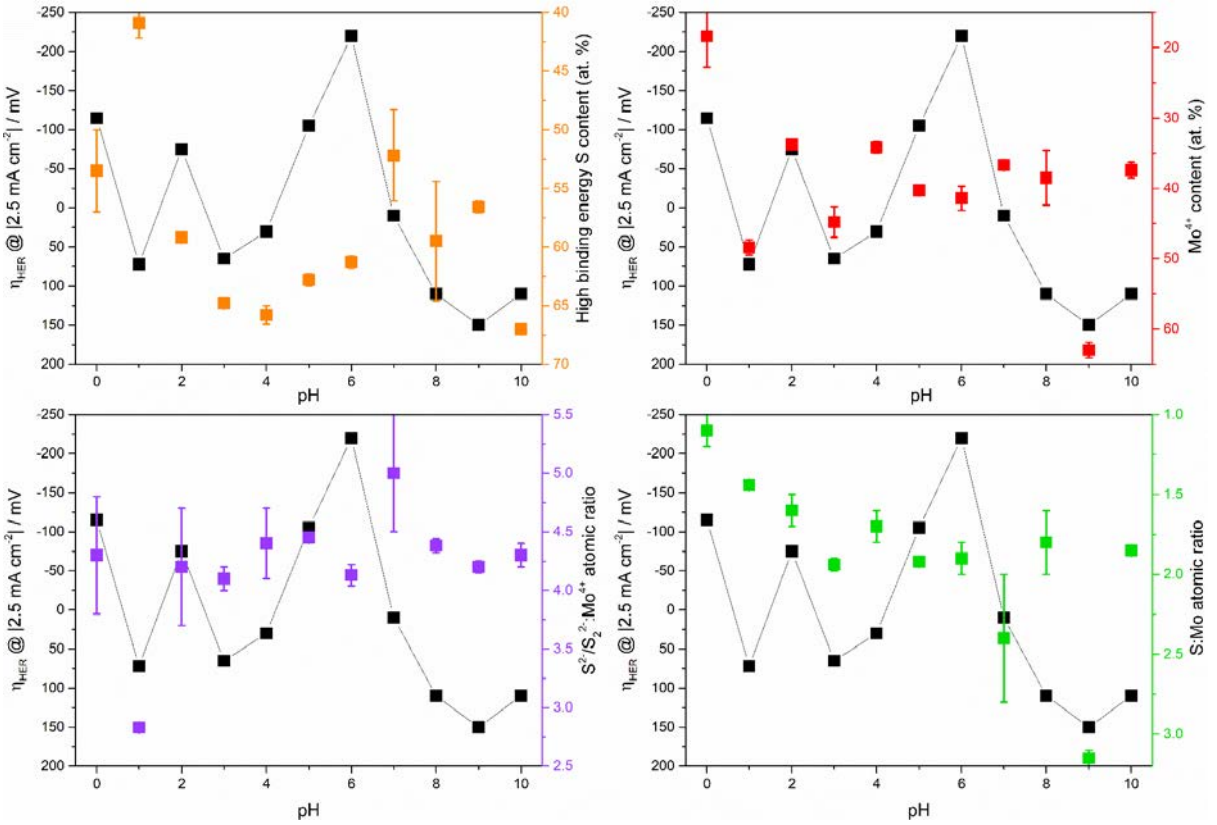

Figure 9.23. Summary of $\eta_{HER}@|2.5\,mA\,cm^{-2}|$as a function several AE-MoS_x descriptors across the 0-10 pH range after oxidative-reductive AE-MoS_x conditioning: a) "high binding energy" $S_2^{2-}{}_{bridging}/S^{2-}{}_{apical}$ content, b) Mo^{4+} content, c) S^{2-}/S_2^{2-} : Mo^{4+} ratio, and d) total S : Mo ratio. At. % units correspond to relative XPS percentages within the Mo 3*d* and S 2*p* deconvoluted components.

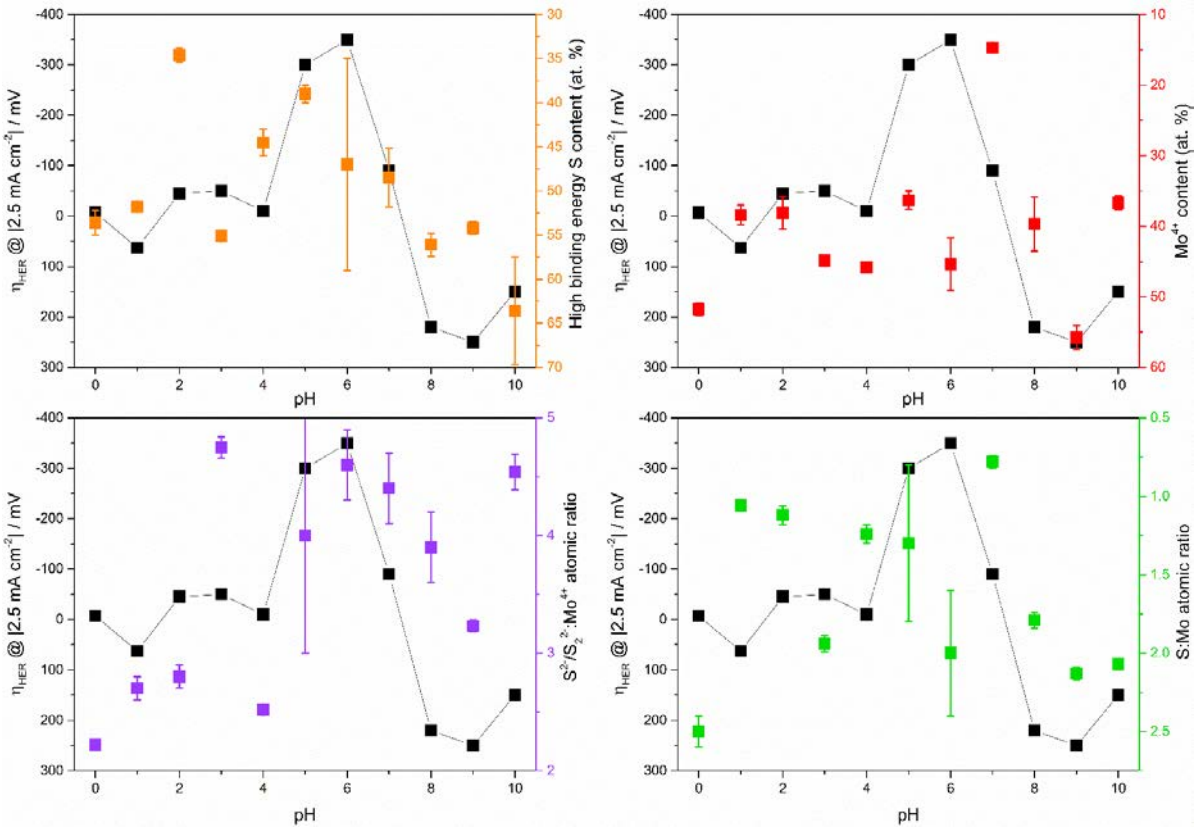

Figure 9.24. Summary of $\eta_{HER}@\,|2.5\,mA\,cm^{-2}|$ as a function several AE-MoS_x descriptors across the 0-10 pH range after reductive AE-MoS_x conditioning: a) "high binding energy" $S_2^{2-}{}_{bridging}/S^{2-}{}_{apical}$ content, b) Mo^{4+} content, c) S^{2-}/S_2^{2-} : Mo^{4+} ratio, and d) total S : Mo ratio. At. % units correspond to relative XPS percentages within the Mo 3*d* and S 2*p* deconvoluted components.

In addition to this, specific pH ranges can be identified where the AE-MoS_x surface is either insensitive or dramatically affected by the electrochemical conditioning methods employed. Samples preconditioned at pH 4 present the lowest overpotential modifications (reductive: -10 mV, electro-oxidative: -15 mV, oxidative-reductive: +30 mV), whereas those conditioned at pH 6 (reductive: -350 mV, electro-oxidative: -290 mV, oxidative-reductive: -220 mV) and pH 9 (reductive: +250 mV, electro-oxidative: +210 mV, oxidative-reductive: +150 mV) present the most positive and negative impact on HER electrocatalysis, respectively. These provide

insight on specific pH regions under which AE-MoS_x activity and/or stability may be exploited for long-term operating conditions.

Thus, we can conclude that monitoring of specific HER descriptors across the whole pH spectrum, specifically those related to sulfide moieties ($S_2^{2-}{}_{bridging}/S^{2-}{}_{apical}$ and S^{2-}/S_2^{2-} : Mo^{4+} ratio), allow the correlation of the experimental hydrogen electrocatalysis observed with surface-dependent AE-MoS_x properties.

9.2.7 AE-MoS_x long-term HER performance: stability and accelerated durability testing

Assessment of the stability and durability of HER catalysts is paramount for their implementation in commercial PEM electrolyzer stacks. However, recent reports have highlighted that no standardized stability test protocol has been adopted in the HER field to evaluate electrocatalytic lifetimes.[52,53] For oxygen evolution electrocatalysts, however, several benchmarking tests have been proposed, most of them comprising chronopotentiometric measurements to monitor catalyst stability (with durations not less than 2 hours)[54] and continuous potential cycling at high voltage scan rates. The latter have proven to give representative information on electrocatalyst durability at shorter timescales, comparable to that obtained at PEM electrolyzer average lifetimes (50000 h).[55] Here we opted to evaluate pristine AE-MoS_x hydrogen evolution stability and durability across the 0-10 pH range by recording, under 1500 rpm stirring, chronopotentiograms of 12 h duration at a constant cathodic current density of -10 mA cm^{-2} (HER benchmarking current density),[28] and by acquiring 3000 cyclic voltammograms at 100 mV s^{-1} scan rate with a cathodic voltage limit set to attain a maximum current density of -10 mA cm^{-2}.

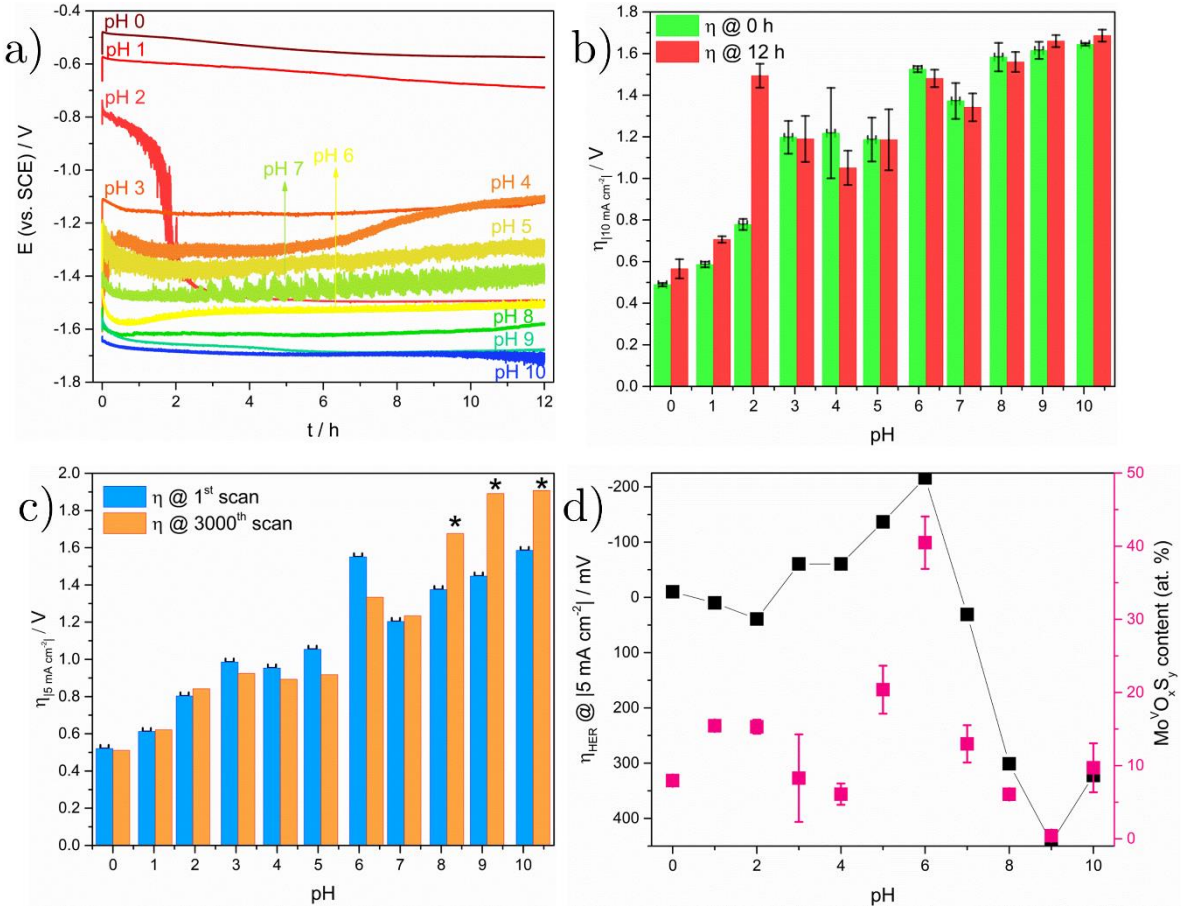

Figure 9.25. a) Representative chronopotentiograms recorded during AE-MoS_x HER stability measurements (12 h galvanostatic electrolysis at j_{geom}= -10 mA cm^{-2}), b) Averaged (±10 min) initial (green) and final (red) overpotentials to sustain j_{geom}= -10 mA cm^{-2} for 12 h, c) Initial (blue) and final (orange) HER $\eta_{HER}@|5\ mA\ cm^{-2}|$obtained during accelerated durability testing on AE-MoS_x (3000 CVs, 100 mV s^{-1}). Values with * indicate approximate overpotentials due to experimental currents not achieving -5 mA cm^{-2} at the evaluated voltage window. d) Summary of $\eta_{HER}@|5\ mA\ cm^{-2}|$as a function $Mo^{5+}O_xS_y$ relative XPS content across the 0-10 pH range after accelerated durability testing.

A compilation of the 12 h stability test results is shown in Figures 9.25a and 9.25b. At very acidic environments ($0 \leq pH \leq 2$) a significant upward increase in both initial ($t = 0 \pm 10$ min) and final ($t = 12$ h $\pm$ 10 min) HER overpotentials was found towards higher pH values. It is

widely established that transition metal sulfides dissolve in acidic media under HER operating conditions due to sulfur atoms loss.[56,57] This property is key in AE-MoS_x, as the electrochemically-induced $S_2^{2-}{}_{bridging}$ cleaving and $S_2^{2-}{}_{terminal}$ dissolution at cathodic potentials, despite of the inevitable sulfur loss, are responsible for the generation of the $S^{2-}{}_{unsat}$ HER active sites. At pH 2, we suspect that the high AE-MoS_x instability, along with the dissolution of the Au electrode layer promoted by the high chloride concentration in the buffered electrolyte (found after physical inspection of the samples' surfaces), explain the dramatic HER overpotential increase. Surprisingly, in mildly acidic conditions ($3 \leq pH \leq 6$) the AE-MoS_x samples present almost unchanged HER performances, slightly improved at pH 4 values (ca. 167 mV lower average overpotential) and to a lesser extent at pH 6 (ca. 45 mV lower average overpotential). Finally, for neutral-to-alkaline environments ($7 \leq pH \leq 10$), the HER continuous performance seems almost constant in neutral pHs (7-8) whereas it clearly worsens in alkaline pHs (9-10), with starting overpotentials increasingly higher towards higher pHs. As mentioned previously, the increasingly higher inherent thermodynamic instability of AE-MoS_x towards alkaline environments supports the worsened HER performance observed.

Upon analysis of the overall initial HER overpotential trends, it is of particular relevance that both the $3 \leq pH \leq 5$ and pH 7 regions break the generally upward trend: these might represent pH environments of AE-MoS_x improved electrochemical activity and stability.

A compilation of the accelerated durability cycling testing for $\eta_{HER}@\,|5\ mA\ cm^{-2}|$across the 0-10 pH range is shown in Figure 9.25c (for representative cycling voltammograms, see Figure 9.26). The experimental trends are in good agreement those obtained for chronopotentiometry experiments: acidic ($0 \leq pH \leq 2$) and neutral-to-alkaline ($7 \leq pH \leq 10$) pH environments present increased HER overpotentials after voltammetric cycling, significantly higher in the alkaline scenario. However, AE-MoS_x tested in mildly pH conditions ($3 \leq pH \leq 6$), contrary to chronopotentiometry experiments, present enhanced HER electrocatalytic activities. This

supports previous experimental evidence that, under these pH conditions, AE-MoS_x HER electrocatalysis does not only seem more favourable (maximized HER activities after electrochemical conditioning for pH 6) but can also be sustained under short duty and accelerated durability testing conditions.

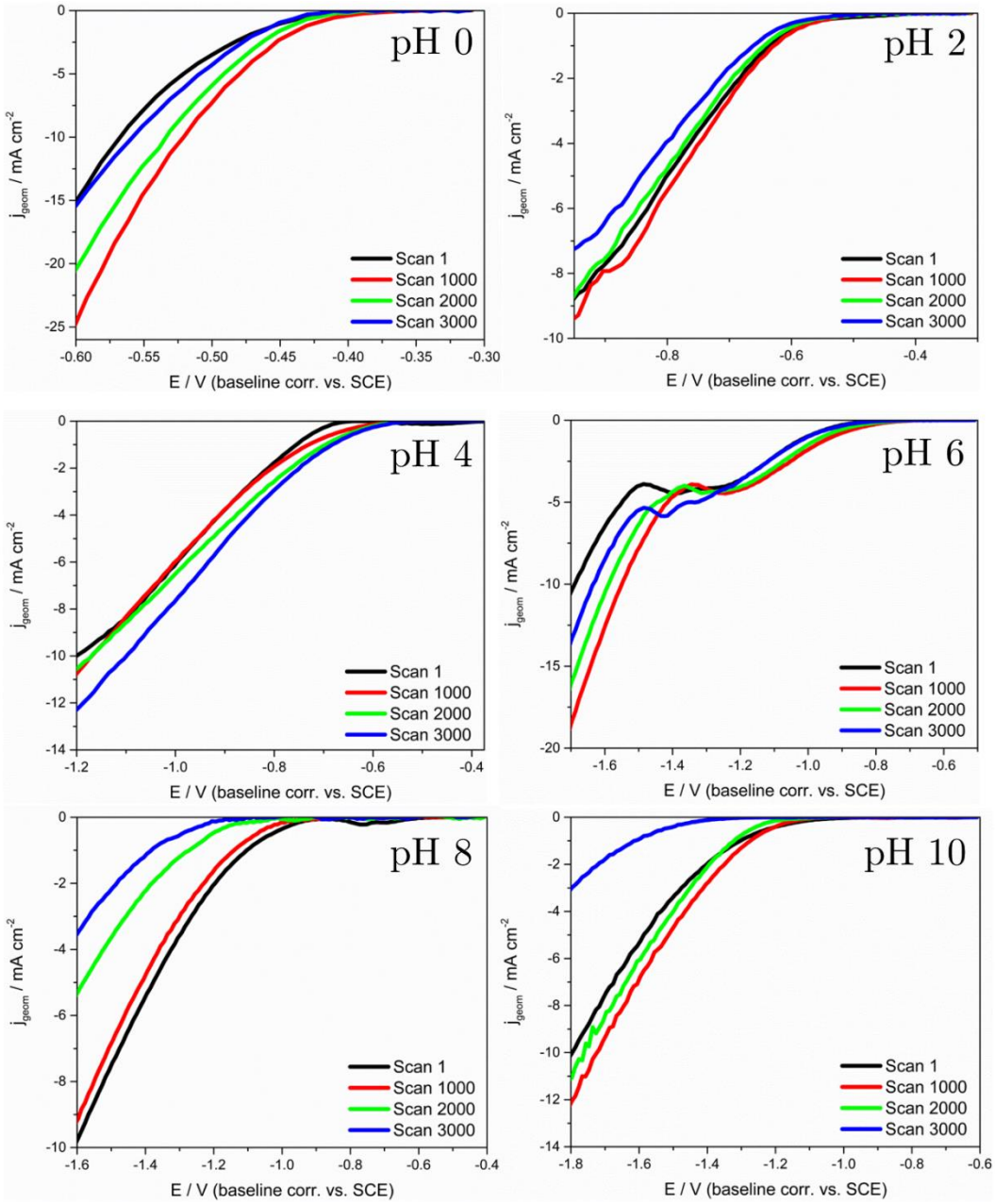

Figure 9.26. Representative voltammograms obtained for AE-MoS_x films during accelerated durability potentiodynamic testing (3000 CVs, 100 mV s^{-1}).

Ex-situ Raman (Figure 9.27) and XPS spectroscopy measurements after accelerated durability tests provide insight on their origin. Compared to pristine AE-MoS_x, both ν(Mo-Mo) and ν(Mo-S) vibration bands in the 150-225 cm^{-1} and 285-360 cm^{-1} wavenumber range, respectively, become increasingly unresolved towards higher pH values leading to their complete disappearance in favour of a broad band from pH 4 upwards. Hence, the previously well-defined AE-MoS_x cluster-based structure is irreversibly modified after accelerated HER operation conditions. Analogously, the $\nu(S_{apical}\text{-Mo})$, $\nu(S\text{-}S)_{terminal}$ and $\nu(S\text{-}S)_{bridging}$ vibrations found at 447, 516 and 555 cm^{-1} in pristine thin films, respectively, undergo substantial modifications.

As previously reported for AE-MoS_x undergoing reductive electrochemical preconditioning, in acidic environments ($0 \leq pH \leq 3$), the signal intensities of $\nu(S\text{-}S)_{terminal}$ and $\nu(S\text{-}S)_{bridging}$ gradually decreased at increasing pH values, the former completely disappearing at pH 1 and the latter blue-shifting and ultimately only observed as a shoulder up to pH 3. Analogously, the $\nu(S_{apical}\text{-Mo})$ vibrational band splits into two additional peaks: one red-shifted (ca. 437 cm^{-1}, ascribed to Mo-S-Mo vibration similar to those found for CE-MoS_x) and another one blue-shifted (ca. 483 cm^{-1}, ascribed to partially-cleaved $S_2^{2-}{}_{terminal}$ moieties), the latter poorly defined toward upward pHs. From mildly acidic to neutral pHs ($4 \leq pH \leq 7$), the Mo=O (ca. 880 cm^{-1}) and $Mo(=O)_2$ (ca. 960 cm^{-1}) vibrations steadily surfacing in acidic pHs govern the Raman spectra, leaving the unresolved (Mo-Mo) and (Mo-S) bands in the 100-600 cm^{-1} overlapped as a shoulder. Finally, the thermodynamic instability of surface molybdenum oxides in alkaline environments implies the dissolution of Mo_xO_y species responsible for Mo=O and $Mo(=O)_2$ vibrations, which ultimately justifies the resurfacing of (Mo-Mo) and (Mo-S) bands from non-dissolved MoS_x.

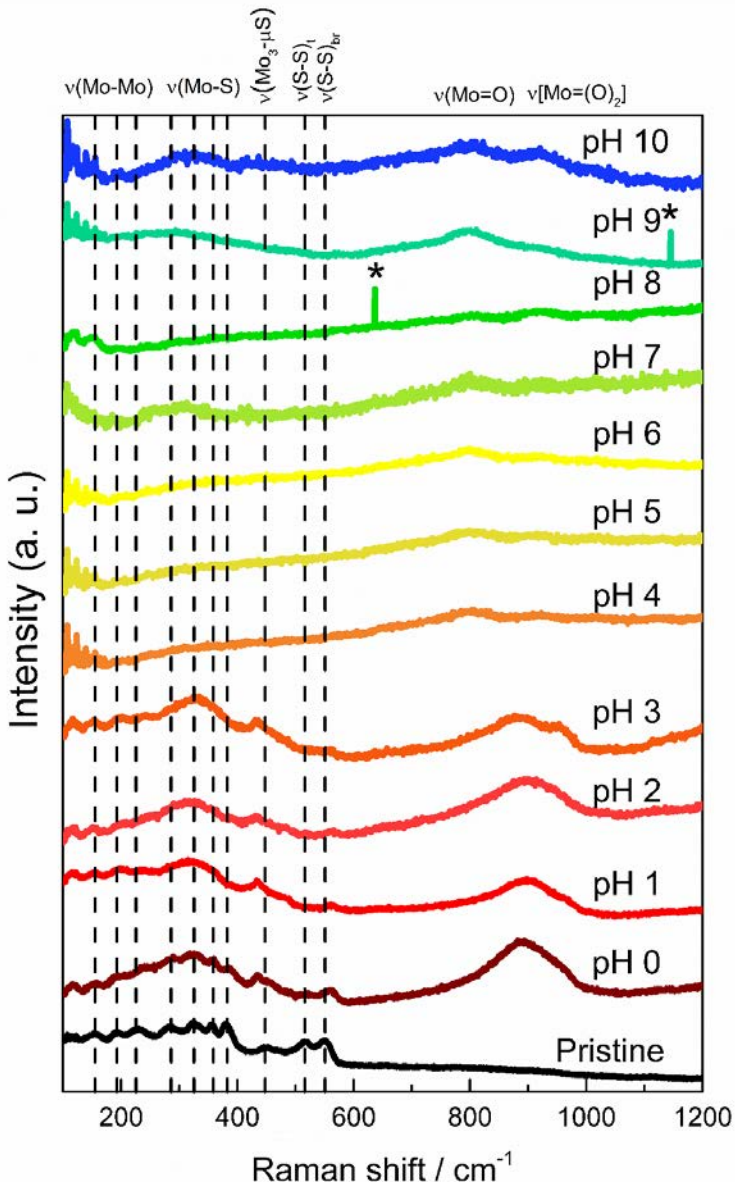

Figure 9.27. Stacked Raman spectra (532 nm laser excitation, 100-1200 cm^{-1} range, intensity-normalized) of pristine (black), and AE-MoS_x thin films after accelerated durability testing (3000 CVs, 100 mV s^{-1}) across the 0-10 pH range. Dashed vertical lines refer to characteristic AE-MoS_x vibration modes. Raman features marked with an asterisk originated from a cosmic ray.

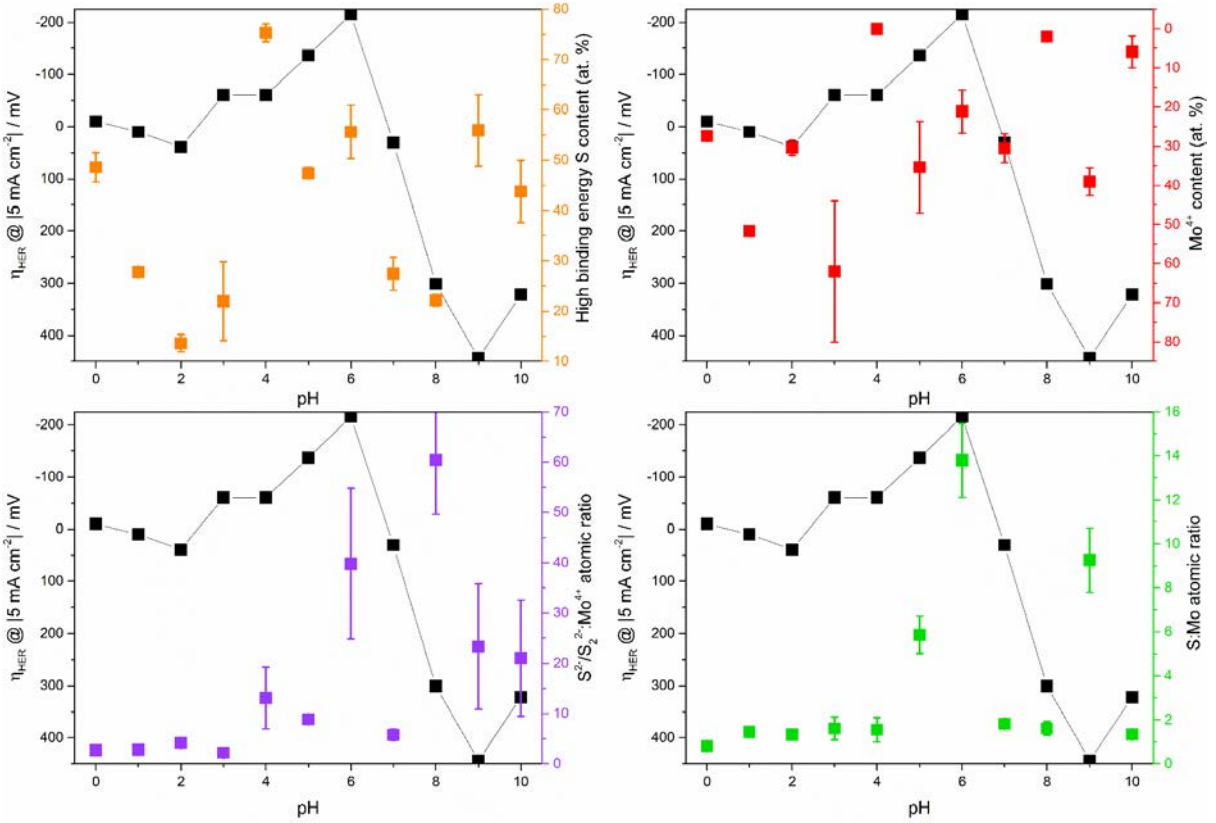

Figure 9.28. Summary of $\eta_{HER}@\,|5\ mA\ cm^{-2}|$ as a function several AE-MoS_x descriptors across the 0-10 pH range after accelerated durability testing on AE-MoS_x(3000 CVs, 100 mV s^{-1}): a) "high binding energy" $S_2^{2-}{}_{bridging}/S^{2-}{}_{apical}$ content, b) Mo^{4+} content, c) S^{2-}/S_2^{2-} : Mo^{4+} ratio, and d) total S : Mo ratio. At. % units correspond to relative XPS percentages within the Mo 3*d* and S 2*p* deconvoluted components.

Component analysis of ex-situ XPS spectra on the freshly tested samples shows no clear trend involving the previously employed HER descriptors (see Figure 9.28). However, when plotting the oxygen-incorporated $Mo^{5+}O_xS_y$ relative surface content along with the $\eta_{HER}@\,|5\ mA\ cm^{-2}|$ across the 0-10 pH range (Figure 9.25d), a clear positive correlation between enhanced HER performances and $Mo^{5+}O_xS_y$ contents was found: at pH 6, where the $Mo^{5+}O_xS_y$ relative surface content is found to be the highest (ca. 40.5± 3.6 at. %), the biggest HER overpotential shift is also achieved (ca. -220 mV). As stated in section 9.2.2, the presence of $E_{peak,2}$ and $E_{peak,3}$ at pH

≥ 5 supported the instability of $Mo^{5+}O_xS_y$ in acidic environments, which is in good agreement with the results obtained in both Raman (faint Mo=O and $Mo(=O)_2$ vibration intensities) and XPS measurements ($Mo^{5+}O_xS_y$ contents lower after electrochemical testing than as-prepared AE-MoS_x: < 18.6± 0.2 at. %) for samples tested in acidic electrolytes. Remarkably, at pH values higher than 4 (i.e. when the HER electrocatalysis is greatly enhanced), the intense Mo=O and $Mo(=O)_2$ vibrations allocated to molybdenum oxide species as well as the sharp increase in oxygen-containing $Mo^{5+}O_xS_y$ surface species indicate a convergence between oxygen incorporation in the AE-MoS_x film and enhanced HER electrocatalysis.

Thus, this leads us to the conclusion that the most active HER AE-MoS_x phase involves, under hydrogen evolving conditions, the formation of oxygen-incorporated (i.e. sulfur deficient) $Mo^{5+}O_xS_y$ species. As the undeniable role of $S_2^{2-}{}_{bridging}$ and $S_2^{2-}{}_{terminal}$ in the HER catalysis has been proven in this study, their selective electrochemical cleaving lead, respectively, to unsaturated sulfur (reaction 9.3a) and molybdenum (reaction 9.3b) sites. We hypothesize, accordingly, that both phenomena synergistically assist in the generation of the HER active sites. Indeed, a very recent report has correlated enhanced hydrogen electrocatalysis in amorphous MoS_x materials at neutral pH values with an internal reorganization of a bridging $S_2^{2-}{}_{bridging}$ ligand to a $S_2^{2-}{}_{terminal}$ configuration by in situ Raman measurements.[58] This reorganization in the Mo_3-thio cluster-like structure was proposed to yield under-coordinated Mo-Mo sites which synergistically promoted the HER. However, the $S_2^{2-}{}_{terminal}$ dissolution found in this study supported by electrochemical, Raman, and XPS experiments leads us to believe that the bridging $S_2^{2-}{}_{bridging}$ ligand adopts a $S^{2-}{}_{unsat}$ configuration instead.

The AE-MoS_x electrocatalysis under hydrogen evolution conditions is then proposed to operate as follows. In acidic pH values ($0 \leq pH < 4$), the predominant HER active sites are those comprising $S^{2-}{}_{unsat}$ formed after $S_2^{2-}{}_{bridging}$ cleaving as unsaturated Mo sites (although more active to the HER) will be prone to (oxy)hydroxide formation by hydration and subsequently

present thermodynamic instability. On the other hand, in mildly acidic to neutral pHs ($4 \leq pH < 7$), the unsaturated Mo^{5+} as found in $Mo^{5+}O_xS_y$ species will no longer dissolve in the electrolyte, compensating for the S^{2-}_{unsat} loss and opening an alternative HER route similar to that proposed by Tran et al.[8] At this stage we must also take into account the variations of the inherent HER kinetics across the studied pH range to understand their interplay with the proposed active sites. At $0 \leq pH \leq 2$, where the AE-MoS_x HER mechanism is expected to undergo by H_3O^+ electroreduction, we believe that the cleaved $S_2^{2-}_{bridging}$ moieties (which act as proton-accepting sites, as suggested by *in operando* Raman studies) are the HER active sites. At higher pH values, as HER electrocatalysis should operate by the water reduction/splitting mechanism, we believe that the freshly-cleaved S^{2-}_{unsat} from $S_2^{2-}_{bridging}$ moieties are less electrocatalytically active, and only when $Mo^{5+}O_xS_y$ species are thermodynamically stable at the surface ($pH > 4$) the HER can be successfully catalysed. As previous *in operando* studies suggest an absence of ν(Mo-H) at hydrogen evolving potentials, we believe that the HER mechanism on $Mo^{5+}O_xS_y$ species necessarily involves the protonation of the Mo=O moieties through O-H bond cleavage and sequential electron transfer. Finally, at neutral to alkaline pHs ($7 \leq pH \leq 10$), the instability of both S^{2-}_{unsat} and $Mo^{5+}O_xS_y$ leads to the prominent formation of solution soluble molybdenum oxides with worsened HER kinetics.

9.3 Conclusions

This chapter has explored the impact of electrolyte pH on the inherent and HER electrochemistry of electrodeposited AE-MoS_x films and its implications in long term operation conditions. Analysis of the pre-catalytic HER features along with EC and XPS using buffered electrolytes have corroborated the simultaneous cleaving of $S_2^{2-}{}_{bridging}$ and $S_2^{2-}{}_{terminal}$ dissolution along with a proposed reduction of $Mo^{5+}O_xS_y$ species to MoO_2 only observed in the $5 \leq pH \leq 10$ range.

The previously reported distinctive EC-dependent electro-oxidation features have been rationalised using PCET theory, demonstrating a modification in the complex electro-oxidation mechanism. Pristine AE-MoS_x satisfies a 1 H^+: 2e^- PCET across the studied pH range ascribed to the oxidation of the Mo^{4+} moieties to Mo^{6+} analogous to crystalline MoS_2, whereas HER pre-conditioned AE-MoS_x presents two distinct electro-oxidation behaviours. In acidic electrolyte this cannot be unambiguously understood: XPS and Raman investigations suggest a mechanism comprising overall $S_2^{2-}{}_{terminal}/S^{2-}{}_{unsat}$ electro-dissolution accompanied by a gradual Mo^{4+}/ Mo^{6+} conversion to generate MoO_x species. In the $7 \leq pH \leq 10$ range, it seems to operate by a sequential 1 H^+: 1e^- PCET arising from partial reinstatement of previously-cleaved $S_2^{2-}{}_{bridging}$ ligands and $S_2^{2-}{}_{terminal}$ ligands dissolution, followed by a 2 H^+: 1e^- PCET corresponding to the oxidation of MoO_2 to MoO_4^{2-}.

Electrochemical conditioning by cycling within reductive/electro-oxidative/oxidative-reductive voltage results in pronounced changes in the HER performance giving an order of $\eta_{HER}@\,|2.5\ mA\ cm^{-2}|$ enhanced/detrimental electrocatalytic effects as follows: reductive (from -350 mV to +250 mV) > electro-oxidative (from -290 mV to + 210 mV) > oxidative-reductive (from -220 mV to + 150 mV). The pH ranges responsible for the most enhanced and detrimental performances are $4 \leq pH \leq 6$ and $8 \leq pH \leq 10$, respectively. The triggered surface

modifications mainly consisted of $S_2^{2-}{}_{bridging}$ cleaving and $S_2^{2-}{}_{terminal}$ dissolution (reduction) and partially-oxidized under-coordinated Mo sites generation with predominance of $S_2^{2-}{}_{terminal}/S^{2-}{}_{unsat}$ moieties (electro-oxidative). Raman spectra analysis corroborated the reductive $S_2^{2-}{}_{bridging}$ cleaving and $S_2^{2-}{}_{terminal}$ dissolution (suppressed vibration modes under reductive potentials), identifying additional bands here ascribed to partially-cleaved S moieties.

Finally, 12 h constant current hold and accelerated cyclic voltammetry experiments revealed that AE-MoS_x films, contrary to conventional testing conditions reported in literature, retain their initial activity and provide more stable performances in the $3 \leq pH \leq 5$ range. Combined analysis of XPS and Raman measurements suggest the oxygen-containing, S-deficient $Mo^{5+}O_xS_y$ surface species as the responsible sites for the HER catalysis in this range. Although cleaved $S_2^{2-}{}_{bridging}$ ligands generating $S^{2-}{}_{unsat}$ proton-accepting sites explain the HER activity of AE-MoS_x in acidic electrolytes, the thermodynamic stability of $Mo^{5+}O_xS_y$ species along with the water reduction HER mechanism satisfied in mildly acidic to alkaline electrolytes explain the key role of $Mo^{5+}O_xS_y$.

The pivotal knowledge gathered from our pH-dependent benchmarking experiments, we believe, will enable to accelerate the deployment TMD-based electrolyzers and shed light into understanding the interplay between surface properties and electroactivity maximization for other earth-abundant HER materials.

References

[1] J. Kibsgaard, T.F. Jaramillo, F. Besenbacher, Building an appropriate active-site motif into a hydrogen-evolution catalyst with thiomolybdate [Mo3S13]2– clusters, Nat. Chem. 6 (2014) 248–253. doi:10.1038/nchem.1853.

[2] R.N. Bhattacharya, C.Y. Lee, F.H. Pollak, D.M. Schleich, Optical study of amorphous MoS3: Determination of the fundamental energy gap, J. Non. Cryst. Solids. 91 (1987) 235–242. doi:10.1016/S0022-3093(87)80306-X.

[3] D. Bélanger, G. Laperriere, B. Marsan, The electrodeposition of amorphous molybdenum sulfide, J. Electroanal. Chem. 347 (1993) 165–183. doi:10.1016/0022-0728(93)80086-W.

[4] H. Vrubel, X. Hu, Growth and activation of an amorphous molybdenum sulfide hydrogen evolving catalyst, ACS Catal. 3 (2013) 2002–2011. doi:10.1021/cs400441u.

[5] D. Merki, S. Fierro, H. Vrubel, X. Hu, Amorphous molybdenum sulfide films as catalysts for electrochemical hydrogen production in water, Chem. Sci. 2 (2011) 1262–1267. doi:10.1039/C1SC00117E.

[6] A. Ambrosi, M. Pumera, Templated Electrochemical Fabrication of Hollow Molybdenum Sulfide Microstructures and Nanostructures with Catalytic Properties for Hydrogen Production, ACS Catal. 6 (2016) 3985–3993. doi:10.1021/acscatal.6b00910.

[7] H.S. Ahn, A.J. Bard, Electrochemical Surface Interrogation of a MoS2 Hydrogen-Evolving Catalyst: In Situ Determination of the Surface Hydride Coverage and the Hydrogen Evolution Kinetics, J. Phys. Chem. Lett. 7 (2016) 2748–2752. doi:10.1021/acs.jpclett.6b01276.

[8] P.D. Tran, T. V. Tran, M. Orio, S. Torelli, Q.D. Truong, K. Nayuki, Y. Sasaki, S.Y. Chiam, R. Yi, I. Honma, J. Barber, V. Artero, Coordination polymer structure and revisited hydrogen evolution catalytic mechanism for amorphous molybdenum sulfide, Nat. Mater. 15 (2016) 640–646. doi:10.1038/nmat4588.

[9] L.R.L. Ting, Y. Deng, L. Ma, Y.J. Zhang, A.A. Peterson, B.S. Yeo, Catalytic Activities of Sulfur Atoms in Amorphous Molybdenum Sulfide for the Electrochemical Hydrogen Evolution Reaction, ACS Catal. 6 (2016) 861–867. doi:10.1021/acscatal.5b02369.

[10] E. Laviron, Electrochemical Reactions with Protonations at Equilibrium Part II. The 1e, 1H+ reaction (four-member square scheme) for a heterogeneous reaction, J. Electroanal. Chem. 124 (1981) 1–7. doi:10.1016/S0022-0728(81)80280-X.

[11] J.-M. Savéant, Electrochemical approach to proton-coupled electron transfers: recent advances, Energy Environ. Sci. 5 (2012) 7718. doi:10.1039/c2ee03241d.

[12] B.Y.W.J. Albery, A Marcus Model for Concerted Proton Transfer, Faraday Discuss. (1982) 245–256.

[13] W.J. Albery, J.R. Knowles, The determination of the rate-limiting step in a proton transfer reaction from the breakdown of the Swain-Schaad relation, J. Am. Chem. Soc. 99 (1977) 637–638. doi:10.1021/ja00444a068.

[14] M.T.M. Koper, Theory of multiple proton-electron transfer reactions and its implications for electrocatalysis, Chem. Sci. 4 (2013) 2710–2723. doi:10.1039/c3sc50205h.

[15] M.T.M. Koper, Theory of the transition from sequential to concerted electrochemical proton-electron transfer, Phys. Chem. Chem. Phys. 15 (2013) 1399–1407. doi:10.1039/c2cp42369c.

[16] Y. Deng, L.R.L. Ting, P.H.L. Neo, Y.-J. Zhang, A.A. Peterson, B.S. Yeo, Operando Raman Spectroscopy of Amorphous Molybdenum Sulfide (MoSx) during the Electrochemical Hydrogen Evolution Reaction: Identification of Sulfur Atoms as Catalytically Active Sites for H + Reduction, ACS Catal. (2016) 7790–7798. doi:10.1021/acscatal.6b01848.

[17] D.W. Redman, M.J. Rose, K.J. Stevenson, Electrodeposition of Amorphous Molybdenum Chalcogenides from Ionic Liquids and Their Activity for the Hydrogen Evolution Reaction, Langmuir. 33 (2017) 9354–9360. doi:10.1021/acs.langmuir.7b00821.

[18] J. Chandrasekaran, M.A. Ansari, S. Sarkar, Aging of ammonium tetrathiomolybdate(VI) in air: an example of induced electron transfer by external oxidant, oxygen, J. Less-Common Met. 134 (1987) 23–25. doi:10.1016/0022-5088(87)90570-4.

[19] Y. Yu, S.Y. Huang, Y. Li, S.N. Steinmann, W. Yang, L. Cao, Layer-dependent electrocatalysis of MoS2 for hydrogen evolution, Nano Lett. 14 (2014) 553–558. doi:10.1021/nl403620g.

[20] X.-Q. Bao, D.Y. Petrovykh, P. Alpuim, D.G. Stroppa, N. Guldris, H. Fonseca, M. Costa, J. Gaspar, C. Jin, L. Liu, Amorphous oxygen-rich molybdenum oxysulfide Decorated p-type silicon microwire Arrays for efficient photoelectrochemical water reduction, Nano Energy. 16 (2015) 130–142. doi:10.1016/j.nanoen.2015.06.014.

[21] M. Pourbaix, Altas of Electrochemical Equilibrium in Aqueous Solutions, Pergamon Press, New York, 1966.

[22] D. McAteer, Z. Gholamvand, N. McEvoy, A. Harvey, E. O'Malley, G.S. Duesberg, J.N. Coleman, Thickness Dependence and Percolation Scaling of Hydrogen Production Rate in MoS 2 Nanosheet and Nanosheet–Carbon Nanotube Composite Catalytic Electrodes, ACS Nano. 10 (2016) 672–683. doi:10.1021/acsnano.5b05907.

[23] Y. Li, Y. Yu, Y. Huang, R.A. Nielsen, W.A. Goddard, Y. Li, L. Cao, Engineering the Composition and Crystallinity of Molybdenum Sulfide for High-Performance Electrocatalytic Hydrogen Evolution, ACS Catal. 5 (2015) 448–455. doi:10.1021/cs501635v.

[24] L.A. Kibler, J.M. Hermann, A. Abdelrahman, A.A. El-Aziz, T. Jacob, New insights on hydrogen evolution at Au single crystal electrodes, Curr. Opin. Electrochem. (2018) 1–6. doi:10.1016/j.coelec.2018.05.013.

[25] L.A. Khanova, L.I. Krishtalik, Kinetics of the hydrogen evolution reaction on gold electrode. A new case of the barrierless discharge, J. Electroanal. Chem. 660 (2011) 224–229. doi:10.1016/j.jelechem.2011.01.016.

[26] A. Kahyarian, B. Brown, S. Nesic, Mechanism of the Hydrogen Evolution Reaction in Mildly Acidic Environments on Gold, J. Electrochem. Soc. 164 (2017) H365–H374. doi:10.1149/2.1061706jes.

[27] T. Ohmori, M. Enyo, Hydrogen evolution reaction on gold electrode in alkaline solutions, Electrochim. Acta. 37 (1992) 2021–2028. doi:10.1016/0013-4686(92)87118-J.

[28] J.D. Benck, T.R. Hellstern, J. Kibsgaard, P. Chakthranont, T.F. Jaramillo, Catalyzing the Hydrogen Evolution Reaction (HER) with Molybdenum Sulfide Nanomaterials, ACS Catal. 4 (2014) 3957–3971. http://pubs.acs.org/doi/abs/10.1021/cs500923c (accessed December 15, 2015).

[29] Y. Zheng, Y. Jiao, M. Jaroniec, S.Z. Qiao, Advancing the electrochemistry of the hydrogen-evolution reaction through combining experiment and theory., Angew. Chemie (International Ed.). 54 (2015) 52–65. doi:10.1002/anie.201407031.

[30] S.J. Rowley-Neale, D.A.C. Brownson, G.C. Smith, D.A.G. Sawtell, P.J. Kelly, C.E. Banks, 2D nanosheet molybdenum disulphide (MoS2) modified electrodes explored towards the hydrogen evolution reaction, Nanoscale. 7 (2015) 18152–18168. doi:10.1039/C5NR05164A.

[31] T.R. Hellstern, J. Kibsgaard, C. Tsai, D.W. Palm, L.A. King, F. Abild-Pedersen, T.F. Jaramillo, Investigating Catalyst–Support Interactions To Improve the Hydrogen Evolution Reaction Activity of Thiomolybdate [Mo3S13]2– Nanoclusters, ACS Catal. (2017) 7126–7130. doi:10.1021/acscatal.7b02133.

[32] D. Kong, H. Wang, J. Cha, M. Pasta, K. Koski, Synthesis of MoS2 and MoSe2 films with vertically aligned layers, Nano Lett. 13 (2013) 1341–1347. http://pubs.acs.org/doi/abs/10.1021/nl400258t (accessed December 15, 2015).

[33] N. Dubouis, C. Yang, R. Beer, L. Ries, D. Voiry, A. Grimaud, Interfacial Interactions as an Electrochemical Tool To Understand Mo-Based Catalysts for the Hydrogen Evolution Reaction, ACS Catal. 8 (2017) 828–836. doi:10.1021/acscatal.7b03684.

[34] I. Ledezma-Yanez, W.D.Z. Wallace, P. Sebastián-Pascual, V. Climent, J.M. Feliu, M.T.M. Koper, Interfacial water reorganization as a pH-dependent descriptor of the hydrogen evolution rate on platinum electrodes, Nat. Energy. 2 (2017) 1–7. doi:10.1038/nenergy.2017.31.

[35] T. Cheng, L. Wang, B. V. Merinov, W.A. Goddard, Explanation of Dramatic pH-Dependence of Hydrogen Binding on Noble Metal Electrode: Greatly Weakened Water Adsorption at High pH, J. Am. Chem. Soc. 140 (2018) 7787–7790. doi:10.1021/jacs.8b04006.

[36] D. Strmcnik, M. Uchimura, C. Wang, R. Subbaraman, N. Danilovic, D. Van Der Vliet, A.P. Paulikas, V.R. Stamenkovic, N.M. Markovic, Improving the hydrogen oxidation reaction rate by promotion of hydroxyl adsorption, Nat. Chem. 5 (2013) 300–306. doi:10.1038/nchem.1574.

[37] J. Zheng, W. Sheng, Z. Zhuang, B. Xu, Y. Yan, Universal dependence of hydrogen oxidation and evolution reaction activity SI, Sci. Adv. 2 (2016) e1501602. doi:10.1126/sciadv.1501602.

[38] S. Haghighat, J.M. Dawlaty, pH Dependence of the Electron-Transfer Coefficient: Comparing a Model to Experiment for Hydrogen Evolution Reaction, J. Phys. Chem. C. 120 (2016) 28489–28496. doi:10.1021/acs.jpcc.6b10602.

[39] N. Mohamad Latiff, L. Wang, C.C. Mayorga-Martinez, Z. Sofer, A.C. Fisher, M. Pumera, Valence and oxide impurities in MoS2 and WS2 dramatically change their electrocatalytic activity towards proton reduction, Nanoscale. 8 (2016) 16752–16760. doi:10.1039/C6NR03086F.

[40] J. Bonde, P.G. Moses, T.F. Jaramillo, J. Norskov, I. Chorkendorff, Hydrogen evolution on nano-particulate transition metal sulfides, Faraday Discuss. 140 (2008) 219–231. doi:10.1039/b814058h.

[41] M. Zafir Mohamad Nasir, Z. Sofer, M. Pumera, Effect of Electrolyte pH on the Inherent Electrochemistry of Layered Transition-Metal Dichalcogenides (MoS 2 , MoSe 2 , WS 2 , WSe 2), ChemElectroChem. 2 (2015) 1713–1718. doi:10.1002/celc.201500259.

[42] D.N. Nguyen, L.N. Nguyen, P.D. Nguyen, T.V. Thu, A.D. Nguyen, P.D. Tran, Crystallization of Amorphous Molybdenum Sulfide Induced by Electron or Laser Beam and Its Effect on H2-Evolving Activities, J. Phys. Chem. C. 120 (2016) 28789–28794. doi:10.1021/acs.jpcc.6b08817.

[43] X. Chia, A. Ambrosi, Z. Sofer, J. Luxa, M. Pumera, Catalytic and Charge Transfer Properties of Transition Metal Dichalcogenides Arising from Electrochemical Pretreatment, ACS Nano. 9 (2015) 5164–5179.

[44] V.S. Saji, C.W. Lee, Molybdenum, molybdenum oxides, and their electrochemistry, ChemSusChem. 5 (2012) 1146–1161. doi:10.1002/cssc.201100660.

[45] T. Weber, J.C. Muijsers, J.W. Niemantsverdriet, Structure of Amorphous MoS3, J. Phys. Chem. 99 (1995) 9194–9200.

[46] J.C. Dupin, D. Gonbeau, I. Martin-Litas, P. Vinatier, A. Levasseur, Amorphous oxysulfide thin films MOySz (M = W, Mo, Ti) XPS characterization: Structural and electronic pecularities, Appl. Surf. Sci. 173 (2001) 140–150. doi:10.1016/S0169-4332(00)00893-X.

[47] G.C. Stevens, T. Edmonds, Electron spectroscopy for chemical analysis spectra of molybdenum sulfides, J. Catal. 37 (1975) 544–547. doi:10.1016/0021-9517(75)90190-6.

[48] J. Torres, J.E. Alfonso, L.D. López-Carreño, XPS and X-ray diffraction characterization of MoO3 thin films prepared by laser evaporation, Phys. Status Solidi C Conf. 2 (2005) 3726–3729. doi:10.1002/pssc.200461782.

[49] B. Hinnemann, P. Moses, J. Bonde, K.P. Jørgensen, J.H. Nielsen, S. Horch, I. Chorkendorff, J.K. Nørskov, Biomimetic hydrogen evolution: MoS2 nanoparticles as catalyst for hydrogen evolution, J. Am. Chem. Soc. 127 (2005) 5308–5309. http://pubs.acs.org/doi/abs/10.1021/ja0504690.

[50] C.-H. Lee, S. Lee, Y.-K. Lee, Y.C. Jung, Y.-I. Ko, D.C. Lee, H.-I. Joh, Understanding the Origin of Formation and Active Sites for Thiomolybdate [Mo $_3$ S $_{13}$] $^{2-}$ Clusters as Hydrogen Evolution Catalyst through the Selective Control of Sulfur Atoms, ACS Catal. 8 (2018) 5221–5227. doi:10.1021/acscatal.8b01034.

[51] C. Tsai, H. Li, S. Park, J. Park, H.S. Han, J.K. Nørskov, X. Zheng, F. Abild-Pedersen, Electrochemical generation of sulfur vacancies in the basal plane of MoS2 for hydrogen evolution, Nat. Commun. 8 (2017) 15113. doi:10.1038/ncomms15113.

[52] P.C.K. Vesborg, B. Seger, I. Chorkendorff, Recent development in hydrogen evolution reaction catalysts and their practical implementation, J. Phys. Chem. Lett. 6 (2015) 951–957. doi:10.1021/acs.jpclett.5b00306.

[53] M. Ledendecker, J.S. Mondschein, O. Kasian, S. Geiger, D. Göhl, M. Schalenbach, A. Zeradjanin, S. Cherevko, R.E. Schaak, K. Mayrhofer, Stability and Activity of Non-Noble-Metal-Based Catalysts Toward the Hydrogen Evolution Reaction, Angew. Chemie - Int. Ed. 56 (2017) 9767–9771. doi:10.1002/anie.201704021.

[54] C.C.L. McCrory, S. Jung, J.C. Peters, T.F. Jaramillo, Benchmarking heterogeneous electrocatalysts for the oxygen evolution reaction., J. Am. Chem. Soc. 135 (2013) 16977–16987. doi:10.1021/ja407115p.

[55] C. Spöri, J.T.H. Kwan, A. Bonakdarpour, D.P. Wilkinson, P. Strasser, The Stability Challenges of Oxygen Evolving Catalysts: Towards a Common Fundamental Understanding and Mitigation of Catalyst Degradation, Angew. Chemie - Int. Ed. 56 (2017) 5994–6021. doi:10.1002/anie.201608601.

[56] N.Q. Tran, V.Q. Bui, H.M. Le, Y. Kawazoe, H. Lee, Anion–Cation Double Substitution in Transition Metal Dichalcogenide to Accelerate Water Dissociation Kinetic for Electrocatalysis, Adv. Energy Mater. 8 (2018) 1–10. doi:10.1002/aenm.201702139.

[57] Y. Sun, C. Liu, D.C. Grauer, J. Yano, J.R. Long, P. Yang, C.J. Chang, Electrodeposited cobalt-sulfide catalyst for electrochemical and photoelectrochemical hydrogen generation from water, J. Am. Chem. Soc. 135 (2013) 17699–17702. doi:10.1021/ja4094764.

[58] Y. Li, R. Nakamura, Structural change of molybdenum sulfide facilitates the electrocatalytic hydrogen evolution reaction at neutral pH as revealed by in situ Raman spectroscopy, Chinese J. Catal. 39 (2018) 401–406. doi:10.1016/S1872-2067(17)62945-0.

Chapter 10

WS_{3-x} electrochemically-decorated iridium electrodes towards highly stable oxygen evolution electrocatalysts in acid

10.1 Introduction

Iridium, currently the state-of-the-art oxygen evolution reaction (OER) electrocatalyst in acidic electrolyte, is a cost-intensive material which suffers greatly from corrosion under OER long-term operating conditions.[1] Alternative compounds, such as transition metal or noble metal free compounds (e.g. pyrochlores or polyoxometalates),[2,3] have proven to be excellent alternatives but the inherently complex synthetic routes involved limit their scalability and implementation in commercial devices. For such reason, researchers have devoted their efforts to mitigate iridium corrosion by modification with corrosion-resistant metal oxides and/or supports as a route to maximize OER catalysts durability whilst retaining their high activity.[4–6] Metal oxide-passivated iridium materials have been generally obtained by physical techniques such as magnetron sputtering, calcination or plasma jet oxidation,[7,8] but these demand cost-intensive apparatus.

In this chapter we explore the decoration of iridium surfaces by a one-step, inexpensive electrochemical route to obtain improved OER stability in acidic environments. This consists on the electrochemical decomposition of a $[WS_4]^{2-}$ aqueous precursor to yield amorphous tungsten sulfide (WS_{3-x}) nanoparticles, process analogous to that described in Chapter 9. The rationale behind WS_{3-x} decoration is that despite of its stability under hydrogen evolution conditions,[9] electrochemical cycling towards oxygen evolving potentials leads to sulfur loss. The remaining insoluble tungsten oxide product[10] is a well-known, highly stable OER catalyst in acidic media under illumination with visible light,[11] also active for the HER.[12] A preliminary study of the $[WS_4]^{2-}$ electrochemical decomposition on iridium electrodes, to ensure the viability of the proposed WS_{3-x} decoration, is followed by a study to optimize the experimental parameters responsible for WS_{3-x} nanoparticle size and surface coverage. Lastly,

short duty and long-term OER testing experiments are carried out to correlate the improved OER stabilities with surface properties using ex-situ SEM and preliminary XPS results.

10.2 Results and discussion

10.2.1 Electrochemical deposition of amorphous tungsten sulfide on iridium

10.2.1.1 Inherent electrochemistry of Ir substrate and $[WS_4]^{2-}$ precursor

The viability of the electrochemical synthesis of WS_{3-x} by decomposition of a $[WS_4]^{2-}$ aqueous precursor was investigated for Si/Cr/Ir electrodes (see Section 4.5 for further details about electrode fabrication). Figure 10.1 shows a set of representative voltammograms obtained after continuous cycling from 0 V to 2.5 V vs. RHE (anodic scan direction) in aqueous electrolytes in the absence (0.1 M $NaClO_4$, Fig. 10.1a) and presence (10mM $(NH_4)_2[WS_4]$, 0.1 M $NaClO_4$, Fig. 10.1b) of the $[WS_4]^{2-}$ aqueous precursor.

In 0.1 M $NaClO_4$, continuous cycling of the Si/Cr/Ir electrode gradually shows the irreversible conversion of polycrystalline metallic iridium to IrO_x. The first cycle shows several redox features which can be subdivided into four regions. Region I, ranging from 0 to 0.5 V, is generally ascribed to the (underpotential) electroadsorption of monoatomic hydrogen (H_{upd}) followed by the oxidative desorption of molecular and monoatomic hydrogen.[13] However, co-existence of the reductive decomposition of electroadsorbed perchlorate anions to chloride,[14–17] and specific adsorption of hydroxide ions[18] in this region has been reported, which supports the voltammogram asymmetry versus the voltage axis. Region II, ranging from 0.5 to 1.1 V, shows a cathodic peak corresponding to the reduction of the compact IrO_x layer formed in regions III and IV,[19] as well as a very faint anodic feature related to OH^- adsorption to form $Ir(OH)_3$.[17,20] Region III, in the 1.1 to 1.75 V range, shows a pair of peaks corresponding

to the Ir^{3+} hydroxide ⇌ Ir^{4+} hydrous oxide transition.[21–24] Finally, region IV (1.75 V upwards) is related to the oxygen evolution reaction (OER), where Ir electrodissolution is also expected to occur.[1,25–27]

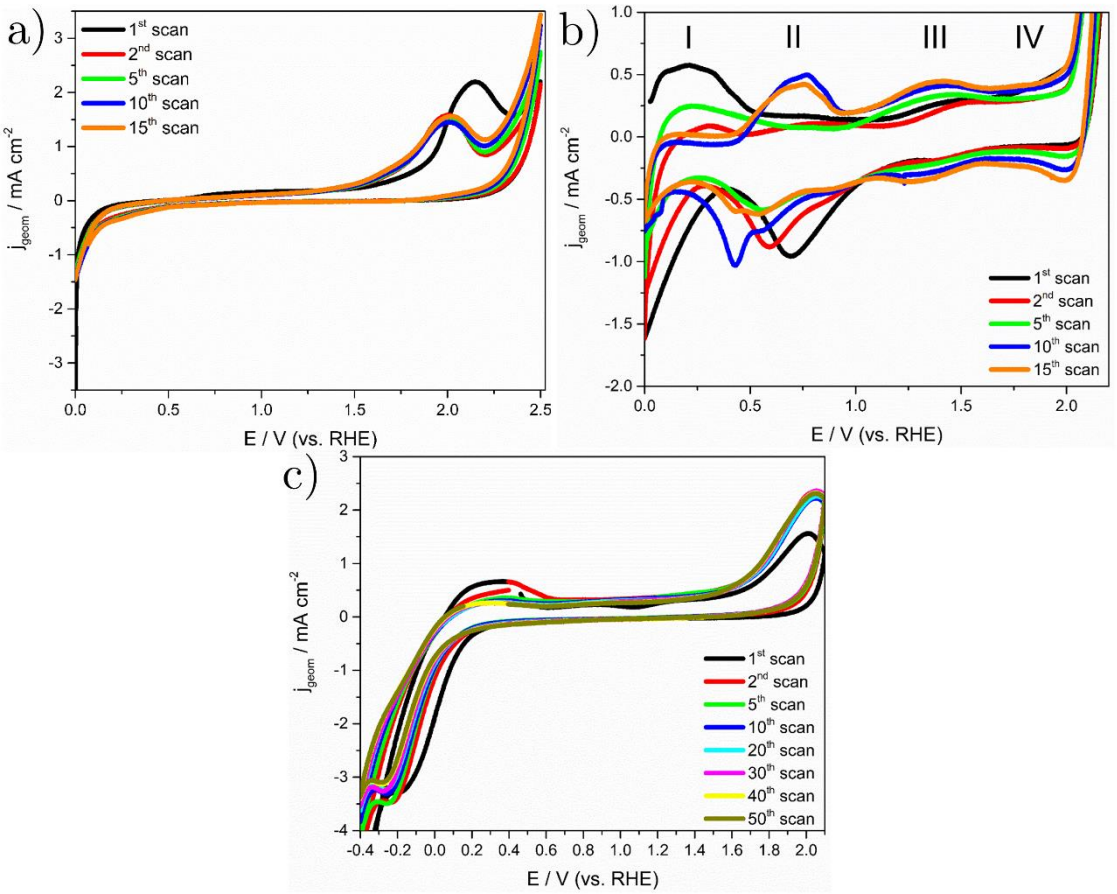

Figure 10.1. Representative voltammograms obtained on 0.25 cm^2 Si/Cr/Ir electrodes by continuous voltage cycling from 0 V to +2.5 V vs. RHE in a) 10 mM $(NH_4)_2[WS_4]$, 0.1 M $NaClO_4$ and b) 0.1 M $NaClO_4$ electrolytes; c) is analogous to a) using a voltage cycling window from -0.4 to +2.1 V vs. RHE (starting potential: +0.4 V). Scan rate: 50 mV s^{-1}.

Upon continuous cycling, electroadsorption/desorption features in region I increasingly disappear, whilst those in regions II and III are more prominent, well-resolved and negatively shifted. This has been previously ascribed to the increased stability (stronger Ir-O bond)[28] of the inner compact anhydrous/outer porous hydrous iridium oxide bilayered structure generated

at potentials higher than 0.5 V vs. RHE.[29] The larger and increased pseudocapacitance during electrochemical cycling observed, besides the growth of the oxide layer, is ascribed to redox transitions coupled to proton intercalation within the porous amorphous oxide matrix.[30,31] The aforementioned oxide cannot be completely reduced, with its partial reduction only taking place at H_{upd} potentials.[26] Thus, the metallic Ir sites formerly available to electroadsorption are gradually blocked by the IrO_x bilayered structure as cycling proceeds. Interestingly, and additional pair of peaks arise in region IV (ca. 1.6 V) over continuous cycling prior to the OER onset: this has been recently ascribed to a conversion of peroxo (O_2^{2-}) to electrophilic superoxo (O_2^-) grops within the iridium oxyhydroxide layer,[32,33] contrary to the previously proposed Ir^{4+} to Ir^{5+} oxidation.[27]

For the $[WS_4]^{2-}$-containing electrochemical bath, a broad electro-oxidative peak centred at ca. 2 V vs. RHE is observed, followed by a cathodic feature with an onset at ca. 0.4 V vs. RHE (reductive peak at ca. -0.25 V, see Figure 10.1c). Interestingly, both redox features present pseudo-stationary peak currents after the first cycle, irrespective of the number of cycles. These electrochemical features are analogous to those obtained upon WS_{3-x} thin film electrodeposition by continuous oxidative-reductive cycling in glassy carbon electrodes.[9] XPS spectra obtained for Ir samples after undergoing 25 cycles within the -0.4 to +2.3 V voltage range (Fig. 10.2a-c) provide insight on the electrochemically-driven oxidative-reductive $[WS_4]^{2-}$ decomposition. A W $4f_{7/2}$:$4f_{5/2}$ spin-orbit doublet with binding energies of ca. 32.3 and 34.5 eV is identified in the W 4*f* high-resolution spectrum (Fig. 10.2a), characteristic of W^{4+} species as expected for WS_{3-x}.[9] The prominent band centred at ca. 166 eV in the S 2*p* spectrum (Fig. 10.2b) denotes the presence of oxidized sulfur moieties (SO_x^{y-}), most likely arising from the low stability towards environment exposure of the S^{2-}/S_2^{2-} moieties during sample transportation and storage, this observed to a lesser extent for MoS_x thin films (see Fig. 9.7 Chapter 9). The sole presence of one Ir $4f_{7/2}$:$4f_{5/2}$ spin-orbit doublet in the high-resolution Ir 4*f*, at binding energies

of ca. 60.2 and 63.3 eV (Fig. 10.2c), indicates that the outermost Ir surface is predominantly found in its metallic state. These results lead us to believe that a WS_{3-x} film is successfully obtained after oxidative-reductive cycling, but ultimately converts to WO_2 after atmosphere exposure.

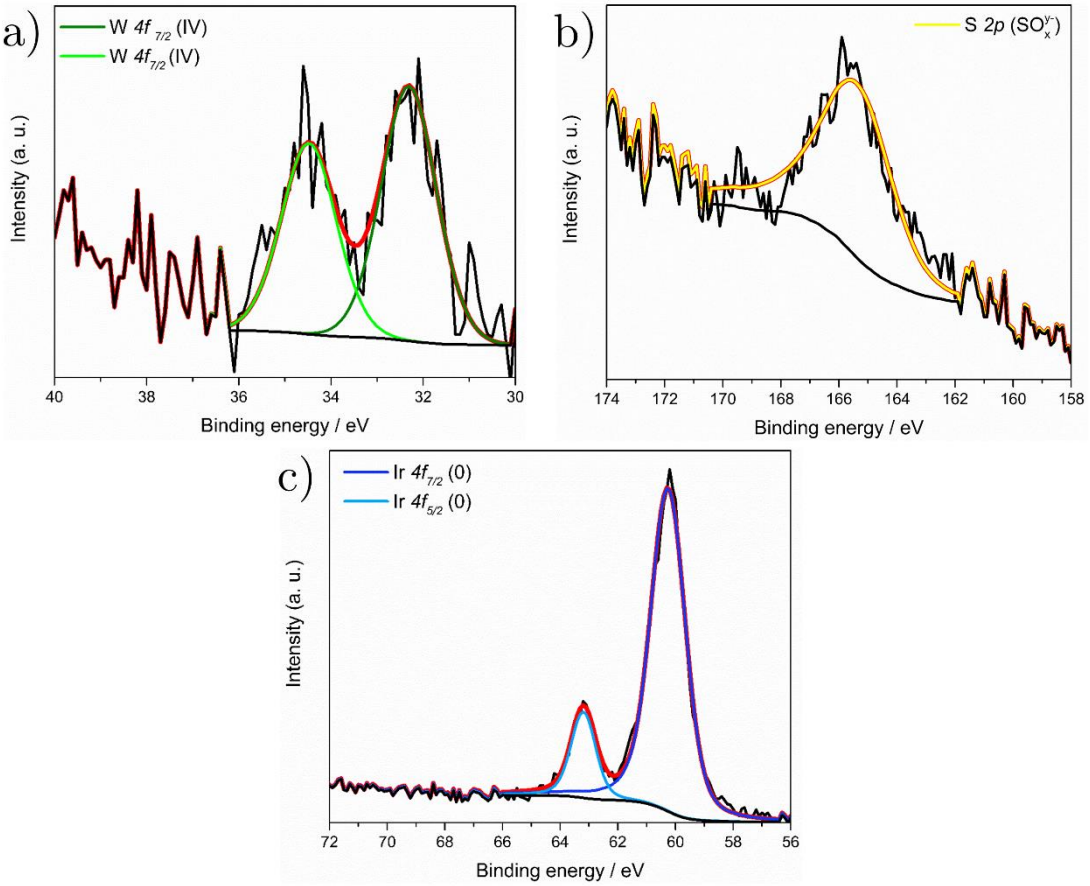

Figure 10.2. High-resolution XPS spectra of a) W 4*f*, b) S 2*p* and c) Ir 4*f*. Labels: W^{4+} $4f_{7/2;5/2}$ (green), S $2p_{3/2:1/2}$ (SO_x^{y-}, yellow), Ir^0 $4f_{7/2;5/2}$ (blue).

Continuing with the voltammetric analysis, there is an evident suppression of the Ir inherent electrochemical features, corroborated when overlapping the first (Figure 10.3a) and 15th (Figure 10.3b) voltammetric cycles obtained in the aforementioned electrolytes. The sharp and high-current OER electrocatalytic feature with onset at ca. 2.0 V and the H_{upd}-hydrogen desorption in the 0-0.5 V region, the most characteristic features for metallic Ir, are no longer

present when cycling in presence of the $[WS_4]^{2-}$ precursor, similarly to features related to IrO_x formation (see insets Figure 10.3). We thus conclude, supported by the XPS results outlined earlier, that WS_{3-x} electrodeposition is also feasible on Ir surfaces, which we presume is substrate-independent, in consonance to previous electrode-dependent investigations of MoS_3 electrodeposition from $[MoS_4]^{2-}$ aqueous baths.[34–36] In addition, inherent Ir electroactivity suppression suggests that the oxidative-reductive cycling deposition mechanism proceeds through a surface-bound pathway which somehow prevents electroadsorption of other aqueous species (namely H^+ and OH^-).

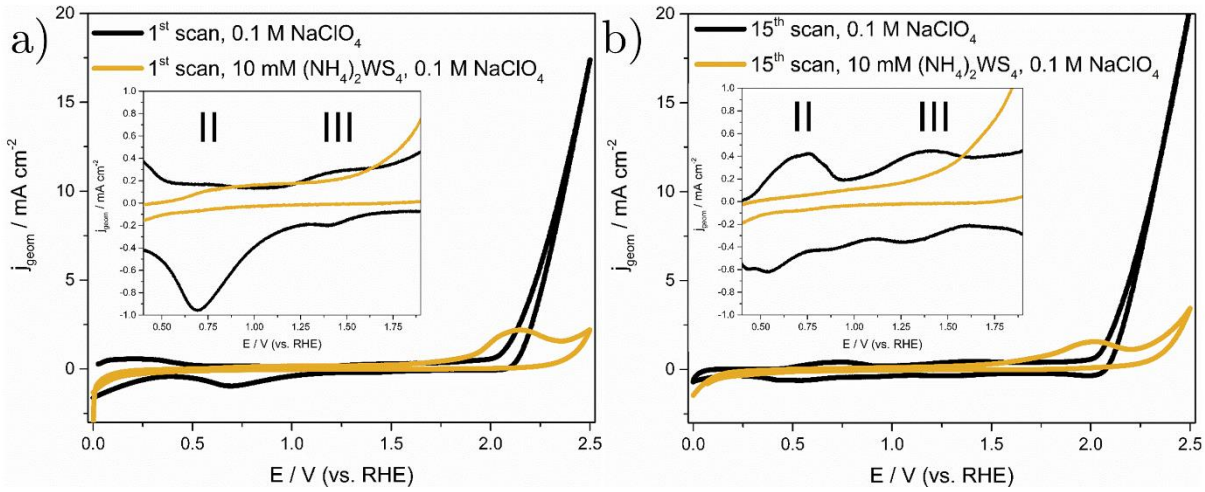

Figure 10.3. Representative a) first and b) 15th (dark yellow) voltammograms obtained by continuous cycling within the 0 V to +2.5 V vs. RHE electrochemical window for 0.25 cm^2 Si/Cr/Ir electrodes in 0.1 M $NaClO_4$ (black) and 10 mM $(NH_4)_2[WS_4]$, 0.1 M $NaClO_4$ (dark yellow) electrolytes. Insets: zoom of the first and 15th voltammograms in the +0.4 to +1.80 V vs. RHE window. Scan rate: 50 mV s^{-1}.

To further corroborate this observation, we evaluated the influence of the voltage cycling window in the $[WS_4]^{2-}$-related electrochemical features. Cycling voltammograms recorded from 0 to 1.6 V vs. RHE (Figure 10.4a), where the upper vertex potential precedes the onset of the $[WS_4]^{2-}$ electro-oxidative event, present two cathodic pre-catalytic peaks (at ca. 0.13 and 0.33

V vs. RHE, respectively) equivalent to those found for H_{upd} on pristine Ir electrodes.[37] This, in conjunction with the absent cathodic feature previously found for the oxidative-reductive cycling treatment, indicates that $[WS_4]^{2-}$ does not undergo any electrochemical reduction unless it is preceded by an electro-oxidative step. Alternatively, if the voltage cyclic window is selected from 0.4 to 2.2 V (Figure 10.4b), where the lower vertex potential precedes the onset of the $[WS_4]^{2-}$ reductive event, the broad $[WS_4]^{2-}$ electro-oxidative feature gradually disappears in favour of the upward anodic current profile characteristic of OER. Consequently, selective cycling in the oxidative range leads to de-activation of the $[WS_4]^{2-}$ anodic deposition pathway, which can be reinstated when cycling towards cathodic currents. This behaviour mirrors that found by Tan et al. for $[WS_4]^{2-}$ electrodeposition in glassy carbon substrates,[9] proposing a plausible electrodeposition mechanism, outlined below

Oxidative adsorption: $$[WS_4]^{2-} \rightarrow WS_3 + 1/8\,S_8 + 2e^- \quad (10.1)$$

Reductive desorption: $$WS_3 + 1/8\,S_8 + 2e^- \rightarrow [WS_4]^{2-} \quad (10.2)$$

WS_3 to WS_2 reductive conversion: $$WS_3 + 2\,H^+ + 2e^- \rightarrow WS_2 + H_2S \quad (10.3)$$

The initial electroadsorption of WS_3 moieties, reaction pathway similar to that proposed in $[MoS_4]^{2-}$ anodic electrodeposition,[34,36] is suggested to be followed by either a conversion of WS_3 to WS_2 or a partial re-dissolution of WS_3, the latter allegedly aggravated at faster scan rates. Passivation of the electroactive surface during oxidative adsorption is suggested to occur due to co-deposition of non-conducting S_8, whilst partial WS_3 to WS_2 conversion and S_8 cathodic electrodissolution are suggested to provide surface sites susceptible to $[WS_4]^{2-}$ oxidative electroadsorption.

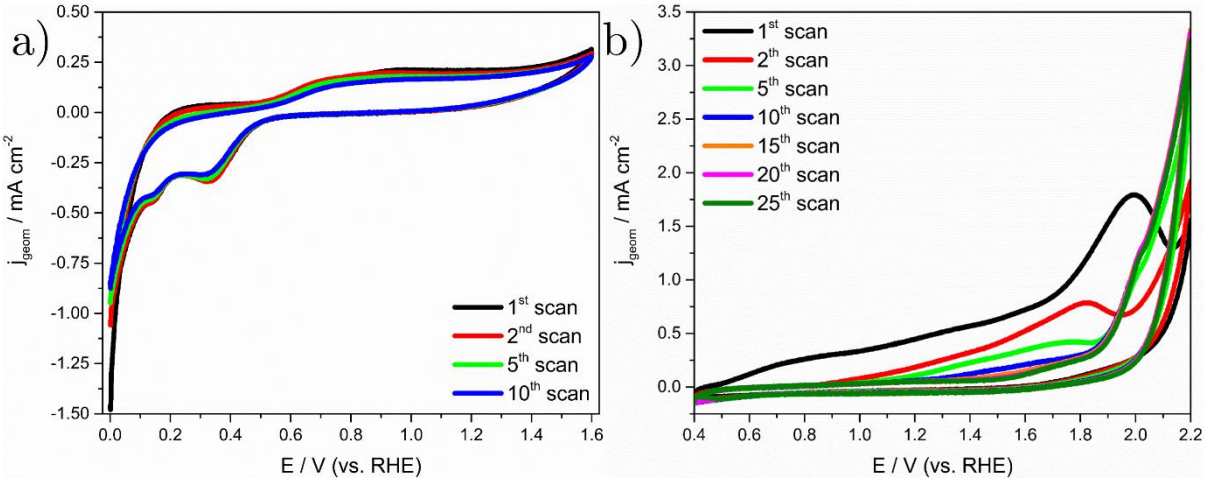

Figure 10.4. Representative voltammograms obtained on 0.25 cm^2 Si/Cr/Ir electrodes by continuous voltage cycling in a 10 mM $(NH_4)_2[WS_4]$, 0.1 M $NaClO_4$ aqueous electrolyte in the voltage windows a) 0 to +1.6 V and b) 0.4 to +2.2 V vs. RHE (starting potential: +0.4 V). Scan rate: 50 mV s^{-1}.

10.2.1.2 Electrodeposition strategy and physical characterization of WS_{3-x} decorated Ir electrodes

Having in mind the previous findings, and our aim to selectively passivate the high surface energy, low coordination number Ir sites to retain OER functionality yet minimizing Ir electrodissolution, WS_{3-x} decoration was carried out by pulsed electrodeposition (PE). The main advantage of PE compared with other conventional electrodeposition methods (cyclic voltammetry, chronoamperometry, chronopotentiometry) is the obtention of nuclei with higher degree of monodispersion (i.e. narrower size distribution), with sizes and coverages modulated by the magnitude and duration of the pulses.[38] A particular mode of PE, known as pulse reverse potential/current (i.e. double anodic-cathodic potential/current pulses) is selected. It consists on alternating anodic and cathodic pulses of equivalent magnitude and duration. This stems from the aim to alternately trigger both $[WS_4]^{2-}$ oxidative electroadsorption and WS_3 to

WS_2 conversion processes, which are proposed to be stoichiometric based on the previously reported deposition mechanism (Eqns. 10.1 and 10.3).

Preliminary studies focused on applying potential-controlled pulses, with anodic pulses applied within the 1.8 to 2.2 V window, and cathodic pulses in the -0.2 to 0.1 V window. These windows were selected to evaluate WS_{3-x} nuclei characteristics when potential pulsing in regions ascribed to the onset, peak potential, and diffusion decay peak regions of both anodic and cathodic processes. Unfortunately, in all cases the high transient currents obtained ($|j_{geom}| > 30$ mA cm^{-2}, see Fig. 10.5a for representative j_{geom}-t profile) resulted in accelerated electrodissolution of the thermally deposited Ir layer, exposing the underlying Cr and Si layers. As this is undesirable for our application, we opted to perform current-controlled pulses, selecting ±500 µA (ca. ±2 mA cm^{-2}), ±700 µA (ca. ±2.8 mA cm^{-2}) and ±900 µA ca. (±3.6 mA cm^{-2}) as pulse currents. These markedly different values were selected after inspection of the oxidative-reductive voltammograms (for representative current pulse profiles see Fig. 10.5b), which approximately correspond to experimental currents observed at the kinetics-controlled, peak potential and diffusion-limited (onset of HER/OER) voltage regions, respectively. The effect of the pulse timescale and total deposition duration on the WS_{3-x} nuclei size and surface coverage was also assessed. Short (62.5 ms), medium (250 ms) and long (1000 ms) pulses are selected, whilst experiment duration was modified between 1 to 10 minutes.

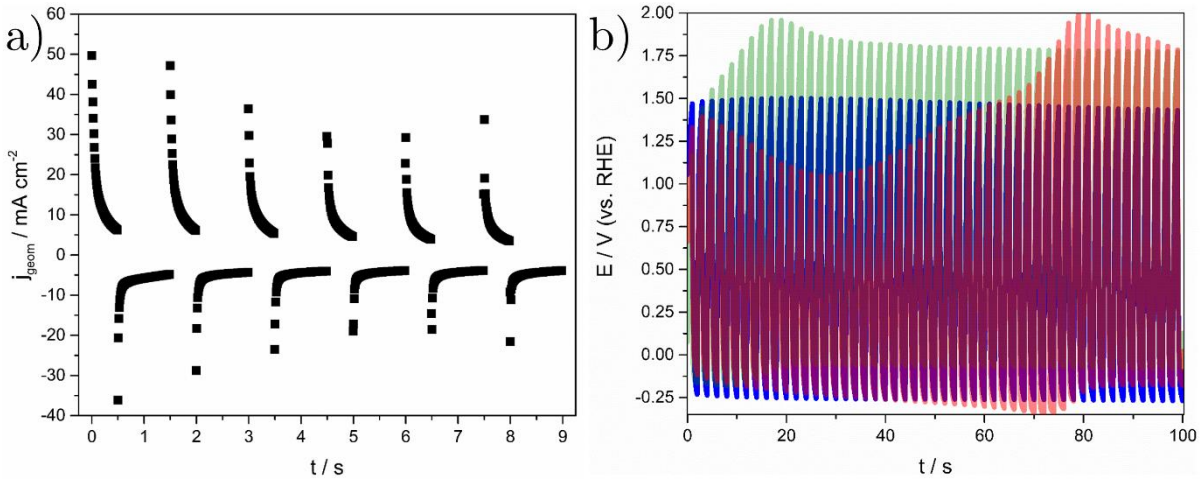

Figure 10.5. a) j_{geom} – t profile obtained during use of pulse reverse potential electrodeposition procedure (+1.8 V, 500 ms; -0.2 V, 1000 ms) and b) E – t profiles obtained during use of pulse reverse current electrodeposition procedure (1000 ms on/off pulses) with current magnitudes of ±500 μA (blue), ±700 μA (green) and ±900 μA (red) on 0.25 cm^2 Si/Cr/Ir electrodes.

Morphology characterization of Si/Cr/Ir electrodes before and after reverse pulsed deposition from a $[WS_4]^{2-}$ aqueous bath was performed by FE-SEM. Micrographs of the as-received Si/Cr/Ir surface (Fig. 10.6a-d) show smooth surfaces with cracks within the Ir layer (lengths: 0.5-15 μm, widths: 10-35 nm) range, and Ir grain sizes of 25±7 nm. The observed cracks are most probably originated from internal stress/strain of the Ir film during thermal deposition, leading to a corrugated profile: their abundance has been found to vary across the wafers employed. For Si/Cr/Ir electrodes undergoing reverse pulse current electrodeposition in a $[WS_4]^{2-}$ aqueous bath, two main conclusions can be drawn based on preliminary SEM micrograph analysis (Figs. 10.7-10.9). First, deposition of WS_{3-x} nuclei seems to occur: amorphous aggregates physically attached to the Ir surface can be identified. Second, the electrodeposition protocol does not seem to significantly modify the inherent Ir surface morphology. Unambiguous identification of the nature of the observed nuclei is not possible with EDX elemental analysis, as the characteristic X-ray lines of both Ir and W cannot be resolved due to their overlapping.

FE-SEM micrographs comparison of Si/Cr/Ir electrodes undergoing pulses of different magnitude for a given pulse duration in a $[WS_4]^{2-}$ aqueous bath are shown in Figure 10.7. It can be clearly seen that pulses of higher magnitude applied in shorter experiment durations yield minimal or not observable Ir surface modification relative to its grain size. We hypothesize that higher magnitude pulses lead towards a lower WS_{3-x} nuclei deposition efficiency, as not only will yield faster depletion rates of the $[WS_4]^{2-}$ species at the electrode-electrolyte interface, but also higher fractions of the charge passed will be allocated to the competing HER/OER processes observed for Ir. Analysis of the micrographs of Si/Cr/Ir electrodes undergoing current pulses of different timescale for a given total experiment duration (Fig. 10.8) show that nuclei size and surface coverage are drastically affected: longer pulses (1000 ms) yield a high density of large nuclei, whilst medium and short pulses presumably yield nuclei sizes and coverages beyond the FE-SEM resolution, if present. We believe that for transient current pulse timescales the electrodeposition kinetics might not be fast enough to fully take place, primarily contributing to the non-faradaic charge-discharge of the electrical double layer, phenomenon which occurs in the μs-ms range depending on the experimental time constant.[39] Further insight on the effect of total experiment duration can be gathered by analysis of the micrographs obtained for the ±500 μA pulsed electrodeposited samples (Fig. 10.9): longer experiment times (≥ 5 mins) yield larger WS_{3-x} nuclei and higher surface coverages (average size: 205±70 nm for 10 mins, 42±11 nm for 5 mins), that cannot be resolved for shorter times (≤ 2.5 mins) due to their small size and/or low coverage. We can then conclude that WS_{3-x} deposition is maximized in terms of nuclei size and surface coverage when selecting ±500 μA pulse currents, long pulse timescales (1000 ms) and longer total pulse reverse current electrodeposition times (10 mins).

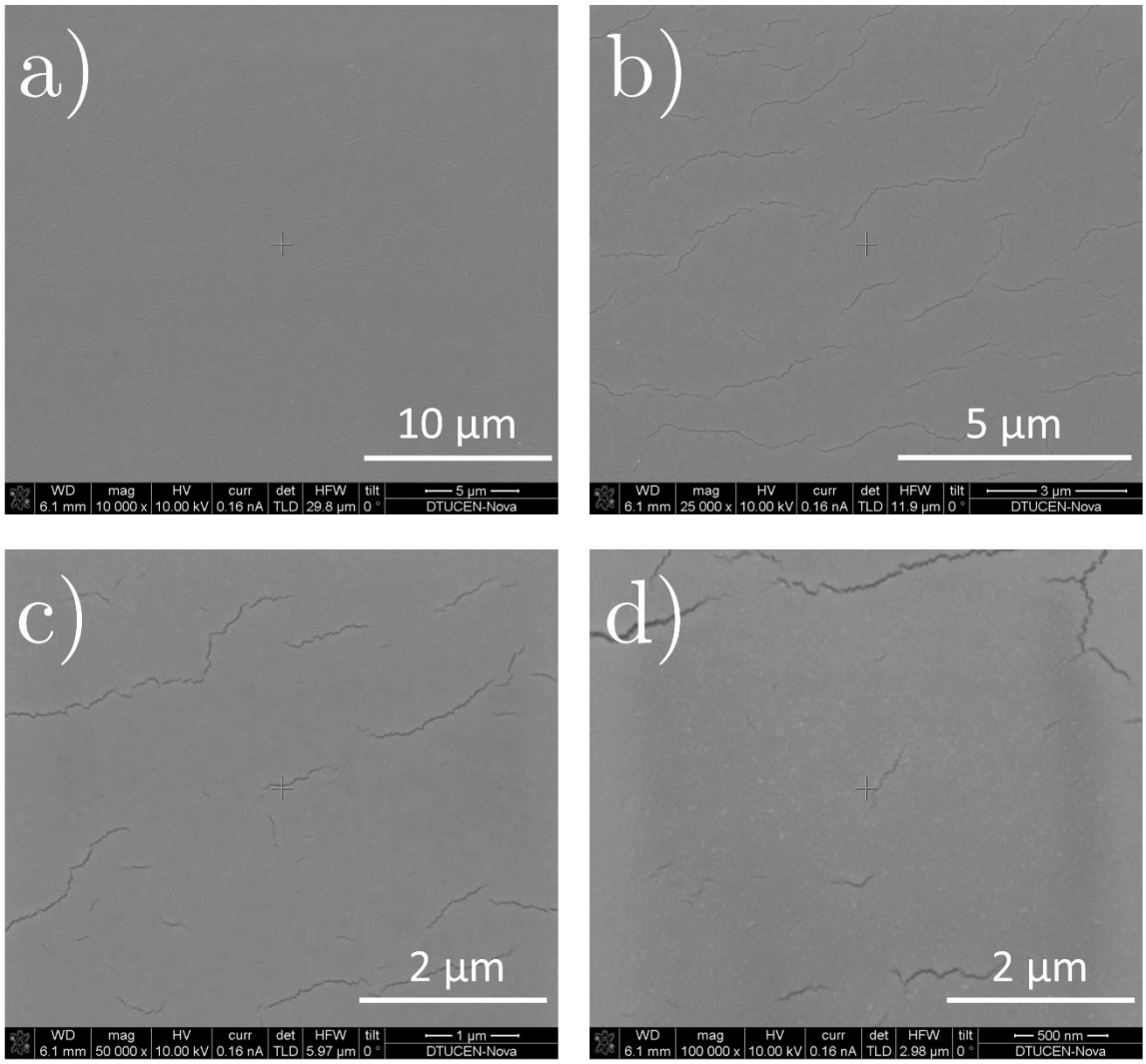

Figure 10.6. FE-SEM micrographs of as-received Si/Cr/Ir electrodes at a) 10000x, b) 25000x, c) 50000x and d) 100000x magnification.

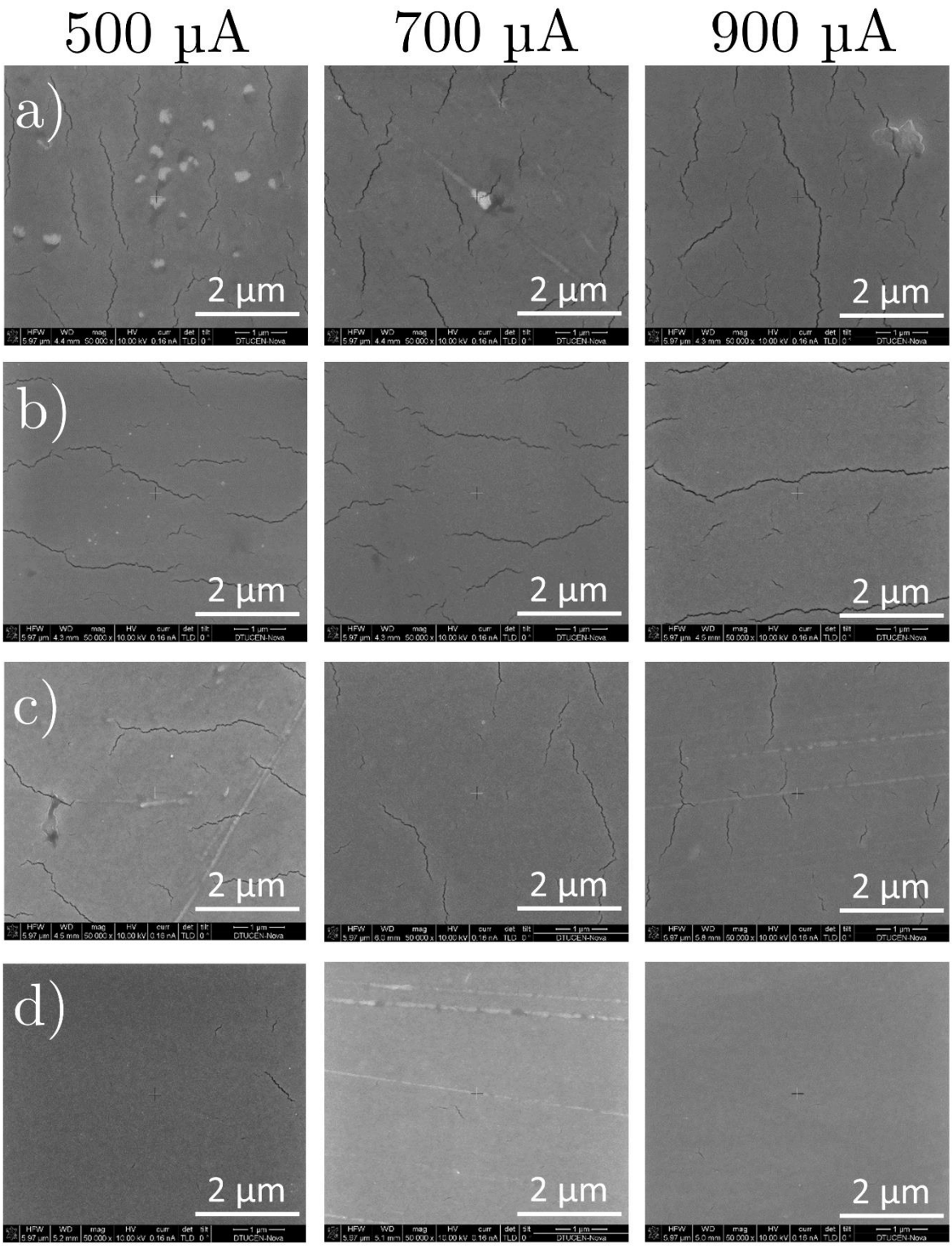

Figure 10.7. FE-SEM micrographs of Si/Cr/Ir electrodes after undergoing ±500-900 µA (pulse duration: 1000 ms), pulse reverse current electrodeposition experiments for a) 10 mins, b) 5 mins, c) 2.5 mins and d) 1 min. Micrographs image magnification: 50000x.

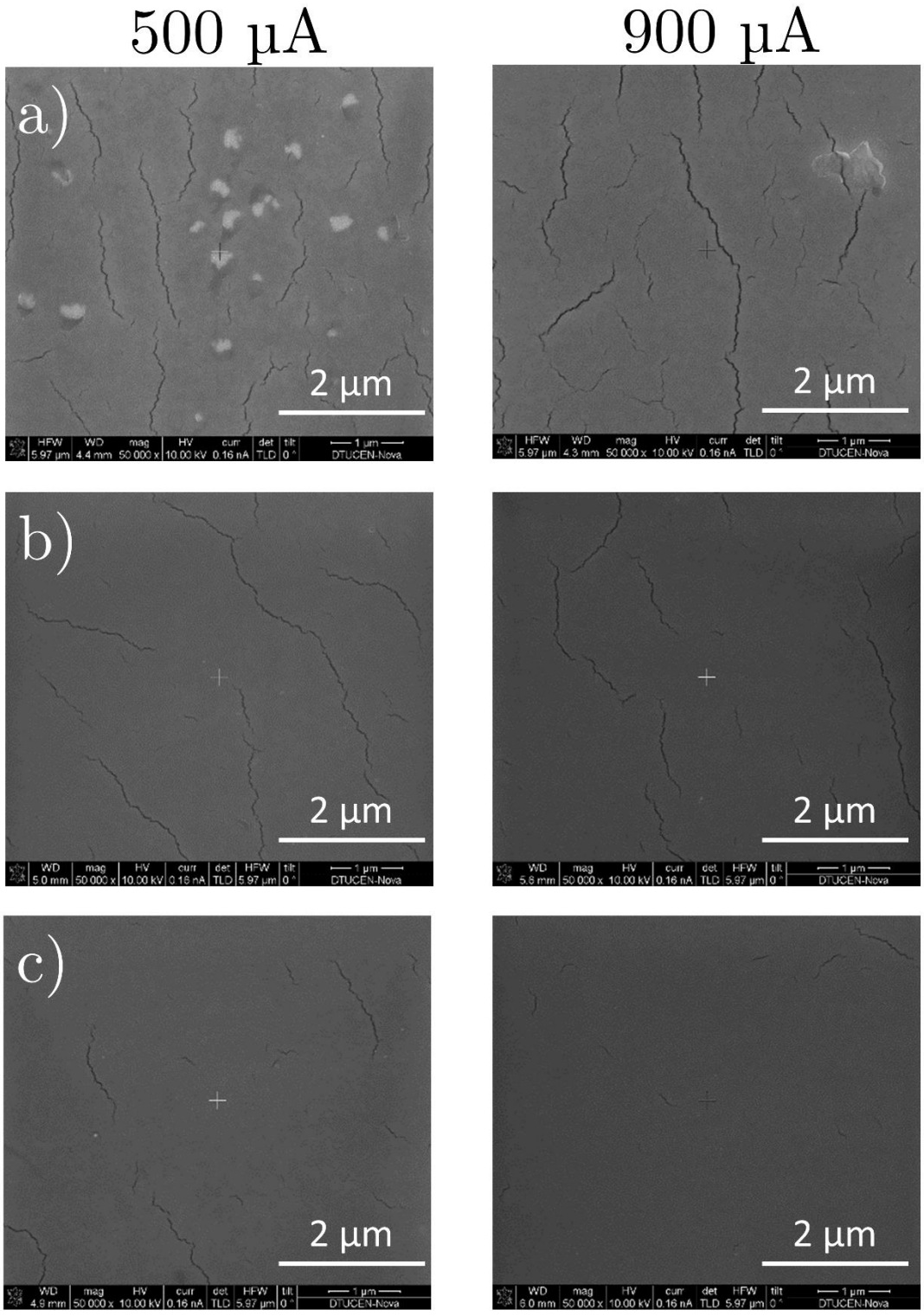

Figure 10.8. FE-SEM micrographs of Si/Cr/Ir electrodes after undergoing ±500 and 900 µA pulse reverse current electrodeposition experiments for 10 mins using a) 1000 ms, b) 250 ms and c) 62.5 ms current pulses. Micrographs image magnification: 50000x.

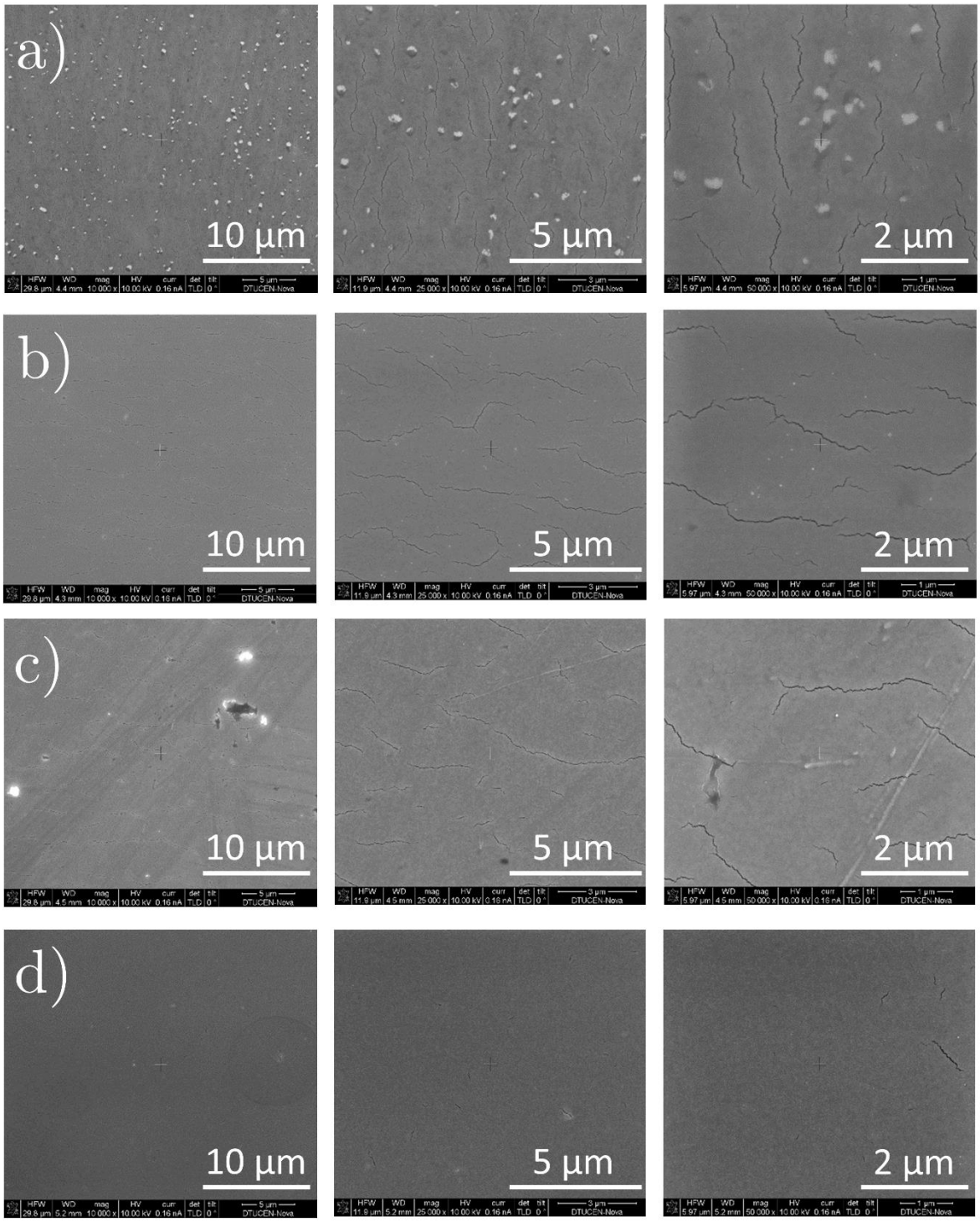

Figure 10.9. FE-SEM micrographs of Si/Cr/Ir electrodes after undergoing ±500 µA, 1000 ms pulse reverse current electrodeposition experiments for a) 10 mins, b) 5 mins, c) 2.5 mins and d) 1 min. Micrographs image magnification: 10000x (left), 25000x (middle) and 50000x (right).

10.2.2 Electrochemical testing of WS_{3-x} decorated Ir electrodes: oxygen evolution reaction (OER)

10.2.2.1 Short-term OER testing

The effect of WS_{3-x} pulse reverse current electrodeposition on Ir electrodes towards the OER was investigated by use of a complex testing protocol (for full details, see section 4.7.4 Materials, equipment and methods). In brief, all samples were electrochemically preconditioned until a pseudo-stationary response was obtained, followed by cyclic voltammetry acquisition in the H_{upd} (0.025 to 0.55 V) and OER (1.0 to 1.60 V) voltage windows to evaluate modifications in the electrochemical active surface area (ECSA) and OER activity before/after OER stability testing. Short-duty stability testing was evaluated by recording chronopotentiograms during 2 hours of the potential required to sustain an anodic current density of +10 mA cm^{-2}, as shown in Figure 10.10. Compared with as-received Ir, which presents an OER potential of 1.729±0.005 V vs RHE after 2 hour testing, the WS_{3-x} decorated Ir electrodes generally present slightly higher OER overpotentials. This result is expected, as WS_{3-x} incorporation at the Ir surface, a material less electrocatalytic to the OER than Ir, which will inevitably partially block highly active OER surface sites, increasing the overall OER overpotential.

However, the most relevant metrics to evaluate the passivating effect of WS_{3-x} on Ir electrodes are the variation in OER overpotential (ΔE_{OER}) after short-duty testing, and the modifications in the mass activities (OER current normalized by Ir loading) and specific activities (OER current normalized by electrochemically active Ir surface area): for mass and specific activity elucidation, see section K Appendix. Among the whole set of samples tested (see Tables K.1-K.3 Appendix), a narrow selection (see Table 10.1) present greatly improved OER metrics. For instance, ΔE_{OER} was reduced by ca. 20 mV (39 mV vs. 59 mV; sample: ±500 µA, 250 ms, 1 min). As for the mass and specific activities, although WS_{3-x} decorated samples generally

presented on-par or worse OER performances prior to stability measurements, these greatly surpassed pristine Ir electrodes after the 2 hour, +10 mA cm^{-2} galvanostatic stability experiments (for representative OER activity voltammograms, see Fig. 10.11a). Best performing samples presented a ca. 1.6 fold (3.1 vs. 1.9 ± 0.3 A mg_{Ir}^{-1} at 1.55 V) and ca. 1.8 fold (1.03 × 10^{-4} vs 5.71 ± 0.1 × 10^{-5} A cm_{Ir}^{-2} at 1.55 V) enhancement in mass and specific activities, respectively.

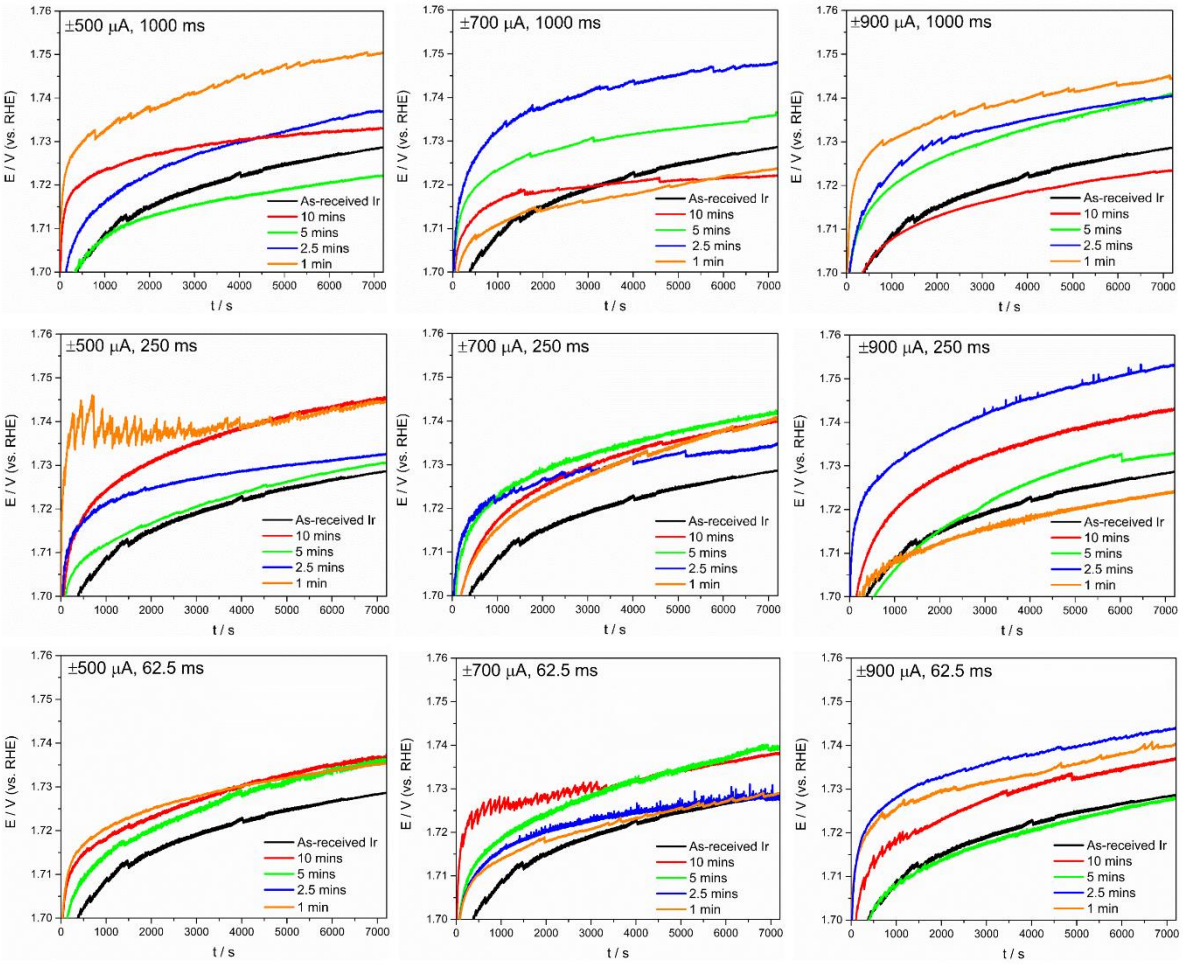

Figure 10.10. Chronopotentiograms recorded for Si/Cr/Ir electrodes before and after undergoing ±500-900 µA pulse reverse current electrodeposition experiments, to sustain j_{geom}= +10 mA cm^{-2} for 2 h. Labels (total electrodeposition time): 10 mins (red), 5 mins (green), 2.5 mins (blue) and 1 min (orange).

Sample	E_{OER,t_0} / V	E_{OER,t_f} / V	ΔE_{OER}/ V	@ 1.51 V			@ 1.55 V		
				j_{geom} / mA cm^{-2}	Mass activity / A mg$_{Ir}^{-1}$	Specific activity / A cm$_{Ir}^{-2}$	j_{geom} / mA cm^{-2}	Mass activity / A mg$_{Ir}^{-1}$	Specific activity / A cm$_{Ir}^{-2}$
As-received Ir	1.670 ± 0.005	1.729 ± 0.005	0.059 ± 0.008	0.23 ± 0.03 0.80 ± 0.03	0.040 ± 0.02 0.31 ± 0.04	6.68 ± 2.5 × 10^{-6} 9.42 ± 0.6 × 10^{-6}	1.70 ± 0.2 4.90 ± 0.5	0.30 ± 0.2 1.90 ± 0.3	5.01 ± 1.9 × 10^{-5} 5.71 ± 0.1 × 10^{-5}
±500 µA, 1000 ms, 10 mins	*1.690 ± 0.007*	*1.73300 ± 0.00005*	*0.043*	*0.15* *1.09*	*0.041* *0.378*	*2.44 × 10^{-6}* *1.39 × 10^{-5}*	*1.14* *6.34*	*0.310* *2.197*	*1.86 × 10^{-5}* *8.11 × 10^{-5}*
±500 µA, 1000 ms, 5 mins	*1.668 ± 0.005*	*1.72220 ± 0.00005*	*0.054*	*0.16* *1.02*	*0.032* *0.320*	*3.30 × 10^{-6}* *1.44 × 10^{-5}*	*1.24* *6.40*	*0.259* *2.006*	*2.64 × 10^{-5}* *9.05 × 10^{-5}*
±500 µA, 250 ms, 5 mins	*1.678 ± 0.005*	*1.73048 ± 0.00004*	*0.053*	*0.20* *1.14*	*0.0298* *0.328*	*6.12 × 10^{-6}* *1.75 × 10^{-5}*	*1.43* *6.71*	*0.210* *1.934*	*4.32 × 10^{-5}* *1.03 × 10^{-4}*
±500 µA, 250 ms, 2.5 mins	1.683 ± 0.006	1.73256 ± 0.00005	0.050	0.21 1.54	0.057 0.589	3.35 × 10^{-6} 1.79 × 10^{-5}	1.5 7.59	0.413 2.902	2.42× 10^{-5} 8.80 × 10^{-5}
±500 µA, 250 ms, 1 min	1.707 ± 0.005	1.74462 ± 0.00007	0.038	0.28 1.59	0.062 0.643	5.60 × 10^{-6} 1.74 × 10^{-5}	1.87 7.52	0.416 3.040	3.73 × 10^{-5} 8.25 × 10^{-5}
±700 µA, 1000 ms, 10 mins	*1.682 ± 0.006*	*1.72205 ± 0.00004*	*0.040*	*1.46* *2.08*	*0.422* *0.731*	*2.24 × 10^{-5}* *2.62 × 10^{-5}*	*-(6.75 @1.54 V)* *- (8.19 @1.54V)*	*- (>1.194)* *- (>2.02)*	*- (>6.33 × 10^{-5})* *- (>7.26 × 10^{-5})*
±700 µA, 1000 ms, 5 mins	1.686 ± 0.006	1.73661 ± 0.00003	0.051	0.18 1.18	0.057 0.451	2.50 × 10^{-6} 1.37 × 10^{-5}	1.33 6.69	0.422 2.558	1.86 × 10^{-5} 7.76 × 10^{-5}
±700 µA, 250 ms, 2.5 mins	*1.683 ± 0.006*	*1.7347 ± 0.0001*	*0.052*	*0.18* *1.44*	*0.052* *0.568*	*2.73 × 10^{-6}* *1.62 × 10^{-5}*	*1.24* *7.12*	*0.360* *2.809*	*1.89 × 10^{-5}* *8.00 × 10^{-5}*
±700 µA, 62.5 ms, 2.5 mins	1.677 ± 0.006	1.7278 ± 0.0004	0.051	0.19 1.42	0.053 0.526	2.96 × 10^{-6} 1.70 × 10^{-5}	1.35 7.33	0.381 2.713	2.12 × 10^{-5} 8.78 × 10^{-5}
±900 µA, 1000 ms, 10 mins	*1.667 ± 0.006*	*1.72343 ± 0.00004*	*0.056*	*0.29* *1.28*	*0.075* *0.418*	*4.83 × 10^{-6}* *1.74 × 10^{-5}*	*2.12* *7.57*	*0.556* *2.471*	*3.58 × 10^{-5}* *1.03 × 10^{-4}*
±900 µA, 250 ms, 5 mins	1.669 ± 0.005	1.73295 ± 0.00009	0.064	0.43 1.5	0.135 0.543	6.05 × 10^{-6} 1.84 × 10^{-5}	2.67 7.95	0.839 2.879	3.7674× 10^{-5} 9.73163× 10^{-5}
±900 µA, 250 ms, 1 min	*1.670 ± 0.006*	*1.7241 ± 0.0001*	*0.054*	*0.35* *1.42*	*0.104* *0.593*	*5.25 × 10^{-6}* *1.5 × 10^{-5}*	*2.53* *7.43*	*0.749* *3.102*	*3.79 × 10^{-5}* *7.89 × 10^{-5}*

Table 10.1. Compilation of the short-duty oxygen evolution activity of WS_{3-x} decorated Ir electrodes after use of ±500-900 µA pulse reverse current electrodeposition. E_{OER,t_0}, E_{OER,t_f} and ΔE_{OER} correspond to the averaged (± 10 s) initial, final and variation, respectively, of the OER overpotentials recorded to sustain j_{geom}= +10 mA cm^{-2} for 2 h. OER activity metrics (j_{geom}, mass activity, specific activity) are reported, for each sample, before (first row) and after (second row) short-duty OER stability measurements.

Sample	R_f (A_{ECSA}/A_{geom})			Relative R_f increase / %		Tafel slope / mV dec^{-1}	
	Before OER	After OER	After 2 h OER stability	After OER	After 2 h OER stability	After OER	After 2 h OER stability
As-received Ir	38 ± 17	76 ± 7	86 ± 8	100	126.32	39 ± 2	45 ± 2
±500 µA, 1000 ms, 10 mins	***61.4***	***71.2***	***78.2***	***15.96***	***27.36***	***41***	***46***
±500 µA, 1000 ms, 5 mins	***47***	***64.6***	***70.7***	***37.45***	***50.43***	***42***	***43***
±500 µA, 250 ms, 5 mins	***33.1***	***57.2***	***65.0***	***72.81***	***96.37***	***43***	***45***
±500 µA, 250 ms, 2.5 mins	62.1	80.2	86.3	29.15	38.97	42	47
±500 µA, 250 ms, 1 min	50.1	72.3	91.2	44.31	82.04	43	46
±700 µA, 1000 ms, 10 mins	**65.2**	**78.3**	**79.3**	**20.09**	**21.63**	**41**	**47**
±700 µA, 1000 ms, 5 mins	71.6	79.0	86.3	10.34	20.53	45	46
±700 µA, 250 ms, 2.5 mins	***65.5***	***83.3***	***89***	***21.37***	***35.88***	***42***	***45***
±700 µA, 62.5 ms, 2.5 mins	63.6	74.9	83.5	17.77	32.29	45	46
±900 µA, 1000 ms, 10 mins	***59.2***	***71.8***	***73.7***	***21.28***	***24.49***	***44***	***45***
±900 µA, 250 ms, 5 mins	70.9	72.7	81.7	2.54	15.23	48	47
±900 µA, 250 ms, 1 min	***66.8***	***89.2***	***94.2***	***33.53***	***41.02***	***44***	***47***

Table 10.2. Compilation of the roughness factor (R_f) values (obtained after integration of the hydrogen desorption region, 0.06 V to ca. 0.45 V vs RHE), their relative increase, and Tafel slope values for pristine and WS_{3-x} decorated Ir electrodes before/after OER activity measurements, and after 2 h OER stability measurements.

The OER geometric current density values obtained prior to OER stability testing can again be explained by the electrocatalytic inertness of WS_{3-x} nuclei towards the OER. Indeed, the first voltammograms recorded towards OER potentials, which present broad electro-oxidative features in the 1 to 1.4 V voltage range not found in consecutive scans, are markedly different between pristine Ir samples and those decorated with WS_{3-x} (Fig. 10.11b). For pristine Ir, tailing of the $Ir(OH)_3$ formation (up to 1.1 V) is still present followed by the characteristic oxygen evolution current. Conversely, for WS_{3-x} decorated samples the $Ir(OH)_3$ formation tailing is absent, observing instead a broad electro-oxidation peak centred at ca. 1.25 V vs RHE, followed by OER shifted towards positive overpotentials.

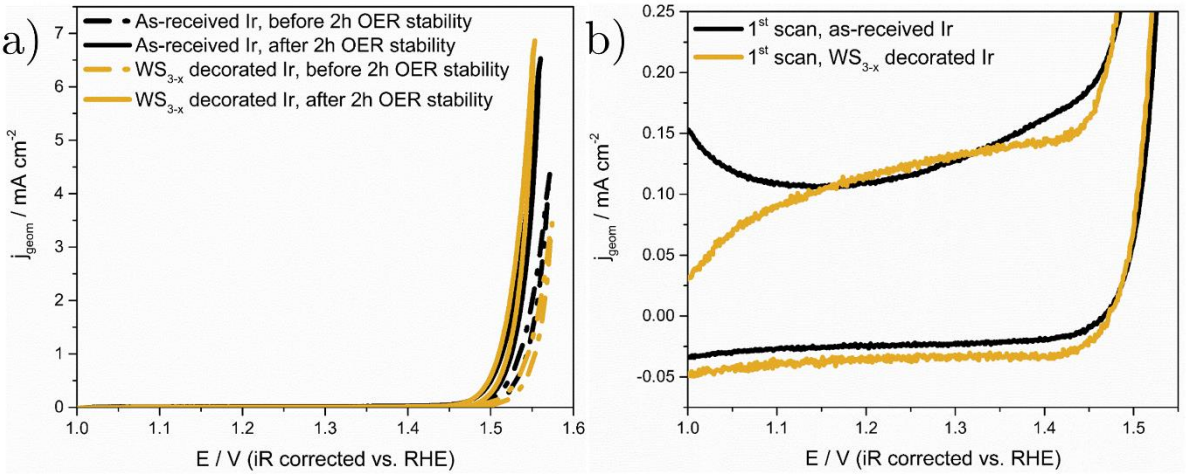

Figure 10.11. Cyclic voltammograms recorded at pristine (black) and WS_{3-x} decorated (±500 µA, 1000 ms, 5 mins; dark yellow) Si/Cr/Ir electrodes a) before (broken line) and after (solid line) undergoing short-duty OER stability experiments: j_{geom}= +10 mA cm^{-2} sustained for 2 h; b) first OER voltammograms recorded for pristine and WS_{3-x} decorated (±700 µA, 250 ms, 10 mins). Voltage window: +1.0 to +1.6 V vs. RHE. Electrolyte: 0.1 M $HClO_4$. Scan rate: 10 mV s^{-1}.

We hypothesize that this feature corresponds to be the irreversible electro-oxidative conversion of W^{4+} centres in WS_{3-x} nuclei to W^{6+} as found in WO_3.[10] Proof of this conversion can be gathered by analyzing the W 4f high resolution XPS spectra of WS_{3-x} decorated Ir samples

after short-duty OER testing (Fig. 10.12): the characteristic W $4f_{7/2}$:$4f_{5/2}$ 4f spin-orbit doublet of W^{4+} species, at binding energies of ca. 32.3 and 34.5 eV, is positively shifted after OER testing by ca. 3.7 eV, yielding a doublet centred at 36 and 38.2 eV. These binding energies are characteristic of W^{6+} species, as found in WO_3.[40,41] This conversion is key in Ir stability maximization, as WO_3 is a thermodynamically stable oxide under strongly anodic potentials in acidic media,[42] but as already mentioned initially hampers the OER electrocatalysis due to partial blocking of OER-active Ir sites.

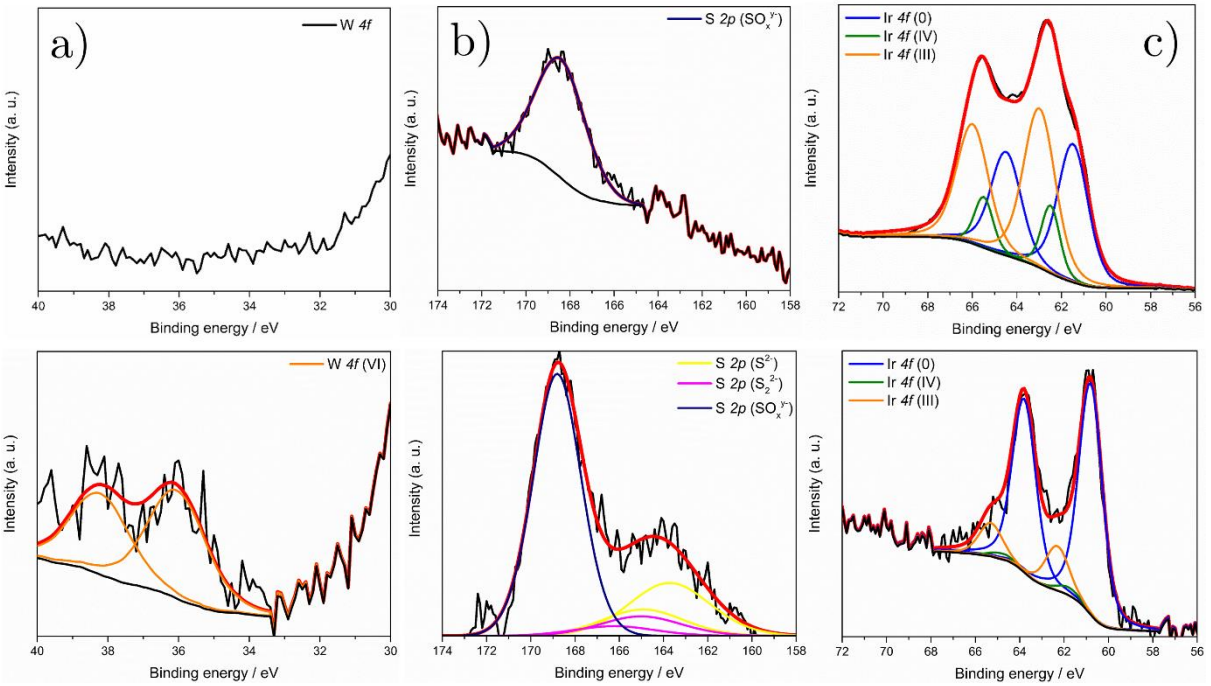

Figure 10.12. High-resolution XPS spectra of a) W 4*f*, b) S 2*p* and c) Ir 4*f* for pristine (top) and WS_{3-x} decorated (±500 µA, 1000 ms, 5 mins; bottom) Ir samples. Labels: W^{6+} $4f_{7/2:5/2}$ (orange), S $2p_{3/2:1/2}$ (S^{2-}, yellow), S $2p_{3/2:1/2}$ (S_2^{2-}, magenta), S $2p_{3/2:1/2}$ (SO_x^{y-}, dark blue), Ir^0 $4f_{7/2:5/2}$ (blue), Ir^{4+} $4f_{7/2:5/2}$ (green) and Ir^{3+} $4f_{7/2:5/2}$ (orange).

Insights on the origin of the improved OER metrics after 2 h stability testing can be gathered by joint analysis of the electrochemistry, FE-SEM and XPS results. Ir surface roughening, monitored qualitatively by FE-SEM, and quantitatively by roughness factor measurements (R_f,

defined here as ECSA normalized per geometric electrode area),[43] can be correlated with Ir electrodissolution: higher R_f, compared with pristine samples, indicate surfaces that present a higher density of Ir sites geometrically accessible to the electrolyte exposed after Ir dissolution at the outermost surface.[44] FE-SEM micrographs show that pristine Ir samples (Fig. 10.14a) present surfaces with increased grain sizes at longer stability experiments, whereas for WS_{3-x} decorated Ir samples (Fig. 10.14b-d) this surface roughening is less severe. Variation in the density and dimensions of the surface cracks are again related to variability within the Si/Cr/Ir wafers employed. Quantitative comparison of R_f values before OER testing (Table 10.2) clearly shows higher values for WS_{3-x} decorated Ir samples (R_f range: 33-71) than for pristine Ir samples ($R_f = 38 \pm 17$). We consequently believe that, during the pulse reverse current electrodeposition step to deposit WS_{3-x}, Ir electrodissolution also occurs besides surface restructuring. Indeed, anodic dissolution due to the irreversible conversion of Ir to IrO_4^{2-} via IrO_x formation is known to occur at $E > 0.9$ V,[1,27] whilst cathodic dissolution occurs at $E \leq 0.1$ V due to IrO_x reduction.[45] These potentials are achieved, or surpassed, during electrodeposition. Interestingly, R_f values of WS_{3-x} decorated Ir samples present significantly lower values after OER activity (57-89 vs 76 ± 7) and OER stability testing (65-94 vs 86 ± 8) than pristine Ir. This seems to indicate that Ir electrodissolution during OER testing is mitigated once Ir samples have undergone WS_{3-x} decoration. Indeed, after OER stability testing, a 126 % relative R_f increase was found for pristine Ir compared with the 15.23 % of the least roughened sample (±900 µA, 250 ms, 5 mins).

Tafel slope analysis of the voltammograms before and after OER short-duty testing (Table 10.2) provides relevant information regarding the electrode kinetics, i.e. the magnitude of the external driving force (overpotential) to increase the OER reaction rate by a factor of 10, but also of the rate-determining reaction step intimately correlated with the electrocatalyst stability.

For the OER, recent studies have shown a correlation between Tafel slope (b) values and dissolution rates.[1] Metals with $b \geq 100$ mV dec^{-1} (Pt, Pd) present slow dissolution rates ($\leq$ 0.001 ng cm^{-2} s^{-1}), whereas metals with Tafel slopes below 50 mV dec^{-1} (Au, Ir, Rh, Ru) present higher dissolution rates (e.g. Au: 2.2 ng cm^{-2} s^{-1}, Ir: 0.022 ng cm^{-2} s^{-1}, Ru: 1.9 ng cm^{-2} s^{-1}). This is due to differences in the OER mechanism. For Pt and Pd, where the rate-determining step is the water de-protonation ($b \approx 120$ mV dec^{-1}),[46] the thin surface oxide layer formed during under OER operating conditions does not participate in the reaction: this is commonly reported as the OER "solution route", as oxygen evolved stems from water electroadsorption and cleaving. On the other hand, in metals such as Ir and Ru, where the rate-limiting step is the de-protonation of adsorbed OH species ($40 \leq b \leq 60$ mV dec^{-1}), the OER proceeds by the "place-exchange" mechanism: adsorbed O species are incorporated in the metal sub-surface sites, generating an oxide layer which is electrochemically restructured during O recombination taking place inside the layer, and ultimately electrodissolved.[47] The thermodynamic instability of these metal oxides under OER conditions was indeed reported.[48] Ir/Ru dissolution consequently assists in the OER process, known as lattice oxygen evolution reaction (LOER): for Ir, this takes place via the formation of IrO_3 and/or IrO_2OH intermediates, or direct dissolution of Ir to Ir^{3+}.[49]

Tafel slope analysis also provides information regarding the nature of the electrode surface, being sensitive to its preparation method and morphology. In particular, metallic Ir electrodes (covered by a thin anhydrous oxide layer) present Tafel slopes of ca. 66 mV dec^{-1},[27] whereas electrochemically grown hydrous iridium oxide on metallic Ir present $b \approx$ 50-40 mV dec^{-1}, with lower slopes found at increasing oxide layer thicknesses.[25] The first indicates a modification in the OER rate-determining step,[50] ascribed to a chemical step where the initially unstable electroadsorbed OH species undergo a rearrangement by a surface reaction. [51]

As-received Ir electrodes present $b \approx 39 \pm 2$ before, and $\approx 45 \pm 2$ mV dec^{-1} after OER testing, respectively. These values are close to 40 mV dec^{-1}, indicating that the OER rate-determining step of the tested electrodes is the adsorbed OH species de-protonation, and that a hydrous iridium oxide overlayer electrochemically grown onto metallic Ir during OER conditioning is the surface species predominantly involved in the OER. With regards to WS_{3-x} decorated samples, Tafel slopes before and after testing range within $b \approx$ 41-48 and $\approx$ 43-47 mV dec^{-1}, respectively. They do not greatly differ from the pristine Ir samples, concluding that the OER mechanism is apparently unaffected by the presence of the WO_3 nuclei. However, their somewhat slightly higher values could indicate either the presence of a thinner/less porous hydrous iridium oxide layer or a mitigated electrochemical restructuring, yielding higher stabilities. The latter is experimentally supported by the lower R_f values for decorated samples after testing.

Having this in mind, the OER mass and specific activity metrics can now be easily explained. Before OER testing, WS_{3-x} decorated samples present mildly higher mass activity and lower specific activity values with respect to the pristine counterparts, due to their higher surface roughness (higher R_f). On the other hand, improved specific activities obtained after 2 h stability testing show that the enhanced OER current densities and mass activities on WS_{3-x} decorated samples do not stem from surface area effects, as the surface roughening on these samples is attenuated (lower R_f and faintly higher Tafel slopes). Thus, alterations in the Ir surface species have to come into play.

Comparison of the deconvoluted high-resolution Ir 4*f* spectra of pristine and WS_{3-x} decorated Ir samples after short-duty OER testing shows clear modifications in the surface species present (Fig. 10.12). In contrast with its pristine counterpart, the WS_{3-x} decorated Ir sample retains its predominantly metallic character, with a minor contribution of two additional W $4f_{7/2}$:$4f_{5/2}$ 4f spin-orbit doublets characteristic of Ir^{4+} (ca. 62.5 and 65.5 eV) and Ir^{3+} (ca. 63 and 66 eV)

as found in IrO_2 or $Ir(OH)_3$, respectively. Quantification of the relative atomic photoemission percentages of the deconvoluted components supports this. The relative abundance of the Ir^0: Ir^{3+}: Ir^{4+} species shifts from an atomic % ratio of 40.0:11.0:48.0 in pristine Ir to 81.5:2.8:15.7 at. % after WS_{3-x} decoration. Thus, the acid-insoluble WO_3 nuclei mitigate the electro-oxidation of Ir towards higher oxidation states prone to electrodissolution, namely Ir^{3+} [49] as found in the electrochemically generated $Ir(OH)_3$ hydrous oxide. This mitigated corrosion consequently supports the lower relative R_f increases and somewhat higher Tafel slopes observed after WS_{3-x} decoration.

10.2.2.2 Long-term OER testing

Next, we evaluated the OER stability of pristine and WS_{3-x} decorated Ir samples in a protocol analogous to that of Section 10.2.2.1, but recording chronopotentiograms for 12 hours to monitor changes in the voltage required to sustain an anodic current density of +10 mA cm^{-2} (see Fig. 10.13b). Although previous reports on in-operando scanning flow cell/inductively coupled plasma mass spectrometry (SFC/ICP-MS) indicated that Ir electrodissolution is higher in the transient stage (shorter timescales, i.e. during IrO_x formation) than in the steady-state (longer timescales, $\gg$ 1000 s),[1] the 6-fold longer OER stability testing duration selected is expected to provide more representative information on the passivating effect of WO_3 for long-term OER applications.

The OER metrics obtained prior to OER stability testing (for values, see Table 10.3) mirror those found for the 2 h-tested Ir samples: geometric current densities (0.46-1.88 vs. 2.58 mA cm^{-2} at 1.55 V) and specific activities (1.49-4.20 $\times$ 10^{-5} vs. 5.24 $\times$ 10^{-5} A cm_{Ir}^{-2} at 1.55 V) are lower for WS_{3-x} decorated than for pristine Ir samples, whilst mass activities are on par or lower (0.165-0.596 vs. 0.56 A mg_{Ir}^{-1} at 1.55 V). After 12 h OER testing, geometric current densities (5.65-7.80 vs. 6.73 mA cm^{-2} at 1.55 V) and mass activities (1.86-2.86 vs. 2.82 A mg_{Ir}^{-1} at 1.55 V) are comparable or lower to those found in pristine Ir electrodes: this would again

initially suggest, disregarding any contribution from electroactive surface area effects, that the OER activity of the WS_{3-x} decorated (WO_3 under OER potentials) Ir electrodes is limited by the passivating effect of the nuclei (for representative OER activity voltammograms, see Fig. 10.13a).

However, improvements in both R_f and specific activities, metrics which enable unambiguous interpretation of the OER stability as they are normalized by the electroactive area, are again prominent (Table 10.4). Namely, R_f relative increases (excluding the ±700 μA, 250 ms, 2.5 mins sample) are within 14.8-44.98 % for WS_{3-x} decorated samples compared with the 91.57 % found for pristine Ir. As for specific activities, all WS_{3-x} decorated samples outperform the pristine Ir counterpart, with the best-performing sample (±700 μA, 1000 ms, 10 mins) presenting a 1.8 fold increase: 1.30×10^{-4} vs 7.12×10^{-5} A cm_{Ir}^{-2} at 1.55 V. Tafel slope analysis of the WS_{3-x} decorated and pristine Ir samples before and after 12 testing follows the same trend found after short-duty testing (Table 10.4): almost invariable, yet slightly higher values before (39-48 vs. 41 mV dec^{-1}) and after (37-47 vs. 44 mV dec^{-1}) OER operation suggest a slower Ir electrodissolution rate for WS_{3-x} decorated samples. Thus, the presence of WO_3 nuclei onto Ir electrodes again results in minimized Ir surface restructuring (mitigated ECSA modifications) and electrodissolution, even under the significantly extended OER operating conditions employed.

The most relevant findings when comparing the results after 12 h and 2h OER stability tests are, strikingly, related to the final OER working potential recorded values (E_{OER,t_f}) and their relative increase versus the starting potential (ΔE_{OER}). Unlike 2 h OER-tested samples, in almost all cases both ΔE_{OER} and E_{OER,t_f} were lower for WS_{3-x} decorated Ir samples than for pristine Ir. (Fig. 10.13b) The improvement, despite of not being numerically large speaking (for the best-performing sample, E_{OER,t_f}= -14 mV, ΔE_{OER} = -43 mV), is foreseen to be amplified, as occurred in our investigations after extending the OER stability testings from 2 to 12 hours,

at longer operating conditions due to the extremely flat E-t profiles observed. Indeed, the samples presenting improvements in these metrics also present higher Tafel slopes, correlated with slower electrodissolution rates as mentioned previously. Thus, the stabilizing effect of WO_3 is not only maintained, but also reinforced, after long-term OER operation conditions, yielding OER metrics which outperform those of pristine Ir surfaces.

Analysis of the Ir surface morphology by FE-SEM micrographs (Fig. 10.14, right column) supports these conclusions. No clear surface modification can be found for WS_{3-x} decorated Ir samples after 12 h OER testing compared with short-duty tested samples, whereas the grain size on pristine Ir surfaces coarsens (quantitative evidence is found in R_f elucidation, Table 10.4). XPS results, unfortunately, are not available by the submission date of this thesis due to technical malfunctions of the XPS instrument which have significantly delayed spectra acquisition.

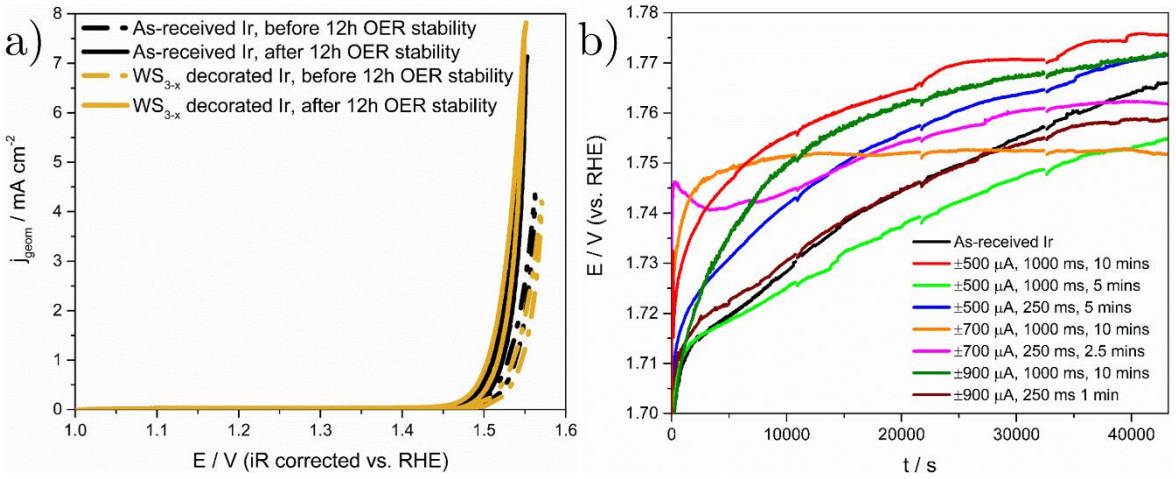

Figure 10.13. Cyclic voltammograms recorded at pristine (black) and WS_{3-x} decorated (±500 µA, 1000 ms, 5 mins; dark yellow) Si/Cr/Ir electrodes a) before (broken line) and after (solid line) undergoing long-term OER stability experiments: j_{geom}= +10 mA cm^{-2} sustained for 12 h. Voltage window: +1.0 to +1.6 V vs. RHE. Scan rate: 10 mV s^{-1}.; b) first OER voltammograms recorded for pristine and WS_{3-x} decorated (±700 µA, 250 ms, 10 mins. Electrolyte: 0.1 M $HClO_4$.

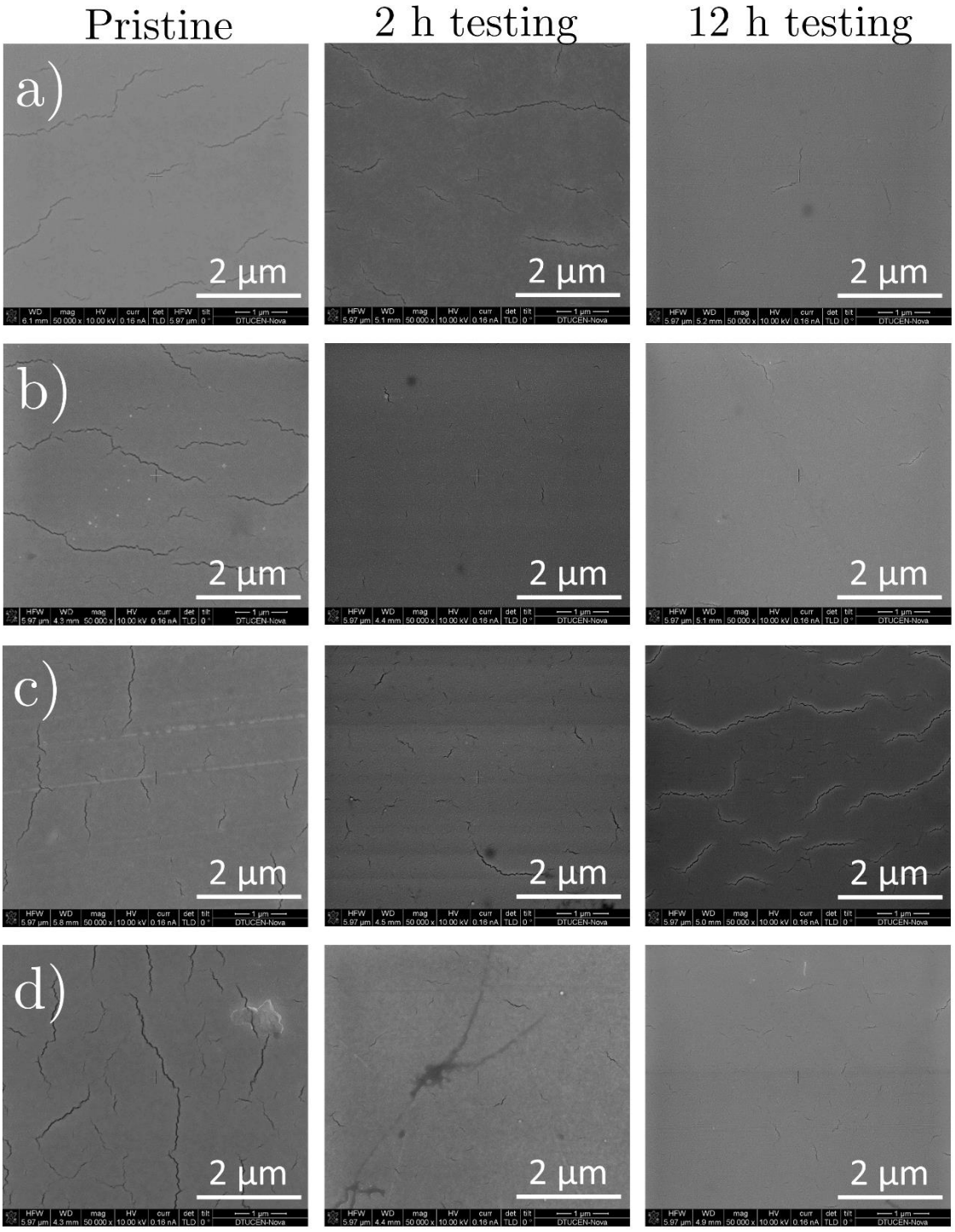

Figure 10.14. FE-SEM micrographs of Si/Cr/Ir electrodes before, after 2 h and after 12 h OER stability testing of a) as-received and WS_{3-x} decorated electrodes by b) ±500 µA, 1000 ms, 5 mins, c) ±700 µA, 1000 ms, 10 mins, and d) ±900 µA, 1000 ms, 10 mins reverse current pulses. Micrographs image magnification: 50000x.

Sample	E_{OER,t_0} / V	E_{OER,t_f} / V	ΔE_{OER}/ V	@ 1.51 V			@ 1.55 V		
				j_{geom} / mA cm^{-2}	Mass activity / A mg_{Ir}^{-1}	Specific activity / A cm_{Ir}^{-2}	j_{geom} / mA cm^{-2}	Mass activity / A mg_{Ir}^{-1}	Specific activity / A cm_{Ir}^{-2}
As-received Ir	1.693 ± 0.003	1.76595 ± 0.00002	0.073	0.36 0.96	0.079 0.40	7.33×10^{-6} 1.02×10^{-5}	2.58 6.73	0.56 2.82	5.24×10^{-5} 7.12×10^{-5}
±500 µA, 1000 ms, 10 mins	*1.726 ± 0.003*	*1.77553 ± 0.00001*	*0.050*	*0.18* *1.41*	*0.042* *0.419*	3.55×10^{-6} 2.10×10^{-5}	- -	- -	- -
±500 µA, 1000 ms, 5 mins	*1.694 ± 0.003*	*1.75484± 0.00005*	*0.061*	*0.28* *1.31*	*0.089* *0.477*	3.94×10^{-6} 1.59×10^{-5}	*1.88* *7.72*	*0.596* *2.81*	2.63×10^{-5} 9.40×10^{-5}
±500 µA, 250 ms, 5 mins	*1.701 ± 0.003*	*1.77158 ± 0.00002*	*0.071*	*0.18* *0.98*	*0.046* *0.342*	3.15×10^{-6} 1.25×10^{-5}	*1.29* *6.46*	*0.328* *2.25*	2.25×10^{-5} 8.24×10^{-5}
±700 µA, 1000 ms, 10 mins	*1.722± 0.003*	*1.75176 ± 0.00003*	*0.030*	*0.058* *0.87*	*0.046* *0.342*	1.87×10^{-6} 1.94×10^{-5}	*0.46* *5.82*	*0.328* *2.25*	1.49×10^{-5} 1.30×10^{-4}
±700 µA, 250 ms, 2.5 mins	*1.741± 0.003*	*1.76180 ± 0.00003*	*0.021*	*0.17* *0.86*	*0.022* *0.283*	5.54×10^{-6} 1.15×10^{-5}	*1.25* *5.65*	*0.165* *1.86*	4.20×10^{-5} 7.59×10^{-5}
±900 µA, 1000 ms, 10 mins	*1.689 ± 0.004*	*1.77166 ± 0.00005*	*0.083*	*0.23* *1.08*	*0.055* *0.340*	4.08×10^{-6} 1.52×10^{-5}	*1.71* *7.80*	*0.419* *2.46*	3.09×10^{-5} 1.10×10^{-4}
±900 µA, 250 ms, 1 min	*1.696 ± 0.003*	*1.75882 ± 0.00006*	*0.063*	*0.26* *1.23*	*0.078* *0.462*	3.80×10^{-6} 1.45×10^{-5}	*1.82* *7.60*	*0.548* *2.86*	2.68×10^{-5} 8.96×10^{-5}

Table 10.3. Compilation of the long-term oxygen evolution activity of WS_{3-x} decorated Ir electrodes after use of ±500-900 µA pulse reverse current electrodeposition at variable pulse timescales and total experiment durations. E_{OER,t_0}, E_{OER,t_f} and ΔE_{OER} correspond to the averaged (± 100 s) initial, final and variation, respectively, of the OER overpotentials recorded to sustain j_{geom}= +10 mA cm^{-2} for 12 h. OER activity metrics (j_{geom}, mass activity, specific activity) are reported, for each sample, before (first row) and after (second row) OER stability measurements.

Sample	R_f (A_{ECSA}/A_{geom})			Relative R_f increase / %		Tafel slope / mV dec^{-1}	
	Before OER	After OER	After 12 h OER stability	After OER	After 12 h OER stability	After OER	After 12 h OER stability
As-received Ir	49.2	75.9	94.5	54.27	91.57	41	44
±500 µA, 1000 ms, 10 mins	51.8	61.1	67.1	17.95	29.54	39	37
±500 µA, 1000 ms, 5 mins	71.6	77.6	82.2	8.38	14.80	48	47
±500 µA, 250 ms, 5 mins	57.4	74.0	78.4	28.92	36.59	45	43
±700 µA, 1000 ms, 10 mins	30.9	35.5	44.8	14.89	44.98	45	44
±700 µA, 250 ms, 2.5 mins	29.8*	69.2	74.5	132.21	150	45	46
±900 µA, 1000 ms, 10 mins	55.3	65.9	71.0	19.17	28.39	41	43
±900 µA, 250 ms, 1 min	67.9	85.0	84.8	25.18	24.89	46	45

Table 10.4. Compilation of the roughness factor (R_f) values (obtained after integration of the hydrogen desorption region, 0.06 V to ca. 0.45 V vs RHE), their relative increase, and Tafel slope values for pristine and WS_{3-x} decorated Ir electrodes before/after OER activity measurements, and after 12 h OER stability measurements. Values labelled with an asterisk (*) indicate that hydrogen desorption integration is affected by ohmic drop, unable to be fully corrected by post-experiment *iR* compensation.

10.3 Conclusions

In this chapter we have evaluated the viability of an electrochemical decoration process on Ir electrodes based on the decomposition of an $[WS_4]^{2-}$ aqueous precursor to yield amorphous tungsten sulfide (WS_{3-x}) nanoparticles. A preliminary evaluation of the electrochemical features of the $[WS_4]^{2-}$ aqueous bath revealed their analogy with previously reported substrates, indicative of a substrate-independent electrodeposition mechanism. The suppressed inherent Ir electrochemistry as well as the hampered HER and OER catalysis after cycling from oxidative to reductive potentials seems to suggest that both the anodic $[WS_4]^{2-}$ electroadsorption and S co-deposition block the Ir surface sites responsible for proton and hydroxyl adsorption. Cycling within the voltage window comprising the $[WS_4]^{2-}$ anodic and cathodic features yields pseudo-stationary electrochemical responses, contrasting with selective cycling within anodic and cathodic voltage windows, which results in increasingly mitigated or absent $[WS_4]^{2-}$ deposition features, respectively. This conforms to the maximized WS_{3-x} deposition yields previously reported by oxidative-reductive cycling.

The pulse reverse current electrodeposition strategy, selected to satisfy the maximized electrodeposition by co-existing anodic and cathodic processes, has been found to be heavily influenced by both current pulse magnitudes and duration. Low magnitude pulses (e.g. ±500 µA) applied at long timescales (1000 ms) provide the larger WS_{3-x} nuclei and higher coverages, and vice versa. We hypothesize that at high magnitudes and shorter timescales, $[WS_4]^{2-}$ depletion, competing electrochemical reactions (HER/OER) and sluggish reaction kinetics limit the electrochemically assisted $[WS_4]^{2-}$ decomposition. Longer electrodeposition durations, predictably, yield larger nuclei sizes. Short and long term OER testing experiments show that WS_{3-x} decorated Ir samples present improved stability metrics, namely lower R_f and ΔE_{OER}, as well as higher specific activities, than their pristine counterparts, this magnified at longer

testing conditions. We hypothesize that the electro-oxidation of WS_{3-x} to the acid-insoluble WO_3 minimizes the electrodissolution of metallic Ir via Ir^{3+} leaching, supported by preliminary XPS measurements and ex-situ imaging. Thus, decoration with corrosion-resistant TMDs is a novel approach towards improving the OER stability of Ir in harsh acidic environments.

References

[1] S. Cherevko, A.R. Zeradjanin, A.A. Topalov, N. Kulyk, I. Katsounaros, K.J.J. Mayrhofer, Dissolution of noble metals during oxygen evolution in acidic media, ChemCatChem. 6 (2014) 2219–2223. doi:10.1002/cctc.201402194.

[2] J. Kim, P.C. Shih, K.C. Tsao, Y.T. Pan, X. Yin, C.J. Sun, H. Yang, High-Performance Pyrochlore-Type Yttrium Ruthenate Electrocatalyst for Oxygen Evolution Reaction in Acidic Media, J. Am. Chem. Soc. 139 (2017) 12076–12083. doi:10.1021/jacs.7b06808.

[3] M. Blasco-Ahicart, J. Soriano-Lopez, J.J. Carbo, J.M. Poblet, J.R. Galan-Mascaros, Polyoxometalate electrocatalysts based on earthabundant metals for efficient water oxidation in acidic media, Nat. Chem. 10 (2018) 24–30. doi:10.1038/NCHEM.2874.

[4] L.C. Seitz, C.F. Dickens, K. Nishio, Y. Hikita, J. Montoya, A. Doyle, C. Kirk, A. Vojvodic, H.Y. Hwang, J.K. Norskov, T.F. Jaramillo, A highly active and stable IrOx/SrIrO3 catalyst for the oxygen evolution reaction, Science (80-.). 353 (2016) 1011–1014.

[5] G. Li, K. Li, L. Yang, J. Chang, R. Ma, Z. Wu, J. Ge, C. Liu, W. Xing, Boosted Performance of Ir Species by Employing TiN as the Support toward Oxygen Evolution Reaction, ACS Appl. Mater. Interfaces. (2018). doi:10.1021/acsami.8b14172.

[6] S. Choe, B.S. Lee, M.K. Cho, H.J. Kim, D. Henkensmeier, S.J. Yoo, J.Y. Kim, S.Y. Lee, H.S. Park, J.H. Jang, Electrodeposited IrO2/Ti electrodes as durable and cost-effective anodes in high-temperature polymer-membrane-electrolyte water electrolyzers, Appl. Catal. B Environ. 226 (2018) 289–294. doi:10.1016/j.apcatb.2017.12.037.

[7] T. Reier, Z. Pawolek, S. Cherevko, M. Bruns, T. Jones, D. Teschner, S. Selve, A. Bergmann, H.N. Nong, R. Schlögl, K.J.J. Mayrhofer, P. Strasser, Molecular insight in structure and activity of highly efficient, low-Ir Ir-Ni oxide catalysts for electrochemical water splitting (OER), J. Am. Chem. Soc. 137 (2015) 13031–13040. doi:10.1021/jacs.5b07788.

[8] S. Kumari, B.P. Ajayi, B. Kumar, J.B. Jasinski, M.K. Sunkara, J.M. Spurgeon, A low-noble-metal $W_{1-x}Ir_xO_{3-\delta}$ water oxidation electrocatalyst for acidic media via rapid plasma synthesis, Energy Environ. Sci. 10 (2017) 2432–2440. doi:10.1039/C7EE02626A.

[9] S.M. Tan, M. Pumera, Bottom-up Electrosynthesis of Highly Active Tungsten Sulfide (WS3-x) Films for Hydrogen Evolution, ACS Appl. Mater. Interfaces. 8 (2016) 3948–3957. doi:10.1021/acsami.5b11109.

[10] A.Y.S. Eng, A. Ambrosi, Z. Sofer, P. Simek, M. Pumera, Electrochemistry of Transition Metal Dichalcogenides : Strong Dependence on the Metal-to-Chalcogen Composition and Exfoliation Method, ACS Nano. 8 (2014) 12185–12198.

[11] S.S. Thind, K. Rozic, F. Amano, A. Chen, Fabrication and photoelectrochemical study of WO3-based bifunctional electrodes for environmental applications, Appl. Catal. B Environ. 176–177 (2015) 464–471. doi:10.1016/j.apcatb.2015.04.033.

[12] A.K. Nayak, M. Verma, Y. Sohn, P.A. Deshpande, D. Pradhan, Highly active tungsten oxide nanoplate electrocatalysts for the hydrogen evolution reaction in acidic and near neutral electrolytes, ACS Omega. 2 (2017) 7039–7047. doi:10.1021/acsomega.7b01151.

[13] S. Motoo, N. Furuya, Hydrogen and oxygen adsorption on Ir (111), (100) and (110) planes, J. Electroanal. Chem. 167 (1984) 309–315. doi:10.1016/0368-1874(84)87078-1.

[14] A. Ahmadi, R.W. Evans, G. Attard, Anion-surface interactions. Part I. Perchlorate decomposition and sulphate adsorption hysteresis studied by voltammetry, J. Electroanal. Chem.

350 (1993) 279–295. doi:10.1016/0022-0728(93)80211-Y.

[15] M.S. Cruz, M.J.G. Tejera, M.C. Villamanan, Reduction Electroquimique de l'Ion ClO4- sur l'Electrode d'Iridium, Electrochim. Acta. 30 (1985) 1563–1569.

[16] G.G. Láng, G. Horányi, Some interesting aspects of the catalytic and electrocatalytic reduction of perchlorate ions, J. Electroanal. Chem. 552 (2003) 197–211. doi:10.1016/S0022-0728(02)01302-5.

[17] T. Pajkossy, L.A. Kibler, D.M. Kolb, Voltammetry and impedance measurements of Ir(1 0 0) electrodes in aqueous solutions, J. Electroanal. Chem. 600 (2007) 113–118. doi:10.1016/j.jelechem.2006.04.016.

[18] A. Ganassin, P. Sebastian, V. Climent, W. Schuhmann, A.S. Bandarenka, J. Feliu, On the pH Dependence of the Potential of Maximum Entropy of Ir(111) Electrodes, Sci. Rep. 7 (2017) 1–14. doi:10.1038/s41598-017-01295-1.

[19] P.G. Pickup, V.I. Birss, A model for anodic hydrous oxide growth at iridium, J. Electroanal. Chem. 220 (1987) 83–100. doi:10.1016/0022-0728(87)88006-3.

[20] J.O. Zerbino, N.R. de Tacconi, A.J. Arvia, The Activation and Deactivation of Iridium Electrodes in Acid Electrolytes, J. Electrochem. Soc. 125 (1978) 1266–1276. doi:10.1149/1.2131661.

[21] J. Juodkazyte, B. Šebeka, I. Valsiunas, K. Juodkazis, Iridium anodic oxidation to Ir(III) and Ir(IV) hydrous oxides, Electroanalysis. 17 (2005) 947–952. doi:10.1002/elan.200403200.

[22] R. Kötz, C. Barbero, O. Haas, Probe beam deflection investigation of the charge storage reaction in anodic iridium and tungsten oxide films, J. Electroanal. Chem. 296 (1990) 37–49. doi:10.1016/0022-0728(90)87231-8.

[23] M.A. Petit, V. Plichon, Anodic electrodeposition of iridium oxide films, J. Electroanal. Chem. 444 (1998) 247–252. doi:10.1016/S0022-0728(97)00570-6.

[24] T.E. Fonseca, M.I. Lopes, M.T.C. Portela, A comparative voltammetric study of the Ir lH , SO , and Ir (HC10 , aqueous interfaces, J. Electroanal. Chem. 415 (1996) 89–96.

[25] S. Cherevko, S. Geiger, O. Kasian, A. Mingers, K.J.J. Mayrhofer, Oxygen evolution activity and stability of iridium in acidic media. Part 2. - Electrochemically grown hydrous iridium oxide, J. Electroanal. Chem. 774 (2016) 102–110. doi:10.1016/j.jelechem.2016.05.015.

[26] S. Cherevko, S. Geiger, O. Kasian, N. Kulyk, J.-P. Grote, A. Savan, B.R. Shrestha, S. Merzlikin, B. Breitbach, A. Ludwig, K.J.J. Mayrhofer, Oxygen and hydrogen evolution reactions on Ru, RuO2, Ir, and IrO2 thin film electrodes in acidic and alkaline electrolytes: A comparative study on activity and stability, Catal. Today. 262 (2016) 170–180. doi:10.1016/j.cattod.2015.08.014.

[27] S. Cherevko, S. Geiger, O. Kasian, A. Mingers, K.J.J. Mayrhofer, Oxygen evolution activity and stability of iridium in acidic media. Part 1.- Metallic iridium, J. Electroanal. Chem. 773 (2016) 69–78. doi:10.1016/j.jelechem.2016.04.033.

[28] B.E. Conway, J. Mozota, Surface and Bulk Processes at Oxidized Iridium Electrodes - II. Conductivity-Switched Behaviour of Thick Oxide Films, Electrochim. Acta. 28 (1983) 9–16.

[29] L.D. Burke, E.J.M.O. Sullivan, Oxygen Gas Evolution on Hydrous Oxides - An Example of Three-Dimensional Electrocatalysis?, J. Electroanal. Chem. 117 (1981) 155–160.

[30] V.I. Birss, C. Bock, H. Elzanowska, Hydrous Ir oxide films: the mechanism of the anodic prepeak reaction, Can. J. Chem. 75 (1997) 1687–1693.

[31] L.D. Burke, D. P. Whelan, A Voltammetric Investigation of the Charge Storage Reactions of Hydrous Iridium Oxide Layers, J. Electroanal. Chem. 162 (1984) 121–141.

[32] V. Pfeifer, T.E. Jones, J.J. Velasco Vélez, R. Arrigo, S. Piccinin, M. Hävecker, A. Knop-Gericke,

R. Schlögl, In situ observation of reactive oxygen species forming on oxygen-evolving iridium surfaces, Chem. Sci. 8 (2017) 2143–2149. doi:10.1039/c6sc04622c.

[33] V.A. Saveleva, L. Wang, D. Teschner, T. Jones, A.S. Gago, K.A. Friedrich, S. Zafeiratos, R. Schlögl, E.R. Savinova, Operando Evidence for a Universal Oxygen Evolution Mechanism on Thermal and Electrochemical Iridium Oxides, J. Phys. Chem. Lett. 9 (2018) 3154–3160. doi:10.1021/acs.jpclett.8b00810.

[34] D. Merki, S. Fierro, H. Vrubel, X. Hu, Amorphous molybdenum sulfide films as catalysts for electrochemical hydrogen production in water, Chem. Sci. 2 (2011) 1262–1267. doi:10.1039/C1SC00117E.

[35] D. Merki, H. Vrubel, L. Rovelli, S. Fierro, X. Hu, Fe, Co, and Ni ions promote the catalytic activity of amorphous molybdenum sulfide films for hydrogen evolution, Chem. Sci. 3 (2012) 2515. doi:10.1039/c2sc20539d.

[36] H. Vrubel, X. Hu, Growth and activation of an amorphous molybdenum sulfide hydrogen evolving catalyst, ACS Catal. 3 (2013) 2002–2011. doi:10.1021/cs400441u.

[37] B. Łosiewicz, R. Jurczakowski, A. Lasia, Kinetics of hydrogen underpotential deposition at iridium in sulfuric and perchloric acids, Electrochim. Acta. 225 (2017) 160–167. doi:10.1016/j.electacta.2016.12.116.

[38] M.S. Chandrasekar, M. Pushpavanam, Pulse and pulse reverse plating-Conceptual, advantages and applications, Electrochim. Acta. 53 (2008) 3313–3322. doi:10.1016/j.electacta.2007.11.054.

[39] A.J. Bard, L.R. Faulkner, Electrochemical Methods: Fundamentals and Applications, 2nd ed., John Wiley and Sons Ltd., New York, 2001. doi:10.1016/B978-0-12-381373-2.00056-9.

[40] A. Katrib, F. Hemming, P. Wehrer, L. Hilaire, G. Maire, The multi-surface structure and catalytic properties of partially reduced WO3, WO2 and WC + O2 or W + O2 as characterized by XPS, J. Electron Spectros. Relat. Phenomena. 76 (1995) 195–200. doi:10.1016/0368-2048(95)02451-4.

[41] A.P. Shpak, A.M. Korduban, L.M. Kulikov, T. V. Kryshchuk, N.B. Konig, V.O. Kandyba, XPS studies of the surface of nanocrystalline tungsten disulfide, J. Electron Spectros. Relat. Phenomena. 181 (2010) 234–238. doi:10.1016/j.elspec.2010.05.030.

[42] M. Pourbaix, Altas of Electrochemical Equilibrium in Aqueous Solutions, Pergamon Press, New York, 1966.

[43] C.C.L. McCrory, S. Jung, I.M. Ferrer, S. Chatman, J.C. Peters, T.F. Jaramillo, Benchmarking HER and OER Electrocatalysts for Solar Water Splitting Devices., J. Am. Chem. Soc. (2015). doi:10.1021/ja510442p.

[44] C. Spöri, J.T.H. Kwan, A. Bonakdarpour, D.P. Wilkinson, P. Strasser, The Stability Challenges of Oxygen Evolving Catalysts: Towards a Common Fundamental Understanding and Mitigation of Catalyst Degradation, Angew. Chemie - Int. Ed. 56 (2017) 5994–6021. doi:10.1002/anie.201608601.

[45] P. Jovanovič, N. Hodnik, F. Ruiz-Zepeda, I. Arčon, B. Jozinović, M. Zorko, M. Bele, M. Šala, V.S. Šelih, S. Hočevar, M. Gaberšček, Electrochemical Dissolution of Iridium and Iridium Oxide Particles in Acidic Media: Transmission Electron Microscopy, Electrochemical Flow Cell Coupled to Inductively Coupled Plasma Mass Spectrometry, and X-ray Absorption Spectroscopy Study, J. Am. Chem. Soc. 139 (2017) 12837–12846. doi:10.1021/jacs.7b08071.

[46] A. Damjanovic, V.I. Birss, D.S. Boudreaux, Electron Transfer Through Thin Anodic Oxide Films during the Oxygen Evolution Reactions at Pt Electrodes: I. Acid Solutions, J. Electrochem. Soc. 138 (1991) 2549–2555.

[47] R. Kötz, H.J. Lewerenz, P. Brüesch, S. Stucki, Oxygen evolution on Ru and Ir electrodes. XPS-

studies, J. Electroanal. Chem. 150 (1983) 209–216. doi:10.1016/S0022-0728(83)80203-4.

[48] T. Binninger, R. Mohamed, K. Waltar, E. Fabbri, P. Levecque, R. Kötz, T.J. Schmidt, Thermodynamic explanation of the universal correlation between oxygen evolution activity and corrosion of oxide catalysts, Sci. Rep. 5 (2015) 1–7. doi:10.1038/srep12167.

[49] O. Kasian, J.P. Grote, S. Geiger, S. Cherevko, K.J.J. Mayrhofer, The Common Intermediates of Oxygen Evolution and Dissolution Reactions during Water Electrolysis on Iridium, Angew. Chemie - Int. Ed. 57 (2018) 2488–2491. doi:10.1002/anie.201709652.

[50] S. Gottesfeld, S. Srinivasan, Electrochemical and Optical Studies of Thick Oxide Layers on Iridium and their Electrocatalytic Activities for the Oxygen Evolution Reaction, J. Electroanal. Chem. 86 (1978) 89–104.

[51] L.A. De Faria, J.F.C. Boodts, S. Trasatti, Electrocatalytic properties of ternary oxide mixtures of composition Ru0.3Ti(0.7-x)CexO2: Oxygen evolution from acidic solution, J. Appl. Electrochem. 26 (1996) 1195–1199. doi:10.1007/BF00243745.

Chapter 11

Conclusions and Outlook

11.1 Summary

This thesis has evaluated several strategies to maximize the HER electrocatalytic activity of TMDs, as well as their applicability as corrosion-resistant materials to improve the electrochemical stability of state-of-the-art Ir materials under OER operation. Tables 11.1 and 11.2 compile, for the ease of the reader, the key findings stemmed from the undertaken strategies, including a critical analysis of their advantages and limitations.

Chapters 5 and 6 have shown the successful fabrication of Ni-MoS_2 hybrid nanoclusters and sulfur-enriched MoS_2 size-selected nanoclusters by a magnetron sputtering and gas condensation technique. Optimization of the deposition parameters (i.e. sputtering power of the dual Ni and MoS_2 targets) enabled the production of nanoclusters containing both Ni and MoS_2 rather than their segregated components with an equivalent mass of $(MoS_2)_{1000}$. HAADF-STEM and EDX measurements showed that both $(MoS_2)_{300}$ and $(Ni\text{-}MoS_2)_{1000}$ presented an incomplete, 3-4 multilayered amorphous structure (peak size distributions of 2.6 and 5.0 nm, respectively) where the Ni and MoS_2 ratios within the hybrid nanoclusters were dependent on the nanocluster size. XPS measurements showed that both $(MoS_2)_{300}$ (1:0.9) and $(Ni\text{-}MoS_2)_{1000}$ (1:1.8) were sulfur-deficient, revealing a partial oxidation of MoS_2 to MoO_3 after atmosphere exposure. An HER electrocatalysis enhancement was found for $(Ni\text{-}MoS_2)_{1000}$ with respect to

$(MoS_2)_{300}$ nanoclusters, stemming from the synergistic effect between Ni and MoS_2 to activate the initially inert S-edge sites to the HER leaving the HER mechanism unaltered (Tafel slope ≈ 120 mV dec^{-1}). This enhancement was fully maximized after 14 h atmosphere exposure, yielding a 100 mV lower HER onset potential and a 3-fold increase in the exchange current density, and ascribed to both the partial electrochemical exfoliation of MoS_2 and the conversion of Ni to the HER-active NiO. Experimental evidence of Mo- and S-edge doping by Ni atoms was additionally obtained by anodic stripping voltammetry experiments.

In order to mitigate the sulfur deficiency found for as-deposited MoS_2 nanoclusters, a post-deposition treatment comprising sulfur evaporation and annealing was explored. It was found that $(MoS_2)_{1000}$ size-selected nanoclusters undergoing this treatment not only presented an extended crystalline order, but also a S-rich nature as confirmed by XPS measurements: the Mo:S ratio shifted from 1:1.9 to 1:4.9. Improved crystallinity and maximized S^{2-} surface content (with minimal size distribution modification), accompanied by the almost complete reduction of oxygen-containing Mo species to Mo^{4+} are responsible for the HER enhancements observed: 200 mV lower onset potential, 2-fold improved TOF values and more than 30-fold increased exchange current densities. These metrics outperform the results obtained by $(Ni\text{-}MoS_2)_{1000}$ hybrid nanoclusters, postulated to be due to the crystalline nature that significantly improves the charge transfer resistance and stability under HER operation.

Chapters 7 and 8 have presented the fabrication of TMD nanoarray structures by sequential nanosphere lithography and plasma etching treatments. Highly-compact, hexagonal close-packed nanosphere monolayers were obtained on MoS_2 and WS_2 crystals, with nanoarray morphologies dependent on the SF_6/C_4F_8 plasma etching duration: ranging from nanocylinders to truncated nanocones for MoS_2, and nanocones of varying aspect ratios for WS_2. Contrasting with previous results reported after MoS_2 plasma etching, XPS analysis of plasma-etched WS_2 samples suggests a minimal oxygen incorporation, yet exposing the 1T phase presumably found

at the nanocone array surfaces. The HER electrocatalytic enhancement (≈200 mV for MoS_2 and ≈100 mV for WS_2) and pseudo steady-state voltammetric profile found after TMD plasma etching were rationalized using the diffusion domain theory previously employed for microelectrode arrays. Transient chronoamperometry and Randles-Ševčík experiments indicated that, for MoS_2, the improved HER electrocatalysis was due to edge site exposure alone, whereas for WS_2 certain aspect ratios presented an additional mass transport contribution. MoS_2 closely-spaced nanoarrays yielded a full overlapping of the individual nanoarrays diffusion profile at the scan rates studied, behaving macroscopically as planar electrodes. In contrast, WS_2 larger nanocone interspacing allowed an additional HER contribution from radial diffusion (macroscopically behaving as the microelectrode array Case 1), where higher nanopillar aspect ratios presented improved geometrically-normalized HER currents due to higher edge site exposure. Evaluation of the electron transfer properties revealed improved electron transfer kinetics for plasma-etched WS_2 nanoarrays compared with their MoS_2 counterparts, explained by the mitigated oxygen incorporation and higher aspect ratios (i.e. maximized edge site exposure) found for WS_2 nanoarrays. However, electrochemical testing after 5-month storage reveals diminished HER performances due to electrochemical restructuring and loss of active sites. An attempt to reinstate the initial HER electrocatalysis of atmospherically-aged plasma-etched WS_2 nanoarrays was conducted by use of an electrochemical sulfidation method previously employed for plasma-etched MoS_2 nanostructures with success. Strikingly, the solution phase sulfidation method yielded worse HER performances but improved electron transfer properties. These results were rationalized by analysing the W:S surface ratio and WO_2 contents by XPS and electrochemical measurements over a 21-day span: WS_2 (electro-)oxidation to WO_2 is detrimental for the HER but also reveals a more electron-conducting species, whereas improved HER performances could be correlated to higher chalcogen-to-metal ratios and 1T phase contents. The unsuccessful incorporation of S^{2-} to WS_2 was ascribed to the formation of the solution-insoluble WO_x during

the sulfidation treatment, contrasting with the acid-soluble MoO_4^{2-} species formed for MoX_2 TMDs.

Chapter 9 has described a thorough evaluation of the inherent electrochemistry of AE-MoS_x thin films, and its implications in both activity and stability across the 0-10 pH range. Analysis of the HER pre-catalytic features preliminary ascribed $E_{peak,1}$, $E_{peak,2}$ and $E_{peak,3}$ to the electrochemical cleaving of $S_2^{2-}{}_{bridging/terminal}$ ligands, reduction of $Mo^{5+}O_xS_y$ to Mo^{4+} species and subsequent reduction of $Mo^{4+}O_xS_y$ to MoO_2, respectively. A pH-dependent HER mechanism of AE-MoS_x was also observed: in the $0 \leq pH \leq 2$ range both Tafel slopes ($b \approx 65 \pm 10$ mV dec^{-1}) and LSVs are practically invariable, related to the HER operating by the H_3O^+ electroreduction mechanism. Conversely, higher pH values yielded increasingly higher Tafel slopes ($b \approx 120$ mV dec^{-1} at pH 5 but >120 mV dec^{-1} at neutral-to-alkaline pHs) and negatively shifted HER LSVs, ascribed to increasingly mass transport limited water reduction mechanism and to the presence of Mo_xO_y surface species with worsened HER kinetics. A preconditioning-dependent modification in the AE-MoS_x electro-oxidation mechanism was found: pristine films presented 1 H^+: 2e^- PCET mechanism equivalent to that observed for crystalline MoS_2, whilst the HER preconditioned AE-MoS_x films presented in neutral-to-alkaline environments a sequential 1 H^+: 1e^- PCET followed by a 2 H^+: 1e^- PCET electro-oxidation mechanism ascribed to the partial reinstatement of previously-cleaved $S_2^{2-}{}_{bridging}$ ligands and $S_2^{2-}{}_{terminal}$ ligands dissolution, and oxidation of MoO_2 to MoO_4^{2-}, respectively. In acidic environments, the mechanism is yet to be fully understood, but yields a Mo^{4+} to Mo^{6+} conversion and overall $S_2^{2-}{}_{terminal}/S^{2-}{}_{unsat}$ electro-dissolution. Electrochemical preconditioning within different voltage windows revealed that the pre-catalytic $E_{peak,1}$ split into peaks $E_{peak,III}$ and $E_{peak,IV}$ upon continuous oxidative-reductive cycling: this provided for the first time, supported by XPS and Raman measurements, electrochemical evidence of the S-S bond cleaving from $S_2^{2-}{}_{terminal}$ (irreversible, $E_{peak,III}$) and $S_2^{2-}{}_{bridging}$ (partially reversible, $E_{peak,IV}$) moieties, respectively. In addition, preconditioning

dramatically modified the HER electrocatalysis in AE-MoS_x films, most notably after reductive cycling ($\eta_{HER}@\,|2.5\,mA\,cm^{-2}|$ shifting from -350 to +250 mV), correlated to experimental surface descriptors such as Mo^{4+} content (electro-oxidative), "high binding energy" $S_2^{2-}{}_{bridging}/S^{2-}{}_{apical}$ relative abundance (reductive) and S^{2-}/S_2^{2-} : Mo^{4+} ratio (oxidative-reductive). Long-term HER chronoamperometric and chronopotentiometric experiments revealed improved AE-MoS_x stabilities in the $3 \leq pH \leq 6$ range. High $Mo^{5+}O_xS_y$ surface contents found by ex-situ XPS in the same pH range suggest a pH-dependent shift of the HER active site species: in acidic environments ($0 \leq pH \leq 2$), the proton-accepting electrochemically-cleaved $S_2^{2-}{}_{bridging}$ moieties are the active sites responsible to catalyze the H_3O^+ electroreduction, but in mildly acidic electrolytes the now-dominating water reduction mechanism suggests the HER to operate via Mo=O moieties (as found in $Mo^{5+}O_xS_y$) through O-H bond cleaving and sequential electron transfer.

Chapter 10 has investigated the potential of WS_{3-x} nanoparticle decoration by electrochemical decomposition from an $[WS_4]^{2-}$ aqueous electrolyte as a strategy to mitigate Ir corrosion under OER operating conditions. The electrochemical features, previously ascribed to $[WS_4]^{2-}$ anodic electroadsorption and WS_3 to WS_2 reductive conversion are identified, suggesting a substrate-insensitive electrodeposition mechanism which suppresses the inherent electrochemical features of Ir. Selective cycling within electrochemical windows solely presenting the anodic or cathodic features indicate a gradual suppression or absence, respectively, of WS_{3-x} electrodeposition upon continuous cycling. A pulse reverse current electrodeposition method, selected to satisfy the need for an alternating oxidative-reductive step, is mostly affected by the magnitude and duration of the pulses: pulses applied at long timescales (1000 ms) and magnitudes similar to that of the $[WS_4]^{2-}$ anodic decomposition onset (±500 µA, ca. ±2 mA cm^{-2}) provide the largest and highest surface coverage of WS_{3-x} nuclei. These conditions prevent low deposition yields, as found in short-lived and high-magnitude pulses, proposed to stem from worsened faradaic

yields (competing reactions such as HER/OER) and sluggish deposition kinetics. OER stability testing after 2 h and 12 h chronopotentiometric testing reveals that WS_{3-x} decorated Ir samples present improved stability metrics (lower R_f and ΔE_{OER}, almost 2-fold improved specific activities) with respect to unmodified Ir samples, magnified at longer testing conditions, without altering the OER mechanism (Tafel slope $b \approx 40$ mV dec^{-1}). Joint analysis of ex-situ FE-SEM micrographs and preliminary XPS data indicate a lower surface roughening, and a conversion of WS_{3-x} to the acid-insoluble WO_3, which mitigates the electro-oxidation of metallic Ir at the outermost surface to the highly-active, yet dissolution-prone Ir^{3+} species such as $Ir(OH)_3$ grown under OER operating conditions.

TMD nanostructuring strategy	Key findings	Benefits	Limitations
Ni-MoS_2 hybrid nanoclusters	- Incorporation of transition metals onto TMDs is achieved in one step - 3-fold increased exchange current density, 100 mV shifted HER onset potential after Ni incorporation	- Degree of Ni incorporation tuneable by magnetron target power - TMs incorporation in absence of surface-blocking capping ligands - Possibility of incorporating exotic TMs unachievable by solvent-based methods	- Non-selective incorporation yields nanoclusters with variable composition - Low loadings (low deposition rate) - Amorphous, S-deficient nature: highly active but unstable at long-term use
Size-selected sulfur-enriched MoS_x nanoclusters	- Over-stoichiometric MoSx nanoclusters obtained after sequential sulfur evaporation and annealing in UHV - More than 30-fold increased exchange current density, 200 mV shifted HER onset potential	- High mass activities: 110.5 mA mg^{-1}, 400 mV at 83.78 ng cm^{-2} loadings - S-enrichment improves MoS_x nanoclusters crystallinity and electrochemical stability - Narrow size distributions due to use of ToF mass filter	- Long deposition times (hours) required for high MoSx loadings - Sulfidation under UHV conditions is necessary: technically challenging
MoS_2/WS_2 nanocone arrays	- Extended, edge-abundant nanocone arrays formed from TMD crystals by plasma etching - Improved HER peak-current density directly correlated with higher nanocone aspect ratios	- At $>$ 40 nm nanocone interspacings: additional HER currents due to morphology-induced hemispherical diffusion - Nanoarray morphology ideal for photoelectrochemical experiments: enhanced light harvesting	- Nanocone morphology irreversibly altered during HER - O_2 plasma yields MoO_x formation in MoS_2: lower stability under HER operation - Range of nanocone aspect ratios limited by diameter of deposited nanospheres

Table 11.1. Compilation of TMD nanostructuring strategies undertaken in this thesis (Chapters 5 to 8), highlighting key findings, benefits and limitations versus the state-of-the-art.

TMD nanostructuring strategy	Key findings	Benefits	Limitations
Anodically electrodeposited MoS_x thin films	- First-time electrochemical evidence of pH-dependent electro-oxidation mechanisms and S-S bond cleaving from $S_2^{2-}{}_{terminal}$ (irreversible) and $S_2^{2-}{}_{bridging}$ moieties under pre-catalytic potentials - pH-dependent HER stability : maximized in the $3 \leq pH \leq 5$ range	- HER activity tuneable by electrochemical conditioning - Loading, stoichiometry and morphology can be tuned by electrodeposition conditions - Substrate-insensitive deposition mechanism allows decoration of any conducting substrate	- Unambiguous understanding of the HER operating mechanism is still pending
WS_{3-x} electrochemically-decorated Ir electrodes	- Novel strategy to decorate Ir electrodes with corrosion-resistant WS_{3-x} nuclei - Improved OER stability metrics: almost 2-fold improved specific activity	- Inexpensive method to mitigate Ir corrosion under OER potentials	- Sluggish WS_{3-x} deposition kinetics yield low faradaic yields and surface decoration.

Table 11.2. Compilation of TMD nanostructuring strategies undertaken in this thesis (Chapters 9 and 10), highlighting key findings, benefits and limitations versus the state-of-the-art.

11.2 Outlook and future work

The conclusions and core findings for the work carried out during this thesis can be critically assessed with respect to the state-of-the art, to subsequently suggest a potential set of experiments to be undertaken in future investigations.

The main advantage of the TMD nanocluster fabrication by magnetron sputtering and gas condensation technique versus the state-of-the art TMD physical preparation methods is the possibility of preparing any TMD nanoclusters under mass selection and accurate loading control just by use of different TMD sputtering targets. This brings the possibility of incorporating any elements by use of a second target (Ni, Chapter 5) or post-deposition treatments (S evaporation, Chapter 6), evaluated in this work, which can open very powerful research lines to bring excellent understanding in size-electrocatalytic activity scaling relations. Indeed, we envisage that preparation of sulfur-enriched, transition metal-doped (Fe, Co, Ni, Pd, Pt) MoS_2 hybrid nanoclusters by a dual target and sulfur evaporation/annealing strategy would clearly outperform the HER activities of the nanoclusters evaluated in Chapters 5 and 6, obtaining a synergy between S-edge site activation and increased presence of the proton-accepting S sites.

The small nanocluster production rate (μg/hour) due to mass-selected deposition, the stochastic cluster condensation and the highly-amorphous nature of the as-deposited MoS_2 nanoclusters, on the other hand, limit the current implementation of size-selected MoS_2 nanoclusters: required loadings of mg cm^{-2} in real electrolyser devices would take hours to be achieved, yielding non-uniform distributions of a highly-active yet unstable catalyst layer. Very recent research efforts for nanoscale production scale-up at the NPRL have yielded the so-called Matrix Assembly Cluster Source (MACS), which enables cluster flux rates of mg/hour: MoS_2

nanocluster production with this method followed by post-deposition annealing would enable industrial application of the deposition technique. Further attempts to improve the electrochemical stability are also essential, and methods which could promote more crystalline nanocluster structures such as the use of strongly interacting supports and higher nanocluster landing energies (i.e. higher anchoring) should be explored.

As for Ni-MoS_2 hybrid nanoclusters, unambiguous understanding of the interaction between Ni and MoS_2 in is still pending, and consequently future characterisation studies should be carried out with techniques such as X-ray absorption spectroscopy (XAS) or EELS, which will provide information of the chemical environment of the incorporated Ni.

We believe that future work in TMD nanocluster production, given the edge-limited HER activity of most TMDs, should be focused on the fabrication of TMD nanoclusters which already present basal planes active to the HER, such as VS_2. TaS_2 or NbS_2: the remarkable activities shown in recent state-of-the-art reports would be fully exploited by the accurate size selection and tuneable loadings. Based on recent reports in the literature, electrochemical exfoliation and/or incorporation of alkali cations would also provide improved charge transfer properties in the MoS_2 nanoclusters.

Plasma-etched MoS_2/WS_2 crystals fabricated in this work yield extended, edge-abundant TMD unique nanoarrayed structures. Their main limitation is, however, their technically challenging preparation method and its operating parameters. The use of O_2 plasma has been shown to be detrimental in group VI TMDs for the HER as acid-soluble MO_x species are formed, which compromises their electrochemical stability. Additionally, the range of nanopillar aspect ratios is limited by the diameter of the polysterene nanospheres employed, where the resulting structures present challenging mass transport properties to characterize, as shown in our work.

To amend these limitations, further investigations on plasma-etched MoS_2/WS_2 nanoarrays should focus in the replacement of the O_2 plasma step by one employing an inert gas (Ar, H_2).

This would not only mitigate oxygen incorporation, but would also promote the extrinsic formation of S vacancies which would further activate the TMD nanoarray structure. Transition metal doping by physical methods such as CVD or PVD would be worth pursuing, as well as the potential incorporation of recently reported dopants (P, B, N) in the reacting plasma to further boost the inherent activity of the TMDs. For future research areas, TMD nanoarrays are very attractive for applications not frequently evaluated in the literature such as photoelectrochemical hydrogen production, biosensing and supercapacitors: dense nanopillar structures promote efficient light harvesting and offer a high surface area susceptible to charge accumulation and detection of electroactive analytes.

Anodically-electrodeposited amorphous MoS_x thin films present great advantages compared to other MoS_x preparation methods such as their low preparation cost, high HER activity (one of the most active pristine MoS_2 materials reported so far) tuneable by electrodeposition conditions, co-deposition of other metals, electrochemical conditioning and backing electrode among others. Our pH-dependent studies reveal very important information on how crucial the electrochemical conditioning and pH environments are to ensure maximized activities and stabilities. However, in all cases the surface characterization techniques to support our conclusions (Raman and XPS) are performed ex-situ, which cannot provide full understanding of the MoS_x thin films under HER operation.

For such reason, future work on these pH-dependent studies would greatly benefit from *in operando* coupled characterization techniques such as near-ambient pressure XPS, Raman or SFC/ICP-MS to unambiguously correlate in real time structural or surface state modifications in MoS_x with the electrochemical data recorded, and corroborate the postulated pH-dependent stability and active site modification. The inherent nanostructuring of AE-MoS_x by hard templates and composite preparation has already been explored in the literature, but a surface-area maximization approach based upon soft templates (e.g. microemulsions) would be relevant

as the pore size distribution and morphology of the resulting MoS_x could be easily tuned by the properties of the colloidal suspension and the electrodeposition parameters.

Lastly, the OER stability enhancement observed after WS_{3-x} decoration on Ir electrodes is hampered by the pulse reverse electrodeposition method needed to yield nuclei instead of homogeneous thin films: the low deposition yield due to the somewhat WS_{3-x} sluggish deposition kinetics affects the degree of incorporation, and it is the main inherent limitation of this particular application of WS_{3-x}. The beneficial role of WS_{3-x} as a corrosion-resistant material for OER electrocatalysts, once the electrodeposition yields are fully maximized and tailored, should be evaluated in future investigations by its use in other state-of-the-art materials, the most suitable candidate being the more active yet more unstable Ru. In addition to this, supplementary XPS measurements (not available at the thesis submission date) should corroborate the synergistic effect of the acid-insoluble WO_3 phase with the further improved Ir OER stabilities. Analogous to AE-MoS_x, coupled in operando techniques such as SFC/ICP-MS would provide direct evidence of the mitigated corrosion rates, and would open the window to the implementation of other corrosion-resistant oxides derived from TMDs.

As a final remark of this work, we should put in context our findings with those recently reported in the literature. Our research has tackled the three most important strategies to enhance the HER activity of MoS_2 reported in the literature: edge site exposure (Chapter 7), activation of initially inactive S edge sites (Chapter 5) and maximization of the inherent electroactivity of the active sites by morphology and electrochemical tailoring (Chapters 6 and 9). The work carried out for size-selected nanoclusters and anodically-electrodeposited amorphous MoS_x has been shown to be on par with the best reports in the literature. The field now heads towards single atom doping and chalcogenide vacancy formation as the main basal plane activation methods to fully maximize HER activity in TMDs whose activity is limited to the edges: some of the future work suggested here aims to align with these efforts. Their

reported enhancements, however, cannot be unambiguously ascribed to one specific effect, as for example non-native metal incorporation will affect to some extent the morphology, electronical and catalytical properties of TMDs. For such reason, systematic understanding of the role of in-plane dopants and vacancies is needed for the field to fully prosper in the forthcoming years, but TMDs remain to be an exciting family of materials with room for increasing number of applications and activity enhancements.

Appendix

A. Non-electrolytic hydrogen production methods

A.1 Hydrocarbon-based methods

Hydrogen production by use of hydrocarbon fossil fuels is the predominant method, specifically 95% of its global production.[1] These are classified in three production methods: steam reforming (SR), partial oxidation (POX) and autothermal reforming (ATR).

SR is a high-temperature reaction (700-900°C) between steam and a light hydrocarbon source (normally natural gas or pure methane) to produce hydrogen and carbon monoxide (syngas) in a first step, followed by a second step at lower temperatures (200-400°C) known as the water-gas shift reaction, which maximizes the hydrogen production yield by oxidation of carbon monoxide in presence of steam, as outlined below.

Reforming $$C_nH_m + n\,H_2O \rightleftharpoons n\,CO + \left(n + \frac{m}{2}\right)H_2 \; (Ap.1.1)$$

Water-gas shift reaction: $$CO + H_2O \rightleftharpoons CO_2 + H_2 \; (Ap.1.2)$$

SR, when using methane, presents a 72% hydrogen production efficiency, yielding a 70-75% hydrogen-rich gas which by posterior purifications results in a 99.95% final hydrogen purity[2,3]: SR accounts for 48% of global hydrogen production.[2] However, high operating and energy costs as well as make this method undesirable in the hydrogen economy.

POX, unlike SR, is an exothermic process where a substoichiometric ratio of hydrocarbon (methane, coal, heavy oil or petroleum coke) and oxygen react by incomplete combustion to yield syngas. Working temperatures range from 900-950°C to 1150-1315°C whether the reaction

is catalytically or thermally-driven.[4] This method, however, presents a lower hydrogen yield (hydrogen:CO ratio 2:1/1:1 vs. 3:1 in SR).[5]

$$C_nH_m + \frac{n}{2}\,O_2 \;\rightleftharpoons\; n\,CO + \left(\frac{m}{2}\right)H_2 \quad (Ap.1.3)$$

ATR is a combination of both POX and SR, whereby the partial combustion of the hydrocarbon source generates the heat necessary to thermally-induce reforming, generating syngas as a product. Although providing lower hydrogen yield than SR, its almost thermodynamically neutral nature makes it attractive from the economic standpoint.

$$C_nH_m + \frac{n}{2}\,O_2 + n\,H_2O \;\rightleftharpoons\; n\,CO_2 + \left(\frac{m}{2}\right)H_2 \quad (Ap.1.4)$$

Coal and biomass can be employed for hydrogen production by their combustion in presence of steam, as an alternative to natural gas and other aforementioned hydrocarbons. This process, known as coal/biomass gasification, in conjunction with the water-gas shift reaction, yields hydrogen by the following chemical reactions

Coal combustion under steam:

$$2C + \frac{1}{2}\,O_2 + 1\,H_2O \;\rightleftharpoons\; 2\,CO + H_2 \quad (Ap.1.5)$$

Biomass combustion under steam:

$$Biomass + heat + steam \;\rightarrow H_2 + CO + CO_2 + CH_4 + hydrocarbons + char \quad (Ap.1.6)$$

Water-gas shift reaction:

$$CO + H_2O \;\rightleftharpoons\; CO_2 + H_2 \quad (Ap.1.7)$$

Coal/biomass gasification is an energy-intensive process (800-950°C needed for fluidised bed reactors, 1200-1500°C for entrained flow reactor), with faster hydrogen production rates than SR or POX, but lower thermal efficiencies (53% for coal, 60% for biomass vs. 65-80% in SR).[6]

All of these processes, unless coupled to carbon capture and sequestration technologies, generate carbon emissions which are undesirable for achieving a fully carbon-free hydrogen economy. For SR, CO_2 emissions are indeed analogous to those obtain by combustion of the hydrocarbon employed. However, these processes might be adequate at early stages to accelerate hydrogen penetration in the energy mix and implement its related infrastructure.

A.2. Biologically-based methods

Attention has been drawn to microorganisms capable of producing hydrogen, due to the lower working temperatures and technological simplicity. These are particularly suitable for waste minimization, as a wide range of biomass types (both dry and wet) can be employed.[7] Bio-hydrogen production can be classified in three main categories: anaerobic digestion, biophotolysis and fermentation (photo-assisted or dark).

In anaerobic digestion, acid-forming bacteria and methane-forming archaea degrade biomass in a two-step, oxygen-free process generating biofuel (methane and CO_2) as well as hydrogen.[8]

Biophotolysis is based upon the photosynthesis taking place at the chloroplasts present in green algae and cyanobacteria under sun irradiation: in excess of sunlight or anaerobic conditions, water can be photolysed by hydrogenase enzymes to form hydrogen and oxygen (Figure A.1a). An indirect biophotolysis pathway also exists where hydrogen is produced after a four-step process: I) production of biomass by photosynthesis, II) concentration of biomass, III) dark aerobic fermentation producing 4 mol hydrogen/mol glucose and 2 mol of acetates, and IV) conversion of acetate to hydrogen.[4]

Dark fermentation is carried out by anaerobic bacteria and green algae on carbohydrate-rich substrates in the dark: contrary to biophotolysis, fermentation of sugars such as glucose not only yields hydrogen but also CO_2, methane and hydrogen sulfide, requiring post-treatment to purify hydrogen.[9] Thus, the theoretical 4 mol hydrogen/mol glucose of the standard fermentation pathway is down to 2.4-3.2 mol hydrogen/mol glucose.[10] In photo-fermentation (Figure A.1b), purple non-sulfur photosynthetic bacteria convert various organic substrates (agricultural effluents, sugars, organic acids)[11] to hydrogen after harvested sunlight at the bacterial photosystems drive proton reduction at nitrogenase enzymes. Nitrogen-deficient conditions are needed to prevent nitrogenase from undergoing N-fixation through ammonia production.

All of these processes present a high potential, particularly in solar-rich countries with a high production of biomass waste,[11] yet they need to circumvent several barriers to maximize their production efficiency. In photo-assisted processes, these mainly consist of sunlight collection efficiency and bacteria strain modification to supress competing photosynthetic and N-fixation routes. For anaerobic/dark processes, careful control of hydrogen partial pressures and pH is needed to prevent formation of reduced molecules through alternative pathways (acetone, ethanol, lactate, etc.) which irreversibly slow down the hydrogen production rate.[12]

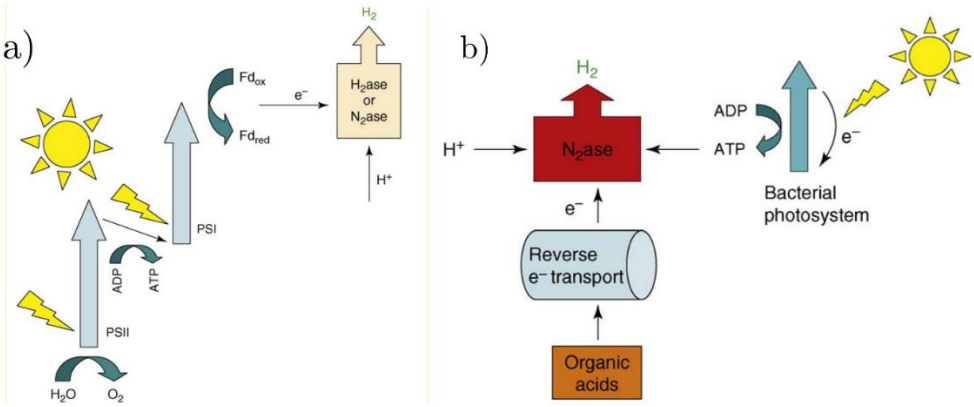

Figure A.1. Schematic diagrams of a) direct biophotolysis and b) photo-fermentation. Reproduced from [13].

A.3 Alternative methods

Hydrogen production can also be achieved at extreme temperature or voltage operating conditions.

In the case of pyrolysis or plasma arc decomposition, hydrocarbons are thermally-decomposed to hydrogen and carbon black, as below

$$C_nH_m \xrightarrow{heat} n\,C + \frac{m}{2}H_2 \quad (Ap.1.8)$$

For methane, this occurs above 980°C, in the absence of oxygen and steam to prevent SR and POX to occur.[14] Compared with the aforementioned hydrocarbon-based methods, pyrolysis yields minimal CO_x emissions, with high hydrogen purities. However, carbon fouling of the reactor and durability of the hydrogen separation membrane employed are challenges to be overcome.

At sufficiently high temperatures (> 2500°C), water can be thermally dissociated into hydrogen and oxygen, process known as thermolysis. Thermochemical water splitting cycles have been proposed as substitutes to thermolysis (ca. 2000-3000 reported),[15] to avoid the challenging hydrogen separation previously required and decrease the operation temperature to values achievable by sustainable heat sources (such as solar thermal collector). Among these, the sulphur-iodine (see Figure A.2)[16], the multi-stage Cu-Cl,[17] and the two-step SnO_2/SnO cycles[18] are suitable candidates for large-scale production of hydrogen.

Waste heat from nuclear power plants can also be employed for thermochemical hydrogen production, but this presents concerns regarding the non-sustainability of uranium ore mining and radioactive waste management. Nonetheless, the large scale implementation of these processes are restricted by the high working temperatures required.

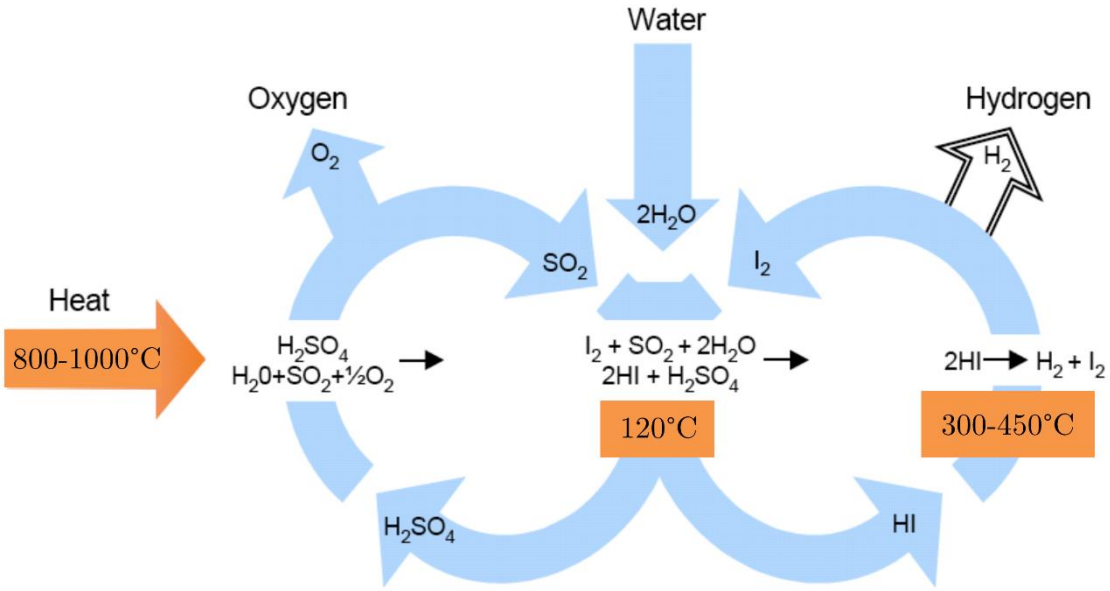

Figure A.2. Schematic of the reaction pathways for the sulphur-iodine thermochemical cycle. Reproduced from [16].

B. Layered transition metal dichalcogenides: optoelectronic properties

B.1 Electronic aspects of layered TMDs

The different symmetry and layer stacking arrangement induces contrasting electronic properties between TMD polymorphs. Namely, group IV and VI single-layered TMDs are generally semiconducting (1-4 eV band gap) or insulating (>4 eV band gap),[19] whilst group V are all metallic.[20] With exceptions (2H-NbX_2, 2H-TaX_2), this indicates that 2H-TMDs present a semiconducting behaviour.

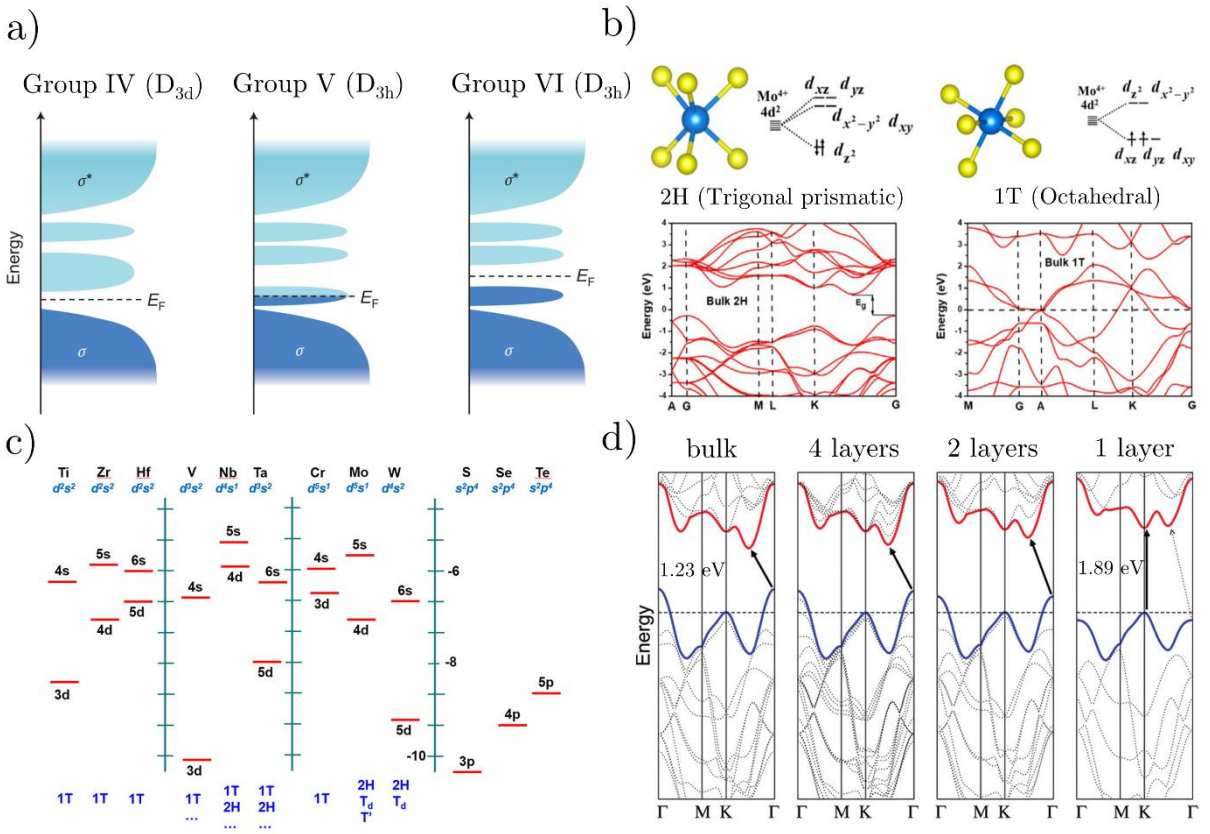

Figure B.1. a) Schematic representation of the M^{4+} d orbital filling within group IV-VI TMDs, located in between the bonding (σ) and antibonding (σ^*) bands, b) Symmetry-induced 4d orbital splitting of 2H- and 1T-MoX_2 with the corresponding MoS_2 calculated band structures, c) Schematic representation of the relative energy levels of metal and chalcogen atoms and d) Calculated indirect-to-direct band gap transition from bulk to monolayer MoS_2. Reproduced from refs. [21–24]

These can be explained by the TMD symmetry-dependent electron pairing of the electronic band structure (occupancy of the σ bonding and σ^* antibonding bands), which near the Fermi level (E_F) is mostly affected by the M^{4+} d-electron count (see Figure B.1a). For TMDs of groups V and VI (2H phase, D_{3h} symmetry), the d electron band of M^{4+} splits into three groups with differentiated energies: I) dz^2, II) degenerate $d_{x^2-y^2}$ and d_{xy}, and III) degenerate d_{xz} and d_{yz}. In contrast, group IV TMDs, with 1T phase and D_{3d} symmetry, present a d electron band

split into two groups: I) degenerate dz^2 and $d_{x^2-y^2}$ and II) degenerate d_{xz}, d_{yz}, and d_{xy}.[21] Electronic band configurations which yield paired electrons lead to semiconducting/insulating properties, and unpaired electron configurations metallic properties. Group IV M^{4+} centres, with "d^0" configuration consequently behave as semiconductors. Group V, as they present an odd electron configuration ("d^1") they will present metallic properties irrespective of the TMD polytype. For Group VI, the even electron configuration ("d^2") yields close-shell electron pairing (2H phase) or unpaired occupation of degenerate electronic energy levels (1T phase).[25] This explains the metallic behaviour observed for 1T-MoX_2/WX_2, contrasting with the semiconducting properties of 2H-MoX_2/WX_2, represented in Figure B.1b.

This general trend is however affected by the relative electronic energies of metal (M^{4+}) and chalcogen (X^{2-}). Within TMDs of a given X^{2-}, M^{4+} of a higher period within a periodic table group present increasing energy gaps with respect to the p orbital X^{2-}, as the d electron energies involved near E_F are higher. Analogously, X^{2-} of higher atomic number from the same M^{4+} TMDs present reduced electron gaps (see Figure B.1c). This leads to, for example, WTe_2 presenting semimetallic properties (band gap ≈ 0.5 eV vs. 1.35 eV for WS_2, see Table 2.1 Chapter 2).

TMD band structures were initially calculated semi-empirically,[26,27] but later evaluated by *ab initio*,[28] augmented-plane-wave[29] and first principle methods such as density functional theory (DFT).[30–33] Band structures were also experimentally measured with several spectroscopic techniques.[24,34–38] Strikingly, TMDs were found to present layer-dependent band structure properties. MoX_2 and WX_2, from bulk to monolayer, present an indirect-to-direct band gap transition conversion (Figure B.1d, for band gap values see Table 2.1 Chapter 2).[39,40] The indirect transition in bulk takes place from the valence band maximum at the Γ point (G point in Figure B.1b) to the conduction band minimum K halfway between the Γ-K lines which, in monolayers, is converted to a K-K direct band gap transition with higher

energies: 1.89 vs. 1.23 eV for MoS_2, 1.98 vs. 1.35 eV for WS_2.[41,42] The gradual increase in band gap by decreasing TMD layer numbers is originated by quantum confinement and interlayer coupling effects, the former theoretically predicted in the 1960's in semiconducting films.[43] The orbitals predominantly contributing to the conduction band states of the K point originate from Mo/W d orbitals localized in between the X-M-X trilayered structure, and thus barely unaffected by interlayer coupling. In contrast, the hybridized Mo d_z^2 and antibonding S p_z orbitals primarily contributing to the Γ point valence band states are strongly affected by interlayer coupling[44]: TMD layer number decrease minimizes the S p_z orbitals coulombic repulsion of neighbouring layers, downshifting Γ valence band energy state relative to K.[45]

The layer-dependent electronic properties in TMDs allow a high degree of band gap tunability, unattainable for graphene, of high interest for electronic applications (e.g. field-effect transistors).[20,46] Indeed, TMDs band gap can be further modulated, generally aiming its reduction, by the following strategies: application of electrical fields,[47,48] mechanical strain,[49–55] hydrostatic pressure, thermal decoupling of adjacent layers,[39] chemical functionalization,[56] alloy formation,[57,58] Rb metal doping,[59,60] and TMD heterostack fabrication.[61,62]

B.2 Optical properties of layered TMDs

Layer-dependent TMD properties are not solely restricted to band gap modifications. The direct band gap found for monolayer TMDs, located within the visible spectrum range, means that incident/emitted photons can possess energies higher than that of the direct band gap, which in turn maximises the absorption/emission efficiencies. This is particularly suitable for optoelectronic applications such as optical switches, photo-detectors and wearable electronics.[20] The indirect-to-direct band gap transition in monolayer MoX_2 and WX_2 TMDs was indeed manifested as emergent photoluminescence (PL, light emission resulting from previous photon adsorption) with a ca. 10^4 quantum yield enhancement for MoS_2,[42] weakened

with increasing TMD layer numbers and finally absent in bulk (Figures B.2a-b).[24,36,40,63] PL quenching, ascribed to the competitive indirect electronic transition in multi-layered TMDs (emerging weak PL band at higher wavelengths), can also be obtained in TMD monolayers by heterostack fabrication with few-layer black phosphorus (Figure B.2c),[64] oxygen plasma treatment,[65] application of lateral electrical fields,[66] room-temperature environment ageing,[67] Au monolayer deposition,[68] electrochemically-induced cation intercalation,[69] or 2H→1T phase conversion induced by chemical exfoliation.[35]

PL can also be modulated by several strategies. Indeed, PL in monolayer TMDs can be reversibly maximized (MoX_2) or quenched (WSe_2) by oxygen and water molecules physisorption,[70] whilst improved PL is obtained after plasma-induced sulfur vacancies formation[71] and subsequent oxygen chemisorption,[72] or chemical doping.[73,74] For few-layer TMDs, PL can be induced by thermal treatments,[39] lateral electrical fields,[66] strain-induced one-dimensional corrugations[75] or inclusion of polymeric interspacers.[76] PL is also extremely affected at the TMD grain boundaries: for MoS_2, mirror twin boundaries (Mo-rich, "n-doped") present quenched PL, whereas for tilt boundaries (S-rich, "p-doped") it is greatly enhanced.[77] A similar effect is found for MX_2 stoichiometry-dependent PL studies: lower X contents yielded worsened PL and vice versa.[78] Finally, the PL emission peak can be red- (lower energy) or blue-shifted (higher energy) by use of different solvent environments[79] and TMD alloy stoichiometries (Figure B.2d).[80]

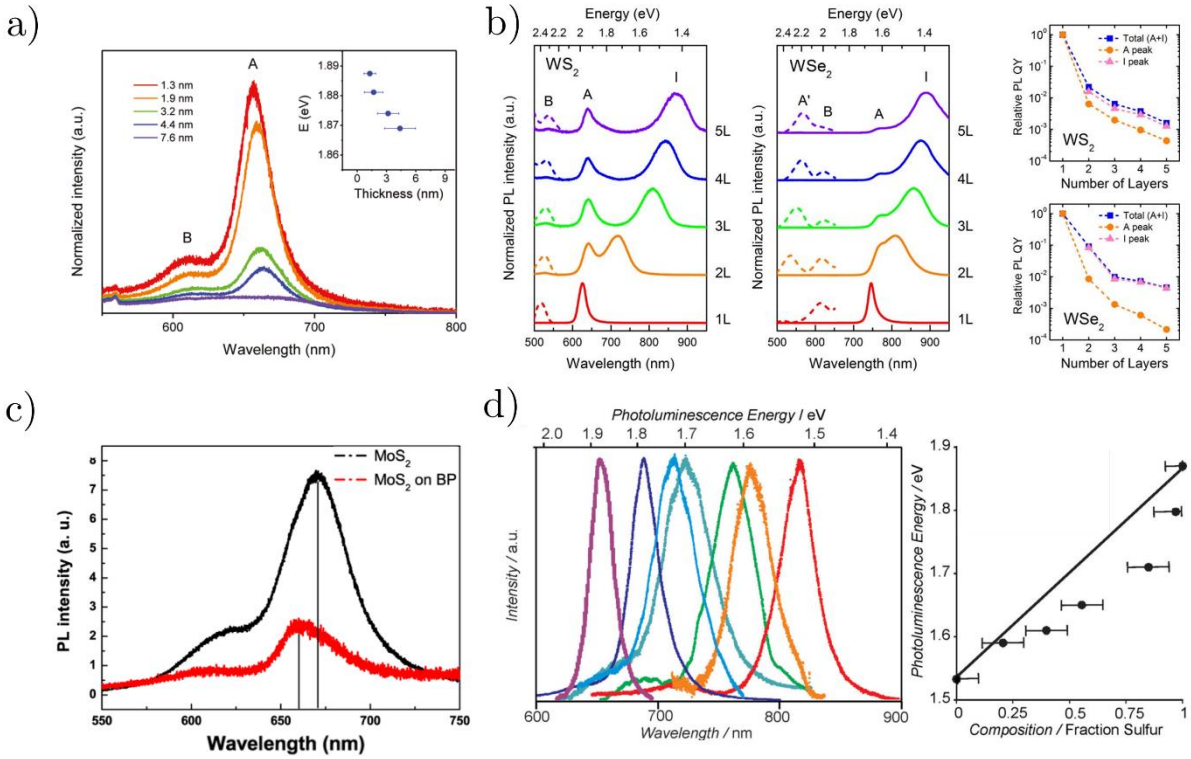

Figure B.2. Thickness-dependent photoluminescence (PL) spectra of a) MoS_2 and b) WS_2 and WSe_2 along with the layer (L) dependent PL energy and intensity. c) PL spectra of MoS_2 before and after heterostack formation with black phosphorous (BP). d) Composition-dependent PL spectra of a $MoS_{2(1-x)}Se_{2x}$ TMD alloy film. Reproduced from refs. [35,40,64,80].

The general explanation behind PL enhancement lies in the stabilization of the excitons (suppression of their non-radiative recombination): for n-type TMDs (MoX_2) this occurs via electron withdrawal (p-type doping) from adsorbed species or modified local stoichiometries. As for PL quenching, several mechanisms come into play depending on the treatment employed: direct-to-indirect band gap conversions, electron donation/withdrawal on n/p-type TMDs (molecule adsorption), interlayer electrical field build-up (heterostacks), and local presence of higher metal centre oxidation states (ageing, oxygen plasma).

Layer-dependent TMD optical properties are also found in Raman spectroscopy. A pioneering study on MoS_2 showed a layer-dependent relative frequency of the in-plane E^1_{2g} and out-of-

plane A_{1g} vibration modes up to 4 layers.[81] With increasing layer number, E^1_{2g} is red-shifted (lower frequency, 385 cm^{-1} for monolayer vs. 383 cm^{-1} in bulk) whereas A_{1g} is blue-shifted (higher frequency, 404 cm^{-1} for monolayer vs. 408 cm^{-1} in bulk); peak widths and intensities varied arbitrarily (Figure B.3a).[82] Similar results were found for other MS_2 TMDs.[83] The relative frequency shift $\Delta\nu$ was found independent on the laser employed.[82] The number of layers, in the case of MoS_2, can be obtained by $\Delta\nu(A_{1g} - E^1_{2g}) = 25.8 - 8.4/N$, N being the number of layers (up to 5).[84] A_{1g} stiffening was attributed to enhanced van der Waals interlayer forces, whilst E^1_{2g} to modified interlayer interactions and dielectric screening of the long-range Coulomb interactions.[85]

Changes in the E^2_{2g} mode frequency (interlayer shear mode, $\nu < 50$ cm^{-1}), ascribed to the in-plane vibration of the X-M-X trilayer parallel to adjacent layers, also reveal information regarding the layer stacking arrangement and also the number of TMD layers present.[86] The E^2_{2g} mode frequency was found to decrease by ca. 0.5 cm^{-1} in MSe_2 TMDs when the interlayer stacking shifted from the 2H to the 3R phase, with a significant intensity drop in the 3R phase.[87] Another low-frequency mode, referred as layer breathing mode due to the out-of-plane B^2_{2g} interlayer vibration involved (i.e. absent in bulk and monolayers), is particularly sensitive to layer stacking[88] and relative orientation between MX_2 interlayers and heterostructures.[89] As a general trend, it was found that increasing TMD layer numbers yield a softening (red-shift) in B^2_{2g} layer breathing modes, and stiffening (blue-shift) in E^2_{2g} shear modes (Figure B.3b).[90–92] As for the relative orientation dependence, a disappearance of the E^2_{2g} shear modes was found in bilayer MoS_2 in the 20-40° rotation range, accompanied by significant frequency shifts and intensity modifications.[89,93]

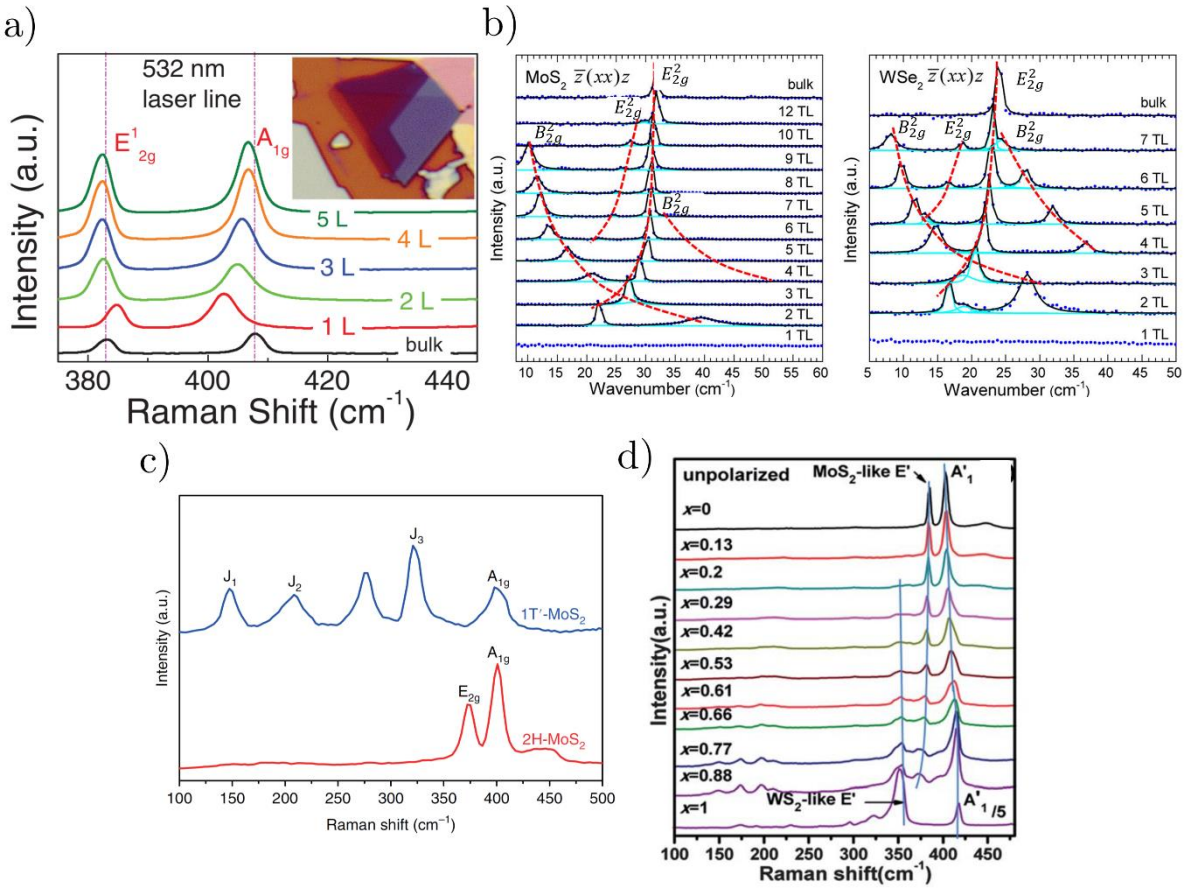

Figure B.3. Layer-dependent frequency shift of a) in-plane E^1_{2g} and out-of-plane A_{1g} MoS_2 modes and b) E^2_{2g} interlayer shear and B^2_{2g} layer breathing modes in MoS_2 and WSe_2. c) Raman spectra of monolayer monolayer 2H-MoS_2 (red) and 1T'-MoS_2 (blue), showing Raman bands J_1, J_2 and J_3. d) Stacked Raman spectra of $Mo_{1-x}W_xS_2$ monolayer alloys for varying W composition (labelled as x). Reproduced from refs. [82,90,94,95].

TMD polytypes can also be identified using Raman spectroscopy. Compared with 2H-MoX_2, the 1T phase of MoX_2 presented three additional bands,[94,96,97] known as J_1, J_2 and J_3 for MoS_2 (at 153, 226, 330 cm^{-1} respectively, see Figure B.3c).[98,99] These bands were recently ascribed to the in-plane shearing mode of one side of the zig-zag chain with respect to the other (J_1), motion of S atoms with respect to the Mo atom layers (J_2) and a relative stretching of a

side of the zig-zag chain relative to the other with a partial out-of-plane component (J_3).[25,100] The phase purity of exfoliated natural molybdenite could also be proved by low-frequency vibration analysis, where mixed 2H-3R MoS_2 stacking arrangements were found.[101]

As occurred in TMD photoluminescence, Raman modes are affected by multiple aspects, such as ion intercalation,[102,103] temperature,[104,105] pressure,[106] strain,[51,52] supporting substrate,[107] electron[108] or laser irradiation,[96,109,110] interlayer coupling,[111] and TMD compositions (elements, chalcogen-to-metal stoichiometry and phase, see Figure B.3d).[65,95,112]

B.3 Other interesting properties and applications of layered TMDs

TMDs, in particular MoS_2, present remarkable mechanical and tribological properties. The Young modulus of monolayer MoS_2 is 270 ± 100 GPa, similar to steel, sustaining significant elastical stretching before full fracture (11%, breaking strength: 23 GPa).[113] What's more, few-layered MoS_2 (5-25 layers) intrinsic strength is maintained,[114] whilst the bending modulus is 3 orders of magnitude higher in three-layer MoS_2 retaining its monolayer flexibility.[115] Thus, MoS_2 is not only one of the strongest semiconductors reported, but also highly flexible, qualities appropriate for wearable (opto)electronic devices. The ultra-low friction coefficient of TMDs is particularly suited for lubricating applications[116,117]: for MoS_2, at room temperature, this is 0.01-0.1.[118] The underlying mechanical energy dissipation mechanism has been primarily ascribed to the stick-slip model: abrupt state transitions of the lamellar sliding structures, whereby the sliding velocity of the TMD surface atoms surpasses by orders of magnitude that of the centre-of-mass.[119,120] Analogous to the aforementioned optoelectronical properties of TMDs, nanoscale friction is layer-dependent, monotonically increasing with increasing layer number.[121]

TMDs have also been reported to exhibit magnetic properties. For bulk MoS_2 and WS_2, the semiconducting 2H phase is reported to be diamagnetic at room temperature, but few-layer

MS_2 present ferromagnetic behaviour in the 10-300 K range,[122,123] and room-temperature ferrimagnetism after proton irradiation due to vacancy formation.[124] Studies on MoS_2 nanostructures have demonstrated that the 1T phase, found in undercoordinated Mo- and S-edge sites or induced by S vacancies in basal planes, is responsible for the observed ferromagnetism.[125] Modelling indicated zig-zag nanoribbons present ferromagnetic and metallic nature, whilst armchair nanoribbons are non-magnetic and semiconducting.[126–128] Although preliminary DFT studies allocated the ferromagnetic properties to the unpaired spins at S- edges,[129] Mo-edge rich nanoplatelets with a zigzag configuration as found in MoS_2 dodecagons present the highest calculated magnetic moment,[130] which is lost after edge reconstruction.[131] Magnetism in TMD materials can also be triggered by 3d transition metal adsorption,[132,133] non-metal atoms adsorption (H, B, C, N, O, F),[134] organolithium exfoliation,[135] uniaxial strain[55] or strained vacancies generation;[136,137] and tuned by molecular adsorption.[138] Besides Mo/WS_2, TMDs with ferromagnetic metals (M = Fe, Mn, V) present ferromagnetic properties[139]: an illustration compiling the magnetic properties of TMDs can be found in Figure B.4a. External magnetic fields applied to TMDs have been reported to induce phenomena such as magnetoresistance[140] and magneto-conductance,[141] the latter via the Hall effect.

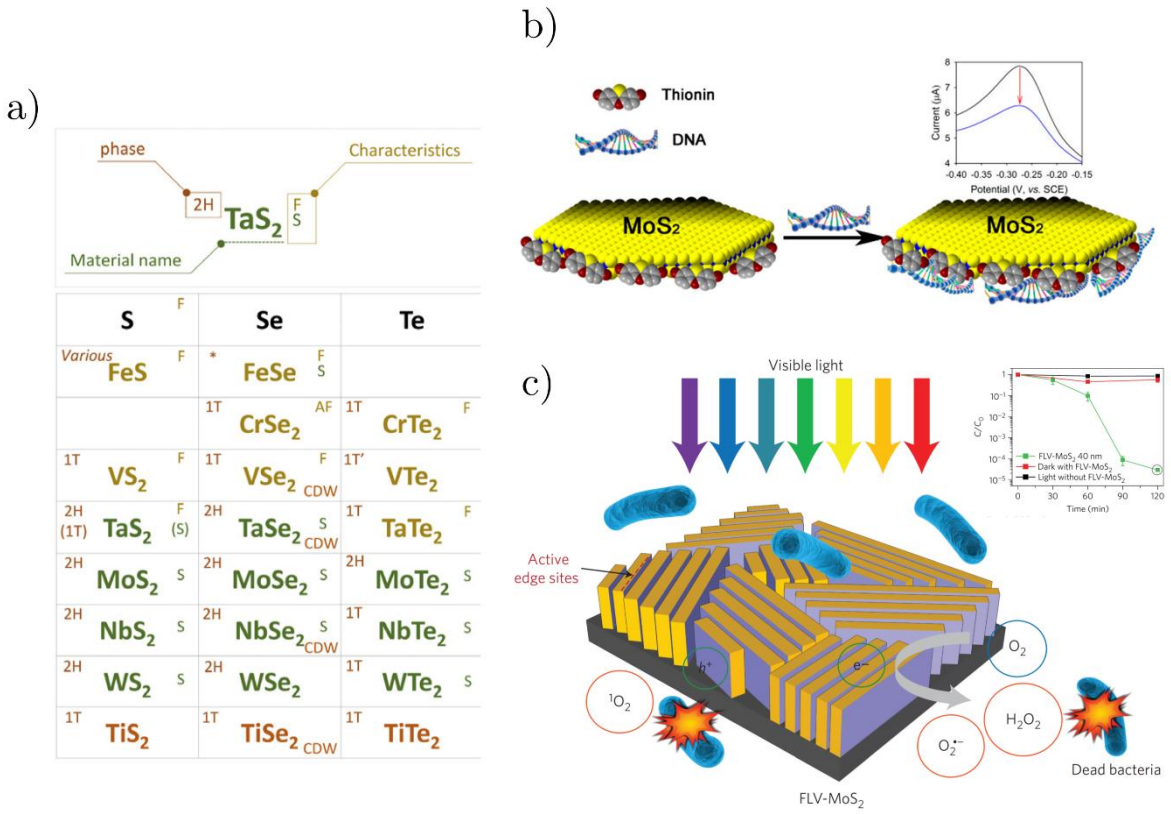

Figure B.4. a) Compilation of 2D TMDs and their physical properties: magnetism (ferromagnetic (F), antiferromagnetic (AF)) and superconductivity (S). b) Schematic of the electrochemical biosensing mechanism of double-stranded DNA by thionin-functionalized MoS_2. c) Schematic of the bacteria inactivation mechanism via few-layer vertically aligned MoS_2 photocatalytic production of reactive oxygen species. Insets of b) and c) show biosensing and disinfection performance of the TMD-based devices. Reproduced from refs. [142–144].

TMDs present a myriad of interesting applications. In biological systems, these range from sensing of relevant biomolecules such as nucleic acids (Figure B.4b),[145] proteins[146] and small molecules (e.g. glucose, dopamine, uric and ascorbic acids, bisphenol and hydrogen peroxide)[147,148] to therapeutic agents drug delivery,[149] whilst water-methanol gas mixtures could also be selectively monitored.[150] Industry-relevant TMD applications have also been reported, such as the preparation of anodes for lithium ion batteries,[151–153] (micro-)supercapacitors,[154] DNA sequencing via TMD nanopore transport,[155] piezoelectric

devices,[142] water disinfection via electrochemical production of hydrogen peroxide (Figure B.4c)[144,156] and removal of water soluble-dyes[157] and heavy metals.[158,159]

C. Hybrid Ni-MoS_2 nanocluster composition calculation

The HAADF intensity (I) of two kinds of elements (A and B) follows the relationship $I_A/I_B = (Z_A/Z_B)^{1.46}$, in which Z is the atomic number, for our microscope calibration[170]. Thus the intensity relationship between Mo, S and Ni can be listed as below:

$$I_{Mo} = 4.09 \times I_S = 1.81 \times I_{Ni} \quad (Ap.3.1)$$

Since the single atom intensity of Mo is much higher than that of S and Ni, we assume the atoms most easily visible in STEM images are Mo. According to the intensity line profile shown in Figure 5.3 Chapter 5, the number of Mo columns intersected by the line and the number of Mo atoms in each column can be obtained. Once all the surface area of the nanocluster is scanned by such lines, the total number of Mo atoms (N_{Mo}) is obtained. The number of S atoms (N_s) in this nanocluster can also be derived on the assumption that the ratio of Mo atoms to S atoms is 1:2. Therefore the composition of the nanocluster can be regarded as: $(MoS_2)_{N_{Mo}}Ni_x$. Now the integrated intensity of the whole nanocluster ($I_{cluster}$) can be given by:

$$(I_{Mo} \times N_{Mo}) + (I_S \times 2N_{Mo}) + (I_{Ni} \times x) = I_{cluster} \quad (Ap.3.2)$$

Since the intensity of the whole nanocluster can be measured from STEM image, against using single Mo atom as the standard, the value of x can be given by combining equations (Ap. 3.1) and (Ap. 3.2):

$$x = 1.81\frac{I_{cluster}}{I_{Mo}} - (2.67 \times N_{Mo}) \quad (Ap.3.3)$$

Then the nanocluster composition is revealed.

D. Alternative XPS spectra peak devonvolution for Ni-MoS_2 and Ni nanoclusters

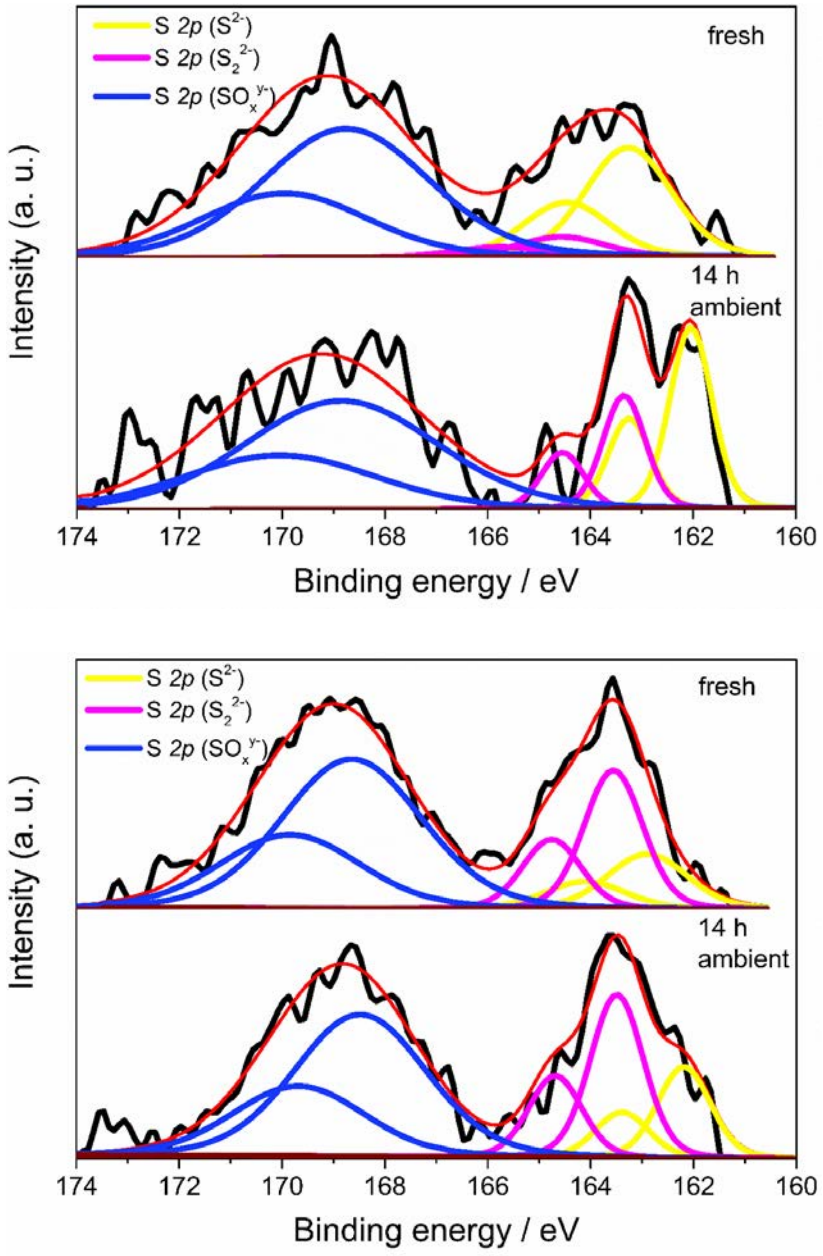

Figure D.1. Fresh and 14 h air exposed high-resolution XPS spectra S 2p (right) for $(MoS_2)_{300}$ nanoclusters (top) and $(Ni\text{-}MoS_2)_{1000}$ nanoclusters (bottom),. Labels: raw spectra (solid black), cumulative peak fit (solid red), S $2p_{3/2:1/2}$ (S^{2-}, yellow), S $2p_{3/2:1/2}$ (S_2^{2-}, magenta) and S $2p_{3/2:1/2}$ (SO_x^{y-}, blue).

E. Hydrogen turnover frequency (TOF) elucidation

E.1 Nickel-molybdenum disulfide hybrid nanoclusters

Estimation of turnover frequency was performed by the deconvolution and integration of the anodic peaks observed after 10 cycles in the 0 to 1.2 V voltage range vs. SCE (0.35 to 1.6 V vs. NHE after calibration). The deconvolution of the first anodic linear sweep was performed in the 0.6 to 1 V and 0.4 to 0.8 V voltage range vs. RHE for $(MoS_2)_{300}$ and $(Ni\text{-}MoS_2)_{1000}$ nanoclusters, respectively.

The formula used for calculating the TOF per-site is the following[179]:

$$TOF\ per\ site = \frac{Total\ hydrogen\ turnovers/cm^2 geometric\ area}{Number\ of\ electrochemically\ active\ sites/cm^2 geometric\ area} \quad (Ap.\ 5.1)$$

The total number of hydrogen turnover events is calculated using the conversion[180]:

$$j_{geom,half\ max}\ \frac{mA}{cm^2_{geom}} \cdot \frac{1\ A}{1000\ mA} \cdot \frac{1\ C/s}{1\ A} \cdot \frac{1\ mol\ e^-}{96485\ C} \cdot \frac{1\ mol\ H_2}{2\ mol\ e^-} \cdot \frac{6.023 \times 10^{23}\ molecules\ H_2}{1\ mol\ H_2}$$

$$= j_{geom,half\ max} * 3.12 \times 10^{15} \frac{molec\frac{H_2}{s}}{cm^2_{geom}}\ per\ \frac{mA}{cm^2_{geom}} \quad (Ap. 5.2)$$

For comparison purposes, the current density is selected at the voltage corresponding to the $(MoS_2)_{300}$ nanoclusters hydrogen evolution peak half maximum (E= -0.749 V, v_{scan}= 25 mV s^{-1}):

For $(MoS_2)_{300}$ nanoclusters:

$$|j_{geom,half\ \max}| * 3.12 \times 10^{15} \frac{molec\frac{H_2}{s}}{cm^2_{geom}}\ per\ \frac{mA}{cm^2_{geom}} = 0.4\ \frac{mA}{cm^2_{geom}} * 3.12 \times 10^{15}$$

$$= 1.25 \times 10^{15} \frac{molec\frac{H_2}{s}}{cm^2_{geom}} \quad (Ap. 5.3)$$

For $(Ni\text{-}MoS_2)_{1000}$ hybrid nanoclusters:

$$|j_{geom,half\ max}| * 3.12 \times 10^{15} \frac{molec \frac{H_2}{s}}{cm^2_{geom}}\ per\ \frac{mA}{cm^2_{geom}} = 0.60\ \frac{mA}{cm^2_{geom}} *\ 3.12 \times 10^{15}$$

$$= 1.87 \times 10^{15} \frac{molec \frac{H_2}{s}}{cm^2_{geom}}\ (Ap.5.4)$$

Calculation of the turnover frequency can also be calculated for the $(Ni\text{-}MoS_2)_{1000}$ hybrid nanoclusters at the $(Ni\text{-}MoS_2)_{1000}$ hydrogen evolution peak half maximum (E= -0.640 V, v_{scan} = 25 mV s^{-1}):

$$|j_{geom,half\ max}| * 3.12 \times 10^{15} \frac{molec \frac{H_2}{s}}{cm^2_{geom}}\ per\ \frac{mA}{cm^2_{geom}} = 0.31\ \frac{mA}{cm^2_{geom}} *\ 3.12 \times 10^{15}$$

$$= 9.56 \times 10^{14} \frac{molec \frac{H_2}{s}}{cm^2_{geom}}\ (Ap.5.5)$$

The total number of electrochemically MoS_2 active edge sites per geometric area is elucidated as it follows:

Assuming that the anodic electrochemical process undergoes the reaction mechanism proposed by Bonde et al.[181], corresponding to the partial oxidation of sulfur in MoS_2

$$MoS_2 + 7\ H_2O \rightarrow MoO_3 + SO_4^{2-} + \frac{1}{2}\ S_2^{2-} + 14H^+ + 11e^-\ (Ap.5.6)$$

The integration of the ASV deconvoluted peaks responsible for the MoS_2 active edge sites oxidation will enable to provide an estimation of the TOF.

Peak integration values obtained for first scan ASV:

$(MoS_2)_{300}$ nanoclusters

- Mo-edge sites: $32.7\ \mu C/cm^2_{geom}$

$(Ni\text{-}MoS_2)_{1000}$ hybrid nanoclusters

- Ni-doped Mo-edge sites (Peak II): $13.4\ \mu C/cm^2_{geom}$
- Ni-doped S-edge sites (Peak III): $26.8\ \mu C/cm^2_{geom}$
- Undoped Mo-edge sites (Peak IV): $14.3\ \mu C/cm^2_{geom}$
- Total active sites integrated charge density: $54.5\ \mu C/cm^2_{geom}$

The peak integrated area (represented in terms of charge density $\langle\sigma_q\rangle$) is converted to MoS_2 active sites/geometric area as follows:

$$\langle\sigma_q\rangle \frac{\mu C}{cm^2_{geom}} \cdot \frac{1\ C}{1\times10^6\ \mu C} \cdot \frac{1\ mol\ e^-}{96485\ C} \cdot \frac{1\ mol\ MoS_2}{11\ mol\ e^-} \cdot \frac{6.023\times10^{23}\ molecules\ MoS_2}{1\ mol\ MoS_2}$$

$$= \langle\sigma_q\rangle * 5.67\times10^{11} \frac{molec\ MoS_2}{cm^2_{geom}}\ (Ap.5.7)$$

For $(MoS_2)_{300}$ nanoclusters:

$$\langle\sigma_q\rangle * 5.67\times10^{11} \frac{molec\ MoS_2}{cm^2_{geom}} = 32.7 * 5.67\times10^{11} \frac{molec\ MoS_2}{cm^2_{geom}} = 1.86\times10^{13} \frac{molec\ MoS_2}{cm^2_{geom}}\ (Ap.5.8)$$

For $(Ni\text{-}MoS_2)_{1000}$ hybrid nanoclusters:

$$\langle\sigma_q\rangle * 5.67\times10^{11} \frac{molec\ MoS_2}{cm^2_{geom}} = 54.5 * 5.67\times10^{11} \frac{molec\ MoS_2}{cm^2_{geom}} = 3.09\times10^{13} \frac{molec\ MoS_2}{cm^2_{geom}}\ (Ap.5.9)$$

Turnover frequency values per active site, at E= -0.749 V and v_{scan}= 25 mV s^{-1}, are:

For $(MoS_2)_{300}$ nanoclusters:

$$TOF\ per\ site = \frac{1.25\times10^{15} \frac{molec \frac{H_2}{s}}{cm^2_{geom}}}{1.86\times10^{13} \frac{molec\ MoS_2}{cm^2_{geom}}} = 67.1 \frac{molec \frac{H_2}{s}}{active\ MoS_2\ sites}\ (Ap.5.10)$$

For $(Ni\text{-}MoS_2)_{1000}$ hybrid nanoclusters (at the $(MoS_2)_{300}$ nanoclusters hydrogen evolution peak half maximum) :

$$TOF\ per\ site = \frac{1.87 \times 10^{15} \frac{molec \frac{H_2}{s}}{cm^2_{geom}}}{3.09 \times 10^{13} \frac{molec\ MoS_2}{cm^2_{geom}}} = 60.3 \frac{molec \frac{H_2}{s}}{active\ MoS_2\ sites} \quad (Ap.5.11)$$

For $(Ni\text{-}MoS_2)_{1000}$ hybrid nanoclusters (at the $(Ni\text{-}MoS_2)_{1000}$ nanoclusters hydrogen evolution peak half maximum) :

$$TOF\ per\ site = \frac{9.56 \times 10^{14} \frac{molec \frac{H_2}{s}}{cm^2_{geom}}}{3.09 \times 10^{13} \frac{molec\ MoS_2}{cm^2_{geom}}} = 30.9 \frac{molec \frac{H_2}{s}}{active\ MoS_2\ sites} \quad (Ap.5.12)$$

E.2 Size-selected, sulfur-enriched molybdenum sulfide nanoclusters

Estimation of the hydrogen turnovers per second can be performed based on the extremely accurate control of the catalyst loading provided by the proprietary lateral time-of-flight mass filter used in our cluster source[178] and the cluster beam deposition current. Other TOF estimation methods commonly reported in the literature (anodic stripping voltammetry, electrochemical capacitance measurements, study of redox mediator electrochemistry) cannot be used due to the ultra-low catalyst loading on our samples (~ng cm^{-2}). The catalyst loading-based method used implies, however, the TOF is not calculated based on the electrochemically active surface area of the nanoclusters (i.e. the active sites accessible by the electrolyte). This means that the final TOF obtained will underestimate the real TOF per-site, but if this metric is calculated in the same manner for all $(MoS_x)_{1000}$ nanoclusters samples then it will provide physically relevant information.

As with our studies on magnetron-sputtered Ni-$(MoS_x)_y$ hybrid nanoclusters, the current density is selected at the voltage corresponding to the as-deposited $(MoS_{1.9})_{1000}$ nanoclusters hydrogen evolution peak half maximum $|j_{geom,half\ max}|$ at a given scan rate (in this case v_{scan}= 50 mV s^{-1})

For $(MoS_{1.9})_{1000}$ nanoclusters deposited at 5% surface coverage, $|\eta_{\text{half max}}|$= 825 mV:

$$|j_{geom,half\ \max}| * 3.12 \times 10^{15} \frac{molec\frac{H_2}{s}}{cm^2_{geom}}\ per\ \frac{mA}{cm^2_{geom}} = 0.303\ \frac{mA}{cm^2_{geom}} *\ 3.12 \times 10^{15}$$

$$= 9.46 \times 10^{14} \frac{molec\frac{H_2}{s}}{cm^2_{geom}}\ (Ap.5.13)$$

For $(MoS_{1.9})_{1000}$ nanoclusters deposited at 20% surface coverage, $|\eta_{\text{half max}}|$= 815 mV:

$$|j_{geom,half\ \max}| * 3.12 \times 10^{15} \frac{molec\frac{H_2}{s}}{cm^2_{geom}}\ per\ \frac{mA}{cm^2_{geom}} = 0.328 \frac{mA}{cm^2_{geom}} *\ 3.12 \times 10^{15}$$

$$= 1.02 \times 10^{15} \frac{molec\frac{H_2}{s}}{cm^2_{geom}}\ (Ap.5.14)$$

Calculation of the turnover frequency is equally performed for the sulfurised and annealed $(MoS_x)_{1000}$ nanoclusters:

For sulfurised and annealed $(MoS_{4.9})_{1000}$ nanoclusters deposited at 5% surface coverage, at $|\eta|$= 825 mV ($|\eta_{\text{half max}}|$ for the as-deposited sample):

$$|j_{geom,half\ \max}| * 3.12 \times 10^{15} \frac{molec\frac{H_2}{s}}{cm^2_{geom}}\ per\ \frac{mA}{cm^2_{geom}} = 0.614\ \frac{mA}{cm^2_{geom}} *\ 3.12 \times 10^{15}$$

$$= 1.92 \times 10^{15} \frac{molec\frac{H_2}{s}}{cm^2_{geom}}\ (Ap.5.15)$$

For sulfurised and annealed $(MoS_{4.9})_{1000}$ nanoclusters deposited at 20% surface coverage, at $|\eta|$= 815 mV ($|\eta_{\text{half max}}|$ for the as-deposited sample):

$$|j_{geom,half\ \max}| * 3.12 \times 10^{15} \frac{molec\frac{H_2}{s}}{cm^2_{geom}}\ per\ \frac{mA}{cm^2_{geom}} = 0.556\ \frac{mA}{cm^2_{geom}} *\ 3.12 \times 10^{15}$$

$$= 1.73 \times 10^{15} \frac{molec\frac{H_2}{s}}{cm^2_{geom}}\ (Ap.5.16)$$

The total number of MoS_2 units per geometric area is elucidated by the following conversion, which assumes the Mo:S stoichiometry to be 1:2, as found in the MoS_2 sputtering target (not far from the 1:1.9±0.1 experimentally found by XPS for as-deposited nanoclusters):

$$(MoS_x)_{1000}, catalyst\ loading\ \left(\frac{ng}{cm^2_{geom}}\right) \cdot \frac{1\ g}{10^9\ ng} \cdot \frac{1\ mol\ MoS_2}{160.07\ g\ MoS_2} \cdot \frac{6.023\times10^{23}\ molecules\ MoS_2}{1\ mol\ MoS_2} =$$

$$(MoS_x)_{1000}, catalyst\ loading\ *\ 3.76\times10^{12}\frac{molecules\ MoS_2}{ng}\ (Ap.5.17)$$

For $(MoS_{1.9})_{1000}$ nanoclusters deposited at 5% surface coverage:

$$(MoS_x)_{1000}, catalyst\ loading\ \left(\frac{ng}{cm^2_{geom}}\right) *\ 3.76\times10^{12}\frac{molecules\ MoS_2}{ng}$$

$$= 83.78\frac{ng}{cm^2_{geom}} * 3.76\times10^{12}\frac{molecules\ MoS_2}{ng}$$

$$= 3.15\times10^{14}\frac{molec\ MoS_2}{cm^2_{geom}}\ (Ap.5.18)$$

For $(MoS_{1.9})_{1000}$ nanoclusters deposited at 20% surface coverage:

$$(MoS_x)_{1000}, catalyst\ loading\ \left(\frac{ng}{cm^2_{geom}}\right) *\ 3.76\times10^{12}\frac{molecules\ MoS_2}{ng}$$

$$= 335.12\frac{ng}{cm^2_{geom}} * 3.76\times10^{12}\frac{molecules\ MoS_2}{ng}$$

$$= 1.26\times10^{15}\frac{molec\ MoS_2}{cm^2_{geom}}\ (Ap.5.19)$$

Turnover frequency values per active site, are:

For $(MoS_{1.9})_{1000}$ nanoclusters deposited at 5% surface coverage:

As deposited:

$$TOF\ per\ site = \frac{9.46 \times 10^{14} \frac{molec\frac{H_2}{s}}{cm^2_{geom}}}{3.15 \times 10^{14} \frac{molec\ MoS_2}{cm^2_{geom}}} = 3.0 \frac{molec\frac{H_2}{s}}{active\ MoS_2\ sites} \quad (Ap.5.20)$$

Sulfurised and annealed:

$$TOF\ per\ site = \frac{1.92 \times 10^{15} \frac{molec\frac{H_2}{s}}{cm^2_{geom}}}{3.15 \times 10^{14} \frac{molec\ MoS_2}{cm^2_{geom}}} = 6.1 \frac{molec\frac{H_2}{s}}{active\ MoS_2\ sites} \quad (Ap.5.21)$$

For $(MoS_{1.9})_{1000}$ nanoclusters deposited at 20% surface coverage:

As deposited:

$$TOF\ per\ site = \frac{1.02 \times 10^{15} \frac{molec\frac{H_2}{s}}{cm^2_{geom}}}{1.26 \times 10^{15} \frac{molec\ MoS_2}{cm^2_{geom}}} = 0.8 \frac{molec\frac{H_2}{s}}{active\ MoS_2\ sites} \quad (Ap.5.22)$$

Sulfurised and annealed:

$$TOF\ per\ site = \frac{1.73 \times 10^{15} \frac{molec\frac{H_2}{s}}{cm^2_{geom}}}{1.26 \times 10^{15} \frac{molec\ MoS_2}{cm^2_{geom}}} = 1.4 \frac{molec\frac{H_2}{s}}{active\ MoS_2\ sites} \quad (Ap.5.23)$$

F. Hydrogen evolution reaction experiments: compilation of results

F.1 Nickel-molybdenum disulfide hybrid nanoclusters

Sample	$\lvert j_{half\ max}\rvert$ / mA cm^{-2}; η / mV	$\lvert j_p\rvert$ / mA cm^{-2}; η/ mV	b / mV dec^{-1}	j_0 / A cm^{-2}	$j_{0,norm}$ / A cm^{-2}	TOF / s^{-1}
Ni_{2200}	0.36; 771	0.72; 869	106	2.8×10^{-11}	-	-
$(MoS_2)_{300}$ fresh	0.31; 766	0.63; 906	133	8.4×10^{-10}	-	-
$(MoS_2)_{300}$ 14 h	0.4; 749	0.81; 923	94	2.7×10^{-11}	2.14×10^{-9}	67.1 (740 mV)
$(Ni\text{-}MoS_2)_{1000}$ fresh	0.35; 683	0.69; 805	118	7.6×10^{-10}	-	-
$(Ni\text{-}MoS_2)_{1000}$ 14 h	0.31; 640	0.60; 769	122	2.1×10^{-9}	1.02×10^{-7}	60.3 (740 mV) 30.9 (650 mV)

Table F.1. Compilation of peak half maximum current density ($j_{half\ max}$), peak current density (j_p), Tafel slope (b), exchange current density (j_0), normalized exchange current density ($j_{0,norm}$) and turnover frequency (TOF) values of the doped/undoped MoS_2 nanoclusters samples evaluated

F.2 Size-selected, sulfur-enriched molybdenum sulfide nanoclusters

Sample	Catalyst loading / mg cm^{-2}	$\|j_{half\ max}\|$ / mA cm^{-2}; $\|\eta_{half\ max}\|$ / mV	b / mV dec^{-1}	j_0 / A cm^{-2}	$j_{0,norm}$ / A cm-2	Mass activity @ $\|j_{half\ max}\|$ / mA mg^{-1}	Mass activity @ 400 mV/ mA mg^{-1}	TOF @ $\|j_{half\ max}\|$ / s^{-1}
$(MoS_x)_{1000}$, 5 % surface coverage	**8.378×10^{-5}**	**0.303; 825**	**145**	**8.85×10^{-10}**	**4.21×10^{-9}**	**3616.6**	**0.5**	**3.0**
$(MoS_x)_{1000}$, 5 % surface coverage S evaporation	**8.378×10^{-5}**	**0.336; 652 (0.614;825)**	**154**	**2.82×10^{-8}**	**1.34×10^{-7}**	**4010.5 (7328.7)**	**110.5**	**3.3 (6.1)**
$(MoS_x)_{1000}$, 20 % surface coverage	**3.351×10^{-4}**	**0.328; 815**	**143**	**7.86×10^{-10}**	**9.4×10^{-10}**	**978.8**	**1.8**	**0.8**
$(MoS_x)_{1000}$, 20 % surface coverage S evaporation	**3.351×10^{-4}**	**0.349; 590 (0.556;815)**	**149**	**5.25×10^{-8}**	**6.24×10^{-8}**	**1041.5 (1659.2)**	**66.9**	**0.9 (1.4)**

Table F.2. Compilation of peak half maximum current density ($j_{half\ max}$), Tafel slope (b), exchange current density (j_0), normalized exchange current density ($j_{0,norm}$), mass activity and turnover frequency (TOF) values of the $(MoS_x)_{1000}$ nanoclusters samples evaluated. Values in parentheses correspond to HER metrics calculated at $|\eta_{half\ max}|$ values of as-deposited nanoclusters.

G. Electrochemical impedance spectroscopy of size-selected, sulfur enriched molybdenum sulfide nanoclusters: fitting parameters

Sample	η / mV	R_{sol}/ Ω	R_{ct}/ Ω	CPE_{ct}/ $F^{-1}s^{1-n}$		R_c / Ω	CPE_c/ $F^{-1}s^{1-n}$		CPE_{sol}/ $F^{-1}s^{1-n}$	
$(MoS_x)_{1000}$ 5% surface coverage	-1100	117.9	1239	8.9×10^{-6}	n: 0.93	4640	1.2×10^{-6}	n: 0.96	1.7×10^{-6}	n: 0.60
$(MoS_x)_{1000}$ 5% surface coverage S evaporation	-1100	89.1	1177	3.8×10^{-5}	n: 0.72	3252	1.0×10^{-6}	n:0.99	1.9×10^{-5}	n: 0.44
$(MoS_x)_{1000}$ 10% surface coverage	-1100	124.8	2162	1.3×10^{-5}	n: 0.92	31176	1.7×10^{-6}	n: 0.96	8.1×10^{-5}	n: 0.06
$(MoS_x)_{1000}$ 10% surface coverage S evaporation	-1100	121.2	1104	4.7×10^{-6}	n: 0.92	11437	2.3×10^{-6}	n :0.97	1.7×10^{-4}	n: 0.15
$(MoS_x)_{1000}$ 20% surface coverage	-1100	112.6	6064	2.0×10^{-5}	n: 0.80	12424	6.1×10^{-7}	n: 1.0	4.7×10^{-6}	n: 0.63
$(MoS_x)_{1000}$ 20% surface coverage S evaporation	-1100	81.8	836	9.2×10^{-4}	n: 0.71	6817	2.9×10^{-6}	n: 0.86	9.9×10^{-5}	n: 0.32

Table G.1. Fit parameters obtained for equivalent circuit model as seen in Figure 4.4 Chapter 4. EIS voltage acquisition: -1.1 V vs. SCE (ca. -0.7 V vs. NHE after Nernstian correction)

H. Literature compilation and comparison of HER performance: state-of-the-art pure MoS_2 and MoS_2-based (hybrid/supported) catalysts

Recent efforts in the literature have focused on producing MoS_2 catalysts which maximize the values of the commonly reported figures of merit: the turnover frequency (a.k.a. TOF, i.e. descriptor of the intrinsic activity per site of a catalyst) and the overpotential to achieve current densities of 10 mA cm^{-2} (i.e. a metric for the total electrode activity, based upon the 12.3% efficiency of an artificial photosynthesis device powered by a 0.1 W cm^{-2} average power of incident sunlight).[182,183]

The latter, however, is generally reported after normalization with the geometric electrode area, irrespectively of the catalyst loading or the electrochemically active surface area of the electrode (catalyst surface geometrically-accessible by the electrolyte, dependent on surface roughness). A recent report by McAteer et al.[184] corroborated that a linear correlation between HER current densities and MoS_2-modified electrode thicknesses was satisfied up to 5 microns. This implies, provided no electrolyte permeation and current collection problems arise, that the hydrogen production rate (and consequently the aforementioned figures of merit) can be boosted up by increasing the MoS_2 catalyst loading at the electrode surface.

Thus, we believe that a more appropriate figure of merit to compare the results reported in the literature is the current density (at a given overpotential or vice versa) normalized by the catalyst loading: the catalyst mass activity. This is a well-established metric for noble-metal based catalysts,[185,186] and provides unambiguous insight on the efficient catalyst utilization. Enclosed here is a list of some of the recently-reported MoS_2 catalysts, along with the relevant HER metrics to allow their comparison.

Catalyst	Catalyst loading / mg cm^{-2}	$\|\eta\|$ @ $\|j_{geom}\|$ = 10 mA cm^{-2} / mV	$\|j_{geom}\|$ @ $\|\eta\|$ = 200 mV / mA cm^{-2}	Tafel slope / mV dec^{-1}	Mass activity @ 10 mA cm^{-2} / mA mg^{-1}	Mass activity @ 200 mV / mA mg^{-1}	TOF (@ $\|\eta\|$) / s^{-1}	Ref.
High purity crystalline bulk 2H-MoS_2	**56.58 × 10^{-3}**	**770**	**ca. 0**	**175**	**176.74**	**n.a.**	**n.a.**	***187***
Bulk 3R-MoS_2	**56.58 × 10^{-3}**	**520**	**0.07**	**113**	**176.874**	**1.24**	**n.a.**	***188***
1T-MoS_2 nanosheets (Li intercalation)	**50 × 10^{-3}**	**ca. 200**	**ca. 10**	**41**	**200**	**200**	**n.a.**	***189***
1T-MoS_2 nanosheets (hydrothermal)	**43 × 10^{-3}**	**175**	**15**	**40**	**232.56**	**348.8**	**n.a.**	***190***
MoS_2 monolayer with S vacancies	**0.28**	**160**	**ca. 37.5**	**54.9**	**35.71**	**133.93**	**n.a.**	***191***
Vertically aligned 1T-MoS_2 nanosheets on 2H-MoS_2 nanosheets	**0.29**	**202**	**ca. 10**	**60**	**34.5**	**34.5**	**n.a.**	***192***
MoS_2 nanosheets with rich in-plane edges	**0.305 × 10^{-3}**	**167**	**ca. 28**	**41**	**32786.9**	**91803.3**	**n.a.**	***193***
Interlayer-expanded MoS_2 nanosheets	**0.28**	**149**	**ca. 50**	**49**	**35.7**	**178.6**	**1.14 (@200 mV)**	***194***
Defect-rich MoS_2 nanosheets (thiourea method)	**0.285**	**ca. 191**	**13**	**50**	**35.1**	**45.6**	**0.725 (@ 300 mV)**	***195***
Defect-rich MoS_2 nanosheets (microdomain method)	**0.285**	**ca. 195**	**ca. 11**	**68**	**35.1**	**38.6**	**0.08 (@ 150 mV)**	***196***

Table H.1. Compilation and comparison of HER performances for recently reported, state-of-the-art pure MoS_2 and MoS_2-based (hybrid/supported) catalysts[187,188,197–206,189,207–216,190,217–220,191–196]

Catalyst	Catalyst loading / mg cm^{-2}	$\|\eta\|$ @ $\|j_{geom}\|$ = 10 mA cm^{-2} / mV	$\|j_{geom}\|$ @ $\|\eta\|$ = 200 mV / mA cm^{-2}	Tafel slope / mV dec^{-1}	Mass activity @ 10 mA cm^{-2} / mA mg^{-1}	Mass activity @ 200 mV / mA mg^{-1}	TOF (@ $\|\eta\|$) / s^{-1}	Ref.
Mesoporous 1T-MoS_2 nanosheets	**0.14**	**153**	**ca. 60**	**43**	**71.4**	**428.6**	**0.5 (@153 mV)**	***197***
Oxygen-incorporated MoS_2 nanosheets	**0.285**	**175**	**ca. 17.5**	**55**	**35.1**	**61.4**	**n.a.**	***198***
Heterogeneous 1T/2H- MoS_2 nanosheets	**0.3368**	**220**	**ca. 4.8**	**61**	**29.7**	**14.2**	**n.a.**	***199***
Defect-rich MoS_2 nanowalls (200 nm thick)	**0.88**	**95**	**ca. 100**	**78**	**11.4**	**113.6**	**n.a.**	***200***
Sulfur-depleted MoS_2 nanocrystals	**16.97×10^{-3}**	**ca. 150**	**52.1**	**29**	**589.3**	**3071.9**	**n.a.**	***201***
Stepped-edge surface-terminated MoS_2 arrays	**3.2**	**104**	**ca. 150**	**59**	**3.1**	**46.9**	**1.51 (@ 200 mV)**	***202***
Polycrystalline MoS_2 thin film (CVD deposition)	**0.3**	**ca. 186**	**ca. 20**	**50-60**	**33.3**	**66.7**	**0.14×10^{-3} (@ 0 mV)**	***203***
Double-gyroid MoS_2 thin film (Electrodeposition + Sulfidization)	**60×10^{-3}**	**ca. 236**	**ca. 4.4**	**50**	**166.7**	**73.3**	**n.a.**	***204***
Edge-terminated MoS_2 thin film	**8.5×10^{-3}**	**n.a.**	**ca. 0.1**	**105-120**	**n.a.**	**12.9**	**0.013 (@ 0 mV)**	***205***

Table H.1. (Continued) Compilation and comparison of HER performances for recently reported, state-of-the-art pure MoS_2 and MoS_2-based (hybrid/supported) catalysts[187,188,197–206,189,207–216,190,217–220,191–196]

Catalyst	Catalyst loading / mg cm^{-2}	$\|\eta\|$ @ $\|j_{geom}\|$ = 10 mA cm^{-2} / mV	$\|j_{geom}\|$ @ $\|\eta\|$ = 200 mV / mA cm^{-2}	Tafel slope / mV dec^{-1}	Mass activity @ 10 mA cm^{-2} / mA mg^{-1}	Mass activity @ 200 mV / mA mg^{-1}	TOF (@ $\|\eta\|$) / s^{-1}	Ref.
Amorphous MoS_3 thin film (CVD deposition)	**0.3**	**ca. 160**	**>20**	**39**	**33.3**	**>66.7**	**0.01-0.03 × 10^{-3} (@ 0 mV)**	***203***
Amorphous MoS_3 thin film (Electrodeposition)	**45 × 10^{-3}**	**ca. 190**	**16.5**	**40**	**222.2**	**366.7**	**n.a.**	***206***
MoS2 nanoparticles on rGO	**0.28**	**ca. 150**	**>20**	**41**	**35.7**	**>71.4**	**n.a.**	***207***
MoS_2 nanosheets on hollow carbon spheres	**0.139**	**198**	**ca. 10**	**49.3**	**71.9**	**≥71.9**	**n.a.**	***208***
MoS_2 on mesoporous graphene	**0.21**	**n.a.**	**100**	**42**	**n.a.**	**476.2**	**n.a.**	***209***
Perpendicularly-grown MoS_2 nanosheets on graphene (@1600 rpm)	**0.204**	**172**	**17.5**	**43**	**49**	**85.8**	**n.a.**	***210***
4 layers-thick MoS_2 nanosheets @ ordered mesoporous carbon	**0.3**	**182**	**ca. 15**	**60**	**33.3**	**50**	**1.45 (@ 200 mV)**	***211***
MoS2 nanoparticles on carbon fiber paper	**3.4-3.9**	**100-115**	**200**	**62**	**2.9-2.6**	**58.8-51.3**	**0.1 (@ 200 mV)**	***212***
MoS2 nanosheets on carbon nanopaper	**0.875**	**80**	**ca. 88**	**41**	**11.4**	**100.7**	**n.a.**	***213***

Table H.1. (Continued) Compilation and comparison of HER performances for recently reported, state-of-the-art pure MoS_2 and MoS_2-based (hybrid/supported) catalysts[187,188,197–206,189,207–216,190,217–220,191–196]

Catalyst	Catalyst loading / mg cm^{-2}	$\|\eta\|$ @ $\|j_{geom}\|$ = 10 mA cm^{-2} / mV	$\|j_{geom}\|$ @ $\|\eta\|$ = 200 mV / mA cm^{-2}	Tafel slope / mV dec^{-1}	Mass activity @ 10 mA cm^{-2} / mA mg^{-1}	Mass activity @ 200 mV / mA mg^{-1}	TOF (@ $\|\eta\|$) / s^{-1}	Ref.
Defect/S-rich MoS_2 nanosheets @ N-doped carbon nanofibers	**0.217**	**135**	**65.6**	**48**	**46.1**	**302.2**	**n.a.**	***214***
MoS_2 nanosheets on porous carbon aerogel	**0.283**	**ca. 200**	**9.7**	**59**	**ca.35.3**	**35.3**	**n.a.**	***215***
Amorphous MoS_2 on G/CNTs hybrid	**3**	**141**	**182**	**41**	**3.3**	**60.7**	**0.14 (@ 200 mV)**	***216***
Sulfur-depleted MoS_2 nanocrystals on expanded GO	**0.202**	**100-150**	**231.5**	**38**	**49.41**	**1143.8**	**8.74 (@ 200 mV)**	***201***
MoS_2 nanosheets on conducting MoO_2	**0.3**	**200**	**10**	**35.6**	**33.3**	**33.3**	**n.a.**	***217***
Vertically aligned MoS_2/Mo_2C on carbon fiber cloth	**1.67**	**63**	**400**	**53**	**6**	**239.5**	**0.17 (@ 150 mV)**	***218***
$MoS_2/CoSe_2$ hybrid (@1600 rpm)	**0.28**	**68**	**75**	**36**	**35.7**	**267.9**	**n.a.**	***219***
MoS_2/black phosphorous hybrid	**0.102**	**85**	**ca. 50**	**68**	**98**	**490.2**	**n.a.**	***220***

Table H.1. (Continued) Compilation and comparison of HER performances for recently reported, state-of-the-art pure MoS_2 and MoS_2-based (hybrid/supported) catalysts[187,188,197–206,189,207–216,190,217–220,191–196]

I. Transition metal dichalcogenide nanoarrays

I.1 Elucidation of mass transport mechanism: peak current vs. square root of scan rate and transient chronoamperometry experiments

Calculation of theoretical $\log(j/A_{domain})$ vs. $\log(\tau)$ curves for Cases 1 and 4 was made based on the following steps.

Calculation of theoretical current expected from a planar electrode by using Cottrell equation:

$$I_{Cottrell} = \frac{zFAD_{H^+}^{1/2} C_{H^+,bulk}}{\pi^{1/2} t^{1/2}} \quad (Ap.9.1)$$

Where z stands for the number of electrons transferred in electrochemical reaction (for $H^+_{(aq)} + 1e^- \rightarrow 1/2\ H_{2(g)}$, n= 1), F for the Faraday constant (96485 C mol^{-1}), A for the geometric area (in cm^2), D_{H^+} for the proton diffusion coefficient ($D_{H^+} \approx 7.9 \times 10^{-5}\ cm^2\ s^{-1}$),[221] $C_{H^+,bulk}$ for the proton concentration in bulk solution (in this report $[H^+] \approx 2 \times 10^{-6}\ mols\ cm^{-3}$) and t for the experimental times recorded during the duration of the transient experiments.

For Case 4, A corresponds to the geometric area of the TMD crystal (A_{geom}). For Case 1, A accounts for the real surface area of the nanoarray, i.e. the nanocone surface area plus the basal surface located between the nanopillars ($A_{nanoc + basal\ plane}$).

The surface area of an individual nanocone was calculated applying the formula for the lateral surface area of a cone. Nanocone height (h_{nanoc}), radius (r_{nanoc}), and interspacing ($d_{interspacing}$) were determined experimentally (see Table 7.1 Chapter 7)

$$A_{nanoc} = \pi\, r_{nanoc}\sqrt{r_{nanoc}^2 + h_{nanoc}^2}\ (Ap\ 9.2)$$

The total surface area of the nanocones contained in the array was calculated by multiplying the number of nanocones which could be contained at the TMD crystal surface assuming a packing factor = 1, times the nanocone packing factor at the TMD surface:

$$A_{nanoc,tot} = A_{nanoc} * \frac{A_{geom}}{\pi r_{nanoc}^2} * \frac{\pi r_{nanoc}^2}{A_{unit\ cell}} = A_{nanoc} * \frac{A_{geom}}{A_{unit\ cell}}\ (Ap.9.3)$$

where

$$A_{unit\ cell} = \left(2\, r_{nanoc} + d_{interspacing}\right)^2\ (Ap.9.4)$$

The total area of the basal surface at the nanocone interstices is calculated with the following expression

$$A_{basal\ plane} = (A_{unit\ cell} - \pi\, r_{nanoc}^2) * \frac{A_{geom}}{A_{unit\ cell}}\ (Ap.9.5)$$

Finally, the total surface area of the nanoarray is obtained by summing the total nanocone and intersticial basal plane surface area:

$$A_{nanoc\,+\,basal\ plane} = A_{nanoc,tot} + A_{basal\ plane}\ (Ap.9.6)$$

Substitution of $I_{Cottrell}$ in the $\log\left(\frac{I}{2\pi zFCDr_{nanoc} * A_{domain}}\right)$ expression.

For both cases 1 and 4, $A_{domain} = \pi r_{domain}^2 = d^2$, d being the nanocone center-to-center distance in cm.

I.2 Elucidation of roughness factor by electrochemical capacitance measurements after solvent-phase electrochemical sulfidation

In order to estimate variations in the plasma-etched WS_2 samples roughness deriving from either the electro-oxidative step occurring during the sulfidation treatment or the HER electrochemical testing, we recorded cyclic voltammograms in the voltage region corresponding to non-faradaic processes arising from the charge/discharge of the electrical double layer (in this case, -0.2 V to 0.2 V vs. NHE).

In voltage sweep experiments, the double layer charging/discharging current I_C can be correlated with the electrochemically active surface area (A_{ECSA}) by the following equation[222]:

$$|I_C| = \nu_{scan} * C_{dl} * A_{ECSA} \quad (Ap.9.7)$$

Thus, a simple linear regression of the I_C values obtained at different scan rates enables to estimate A_{ECSA}, dependent on the inherent capacitance of the surface. If the same experiments are performed to a geometrically flat surface of the same material, the ratio $|I_C|/|I_{C,flat}|$ would enable to estimate a true roughness factor

$$Rf = A_{ECSA}/A_{geom} \quad (Ap.9.8)$$

However, as we do not possess a perfectly flat WS_2 electrode standard to compare the $|I_C|$ values to, we opted to plot the charging/discharging current density $|j_C| = |I_C|/A_{geom}$ vs. the scan rate ν_{scan}. This will enable us to obtain the electrical double layer capacitance values C_{dl} (in $\mu F\ cm^{-2}_{geom}$) for the pre-sulfidated, post-sulfidated, 8-day atmosphere exposed, 15-day

atmosphere exposed and 22-day atmosphere exposed samples. The ratio of all C_{dl} values vs. the C_{dl} value obtained for the pre-sulfidated sample will lead to a relative roughness factor (Rf), which will enable us to account for modifications in the real surface area along the duration of the sulfidation experiments.

$$Rf = \frac{A_{ECSA}}{A_{ECSA,\ pre-sulfidated}} \quad (Ap.9.9)$$

WS_2	SF_6/C_4F_8 plasma etching time / s		Pre-sulfidated	Day 1	Day 8	Day 15	Day 22
	31 ± 1	Double layer electrochemical capacitance C_{dl} / $\mu F\ cm^{-2}_{geom}$	5695	4800	3185	2710	3480
		Relative roughness factor	1	0.84	0.56	0.48	0.61
	61 ± 1	Double layer electrochemical capacitance C_{dl} / $\mu F\ cm^{-2}_{geom}$	1710	2455	2335	1555	1900
		Relative roughness factor	1	1.44	1.37	0.91	1.12

Table I.1. Compilation of C_{dl} and Rf values for 31 ± 1 s (R= 2, Z= 6.4) and 61 ± 1 s atmospherically aged, sulfidation treated, plasma-etched WS_2 samples after weekly electrochemical testing over a three week ambient exposure period

J. AE-MoS_x Raman mode values: compilation before/after electrochemical preconditioning

	Raman shift / cm^{-1}													
Sample	$v\ (Mo-Mo)$			$v\ (Mo-S)$				E^1_{2g}	A_{1g}	$v\ (Mo_3-\mu S)$	$v\ (S-S)_t$,weak	$v\ (S-S)_t$	$v\ (S-S)_{br}$	$v\ (Mo=O)$
As-received	155	201	225	287	325		358	382	405	447		516	555	
pH 0	151	201	227	306	325		361	381	408	449	493	519		
pH 1	155	191	234	286	325		359	383		450		519	552	
pH 2	155	193	232	286	327		358	382		452		518	555	
pH 3	155	200	225	287	325	341	355	380	405	453	492	517	555	
pH 4	155	195	230	285	324		357	380	405	452		517	55	
pH 5	155	198	225	291	325		354	378	404	450		517	552	730
pH 6	155	199	225	291	324	341	355	380	404	452	490	514	553	730
pH 7	155	199	226	285	324		355	380	405	455	492	516	553	734
pH 8	153	200	225	285	325	341	355	380	404	452	490	520	555	730
pH 9	155	200	224	289	325	341	355	380	404	451	490	517	553	732
pH 10	155	199	224	291	325		355	378	404	452	490	515	553	730

Table J.1. Compilation of the characteristic Raman mode values found for pristine and electro-oxidized AE-MoS_x thin films across the 0-10 pH range, shown in Figure 9.12.

	Raman shift / cm^{-1}											
Sample	$\nu\ (Mo-Mo)$			$\nu\ (Mo-S)$			E^1_{2g}	A_{1g}	$\nu\ (Mo_3-\mu S)$	$\nu\ (S-S)_t$,weak	$\nu\ (S-S)_t$	$\nu\ (S-S)_{br}$
As-received	**155**	**202**	**225**	**287**	**325**	**358**	**382**	**405**	**447**		**516**	**555**
pH 0	**156**	**203**	**251**		**339**		**394**		**438**	**494**		**566**
pH 1	**154**	**195**	**233**	**289**	**327**	**357**	**383**	**407**	**435**		**520**	**555**
pH 2	**153**	**202**	**236**	**291**	**330**	**358**	**378**	**405**	**435**	**483**	**514**	**555**
pH 3	**155**	**199**	**235**	**291**		**357**		**407**	**449**		**520**	**553**
pH 4	**156**	**204**	**229**	**291**	**328**	**357**	**382**	**408**	**454**		**516**	**555**
pH 5	**155**	**200**	**230**	**287**	**329**	**358**	**381**	**402**	**446**	**491**	**517**	**550**
pH 6	**156**	**195**	**234**	**285**	**326**	**358**	**380**		**447**		**514**	**550**
pH 7	**156**	**199**	**238**	**288**	**333**	**361**	**387**	**408**	**453**	**489**	**520**	**556**
pH 8	**155**	**196**	**243**	**291**	**330**	**359**	**382**		**448**		**521**	**556**
pH 9	**152**	**200**	**226**	**285**	**325**	**357**	**380**	**404**	**453**		**515**	**552**
pH 10	**155**	**195**	**232**	**287**	**329**	**360**	**383**		**454**		**517**	**555**

Table J.2. Compilation of the characteristic Raman mode values found for pristine and AE-MoS_x thin films electrochemically conditioned by oxidative-reductive cycling across the 0-10 pH range, shown in Figure 9.19a.

	Raman shift / cm^{-1}											
Sample	$\nu\ (Mo-Mo)$			$\nu\ (Mo-S)$			E^1_{2g}	A_{1g}	$\nu\ (Mo_3-\mu S)$	$\nu\ (S-S)_t$,weak	$\nu\ (S-S)_t$	$\nu\ (S-S)_{br}$
As-received	**155**	**202**	**225**	**287**	**325**	**358**	**382**	**405**	**447**		**516**	**555**
pH 0	**156**	**199**	**243**	**298**	**337**	**358**	**385**		**438**	**490**		**561**
pH 1	**153**	**202**	**236**	**291**	**330**	**355**	**378**	**407**	**435**	**486**	**514**	**555**
pH 2	**155**	**197**	**230**	**287**	**327**	**358**	**380**	**404**	**448**		**518**	**555**
pH 3	**154**	**195**	**230**	**287**	**325**	**357**	**377**	**404**	**445**		**517**	**551**
pH 4	**155**	**200**	**225**	**295**		**357**	**377**	**407**	**435**	**492**		**561**
pH 5	**152**	**200**	**226**	**291**	**330**	**360**	**380**	**405**	**445**	**492**	**519**	**556**
pH 6	**156**	**200**	**226**	**285**	**328**	**358**	**380**	**405**	**454**	**492**	**520**	**551**
pH 7	**156**	**200**	**244**	**297**	**324**	**359**	**386**	**407**	**441**		**520**	**560**
pH 8	**155**	**193**	**230**	**287**	**325**	**355**	**380**		**449**		**515**	**5450**
pH 9	**155**	**203**	**254**	**284**	**315**	**360**		**416**		**469**		
pH 10	**155**	**195**	**235**	**289**	**329**	**359**	**383**		**449**		**517**	**555**

Table J.3. Compilation of the characteristic Raman mode values found for pristine and AE-MoS_x thin films electrochemically conditioned by reductive cycling across the 0-10 pH range, shown in Figure 9.19b.

	Raman shift / cm^{-1}										
Sample	$v\ (Mo-Mo)$			$v\ (Mo-S)$			E^1_{2g}	A_{1g}	$v\ (Mo_3-\mu S)$	$v\ (S-S)_t$	$v\ (S-S)_{br}$
As-received	**155**	**202**	**225**	**287**	**325**	**358**	**382**	**405**	**447**	**516**	**555**
pH 0	**156**	**204**	**229**	**290**	**328**	**357**	**382**	**408**	**454**	**516**	**550**
pH 1	**156**	**197**	**236**	**287**	**328**	**358**	**383**	**407**	**435**	**520**	**558**
pH 2	**156**	**195**	**229**	**284**	**326**	**357**	**380**	**405**	**449**	**517**	**553**
pH 3	**153**	**199**	**233**	**289**	**328**	**355**	**380**	**404**	**446**	**520**	**555**
pH 4	**156**	**194**	**232**	**290**	**328**	**358**	**383**		**457**	**520**	**555**
pH 5	**155**	**193**	**233**	**286**	**324**	**357**	**381**		**450**	**518**	**551**
pH 6	**155**	**195**	**244**	**291**	**331**	**357**	**383**	**403**	**452**	**517**	**557**
pH 7	**155**	**200**	**227**	**286**	**329**	**357**	**381**	**405**	**452**	**515**	**553**
pH 8	**153**	**199**	**240**	**288**	**334**	**358**	**381**	**403**	**458**	**521**	**555**
pH 9	**155**	**199**	**229**	**288**	**327**	**356**	**380**	**404**	**452**	**517**	**551**
pH 10	**156**	**195**	**232**	**287**	**326**	**359**	**382**	**404**	**452**	**516**	**553**

Table J.4. Compilation of the characteristic Raman mode values found for pristine and AE-MoS_x thin films electrochemically conditioned by electro-oxidative cycling across the 0-10 pH range, shown in Figure 9.20

K. Tungsten sulfide-decorated iridium electrodes

K.1 Elucidation of OER normalized metrics: mass and specific activity

Normalization of oxygen evolution metrics is paramount in order to compare experimental results with those reported in the literature. Although catalyst preparation technique, electrochemical setup and testing conditions play a role, both catalyst loading and electrochemically active surface area (ECSA) are parameters which can be experimentally elucidated and give insight into mass and surface-dependent properties of the electrocatalysts.

K.1.1 Mass activity calculation

Mass activity measurements are generally reported in $A\,mg_M^{-1}$, mg_M being the mass (in mg) of the electrocatalyst tested. This metric is especially useful in nanoparticle electrocatalysis, as nanocatalysts are generally tested by drop-casting of a liquid suspension onto a conductive electrode. Homogeneous, high-quality nanocatalyst films will present higher mass activities than poorly deposited films for a given catalyst loading, and vice versa, due to lower working electrode coverages and nanoparticle agglomeration effects.[186,223,224] In our present work, we employ thermally deposited Ir thin film electrodes, with an average thickness of 100 nm (1 $\times$ 10^{-5} cm) as provided by the manufacturer. Iridium mass loading onto the electrodes, m_{Ir}, can be elucidated if the geometrical electrode area (A_{geom}, in cm^2) and the density of polycrystalline Ir ($\rho_{Ir} = 22.5622\ g\ cm^{-3}$) are employed:

$$m_{Ir}\,(g) = A_{geom} * 1 \times 10^{-5}\ cm * 22.5622\ g\ cm^{-3}\ (Ap.11.1)$$

where A_{geom} is experimentally obtained by contour calculation of electrode images using the software ImageJ after pixel ratio calibration.

Next, the electrochemical active surface area (ECSA) of the Si/Cr/Ir electrodes is evaluated by integrating the charge underneath the anodic sweep voltammogram region acquired from 0.025 to 0.55 V vs. RHE, in particular in the region from 0.06 to ca. 0.4 V vs. RHE. This corresponds to the voltage window under which full electrochemical desorption of a monoatomic hydrogen monolayer, previously adsorbed by hydrogen underpotential deposition (H_{UPD}), takes place. Studies on Ir (and other platinum group metal) single crystals have accurately correlated hydrogen coverages with Ir atom population density at the outermost surface.[225–228] For polycrystalline Ir (where no crystallographic plane is preferentially exposed), this charge is estimated to be $Q_{Ir,poly} = 179\ \mu C\ cm^{-2}$.[229,230] Thus, normalization of the integrated hydrogen desorption charge ($Q_{H,des}$, in C) at a given scan rate ν_{scan} (in V s^{-1}) versus that expected for a full monoatomic hydrogen monolayer will enable to estimate the electrochemically active Ir surface sites in our electrodes of interest. The ECSA is estimated with the following formula

$$ECSA\ (cm^2 g^{-1}) = \frac{Q_{H,des}/\nu_{scan}}{Q_{Ir,poly} * m_{Ir}} \quad (Ap.11.2)$$

Finally, the mass activity can be calculated at a given OER overpotential using the following expression

$$Mass\ activity\ (A\ mg_{Ir}^{-1}) = \frac{ECSA * j_{geom}\ (A\ cm_{geom}^{-2})}{1000} \quad (Ap.11.3)$$

K.1.2 Specific activity calculation

Elucidation of specific activities on Si/Cr/Ir electrodes for the OER, reported here as $A\ cm_{Ir}^{-2}$, will mirror the methodology recently reported by McCrory et al.,[231] employed with success for Ir catalysts. This methodology, however, is reported as a guideline to compare relative modifications in specific activities rather than absolute values of OER turnover frequencies:

highly-porous surfaces will present mass transport limitations, which yield underestimated values with this methodology.

Firstly, an experimental roughness factor (R_f) is calculated by normalizing the ECSA (calculated without accounting for Ir loading) with the geometric electrode area

$$R_f\left(cm_{Ir}^2\ cm_{geom}^{-2}\right) = \frac{Q_{H,des}/Q_{Ir,poly}}{A_{geom}} \quad (Ap.11.4)$$

Finally, the specific activity (also known as specific geometric current density) is obtained by normalizing the geometric current density at a given OER overpotential by R_f

$$j_{specific}(A\ cm_{Ir}^{-2}) = \frac{j_{geom}\left(A\ cm_{geom}^{-2}\right)}{R_f} \quad (Ap.11.5)$$

Sample	E_{OER,t_0} / V	E_{OER,t_f} / V	ΔE_{OER}/ V	@ 1.51 V			@ 1.55 V		
				j_{geom} / mA cm^{-2}	Mass activity / A mg_{Ir}^{-1}	Specific activity / A cm_{Ir}^{-2}	j_{geom} / mA cm^{-2}	Mass activity / A mg_{Ir}^{-1}	Specific activity / A cm_{Ir}^{-2}
As-received Ir	1.670 ± 0.005	1.729 ± 0.005	0.059 ± 0.008	0.23 ± 0.03 0.80 ± 0.03	0.040 ± 0.02 0.31 ± 0.04	$6.68 \pm 2.5 \times 10^{-6}$ $9.42 \pm 0.6 \times 10^{-6}$	1.70 ± 0.2 4.90 ± 0.5	0.30 ± 0.2 1.90 ± 0.3	$5.01 \pm 1.9 \times 10^{-5}$ $5.71 \pm 0.1 \times 10^{-5}$
±500 µA, 1000 ms, 10 mins	1.690 ± 0.007	1.73300 ± 0.00005	0.043	0.15 1.09	0.041 0.378	2.44×10^{-6} 1.39×10^{-5}	1.14 6.34	0.310 2.197	1.86×10^{-5} 8.11×10^{-5}
±500 µA, 1000 ms, 5 mins	1.668 ± 0.005	1.72220 ± 0.00005	0.054	0.16 1.02	0.032 0.320	3.30×10^{-6} 1.44×10^{-5}	1.24 6.40	0.259 2.006	2.64×10^{-5} 9.05×10^{-5}
±500 µA, 1000 ms, 2.5 mins	1.672 ± 0.006	1.73695 ± 0.00006	0.065	0.23 0.90	0.065 0.324	3.52×10^{-6} 1.11×10^{-5}	1.60 5.07	0.459 1.820	2.47×10^{-5} 6.26×10^{-5}
±500 µA, 1000 ms, 1 min	1.696 ± 0.006	1.75039 ± 0.00004	0.054	0.11 0.88	0.030 0.337	1.62×10^{-6} 1.02×10^{-5}	0.83 4.87	0.237 1.868	1.28×10^{-5} 5.63×10^{-5}
±500 µA, 250 ms, 10 mins	1.678± 0.006	1.7454 ± 0.0001	0.067	0.02 1.01	0.006 0.283	4.39×10^{-7} 1.60×10^{-5}	0.2 5.44	0.048 1.522	3.75×10^{-6} 8.62×10^{-5}
±500 µA, 250 ms, 5 mins	1.678 ± 0.005	1.73048 ± 0.00004	0.053	0.20 1.14	0.0298 0.328	6.12×10^{-6} 1.75×10^{-5}	1.43 6.71	0.210 1.934	4.32×10^{-5} 1.03×10^{-4}
±500 µA, 250 ms, 2.5 mins	1.683 ± 0.006	1.73256 ± 0.00005	0.050	0.21 1.54	0.057 0.589	3.35×10^{-6} 1.79×10^{-5}	1.5 7.59	0.413 2.902	2.42×10^{-5} 8.80×10^{-5}
±500 µA, 250 ms, 1 min	1.707 ± 0.005	1.74462 ± 0.00007	0.038	0.28 1.59	0.062 0.643	5.60×10^{-6} 1.74×10^{-5}	1.87 7.52	0.416 3.040	3.73×10^{-5} 8.25×10^{-5}
±500 µA, 62.5 ms, 10 mins	1.681 ± 0.006	1.7367 ± 0.0004	0.056	0.19 1.52	0.058 0.611	2.67×10^{-6} 1.68×10^{-5}	1.35 7.33	0.418 2.945	1.93×10^{-5} 8.09×10^{-5}
±500 µA, 62.5 ms, 5 mins	1.679 ± 0.006	1.7359 ± 0.0002	0.057	0.24 1.7	0.077 0.705	3.42×10^{-6} 1.82×10^{-5}	1.65 -	0.521 -	2.31×10^{-5} -
±500 µA, 62.5 ms, 2.5 mins	1.688 ± 0.006	1.814 ± 0.001	0.126	0.14 1.17	0.034 0.359	2.39×10^{-6} 1.69×10^{-5}	0.97 5.86	0.245 1.796	1.70×10^{-5} 8.47×10^{-5}
±500 µA, 62.5 ms, 1 min	1.682 ± 0.006	1.73538 ± 0.00005	0.053	0.15 0.88	0.045 0.327	2.34×10^{-6} 1.04×10^{-5}	1.20 5.0	0.348 1.864	1.83×10^{-5} 5.94×10^{-5}

Table K.1. Compilation of the short-duty oxygen evolution activity of WS_{3-x} decorated Ir electrodes after use of ±500 µA pulse reverse current electrodeposition at variable pulse timescales and total experiment durations. E_{OER,t_0}, E_{OER,t_f} and ΔE_{OER} correspond to the averaged (± 10 s) initial, final and variation, respectively, of the OER overpotentials recorded to sustain j_{geom}= +10 mA cm^{-2} for 2 h. OER activity metrics are reported, for each sample, before (first row) and after (second row) short-duty OER stability measurements.

Sample	E_{OER,t_0} / V	E_{OER,t_f} / V	ΔE_{OER}/ V	@ 1.51 V			@ 1.55 V		
				j_{geom} / mA cm^{-2}	Mass activity / A mg$_{Ir}^{-1}$	Specific activity / A cm$_{Ir}^{-2}$	j_{geom} / mA cm^{-2}	Mass activity / A mg$_{Ir}^{-1}$	Specific activity / A cm$_{Ir}^{-2}$
As-received Ir	1.670 ± 0.005	1.729 ± 0.005	0.059 ± 0.008	0.23 ± 0.03 0.80 ± 0.03	0.040 ± 0.02 0.31 ± 0.04	6.68 ± 2.5 × 10^{-6} 9.42 ± 0.6 × 10^{-6}	1.70 ± 0.2 4.90 ± 0.5	0.30 ± 0.2 1.90 ± 0.3	5.01 ± 1.9 × 10^{-5} 5.71 ± 0.1 × 10^{-5}
±700 µA, 1000 ms, 10 mins	1.682 ± 0.006	1.72205 ± 0.00004	0.040	1.46 2.08	0.422 0.731	2.24 × 10^{-5} 2.62 × 10^{-5}	- -	- (>1.194) - (>2.02)	- (>6.33 × 10^{-5}) - (>7.26 × 10^{-5})
±700 µA, 1000 ms, 5 mins	1.686 ± 0.006	1.73661 ± 0.00003	0.051	0.18 1.18	0.057 0.451	2.50 × 10^{-6} 1.37 × 10^{-5}	1.33 6.69	0.422 2.558	1.86 × 10^{-5} 7.76 × 10^{-5}
±700 µA, 1000 ms, 2.5 mins	1.687 ± 0.006	1.74797 ± 0.00003	0.061	0.21 0.94	0.061 0.331	3.32 × 10^{-6} 1.19 × 10^{-5}	1.52 5.57	0.433 1.950	2.37 × 10^{-5} 7.05 × 10^{-5}
±700 µA, 1000 ms, 1 min	1.675 ± 0.007	1.87766 ± 0.00006	0.203	0.15 0.79	0.040 0.269	2.61 × 10^{-6} 1.04 × 10^{-5}	1.15 3.41	0.298 1.154	1.97 × 10^{-5} 4.47 × 10^{-5}
±700 µA, 250 ms, 10 mins	1.668 ± 0.006	1.73993 ± 0.00006	0.072	0.28 1.38	0.091 0.564	3.86 × 10^{-6} 1.50 × 10^{-5}	1.8 6.88	0.581 2.812	2.47 × 10^{-5} 7.46 × 10^{-5}
±700 µA, 250 ms, 5 mins	1.249 ± 0.006	1.7420 ± 0.0001	0.493	0.42 1.29	0.135 0.500	5.78 × 10^{-6} 1.48 × 10^{-5}	2.8 6.69	0.900 2.592	3.86 × 10^{-5} 7.65 × 10^{-5}
±700 µA, 250 ms, 2.5 mins	1.683 ± 0.006	1.7347 ± 0.0001	0.052	0.18 1.44	0.052 0.568	2.73 × 10^{-6} 1.62 × 10^{-5}	1.24 7.12	0.360 2.809	1.89 × 10^{-5} 8.00 × 10^{-5}
±700 µA, 250 ms, 1 min	1.672 ± 0.006	1.7403 ± 0.0001	0.068	0.45 1.5	0.155 0.612	5.80 × 10^{-6} 1.63 × 10^{-5}	2.81 7.31	0.968 2.981	3.61 × 10^{-5} 7.94 × 10^{-5}
±700 µA, 62.5 ms, 10 mins	1.690 ± 0.006	1.73811 ± 0.00006	0.048	0.19 1.36	0.050 0.528	3.32 × 10^{-6} 1.55 × 10^{-5}	1.35 7.0	0.348 2.716	2.32 × 10^{-5} 8.00 × 10^{-5}
±700 µA, 62.5 ms, 5 mins	1.679 ± 0.006	1.7394 ± 0.0002	0.060	0.23 1.1	0.078 0.461	2.88 × 10^{-6} 1.16 × 10^{-5}	1.65 6.0	0.573 2.512	2.11 × 10^{-5} 6.35 × 10^{-5}
±700 µA, 62.5 ms, 2.5 mins	1.677 ± 0.006	1.7278 ± 0.0004	0.051	0.19 1.42	0.053 0.526	2.96 × 10^{-6} 1.70 × 10^{-5}	1.35 7.33	0.381 2.713	2.12 × 10^{-5} 8.78 × 10^{-5}
±700 µA, 62.5 ms, 1 min	1.678 ± 0.006	1.73538 ± 0.00006	0.057	0.17 0.87	0.036 0.309	3.51 × 10^{-6} 1.07 × 10^{-5}	1.31 5.09	0.281 1.821	2.70 × 10^{-5} 6.30 × 10^{-5}

Table K.2. Compilation of the short-duty oxygen evolution activity of WS_{3-x} decorated Ir electrodes after use of ±700 µA pulse reverse current electrodeposition at variable pulse timescales and total experiment durations. E_{OER,t_0}, E_{OER,t_f} and ΔE_{OER} correspond to the averaged (± 10 s) initial, final and relative variation, respectively, of the OER overpotentials recorded to sustain j_{geom}= +10 mA cm^{-2} for 2 h. OER activity metrics are reported, for each sample, before (first row) and after (second row) short-duty OER stability measurements.

Sample	E_{OER,t_0} / V	E_{OER,t_f} / V	ΔE_{OER}/ V	1.51 V			1.55 V		
				j_{geom} / mA cm^{-2}	Mass activity / A mg_{Ir}^{-1}	Specific activity / A cm_{Ir}^{-2}	j_{geom} / mA cm^{-2}	Mass activity / A mg_{Ir}^{-1}	Specific activity / A cm_{Ir}^{-2}
As-received Ir	1.670 ± 0.005	1.729 ± 0.005	0.059 ± 0.008	0.23 ± 0.03 0.80 ± 0.03	0.040 ± 0.02 0.31 ± 0.04	$6.68 \pm 2.5 \times 10^{-6}$ $9.42 \pm 0.6 \times 10^{-6}$	1.70 ± 0.2 4.90 ± 0.5	0.30 ± 0.2 1.90 ± 0.3	$5.01 \pm 1.9 \times 10^{-5}$ $5.71 \pm 0.1 \times 10^{-5}$
±900 µA, 1000 ms, 10 mins	1.667 ± 0.006	1.72343 ± 0.00004	0.056	0.29 1.28	0.075 0.418	4.83×10^{-6} 1.74×10^{-5}	2.12 7.57	0.556 2.471	3.58×10^{-5} 1.03×10^{-4}
±900 µA, 1000 ms, 5 mins	1.680 ± 0.006	1.74086 ± 0.00005	0.061	0.22 1.01	0.048 0.318	4.58×10^{-6} 1.42×10^{-5}	1.64 5.38	0.354 1.696	3.37×10^{-5} 7.56×10^{-5}
±900 µA, 1000 ms, 2.5 mins	1.677 ± 0.006	1.74043 ± 0.00004	0.063	0.29 0.82	0.086 0.234	4.37×10^{-6} 1.27×10^{-5}	2.11 4.87	0.621 1.394	3.18×10^{-5} 7.54×10^{-5}
±900 µA, 1000 ms, 1 min	0.926 ± 0.004	1.74443 ± 0.00004	0.818	0.14 0.93	0.04 0.349	2.11×10^{-6} 1.09×10^{-5}	0.97 5.24	0.281 1.972	1.49×10^{-5} 6.17×10^{-5}
±900 µA, 250 ms, 10 mins	1.670 ± 0.006	1.7430 ± 0.0001	0.073	0.16 1.18	0.029 0.423	4.08×10^{-6} 1.46×10^{-5}	1.17 6.17	0.207 2.209	2.93×10^{-5} 7.64×10^{-5}
±900 µA, 250 ms, 5 mins	1.669 ± 0.005	1.73295 ± 0.00009	0.064	0.43 1.5	0.135 0.543	6.05×10^{-6} 1.84×10^{-5}	2.67 7.95	0.839 2.879	3.7674×10^{-5} 9.73163×10^{-5}
±900 µA, 250 ms, 2.5 mins	1.693 ± 0.004	1.75302 ± 0.00007	0.060	0.33 1.52	0.068 0.514	7.10×10^{-6} 1.99×10^{-5}	2.24 7.54	0.462 2.548	4.81×10^{-5} 9.89×10^{-5}
±900 µA, 250 ms, 1 min	1.670 ± 0.006	1.7241 ± 0.0001	0.054	0.35 1.42	0.104 0.593	5.25×10^{-6} 1.5×10^{-5}	2.53 7.43	0.749 3.102	3.79×10^{-5} 7.89×10^{-5}
±900 µA, 62.5 ms, 10 mins	1.673 ± 0.006	1.7369 ± 0.0001	0.064	0.33 1.31	0.108 0.517	4.45×10^{-6} 1.47×10^{-5}	2.18 6.69	0.715 2.639	2.95×10^{-5} 7.52×10^{-5}
±900 µA, 62.5 ms, 5 mins	1.20 ± 0.3	1.7279 ± 0.0001	0.528	0.31 1.23	0.100 0.477	4.25×10^{-6} 1.41×10^{-5}	2.24 6.57	0.724 2.546	3.07×10^{-5} 7.52×10^{-5}
±900 µA, 62.5 ms, 2.5 mins	1.688 ± 0.006	1.74375 ± 0.00005	0.056	0.16 0.90	0.049 0.355	2.31×10^{-6} 1.02×10^{-5}	1.24 5.21	0.379 2.051	1.80×10^{-5} 5.87×10^{-5}
±900 µA, 62.5 ms, 1 min	1.691 ± 0.006	1.7403± 0.0001	0.049	0.15 0.83	0.037 0.292	2.63×10^{-6} 1.05×10^{-5}	1.21 4.74	0.303 1.666	2.14×10^{-5} 5.98×10^{-5}

Table K.3. Compilation of the short-duty oxygen evolution activity of WS_{3-x} decorated Ir electrodes after use of ±700 µA pulse reverse current electrodeposition at variable pulse timescales and total experiment durations. E_{OER,t_0}, E_{OER,t_f} and ΔE_{OER} correspond to the averaged (± 10 s) initial, final and relative variation, respectively, of the OER overpotentials recorded to sustain j_{geom}= +10 mA cm^{-2} for 2 h. OER activity metrics are reported, for each sample, before (first row) and after (second row) short-duty OER stability measurements.

References

[1] C. Philibert, Renewable Energy for Industry. From green energy to green materials and fuels, Int. Energy Agency. (2017) 72. doi:10.1111/j.1365-2990.2010.01130.x.

[2] T. da Silva Veras, T.S. Mozer, D. da Costa Rubim Messeder dos Santos, A. da Silva César, Hydrogen: Trends, production and characterization of the main process worldwide, Int. J. Hydrogen Energy. 42 (2017) 2018–2033. doi:10.1016/j.ijhydene.2016.08.219.

[3] S. Sharma, S.K. Ghoshal, Hydrogen the future transportation fuel: From production to applications, Renew. Sustain. Energy Rev. 43 (2015) 1151–1158. doi:10.1016/j.rser.2014.11.093.

[4] A.M. Abdalla, S. Hossain, O.B. Nisfindy, A.T. Azad, M. Dawood, A.K. Azad, Hydrogen production, storage, transportation and key challenges with applications: A review, Energy Convers. Manag. 165 (2018) 602–627. doi:10.1016/j.enconman.2018.03.088.

[5] J.D. Holladay, J. Hu, D.L. King, Y. Wang, An overview of hydrogen production technologies, Catal. Today. 139 (2009) 244–260. doi:10.1016/j.cattod.2008.08.039.

[6] M.N. Manage, D. Hodgson, N. Milligan, S.J.R. Simons, D.J.L. Brett, A techno-economic appraisal of hydrogen generation and the case for solid oxide electrolyser cells, Int. J. Hydrogen Energy. 36 (2011) 5782–5796. doi:10.1016/j.ijhydene.2011.01.075.

[7] Options for producing low-carbon hydrogen at scale: Policy Briefing, 2018.

[8] K. Stamatelatou, G. Antonopoulou, P. Michailides, Biomethane and biohydrogen production via anaerobic digestion/fermentation, Woodhead Publishing Limited, 2014. doi:10.1533/9780857097385.2.476.

[9] M. Ni, D.Y.C. Leung, M.K.H. Leung, K. Sumathy, An overview of hydrogen production from biomass, Fuel Process. Technol. 87 (2006) 461–472. doi:10.1016/j.fuproc.2005.11.003.

[10] K.L. Kovács, G. Maróti, G. Rákhely, A novel approach for biohydrogen production, Int. J. Hydrogen Energy. 31 (2006) 1460–1468. doi:10.1016/j.ijhydene.2006.06.011.

[11] A.J. Stephen, S.A. Archer, R.L. Orozco, L.E. Macaskie, Advances and bottlenecks in microbial hydrogen production, Microb. Biotechnol. 10 (2017) 1120–1127. doi:10.1111/1751-7915.12790.

[12] E.W.J. Van Niel, P.A.M. Claassen, A.J.M. Stams, Substrate and product inhibition of hydrogen production by the extreme thermophile, Caldicellulosiruptor saccharolyticus, Biotechnol. Bioeng. 81 (2003) 255–262. doi:10.1002/bit.10463.

[13] P.C. Hallenbeck, D. Ghosh, Advances in fermentative biohydrogen production: the way forward?, Trends Biotechnol. 27 (2009) 287–297. doi:10.1016/j.tibtech.2009.02.004.

[14] P. Nikolaidis, A. Poullikkas, A comparative overview of hydrogen production processes, Renew. Sustain. Energy Rev. 67 (2017) 597–611. doi:10.1016/j.rser.2016.09.044.

[15] S.Z. Baykara, Hydrogen: A brief overview on its sources, production and environmental impact, Int. J. Hydrogen Energy. 43 (2018) 10605–10614. doi:10.1016/j.ijhydene.2018.02.022.

[16] P. Mathias, 68th Annual Meeting of the Society of Chemical Engineers, Tokyo, 2003.

[17] M.F. Orhan, I. Dincer, M.A. Rosen, Energy and exergy assessments of the hydrogen production step of a copper-chlorine thermochemical water splitting cycle driven by nuclear-based heat, Int. J. Hydrogen Energy. 33 (2008) 6456–6466. doi:10.1016/j.ijhydene.2008.08.035.

[18] S. Abanades, P. Charvin, F. Lemont, G. Flamant, Novel two-step SnO2/SnO water-splitting cycle for solar thermochemical production of hydrogen, Int. J. Hydrogen Energy. 33 (2008) 6021–6030. doi:10.1016/j.ijhydene.2008.05.042.

[19] M. Velický, P.S. Toth, From two-dimensional materials to their heterostructures: An electrochemist's perspective, Appl. Mater. Today. 8 (2017) 68–103. doi:10.1016/j.apmt.2017.05.003.

[20] Q.H. Wang, K. Kalantar-Zadeh, A. Kis, J.N. Coleman, M.S. Strano, Electronics and optoelectronics of two-dimensional transition metal dichalcogenides, Nat. Nanotechnol. 7 (2012) 699–712. doi:10.1038/nnano.2012.193.

[21] M. Chhowalla, H.S. Shin, G. Eda, L.J. Li, K.P. Loh, H. Zhang, The chemistry of two-dimensional layered transition metal dichalcogenide nanosheets, Nat. Chem. 5 (2013) 263–275. doi:10.1038/nchem.1589.

[22] W. Zhao, J. Pan, Y. Fang, X. Che, D. Wang, K. Bu, F. Huang, Metastable MoS2: Crystal Structure, Electronic Band Structure, Synthetic Approach and Intriguing Physical Properties, Chem. - A Eur. J. 24 (2018) 15942–15954. doi:10.1002/chem.201801018.

[23] Vincenzo Grasso, Electronic Structure and Electronic Transitions in Layered Materials, 1st ed., Springer Science, 1986. doi:10.1007/978-94-009-4542-5.

[24] A. Splendiani, L. Sun, Y. Zhang, T. Li, J. Kim, C.Y. Chim, G. Galli, F. Wang, Emerging photoluminescence in monolayer MoS2, Nano Lett. 10 (2010) 1271–1275. doi:10.1021/nl903868w.

[25] D. Voiry, A. Mohite, M. Chhowalla, Phase engineering of transition metal dichalcogenides, Chem. Soc. Rev. 44 (2015) 2702–2712. doi:10.1039/c5cs00151j.

[26] R.A. Bromley, R.B. Murray, The band structures of some transition metal dichalcogenides. I. A semiempirical tight binding method, J. Phys. C Solid State Phys. 5 (1972) 738–745. doi:10.1177/1090198117715667.

[27] R.A. Bromley, A semi-empirical tight-binding calculation of the band structure of MoS2, Phys. Lett. A. 33 (1970) 242–243. doi:10.1016/0375-9601(70)90756-5.

[28] S.K. Mahatha, K.D. Patel, K.S.R. Menon, Electronic structure investigation of MoS 2 and MoSe 2 using angle-resolved photoemission spectroscopy and abinitio band structure studies, J. Phys. Condens. Matter. 24 (2012). doi:10.1088/0953-8984/24/47/475504.

[29] L.F. Mattheiss, Band structures of transition-metal-dichalcogenide layer compounds, Phys. Rev. B. 8 (1973) 3719–3740. doi:10.1103/PhysRevB.8.3719.

[30] L.F. Mattheiss, Energy Bands for 2H-NbSe2 and 2H-MoS2, Phys. Rev. Lett. 30 (1973) 784–787. http://search.proquest.com/psycinfo/docview/617514079/C1E6BB3741EF4493PQ/302?accountid=15115#.

[31] K. Kobayashi, J. Yamauchi, Electronic structure and scanning-tunneling-microscopy image of molybdenum dichalcogenide surfaces, Phys. Rev. B. 51 (1995) 17085–17095. doi:10.1103/PhysRevB.51.17085.

[32] A.H. Reshak, S. Auluck, Band structure and optical response of 2H-Mo X2 compounds (X=S, Se, and Te), Phys. Rev. B - Condens. Matter Mater. Phys. 71 (2005) 1–6. doi:10.1103/PhysRevB.71.155114.

[33] N.J. Doran, Electronic structure and band theory of transition metal dichalcogenides, Phys. B+C. 99 (1980) 227–237. doi:10.1016/0378-4363(80)90237-5.

[34] F.R. Shepherd, P.M. Williams, Photoemission studies of the band structures of transition metal dichalcogenides. II. Groups VA and VIA, J. Phys. C Solid State Phys. 7 (1974) 4427–4440. doi:10.1088/0022-3719/7/23/029.

[35] G. Eda, H. Yamaguchi, D. Voiry, T. Fujita, M. Chen, M. Chhowalla, Photoluminescence from chemically exfoliated MoS 2, Nano Lett. 11 (2011) 5111–5116. doi:10.1021/nl201874w.

[36] H.R. Gutiérrez, N. Perea-López, A.L. Elías, A. Berkdemir, B. Wang, R. Lv, F. López-Urías, V.H. Crespi, H. Terrones, M. Terrones, Extraordinary room-temperature photoluminescence in triangular WS 2 monolayers, Nano Lett. 13 (2013) 3447–3454. doi:10.1021/nl3026357.

[37] T. Eknapakul, P.D.C. King, M. Asakawa, P. Buaphet, R.H. He, S.K. Mo, H. Takagi, K.M. Shen, F. Baumberger, T. Sasagawa, S. Jungthawan, W. Meevasana, Electronic structure of a quasi-freestanding MoS2monolayer, Nano Lett. 14 (2014) 1312–1316. doi:10.1021/nl4042824.

[38] W. Jin, P.C. Yeh, N. Zaki, D. Zhang, J.T. Sadowski, A. Al-Mahboob, A.M. Van Der Zande, D.A. Chenet, J.I. Dadap, I.P. Herman, P. Sutter, J. Hone, R.M. Osgood, Direct measurement of the thickness-dependent electronic band structure of MoS2 using angle-resolved photoemission spectroscopy, Phys. Rev. Lett. 111 (2013) 1–5. doi:10.1103/PhysRevLett.111.106801.

[39] S. Tongay, J. Zhou, C. Ataca, K. Lo, T.S. Matthews, J. Li, J.C. Grossman, J. Wu, Thermally driven crossover from indirect toward direct bandgap in 2D Semiconductors: MoSe2versus MoS2, Nano Lett. 12 (2012) 5576–5580. doi:10.1021/nl302584w.

[40] W. Zhao, Z. Ghorannevis, L. Chu, M. Toh, C. Kloc, P.H. Tan, G. Eda, Evolution of electronic structure in atomically thin sheets of ws2and wse2, ACS Nano. 7 (2013) 791–797. doi:10.1021/nn305275h.

[41] M. Ye, D. Winslow, D. Zhang, R. Pandey, Y. Yap, Recent Advancement on the Optical Properties of Two-Dimensional Molybdenum Disulfide (MoS2) Thin Films, Photonics. 2 (2015) 288–307. doi:10.3390/photonics2010288.

[42] K.F. Mak, C. Lee, J. Hone, J. Shan, T.F. Heinz, Atomically thin MoS2: A new direct-gap semiconductor, Phys. Rev. Lett. 105 (2010) 2–5. doi:10.1103/PhysRevLett.105.136805.

[43] V.B. Sandomirskii, Quantum Size Effect in a Semimetal Film, Sov. Phys. JETP. 25 (1967) 101.

[44] I. Song, C. Park, H.C. Choi, Synthesis and properties of molybdenum disulphide: from bulk to atomic layers, RSC Adv. 5 (2015) 7495–7514. doi:10.1039/C4RA11852A.

[45] V. Sorkin, H. Pan, H. Shi, S.Y. Quek, Y.W. Zhang, Nanoscale transition metal dichalcogenides: Structures, properties, and applications, Crit. Rev. Solid State Mater. Sci. 39 (2014) 319–367. doi:10.1080/10408436.2013.863176.

[46] B. Radisavljevic, A. Radenovic, J. Brivio, V. Giacometti, A. Kis, Single-layer MoS2transistors, Nat. Nanotechnol. 6 (2011) 147–150. doi:10.1038/nnano.2010.279.

[47] A. Ramasubramaniam, D. Naveh, E. Towe, Tunable band gaps in bilayer transition-metal dichalcogenides, Phys. Rev. B - Condens. Matter Mater. Phys. 84 (2011) 1–10. doi:10.1103/PhysRevB.84.205325.

[48] N. Zibouche, P. Philipsen, A. Kuc, T. Heine, Transition-metal dichalcogenide bilayers: Switching materials for spintronic and valleytronic applications, Phys. Rev. B - Condens. Matter Mater. Phys. 90 (2014) 1–6. doi:10.1103/PhysRevB.90.125440.

[49] E. Scalise, M. Houssa, G. Pourtois, V. Afanas'ev, A. Stesmans, Strain-induced semiconductor to metal transition in the two-dimensional honeycomb structure of MoS 2, Nano Res. 5 (2012) 43–48. doi:10.1007/s12274-011-0183-0.

[50] S. Bhattacharyya, A.K. Singh, Semiconductor-metal transition in semiconducting bilayer sheets of transition-metal dichalcogenides, Phys. Rev. B - Condens. Matter Mater. Phys. 86 (2012) 1–7. doi:10.1103/PhysRevB.86.075454.

[51] H.J. Conley, B. Wang, J.I. Ziegler, R.F. Haglund, S.T. Pantelides, K.I. Bolotin, Bandgap engineering of strained monolayer and bilayer MoS2, Nano Lett. 13 (2013) 3626–3630.

doi:10.1021/nl4014748.

[52] S.B. Desai, G. Seol, J.S. Kang, H. Fang, C. Battaglia, R. Kapadia, J.W. Ager, J. Guo, A. Javey, Strain-induced indirect to direct bandgap transition in multilayer WSe2, Nano Lett. 14 (2014) 4592–4597. doi:10.1021/nl501638a.

[53] S. Bhattacharyya, T. Pandey, A.K. Singh, Effect of strain on electronic and thermoelectric properties of few layers to bulk MoS2., Nanotechnology. 25 (2014) 465701. doi:10.1088/0957-4484/25/46/465701.

[54] B. Ouyang, Z. Mi, J. Song, Bandgap Transition of 2H Transition Metal Dichalcogenides: Predictive Tuning via Inherent Interface Coupling and Strain, J. Phys. Chem. C. 120 (2016) 8927–8935. doi:10.1021/acs.jpcc.5b12677.

[55] P. Lu, X. Wu, W. Guo, X.C. Zeng, Strain-dependent electronic and magnetic properties of MoS 2 monolayer, bilayer, nanoribbons and nanotubes, Phys. Chem. Chem. Phys. 14 (2012) 13035–13040. doi:10.1039/c2cp42181j.

[56] S. Dey, H.S.S.R. Matte, S.N. .Shirodkar, U. V. Waghmare, C.N.R. Rao, Charge-transfer Interaction between Few-layer MoS2 and Tetrathiafulvalene, Chem. an Asian J. 8 (2013) 1780–1784.

[57] F. Cui, Q. Feng, J. Hong, R. Wang, Y. Bai, X. Li, D. Liu, Y. Zhou, X. Liang, X. He, Z. Zhang, S. Liu, Z. Lei, Z. Liu, T. Zhai, H. Xu, Synthesis of Large-Size 1T′ ReS2xSe2(1—x) Alloy Monolayer with Tunable Bandgap and Carrier Type, Adv. Mater. 29 (2017) 1–9. doi:10.1002/adma.201705015.

[58] S. Susarla, A. Kutana, J.A. Hachtel, V. Kochat, A. Apte, R. Vajtai, J.C. Idrobo, B.I. Yakobson, C.S. Tiwary, P.M. Ajayan, Quaternary 2D Transition Metal Dichalcogenides (TMDs) with Tunable Bandgap, Adv. Mater. 29 (2017) 1–8. doi:10.1002/adma.201702457.

[59] B.S. Kim, W.S. Kyung, J.J. Seo, J.Y. Kwon, J.D. Denlinger, C. Kim, S.R. Park, Possible electric field induced indirect to direct band gap transition in MoSe2, Sci. Rep. 7 (2017) 3–8. doi:10.1038/s41598-017-05613-5.

[60] M. Kang, B. Kim, S.H. Ryu, S.W. Jung, J. Kim, L. Moreschini, C. Jozwiak, E. Rotenberg, A. Bostwick, K.S. Kim, Universal Mechanism of Band-Gap Engineering in Transition-Metal Dichalcogenides, Nano Lett. 17 (2017) 1610–1615. doi:10.1021/acs.nanolett.6b04775.

[61] H. Terrones, F. López-Urías, M. Terrones, Novel hetero-layered materials with tunable direct band gaps by sandwiching different metal disulfides and diselenides., Sci. Rep. 3 (2013) 1549. doi:10.1038/srep01549.

[62] N. Lu, H. Guo, L. Li, J. Dai, L. Wang, W.N. Mei, X. Wu, X.C. Zeng, MoS2/MX2heterobilayers: Bandgap engineering via tensile strain or external electrical field, Nanoscale. 6 (2014) 2879–2886. doi:10.1039/c3nr06072a.

[63] T. Korn, S. Heydrich, M. Hirmer, J. Schmutzler, C. Schuller, Low-temperature photocarrier dynamics in monolayer MoS2, Appl. Phys. Lett. 99 (2011) 102109. doi:10.1063/1.3636402.

[64] J. Yuan, S. Najmaei, Z. Zhang, J. Zhang, S. Lei, P.M. Ajayan, B.I. Yakobson, J. Lou, Photoluminescence Quenching and Charge Transfer in Arti fi cial Heterostacks of Monolayer Transition Black Phosphorus, ACS Nano. 9 (2015) 555–563.

[65] N. Kang, H.P. Paudel, M.N. Leuenberger, L. Tetard, S.I. Khondaker, Photoluminescence quenching in single-layer MoS2via oxygen plasma treatment, J. Phys. Chem. C. 118 (2014) 21258–21263. doi:10.1021/jp506964m.

[66] Z. He, Y. Sheng, Y. Rong, G. Do Lee, J. Li, J.H. Warner, Layer-dependent modulation of tungsten disulfide photoluminescence by lateral electric fields, ACS Nano. 9 (2015) 2740–2748. doi:10.1021/nn506594a.

[67] J. Gao, B. Li, J. Tan, P. Chow, T.M. Lu, N. Koratkar, Aging of Transition Metal Dichalcogenide Monolayers, ACS Nano. 10 (2016) 2628–2635. doi:10.1021/acsnano.5b07677.

[68] U. Bhanu, M.R. Islam, L. Tetard, S.I. Khondaker, Photoluminescence quenching in gold-MoS 2 hybrid nanoflakes, Sci. Rep. 4 (2014) 1–5. doi:10.1038/srep05575.

[69] Y. Wang, J.Z. Ou, S. Balendhran, A.F. Chrimes, M. Mortazavi, D.D. Yao, M.R. Field, K. Latham, V. Bansal, J.R. Friend, S. Zhuiykov, N. V Medhekar, M.S. Strano, K. Kalantar-zadeh, W.E.T. Al, Electrochemical Control of Photoluminescence in Two-Dimensional MoS 2 Nano flakes, ACS Nano. 7 (2013) 10083–10093.

[70] S. Tongay, J. Zhou, C. Ataca, J. Liu, J.S. Kang, T.S. Matthews, L. You, J. Li, J.C. Grossman, J. Wu, Broad-range modulation of light emission in two-dimensional semiconductors by molecular physisorption gating, Nano Lett. 13 (2013) 2831–2836. doi:10.1021/nl4011172.

[71] S. Tongay, J. Suh, C. Ataca, W. Fan, A. Luce, J.S. Kang, J. Liu, C. Ko, R. Raghunathanan, J. Zhou, F. Ogletree, J. Li, J.C. Grossman, J. Wu, Defects activated photoluminescence in two-dimensional semiconductors: Interplay between bound, charged, and free excitons, Sci. Rep. 3 (2013) 1–5. doi:10.1038/srep02657.

[72] H. Nan, Z. Wang, W. Wang, Z. Liang, Y. Lu, Q. Chen, D. He, P. Tan, F. Miao, X. Wang, J. Wang, Z. Ni, Strong photoluminescence enhancement of MoS2through defect engineering and oxygen bonding, ACS Nano. 8 (2014) 5738–5745. doi:10.1021/nn500532f.

[73] S. Mouri, Y. Miyauchi, K. Matsuda, Tunable photoluminescence of monolayer MoS2via chemical doping, Nano Lett. 13 (2013) 5944–5948. doi:10.1021/nl403036h.

[74] N. Peimyoo, W. Yang, J. Shang, X. Shen, Y. Wang, T. Yu, Chemically Driven Tunable Light Emission of Charged and Neutral Excitons in Monolayer WS2, ACS Nano. 8 (2014) 11320–11329.

[75] K.P. Dhakal, S. Roy, H. Jang, X. Chen, W.S. Yun, H. Kim, J. Lee, J. Kim, J.H. Ahn, Local Strain Induced Band Gap Modulation and Photoluminescence Enhancement of Multilayer Transition Metal Dichalcogenides, Chem. Mater. 29 (2017) 5124–5133. doi:10.1021/acs.chemmater.7b00453.

[76] P. Joo, K. Jo, G. Ahn, D. Voiry, H. Jeong, S. Ryu, M. Chhowalla, B. Kim, Functional Polyelectrolyte Nanospaced MoS2 Multilayers for Enhanced Photoluminescence, Nano Lett. 14 (2014) 6456–6462. http://pubs.acs.org/doi/abs/10.1021/nl502883a (accessed April 21, 2015).

[77] A.M. Van Der Zande, P.Y. Huang, D.A. Chenet, T.C. Berkelbach, Y. You, G.H. Lee, T.F. Heinz, D.R. Reichman, D.A. Muller, J.C. Hone, Grains and grain boundaries in highly crystalline monolayer molybdenum disulphide, Nat. Mater. 12 (2013) 554–561. doi:10.1038/nmat3633.

[78] I.S. Kim, V.K. Sangwan, D. Jariwala, J.D. Wood, S. Park, K.S. Chen, F. Shi, F. Ruiz-Zepeda, A. Ponce, M. Jose-Yacaman, V.P. Dravid, T.J. Marks, M.C. Hersam, L.J. Lauhon, Influence of stoichiometry on the optical and electrical properties of chemical vapor deposition derived MoS2, ACS Nano. 8 (2014) 10551–10558. doi:10.1021/nn503988x.

[79] N. Mao, Y. Chen, D. Liu, J. Zhang, L. Xie, Solvatochromic effect on the photoluminescence of MoS2monolayers, Small. 9 (2013) 1312–1315. doi:10.1002/smll.201202982.

[80] J. Mann, Q. Ma, P.M. Odenthal, M. Isarraraz, D. Le, E. Preciado, D. Barroso, K. Yamaguchi, G. Von Son Palacio, A. Nguyen, T. Tran, M. Wurch, A. Nguyen, V. Klee, S. Bobek, D. Sun, T.F. Heinz, T.S. Rahman, R. Kawakami, L. Bartels, 2-Dimensional transition metal dichalcogenides with tunable direct band gaps: MoS2(1-x)Se2x monolayers, Adv. Mater. 26 (2014) 1399–1404. doi:10.1002/adma.201304389.

[81] C. Lee, H. Yan, L. Brus, T. Heinz, J. Hone, S. Ryu, Anomalous lattice vibrations of single-and few-layer MoS2, ACS Nano. 4 (2010) 2695–700. doi:10.1021/nn1003937.

[82] H. Li, Q. Zhang, C.C.R. Yap, B.K. Tay, T.H.T. Edwin, A. Olivier, D. Baillargeat, From bulk to

monolayer MoS 2: Evolution of Raman scattering, Adv. Funct. Mater. 22 (2012) 1385–1390. doi:10.1002/adfm.201102111.

[83] A. Berkdemir, H.R. Gutiérrez, A.R. Botello-Méndez, N. Perea-López, A.L. Elías, C.I. Chia, B. Wang, V.H. Crespi, F. López-Urías, J.C. Charlier, H. Terrones, M. Terrones, Identification of individual and few layers of WS2 using Raman Spectroscopy, Sci. Rep. 3 (2013) 1–8. doi:10.1038/srep01755.

[84] X. Zhang, X.F. Qiao, W. Shi, J. Bin Wu, D.S. Jiang, P.H. Tan, Phonon and Raman scattering of two-dimensional transition metal dichalcogenides from monolayer, multilayer to bulk material, Chem. Soc. Rev. 44 (2015) 2757–2785. doi:10.1039/c4cs00282b.

[85] A. Molina-Sánchez, L. Wirtz, Phonons in single-layer and few-layer MoS2 and WS2, Phys. Rev. B - Condens. Matter Mater. Phys. 84 (2011) 1–8. doi:10.1103/PhysRevB.84.155413.

[86] X. Zhang, Q.H. Tan, J. Bin Wu, W. Shi, P.H. Tan, Review on the Raman spectroscopy of different types of layered materials, Nanoscale. 8 (2016) 6435–6450. doi:10.1039/c5nr07205k.

[87] A.A. Puretzky, L. Liang, X. Li, K. Xiao, K. Wang, M. Mahjouri-Samani, L. Basile, J.C. Idrobo, B.G. Sumpter, V. Meunier, D.B. Geohegan, Low-Frequency Raman Fingerprints of Two-Dimensional Metal Dichalcogenide Layer Stacking Configurations, ACS Nano. 9 (2015) 6333–6342. doi:10.1021/acsnano.5b01884.

[88] X. Zhang, W.P. Han, J.B. Wu, S. Milana, Y. Lu, Q.Q. Li, A.C. Ferrari, P.H. Tan, Raman spectroscopy of shear and layer breathing modes in multilayer MoS2, Phys. Rev. B - Condens. Matter Mater. Phys. 87 (2013) 1–8. doi:10.1103/PhysRevB.87.115413.

[89] C.H. Lui, Z. Ye, C. Ji, K.C. Chiu, C.T. Chou, T.I. Andersen, C. Means-Shively, H. Anderson, J.M. Wu, T. Kidd, Y.H. Lee, R. He, Observation of interlayer phonon modes in van der Waals heterostructures, Phys. Rev. B - Condens. Matter Mater. Phys. 91 (2015) 1–7. doi:10.1103/PhysRevB.91.165403.

[90] Y. Zhao, X. Luo, H. Li, J. Zhang, P.T. Araujo, C.K. Gan, J. Wu, H. Zhang, S.Y. Quek, M.S. Dresselhaus, Q. Xiong, Interlayer breathing and shear modes in few-trilayer MoS2 and WSe2, Nano Lett. 13 (2013) 1007–1015. doi:10.1021/nl304169w.

[91] G. Froehlicher, E. Lorchat, F. Fernique, C. Joshi, A. Molina-Sánchez, L. Wirtz, S. Berciaud, Unified Description of the Optical Phonon Modes in N-Layer MoTe2, Nano Lett. 15 (2015) 6481–6489. doi:10.1021/acs.nanolett.5b02683.

[92] M. O'Brien, N. McEvoy, D. Hanlon, T. Hallam, J.N. Coleman, G.S. Duesberg, Mapping of Low-Frequency Raman Modes in CVD-Grown Transition Metal Dichalcogenides: Layer Number, Stacking Orientation and Resonant Effects, Sci. Rep. 6 (2016) 1–11. doi:10.1038/srep19476.

[93] S. Huang, L. Liang, X. Ling, A.A. Puretzky, D.B. Geohegan, B.G. Sumpter, J. Kong, V. Meunier, M.S. Dresselhaus, Low-Frequency Interlayer Raman Modes to Probe Interface of Twisted Bilayer MoS2, Nano Lett. 16 (2016) 1435–1444. doi:10.1021/acs.nanolett.5b05015.

[94] Y. Yu, G.H. Nam, Q. He, X.J. Wu, K. Zhang, Z. Yang, J. Chen, Q. Ma, M. Zhao, Z. Liu, F.R. Ran, X. Wang, H. Li, X. Huang, B. Li, Q. Xiong, Q. Zhang, Z. Liu, L. Gu, Y. Du, W. Huang, H. Zhang, High phase-purity 1T′-MoS2- and 1T′-MoSe2-layered crystals, Nat. Chem. 10 (2018) 638–643. doi:10.1038/s41557-018-0035-6.

[95] Y. Chen, D.O. Dumcenco, Y. Zhu, X. Zhang, N. Mao, Q. Feng, M. Zhang, J. Zhang, P.H. Tan, Y.S. Huang, L. Xie, Composition-dependent Raman modes of Mo1-xWxS2monolayer alloys, Nanoscale. 6 (2014) 2833–2839. doi:10.1039/c3nr05630a.

[96] S. Cho, S. Kim, J.H. Kim, J. Zhao, J. Seok, D.H. Keum, J. Baik, D. Choe, K.J. Chang, K. Suenaga, S.W. Kim, Y.H. Lee, H. Yang, Phase patterning for ohmic homojunction contact in MoTe2, Science (80-.). 349 (2015) 625–628.

[97] A.L. Friedman, A.T. Hanbicki, F.K. Perkins, G.G. Jernigan, J.C. Culbertson, P.M. Campbell, Evidence for Chemical Vapor Induced 2H to 1T Phase Transition in MoX2(X = Se, S) Transition Metal Dichalcogenide Films, Sci. Rep. 7 (2017) 1–9. doi:10.1038/s41598-017-04224-4.

[98] S. Jiménez Sandoval, D. Yang, R.F. Frindt, J.C. Irwin, Raman study and lattice dynamics of single molecular layers of <math display="inline"> <mrow> <msub> <mrow> <mi mathvariant="normal">MoS</mi> </mrow> <mrow> <mn>2</mn> </mrow> </msub> </mrow> </math>, Phys. Rev. B. 44 (1991) 3955–3962. doi:10.1103/PhysRevB.44.3955.

[99] D. Yang, S. Jiménez Sandoval, W.M.R. Divigalpitiya, J.C. Irwin, R.F. Frindt, Structure of single-molecular-layer MoS2, Phys. Rev. B. 43 (1991) 12053–12056.

[100] M. Calandra, Chemically exfoliated single-layer MoS 2: Stability, lattice dynamics, and catalytic adsorption from first principles, Phys. Rev. B - Condens. Matter Mater. Phys. 88 (2013) 1–6. doi:10.1103/PhysRevB.88.245428.

[101] J.-U. Lee, K. Kim, S. Han, G.H. Ryu, Z. Lee, H. Cheong, Raman Signatures of Polytypism in Molybdenum Disulfide., ACS Nano. (2016). doi:10.1021/acsnano.5b05831.

[102] S. Balendhran, J.Z. Ou, M. Bhaskaran, S. Sriram, S. Ippolito, Z. Vasic, E. Kats, S. Bhargava, S. Zhuiykov, K. Kalantar-Zadeh, Atomically thin layers of MoS2via a two step thermal evaporation-exfoliation method, Nanoscale. 4 (2012) 461–466. doi:10.1039/c1nr10803d.

[103] W. Shi, M.L. Lin, Q.H. Tan, X.F. Qiao, J. Zhang, P.H. Tan, Raman and photoluminescence spectra of two-dimensional nanocrystallites of monolayer WS2and WSe2, 2D Mater. 3 (2016). doi:10.1088/2053-1583/3/2/025016.

[104] A.S. Pawbake, M.S. Pawar, S.R. Jadkar, D.J. Late, Large area chemical vapor deposition of monolayer transition metal dichalcogenides and their temperature dependent Raman spectroscopy studies, Nanoscale. 8 (2016) 3008–3018. doi:10.1039/c5nr07401k.

[105] G.P. Srivastava, I.O. Thomas, Temperature-dependent Raman linewidths in transition-metal dichalcogenides, Phys. Rev. B. 98 (2018) 1–8. doi:10.1103/PhysRevB.98.035430.

[106] A.P. Nayak, T. Pandey, D. Voiry, J. Liu, S.T. Moran, A. Sharma, C. Tan, C.H. Chen, L.J. Li, M. Chhowalla, J.F. Lin, A.K. Singh, D. Akinwande, Pressure-dependent optical and vibrational properties of monolayer molybdenum disulfide, Nano Lett. 15 (2015) 346–353. doi:10.1021/nl5036397.

[107] M. Buscema, G.A. Steele, H.S.J. van der Zant, A. Castellanos-Gomez, The effect of the substrate on the Raman and photoluminescence emission of single-layer MoS2, Nano Res. 7 (2014) 1–11. doi:10.1007/s12274-014-0424-0.

[108] W.M. Parkin, A. Balan, L. Liang, P.M. Das, M. Lamparski, C.H. Naylor, J.A. Rodríguez-Manzo, A.T.C. Johnson, V. Meunier, M. Drndić, Raman Shifts in Electron-Irradiated Monolayer MoS2, ACS Nano. 10 (2016) 4134–4142. doi:10.1021/acsnano.5b07388.

[109] D.N. Nguyen, L.N. Nguyen, P.D. Nguyen, T.V. Thu, A.D. Nguyen, P.D. Tran, Crystallization of Amorphous Molybdenum Sulfide Induced by Electron or Laser Beam and Its Effect on H2-Evolving Activities, J. Phys. Chem. C. 120 (2016) 28789–28794. doi:10.1021/acs.jpcc.6b08817.

[110] B.C. Windom, W.G. Sawyer, D.W. Hahn, A raman spectroscopic study of MoS 2 and MoO 3: Applications to tribological systems, Tribol. Lett. 42 (2011) 301–310. doi:10.1007/s11249-011-9774-x.

[111] S. Tongay, W. Fan, J. Kang, J. Park, U. Koldemir, J. Suh, D.S. Narang, K. Liu, J. Ji, J. Li, R. Sinclair, J. Wu, Tuning interlayer coupling in large-area heterostructures with CVD-grown MoS2 and WS2 monolayers, Nano Lett. 14 (2014) 3185–3190. doi:10.1021/nl500515q.

[112] S.J.R. Tan, S. Sarkar, X. Zhao, X. Luo, Y.Z. Luo, S.M. Poh, I. Abdelwahab, W. Zhou, T. Venkatesan, W. Chen, S.Y. Quek, K.P. Loh, Temperature- and Phase-Dependent Phonon

Renormalization in 1T'-MoS2, ACS Nano. 12 (2018) 5051–5058. doi:10.1021/acsnano.8b02649.

[113] S. Bertolazzi, J. Brivio, A. Kis, Stretching and breaking of ultrathin MoS2, ACS Nano. 5 (2011) 9703–9709. doi:10.1021/nn203879f.

[114] A. Castellanos-Gomez, M. Poot, G.A. Steele, H.S.J. Van Der Zant, N. Agraït, G. Rubio-Bollinger, Elastic properties of freely suspended MoS2nanosheets, Adv. Mater. 24 (2012) 772–775. doi:10.1002/adma.201103965.

[115] G. Casillas, U. Santiago, H. BarroÌn, D. Alducin, A. Ponce, M. José-Yacamán, Elasticity of MoS2sheets by mechanical deformation observed by in situ electron microscopy, J. Phys. Chem. C. 119 (2015) 710–715. doi:10.1021/jp5093459.

[116] G. Salomon, A.W.J. De Gee, J.H. Zaat, Mechano-chemical factors in MoS2-film lubrication, Wear. 7 (1964) 87–101. doi:10.1016/0043-1648(64)90081-X.

[117] P.D. Fleischauer, J.R. Lince, P.A. Bertrand, R. Bauer, Electronic Structure and Lubrication Properties of MoS2: A Qualitative Molecular Orbital Approach, Langmuir. 5 (1989) 1009–1015. doi:10.1021/la00088a022.

[118] M. Dallavalle, N. Sändig, F. Zerbetto, Stability, dynamics, and lubrication of MoS 2 platelets and nanotubes, Langmuir. 28 (2012) 7393–7400. doi:10.1021/la300871q.

[119] S. Cahangirov, C. Ataca, M. Topsakal, H. Sahin, S. Ciraci, Frictional figures of merit for single layered nanostructures, Phys. Rev. Lett. 108 (2012) 1–5. doi:10.1103/PhysRevLett.108.126103.

[120] A. Socoliuc, R. Bennewitz, E. Gnecco, E. Meyer, Transition from stick-slip to continuous sliding in atomic friction: Entering a new regime of ultralow friction, Phys. Rev. Lett. 92 (2004) 1–4. doi:10.1103/PhysRevLett.92.134301.

[121] C. Lee, C. Lee, Q. Li, W. Kalb, X. Liu, H. Berger, Frictional Characteristics of Atomically Thin Sheets, Science (80-.). 328 (2011) 76. doi:10.1126/science.1184167.

[122] S. Tongay, S.S. Varnoosfaderani, B.R. Appleton, J. Wu, A.F. Hebard, Magnetic properties of MoS 2: Existence of ferromagnetism, Appl. Phys. Lett. 101 (2012). doi:10.1063/1.4753797.

[123] X. Mao, Y. Xu, Q. Xue, W. Wang, D. Gao, Ferromagnetism in exfoliated tungsten disulfide nanosheets, Nanoscale Res. Lett. 8 (2013) 430. doi:10.1186/1556-276X-8-430.

[124] S. Mathew, K. Gopinadhan, T.K. Chan, X.J. Yu, D. Zhan, L. Cao, A. Rusydi, M.B.H. Breese, S. Dhar, Z.X. Shen, T. Venkatesan, J.T.L. Thong, Magnetism in MoS2induced by proton irradiation, Appl. Phys. Lett. 101 (2012). doi:10.1063/1.4750237.

[125] L. Cai, J. He, Q. Liu, T. Yao, L. Chen, W. Yan, F. Hu, Y. Jiang, Y. Zhao, T. Hu, Z. Sun, S. Wei, Vacancy-induced ferromagnetism of MoS2 nanosheets, J. Am. Chem. Soc. 137 (2015) 2622–2627. doi:10.1021/ja5120908.

[126] Y. Li, Z. Zhou, S. Zhang, Z. Chen, MoS 2 Nanoribbons : High Stability and Unusual Electronic and Magnetic Properties, J. Am. Chem. Soc. (2008) 16739–16744. doi:10.1021/ja805545x.

[127] A.R. Botello-Méndez, F. López-Urías, M. Terrones, H. Terrones, Metallic and ferromagnetic edges in molybdenum disulfide nanoribbons, Nanotechnology. 20 (2009). doi:10.1088/0957-4484/20/32/325703.

[128] H. Pan, Y.W. Zhang, Edge-dependent structural, electronic and magnetic properties of MoS 2 nanoribbons, J. Mater. Chem. 22 (2012) 7280–7290. doi:10.1039/c2jm15906f.

[129] A. Vojvodic, B. Hinnemann, J.K. Nørskov, Magnetic edge states in MoS2 characterized using density-functional theory, Phys. Rev. B - Condens. Matter Mater. Phys. 80 (2009) 1–11. doi:10.1103/PhysRevB.80.125416.

[130] D. Cao, T. Shen, P. Liang, X. Chen, H. Shu, Role of chemical potential in flake shape and edge

properties of monolayer MoS2, J. Phys. Chem. C. 119 (2015) 4294–4301. doi:10.1021/jp5097713.

[131] W. Zhou, X. Zou, S. Najmaei, Z. Liu, Y. Shi, J. Kong, J. Lou, P.M. Ajayan, B.I. Yakobson, J.C. Idrobo, Intrinsic structural defects in monolayer molybdenum disulfide, Nano Lett. 13 (2013) 2615–2622. doi:10.1021/nl4007479.

[132] C. Ataca, S. Ciraci, Functionalization of single-layer Mos2honeycomb structures, J. Phys. Chem. C. 115 (2011) 13303–13311. doi:10.1021/jp2000442.

[133] J. Wang, F. Sun, S. Yang, Y. Li, C. Zhao, M. Xu, Y. Zhang, H. Zeng, Robust ferromagnetism in Mn-doped MoS2nanostructures, Appl. Phys. Lett. 109 (2016) 1–6. doi:10.1063/1.4961883.

[134] Y. Ma, Y. Dai, M. Guo, C. Niu, J. Lu, B. Huang, Electronic and magnetic properties of perfect, vacancy-doped, and nonmetal adsorbed MoSe2, MoTe2 and WS2 monolayers, Phys. Chem. Chem. Phys. 13 (2011) 15546–15553. doi:10.1039/c1cp21159e.

[135] J. Luxa, O. Jankovský, D. Sedmidubský, R. Medlín, M. Maryško, M. Pumera, Z. Sofer, Origin of exotic ferromagnetic behavior in exfoliated layered transition metal dichalcogenides MoS2 and WS2, Nanoscale. 8 (2016) 1960–1967. doi:10.1039/c5nr05757d.

[136] S.W. Han, Y. Park, Y.H. Hwang, W.G. Lee, S.C. Hong, Investigation of electron irradiation-induced magnetism in layered MoS2single crystals, Appl. Phys. Lett. 109 (2016). doi:10.1063/1.4971192.

[137] H. Zheng, B. Yang, D. Wang, R. Han, X. Du, Y. Yan, Tuning magnetism of monolayer MoS2 by doping vacancy and applying strain, Appl. Phys. Lett. 104 (2014) 4–9. doi:10.1063/1.4870532.

[138] C.N.R. Rao, H.S.S.R. Matte, K.S. Subrahmanyam, U. Maitra, Unusual magnetic properties of graphene and related materials, Chem. Sci. 3 (2012) 45–52. doi:10.1039/c1sc00726b.

[139] C. Ataca, H. Şahin, S. Ciraci, Stable, single-layer MX2transition-metal oxides and dichalcogenides in a honeycomb-like structure, J. Phys. Chem. C. 116 (2012) 8983–8999. doi:10.1021/jp212558p.

[140] W. Jie, Z. Yang, F. Zhang, G. Bai, C.W. Leung, J. Hao, Observation of Room-Temperature Magnetoresistance in Monolayer MoS2by Ferromagnetic Gating, ACS Nano. 11 (2017) 6950–6958. doi:10.1021/acsnano.7b02253.

[141] A.T. Neal, H. Liu, J. Gu, P.D. Ye, Magneto-transport in MoS2: Phase coherence, spin-orbit scattering, and the hall factor, ACS Nano. 7 (2013) 7077–7082. doi:10.1021/nn402377g.

[142] W. Choi, N. Choudhary, G.H. Han, J. Park, D. Akinwande, Y.H. Lee, Recent development of two-dimensional transition metal dichalcogenides and their applications, Mater. Today. 20 (2017) 1–15. doi:10.1016/j.mattod.2016.10.002.

[143] T. Wang, R. Zhu, J. Zhuo, Z. Zhu, Y. Shao, M. Li, Direct detection of DNA below ppb level based on thionin-functionalized layered MoS2 electrochemical sensors, Anal. Chem. 86 (2014) 12064–12069. doi:10.1021/ac5027786.

[144] C. Liu, D. Kong, P.C. Hsu, H. Yuan, H.W. Lee, Y. Liu, H. Wang, S. Wang, K. Yan, D. Lin, P.A. Maraccini, K.M. Parker, A.B. Boehm, Y. Cui, Rapid water disinfection using vertically aligned MoS2 nanofilms and visible light, Nat. Nanotechnol. 11 (2016) 1098–1104. doi:10.1038/nnano.2016.138.

[145] A.H. Loo, A. Bonanni, Z. Sofer, M. Pumera, Transitional Metal/Chalcogen Dependant Interactions of Hairpin DNA with Transition Metal Dichalcogenides, MX2., Chemphyschem. 16 (2015) 2304–6. doi:10.1002/cphc.201500311.

[146] Y.H. Wang, K.J. Huang, X. Wu, Recent advances in transition-metal dichalcogenides based electrochemical biosensors: A review, Biosens. Bioelectron. 97 (2017) 305–316. doi:10.1016/j.bios.2017.06.011.

[147] Y. Hu, Y. Huang, C. Tan, X. Zhang, Q. Lu, M. Sindoro, X. Huang, W. Huang, L. Wang, H. Zhang, Two-dimensional transition metal dichalcogenide nanomaterials for biosensing applications, Mater. Chem. Front. 1 (2017) 24–36. doi:10.1039/c6qm00195e.

[148] M. Pumera, A.H. Loo, Layered transition-metal dichalcogenides (MoS2 and WS2) for sensing and biosensing, TrAC Trends Anal. Chem. 61 (2014) 49–53. doi:10.1016/j.trac.2014.05.009.

[149] K. Kalantar-zadeh, J.Z. Ou, T. Daeneke, M.S. Strano, M. Pumera, S.L. Gras, Two-Dimensional Transition Metal Dichalcogenides in Biosystems, Adv. Funct. Mater. 25 (2015) 5086–5099. doi:10.1002/adfm.201500891.

[150] C.C. Mayorga-Martinez, A. Ambrosi, A.Y.S. Eng, Z. Sofer, M. Pumera, Metallic 1T-WS 2 for Selective Impedimetric Vapor Sensing, Adv. Funct. Mater. 25 (2015) 5611–5616. doi:10.1002/adfm.201502223.

[151] K. Chang, W. Chen, L -Cysteine-assisted synthesis of layered MoS2/graphene composites with excellent electrochemical performances for lithium ion batteries, ACS Nano. 5 (2011) 4720–4728. doi:10.1021/nn200659w.

[152] H. Hwang, H. Kim, J. Cho, MoS2 nanoplates consisting of disordered graphene-like layers for high rate lithium battery anode materials, Nano Lett. 11 (2011) 4826–4830. doi:10.1021/nl202675f.

[153] J. Xiao, D. Choi, L. Cosimbescu, P. Koech, J. Liu, J.P. Lemmon, Exfoliated MoS2 nanocomposite as an anode material for lithium ion batteries, Chem. Mater. 22 (2010) 4522–4524. doi:10.1021/cm101254j.

[154] M. Acerce, D. Voiry, M. Chhowalla, Metallic 1T phase MoS2nanosheets as supercapacitor electrode materials, Nat. Nanotechnol. 10 (2015) 313–318. doi:10.1038/nnano.2015.40.

[155] B. Luan, R. Zhou, Spontaneous Transport of Single-Stranded DNA through Graphene-MoS2Heterostructure Nanopores, ACS Nano. 12 (2018) 3886–3891. doi:10.1021/acsnano.8b01297.

[156] D. Sarkar, B. Mondal, A. Som, S.J. Ravindran, S.K. Jana, C.K. Manju, T. Pradeep, Holey MoS $_2$ Nanosheets with Photocatalytic Metal Rich Edges by Ambient Electrospray Deposition for Solar Water Disinfection, Glob. Challenges. 1800052 (2018) 1800052. doi:10.1002/gch2.201800052.

[157] A.T. Massey, R. Gusain, S. Kumari, O.P. Khatri, Hierarchical Microspheres of MoS2Nanosheets: Efficient and Regenerative Adsorbent for Removal of Water-Soluble Dyes, Ind. Eng. Chem. Res. 55 (2016) 7124–7131. doi:10.1021/acs.iecr.6b01115.

[158] Z. Wang, B. Mi, Environmental Applications of 2D Molybdenum Disulfide (MoS2) Nanosheets, Environ. Sci. Technol. 51 (2017) 8229–8244. doi:10.1021/acs.est.7b01466.

[159] W.Y. Zhou, S.S. Li, X.Y. Xiao, S.H. Chen, J.H. Liu, X.J. Huang, Defect- and phase-engineering of Mn-mediated MoS2 nanosheets for ultrahigh electrochemical sensing of heavy metal ions: chemical interaction-driven in situ catalytic redox reactions, Chem. Commun. 54 (2018) 9329–9332. doi:10.1039/c8cc04575e.

[160] R.J. Keyse, A.J. Garratt-Reed, P.J. Goodhew, G.W. Lorimer, Introduction to Scanning Transmission Electron Microscopy, 1st ed., BIOS Scientific Publishers, Oxford, 1998.

[161] Z.Y. Li, N.P. Young, M. Di Vece, S. Palomba, R.E. Palmer, a L. Bleloch, B.C. Curley, R.L. Johnston, J. Jiang, J. Yuan, Three-dimensional atomic-scale structure of size-selected gold nanoclusters., Nature. 451 (2008) 46–8. doi:10.1038/nature06470.

[162] Dawn Michelle Foster, Production and characterisation by scanning transmission electron microscopy of size-selected noble metal nanoclusters, University of Birmingham, 2017.

[163] D.B. Williams, C.B. Carter, Transmission Electron Microscopy: A Textbook for Materials

Science, Springer Science & Business Media, 2009.

[164] Energy-dispersive X-ray spectroscopy, (n.d.). http://en.stonkcash.com/energy-dispersive-x-ray-spectrometry/ (accessed October 13, 2018).

[165] Y. Wang, Y. Li, C. Rong, J.P. Liu, Sm-Co hard magnetic nanoparticles prepared by surfactant-assisted ball milling, Nanotechnology. 18 (2007). doi:10.1088/0957-4484/18/46/465701.

[166] V. M. Chakka, B. Altuncevahir, Z.Q. Jin, Y. Li, J.P. Liu, Magnetic nanoparticles produced by surfactant-assisted ball milling, J. Appl. Phys. 99 (2006) 08E912. doi:10.1063/1.2170593.

[167] Walt A. de Heer, The physics of simple metal clusters: experimental aspects and simple models, Rev. Mod. Phys. 65 (1993) 611–676.

[168] S. Vajda, M.G. White, Catalysis Applications of Size-Selected Cluster Deposition, ACS Catal. 5 (2015) 7152–7176. doi:10.1021/acscatal.5b01816.

[169] K.-J. Hu, S.R. Plant, P.R. Ellis, C.M. Brown, P.T. Bishop, R.E. Palmer, The effects of 1-pentyne hydrogenation on the atomic structures of size-selected Au N and Pd N (N = 923 and 2057) nanoclusters, Phys. Chem. Chem. Phys. 16 (2014) 26631–26637. doi:10.1039/C4CP02686A.

[170] Z.W. Wang, R.E. Palmer, Intensity calibration and atomic imaging of size-selected Au and Pd clusters in aberration-corrected HAADF-STEM, J. Phys. Conf. Ser. 371 (2012) 012010. doi:10.1088/1742-6596/371/1/012010.

[171] M.J. Cuddy, K.P. Arkill, Z.W. Wang, H.-P. Komsa, A. V Krasheninnikov, R.E. Palmer, Fabrication and atomic structure of size-selected, layered MoS2 clusters for catalysis., Nanoscale. 6 (2014) 12463–12469. doi:10.1039/c4nr04317k.

[172] C.E. Blackmore, N. V Rees, R.E. Palmer, Modular construction of size-selected multiple-core Pt-TiO2 nanoclusters for electro-catalysis., Phys. Chem. Chem. Phys. (2015). doi:10.1039/c5cp00285k.

[173] S.J. Carroll, S. Pratontep, M. Streun, R.E. Palmer, Pinning of size-selected Ag clusters on graphite surfaces, J. Chem. Phys. 113 (2000) 7723–7727. doi:10.1063/1.1322657.

[174] S. Gibilisco, M. Di Vece, S. Palomba, G. Faraci, R.E. Palmer, Pinning of size-selected Pd nanoclusters on graphite, J. Chem. Phys. 125 (2006) 8–11. doi:10.1063/1.2337288.

[175] D. Escalera-López, Y. Niu, S.J. Park, M. Isaacs, K. Wilson, R.E. Palmer, N. V. Rees, Hydrogen evolution enhancement of ultra-low loading, size-selected molybdenum sulfide nanoclusters by sulfur enrichment, Appl. Catal. B Environ. 235 (2018) 84–91. doi:10.1016/j.apcatb.2018.04.068.

[176] C.E. Blackmore, Experimental and Theoretical Studies of the Atomic Structure of Platinum-based Nanoclusters, University of Birmingham, 2016.

[177] S. Pratontep, S.J. Carroll, C. Xirouchaki, M. Streun, R.E. Palmer, Size-selected cluster beam source based on radio frequency magnetron plasma sputtering and gas condensation, Rev. Sci. Instrum. 76 (2005) 045103. doi:10.1063/1.1869332.

[178] B. von Issendorff, R.E. Palmer, A new high transmission infinite range mass selector for cluster and nanoparticle beams, Rev. Sci. Instrum. 70 (1999) 4497. doi:10.1063/1.1150102.

[179] J.D. Benck, Z. Chen, L.Y. Kuritzky, A.J. Forman, T.F. Jaramillo, Amorphous Molybdenum Sul fi de Catalysts for Electrochemical Hydrogen Production: Insights into the Origin of their Catalytic Activity, ACS Catal. 2 (2012) 1916–1923.

[180] Z. Chen, D. Cummins, B.N. Reinecke, E. Clark, M.K. Sunkara, T.F. Jaramillo, Core-shell MoO 3-MoS 2 Nanowires for Hydrogen Evolution : A Functional Design for Electrocatalytic Materials, Nano Lett. 11 (2011) 4168–4175.

[181] J. Bonde, P.G. Moses, T.F. Jaramillo, J. Norskov, I. Chorkendorff, Hydrogen evolution on nano-

particulate transition metal sulfides, Faraday Discuss. 140 (2008) 219–231. doi:10.1039/b814058h.

[182] J.D. Benck, T.R. Hellstern, J. Kibsgaard, P. Chakthranont, T.F. Jaramillo, Catalyzing the Hydrogen Evolution Reaction (HER) with Molybdenum Sulfide Nanomaterials, ACS Catal. 4 (2014) 3957–3971. http://pubs.acs.org/doi/abs/10.1021/cs500923c (accessed December 15, 2015).

[183] I. Roger, M.A. Shipman, M.D. Symes, Earth-abundant catalysts for electrochemical and photoelectrochemical water splitting, Nat. Rev. Chem. 1 (2017) 0003. doi:10.1038/s41570-016-0003.

[184] D. McAteer, Z. Gholamvand, N. McEvoy, A. Harvey, E. O'Malley, G.S. Duesberg, J.N. Coleman, Thickness Dependence and Percolation Scaling of Hydrogen Production Rate in MoS 2 Nanosheet and Nanosheet–Carbon Nanotube Composite Catalytic Electrodes, ACS Nano. 10 (2016) 672–683. doi:10.1021/acsnano.5b05907.

[185] Y. Garsany, J. Ge, J. St-Pierre, R. Rocheleau, K.E. Swider-Lyons, Analytical Procedure for Accurate Comparison of Rotating Disk Electrode Results for the Oxygen Reduction Activity of Pt/C, J. Electrochem. Soc. 161 (2014) F628–F640. doi:10.1149/2.036405jes.

[186] K.J.J. Mayrhofer, D. Strmcnik, B.B. Blizanac, V. Stamenkovic, M. Arenz, N.M. Markovic, Measurement of oxygen reduction activities via the rotating disc electrode method: From Pt model surfaces to carbon-supported high surface area catalysts, Electrochim. Acta. 53 (2008) 3181–3188. doi:10.1016/j.electacta.2007.11.057.

[187] R.J. Toh, Z. Sofer, J. Luxa, M. Pumera, Ultrapure Molybdenum Disulfide Shows Enhanced Catalysis for Hydrogen Evolution over Impurities-Doped Counterpart, ChemCatChem. 9 (2017) 1168–1171. doi:10.1002/cctc.201601561.

[188] R.J. Toh, Z. Sofer, J. Luxa, D. Sedmidubský, M. Pumera, 3R phase of MoS $_2$ and WS $_2$ outperforms the corresponding 2H phase for hydrogen evolution, Chem. Commun. 53 (2017) 3054–3057. doi:10.1039/C6CC09952A.

[189] D. Voiry, M. Salehi, R. Silva, T. Fujita, M. Chen, Conducting MoS2 nanosheets as catalysts for hydrogen evolution reaction, Nano Lett. 13 (2013) 6222–6227. http://pubs.acs.org/doi/abs/10.1021/nl403661s.

[190] X. Geng, W. Sun, W. Wu, B. Chen, A. Al-Hilo, M. Benamara, H. Zhu, F. Watanabe, J. Cui, T.P. Chen, Pure and stable metallic phase molybdenum disulfide nanosheets for hydrogen evolution reaction, Nat. Commun. 7 (2016) 1–7. doi:10.1038/ncomms10672.

[191] Y. Xu, L. Wang, X. Liu, S. Zhang, C. Liu, D. Yan, Y. Zeng, Y. Pei, Y. Liu, S. Luo, Monolayer MoS $_2$ with S vacancies from interlayer spacing expanded counterparts for highly efficient electrochemical hydrogen production, J. Mater. Chem. A. 4 (2016) 16524–16530. doi:10.1039/C6TA06534A.

[192] J. Yang, K. Wang, J. Zhu, C. Zhang, T. Liu, Self-templated growth of vertically aligned 2H-1T MoS2 for efficient electrocatalytic hydrogen evolution, ACS Appl. Mater. Interfaces. 8 (2016) 31702–31708. doi:10.1021/acsami.6b11298.

[193] H. Huang, L. Chen, C. Liu, X. Liu, S. Fang, W. Liu, Y. Liu, Hierarchically Nanostructured MoS2 with Rich In-plane Edges as a High-performance Electrocatalyst for Hydrogen Evolution Reaction, J. Mater. Chem. A. 4 (2016) 14577–14585. doi:10.1039/C6TA06174E.

[194] M.-R. Gao, M.K.Y. Chan, Y. Sun, Edge-terminated molybdenum disulfide with a 9.4-Å interlayer spacing for electrochemical hydrogen production., Nat. Commun. 6 (2015) 7493. doi:10.1038/ncomms8493.

[195] J. Xie, H. Zhang, S. Li, R. Wang, X. Sun, M. Zhou, J. Zhou, X.W.D. Lou, Y. Xie, Defect-rich MoS2 ultrathin nanosheets with additional active edge sites for enhanced electrocatalytic hydrogen evolution., Adv. Mater. 25 (2013) 5807–13. doi:10.1002/adma.201302685.

[196] Z. Wu, B. Fang, Z. Wang, C. Wang, Z. Liu, F. Liu, W. Wang, A. Alfantazi, D. Wang, D.P. Wilkinson, MoS 2 Nanosheets : A Designed Structure with High Active Site Density for the Hydrogen Evolution Reaction, (2013).

[197] Y. Yin, J. Han, Y. Zhang, X. Zhang, P. Xu, Q. Yuan, L. Samad, X. Wang, Y. Wang, Z. Zhang, P. Zhang, X. Cao, B. Song, S. Jin, Contributions of Phase, Sulfur Vacancies, and Edges to the Hydrogen Evolution Reaction Catalytic Activity of Porous Molybdenum Disulfide Nanosheets, J. Am. Chem. Soc. 138 (2016) 7965–7972. doi:10.1021/jacs.6b03714.

[198] J. Xie, J. Zhang, S. Li, F. Grote, X. Zhang, H. Zhang, R. Wang, Y. Lei, B. Pan, Y. Xie, Controllable disorder engineering in oxygen-incorporated MoS2 ultrathin nanosheets for efficient hydrogen evolution, J. Am. Chem. Soc. 135 (2013) 17881–17888. doi:10.1021/ja408329q.

[199] Z. Liu, Z. Gao, Y. Liu, M. Xia, R. Wang, N. Li, Heterogeneous Nanostructure Based on 1T-Phase MoS $_2$ for Enhanced Electrocatalytic Hydrogen Evolution, ACS Appl. Mater. Interfaces. 9 (2017) 25291–25297. doi:10.1021/acsami.7b05775.

[200] J. Xie, H. Qu, J. Xin, X. Zhang, G. Cui, X. Zhang, J. Bao, B. Tang, Y. Xie, Defect-rich MoS2 nanowall catalyst for efficient hydrogen evolution reaction, Nano Res. 10 (2017) 1178–1188. doi:10.1007/s12274-017-1421-x.

[201] L. Lin, N. Miao, Y. Wen, S. Zhang, P. Ghosez, Z. Sun, D.A. Allwood, Sulfur-Depleted Monolayered Molybdenum Disulfide Nanocrystals for Superelectrochemical Hydrogen Evolution Reaction, ACS Nano. 10 (2016) 8929–8937. doi:10.1021/acsnano.6b04904.

[202] J. Hu, B. Huang, C. Zhang, Z. Wang, Y. An, D. Zhou, H. Lin, M.K.H. Leung, S. Yang, Engineering stepped edge surface structures of MoS2 sheet stacks to accelerate the hydrogen evolution reaction, Energy Environ. Sci. 10 (2017) 593–603. doi:10.1039/C6EE03629E.

[203] Y. Li, Y. Yu, Y. Huang, R.A. Nielsen, W.A. Goddard, Y. Li, L. Cao, Engineering the Composition and Crystallinity of Molybdenum Sulfide for High-Performance Electrocatalytic Hydrogen Evolution, ACS Catal. 5 (2015) 448–455. doi:10.1021/cs501635v.

[204] J. Kibsgaard, Z. Chen, B.N. Reinecke, T.F. Jaramillo, Engineering the surface structure of MoS2 to preferentially expose active edge sites for electrocatalysis., Nat. Mater. 11 (2012) 963–969. doi:10.1038/nmat3439.

[205] D. Kong, H. Wang, J. Cha, M. Pasta, K. Koski, Synthesis of MoS2 and MoSe2 films with vertically aligned layers, Nano Lett. 13 (2013) 1341–1347. http://pubs.acs.org/doi/abs/10.1021/nl400258t (accessed December 15, 2015).

[206] H. Vrubel, X. Hu, Growth and activation of an amorphous molybdenum sulfide hydrogen evolving catalyst, ACS Catal. 3 (2013) 2002–2011. doi:10.1021/cs400441u.

[207] Y. Li, H. Wang, L. Xie, Y. Liang, MoS2 nanoparticles grown on graphene: an advanced catalyst for the hydrogen evolution reaction, J. Am. Chem. Soc. 133 (2011) 7296–7299. http://pubs.acs.org/doi/abs/10.1021/ja201269b (accessed December 15, 2015).

[208] W. Li, Z. Zhang, W. Zhang, S. Zou, MoS $_2$ Nanosheets Supported on Hollow Carbon Spheres as Efficient Catalysts for Electrochemical Hydrogen Evolution Reaction, ACS Omega. 2 (2017) 5087–5094. doi:10.1021/acsomega.7b00755.

[209] L. Liao, J. Zhu, X. Bian, L. Zhu, M.D. Scanlon, H.H. Girault, B. Liu, MoS 2 Formed on Mesoporous Graphene as a Highly Active Catalyst for Hydrogen Evolution, Adv. Funct. Mater. 23 (2013) 5326–5333. doi:10.1002/adfm.201300318.

[210] Z.H. Deng, L. Li, W. Ding, K. Xiong, Z.D. Wei, Synthesized ultrathin MoS $_2$ nanosheets perpendicular to graphene for catalysis of hydrogen evolution reaction, Chem. Commun. 51 (2015) 1893–1896. doi:10.1039/C4CC08491H.

[211] B. Seo, G.Y. Jung, Y.J. Sa, H.Y. Jeong, J.Y. Cheon, J.H. Lee, H.Y. Kim, J.C. Kim, H.S. Shin,

S.K. Kwak, S.H. Joo, Monolayer-precision synthesis of molybdenum sulfide nanoparticles and their nanoscale size effects in the hydrogen evolution reaction, ACS Nano. 9 (2015) 3728–3739. doi:10.1021/acsnano.5b00786.

[212] H. Wang, Z. Lu, D. Kong, J. Sun, T.M. Hymel, Y. Cui, Electrochemical Tuning of MoS2 Nanoparticles on Three-Dimensional Substrate for Efficient Hydrogen Evolution, ACS Nano. 8 (2014) 4940–4947.

[213] T.-N. Ye, L.-B. Lv, M. Xu, B. Zhang, K.-X. Wang, J. Su, X.-H. Li, J.-S. Chen, Hierarchical carbon nanopapers coupled with ultrathin MoS2 nanosheets: Highly efficient large-area electrodes for hydrogen evolution, Nano Energy. 15 (2015) 335–342. doi:10.1016/j.nanoen.2015.04.033.

[214] Y. Guo, X. Zhang, X. Zhang, T. You, Defect- and S-rich ultrathin MoS 2 nanosheet embedded N-doped carbon nanofibers for efficient hydrogen evolution, J. Mater. Chem. A. 3 (2015) 15927–15934. doi:10.1039/C5TA03766B.

[215] Y. Zhang, L. Zuo, Y. Huang, L. Zhang, F. Lai, W. Fan, T. Liu, In-Situ Growth of Few-Layered MoS2 Nanosheets on Highly Porous Carbon Aerogel as Advanced Electrocatalysts for Hydrogen Evolution Reaction, ACS Sustain. Chem. Eng. 3 (2015) 3140–3148. doi:10.1021/acssuschemeng.5b00700.

[216] K.C. Pham, Y.H. Chang, D.S. McPhail, C. Mattevi, A.T.S. Wee, D.H.C. Chua, Amorphous Molybdenum Sulfide on Graphene-Carbon Nanotube Hybrids as Highly Active Hydrogen Evolution Reaction Catalysts, ACS Appl. Mater. Interfaces. 8 (2016) 5961–5971. doi:10.1021/acsami.5b09690.

[217] R.D. Nikam, A.Y. Lu, P.A. Sonawane, U.R. Kumar, K. Yadav, L.J. Li, Y.T. Chen, Three-Dimensional Heterostructures of MoS2 Nanosheets on Conducting MoO2 as an Efficient Electrocatalyst to Enhance Hydrogen Evolution Reaction, ACS Appl. Mater. Interfaces. 7 (2015) 23328–23335. doi:10.1021/acsami.5b07960.

[218] Z. Zhao, F. Qin, S. Kasiraju, L. Xie, M.K. Alam, S. Chen, D. Wang, Z. Ren, Z. Wang, L.C. Grabow, J. Bao, Vertically Aligned MoS $_2$ /Mo $_2$ C hybrid Nanosheets Grown on Carbon Paper for Efficient Electrocatalytic Hydrogen Evolution, ACS Catal. (2017) 7312–7318. doi:10.1021/acscatal.7b02885.

[219] M.-R. Gao, J.-X. Liang, Y.-R. Zheng, Y.-F. Xu, J. Jiang, Q. Gao, J. Li, S.-H. Yu, An efficient molybdenum disulfide/cobalt diselenide hybrid catalyst for electrochemical hydrogen generation., Nat. Commun. 6 (2015) 5982. doi:10.1038/ncomms6982.

[220] R. He, J. Hua, A. Zhang, C. Wang, J. Peng, W. Chen, J. Zeng, Molybdenum Disulfide-Black Phosphorus Hybrid Nanosheets as a Superior Catalyst for Electrochemical Hydrogen Evolution, Nano Lett. 17 (2017) 4311–4316. doi:10.1021/acs.nanolett.7b01334.

[221] H. Li, M. Du, M.J. Mleczko, A.L. Koh, Y. Nishi, E. Pop, A.J. Bard, X. Zheng, Kinetic Study of Hydrogen Evolution Reaction over Strained MoS2 with Sulfur Vacancies Using Scanning Electrochemical Microscopy, J. Am. Chem. Soc. 138 (2016) 5123–5129. doi:10.1021/jacs.6b01377.

[222] A.J. Bard, L.R. Faulkner, Electrochemical Methods: Fundamentals and Applications, 2nd ed., John Wiley and Sons Ltd., New York, 2001. doi:10.1016/B978-0-12-381373-2.00056-9.

[223] M. Inaba, J. Quinson, J.R. Bucher, M. Arenz, On the Preparation and Testing of Fuel Cell Catalysts Using the Thin Film Rotating Disk Electrode Method, J. Vis. Exp. (2018) 1–10. doi:10.3791/57105.

[224] M. Inaba, J. Quinson, M. Arenz, pH matters: The influence of the catalyst ink on the oxygen reduction activity determined in thin film rotating disk electrode measurements, J. Power Sources. 353 (2017) 19–27. doi:10.1016/j.jpowsour.2017.03.140.

[225] S. Motoo, N. Furuya, Hydrogen and oxygen adsorption on Ir (111), (100) and (110) planes, J. Electroanal. Chem. 167 (1984) 309–315. doi:10.1016/0368-1874(84)87078-1.

[226] K.A. Soliman, F.C. Simeone, L.A. Kibler, Electrochemical behaviour of nano-faceted Ir(2 1 0), Electrochem. Commun. 11 (2009) 31–33. doi:10.1016/j.elecom.2008.10.017.

[227] K.A. Soliman, D.M. Kolb, L.A. Kibler, T. Jacob, Restructuring of an Ir(210) electrode surface by potential cycling, Beilstein J. Nanotechnol. 5 (2014) 1349–1356. doi:10.3762/bjnano.5.148.

[228] J. Wei, Y.L. Zheng, Z.Y. Li, M. Le Xu, Y.X. Chen, S. Ye, Electrochemistry of Oxygen at Ir Single Crystalline Electrodes in Acid, Electrochim. Acta. 246 (2017) 329–337. doi:10.1016/j.electacta.2017.05.103.

[229] R. Woods, Hydrogen adsorption on platinum, iridium and rhodium electrodes at reduced temperatures and the determination of real surface area, J. Electroanal. Chem. 49 (1974) 217–226. doi:10.1016/S0022-0728(74)80229-9.

[230] S.M. Alia, K.E. Hurst, S.S. Kocha, B.S. Pivovar, Mercury Underpotential Deposition to Determine Iridium and Iridium Oxide Electrochemical Surface Areas, J. Electrochem. Soc. 163 (2016) F3051–F3056. doi:10.1149/2.0071611jes.

[231] C.C.L. McCrory, S. Jung, I.M. Ferrer, S. Chatman, J.C. Peters, T.F. Jaramillo, Benchmarking HER and OER Electrocatalysts for Solar Water Splitting Devices., J. Am. Chem. Soc. (2015). doi:10.1021/ja510442p.